

ISSN 2312-4334

MINISTRY OF EDUCATION AND SCIENCE OF UKRAINE

East European Journal of Physics

No 3. 2021

2021

East European Journal of Physics

EEJP is an international peer-reviewed journal devoted to experimental and theoretical research on the nuclear physics, cosmic rays and particles, high-energy physics, solid state physics, plasma physics, physics of charged particle beams, plasma electronics, radiation materials science, physics of thin films, condensed matter physics, functional materials and coatings, medical physics and physical technologies in an interdisciplinary context.

Published quarterly in hard copy and online by V.N. Karazin Kharkiv National University Publishing.
ISSN 2312-4334 (Print), ISSN 2312-4539 (Online)

The editorial policy is to maintain the quality of published papers at the highest level by strict peer review.

Approved for publication by the Academic Council of the V.N. Karazin Kharkiv National University (September 27, 2021; Protocol No. 10). EEJP registered by the order of Ministry of Education and Science of Ukraine No. 1643 of 28.12.2019, and included in the list of scientific professional editions of Ukraine (category "A", specialty: 104, 105), in which can be published results of dissertations for obtaining Ph.D. and Dr. Sc. degrees in physical and mathematical sciences.

The Journal is a part of the Web of Science Core Collection (ESCI) scientometric platform and indexed by SCOPUS.

Editor-in-Chief

☉Azarenkov N.A., *Academician of NAS of Ukraine, Professor, V.N. Karazin Kharkiv National University, Kharkiv, Ukraine*

Deputy editor

☉Hirka I.O., *Corresponding Member of NAS of Ukraine, Professor, V.N. Karazin Kharkiv National University, Kharkiv, Ukraine*

Editorial Board

☉Adamenko I.N., *Professor, V.N. Karazin Kharkiv National University, Ukraine*

☉Antonov A.N., *D.Sc., Professor, Institute of Nuclear Research and Nuclear Energy, Sofia, Bulgaria*

☉Barannik E.A., *D.Sc., Professor, V.N. Karazin Kharkiv National University, Ukraine*

☉Beresnev V.M., *D.Sc., Professor, V.N. Karazin Kharkiv National University, Ukraine*

☉Berezhnoy Yu.A., *D.Sc., Professor, V.N. Karazin Kharkiv National University, Ukraine*

☉Bizyukov A.A., *D.Sc., Professor, V.N. Karazin Kharkiv National University, Ukraine*

☉Bragina L.L. *D.Sc., Professor, STU "Kharkiv Polytechnic Institute", Ukraine*

☉Broda B., *D.Sc., University of Lodz, Poland*

☉Dragovich B.G., *D.Sc., University of Belgrade, Serbia*

☉Duplij S.A., *D.Sc., Center for Information Technology (ZIV), Westfälische Wilhelms-Universität Münster, Münster, Germany*

☉Garkusha I.E., *Corresponding Member of NAS of Ukraine, NSC Kharkiv Institute of Physics and Technology, Ukraine*

☉Grekov D.L., *D.Sc., NSC Kharkiv Institute of Physics and Technology, Ukraine*

☉Karnaukhov I.M., *Academician of NAS of Ukraine, NSC Kharkiv Institute of Physics and Technology, Ukraine*

☉Korchin A.Yu., *D.Sc., NSC Kharkiv Institute of Physics and Technology, Ukraine*

☉Krivoruchenko M.I., *D.Sc., Institute for Theoretical and Experimental Physics, Moscow, Russia*

☉Lazurik V.T., *D.Sc., Professor, V.N. Karazin Kharkiv National University, Ukraine*

☉Mel'nik V.N., *D.Sc., Institute of Radio Astronomy, Kharkiv, Ukraine*

☉Merenkov N.P., *D.Sc., NSC Kharkiv Institute of Physics and Technology, Ukraine*

☉Neklyudov I.M., *Academician of NAS of Ukraine, NSC Kharkiv Institute of Physics and Technology, Ukraine*

☉Noterdaeme J.-M., *D.Sc., Max Planck Institute for Plasma Physics, Garching, Germany*

☉Nurmagambetov A.Yu., *D.Sc., Professor, NSC Kharkiv Institute of Physics and Technology, Ukraine*

☉Ostrikov K.N., *D.Sc., Plasma Nanoscience Centre Australia, Clayton, Australia*

☉Peletminsky S.V., *Academician of NAS of Ukraine, NSC Kharkiv Institute of Physics and Technology, Ukraine*

☉Pilipenko N.N., *D.Sc. in Technical Sciences, NSC Kharkiv Institute of Physics and Technology, Ukraine*

☉Radinschi I., *D.Sc., Gheorghe Asachi Technical University, Iasi, Romania*

☉Slyusarenko Yu.V., *Academician of NAS of Ukraine, NSC Kharkiv Institute of Physics and Technology, Ukraine*

☉Smolyakov A.I., *University of Saskatchewan, Saskatoon, Canada*

☉Shul'ga N.F., *Academician of NAS of Ukraine, NSC Kharkiv Institute of Physics and Technology, Ukraine*

☉Tkachenko V.I., *D.Sc., NSC Kharkiv Institute of Physics and Technology, Ukraine*

☉Yegorov O.M., *D.Sc., NSC Kharkiv Institute of Physics and Technology, Ukraine*

Executive Secretary

☉Hirnyk S.A., *Ph.D., V.N. Karazin Kharkiv National University, Kharkiv, Ukraine*

Department of Physics and Technologies, V.N. Karazin Kharkiv National University

Kurchatov av., 31, office 402, Kharkiv, 61108, Ukraine

Tel: +38-057-335-18-33,

E-mail: eejp@karazin.ua,

Web-pages: <http://periodicals.karazin.ua/eejp> (Open Journal System)

Certificate of State registration No.20644-10464P, 21.02.2014

REVIEW

- A Review on Processing Routes, Properties, and Applications of Titanium Metal Matrix Composite** 5
Hrudayanjali Pathi, Tapan Kumar Mishri, Sasmita Rani Panigrahi, Bijayalaxmi Kuanar, Biswajit Dalai

Огляд шляхів обробки, властивостей, застосування та складних проблем, що пов'язані з титаново-металевими матричними композитами

Хрудаянджалі Патх, Тіпан Кумар Мішрі, Шасміта Рані Паніграхі, Біджаялакшмі Куанар, Бісваджіт Далай

ORIGINAL ARTICLES

- Nonlinear Cone Model for Investigation of Runaway Electron Synchrotron Radiation Spot Shape** 18
Igor M. Pankratov, Volodymyr Y. Bochko

Дослідження форми плями синхротронного випромінювання електронів-втікачів в моделі випромінювання спрямованого уздовж поверхні конуса їх швидкостей

І.М. Панкратов, В.Ю. Бочко

- Enhancing the Diffusion in Underdamped Space-Periodic Systems by Applying External Low-Frequency Fields** 25
Ivan G. Marchenko, V. Yu. Aksenova, I. I. Marchenko

Посилення дифузії в недодемпфованих просторово-періодичних системах зовнішніми низькочастотними полями

І.Г. Марченко, В.Ю. Аксенова, І.І. Марченко

- Sputtering of Oxides from LaNi₅ Surface** 30
Viktor A. Litvinov, Ivan I. Okseniuk, Dmitriy I. Shevchenko, Valentin V. Bobkov

Розплення оксидів з поверхні LaNi₅

В.О. Літвінов, І.І. Оксенюк, Д.І. Шевченко, В.В. Бобков

- Tenoselectrical Properties of Electron-Irradiated N-Si Single Crystals** 37
Sergiy Luniov, Petro Nazarchuk, Volodymyr Maslyuk

Тензоелектричні властивості опромінених електронами монокристалів n-Si

Сергій Луньов, Петро Назарчук, Володимир Маслюк

- Structure and Physical Properties of Cast and Splat-Quenched CoCr_{0.8}Cu_{0.64}FeNi High Entropy Alloy** 43
Oleksandr I. Kushnerov, Valerii F. Bashev

Структура та фізичні властивості високоентропійного сплаву CoCr_{0.8}Cu_{0.64}FeNi у литому та загартованому з рідини стані

О.І. Кушнеров, В.Ф. Башев

- Peculiarities in the Structure Formation and Corrosion of Quasicrystalline Al₆₅Co₂₀Cu₁₅ Alloy in Neutral and Acidic Media** 49
Olena V. Sukhova, Volodymyr A. Polonsky

Особливості структуроутворення та корозії квазікристалічного сплаву Al₆₅Co₂₀Cu₁₅ в нейтральному та кислих середовищах

Олена В. Сухова, Володимир А. Полонський

- Determination of Calibration X-Ray Beam Qualities and Establish a Set of Conversion Coefficients for Calibration of Radiation Protection Devices Used in Diagnostic Radiology** 55

Tanjim Siddiqua, Md. Shakilur Rahman, Md. Sanaullah, Zohora Akter Mitu, Imran Hossain, Sadeka Sultana Rubai

Визначення якості калібрування рентгенівського випромінювання та встановлення набору коефіцієнтів перетворення для калібрування пристроїв радіаційного захисту, що використовуються в діагностичній радіології

Танджим Сіддікуа, Мд. Шакілур Рахман, Мд. Санаулах, Зохора Актер Міту, Імран Хусейн, Садека Султана Рубаї

- Fundamental Physical Properties of LiInS₂ and LiInSe₂ Chalcopyrite Structured Solids** 62
Jyoti Kumari, Shalini Tomar, Sukhendra, Banwari Lal Choudhary, Upasana Rani, Ajay Singh Verma

Основні фізичні властивості структурованих сполук халькопіриту LiInS₂ та LiInSe₂

Джуоті Кумарі, Шаліні Томар, Сухендра, Банварі Лал Чоудхарі, Упасана Рані, Аджай Сінх Верма

- Synthesis and Characterization of Methylammonium Lead Bromide Perovskite Based Photovoltaic Device** 70
Shaily Choudhary, Shalini Tomar, Depak Kumar, Sudesh Kumar, Ajay Singh Verma

Синтез і характеристика фотоелектричного пристрою на основі перовскитного метіламмонійного броміду свинцю

Шайлі Чоудхарі, Шаліні Томар, Діпак Кумар, Судеш Кумар, Аджай Сінх Верма






- Investigations of Lead Free Halides in Sodium Based Double Perovskites Cs₂NaBiX₆(X=Cl, Br, I): an Ab Initio Study** 74
Shaily Choudhary, Shalini Tomar, Depak Kumar, Sudesh Kumar, Ajay Singh Verma

Дослідження безсвинцевих галідів у подвійних перовскітах на основі натрію Cs₂NaBiX₆ (X=Cl, Br, I): неемперічне (ab initio) дослідження

Шайлі Чоудхарі, Шаліні Томар, Діпак Кумар, Судеш Кумар, Аджай Сінх Верма

- The Plasma Parameters of Penning Discharge with Negatively Biased Metal Hydride Cathode at Longitudinal Emission of H^- Ions** 81
Ihor Sereda, Yaroslav Hrechko, Ievgeniia Babenko
Параметри плазми розряду Пеннінга з негативно-зміщеним металогідридним катодом при поздовжній емісії іонів H^-
I. Серєда, Я. Грєчко, Є. Бабєнко
- Study of the Mechanical Properties of Shell of Fuel Elements from Zr1% Nb Alloys at Radial Stresses Similar to Reactor Conditions** 87
V.I. Savchenko, N.N. Belash, Y.A. Krainyuk, Voyevodin V.N.
Дослідження механічних властивостей оболонок ТВЕЛ з Zr1%Nb сплавів при радіальних напруженнях, аналогічних реакторним умовам
В.І. Савченко, М.М. Бєлаш, Є.О. Країнюк, В.М. Восводін
- Bremsstrahlung Generation by 7.5 Mev Electrons in Converters Made of Different Materials** 91
Vladimir G. Rudychev, Nikolay A. Azarenkov, Igor A. Girka, Yegor V. Rudychev
Генерація гальмівного випромінювання електронами з енергією 7.5 Мев в конвертерах з різних матеріалів
В.Г. Рудичев, М.О. Азарєнков, І.О. Гірка, Є.В. Рудичев
- Formation of Optical Images with Synchrotron Radiation Flux of Relativistic Electrons in the X-Ray Generator "Nestor"** 97
Aleksandr Mazmanishvili, Nataliya Moskalets
Формування оптичних зображень потоком квантів синхротронного випромінювання релятивістських електронів в рентгенівському генераторі «Нєстор»
О.С. Мазманішвілі, Н.В. Москалець
- The Impact of Pulse Plasma Treatment on the Operating Characteristics of Steel 40X10C2M: Experiment and Numerical Simulations** 102
Nikolay A. Savinkov, Oleh M. Bulanchuk, Aleksander A. Bizyukov
Вплив імпульсної плазмової обробки на мікротвердість сталі 40X10C2M: експеримент і чисельне моделювання
М.О. Савінков, О.М. Буланчук, О.А. Бізюков
- Research and Development of Fuel Rods Metallurgically Bonded with Fuel Cladding for Nuclear Installations** 110
Nikolay N. Belash, Anton V. Kushtym, Vladimir V. Zigunov, Elena A. Slabospyska, Gennadiy A. Holomeyev, Ruslan L. Vasilenko, Aleksandr I. Tymoshenko
Розробка та дослідження ТВЕЛів з металургійним з'єднанням сердечника і оболонки для ядерних установок
М.М. Бєлаш, А.В. Кушитим, В.В. Зігунов, О.О. Слабоспицька, Г.О. Холомєєв, Р.Л. Василенко, О.І. Тимошенко
- Degradation Mechanisms of the Detector Properties of CdTe and CdZnTe Under the Influence of Gamma Irradiation** 116
Alexandr I. Kondrik
Механізми деградації детекторних властивостей CdTe та CdZnTe під впливом гамма-опромінення
О.І. Кондрік
- Influence of Formation Conditions, Subsequent Annealing and Ion Irradiation on the Prop-erties of Nanostructured Coatings Based on Amorphous Carbon with Gold, Silver and Nitrogen Additives** 124
Aleksandr Kolpakov, Aleksandr Poplavsky, Maksim Yapyntsev, Vseslav Novikov, Sergey Manokhin, Igor Goncharov, Marina Galkina, Vyacheslav Beresnev
Вплив умов формування, відпалу та іонного опромінення на властивості наноструктурних покриттів на основі аморфного вуглецю з добавками золота, срібла та азоту
О. Колпаков, О. Поплавський, М. Япрінцев, В. Новіков, С. Манохин, І. Гончаров, М. Галкіна, В. Берєснев
- Beam Scanning Controller for Proton-Beam Writing** 134
S.V. Kolinko, I.S. Kolinko, N.E. Polozhii, A.G. Ponomarev
Система керування скануванням пучка для протонної променевої литографії
С.В. Колінко, І.С. Колінко, Г.С. Положій, О.Г. Пономарьов
- Influence of the Order of Ion Implantation on Luminescent Spectrum of ZnSe Nanocrystals** 141
Anna Boichenko, Sergiy Kononenko, Fadei Komarov, Oganés Kalantaryan, Vitaliy Zhurenko, Stanislav Avotin, Nikolay Rokhmanov
Вплив порядку йонної імплантації на люмінесцентний спектр нанокристалів ZnSe
Г. Бойченко, С. Кононенко, Ф. Комаєров, О. Калантар'ян, В. Журєнко, С. Авотін, М. Рохманов
- Fast Electromagnetic Waves on Metamaterial's Boundary: Modeling of Gain** 145
V.K. Galaydych, A.E. Sporov, V.P. Olefir, M.O. Azarenkov
Швидкі електромагнітні хвилі на межі метаматеріалу: моделювання підсилення
В.К. Галайдич, О.Є. Споров, В.П. Олєфір, М.О. Азарєнков
- Determination of Uranium Isotopic Ratios by HRGS Using Various Efficiency Calibration Approaches** 151
Dmytro V. Kutnii, Dmytro D. Burdeynyi
Гамма-спектрометричне (hrgs) визначення ізотопних співвідношень урану з використанням різних підходів калібрування по ефективності
Д.В. Кутній, Д.Д. Бурдейний
- ANNOUNCEMENT
- V.M. Kuklin, *Selected Chapters (Theoretical Physics)*, (V.N. Karazin KHNU, Kharkiv, 2021), pp. 244. 160

A REVIEW ON PROCESSING ROUTES, PROPERTIES, APPLICATIONS, AND CHALLENGES OF TITANIUM METAL MATRIX COMPOSITE[†]

 Hrudayanjali Pathi^a,  Tapan Kumar Mishri^a,  Sasmita Rani Panigrahi^a,
 Bijayalaxmi Kuanar^{b†},  Biswajit Dalai^{b*}

^aPG Research Scholar, Department of physics, School of Sciences, GIET University, Gunupur 765022, Odisha, India

^bDepartment of physics, School of Sciences, GIET University, Gunupur 765022, Odisha, India

*Corresponding author: biswajit@giet.edu, [†]bkkuanar@giet.edu

Received June 4, 2021; revised August 31, 2021; accepted September 12, 2021

Titanium is currently familiar for its light weight, high strength, and non-reactive nature over all the metals. Titanium metal matrix composites (TMCs) are very popular in the field of aerospace, automotive, defense, and biomedical because of their high specific strength, light weight, and biocompatibility nature. Some of the extensively used fabrication methods like powder metallurgy (PM), additive manufacturing (AM), and spark plasma sintering (SPS) have been reviewed here with some of the properties of TMCs. By varying various types of reinforcements, it is possible to achieve the required properties as per industrial and modern applications in TMC. This study also includes the consequence of sintering temperature on properties of TMCs like physical, mechanical, and structural. Titanium alloys are showing good mechanical and biomedical properties when reinforced with carbon fibers, borides, ceramics, and plenty of other materials as continuous fiber or discontinuous particulates and whiskers. In this paper, the applications of TMCs in aerospace, automobile, biomedical, and defense have been narrated. Besides all these favorable properties and applications, TMCs can't be used extensively in the said applications because of their high cost and difficulty in machining, that discussed in this paper over various challenges of TMCs. The cost reduction can be done by making Ti - super alloys. In addition, there is a necessity for an effective cooling system during the machining of TMCs to enhance machinability and some of the effective methods which may enhance the machinability of TMCs were also discussed.

Keywords: Ti MMC; PM; AM; SPS; Challenges

PACS: 62.23. Pq, 62.20.-x, 62.20.de, 62.20.fk, 72.80. Tm

INTRODUCTION

The surrounding world is filled with composite materials which help mankind to live a better life. Titanium-MMCs (TMCs) are of greater interest within the field of aerospace and automobile industries due to their lightweight and high specific strength, i.e., strength to weight ratio. The characteristics of composite materials are much better than the individual constituents. The essential concept is to integrate the reinforcement material into the matrix material to get some desirable properties. Metal matrix composites (MMCs) are a bunch of materials having metals or metallic alloys as their major component (matrix) and are reinforced (continuously or discontinuously) by other materials like metals, ceramics or polymers. These are very fashionable within the field of engineering due to some superior properties like high thermal and electrical conductivity, high strength and stiffness, high specific strength, lightweight, low coefficient of thermal expansion, biocompatibility, resistance to high temperature, etc [1-4]. The foremost common MMCs are made of aluminum, copper, titanium, magnesium, iron, and nickel. Titanium and its alloys are fast becoming a component of serious research interest for a good range of applications like automotive, aerospace industries, aviation, chemical industries due to its high specific strength, specific rigidity, and excellent mechanical properties [2]. The foremost commonly used aerospace Ti- MMC is ($\alpha+\beta$) alloy, Ti- 6Al- 4V [5]. Titanium alloys with a temperature capability approaching 760 °C, the TMCs offer a possible 50% weight reduction in hot compressor sections to use in airframe applications and aircraft engines [6]. The higher biocompatibility and corrosion resistance of TMCs lead it to be the primary choice in osteosynthesis systems utilized in oral, maxillofacial surgery, and tissue engineering [3, 7]. Again, 37 % porous chemically pure Ti (CP- Ti) and Ti- TiB composite samples produced by selective laser melting (SLM) have a coefficient of elasticity near that of human bone. Their compressibility, good wear resistance, and porosity made them a typical material in biomedical [1, 8].

The common reinforcement of TMCs is split into two groups based on the shape of reinforcements, i.e., continuously reinforced TMCs (CTiMCR) and discontinuously reinforced TMCs (DTiMCR) as shown in Fig. 1. Particulate, whisker (needle-shaped), and short fibers are employed as discontinuously reinforced composites, whereas long fiber and sheets are used as continuously reinforced composites. Sometimes, nanoparticles are used as reinforcements to produce light MMCs with high ductility, high hardness, and high toughness [9, 10]. Discontinuously reinforced titanium composites are usually composed of borides or carbides, embedded in titanium matrix [2]. Here the addition of appropriate reinforcement by a novel processing strategy is very important to optimize the mechanical properties of DRTMCs. The foremost prominent discontinuous reinforcements are TiC, TiN, TiCN, TiB₂, SiC, Al₅Y₃O₁₂, Al₂O₃, and Si₃N₄ in both whisker and particulate forms. Many of the reinforcements exhibit clean interfaces free from any diffusional alloying or reactions with the Ti matrix [8]. To get tailored unique distribution of

[†] Cite as: H. Pathi, T.K. Mishri, S.R. Panigrahi, B. Kuanar, B. Dalai, East. Eur. J. Phys. 3, 5 (2021), <https://doi.org/10.26565/2312-4334-2021-3-01>

© H. Pathi, T.K. Mishri, S. R. Panigrahi, B. Kuanar, B. Dalai, 2021

reinforcements inside TMCs, additive manufacturing and laser deposition techniques are very helpful [11]. Discontinuous (or particulate) reinforced composites are less expensive to fabricate and their properties are nearly isotropic. Continuously reinforced titanium matrix composites are expensive, due to high fiber costs and limited formability, and their properties are highly anisotropic. Particulate reinforced titanium matrix composites are being considered for wear, erosion, and corrosion-resistant applications [12, 13].

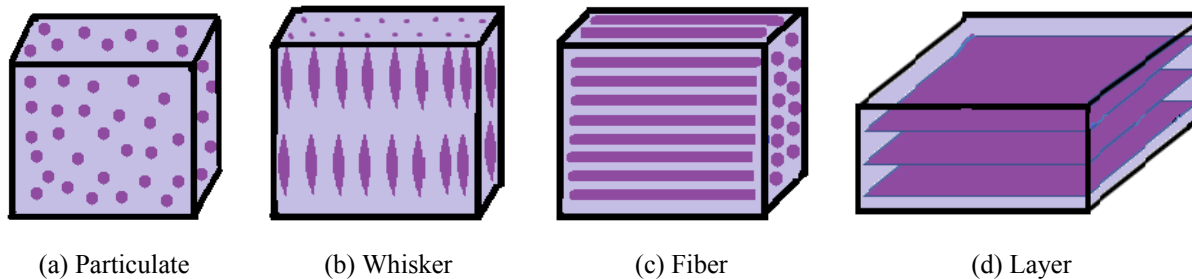


Figure 1. Reinforcement of TMCs (a) Particulate, (b) Whisker, (c) Fiber and (d) Layer

Ceramic particles as reinforcements on titanium metal matrix composites represent a possible improvement in its properties and an increase within the utmost service temperature. Reinforcing Ti with a steady ceramic phase can noticeably improve its modulus, hardness, wear resistance, additionally as yield strength but the resultant tensile ductility is sometimes poor or perhaps near zero [14-17]. The role of reinforcement in a metal matrix composite is to finish the shortcomings of metal and to make it an ideal choice for industrial applications. The coefficient of elasticity of metals is within the range of 45 GPa to 407 GPa. Its value is 106 GPa for Titanium which isn't sufficient for a few industrial applications. Thus, the reinforcement for TMC to increase the coefficient of elasticity has been discussed. The elastic modulus of the composite (E_C) is given by the addition of products of elastic modulus (E_M or E_R) and volume fraction (V_M or V_R) of different components:

$$E_C = E_M \times V_M + E_R \times V_R \quad (1)$$

The thermal expansion is not a greater challenge for metals ($8.5 \times 10^{-6} K^{-1}$). So, the reinforcement can have a little less or very near value of the coefficient of thermal expansion to the metal. The values of Elastic modulus and Coefficient of thermal expansion of some common reinforcements are put together in the following Table 1.

Table 1. The relative properties of some of the reinforcements [9, 18-21].

Reinforcement	Elastic modulus (or Young's modulus) (GPa)	Coefficient of thermal expansion ($10^{-6} K^{-1}$)
TiB	550	8.60
TiC	460	6.52 - 7.4
TiN	250	8.3 - 9.3
SiC	420	4.3 - 4.63
TiB ₂	529	4.6 - 8.1
B ₄ C	449	4.5 - 4.8
Al ₂ O ₃	350	8.1
Si ₃ N ₄	320	3.2
Ti-6Al-4V	115	8.8
Graphene	~1000	-4.8
CNTs	~1000	21
La ₂ O ₃	-	5.8 - 12.1
Alpha-Ti	105	8.8

FABRICATION TECHNIQUES

The fabrication technique is an important aspect of a material that determines the physical, mechanical, and biological properties of composite material along with its surface finishing and cost. Various types of techniques are used to manufacture TiMMCs, out of which powder metallurgy, additive manufacturing, and spark plasma sintering are very popular.

POWDER METALLURGY (PM)

In the PM fabrication technique, the metal removal process is usually avoided so that the yield loss is decreased while manufacturing the fabric which ends up lowering the prices and material wastage as compared to the casting process. It's an efficient process of controlling the components, i.e., matrix and reinforcement dispersion ratio in a very powder form using the varied jar, ball milling methods, etc within the composites [22, 23]. The powder metallurgy routes are applicable for advanced materials for Aerospace, like functionally graded materials. Titanium is reinforced

with Carbon nanotubes (CNTs) and graphite via powder metallurgy and hot-extrusion (HE) [24]. PM processing is extremely useful within the production of military ground vehicles at a lower cost. Initially, the metallic powder of titanium is created within the metallurgy process. This process consists of two major parts: (i) preparation of starting material (mixing, milling, and mechanical alloying) and (ii) densification of the prepared powder mixture (cold or hot pressing, sintering, forging, etc.) [25].

MILLING AND MIXING PROCESS (MMP) OF PM

The pure form of titanium is taken in the cavity of ball milling with spherical steel balls inside it. Then the reinforcement particles were added to it. It grinds the mixture into fine powder. The schematic diagram of milling and mixing has been shown in Fig. 2.

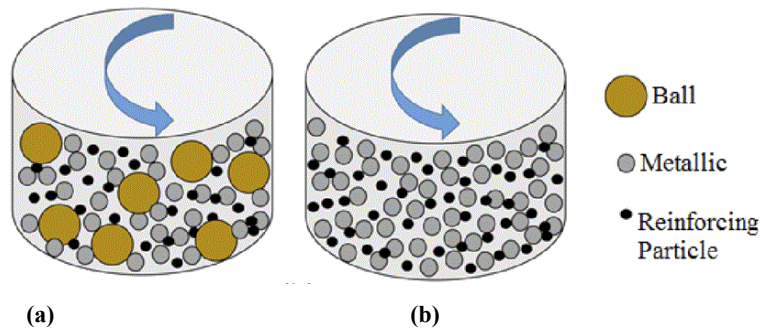


Figure 2. Mixing of metallic particles with reinforcements (a) Ball milling and (b) Regular mixing processes [26].

MECHANICAL ALLOYING (MA) OF PM

This is a popular method that is used for alloying materials which are difficult or impossible to combine through conventional melting methods. The mechanical alloying of Ti with graphite particles is shown in Fig. 3.

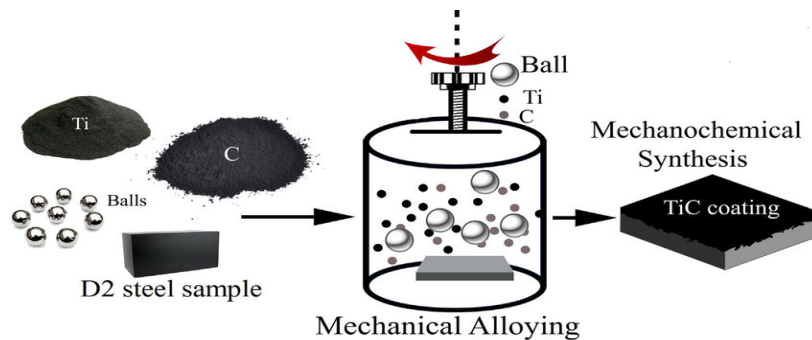


Figure 3. Schematic diagram of MA process to prepare TiC [27].

ISOSTATIC PRESSING OF PM

Isostatic pressing can be performed at (a) elevated temperatures, known as hot isostatic pressing (HIP), or (b) ambient temperatures, known as cold isostatic pressing (CIP). Hot isostatic pressing can be used to manufacture metal components directly or to densify parts from other powder metallurgy processes.

SINTERING PROCESS OF PM

It is the process of compacting the powder to form a solid mass material by applying pressure or heat without melting the material. So, the sintering temperature is less than the melting point. Change of powder to a solid mass or grain is shown in Fig. 4.

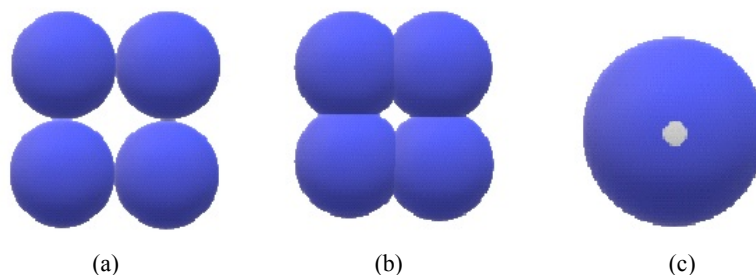


Figure 4. Different stages of the sintering process: (d) Before sintering, (e) During sintering, and (f) After sintering [28].

Before sintering, the grain size is small with big pores in between them. Whereas the grain size increases and the pore size decreases gradually during sintering. Finally, a big grain can be obtained with a small pore inside it. In this stage, the grain size is affected by the sintering temperature.

Table 2. Effect of sintering temperature on grain size [29].

Sample	Grain size at different Sintering temperature	
	1200 °C	1300 °C
Ti-5.1% (4140) alloy	71 ± 9 μm	97 ± 12 μm
Ti-7.1% (4140) alloy	98 ± 8 μm	121 ± 18 μm

Here, it was observed that with the temperature rise, the grain size increases. The increased grain size leads to a larger grain boundary. The strength of a material increases with its grain boundary. During the sintering process, the properties of the material vary with the sintering temperature. The variations of density, porosity, and micro hardness have been plotted in Fig. 5.

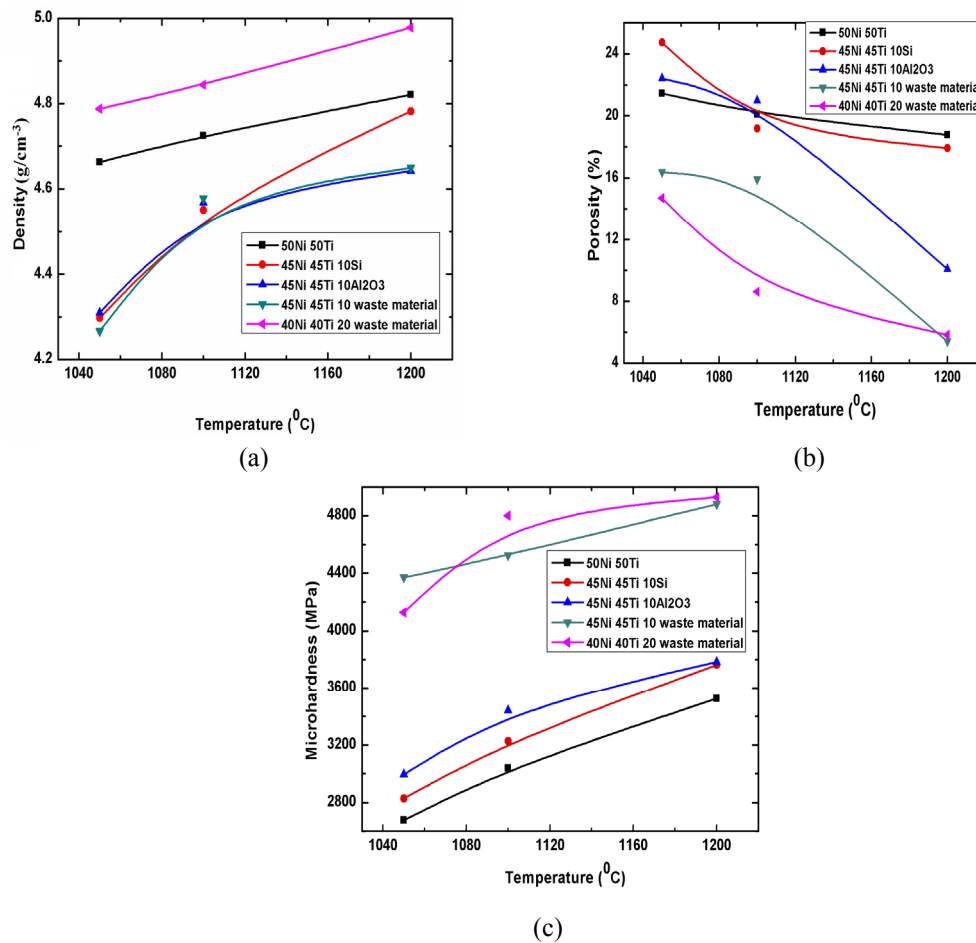


Figure 5. Variations of (a) density, (b) porosity, and (c) micro hardness with sintering temperature [30].

As the sintering temperature increases, the material starts softening and the grains (particles or molecules) seem to diffuse with the surrounding particles or molecules without melting. This happens because of the higher liquid phase transitions at higher temperatures. So, density increases, and porosity decreases with an increase in sintering temperature. As the porosity and air gap decrease with an increase in temperature, the micro hardness increases, and the material, with greater micro hardness value, can be used to manufacture different parts of automobiles and aircraft.

FORGING PROCESS (FP) OF PM

The schematic diagram representing powder metallurgy methods with their different processes and stages has been shown in Fig. 7.

It can be classified into three categories, i.e. (i) Cold forging: In this method forging is done at atmospheric or room temperature, (ii) Warm forging: In this method forging is done above atmospheric or room temperature but below the recrystallization temperature of matter and (iii) Hot forging: In this method forging is done above the recrystallization temperature of matter.

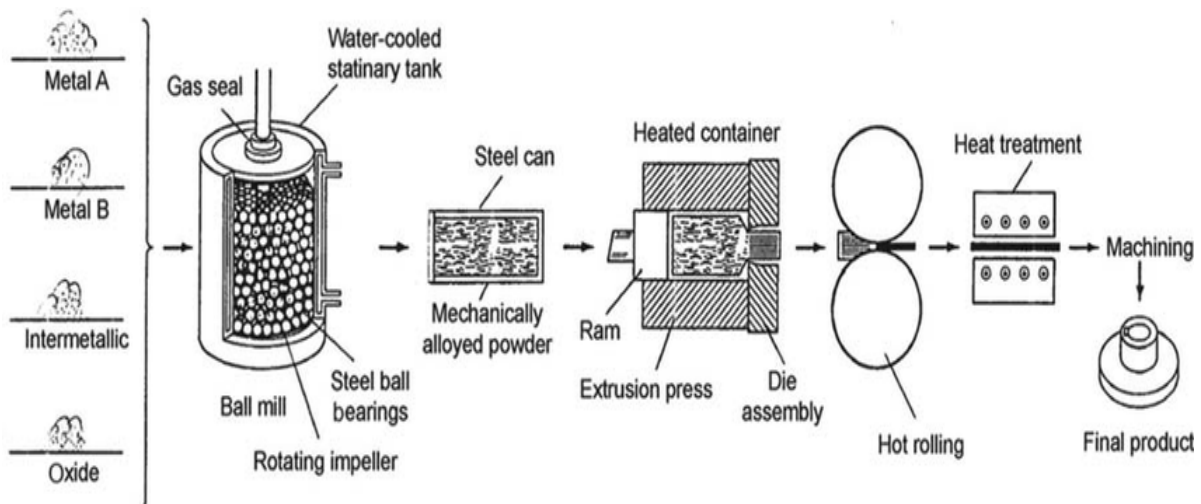


Figure 6. Different steps involved in the manufacturing of a product from powders by mechanical alloying [31].

ADDITIVE MANUFACTURING (AM)

It is a popular method to fabricate composite materials because of its low prototyping and manufacturing cost and also because of the easy method of fabrication. It needs a computer and 3D CAD (computer-aided design) software to sketch the fabric prototype. Once the 3D CAD sketch is produced, the AM manufacturing equipment starts the assembly process by reading the information from CAD files and adds layer upon layer of the fabric (in liquid or powder or sheet form) to fabricate a desired 3D stuff. The fundamental steps of AM method are creating a CAD 3D model, creating STL (standard tessellation language) files, manipulation of STL files in AM equipment, completing the method of building, removal and cleaning up, post-processing and implementation. AM is transforming the practice of drugs and making work easier for architects [32]. The productivity of fabric may be increased by AM fabrication technique. The common application of AM is to style the net-shaped plastic parts without the employment of high cost and time-consuming special tools, like injection molds [33]. AM process is generally utilized in the assembly of lightweight materials to scale back the burden of vehicles in automotive and aerospace applications due to its ability to create lightweight net-shaped frames; it is accustomed to manufacture complex honeycomb-shaped cross-sectional areas [34].

Some of the AM techniques used for the fabrication of TMCs are –

- Selective laser melting (SLM): It is an AM process that uses a high-density laser beam to melt and fuse the metallic powder in any specific region (point or line) or layer by layer. High power laser beam fuses the consecutive layers to form a 3D object by following CAD and STL files.
- Laser-engineered net shaping (LENS): It uses a high-power laser beam to form a highly dense product. The metallic or ceramic powder is injected into the hot molten pool of metal through the nozzle by following CAD. Directed energy deposition is another name of LENS (Fig. 7) and it is used to add some extra material to the existing component or to repair any instrument.

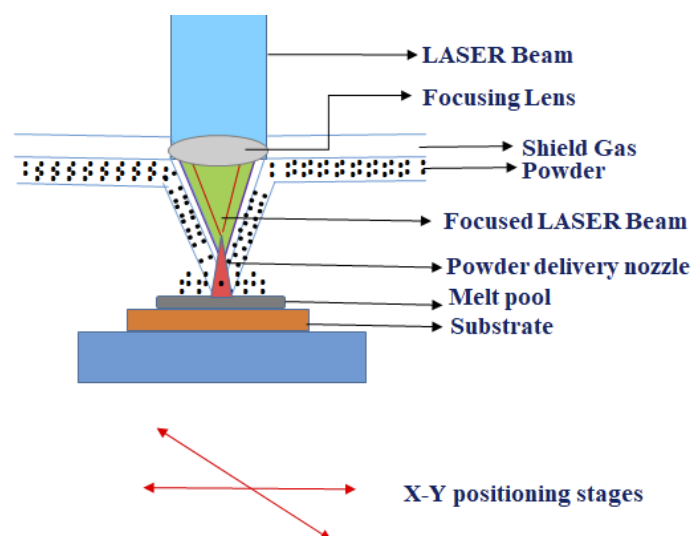


Figure 7. Schematic diagram of Laser engineered net shaping (LENS) [35].

- Direct laser deposition (DLD): It is a process of direct energy deposition (DED) that is very helpful in producing complex customized parts or repairing them. Some AM fabrication methods are presented in Table 3.

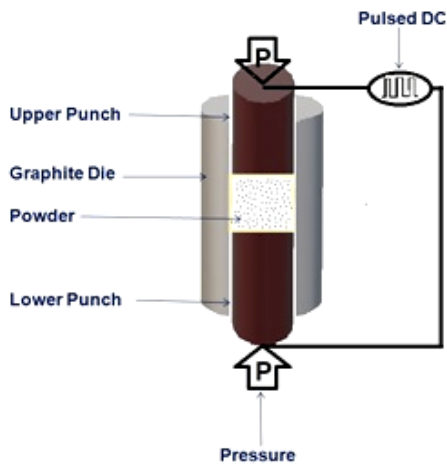
Table 3. AM techniques used for the fabrication of TMCs.

Matrix	Reinforcement	Method of fabrication
Ti	TiB	LENS [35], SLM [36]
Ti	TiC	SLM [37,38]
Ti	TiB and TiC	DLD [39]
Ti	TiC, unmelt SiC, TiSi ₂ , Ti ₅ Si ₃	LENS [40]
Ti	TiN	SLM [41]
Ti	Ta	SLM [42]
Ti-6Al-4V	TiB ₂	DED [43]
Ti-6Al-4V	TiN	LENS [44]
Ti-6Al-4V	TiB and TiN	LENS [45]
Ti-6Al-4V	Mo	SLM [46]

* SLM: Selective Laser Melting, LENS: Laser engineered net shaping, DLD: Direct Laser Deposition, DED: Direct energy deposition

SPARK PLASMA SINTERING (SPS)

It is an emerging powder consolidation technique during which uniaxial force and pulsed DC are employed under low air pressure. A schematic diagram of the SPS process with its different components is shown in Fig. 8.



Instrumentation: the SPS process is administered within the SPS machine having the founded (i) vertical single-axis pressurization, (ii) water-cooled chamber, (iii) atmospheric control, (iv) vacuum exhaust unit, (v) Sintering DC generator, and (vi) SPS controller [47, 50].

EXPERIMENTAL PROCESS OF SPS

The sample powder is held between the punch and the graphite dies. The temperature is quickly raised to 1000 to 2500 °C (which is 200 to 500 °C less than the conventional sintering process) resulting in the formation of the high-quality sintered compact within 5 to 20 mins by the following vaporization, melting, and sintering [48]. During the sintering process, different atmospheres like hydrogen, inert gas, nitrogen, argon, natural gas, dissociated ammonia, and vacuum are used. Vacuum atmosphere is generally used for titanium for its high reactivity. The processing is carried out in 3 stages, i.e., Plasma heating, Joule heating, and Plastic deformation, shown in Fig. 9.

Figure 8. Schematic diagram of SPS [47, 50]

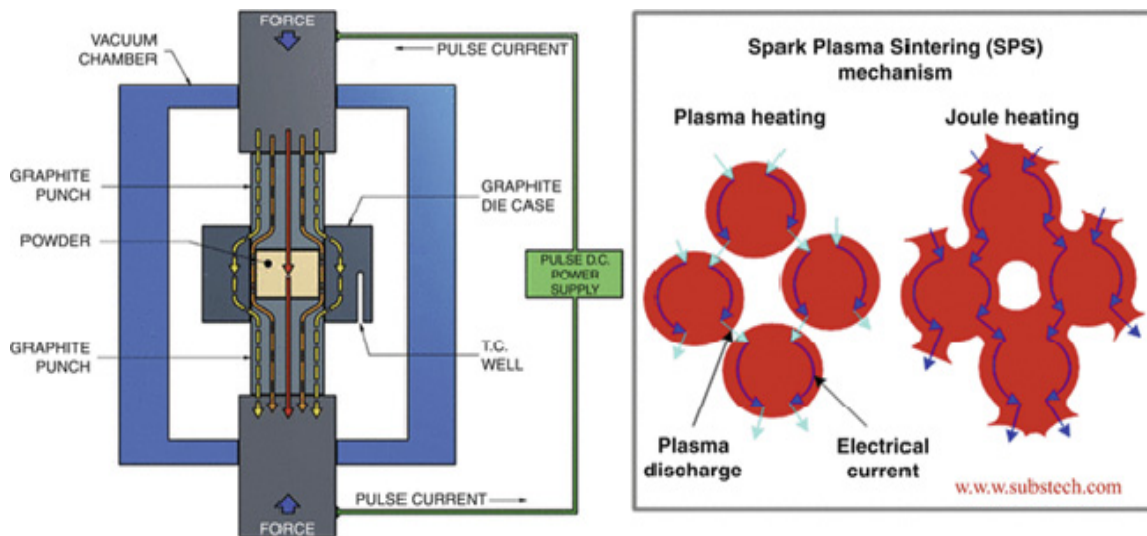


Figure 9. Pulsed DC along with the plasma heating and joule heating [49].

The details are given below.

a. Plasma heating: The electrical discharge among the powder particles results in heating of particle surface around 1000 to 2500 °C. The high temperature causes the vaporization of impurities to purify and activate the particle surface. Because of micro-plasma discharge, the generated heat is equally distributed among particles of the sample. Due to high temperatures, the particles melt and fuse to form a connection between them.

b. Joule heating: It is generated by pulsed DC which flows from particle to particle through the neck and causes diffusion of atoms and molecules enhancing their growth. The rapid rise and drop in temperature diminish the growth of material grain. So, this method can be used in the manufacturing of nanocomposites [50].

c. Plastic deformation: The soft material sample goes through plastic deformation under uniaxial force. The material is densified because of plastic deformation as well as diffusion. So, it is a better option for densification (around 94-99 % of theoretical value) of nanocomposites at a lower temperature than the conventional methods [48, 51-53].

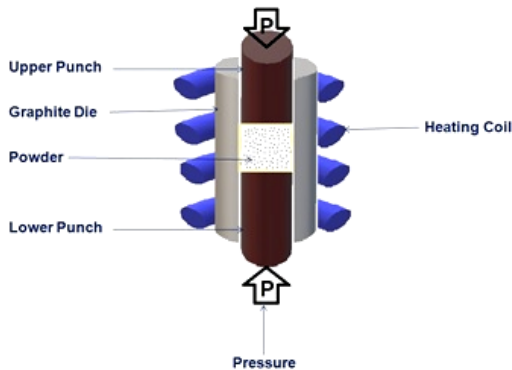


Figure 10. HP process with its different components [47, 50].

SPS is very similar to hot pressing (HP) in which an external heating source is used as shown in Fig. 10, but in SPS, an electric pulse is used to heat the sample powder from outside (through graphite dies) as well as from inside (by plasma discharge). SPS process is having very faster solute homogenization as compared to HP because of the joules heating. So SPS gives better results than HP [54]. The difference between the SPS (with pulsed DC) and HP (with external heating source) can be observed from fig 9 and fig 10. Even if the sintering temperature in SPS is less than the conventional sintering process, it plays a vital role in changing the mechanical properties of a composite material. Here the graphical plot of variations in density, hardness, and flexure strength with sintering temperature has been shown in Fig. 11. With a rise in sintering temperature, the number of pores decreases which results in the densification of the material. Hence

density increases slightly as sintering temperature increases. The hardness of both samples (Fig. 11) was decreased with rising in sintering temperature. The two samples show the best 3-point-bending test result at 1150 °C as the flexure strength is maximum at this sintering temperature.

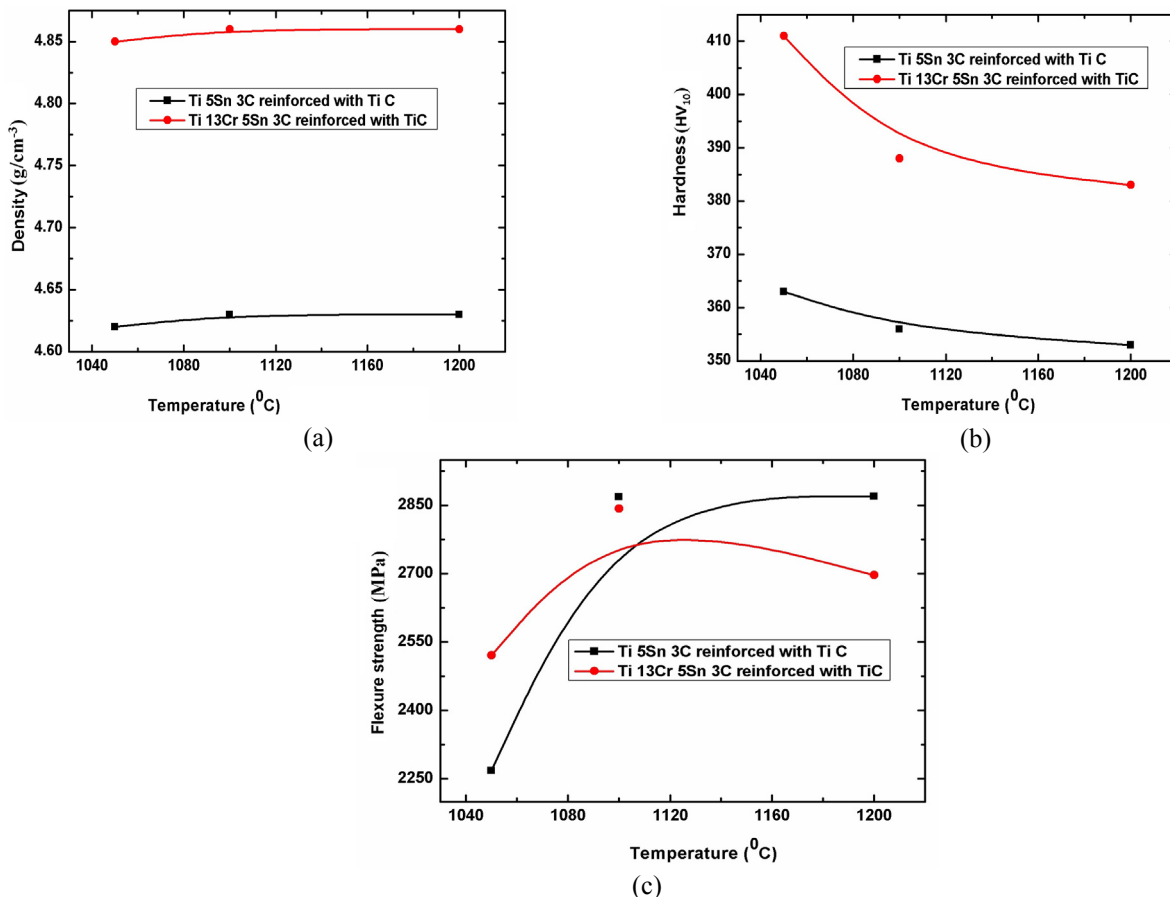


Figure 11. Variation of properties (a) density, (b) hardness, and (c) flexure strength of composites at different sintering temperatures in SPS [55].

PROPERTIES OF TMCs

Comparative Properties of Ti MMCs and Super alloys: TiMMC’s have a metal strength greater than Aluminum Alloy if 6Al-4V titanium alloy is used. The values of some properties are presented in Table 4.

Table 4. Comparative properties of TMC, Ti-Al MMC, and super alloys.

Property	Conventional TiMMC	Ti Aluminide TiMMC	Superalloys
Density (g/cm ³)	4.04	4.18	8.3
0° Stiffness (GPa)	200	242	207
90° Stiffness (GPa)	145	200	207
Max use temp. (°C)	538	760	1090
0° CTE (°C ⁻¹ × 10 ⁻⁶)	7.20	7.92	13.0
90° CTE (°C ⁻¹ × 10 ⁻⁶)	8.91	9.18	13.0

* 0° → Along the direction of Fiber and 90° → Transverse to Direction of Fiber [6, 56, 57].

It has been observed that types of reinforcement, the quantity of reinforcement, and processing routes change the property of composite material. A quantitative study on the physical and mechanical properties of different TMCs with their processing routes is presented in Table 5.

Table 5. Physical and mechanical properties of different TMCs with their processing routes.

Matrix	Reinforcement with volume %	Processing route	Properties				References
			Density	Hardness	Strength (MPa)	Ductility %	
Ti	24% TiB	SPS	4.90 g/cm ³	710 HV	-	-	[58]
	38.5% TiB		4.75 g/cm ³	890 HV	-	-	
	20.6% TiB	HIP (PM)	4.92 g/cm ³	658 HV	-	-	
	38.3% TiB		4.90 g/cm ³	823 HV	-	-	
	17.6% TiB	PM	4.20 g/cm ³	424 HV	-	-	
37.9% TiB	4.68 g/cm ³		618 HV	-	-		
Ti-64	Zr based MG	SLM	-	-	> 1000	20*	[59]
Ti	1.0 wt% CNTs	SPS+HE	-	292 HV	625	-	[60]
	2.0 wt% CNTs		-	336 HV	662	-	
	3.0 wt% CNTs		-	367 HV	853	-	
Ti-4.5 Al-6.8 Mo-1.5 Fe	5% TiB	HVC (PM)	97.90%*	335 HV	1038	2.19	[61]
	10% TiB		98.20%*	392 HV	1147	-	
	15% TiB		98.30%*	428 HV	741	-	
	20% TiB		96.10%*	445 HV	521	-	
Ti	4% TiB + 0.97% TiC	PM	-	-	876	14.2	[62]
	6.49% TiB + 1.61% TiC		-	-	995	7.8	
	10.93% TiB + 2.81% TiC		-	-	1138	2.6	
Ti	0.2wt% of MWCNTs	SPS	99.69%*	2 GPa	898	-	[63]
	0.4 wt% of MWCNTs		99.44%*	2.18 GPa	1092	-	
	0.6 wt% of MWCNTs		99.31%*	2.3 GPa	1052	-	
	0.8 wt% of MWCNTs		99.13%*	2.39 GPa	1015	-	
	1.0 wt% of MWCNTs		99.01%*	2.4 GPa	853	-	
Ti-6Al-4V	5% TiC	SPS	99.7%*	-	995	-	[64]
	10% TiC		99.6%*	-	1060	-	
Ti	0.5 wt% MLGs	SPS	-	15.39 GPa	-	-	[65]
	1.5 wt% MLGs		-	14.54 GPa	-	-	
Ti	B + 1 vol% CNTs	SPS	99.3%*	33 GPa	-	-	[66]
	B + 2 vol% CNTs		98.7%*	29 GPa	-	-	
	B + 4 vol% CNTs		97.6%*	28 GPa	-	-	
	B + 6 vol% CNTs		96.0%*	25 GPa	-	-	
Ti	0.5 vol% B4C	PM + HE	-	-	916	2.6	[67]
Ti-15Mo	TiB	SPS	-	22%*	1480	-	[68]

Matrix	Reinforcement with volume %	Processing route	Properties				References
			Density	Hardness	Strength (MPa)	Ductility %	
Ti-Ni	1 wt% of CCS	SPS	96.4%*	289.40 HV#	669.75	-	[69]
	3 wt% of CCS		98.9%*	296.81 HV#	686.90	-	
	5 wt% of CCS		99.9%*	319.71 HV#	739.90	-	

CNT: Carbon Nano Tube, MWCNT: Multiwalled carbon nanotubes, MLG: Multi-layer graphene, CCS: Carbonized coconut shell, HIP: Hot isostatic pressing, HE: Hot extrusion, HVC: High-velocity compaction, HV: Vickers Hardness, * Relative, # Micro hardness.

APPLICATIONS

There are many important applications of TiMMCs in various sectors such as Aerospace, Biomedical, Automotive, Defense, etc. that shown in Fig. 12.

AEROSPACE

TMCs are extensively used in the aerospace industries to make aircrafts lightweight, erosion-resistant, and protect the aircraft from foreign objects and birds.

- The usage of TMCs in US fighter aircraft [2]
- Ti-6Al-2Sn-4Zr-6Mo is used to manufacture an aero-engine which is having excellent creep resistance, heat resistance up to 450 °C and can be elongated up to 10% with a yield strength of 1105 MPa. Ti-5Al-2Sn-2Zr-4Mo-4Cr having a heat resistance of 350 °C with tensile strength and yield strength of 1250 MPa and 1150 MPa respectively. It is used to manufacture the shaft and fan with a greater damage tolerance ability [70].
- Rolls Royce starts manufacture of world's largest fan blades for an aircraft. The weight of the ultra-fan has been reduced up to 680 kgs. The weight reduction is due to the carbon titanium fan blades and composite casing [71].

BIOMEDICAL

Titanium could be a non-reactive, biocompatible, and corrosion-resistant metal that may be employed in bone and dental implants. It is resistant to body fluids.

- CP-Ti, Ti-6Al-4V, Ti-24Nb-4Zr-8Sn, Ti-TiB/TiC, and Ti-6Al-7Nb are the popular composites utilized in biomedical as these materials show mechanical and biomedical properties almost like human bone [8].
- 37% porous CP Ti and Ti-TiB produced by the SLM process are having a modulus of elasticity near human bone [1].
- Porous ceramic reinforced Ti composites are produced by additive manufacturing complete all the strain of orthopedic implant applications at a lower cost [72].

AUTOMOTIVE

Mainly titanium is employed in automobiles for weight reduction. The weight reduction ultimately reduces the fuel and power consumption and air resistance of the vehicle.

- Titanium is employed to manufacture the engine valve train and connecting rods to reduce the inertial force in a reciprocating engine. The primary motive force in vehicles is provided by the electric motor. The nonmagnetic and relatively higher electrical resistance nature of titanium reduces the eddy current loss in electrical motors [73].
- Ti-6Al-4V is that the main component of connecting rods, intake valves, and wheel hubs because of its high tensile strength up to 1050 MPa and yield strength up to 950 MPa. Ti-6Al-4Sn-4Zr-1Nb-1Mo-0.2Si (Reinforced with 5% TiB) could be a material for the assembly of exhaust valves having a yield strength of 1150 MPa [74].
- Conventional TiMMCs supported strengthening with discontinuous TiB or TiC reinforcements have realized a wide application in automobiles.
- An exhaust valve with a non-porous cast Ti-44Al-8Nb-1B has been processed and examined using an X-Ray beam [75].

DEFENSE

The high ballistic impact resistance and high strength to weight ratio of titanium composites made it a good choice for armor and aviation material in defense. It can reduce the weight of the vehicle up to 40 -50% so that the fuel consumption will be less and the vehicle movement will be free.

- Ti-6Al-4V is having a greater ballistic resistance as compared to rolled homogeneous armor (RHA) steel. It is having a mass efficiency rating of 1.5 when the value for RHA steel is taken as 1 with a lesser weight.
- Ceramic reinforced titanium composites are showing good elastic modulus, good wear resistance, and high yield strength. A reliable armor material can be produced with a different defeat mechanism by ceramic reinforced Ti with TiB ceramic [15, 76].

- Layered composite material armor for helicopters has been developed with Titanium Alloy-Ceramics-Polymer-based lightweight composites which protect ammunitions to critical parts of the helicopters [77].
- TMCs can also be used in the production of body armors weighing only 8-10 kg (bulletproof jacket) and aviation on some parts of fighter jets, aircraft, and military ground vehicles.



Figure 12. Different applications of TiMMCs

VARIOUS CHALLENGES

Even if TMCs are having many unique properties, their use is limited in the automotive and aerospace industries because of the following reasons.

- High cost: Titanium is a high-cost metal as compared to aluminum and iron in the current market. So, it is used in those fields which can get more efficiency and weight reduction as compared to its cost as in the case of aerospace industries where the fly-to-buy ratio is analyzed before its use.
- Low availability of the material: The relative abundance of titanium on earth is just 0.63% whereas, the relative abundance of aluminum and iron is 8.1% and 5% respectively.
- Difficulty in machining: Due to high strength, low thermal conductivity, and chemical reactivity with the tool material at elevated temperature, it makes a hazard to the tool and reduces the tool life.
- Spring-back and chatter effect: The low young's modulus value of Ti alloys and composites leads to the spring-back and chatter effect resulting in the poor surface quality of the product.

The machining difficulties can be solved by using high-pressure coolant during cutting and drilling operations. But the coolants are of high cost. Current research focuses on the design of an effective cooling system. Some of the popular cooling systems are-

- Cryogenic liquid nitrogen: It reduces the cutting temperature (around 28 - 61%), the surface roughness (around 4.36- 51.67 %), thrust force (around 14%) of Ti-6Al-4V as compared to the wet coolant. It also increases the tool life [78].
- Minimum quantity lubrication: The drilling temperature decreases effectively by using the MQL method during the material removal process because it reduces the drill wear when drilling the compound stacks [79].
- Low-frequency vibration-assisted drilling: This technique helps reduce the mechanical and thermal load of the material removal process of carbon epoxy composite Ti-6Al-4V which is very useful in aerospace industries [80].
- Carbon dioxide-based cooling system: Vortex tube-based cooling system assistance machining can increase the effectiveness of the machining in terms of cutting temperature and surface roughness. In this method, different types of coolants can be used where CO₂ gas is providing better results [81]. This cooling system reduces the cutting temperature (around 46.6%) and surface roughness (around 46%) as compared to dry machining [82].

CONCLUSIONS






Titanium metal matrix composites (Ti-MMCs), as a replacement generation of materials, have various potential applications within the biomedical, defense, aerospace, and automotive industries. For a specific potential application, the manufacturing route is restricted. Such as SPS is a better method for the manufacturing of nanocomposites and dense materials. Similarly, additive manufacturing is used to reduce production costs and PM is used to manufacture armors at a lower cost. Depending upon the porosity of TMC, its application is specified in various fields. Porous materials are used in biomedical (37% Ti-TiB) whereas dense materials are used in automotive sectors (cast Ti-44Al-

8Nb-1B). Even if TMCs full fill many mechanical and biomedical requirements, their higher cost and machining difficulties limit their usages in different industries. For aerospace applications, it should have a good fly-to-buy ratio. Otherwise, it will affect the final production cost of aircraft. The cost of TMCs can be reduced to some extent by changing the processing route. But it is not sufficient to compete with other composites in the market. The cost reduction can also be done by making Ti alloys (producing a matrix material containing Ti with other metals like aluminum, iron, etc in nearly equal proportion just like in super alloys). An effective cooling system can overcome machining difficulties. Now-a-days research is going on to reduce the assembly cost of raw Titanium and designing of an effective cooling system. More insight into the research field of composites is required to know the reason for its high cost. Once the reason is very clear then the cost can be reduced which in turn increases the usage of high strength and light weight TMCs in different applications without any second thought.

ACKNOWLEDGEMENT

The authors are grateful to the President, Vice President, Registrar and HOD (School of Sciences) of GIET University for motivation. The authors are thankful to Prof. C. Suryanarayana, Departments of Mechanical and Aerospace Engineering, and Materials Science and Engineering, University of Central Florida, U.S.A.; Mr. Eskandar Fereiduni, Department of Mechanical Engineering, McMaster University, Canada; Dr. Farhad Saba, Department of Materials Science and Engineering, Ferdowsi University of Mashhad, Iran and Dr. Keqin Yang, Department of Physics and Astronomy, Clemson University, USA for their useful input in preparing our review article.

ORCID IDs

 **Hrudayanjali Pathi**, <https://orcid.org/0000-0001-9361-7015>;
  **Tapan Kumar Mishri**, <https://orcid.org/0000-0003-1017-3119>;
 **Sasmita Rani Panigrahi**, <https://orcid.org/0000-0003-2623-0552>;
  **Bijayalaxmi Kuanar**, <https://orcid.org/0000-0003-3187-9049>;
 **Biswajit Dalai**, <https://orcid.org/0000-0001-8401-7501>;

REFERENCES

- [1] H. Attar, S.E. Haghghi, D. Kent, and M.S. Dargusch, *Int. J. Machine Tools and Manufact.* **133**, 85-102 (2018), <https://doi.org/10.1016/j.ijmachtools.2018.06.003>
- [2] M.D. Hayat, H. Singh, Z. He, and P. Cao, *Composites Part A: Applied Science and Manufacturing*, **121**, 418-438 (2019), <https://doi.org/10.1016/j.compositesa.2019.04.005>
- [3] B. Gareb, C.C. Roossien, N.B.V. Bakelen, G.J. Verkerke, A. Vissink, R.R. Bos, and B.V. Minnen, *Scientific reports*, **10**, 1 (2020), <https://doi.org/10.1038/s41598-020-75299-9>
- [4] M. Haghshenas, "Metal-Matrix Composites," *Modul Mater Sci Mater Eng.*, 1–28, (2016).
- [5] K.M. Rahman, V.A. Vorontsov, S.M. Flitcroft, and D. Dye, *Adv Eng Mater*, **19**, 1700027 (2017), <https://doi.org/10.1002/adem.201700027>
- [6] S.A. Singerman, J.J. Jackson, and Pratt & Whitney. West Palm Beach FL. *Superalloys: The Minerals, Metals & Materials Society*, 579 (1996).
- [7] J. Lee, H. Lee, K.H. Cheon, C. Park, T.S. Jang, H.E. Kim, and H.D. Jung, *Additive Manufacturing*, **30**, 100883 (2019), <https://doi.org/10.1016/j.addma.2019.100883>
- [8] L.C. Zhang, and H. Attar, *Advanced engineering materials*, **18**, 463-475, (2015), <https://doi.org/10.1002/adem.201500419>
- [9] S. Jayalxmi, R.A. Singh, and M. Gupta, *Indian journal of advances in chemical science*, **S1**, 288 (2016).
- [10] M.S. Abd-Elwahed, A.F. Ibrahim, and M.M. Reda, *Journal of Mterials Research and Technology*, **9**, 8528-8535 (2020), <https://doi.org/10.1016/j.jmrt.2020.05.021>
- [11] Jiao Y., Huang L., Geng L., *Journals of alloys and compounds*, **767**, 1196-1215 (2018), <https://doi.org/10.1016/j.jallcom.2018.07.100>
- [12] V. Amigó, M.D. Salvador, and A.V.F. Romero, *Materials science forum*, **534**, 817-820 (2007), <https://doi.org/10.4028/www.scientific.net/MSF.534-536.817>
- [13] V Amigo., E. Klyastskina, V. Bonache, J. Candel, and F. Romero, *Congress et Exhibition* , 237 (2005).
- [14] S.C. Tjong, and Y.W. Mai, *Composites Science and Technology*, **68**, 583-601 (2008), <https://doi.org/10.1016/j.compscitech.2007.07.016>
- [15] Tingting Song, Bing Liu, Jie Tian, and Ma Qian*. *Shudong Luo, Advanced Engineering Materials*, **21**, no. 7, (2019), <https://doi.org/10.1002/adem.201801331>
- [16] S. Ehtemam-Haghghi, G. Cao, and L.C. Zhang, *Journal of Alloys and Compounds*, **692**, 892-897 (2017), <https://doi.org/10.1016/j.jallcom.2016.09.123>
- [17] S Wang, LJ Huang, L Geng, F Scarpa, Y Jiao, HX Peng, *Scientific reports*, **7**(1), 1-13 (2017), <https://doi.org/10.1038/srep40823>
- [18] T.M.T. Godfrey, P.S. Goodwin, and C.M.W. Close, *Advanced Engineering Materials*, **2**(3), 85-91 (2000) [https://doi.org/10.1002/\(SICI\)1527-2648\(200003\)2:3<85::AID-ADEM85>3.0.CO;2-U](https://doi.org/10.1002/(SICI)1527-2648(200003)2:3<85::AID-ADEM85>3.0.CO;2-U)
- [19] T. Saito, H. Takamiya, and T. Furuta, *Materials Science and Engineering: A*, **243**, 273-278 (1998), [https://doi.org/10.1016/S0921-5093\(97\)00813-7](https://doi.org/10.1016/S0921-5093(97)00813-7)
- [20] T.M.T. Godfrey, A. Wisbey, P.S. Goodwin, K. Bagnall, and C.M.W. Close, *Materials Science and Engineering: A*, **282**, 240-250 (2000), [https://doi.org/10.1016/S0921-5093\(99\)00699-1](https://doi.org/10.1016/S0921-5093(99)00699-1)
- [21] K.B. Panda, and K.S.R. Chandran, *Adv Mater Processes*, **160**, 59 (2002).
- [22] A. Pasha, B.M. Rajaprakash, and A.C. Manjunath, *Material Science Research India*, **17**, 201-206 (2020), <http://dx.doi.org/10.13005/msri/170302>
- [23] A. Fregeac, F. Ansart, S. Selezneff, and C. Estournès, *Ceramics International*, **45**, 23740-23749 (2019), <http://dx.doi.org/10.1016/j.ceramint.2019.08.090>

- [24] S. Li, B. Sun, H. Imai, T. Mimoto, and K. Kondoh, *Composites Part A: Applied Science and Manufacturing*, **48**, 57-66 (2013), <https://doi.org/10.1016/j.compositesa.2012.12.005>
- [25] J. Ruzic, M. Simić, N. Stoimenov, D. Božić, and, J. Stašić, *Metallurgical and Materials Engineering*, **27**, (2021), <https://doi.org/10.30544/629>
- [26] E. Fereiduni, A. Ghasemi, and, M. Elbestawi, *Aerospace*, **7**, 77, (2020), <https://doi.org/10.3390/aerospace7060077>
- [27] F. Saba, E. Kabiri, J.V. Khaki, and M.H. Sabzevar, *Powder Technology*, **288**, 76-86 (2016), <https://doi.org/10.1016/j.powtec.2015.10.030>
- [28] A. Aytumur, S. Koçyiğit, and I. Uslu, *Journal of Inorganic and Organometallic Polymers and Materials*, **24**, 927-932 (2014), <https://doi.org/10.1007/s10904-014-0064-6>
- [29] L. Bolzoni, E.M.R. Navas, and, E. Gordo, *Materials Science and Engineering: A*, **687**, 47-53 (2017), <https://doi.org/10.1016/j.msea.2017.01.049>
- [30] M.F.S.H. Zawrah, I.M.H. Allah, M.H. Ata, and H. Shouib, *Materials Research Express*, **6**, (2019), <https://doi.org/10.1088/2053-1591/ab316e>
- [31] C. Suryanarayana, and A. Al-Joubori, in: *Encyclopedia of Iron, Steel, and Their Alloys*, (eBook Published, Boca Raton, 2016), pp. 159-177, <https://doi.org/10.1081/E-EISA-120053049>.
- [32] H.A. Hegab, *Manufacturing Review*, **3**, 11 (2016), <https://doi.org/10.1051/mfreview/2016010>
- [33] J. P. Kruth, M. C. Leu, and T. Nakagawa, *CIRP Ann. - Manuf. Technol.*, **47**, 525 (1998), [https://doi.org/10.1016/S0007-8506\(07\)63240-5](https://doi.org/10.1016/S0007-8506(07)63240-5)
- [34] K.V. Wong, and A Hernandez, *International Scholarly Research Network ISRN Mechanical Engineering*. **2012**, 1 (2012), <https://doi.org/10.5402/2012/208760>.
- [35] Y. Hu, W. Cong, X. Wang, Y. Li, F. Ning, and H. Wang, *Compos. Part B Eng.*, **133**, 91-100 (2018), <https://doi.org/10.1016/j.compositesb.2017.09.019>
- [36] H. Attar et al., *Mater. Sci. Eng. A*, **625**, 350-356 (2015), <https://doi.org/10.1016/j.msea.2014.12.036>
- [37] D. Gu, G. Meng, C. Li, W. Meiners, and R. Poprawe, *Scr. Mater.* **67**, 185-188 (2012), <https://doi.org/10.1016/j.scriptamat.2012.04.013>
- [38] D. Gu, Y. C. Hagedorn, W. Meiners, K. Wissenbach, and R. Poprawe, *Compos. Sci. Technol.*, **71**, 1612-1620 (2011), <https://doi.org/10.1016/j.compscitech.2011.07.010>
- [39] Y. Zhang, J. Sun, and R. Vilar, *J. Mater. Process. Technol.*, **211**, 597-601 (2011), <https://doi.org/10.1016/j.jmatprotec.2010.11.009>
- [40] M. Das, V.K. Balla, D. Basu, S. Bose, and A. Bandyopadhyay, *Scr. Mater.* **63**, 438-441 (2010), <https://doi.org/10.1016/j.scriptamat.2010.04.044>
- [41] D. Gu, C. Hong, and G. Meng, *Metall Mater Trans A*, **43**, 697-708 (2012), <https://doi.org/10.1007/s11661-011-0876-8>
- [42] S.L. Sing, F.E. Wiria, and W.Y. Yeong, *Int. J. Refract. Met. Hard Mater.* **77**, 120-127 (2018), <https://doi.org/10.1016/j.ijrmhm.2018.08.006>
- [43] P.K. Farayibi, T.E. Abioye, A. Kennedy, and A.T. Clare, *J. Manuf. Process.* **45**, 429-437 (2019), <https://doi.org/10.1016/j.jmapro.2019.07.029>
- [44] V.K. Balla, A. Bhat, S. Bose, and A. Bandyopadhyay, *J. Mech. Behav. Biomed. Mater.* **6**, 9-20 (2012), <https://doi.org/10.1016/j.jmbbm.2011.09.007>
- [45] M. Das et al., *J. Mech. Behav. Biomed. Mater.* **29**, 259-271 (2014), <https://doi.org/10.1016/j.jmbbm.2013.09.006>
- [46] B. Vrancken, L.Thijs, J.P. Kruth., and J. Van Acta Materialia, **68**, 150-158 (2014). <https://doi.org/10.1016/j.actamat.2014.01.018>
- [47] Sairam, K., et al. *International Journal of Refractory Metals and Hard Materials* **42**, 185-192, (2014). <https://doi.org/10.1016/j.ijrmhm.2013.09.004>
- [48] M. Suárez, A. Fernández, J.L. Menéndez, R.Torrecillas, H.U.Kessel, J.Hennicke, R.Kirchner, and T.Kessel, in: *Sintering applications*, edited by Burcu Ertuğ, (InTech, Croatia, 2013), pp. 319-342, <https://doi.org/10.5772/53706>
- [49] K. Yang, D. Hitchcock, J. He, and A.M. Rao, *Tuning Electrical Properties of Carbon Nanotubes via Spark Plasma Sintering, Encyclopedia of Nanotechnology*; (Springer, Berlin/Heidelberg, Germany, 2012), pp. 2780-2788, https://doi.org/10.1007/978-90-481-9751-4_169
- [50] N. Saheb et al., *J. Nanomater*, **2012**, 983470-82 (2012), <https://doi.org/10.1155/2012/983470>
- [51] K. Vasanthakumar and S. R. Bakshi, *Ceram. Int.*, **44**, 484-494 (2018), <https://doi.org/10.1016/j.ceramint.2017.09.202>
- [52] A. Borrell, M. D. Salvador, V. García-Rocha, A. Fernández, E. Chicardi, and F. J. Gotor, *Mater. Sci. Eng. A*, **543**, 173-179, (2012), <https://doi.org/10.1016/j.msea.2012.02.071>
- [53] Y.F. Yang, and M. Qian, in: *Titanium powder metallurgy, Science, Technology and Applications*, (Elsevier, 2015), pp. 219-235, <https://doi.org/10.1016/B978-0-12-800054-0.00013-7>
- [54] N. Gupta, and B. Basu, in: *Intermetallic Matrix Composites, Properties and Applications*, (Elsevier, 2018), pp. 243-302, <https://doi.org/10.1016/B978-0-85709-346-2.00010-8>
- [55] M. Zadra, and L. Girardini, *Mater. Sci. Eng. A*, **608**, 155-163 (2014), <https://doi.org/10.1016/j.msea.2014.04.066>
- [56] T.E. O'Connell, *Production of Titanium Aluminide Products*, Report AFWAL-TR-83-4050, Wright-Patterson AFB OH, (1983).
- [57] J.J. Jackson, et al, *Titanium Aluminide Composites*, (NASP Contractor Report 1112, NASP JPO, Wright-Patterson AFB OH, (1991).
- [58] M. Selva Kumar, P. Chandrasekar, P. Chandramohan, and M. Mohanraj, *Mater. Charact.* **73**, 43-51, (2012), <https://doi.org/10.1016/j.matchar.2012.07.014>
- [59] X.J. Shen, C. Zhang, Y.G. Yang, and L. Liu, *Addit. Manuf.* **25**, 499-510 (2019), <https://doi.org/10.1016/j.addma.2018.12.006>
- [60] K. Kondoh, T. Threrujirapong, J. Umeda, and B. Fugetsu, *Compos. Sci. Technol.* **72**, 1291-7 (2012), <https://doi.org/10.1016/j.compscitech.2012.05.002>
- [61] Z. Yan, F. Chen, Y. Cai, and Y. Zheng, *Powder Technol.* **267**, 309-314 (2014), <https://doi.org/10.1016/j.powtec.2014.07.048>

- [62] S. Li, K. Kondoh, H. Imai, B. Chen, L. Jia, and J. Umeda, *Mater. Sci. Eng. A*, **628**, 75-83 (2015), <https://doi.org/10.1016/j.msea.2015.01.033>
- [63] F.C. Wang et al., *Carbon N.Y.*, **95**, pp. 396-407, (2015), <https://doi.org/10.1016/j.carbon.2015.08.061>
- [64] M.A. Lagos, I. Agote, G. Atxaga, O. Adarraga, and L. Pambaguian, *Mater. Sci. Eng. A*, **655**, 44-49 (2016), <https://doi.org/10.1016/j.msea.2015.12.050>
- [65] Y. Song et al., *Mater. Des.* **109**, 256-263 (2016), <https://doi.org/10.1016/j.matdes.2016.07.077>
- [66] N.S. Karthiselva, and S.R. Bakshi, *Mater. Sci. Eng. A*, **663**, 38-48 (2016), <https://doi.org/10.1016/j.msea.2016.03.098>
- [67] S. Li et al., *Mater. Des.* **95**, 127-132 (2016), <https://doi.org/10.1016/j.matdes.2016.01.092>
- [68] S. Zherebtsov, M. Ozerov, M. Klimova, D. Moskovskikh, N. Stepanov, and G. Salishchev, *Metals* **9**, 1175 (2019), <https://doi.org/10.3390/met9111175>
- [69] P. Odetola, A. P. Popoola, E. Ajenifuja, and O. Popoola, *J. Met. Mater. Miner.* **30**, 119-127 (2020),
- [70] P. Singh, H. Pungotra, and N.S. Kalsi, *Materials Today: Proceedings*, **4**, 8971-8982 (2017), <https://doi.org/10.1016/j.matpr.2017.07.249>
- [71] C. Sandu, S. Vintilă, M. Sima, F. Zavodnic, T. Tipa, and C. Olariu, *Int. J. Systems Appl. Eng. Dev.* **12**, 168 (2018).
- [72] H. Attar, S. Ehtemam-Haghighi, N. Soro, D. Kent, and M.S. Dargusch, *J. Alloys Compd.* **827**, 154263 (2020), <https://doi.org/10.1016/j.jallcom.2020.154263>
- [73] T. Furuta, *Titanium for Consumer Applications: Real-World Use of Titanium*, (Elsevier, 2019), pp. 77–90, <https://doi.org/10.1016/B978-0-12-815820-3.00006-X>
- [74] O. Schauerer, *Advanced Engineering Materials*, **5**, 411-418, (2003), <https://doi.org/10.1002/adem.200310094>
- [75] A.K. Sachdev, K.Kulkarni, Z.Z. Fang, R.Yang, and V. Girshov. *JOM*, **64**, 553-565 (2012), <http://doi.org/10.1007/s11837-012-0310-8>
- [76] A. Pettersson, P. Magnusson, P. Lundberg, and M. Nygren, *Int. J. Impact Eng.*, **32**, 387-399 (2005), <https://doi.org/10.1016/j.ijimpeng.2005.04.003>
- [77] A. Paman, G. Sukumar, B. Ramakrishna, and V. Madhu, *Int. J. Prot. Structures*, **11**, 185-208 (2020), <https://doi.org/10.1177/2041419619860533>
- [78] L.S. Ahmed, and M.P. Kumar, *Mat. Manufact. Processes*, **31**(7), 951-959 (2016), <https://doi.org/10.1080/10426914.2015.1048475>
- [79] J. Xu, M. Ji, M.C.F. Ren, *Mat. Manufact. Processes*, **32**(12), 1401-1410 (2019), <https://doi.org/10.1080/10426914.2019.1661431>
- [80] J. Xu, C. Li, M. Chen, and, F. Ren, *Mat. Manufact. Processes*, **34**, 1182-1193, (2019) <https://doi.org/10.1080/10426914.2019.1615085>
- [81] K. Mahapatro, and V. Pasam, *Smart and Sustainable Manufact. Systems*, **4**, 62-80 (2020), <https://doi.org/10.1520/SSMS20200016>
- [82] K. Mahapatro, G. Mahendra, A. Markandeya, and P.V. Krishna, *Smart and Sustainable Manufact. Systems*, **5**, 47- 64 (2021), <https://doi.org/10.1520/SSMS20200041>

ОГЛЯД ШЛЯХІВ ОБРОБКИ, ВЛАСТИВОСТЕЙ, ЗАСТОСУВАННЯ ТА СКЛАДНИХ ПРОБЛЕМ, ЩО ПОВ'ЯЗАНІ З ТИТАНОВО-МЕТАЛЕВИМИ МАТРИЧНИМИ КОМПОЗИТАМИ

Хрудаянджалі Патх, Тапан Кумар Мішрі, Шасміта Рані Паніграхі, Біджаялакшмі Куанар, Бісваджіт Далай

Фізичний факультет, наукова школа, університет GIET, Гунупур 765022, Одіша, Індія

На сьогоднішній день титан відрізняється своєю малою вагою, високою міцністю та неактивною природою в порівнянні з усіма металами. Титаново-металеві матричні композити (ТМК) є дуже популярними в галузях аерокосмічної, автомобільної промисловості, в оборонній та біомедичній сферах через їх високу питому міцність, малу вагу та біологічну сумісність. Деякі з широко використовуваних методів виробництва, таких як порошкова металургія (ПМ), адитивне виробництво (АВ) та іскрове плазмове спікання (ІПС), були розглянуті в цій роботі з урахуванням деяких властивостей ТМК. Змінюючи різні типи армування, можна досягти необхідних властивостей відповідно до промислових та сучасних застосувань у ТМК. Це дослідження також включає наслідки впливу температури спікання на такі властивості ТМК, як фізичні, механічні та структурні. Сплави титану демонструють хороші механічні та біомедичні властивості при армуванні вуглецевими волокнами, боридами, керамікою та багатьма іншими матеріалами у вигляді суцільних волокон або переривчастих частинок та вусів (ниткоподібних кристалів). У цій роботі йдеться про застосування ТМК в аерокосмічній, автомобільній, біомедичній та оборонній сферах. Незважаючи на усі ці сприятливі властивості та застосування, ТМК не можуть широко використовуватися у зазначених галузях через їх високу вартість та труднощі в обробці. Зниження вартості можна здійснити шляхом виготовлення Ті – суперсплавів. Крім того, для покращення технологічної обробки існує необхідність у ефективній системі охолодження під час механічної обробки ТМК. Були також розглянуті деякі ефективні методи, які можуть поліпшити оброблюваність ТМК.

Ключові слова: Ті ММК; ПМ; АВ; ІПС; складні проблеми

NONLINEAR CONE MODEL FOR INVESTIGATION OF RUNAWAY ELECTRON SYNCHROTRON RADIATION SPOT SHAPE[†]

 Igor M. Pankratov^{a,b,*},  Volodymyr Y. Bochko^a

^aV.N. Karazin Kharkiv National University, 61022 Kharkiv, Ukraine

^bInstitute of Plasma Physics, NSC “Kharkiv Institute of Physics and Technology”
Akademichna Str.1, 61108 Kharkiv, Ukraine

*Corresponding Author: pankratov@kipt.kharkov.ua

Received June 16, 2021; revised July 26, 2021; accepted July 27, 2021

The runaway electron event is the fundamental physical phenomenon and tokamak is the most advanced conception of the plasma magnetic confinement. The energy of disruption generated runaway electrons can reach as high as tens of mega-electron-volt and they can cause a catastrophic damage of plasma-facing-component surfaces in large tokamaks and International Thermonuclear Experimental Reactor (ITER). Due to its importance, this phenomenon is being actively studied both theoretically and experimentally in leading thermonuclear fusion centers. Thus, effective monitoring of the runaway electrons is an important task. The synchrotron radiation diagnostic allows direct observation of such runaway electrons and an analysis of their parameters and promotes the safety operation of present-day large tokamaks and future ITER. In 1990 such diagnostic had demonstrated its effectiveness on the TEXTOR (Tokamak Experiment for Technology Oriented Research, Germany) tokamak for investigation of runaway electrons beam size, position, number, and maximum energy. Now this diagnostic is installed practically on all the present-day's tokamaks. The parameter $v_{\perp}/|v_{\parallel}|$ strongly influences on the runaway electron synchrotron radiation behavior (v_{\parallel} is the longitudinal velocity, v_{\perp} is the transverse velocity with respect to the magnetic field \vec{B}). The paper is devoted to the theoretical investigation of runaway electron synchrotron radiation spot shape when this parameter is not small that corresponds to present-day tokamak experiments. The features of the relativistic electron motion in a tokamak are taken into account. The influence of the detector position on runaway electron synchrotron radiation data is discussed. Analysis carried out in the frame of the nonlinear cone model. In this model, the ultrarelativistic electrons emit radiation in the direction of their velocity \vec{v} and the velocity vector runs along the surface of a cone whose axis is parallel to the magnetic field \vec{B} . The case of the small parameter $v_{\perp}/|v_{\parallel}|$ ($v_{\perp}/|v_{\parallel}| \ll 1$, linear cone model) was considered in the paper: *Plasma Phys. Rep.* **22**, 535 (1996) and these theoretical results are used for experimental data analysis.

Keywords: diagnostic of runaway electrons, ultrarelativistic electrons, synchrotron radiation spot shape, nonlinear cone model, large tokamak safety operation.

PACS: 52.25.Os, 52.55.Fa, 52.70.-m

The generation of runaway electrons during disruptions poses a potential threat to the safe operation of large tokamaks. The energy of these electrons can reach as high as tens of MeV, which could lead to a serious damage of plasma-facing-component surfaces in large devices like ITER (under construction in France) (see, e. g. [1, 2]). Numerical calculations for ITER suggest about 70% of thermal current may be converted into runaway current during a disruption by avalanche mechanism [2]. Thus, effective monitoring of these high-energy runaway electrons is an emerging safety issue of the tokamak operation. The most powerful diagnostic for runaway monitoring is diagnostic based on their synchrotron radiation [3]. For the first time, this diagnostic was used in TEXTOR [4] to study the parameters of runaway electrons (beam size and position, number, and maximum energy of runaways). Now it is a routine diagnostic for present-day tokamaks: such as Joint European Torus (JET, Great Britain), Axially Symmetric Divertor Experiment (ASDEX Upgrade, Germany), DubletIII-D and Alcator C-Mod (USA), Frascati Tokamak Upgrade (FTU, Italy), *Tokamak a Configuration Variable* (TCV, Switzerland), Experimental Advanced Superconducting Tokamak (EAST, China), Korea Superconducting Tokamak Advanced Research (KSTAR, South Korea). The first correct theoretical analysis of the synchrotron radiation of runaway electrons with taking into account features of the relativistic electron motion in a tokamak (motion along tokamak helical magnetic field with the longitudinal velocity v_{\parallel} , cyclotron gyration motion around the guiding centre with the finite transverse velocity v_{\perp} with respect to the magnetic field and the vertical centrifugal drift of guiding centre motion with velocity v_{dr}) and detector position was carried out in Ref. [5] where cone model was used. Note, the finite value of parameter $v_{\perp}/|v_{\parallel}|$ strongly influences on the runaway electron synchrotron radiation behavior but in Ref. [5] only the case of $v_{\perp}/|v_{\parallel}| \ll 1$ was studied (linear cone model).

The highly relativistic particles emit radiation in the direction of their velocity vector [6], in this approximation, the velocity vector \vec{v} runs along the surface of a cone whose axis is parallel to the magnetic field \vec{B} . Because of in tokamak

[†] **Cite as:** I.M. Pankratov, and V.Y. Bochko, East. Eur. J. Phys. **3**, 18 (2021), <https://doi.org/10.26565/2312-4334-2021-3-02>

experiments the inequality $v_{\perp}/|v_{\parallel}| \gg \gamma^{-1}$ takes place, the small uncertainty introduced by the angular broadening of radiation, $\sim \gamma^{-1}$, was neglected, $\gamma = (1 - v^2/c^2)^{-1/2}$ is the relativistic factor. This model demonstrates good agreement with the full models [7]. Note that for the detailed investigation of runaway beam parameters both analysis of runaway electron synchrotron radiation spot shape and synchrotron radiation spectra must be carried out [8, 9].

NONLINEAR CONE MODEL EQUATIONS

We shall use the toroidal (r, θ, ζ) and Cartesian (x, y, z) coordinate systems, θ and ζ are the poloidal and toroidal angles (see Fig. 1), respectively. The tokamak confinement magnetic field was taken in the form:

$$\vec{B}(r, \vartheta) = \frac{B_{0\zeta}R_0}{R} \left(\pm \vec{e}_{\zeta} + \frac{r}{q(r)R_0} \vec{e}_{\theta} \right), \tag{1}$$

The circular transverse cross sections of the magnetic surfaces in a tokamak are assumed and the displacements of the magnetic surfaces relative to each other are neglected, $R = R_0 - r \cos \theta$, R_0 is the major radius of the magnetic surfaces, $q(r)$ is the tokamak safety factor. The drift surfaces of runaways with small radius r_e strongly deviate from magnetic surfaces with radius r because of the drift shift δ_e [5]:

$$r = \sqrt{r_e^2 - \delta_e^2 \sin^2 \theta} - \delta_e \cos \theta. \tag{2}$$

In present day tokamaks the drift orbits are shifted to low magnetic field side. The runaway electrons on the same drift surface in the low field side are located on a magnetic surface with a larger radius than electrons in the high field side.

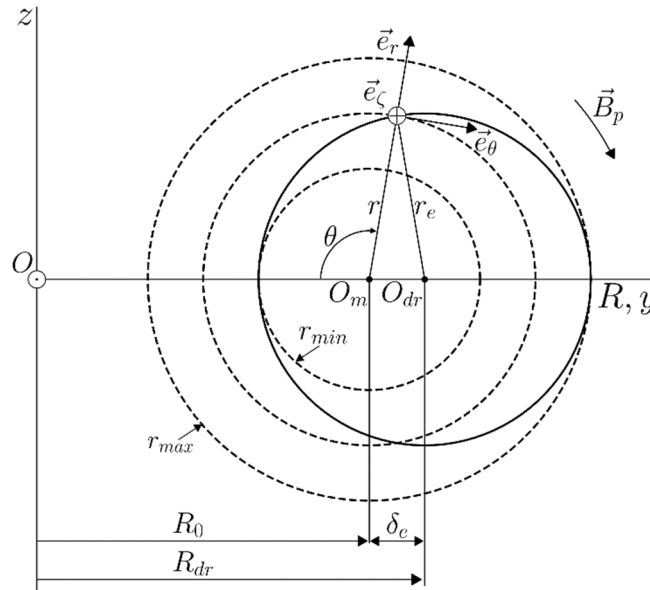


Figure 1. The cross-sections (through the plane $\zeta = \pi/2$) of the magnetic surfaces (dashed circles) with a center at the point O_m and the drift surface with shift δ_e (solid circle) at a center O_{dr} are plotted, r_{min} and r_{max} are minimal and maximal minor radii of magnetic surfaces corresponding to this drift surface. The x-axis is directed toward the detector. The direction of the poloidal magnetic field \vec{B}_p is shown.

Radiation is recorded by the detector if the condition

$$\left[\vec{v} \times (\vec{R}_e - \vec{Q}_{det}) \right] = 0 \tag{3}$$

is satisfied. In Cartesian coordinates, the radius vector of the position of the detector is represented in the next way:

$$\vec{Q}_{det} = D\vec{e}_x + Y_{det}\vec{e}_y + Z_{det}\vec{e}_z, \tag{4}$$

where $D > 0$ is the distance from the detector to the plane $\zeta = \pi/2$ (see Fig. 2).

Recall the main results of the linear cone model (see Ref. [5]). For the case of the small values $v_{\perp}/|v_{\parallel}|$ ($v_{\perp}/|v_{\parallel}| \ll r/q(r)R_0$), when the detector is situated in the plane $z = 0$ ($Z_{det} = 0$), the detector can record electrons for which

$$\tan \theta \approx \pm D / q(r)R_0, \quad (5)$$

i.e., the detector records electrons only from a small part of the beam cross section, which has the shape of a curved strip of varying width. If $v_{\perp} / |v_{\parallel}| \gtrsim r / q(r)R_0$, the detector records a large asymmetrical spot. Note that the influence of drift orbit shift (see Eq. (2)) of high relativistic runaways on the camera record possibility is the main reason why an asymmetrical synchrotron radiation spot can be observed in present day tokamak experiments. When the large orbit shift of runaway electrons takes place, the synchrotron radiation in the low field side cannot be detected.

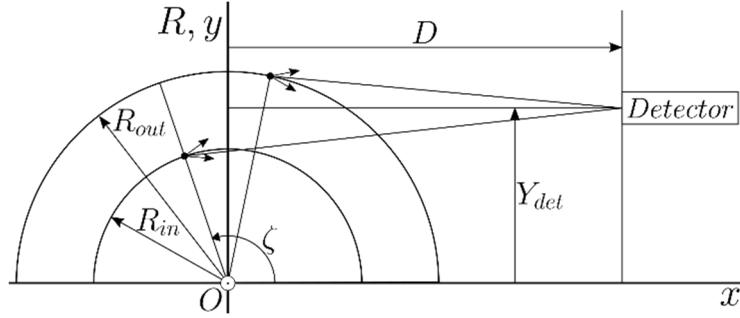


Figure 2. Relative positions of the runaway electrons beam and the detector are shown. For simplicity, case of the plane $z = 0$ and $Z_{det} = 0$ are presented, R_{in} and R_{out} are the inner and outer major radii of the beam in this plane, the cones of radiation emitted by electrons are represented schematically.

The experimental observations of runaway electron synchrotron radiation spot shape (see, e.g. [7, 9, 10, 11]) are in good agreement with the theoretical results of Ref. [5]. The observation of asymmetrical ring-like synchrotron radiation spot shape from runaway electron beams in the EAST experiments has been explained by the large orbit shift [9]. The theory of Ref. [5] may also be applied for data interpretation of a new RE diagnostic called the ‘‘Gamma Ray Imager’’ (GRI) which is deployed on the DIII-D tokamak [12].

In present-day tokamaks during runaway discharge the parameter $v_{\perp} / |v_{\parallel}|$ may achieve the value of the order of 0.5 (see, e.g. [11]). The paper is devoted to the nonlinear cone model for the investigation of runaway electron synchrotron radiation spot shape in such situations. For a magnetic field with small nonuniformity it is convenient to present the electron velocity \vec{v} and the radius vector \vec{R}_e in the following way [13]:

$$\vec{v} = v_{\parallel} \vec{\tau}_0 + v_{\perp} (\vec{\tau}_1 \cos \alpha + \vec{\tau}_2 \sin \alpha), \quad (6)$$

$$\vec{R}_e = R_0 \vec{e}_R + r \vec{\tau}_1 + \frac{v_{\perp}}{\omega_B} (\vec{\tau}_1 \sin \alpha - \vec{\tau}_2 \cos \alpha), \quad (7)$$

where

$$\vec{e}_R = \vec{e}_x \cos \zeta + \vec{e}_y \sin \zeta, \quad \alpha \approx \omega_b, \quad \omega_b(r, \theta) = eB(r, \theta) / \gamma m_e c \quad (e > 0). \quad (8)$$

The right-hand triplet of the vectors is taken in the form:

$$\vec{\tau}_0 = \frac{\vec{B}}{B} = \frac{\pm \vec{e}_z + (r/q(r)R_0) \vec{e}_\theta}{\sqrt{1 + (r/qR_0)^2}}, \quad \vec{\tau}_1 = [\vec{\tau}_2 \times \vec{\tau}_0] = \vec{e}_r, \quad \vec{\tau}_2 = [\vec{\tau}_0 \times \vec{\tau}_1] = \frac{\pm \vec{e}_\theta - (r/q(r)R_0) \vec{e}_z}{\sqrt{1 + (r/qR_0)^2}}. \quad (9)$$

In tokamaks, the change of nonuniform magnetic field is small in comparison with the Larmor radius of the ultra-relativistic electron with tens of MeV energy. Hence to investigate Eqs. (3, 6, 7) the well-known asymptotic methods [13] may be used. The changes of variables (Eqs. (25.32) from Ref. [13]) are used (see appendix). With the triplet of the vectors (9) these changes of variables take the form:

$$v_{\parallel} = \bar{v}_{\parallel} + \frac{1}{\omega_B} \frac{\bar{v}_{\parallel} \bar{v}_{\perp}}{\sqrt{1 + (\bar{r}/qR_0)^2}} \left[\frac{\sin \bar{\alpha}}{\sqrt{1 + (\bar{r}/qR_0)^2}} \left(\frac{\cos \bar{\theta}}{R} - \frac{\bar{r}}{(qR_0)^2} \right) \pm \frac{\cos \bar{\alpha} \sin \bar{\theta}}{R} \right] - \frac{\bar{v}_{\perp}^2}{4\omega_B R} \frac{\bar{r}/qR_0}{\sqrt{1 + (\bar{r}/qR_0)^2}} \left[\sin 2\bar{\alpha} \sin \bar{\theta} \mp \frac{\cos 2\bar{\alpha} \cos \bar{\theta}}{\sqrt{1 + (\bar{r}/qR_0)^2}} \right], \quad (10a)$$

$$v_{\perp} = \bar{v}_{\perp} - \frac{1}{\omega_B} \frac{\bar{v}_{\parallel}^2}{\sqrt{1+(\bar{r}/qR_0)^2}} \left[\frac{\sin \bar{\alpha}}{\sqrt{1+(\bar{r}/qR_0)^2}} \left(\frac{\cos \bar{\theta}}{R} - \frac{\bar{r}}{(qR_0)^2} \right) \pm \frac{\cos \bar{\alpha} \sin \bar{\theta}}{R} \right] + \frac{\bar{v}_{\parallel} \bar{v}_{\perp}}{4\omega_B R} \frac{\bar{r}/qR_0}{\sqrt{1+(\bar{r}/qR_0)^2}} \left[\sin 2\bar{\alpha} \sin \bar{\theta} \mp \frac{\cos 2\bar{\alpha} \cos \bar{\theta}}{\sqrt{1+(\bar{r}/qR_0)^2}} \right], \quad (10b)$$

$$\alpha = \bar{\alpha} - \frac{1}{\omega_B} \frac{1}{\sqrt{1+(\bar{r}/qR_0)^2}} \left\{ \mp \frac{\bar{v}_{\parallel}^2}{\bar{v}_{\perp}} \frac{\sin \bar{\alpha} \sin \bar{\theta}}{R} + \frac{1}{\bar{v}_{\perp}} \frac{\cos \bar{\alpha}}{\sqrt{1+(\bar{r}/qR_0)^2}} \left[\bar{v}_{\parallel}^2 \left(\frac{\cos \bar{\theta}}{R} - \frac{\bar{r}}{(qR_0)^2} \right) - \bar{v}_{\perp}^2 \left(\frac{1}{\bar{r}} - \frac{(\bar{r}/qR_0)^2 \cos \bar{\theta}}{R} \right) \right] \right\} + \frac{\bar{v}_{\parallel}}{4\omega_B R} \frac{\bar{r}/qR_0}{\sqrt{1+(\bar{r}/qR_0)^2}} \left[\cos 2\bar{\alpha} \sin \bar{\theta} \pm \frac{\sin 2\bar{\alpha} \cos \bar{\theta}}{\sqrt{1+(\bar{r}/qR_0)^2}} \right] - \frac{\bar{v}_{\perp}}{\omega_B R} \left[\cos \bar{\theta} \cos \bar{\alpha} \mp \frac{\sin \bar{\theta} \sin \bar{\alpha}}{\sqrt{1+(\bar{r}/qR_0)^2}} \right] - \frac{\bar{v}_{\perp}}{\omega_B qR_0} \frac{\bar{r}/qR_0}{1+(\bar{r}/qR_0)^2} \cos \bar{\alpha}. \quad (10c)$$

Here averaging of variables is determined in the usual way: $\bar{f} = (1/2\pi) \int_0^{2\pi} f d\alpha$.

For simplicity below the line over averaged variables is omitted. After substitutions of these changes of variables (10a, b, c) in Eq. (6) the components of electron velocity take the form:

$$v_x = \cos \Delta \left[\mp v_{\parallel} + v_{\perp} \frac{r}{qR_0} \sin \alpha - \frac{v_{\parallel}^2}{\omega_B R} \frac{r}{qR_0} \cos \theta - \frac{v_{\parallel} v_{\perp}}{\omega_B R} \sin(\theta \pm \alpha) \pm \frac{v_{\parallel} v_{\perp}}{\omega_B qR_0} \frac{r}{qR_0} \sin \alpha + \frac{v_{\perp}^2}{\omega_B qR_0} \cos^2 \alpha \right] + \sin \Delta \left[-v_{\parallel} \frac{r}{qR_0} \sin \theta + v_{\perp} \cos(\theta \pm \alpha) \mp \frac{v_{\parallel}^2}{\omega_B qR_0} \frac{r}{qR_0} \sin \theta \mp \frac{v_{\parallel} v_{\perp}}{\omega_B R} \frac{r}{qR_0} \sin(\theta \pm \alpha) \sin \theta \mp \frac{v_{\parallel} v_{\perp}}{4\omega_B R} \frac{r}{qR_0} \cos \alpha \mp \frac{v_{\perp}^2}{\omega_B r} \sin(\theta \pm \alpha) \cos \alpha \pm \frac{v_{\perp}^2}{\omega_B R} \cos(\theta \pm \alpha) \sin(\theta \pm \alpha) \right], \quad (11a)$$

$$v_y = \cos \Delta \left[v_{\parallel} \frac{r}{qR_0} \sin \theta - v_{\perp} \cos(\theta \pm \alpha) \pm \frac{v_{\parallel}^2}{\omega_B qR_0} \frac{r}{qR_0} \sin \theta \pm \frac{v_{\parallel} v_{\perp}}{\omega_B R} \frac{r}{qR_0} \sin(\theta \pm \alpha) \sin \theta \pm \frac{v_{\parallel} v_{\perp}}{4\omega_B R} \frac{r}{qR_0} \cos \alpha \pm \frac{v_{\perp}^2}{\omega_B r} \sin(\theta \pm \alpha) \cos \alpha \mp \frac{v_{\perp}^2}{\omega_B R} \cos(\theta \pm \alpha) \sin(\theta \pm \alpha) \right] + \sin \Delta \left[\mp v_{\parallel} + v_{\perp} \frac{r}{qR_0} \sin \alpha - \frac{v_{\parallel}^2}{\omega_B R} \frac{r}{qR_0} \cos \theta - \frac{v_{\parallel} v_{\perp}}{\omega_B R} \sin(\theta \pm \alpha) \pm \frac{v_{\parallel} v_{\perp}}{\omega_B qR_0} \frac{r}{qR_0} \sin \alpha + \frac{v_{\perp}^2}{\omega_B qR_0} \cos^2 \alpha \right], \quad (11b)$$

$$v_z = v_{\parallel} \frac{r}{qR_0} \cos \theta + v_{\perp} \sin(\theta \pm \alpha) \mp \frac{v_{\parallel}^2 + 0.5v_{\perp}^2}{\omega_B R} \pm \frac{v_{\parallel}^2}{\omega_B qR_0} \frac{r}{qR_0} \cos \theta \pm \frac{v_{\parallel} v_{\perp}}{\omega_B R} \frac{r}{qR_0} \sin(\theta \pm \alpha) \cos \theta \pm \frac{v_{\parallel} v_{\perp}}{4\omega_B R} \frac{r}{qR_0} \sin \alpha \mp \frac{v_{\perp}^2}{2\omega_B R} \cos 2(\theta \pm \alpha) \pm \frac{v_{\perp}^2}{\omega_B r} \cos(\theta \pm \alpha) \cos \alpha \quad (11c)$$

and components of coordinates (from Eq. (7)):

$$X_e = -(R_0 - r \cos \theta) \sin \Delta, \quad Y_e = (R_0 - r \cos \theta) \cos \Delta, \quad Z_e = r \sin \theta \mp \frac{v_{\perp}}{\omega_B} \cos(\theta \pm \alpha), \quad (12)$$

where $\zeta = \pi/2 + \Delta$. The terms that are proportional to small parameter $(r/q(r)R_0)^2 \ll 1$ are omitted.

By inserting equations 11(a, b, c) and 12 into Eq. (3), the expressions that allow analysis of the synchrotron radiation emitted by runaway electrons in tokamaks are obtained ($v_{\perp}/|v_{\parallel}| \gg r/q(r)R_0$). From expression

$$(Z_e - Z_{\text{det}})v_x = (X_e - D)v_z \quad (13)$$

we get:

$$\begin{aligned} & \pm \left[r \sin \theta \mp \frac{v_{\perp}}{\omega_B} \cos(\theta \pm \alpha) - Z_{\text{det}} \right] \left[\cos \Delta \mp \sin \Delta \frac{v_{\perp}}{v_{\parallel}} \cos(\theta \pm \alpha) \right] = \\ & = \left[D + (R_0 - r \cos \theta) \sin \Delta \right] \left[\frac{r}{qR_0} \cos \theta + \frac{v_{\perp}}{v_{\parallel}} \sin(\theta \pm \alpha) \mp \frac{1}{v_{\parallel}} \frac{v_{\perp}^2 + 0.5v_{\perp}^2}{\omega_B R_0} \pm \frac{v_{\perp}}{v_{\parallel}} \frac{v_{\perp}}{\omega_B r} \cos(\theta \pm \alpha) \cos \alpha \right]. \end{aligned} \quad (14)$$

From expression

$$(X_e - D)v_y = (Y_e - Y_{\text{det}})v_x \quad (15)$$

we get:

$$\sin \Delta \left[1 \pm \frac{Y_{\text{det}}}{D} \frac{v_{\perp}}{v_{\parallel}} \cos(\theta \pm \alpha) \right] = \frac{Y_{\text{det}} \cos \Delta - (R_0 - r \cos \theta)}{D} \mp \cos \Delta \frac{v_{\perp}}{v_{\parallel}} \cos(\theta \pm \alpha). \quad (16)$$

In Eqs. (14) and (16) the small terms that are of the order of $(v_{\perp}^2 / \omega_B qR_0)(r / qR_0)$, $(v_{\perp} v_{\perp} / \omega_B qR)(r / qR_0)$ and $v_{\perp}^2 / \omega_B R$ are omitted. The solution of Eq. (16) has the next form:

$$\cos \Delta = \frac{\left[1 \pm \frac{Y_{\text{det}}}{D} \frac{v_{\perp}}{v_{\parallel}} \cos(\theta \pm \alpha) \right] \left\{ \left[1 + (Y_{\text{det}} / D)^2 \right] \left[1 + (v_{\perp} / v_{\parallel})^2 \cos^2(\theta \pm \alpha) \right] - (R / D)^2 \right\}^{1/2} + \left(\frac{R}{D} \right) \left[\frac{Y_{\text{det}}}{D} \mp \frac{v_{\perp}}{v_{\parallel}} \cos(\theta \pm \alpha) \right]}{\left[1 + (Y_{\text{det}} / D)^2 \right] \left[1 + (v_{\perp} / v_{\parallel})^2 \cos^2(\theta \pm \alpha) \right]}, \quad (17)$$

$$\sin \Delta = \frac{\left[\frac{Y_{\text{det}}}{D} \mp \frac{v_{\perp}}{v_{\parallel}} \cos(\theta \pm \alpha) \right] \left\{ \left[1 + (Y_{\text{det}} / D)^2 \right] \left[1 + (v_{\perp} / v_{\parallel})^2 \cos^2(\theta \pm \alpha) \right] - (R / D)^2 \right\}^{1/2} - \left(\frac{R}{D} \right) \left[1 \pm \frac{Y_{\text{det}}}{D} \frac{v_{\perp}}{v_{\parallel}} \cos(\theta \pm \alpha) \right]}{\left[1 + (Y_{\text{det}} / D)^2 \right] \left[1 + (v_{\perp} / v_{\parallel})^2 \cos^2(\theta \pm \alpha) \right]}. \quad (18)$$

The synchrotron radiation of runaway electron may be detected by the camera only if the next inequality holds (solution of Eqs, (17), (18) exists):

$$\left[1 + (Y_{\text{det}} / D)^2 \right] \left[1 + (v_{\perp} / v_{\parallel})^2 \cos^2(\theta \pm \alpha) \right] \geq (R / D)^2. \quad (19)$$

DISCUSSIONS

For $v_{\perp} / |v_{\parallel}| \ll 1$ the equations (14, 16) correspond to the linear cone model equations of Ref. [5]:

$$\pm (r \sin \theta - Z_{\text{det}}) \approx \left[\frac{r}{qR_0} \cos \theta + \frac{v_{\perp}}{v_{\parallel}} \sin(\theta \pm \alpha) \mp \frac{1}{v_{\parallel}} \frac{v_{\perp}^2 + 0.5v_{\perp}^2}{\omega_B R_0} \right] (D + R \sin \Delta), \quad (20)$$

$$\sin \Delta \approx \pm \frac{r}{qR_0} \sin \theta \mp \frac{v_{\perp}}{v_{\parallel}} \cos(\theta \pm \alpha) + \frac{Y_{\text{det}} - R}{D}, \quad \cos \Delta \approx 1. \quad (21)$$

The upper signs in the equations of the paper correspond to the case when the magnetic field \vec{B} is directed away from the detector, and for the lower sign field is directed toward the detector. For the electron moving toward the detector the longitudinal velocity v_{\parallel} is negative for upper sign ($v_{\parallel} < 0$) and positive for lower sign ($v_{\parallel} > 0$). Hence:

$$\cos \Delta = \frac{\left[1 - \frac{Y_{\text{det}}}{D} \frac{v_{\perp}}{|v_{\parallel}|} \cos(\theta \pm \alpha) \right] \left\{ \left[1 + (Y_{\text{det}} / D)^2 \right] \left[1 + (v_{\perp} / v_{\parallel})^2 \cos^2(\theta \pm \alpha) \right] - (R / D)^2 \right\}^{1/2} + \left(\frac{R}{D} \right) \left[\frac{Y_{\text{det}}}{D} + \frac{v_{\perp}}{|v_{\parallel}|} \cos(\theta \pm \alpha) \right]}{\left[1 + (Y_{\text{det}} / D)^2 \right] \left[1 + (v_{\perp} / v_{\parallel})^2 \cos^2(\theta \pm \alpha) \right]}, \quad (22)$$

$$\sin \Delta = \frac{\left[\frac{Y_{\text{det}}}{D} + \frac{v_{\perp}}{|v_{\parallel}|} \cos(\theta \pm \alpha) \right] \left\{ \left[1 + (Y_{\text{det}} / D)^2 \right] \left[1 + (v_{\perp} / v_{\parallel})^2 \cos^2(\theta \pm \alpha) \right] - (R / D)^2 \right\}^{1/2} - \left(\frac{R}{D} \right) \left[1 - \frac{Y_{\text{det}}}{D} \frac{v_{\perp}}{|v_{\parallel}|} \cos(\theta \pm \alpha) \right]}{\left[1 + (Y_{\text{det}} / D)^2 \right] \left[1 + (v_{\perp} / v_{\parallel})^2 \cos^2(\theta \pm \alpha) \right]}. \quad (23)$$

First situation when $Y_{det}/D > 1$ is considered. If $1 - (Y_{det}/D)(v_{\perp}/|v_{\parallel}|)\cos(\theta \pm \alpha) \geq 0$, then $\cos \Delta \geq 0$ and

$$\sin \Delta \geq 0, \text{ if } \left[(Y_{det}/D) + (v_{\perp}/|v_{\parallel}|)\cos(\theta \pm \alpha) \right]^2 \geq (R/D)^2, \tag{24}$$

$$\sin \Delta \leq 0, \text{ if } \left[(Y_{det}/D) + (v_{\perp}/|v_{\parallel}|)\cos(\theta \pm \alpha) \right]^2 \leq (R/D)^2. \tag{25}$$

If $1 - (Y_{det}/D)(v_{\perp}/|v_{\parallel}|)\cos(\theta \pm \alpha) \leq 0$, then $\sin \Delta \geq 0$ and

$$\cos \Delta \geq 0, \text{ if } \left[(Y_{det}/D)(v_{\perp}/|v_{\parallel}|)\cos(\theta \pm \alpha) - 1 \right]^2 \leq (R/D)^2, \tag{26}$$

$$\cos \Delta \leq 0, \text{ if } \left[(Y_{det}/D)(v_{\perp}/|v_{\parallel}|)\cos(\theta \pm \alpha) - 1 \right]^2 \geq (R/D)^2. \tag{27}$$

Second situation is when $Y_{det}/D < 1$. If $(Y_{det}/D) + (v_{\perp}/|v_{\parallel}|)\cos(\theta \pm \alpha) \geq 0$, then $\cos \Delta \geq 0$ and $\sin \Delta \geq 0$ or $\sin \Delta \leq 0$ if inequality (24) or (25) holds, respectively.

If $(Y_{det}/D) + (v_{\perp}/|v_{\parallel}|)\cos(\theta \pm \alpha) \leq 0$, then $\sin \Delta \leq 0$ and $\cos \Delta \geq 0$ or $\cos \Delta \leq 0$ if inequality (27) or (26) holds, respectively.

In Eqs. (14), (16) the parameter $v_{\perp}/|v_{\parallel}|$ is not small, the solution of Eq. (14) exists only if $|\sin(\theta \pm \alpha)| \ll 1$ and $|\cos(\theta \pm \alpha)| \approx 1$ ($r \ll D$, $Z_{det} \sim r$). Very important conclusion: for each poloidal angle θ the synchrotron radiation of runaway electron is detected by the camera for certain values of α only.

CONCLUSIONS

The analytical expressions that allow analysis of the synchrotron radiation emitted by runaway electrons in tokamaks have been obtained, the finite ratio v_{\perp}/v_{\parallel} the order of 0.5, the tokamak safety factor $q(r)$, the horizontal displacement δ_e of the drift surfaces of electrons with respect to the magnetic surfaces, and the position of the detector are taken into account. This situation corresponds to present-day tokamak runaway electron experiments.

It has been shown that besides the parameter $v_{\perp}/|v_{\parallel}|$, the ratio Y_{det}/D is also a key parameter for the analysis of the synchrotron radiation spot shape. It should be noted that for each poloidal angle θ the synchrotron radiation of runaway electron is detected by the camera for certain values of α (cyclotron rotation angle) only.

APPENDIX

For readers convenience the equations that corresponds to Eqs. 25.32 of Ref. 13 are presented:

$$v_{\parallel} = \bar{v}_{\parallel} + \frac{\bar{v}_{\parallel}\bar{v}_{\perp}}{\omega_B} [\bar{\tau}_1(\bar{\tau}_0\nabla)\bar{\tau}_0 \sin \bar{\alpha} - \bar{\tau}_2(\bar{\tau}_0\nabla)\bar{\tau}_0 \cos \bar{\alpha}] + \frac{\bar{v}_{\perp}^2}{4\omega_B} \{ [\bar{\tau}_1(\bar{\tau}_1\nabla)\bar{\tau}_0 - \bar{\tau}_2(\bar{\tau}_2\nabla)\bar{\tau}_0] \sin 2\bar{\alpha} - [\bar{\tau}_1(\bar{\tau}_2\nabla)\bar{\tau}_0 + \bar{\tau}_2(\bar{\tau}_1\nabla)\bar{\tau}_0] \cos 2\bar{\alpha} \}, \tag{A1}$$

$$v_{\perp} = \bar{v}_{\perp} + \frac{\bar{v}_{\parallel}^2}{\omega_B} [\bar{\tau}_2(\bar{\tau}_0\nabla)\bar{\tau}_0 \cos \bar{\alpha} - \bar{\tau}_1(\bar{\tau}_0\nabla)\bar{\tau}_0 \sin \bar{\alpha}] + \frac{\bar{v}_{\parallel}\bar{v}_{\perp}}{4\omega_B} \{ [\bar{\tau}_1(\bar{\tau}_2\nabla)\bar{\tau}_0 + \bar{\tau}_2(\bar{\tau}_1\nabla)\bar{\tau}_0] \cos 2\bar{\alpha} - [\bar{\tau}_1(\bar{\tau}_1\nabla)\bar{\tau}_0 - \bar{\tau}_2(\bar{\tau}_2\nabla)\bar{\tau}_0] \sin 2\bar{\alpha} \}, \tag{A2}$$

$$\alpha = \bar{\alpha} - \frac{1}{\omega_B} \left\{ \frac{1}{\bar{v}_{\perp}} [\bar{v}_{\parallel}^2 \bar{\tau}_1(\bar{\tau}_0\nabla)\bar{\tau}_0 - \bar{v}_{\perp}^2 \bar{\tau}_2(\bar{\tau}_2\nabla)\bar{\tau}_1] \cos \bar{\alpha} - \frac{1}{\bar{v}_{\perp}} [\bar{v}_{\perp}^2 \bar{\tau}_1(\bar{\tau}_1\nabla)\bar{\tau}_2 - \bar{v}_{\parallel}^2 \bar{\tau}_2(\bar{\tau}_0\nabla)\bar{\tau}_0] \sin \bar{\alpha} \right\} - \frac{\bar{v}_{\parallel}}{4\omega_B} \{ [\bar{\tau}_1(\bar{\tau}_1\nabla)\bar{\tau}_0 - \bar{\tau}_2(\bar{\tau}_2\nabla)\bar{\tau}_0] \cos 2\bar{\alpha} + [\bar{\tau}_1(\bar{\tau}_2\nabla)\bar{\tau}_0 + \bar{\tau}_2(\bar{\tau}_1\nabla)\bar{\tau}_0] \sin 2\bar{\alpha} \} - \frac{\bar{v}_{\perp}}{\omega_B^2} (\bar{\tau}_1 \cos \bar{\alpha} + \bar{\tau}_2 \sin \bar{\alpha}) \nabla \omega_B, \tag{A3}$$

$$\bar{R}_e = R_0 \bar{e}_R + \bar{r} \bar{\tau}_1 + \frac{\bar{v}_{\perp}}{\omega_B} (\bar{\tau}_1 \sin \bar{\alpha} - \bar{\tau}_2 \cos \bar{\alpha}). \tag{A4}$$

ORCID IDs

 Igor M. Pankratov, <https://orcid.org/0000-0001-5876-4618>;  Volodymyr Y. Bochko, <https://orcid.org/0000-0003-2109-968X>

REFERENCES

- [1] B.N. Breizman, P. Aleynikov, E.M. Hollmann, and M. Lehnen, Nuclear Fusion, **59**, 083001 (2019), <https://doi.org/10.1088/1741-4326/ab1822>
- [2] T.C. Hender, J.C. Wesley, J. Bialek, A. Bondeson, A.H. Boozer, R.J. Buttery, A. Garofalo, et al. Nuclear Fusion, **47**, 128 (2007), <https://doi.org/10.1088/0029-5515/47/6/S03>
- [3] R. Jaspers, N.J. Lopes Cardozo, A.J.H. Donne, H.L.M. Widdershoven, and K.H. Finken, Review Sci. Instruments, **72-II**, 466 (2001), <https://doi.org/10.1063/1.1318245>
- [4] K.H. Finken, J.G. Watkins, D. Rusbuldt, W.J. Corbett, K.H. Dippel, D.M. Goebel, and R.A. Moyer, Nuclear Fusion, **30**, 859 (1990), <https://doi.org/10.1088/0029-5515/30/5/005>
- [5] I.M. Pankratov, Plasma Physics Reports, **22**, 535 (1996), https://www.researchgate.net/profile/Igor-Pankratov/publication/252431545_Analysis_of_the_synchrotron_radiation_emitted_by_runaway_electrons/links/0deec52c98ac368d5c000000/Analysis-of-the-synchrotron-radiation-emitted-by-runaway-electrons.pdf
- [6] L.D. Landau, and E.M. Lifshitz, *The classical theory of fields* (Pergamon press).
- [7] M. Hoppe O. Embréus, R.A. Tinguely, R.S. Granetz, A. Stahl, and T. Fülöp, Nuclear Fusion **58**, 026032 (2018), <https://doi.org/10.1088/1741-4326/aa9abb>
- [8] I.M. Pankratov, Plasma Physics Reports, **25**, 145 (1999), https://inis.iaea.org/search/search.aspx?orig_q=RN:35003886
- [9] R.J. Zhou, I.M. Pankratov, L.Q. Hu, M. Xu, and J.H. Yang, Physics of Plasmas, **21**, 063302 (2014), <https://doi.org/10.1063/1.4881469>
- [10] I. Entrop, R. Jaspers, N.J.L. Cardozo, and K.H. Finken, Plasma Physics and Controlled Fusion, **41**, 377 (1999), <https://doi.org/10.1088/0741-3335/41/3/004>
- [11] J.H. Yu, E.M. Hollmann, N. Commaux, N.W. Eidietis, D.A. Humphreys, A.N. James, T.C. Jernigan, and R.A. Moyer, Physics of Plasmas, **20**, 042113 (2013), <https://doi.org/10.1063/1.4801738>
- [12] C. Paz-Soldan, C.M. Cooper, P. Aleynikov, N.W. Eidietis, A. Lvovskiy, D.C. Pace, D.P. Brennan, E.M. Hollmann, C. Liu, R.A. Moyer, and D. Shiraki, Physics of Plasmas, **25**, 056105 (2018), <https://doi.org/10.1063/1.5024223>
- [13] N.N. Bogoliubov, Y.A. Mitropolsky, *Asymptotic methods in theory of non-linear oscillations* (Gordon and Breach Science Publishers, 1961).

ДОСЛІДЖЕННЯ ФОРМИ ПЛЯМИ СИНХРОТРОННОГО ВИПРОМІНЮВАННЯ ЕЛЕКТРОНІВ-ВТІКАЧІВ В МОДЕЛІ ВИПРОМІНЮВАННЯ СПРЯМОВАНОГО УЗДОВЖ ПОВЕРХНІ КОНУСА ЇХ ШВИДКОСТЕЙ

I.M. Панкратов^{a,b}, В.Ю. Бочко^a

^aХарківський національний університет імені В.Н. Каразіна, м. Свободи 4, 61022 Харків, Україна

^bІнститут фізики плазми, ННЦ "Харківський фізико-технічний інститут"

вул. Академічна 1, 61108 Харків, Україна

Електрони-втікачі – це фундаментальне фізичне явище, а токамак – найбільш просунута концепція магнітного утримання плазми. Енергія електронів-втікачів, які утворюються під час зривів розряду, може досягати десятків мегаелектронвольт, потрапляння яких на конструкційні елементи сучасних великих токамаків і споруджуваного міжнародного токамака-реактора ITER може призвести до катастрофічних наслідків. Внаслідок актуальності, дане явище активно досліджується як теоретично, так і експериментально у провідних термоядерних центрах. Ефективний моніторинг електронів-втікачів є важливою задачею. Діагностика, що базується на синхротронному випромінюванні електронів-втікачів, дозволяє як безпосереднє їх спостереження, так і аналіз параметрів цих електронів, що сприяє безпечній роботі сучасних токамаків та майбутнього токамаку-реактора ITER. В 1990 році дана діагностика показала свою ефективність на токамаці TEXTOR для дослідження радіусу пучка, розташування, кількості та максимальної енергії електронів-втікачів. Ця діагностика встановлена на більшості сучасних токамаків. Параметр $v_{\perp}/|v_{\parallel}|$ виявляє сильний вплив на поведінку синхротронного випромінювання електронів-

втікачів (v_{\parallel} - поздовжня, а v_{\perp} - поперечна швидкість по відношенню до магнітного поля \vec{B}). В статті теоретично вивчається форма плями синхротронного випромінювання електронів-втікачів, коли цей параметр не малий, що відповідає теперішнім експериментам на токамаках. Ураховані особливості руху релятивістського електрона в токамаці. Проаналізовано вплив розташування детектора на спостереження синхротронного випромінювання електронів – втікачів. Аналіз проведено у межах нелінійної моделі поверхні «конуса швидкостей». В цій моделі випромінювання ультрарелятивістських електронів спрямовано уздовж вектору їх швидкості \vec{v} , а вектор швидкості спрямовано уздовж поверхні конуса з віссю паралельній магнітному полю \vec{B} . Раніше випадок малого параметру $v_{\perp}/|v_{\parallel}|$ ($v_{\perp}/|v_{\parallel}| \ll 1$, лінійна модель) розглянуто в статті: Фізика плазми, **22**, 588 (1996), ці теоретичні результати використовуються для аналізу експериментальних даних.

Ключові слова: діагностика електронів-втікачів, ультрарелятивістські електрони, форма плями синхротронного випромінювання, нелінійна модель поверхні конуса швидкостей, безпека роботи токамака.

ENHANCING THE DIFFUSION IN UNDERDAMPED SPACE-PERIODIC SYSTEMS BY APPLYING EXTERNAL LOW-FREQUENCY FIELDS[†]

 Ivan G. Marchenko^{a,b,‡},  Viktoriia Yu. Aksenova^{a,*},  Igor I. Marchenko^{c,#}

^aNational Science Center «Kharkiv Institute for Physics Technology

1 Akademichna St., city of Kharkiv, 61108, Ukraine

^bV.N. Karazin Kharkiv National University

4 Svobody Square, city of Kharkiv, 61022, Ukraine

^cNTU «Kharkiv Polytechnic Institute

2 Kirpicheva St., city of Kharkiv 61002, Ukraine

*Corresponding Author: aksenova@kipt.kharkov.ua

[‡]E-mail: march@kipt.kharkov.ua, [#]E-mail: igor.marchenko@hotmail.com

Received June 11, 2021; revised July 5, 2021; accepted July 28, 2021

This paper is devoted to the studies of the opportunities for the intensification of the particle diffusion in the periodic structures, for example the crystals that are exposed to the action of the time-periodic fields of a different nature. These can be acoustic or electromagnetic fields. The trivial one-dimensional model of the motion of the particles in the potential lattice field under the thermal equilibrium has been used. The paper studies the interaction of rectangular fields with the frequencies less than $0.01 \omega_0$, where ω_0 is the frequency of natural small vibrations of the particles in the systems with the low dissipation. The selected friction coefficient in dimensionless units is equal to $\gamma' = 0.03$. The amplitude dependence of the intensification of the diffusion D under the action of the fields of a different frequency has been studied. It was shown that the diffusion coefficient can be increased by several orders of magnitude by applying the field of an appropriate amplitude and frequency. A maximum diffusion intensification is attained at $\omega \rightarrow 0$. A maximum attained value of the diffusion coefficient at the periodic force corresponds to the case of the action of the constant force. However, at low frequencies a maximum intensification is only possible in the narrow range of field amplitudes $F' \propto \gamma'$. A further increase in the field amplitude results in a decrease of the diffusion coefficient and it attains the value of the coefficient of the particle diffusion in the viscous medium $D_{vis} = k'T' / \gamma'$, where k' is the Boltzmann coefficient and T' is the temperature. An increase in the frequency of the external force results in the extension of the range of forces at which $D > D_{vis}$, however the value of the diffusion intensification is decreased. It was shown that the exceed of a certain threshold value of the amplitude of the external field results in the gain of the diffusion coefficient at least by the value of $\eta = (k'T' e^{\varepsilon/k'T'}) / (\gamma'D_0)$, where ε is the value of the energy barrier during the passage of the particle from one cell of the one-dimensional lattice to another. The obtained data open prospects for the development of new technologies to exercise control over diffusion processes. It is of great importance for the production of nanomaterials with the specified structure, creation of the surface nanostructures, etc.

Keywords: Brownian motion, computer simulation, crystals, diffusion, Langevin equations, periodic fields, periodic systems.

PACS: 05.40.-a, 02.50.Ey, 68.43.Jk, 66.30.J-

The process of the creation of the appropriate micro- and nanostructure of the materials is reduced in many respects to the finding of an opportunity for the control over diffusion processes [1]. Up to this day, the temperature was the main parameter of such a control. The diffusion is intensified with an increase in temperature and it results in the activation of other thermal processes. From the standpoint of the technology, it is important to know how to control the diffusion of the certain types of defects or atoms without changing the medium temperature. The application of the external fields of a different nature can solve this problem on the whole.

The latest experimental investigations are indicative of that the diffusion mobility can efficiently be controlled using external fields. A huge increase in the diffusion was observed during the investigations carried out to study the motion of paramagnetic particles across the surface of garnet ferrites exposed to the action of external time-periodic magnetic fields [2]. The intensification of the diffusivity by several orders of magnitude was observed when studying the particle diffusion in the colloids with optical traps [3]. However, the physical basics of such diffusion intensification are still not very clear.

Earlier, the diffusion intensification carried out by using theoretical methods was mainly studied under the action of constant force. It was established that the diffusion mobility of the particles can essentially be increased under the action of the force both in underdamped [4] and overdamped systems [5]. It was shown in [6] that the particle diffusion coefficient can be increased in the periodic lattice by many orders of magnitude under the action of the constant external force in the narrow force range specified by the dissipative properties of the medium. The paper [7] gives analytical expressions to compute the gaining in the diffusion coefficient depending on the friction coefficient for underdamped systems. The paper [8] gives the plotted diagram of the existence of the domains that allow for the efficient control of

[†]Cite as: I.G. Marchenko, V.Yu. Aksenova, I.I. Marchenko, East. Eur. J. Phys. 3, 25 (2021), <https://doi.org/10.26565/2312-4334-2021-3-03>

the diffusion by external constant fields. It was shown that the phenomenon of the so-called temperature-abnormal diffusion (TAD) is realized in such domains. In the case of the TAD, the diffusion coefficient is increased with the temperature drop. At first glimpse, it runs counter to our intuitive notions of diffusion processes. However, it should be noted that such a phenomenon is realized only in the systems that are far from the equilibrium.

As a rule, it is a rather complicated task to realize the conditions for the action of the constant force on a technological level. In practice, it is more promising to apply time-varying fields. Acoustic or electromagnetic fields can be used for such purpose. The authors of [9] showed that the applied periodic field can have a great effect on the diffusion coefficient in the overdamped system. The paper [10] studied diffusion processes under the action of periodic fields in underdamped systems. It was shown that considerable diffusion intensification occurs at much lower vibration amplitudes of the external field in comparison to the overdamped case. Only narrow range of the amplitudes of the periodic force was studied near a maximum value of the coefficient gain at a constant force. However, a change in the diffusion coefficient in the wide amplitude range was not studied. The main purpose of this research was to study the amplitude dependences of the diffusion intensification under the action of the external low-frequency periodic fields.

SIMULATION METHODS

The motion of Brownian particles on the one-dimensional lattice under the action of the time-periodic force $F(t)$ was described by the Langevin equation:

$$m \ddot{x} = -\frac{\partial}{\partial x} U(x) - \gamma \dot{x} + F_t(t) + \sqrt{2\gamma Q} \xi(t), \quad (1)$$

where t is the time, x is the particle coordinate, m is its mass, γ is the friction coefficient, $\xi(t)$ is the white Gaussian noise with the intensity set to unity. The point above denotes the differentiation in time. The thermal energy is $Q = kT$, where k is the Boltzmann constant and T is the temperature.

To look into physical causes for the intensified diffusion under the action of the periodic force we will consider by analogy to [10] the particle motion under the action of the rectangular periodic field.

$$F_t(t) = F \text{sign}(\sin(\omega t)) \quad (2)$$

Where ω is the angular frequency of the external force and F is its amplitude.

The given type of the external field has an advantage over the sinusoidal field from the standpoint of the simplicity of the interpretation of physical results, because under such action the particle ensemble moves in the fixed potential at each half-period. It considerably simplifies the analysis of the obtained data. The use of the sinusoidal dependence, as it was shown in [10], has no effect on the main physical results that remain unchanged and it only varies the obtained numerical values.

The potential particle energy of U in the one-dimensional lattice was equal to:

$$U(x) = -\frac{U_0}{2} \cos\left(\frac{2\pi}{a} x\right), \quad (3)$$

where a is the one-dimensional lattice period, and U_0 is the potential barrier height.

The moving particle is exposed to the action of the periodic force exerted by the lattice F_{lat} :

$$F_{lat} = -\frac{\partial U}{\partial x} = F_0 \sin\left(\frac{2\pi}{a} x\right). \quad (4)$$

The value of $F_0 = \frac{\pi}{a} U_0$ that is called a critical force corresponds to a minimum acting force required for the overcoming of the energy barrier in the viscous medium and that energy barrier separates two neighboring positions of the particles on the one-dimensional lattice.

The parameters of the used space-periodic potential were similar to those described in [6-8], i.e. $U_0 = 0,08$ eV, $a = 2,0$ Å. The particle mass corresponded to the hydrogen mass and it was equal to 1 atomic mass unit.

The stochastic equation (1) was solved numerically for each particle with the time step less than 0.01 of the natural period of vibrations $\tau_0 = a(2m/U_0)^{1/2}$. The statistical averaging was carried out in terms of the ensemble with the particle number of at least $N = 5 \cdot 10^4$. The initial conditions were the same as in [6-8].

To analyze the simulation data it is convenient to change to non-dimensional values [11-12].

After the transformation of

$$x' = \frac{2\pi}{a} x, \quad t' = \frac{t}{\tau_0} \quad (5)$$

and assuming that the non-dimensional mass $m = 1$, we will obtain a maximum simple equation form (1):

$$\ddot{x}' = -\sin x' - \gamma' x' + F'(t') + \sqrt{2\gamma'T'}\zeta(t'), \tag{6}$$

Non-dimensional units are relating to the force, friction coefficient and the temperature as follows:

$$\gamma' = \gamma \frac{\tau_0}{2\pi m}, \quad F' = \frac{F}{F_0}, \quad T' = \frac{2kT}{U_0}. \tag{7}$$

The value of $\gamma' \approx 0.032$ for the given investigation was the same as in the case of previous investigations [6-8]. The diffusion coefficient was calculated in terms of the dispersion $\sigma^2 = \langle (x' - \langle x' \rangle)^2 \rangle$ for the moving particle ensemble distribution when the time tends to the infinity:

$$D = \lim_{t \rightarrow \infty} \frac{\sigma^2}{2t}, \tag{8}$$

where the brackets $\langle \dots \rangle$ denote the ensemble averaging.

To improve the computation accuracy at the limited time the diffusion coefficient was calculated in the following manner. Each computation anticipated the determination of the time t_{lin} required for the attainment of the linear dispersion-time dependence. The one-dimensional lattice diffusion coefficient was defined as $1/2$ of the curve slope $\sigma^2(t)$. The linear dependence was obtained by the simulation data diddling using the method of least squares at the time of $t > 100t_{lin}$. The diddling reliability was within 0.999 in all cases.

THE OBTAINED RESULTS AND DISCUSSION

Let's consider a change in the diffusion mobility of the particles under the external periodic force. To clarify the gain rate of the diffusion coefficient we calculated first the diffusion coefficients of the particles $D_{lat}(T')$ in the absence of the external force. In Fig. 1, the dependence of $D_{lat}(T')$ is represented by hollow markers. It has the form of the Arrhenius curve that is peculiar for crystalline materials $D_{lat}(T') = D_0 e^{-\varepsilon/kT'}$, where ε is the value of the energy barrier when the particle passes from one cell of the one-dimensional lattice to another. And the diffusion coefficient of free particles is exponentially decreased with an increase in the reciprocal temperature.

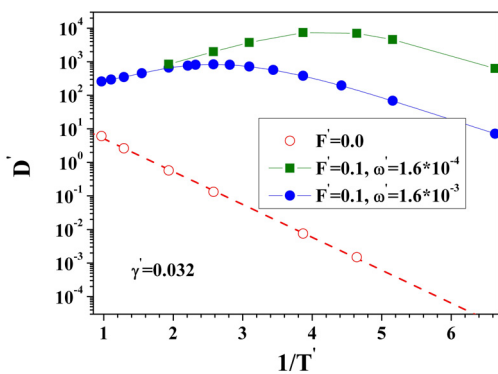


Figure 1. The dependences of diffusion coefficients on the reciprocal temperature. Empty markers denote the external force $F' = 0.0$, filled markers denote the external periodic force $F' = 0.1$ (it corresponds to a maximum diffusion coefficient at a constant force), The friction coefficient is $\gamma' = 3 \cdot 10^{-2}$. Square markers represent the frequency $\omega' = 10^{-4}$, circles indicate the frequency $\omega' = 10^{-3}$.

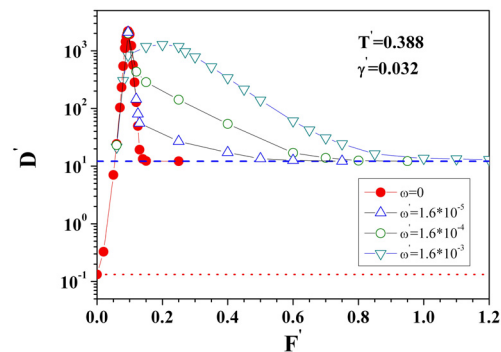


Figure 2. The dependences of diffusion coefficients on the vibration amplitude of the external periodic force F' for different frequencies of ω' . The dotted line shows the value of the diffusion coefficient in the periodic lattice in the absence of the external force. The dashed line shows the value of the diffusion coefficient in the viscous unstructured medium. $T' = 0.388$, $\gamma' = 3 \cdot 10^{-2}$.

The use of the external constant field ($\omega' = 0$) results in the enhanced diffusion mobility of the particles. This gain rate depends to a great extent on the value of external force. In Fig. 2, the filled markers show the dependence of the diffusion coefficient on the value of applied force at a constant temperature of the thermostat. The dotted line in this Figure shows the value of the diffusion coefficient D_{lat} of the particles in the one-dimensional lattice in the absence of

the external force. The dashed line in this Figure shows the value of the diffusion coefficient in the viscous medium of $D_{vis} = k'T'/\gamma'$ in the absence of external forces. It can be seen that the diffusion rises sharply in the narrow range of applied forces. A maximum value of D' is attained at $F' \approx 0.1$. Fig. 1 gives the temperature dependences of the diffusion coefficient of the particles at the same force amplitude value for the two different frequencies. The Figure shows that the application of external periodic field also increases the diffusion mobility of the particles by several orders of magnitude in the wide temperature range. Moreover, the diffusion coefficient is increased in the specified temperature range with the temperature drop. It is the range of the so-called temperature – abnormal diffusion. By decreasing the external force frequency we extend this temperature range. In other words, by changing the external force frequency we can efficiently control the diffusion coefficient at the given temperature.

Let's consider in detail a change in the dependence of the diffusion coefficient on the amplitude of external vibrations for different frequencies of the external force. Fig. 2 shows such dependencies for the fixed temperature of $T' = 0.388$. It can be seen that for the frequency range in question, D' is always increased from the value of D_{lat} , attaining a certain maximum value of D_{max} , and then it drops to the value of D_{vis} . A further increase in the amplitude results in no change of the diffusion coefficient. It means that in the case of exceed of a certain critical amplitude value

we observe the gain in the diffusion coefficient as a minimum by the value of $\eta = D_{vis} / D_{lat} = \frac{k'T'e^{\varepsilon/k'T'}}{\gamma'D_0}$.

The highest diffusion intensification is observed at low frequencies. At the frequency of $\omega' = 1.6 \cdot 10^{-5}$, the curve of $D'(F'; \omega')$ coincides with the curve of a change in the diffusion coefficient under the action of the static force $F' \leq 0.13$. It is well-known [12] that the so-called running and locked solutions can exist simultaneously in underdamped periodic systems. It was shown earlier [13] that an increase in the diffusion coefficient under the action of the constant force occurs due to the appearance of the localized and moving particles in the ensemble of the “populations” particles under the action of the thermal noise. The solution of equation (1) with no random force showed that running stationary solutions are unavailable in studied frequency and amplitude ranges. At each half-period, the particles change to the moving state and make long jumps. Afterwards, these are returned to the localized state and begin their motion from new nodes. As a matter of fact, the diffusion is intensified.

A specific feature of the low-frequency vibrations of a low amplitude is that the particle velocity distributions of $n(V')$ coincide during the half-period for constant and periodic forces. Therefore, at low frequencies ($\omega' = 1.6 \cdot 10^{-5}$) up to the values of $F' \approx 0.13$ the curve of $D'(F')$ coincides with the curve for the case of $\omega = 0$. At high amplitude values, the diffusion coefficient scarcely differs from D_{vis} . The increase in the frequency up to the value of $\omega' = 1.6 \cdot 10^{-4}$ provides a noticeable difference of the diffusion coefficient in contrast to $D'(F'; \omega = 0)$ at $F' > 0.12$. At the frequencies above $\omega' > 1.6 \cdot 10^{-3}$ the diffusion coefficient of $D(\omega)$ fails to attain the value of D_{max} and it considerably differs from $D'(F'; 0)$. In other words, a certain specific frequency range exists and it permits maximum diffusion intensification by varying the amplitude of external vibrations. At the same time, the amplitude range in which $D'(\omega') > D_{vis}$ is extended with an increase in frequency. In this case, the curve maximum $D'(F'; \omega)$ is shifted towards the range of higher amplitudes.

Hence, we showed that the action of the periodic field always results in the enhancement of diffusion processes. A maximum intensification is observed at low frequencies in the narrow amplitude range. An increase in the frequency extends the intensified diffusion domain. It is related to the fact that the diffusion intensification mechanism differs in the case of constant and periodic fields. In the case of the constant field, the diffusion coefficient is defined by the stationary particle distribution between the two ensembles, in particular, the “running” and “localized” states. In the case of the action of the periodic field throughout the period the particle velocity distribution function is changed all the time [14].

CONCLUSIONS

This paper delves into the studies of the intensification of the particle diffusion in the one-dimensional space lattice exposed to the action of the external low-frequency time-periodic fields. It was shown that the diffusion coefficient can be increased by several orders of magnitude by applying the field of an appropriate amplitude and frequency. A maximum diffusion intensification is observed at $\omega \rightarrow 0$. For the studied frequency range we can state that the diffusion coefficient tends to the diffusion coefficient in the viscous medium at increased force amplitudes. The obtained data open prospects for the development of new technologies to exercise control over diffusion processes. It is of great importance for the production of nanomaterials with the specified structure, creation of the surface nanostructures, etc.

ORCID IDs

 Ivan G. Marchenko, <https://orcid.org/0000-0003-4231-7463>;  Viktoriia Yu. Aksenova, <https://orcid.org/0000-0003-4231-7463>;
 Igor I. Marchenko, <https://orcid.org/0000-0002-3071-9169>

REFERENCES

- [1] H.J. Frost, M. F. Ashby, *Deformation-mechanism maps: the plasticity and creep of metals and ceramics* (Pergamon press, Oxford, 1982) p. 165.
- [2] P. Tierno, T. Reimann, H. Johansen, and F. Sagués, *Phys. Rev. Lett.* **105**, 230602 (2010), <https://journals.aps.org/prl/abstract/10.1103/PhysRevLett.105.230602>
- [3] S.H. Lee, and D. G. Grier, *Phys. Rev. Lett.* **96**, 190601 (2006), <https://journals.aps.org/prl/abstract/10.1103/PhysRevLett.96.190601>
- [4] G. Costantini, and F. Marchesoni, *Europhys. Lett.* **48**, 491 (1999), <https://doi.org/10.1209/epl/i1999-00510-7>
- [5] P. Reimann, C. Van den Broeck, H. Linke, P. Hänggi, J.M. Rubí, and A. Pérez-Madrid, *Phys. Rev.* **E65**, 031104 (2002), <https://doi.org/10.1103/PhysRevE.65.031104>
- [6] I.G. Marchenko, and I.I. Marchenko, *Europhys. Lett.* **100**, 5005 (2012), <https://doi.org/10.1134/S0021364012030083>
- [7] I.G. Marchenko, I.I. Marchenko, and V.I. Tkachenko, *JETP Letters* **106**(4), 242 (2017), <https://doi.org/10.1134/S002136401716010X>
- [8] I.G. Marchenko, I.I. Marchenko, and V.I. Tkachenko, *JETP Letters* **109**(1), 671 (2019), <https://doi.org/10.1134/S0021364019100126>
- [9] D. Speer, R. Eichhorn, and P. Reimann, *Europhys. Lett.* **97**, 60004 (2012), <https://iopscience.iop.org/article/10.1209/0295-5075/97/60004>
- [10] I.G. Marchenko, I.I. Marchenko, and A.V. Zhiglo, *Phys. Rev.* **E97**, 012121 (2018), <https://doi.org/10.1103/PhysRevE.97.012121>
- [11] J. Spiechowicz, and J. Luczka, *Phys. Rev.* **E101**, 032123 (2020), <https://doi.org/10.1103/PhysRevE.101.032123>
- [12] H. Risken, *The Fokker-Planck Equation and Methods of Solution and Applications* (Springer, 1989), pp. 485, <https://doi.org/10.1007/978-3-642-61544-3>
- [13] I.G. Marchenko, I.I. Marchenko, and A.V. Zhiglo, *Europ. Phys.* **B87**, 10 (2014), <https://doi.org/10.1140/epjb/e2013-40866-7>
- [14] I.G. Marchenko, and I.I. Marchenko, *JETP Letters*, **95**(3), 137 (2012), <https://doi.org/10.1134/S0021364012030083>

**ПОСИЛЕННЯ ДИФУЗІЇ В НЕДОДЕМПФОВАНИХ ПРОСТОРОВО-ПЕРІОДИЧНИХ СИСТЕМАХ
ЗОВНІШНІМИ НИЗЬКОЧАСТОТНИМИ ПОЛЯМИ**

І.Г. Марченко^{a,b}, В.Ю. Аксенова^a, І.І. Марченко^c

^aНаціональний науковий центр «Харківський фізико-технічний інститут»
бул. Академічна, 1 м. Харків, Україна, 61108

^bХарківський національний університет імені В.Н. Каразіна
м. Свободи, 4 м. Харків, Україна, 61022

^cНТУ «Харківський політехнічний інститут»
бул. Кирпичова, 2, м. Харків, Україна, 61002

Робота присвячена дослідженню можливості посилення дифузії частинок в періодичних структурах, таких як кристали, за допомогою впливу на них зовнішніми періодичними в часі полями різної природи. В якості таких можуть виступати акустичні або електромагнітні поля. Використана найпростіша одномірна модель руху частинок, що знаходяться в потенційному полі решітки та в тепловій рівновазі з термостатом. В роботі вивчено вплив прямокутного поля з частотами менше $0.01 \omega_0$, де ω_0 – частота власних малих коливань частинок у системах із малою дисипацією. Обраний коефіцієнт тертя в безрозмірних одиницях дорівнював $\gamma' = 0.03$. Вивчена амплітудна залежність посилення дифузії D під впливом полів різної частоти. Показано, що коефіцієнт дифузії може бути посилений на кілька порядків із застосуванням поля відповідної амплітуди і частоти. Найбільше посилення дифузії досягається при $\omega \rightarrow 0$. Максимально досяжене значення коефіцієнта дифузії при періодичному впливі відповідає випадку впливу постійної сили. Однак при низьких частотах максимальне посилення можливо тільки у вузькому діапазоні амплітуд поля $F' \propto \gamma'$. При подальшому збільшенні амплітуди поля коефіцієнт дифузії зменшується та досягає величини коефіцієнта дифузії частинок у в'язкому середовищі $D_{vis} = k'T'/\gamma'$, де k' – коефіцієнт Больцмана, а T' – температура. Збільшення частоти зовнішнього впливу призводить до розширення інтервалу сил, при яких $D > D_{vis}$, однак величина посилення дифузії зменшується. Показано, що при перевищенні деякого порогового значення амплітуди зовнішнього поля спостерігається посилення коефіцієнта дифузії як мінімум на значення $\eta = (k'T' e^{\varepsilon/k'T'}) / (\gamma' D_0)$, де ε – величина енергетичного бар'єра при переході частинки з однієї комірки одновимірної решітки в іншу. Отримані результати відкривають перспективи створення нових технологій управління процесами дифузії. Це має велике значення для отримання наноматеріалів із заданою структурою, створення поверхневих наноструктур і т.п.

Ключові слова: броунівський рух, дифузія, комп'ютерне моделювання, кристали, періодичні поля, рівняння Ланжевена.

SPUTTERING OF OXIDES FROM LaNi_5 SURFACE[†]

✉ Viktor A. Litvinov, ✉ Ivan I. Okseniuk, ✉ Dmitriy I. Shevchenko, ✉ Valentin V. Bobkov*

*V.N. Karazin Kharkiv National University**4 Svobody Sq., Kharkiv 61022, Ukraine***Corresponding Author: bobkov@karazin.ua, tel. +380-50-641-23-71*

Received May 31, 2021; revised September 21, 2021; accepted September 23, 2021

The changes in chemical composition of the intermetallic alloy LaNi_5 surface monolayers were studied using secondary ion mass spectrometry (SIMS) in the process of the alloy interaction with oxygen. The investigated samples were pellets made by pressing the fine-grained LaNi_5 alloy. Ar^+ ions having energies of 10-18 keV were used as primary ions. The primary beam current density was 9-17 $\mu\text{A}\cdot\text{cm}^{-2}$, which corresponds to the dynamic SIMS mode. The emission intensities of secondary ions were measured within the dynamic range of at least 6 orders of magnitude. Before the measurements, the samples were annealed in residual vacuum at a temperature of ~ 1000 K. After the annealing, the sample surface was cleaned using the primary ion beam until the mass-spectrum composition and secondary ion emission intensity stabilized completely. The gas phase composition was monitored using a gas mass spectrometer. The conducted studies showed that a complex chemical structure including oxygen, lanthanum and nickel is formed on the surface and in the near-surface region of LaNi_5 as a result of its exposure to oxygen. Oxygen forms strong chemical bonds in such a structure with both components of the alloy. This is evidenced by the presence of a large set of oxygen containing emissions of positive and negative secondary ions with lanthanum, with nickel, and oxygen containing lanthanum-nickel cluster secondary ions in mass spectra. The resulting oxide compounds have a bulk structure and occupy dozens of monolayers. In such a bulk oxide structure, the outer monolayers are characterized by the highest ratio of oxygen atom number to the number of matrix atoms. This ratio decreases along the transition from surface to the underlying monolayers. This process occurs uniformly, without any phase transformation. The observed secondary ions are not a product of association between sputtered surface fragments and oxygen in the gas phase at the fly-off stage after sputter-ejection, but they are products of the oxide compounds being sputtered, hence they characterize the composition of surface and near-surface region.

Keywords: SIMS, LaNi_5 intermetallic alloy, oxygen, surface, oxides.**PACS:** 34.35.+a, 79.20.Rf, 88.30.

LaNi_5 intermetallic alloy is of great importance among other hydrogen storage materials for a number of technical applications. It is used in systems for stationary accumulation and transport of hydrogen, for thermosorption compression, catalysis, hydrogen purification, separation of its isotopes, as well as in fuel cells. The alloy has a high hydrogen capacity, high cyclic stability and can be activated or reactivated easily. LaNi_5 alloy is able to absorb and release a large amount of hydrogen at near room temperatures and relatively low pressures [1-3]. The hydride phase $\text{LaNi}_5\text{H}_{6.7}$ contains 1.4-wt. % hydrogen. The enthalpy of hydride formation is 15.7 kJ/mol·H, the enthalpy of decomposition is 15.1 kJ/mol·H [4].

It is well known that one of the main problems of most hydride-forming alloys limiting their practical application is their susceptibility to surface contamination by reactive gases like oxygen. Oxygen on the surface of the alloys produces a reactive effect, i.e., it initiates a chemical reaction that results in volumetric corrosion of the alloy and, as a result, irreversible reduction of the hydrogen capacity. The high activation energy between the physisorption and chemisorption states of hydrogen on the oxidized surface prevents dissociative chemisorption and associative desorption. Molecular hydrogen cannot penetrate the oxide surface layer to dissociate on the metal surface below the oxide. On the other hand, dissolved hydrogen cannot leave the surface because associative desorption is prevented [5]. Even low oxygen concentrations in hydrogen gas can cause problems with repeated cycling of an alloy [6].

These problems, in principle, are also relevant for the intermetallic LaNi_5 alloy, but unlike most hydride-forming alloys, LaNi_5 is relatively resistant to oxygen impurities in hydrogen. Traces of oxygen, which are always present in varying amounts in hydrogen, do not catastrophically poison the active surface of LaNi_5 when multiple cycles of hydrogen absorption-desorption are performed. During the first few cycles, oxygen absorption-desorption does have a poisoning effect on LaNi_5 , but as cycling continues in hydrogen with oxygen admixture, the kinetics and hydrogen capacity are substantially restored. After this initial transition period, oxygen becomes a classical reactant, i.e., it produces a reactive effect and slowly converts lanthanum atoms into La_2O_3 or various lanthanum hydrates or hydroxides [7-11].

The specific effect of oxygen on LaNi_5 is explained by a number of authors as follows. Lanthanum diffuses to the surface in the surface layer of a freshly prepared LaNi_5 sample since the surface energy of lanthanum is lower than that of nickel; the surface is enriched with lanthanum, achieving thermodynamic equilibrium state [12, 13]. Given that there is some preferential oxidation of lanthanum over nickel, the interaction with oxygen produces La_2O_3 or $\text{La}(\text{OH})_3$. Some surface nickel is also thought to be oxidized. The resulting complex oxides are disproportionated by surface diffusion,

[†] **Cite as:** V.A. Litvinov, I.I. Okseniuk, D.I. Shevchenko, and V.V. Bobkov. East. Eur. J. Phys. 3, 30 (2021), <https://doi.org/10.26565/2312-4334-2021-3-04>

resulting in the formation of composite films of nickel clusters within the stable lanthanum oxide or hydroxide [11]. Such clusters are catalytically active. Metallic nickel catalyzes hydrogen dissociation being the first stage of the hydrogen absorption process. Segregation and reduction of Ni occurs in each hydrogenation cycle. This process represents the mechanism of LaNi₅ active surface self-regeneration. Thus, according to the above, oxygen causes the separation of the alloy components into lanthanum oxidation products (oxides or hydroxides) and nickel clusters.

A somewhat different picture is given in papers [14-16]. According to these authors, exposure of LaNi₅ to oxygen leads to complete oxidation of surface lanthanum to La₂O₃. All the nickel present on the surface is also oxidized. Its oxides consist of NiO, Ni(OH)₂, and Ni₂O₃, but the latter two components exist only in a few upper monolayers. The La₂O₃ layer extends to a greater depth than the NiO layer. The latter is present only as thin oxide layers. Thus, it is believed that the NiO oxide is distributed over the La₂O₃ surface and essentially behaves as a system on a metal carrier, which has a higher catalytic activity towards hydrogen.

It was also shown in [17, 18] that although lanthanum oxidizes quite rapidly when exposed to oxygen, nickel oxide is present in the first few surface monolayers along with lanthanum oxide. The authors believe that the lanthanum-rich oxide layer is important not because it provides large nickel clusters on the surface, but rather because it protects the underlying material, i.e., the LaNi₅ itself. In [19] it was shown that when LaNi₅ is exposed to oxygen, only the lanthanum atoms are oxidized, not the nickel atoms. Nickel segregation occurs in each hydrogen sorption-desorption cycle. The lanthanum in this model actually serves as a gas absorber that provides the formation of pure nickel clusters.

Thus, the above hypotheses indicate that at present there is no consensus on the processes and results of interaction between oxygen with the LaNi₅ intermetallic alloy surface. There is no consensus on how the alloy components react to the presence of oxygen and which chemical compounds are in fact formed on the surface. This fact gives grounds for further research.

The purpose of this work is to study the chemical composition of surface monolayers of LaNi₅ intermetallic alloy during interaction with oxygen as well as to study the change in this composition depending on oxygen pressure and on the depth of oxygen location by using the secondary ion mass spectrometry method.

RESEARCH METHODS

The chemical composition of the alloy surface, as well as the change in this composition depending on the experimental conditions, was studied using the secondary ion mass spectrometry method. This method makes it possible to directly detect hydrogen and its compounds, as well as to study the changes in the composition of such compounds depending on the experimental conditions.

The samples under study were pellets pressed from moderately fine-grained (less than 1 mm) LaNi₅ alloy. Ar⁺ ions with energies of 10 keV in the analysis of positive ions and 18 keV in the analysis of negative secondary ions were used as primary ions. The primary beam current density and vacuum conditions corresponded to the SIMS dynamic mode. The experimental setup was equipped with an energy filter for secondary ions, which allowed measuring the emission intensities of only low-energy secondary ions that mostly characterized the presence and composition of chemical compounds on the surface under study. The emission intensities of secondary ions were measured within the dynamic range of at least 6 orders of magnitude. The samples were annealed before the measurements in a residual vacuum at a temperature of ~ 1000 K in order to partially clean the surface from chemical compounds that are either desorbed or dissolved into the volume of the material during annealing. After the annealing, the sample surface was cleaned using the primary ion beam until the mass-spectrum composition and secondary ion emission intensity stabilized completely. The composition of the gas phase was monitored using a gas mass spectrometer, which also was used for measuring small partial pressures of gases in the vacuum chamber after the necessary calibrations had been performed. In the cases when the multi-atomic secondary ion emissions are complexly overlapped by their mass numbers, their specific contributions were separated according to the usual procedure, taking into account the natural distribution of isotopes. The temperature of the alloy sample during the measurements, including studies of oxygen interaction with the alloy, was ~ 325 K.

EXPERIMENTAL RESULTS

After the annealing and cleaning of the sample with the primary beam, the mass spectra of both positive and negative secondary ions were measured. The analysis of the spectra showed that they contain numerous emissions of atomic and cluster ions of the alloy components. There are also emissions of ions that indicate the interaction between the alloy atoms on the surface with the gas phase and bulk impurities, i.e., emissions corresponding to compounds of lanthanum and nickel with hydrogen, oxygen, and carbon. This indicates that even after annealing and primary beam cleaning there are some chemical compounds which include hydrides, oxides, hydroxides and carbides on the surface of the samples studied. Similar results regarding the mass spectra composition of secondary ions sputtered from the LaNi₅ surface are given in [20-22].

In the further experiments, the mass spectra of positive and negative secondary ions at elevated oxygen partial pressures of $6.6 \cdot 10^{-7}$ to $8.8 \cdot 10^{-4}$ Pa and residual hydrogen partial pressure were measured. Such mass spectra contain a large set of oxygen-containing emissions of positive and negative secondary ions. Emissions of oxygen-containing ions, which include lanthanum atoms, were the most intensive in the positive ion spectra. In the spectra of negative ions, there

was a large set of oxygen-containing ion emissions, which included nickel atoms. There were also a large number of oxygen-containing emissions of complex secondary ions that include lanthanum, nickel, and oxygen atoms with various atomic ratios. In spite of the fact that the residual partial pressure of hydrogen in the sample chamber during the experiments is $4\text{-}5 \cdot 10^{-6}$ Pa, there was emission of hydroxide ions in the spectra, along with the emission of corresponding oxide ions.

We also measured the dependences of the emissions intensities for a number of oxygen-containing secondary ions on the oxygen partial pressure in the sample chamber at the residual hydrogen partial pressure. The positive secondary ion spectra were measured at the primary beam current density of $9 \mu\text{A}\cdot\text{cm}^{-2}$ and the negative secondary ion spectra were measured at the primary beam current density of $17 \mu\text{A}\cdot\text{cm}^{-2}$. Figures 1a, 2a, 3a, 4a show examples of the most characteristic intensity dependences on oxygen partial pressure measured for some positive and negative oxygen-containing secondary ions with lanthanum and nickel, as well as for some intermetallic lanthanum-nickel ions.

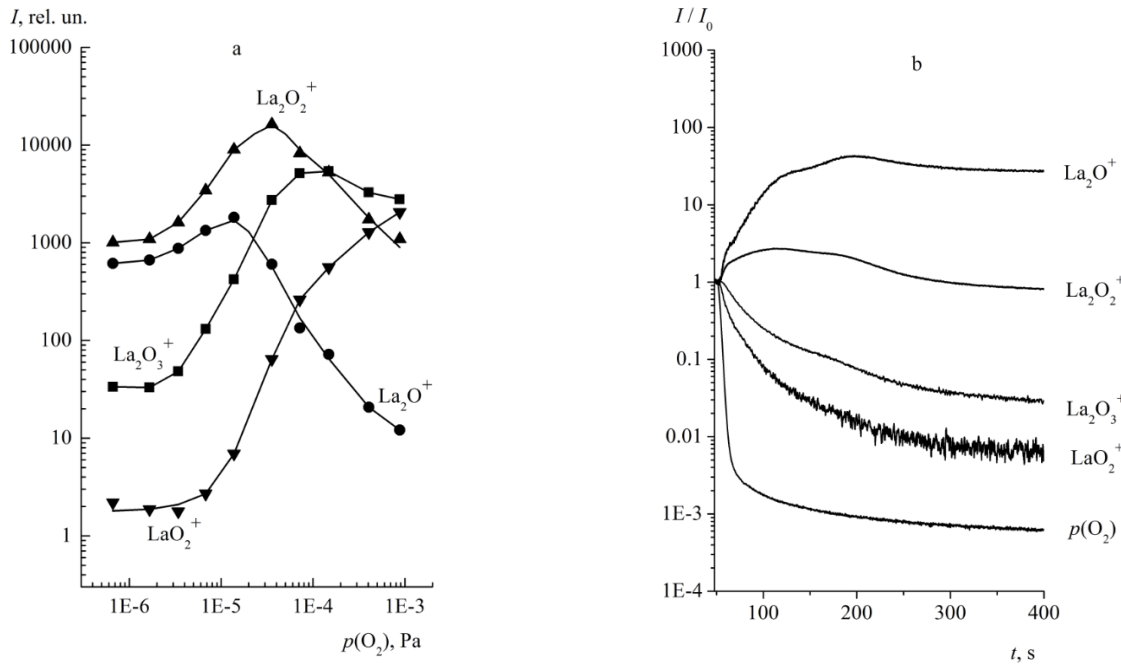


Figure 1. a: Dependences of the emission intensities of positive secondary ions with two lanthanum atoms on the oxygen partial pressure; b: Dependences of the emission intensities of positive secondary ions with lanthanum on sputtering time after the exposure in oxygen.

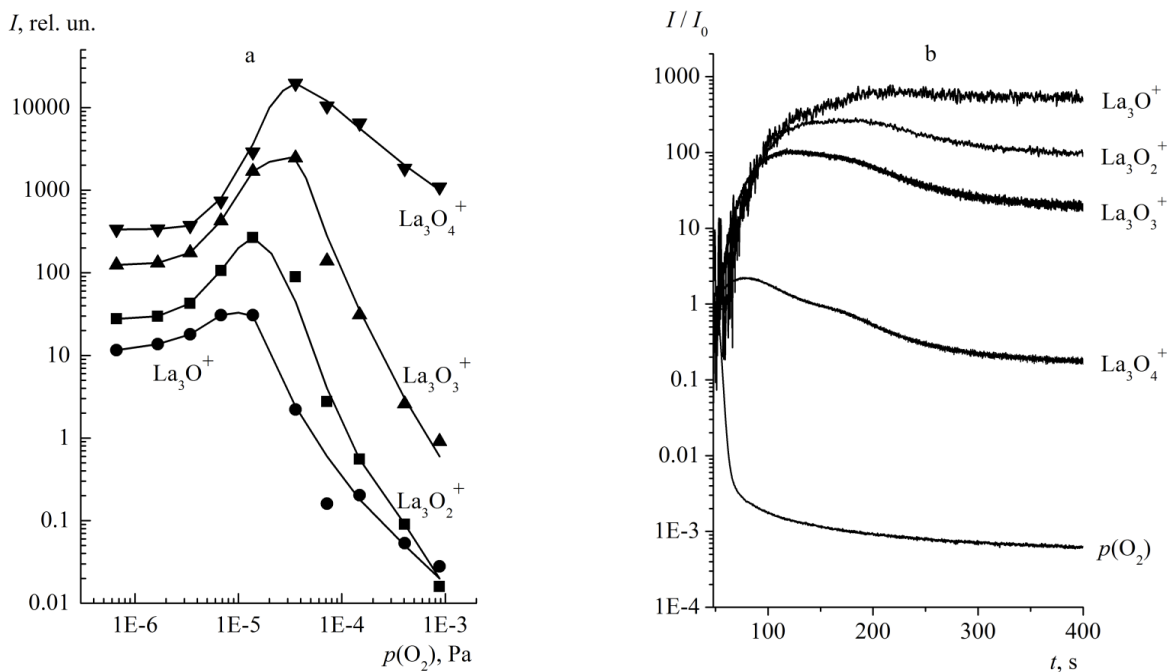


Figure 2. a: Dependences of emission intensities of positive secondary ions with three lanthanum atoms on oxygen partial pressure; b: Dependences of emission intensities of positive secondary ions with lanthanum on sputtering time after the exposure in oxygen.

As a continuation of studying the interaction between LaNi_5 and oxygen, the experiments were conducted to obtain the dependences of the emission intensities for previously studied secondary ions on the sputtering time after the sample exposure to oxygen. An oxide structure, which, as noted above, is characterized by a set of oxygen-containing secondary ions and by the ratio of their emission intensities, was formed on the sample surface at the increased oxygen partial pressure. This structure was then sputtered by the primary beam. As the sputtering proceeded, changes in the emission intensities of the selected secondary ions were recorded.

These experiments were carried out as follows. After the surface of the sample was cleaned by the primary beam in a residual vacuum with continuous recording of the selected ion emission intensity, oxygen was injected into the chamber up to a pressure of $\sim 3.3 \cdot 10^{-4}$ Pa. After 46-48 seconds, the oxygen inlet was shut off and then the time dependences of the secondary ion emission intensity and oxygen pressure in the sample chamber were measured. The oxygen pressure was recorded using a gas mass spectrometer. Fig. 1b, 2b, 3b show the measurement results at the sputtering stage after shutting off the oxygen inlet for oxygen-containing positive ions with lanthanum and for negative ions with nickel. For comparison convenience, the real emission intensities in these figures are divided by the intensity at the time point corresponding to the oxygen shutting off. Thus, the curves in Figs. 1b, 2b, 3b show how many times the emission intensity changes during the sputtering time with respect to the starting point. The same figures show the dependences of the oxygen partial pressure in the chamber also normalized to their initial value.

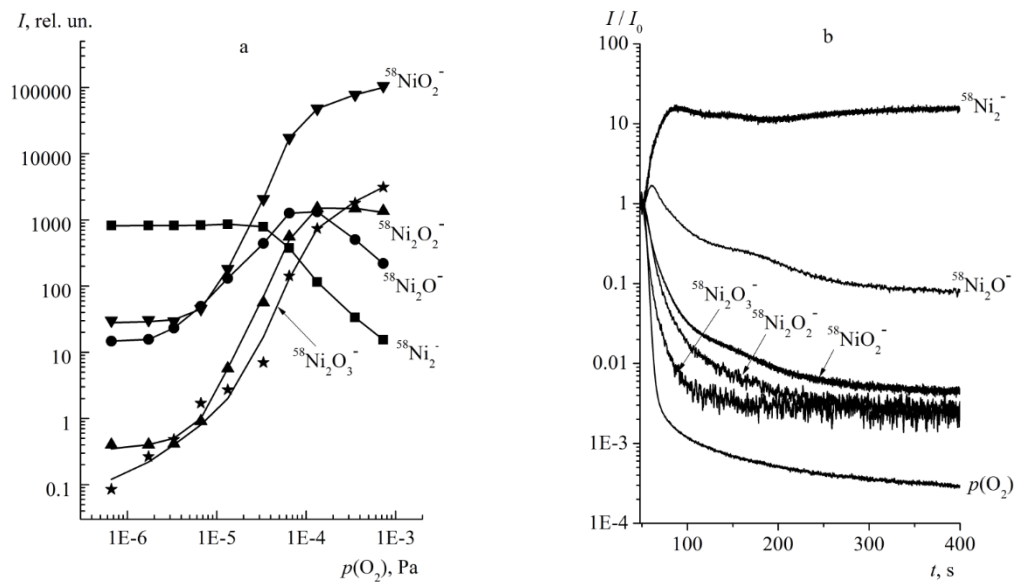


Figure 3. a: Dependences of emission intensities of negative secondary ions with nickel on oxygen partial pressure; b: Dependences of emission intensities of negative secondary ions with nickel on sputtering time after the exposure in oxygen.

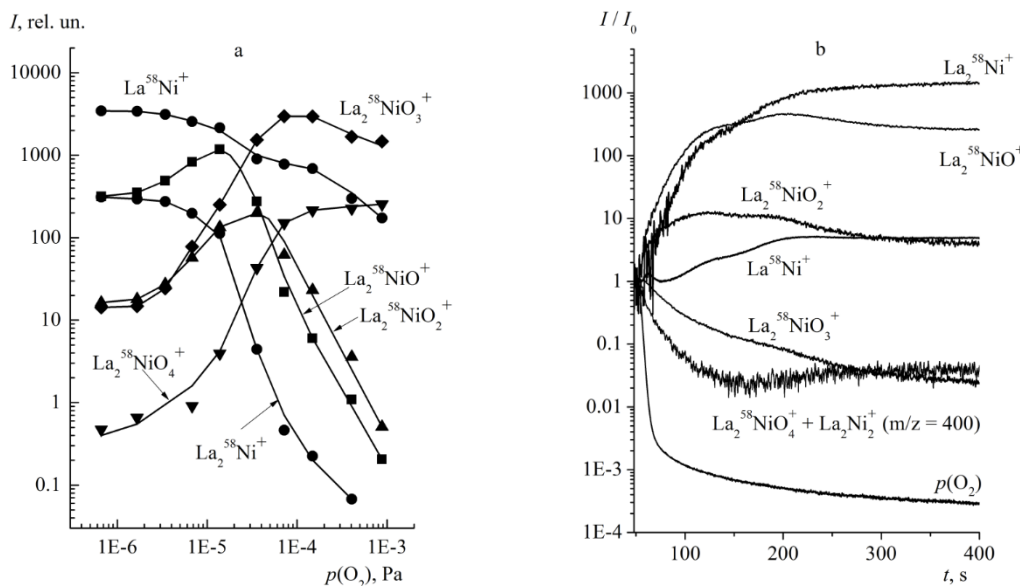


Figure 4. a: Dependences of emission intensities of complex secondary ions with lanthanum and nickel on oxygen partial pressure; b: Dependences of emission intensities of complex secondary ions with lanthanum and nickel on sputtering time after the exposure in oxygen.

Fig. 4b shows the results of measurements at the sputtering stage for complex secondary ions with lanthanum and nickel. In this case, the oxide sputtering experiment was slightly modified. After the sample surface was cleaned with the primary beam in the residual vacuum, the primary beam was shut off. Oxygen was injected into the chamber up to the partial pressure of $3.3 \cdot 10^{-4}$ Pa. After holding for ~ 50 seconds, the oxygen inlet was shut off, the primary beam was switched on and the sputtering began at this moment. As in the previous case, the actual emission intensities in this figure are normalized to the intensity at the point corresponding to the primary beam turning on. This sequence of actions, compared to the previous, makes it possible to estimate the influence of the primary beam on the oxidation processes.

The curve labeled in Fig. 4b as $\text{La}_2^{58}\text{NiO}_4^+ + \text{La}_2\text{Ni}_2^+$ represents the sum of $\text{La}_2^{58}\text{NiO}_4^+$ and La_2Ni_2^+ secondary ion emissions (400 amu); separation of their specific contributions was not performed, since the signal recording was performed in continuous mode (in contrast to the curve for $\text{La}_2^{58}\text{NiO}_4^+$ in Fig. 4a). It is thus taken into account, that at the indicated experimental conditions the contribution of La_2Ni_2^+ ions to the total signal is insignificant.

RESULTS DISCUSSION

The basis for the secondary ion mass spectrometry method, which makes it possible to infer a conclusion about the surface composition based on the analysis of measurement results, is the following model. An impact of a primary ion on a solid body initiates a cascade of binary collisions of target atoms. Sputtering of secondary ions from the surface occurs when a sufficiently energetic cascade approaches the surface. [23]. In the sputtering process, multi-atomic complexes as part of the surface and near-surface regions are sputtered along with single-atomic or two-atomic particles. Since the sputtered secondary ions are part of the surface and near-surface region, the composition diversity of positive and negative secondary ions observed in secondary ion spectra is determined exclusively by the surface and near-surface monolayer composition of the solid from which the sputtering takes place. A change in the surface composition also determines the trends of the secondary ion emission intensity dependences on the experimental parameters.

Obviously, the comparison of the secondary ion mass spectra composition with specific chemical compounds on the surface should be done with caution. It should be kept in mind that chemical compounds on the surface correspond to a much greater extent to the composition of the neutral rather than ionic component of the sputtering products. The composition of sputtered multi-atomic ions can be influenced by the processes of charge acquisition and retention.

The analysis of the results obtained in the present work allows us to conclude that oxygen forms strong chemical bonds with both alloy components when it enters the surface of the LaNi_5 alloy. This is also evidenced by the presence of a large set of secondary ions of $\text{La}_n\text{O}_m^\pm$ and $\text{Ni}_n\text{O}_m^\pm$ type, as well as by the presence of multi-atomic secondary ions comprising both alloy components like the $\text{La}_n\text{Ni}_m\text{O}_k^\pm$ type (where n , m and k may take different values in the case of positive and negative ions). The presence of such emissions in the mass spectrum suggests that when oxygen adsorbs on the LaNi_5 surface, it not only forms strong chemical bonds with both alloy components, but also forms a common structure consisting of lanthanum, nickel and oxygen.

As can be seen from Figs. 1a-4a, the emission intensities of most oxygen-containing secondary ions pass through a maximum as oxygen pressure increases. Moreover, the more oxygen atoms in the composition of a secondary ion are per metal atom, the higher the oxygen pressure at the point where the maximum is observed for such ions. There are also secondary ions which emission intensities only tend to plateau with increasing oxygen partial pressure. The observed dependences of the emission intensity on the oxygen partial pressure reflect the process of oxygen concentration increasing in the formed oxide structure. In other words, the observed dependences indicate that as the partial pressure of oxygen increases, an oxide structure in which the ratio of oxygen atoms to the number of matrix atoms increases is realized on the surface and in the near-surface region of the LaNi_5 sample. From the point of view of the analysis method used, for each specific value of oxygen partial pressure the formed oxide structure is characterized by a certain ratio of emission intensities of oxygen-containing secondary ions.

It should be emphasized that the oxygen concentration on the surface, and so the equilibrium surface coverage with oxygen-containing chemical compounds in our experimental conditions is determined by the dynamic equilibrium between the processes of oxygen adsorption from the gas phase and sputtering by the primary beam. There are also the effects of ion beam mixing. Analysis of the results obtained at oxide sputtering shows the following. The oxygen partial pressure $p(\text{O}_2)$ in the sample chamber, after the shut off drops by two orders of magnitude during ~ 10 seconds. At the same time, the emission intensity of secondary ions changes much more slowly. For some secondary ions, the emission intensity grows with the sputtering time; for others it decreases, and for some ions, it passes through a maximum. This applies to lanthanum ions, nickel ions, and complex lanthanum-nickel ions in Fig. 1b-4b. This behavior of the emission intensity dependences on sputtering time for the selected ions correlates well with the oxygen dependences for these ions in Figs. 1a-4a. Qualitatively, the course of the dependences of the ion emission intensity on sputtering time repeats in reverse order the course of the corresponding dependences obtained when the partial pressure of oxygen is increased.

This correlation allows us to state that in sputtering experiments, after pumping oxygen out of the chamber, and as the formed oxides are being sputtered, the situation on the surface is the opposite of the one that occurs when the partial pressure of oxygen increases, and when the number of oxygen atoms per matrix atom in the surface structure increases. Namely, as the oxygen-containing structure formed at the maximum partial pressures of oxygen in our experiments is sputtered, the number of oxygen atoms per matrix atom decreases.

The data shown in Fig. 1b-4b evidence that the sputtering of the formed oxides continues for hundreds of seconds. This indicates that the formed oxide compounds have a bulk structure and occupy dozens of monolayers. In such a bulk oxide structure, the outer monolayers are characterized by the highest oxygen concentration. The oxygen concentration decreases along the transition to the underlying monolayers.

The sputtering results obtained after the exposure in oxygen under the primary beam (Figs. 1b-3b) and after the exposure with the primary beam turned off (Fig. 4b) allow a qualitatively similar interpretation. This suggests that the primary beam does not significantly affect the LaNi₅ oxidation processes, while introducing the sputtering and ion beam mixing factors.

Among other things, the results of the conducted sputtering experiments show that there is no direct correlation between the change in the oxygen partial pressure with time and the change in the intensity of oxygen-containing secondary ion emission with time. This is direct evidence that the observed secondary ions are not a product of association of sputtered surface fragment with oxygen in the gas phase at the fly-off stage, but are the products of oxide compounds being sputtered and do characterize the surface and near-surface region composition.

CONCLUSION

SIMS studies of the chemical composition of LaNi₅ alloy surface monolayers during interaction of the alloy with oxygen showed the following. As a result of the interaction between oxygen and the alloy sample, a complex chemical structure including oxygen, lanthanum and nickel is formed on the LaNi₅ surface and in the near-surface region. Oxygen in such a structure forms strong chemical bonds with both alloy components. This is evidenced by the presence of a large set of oxygen-containing emissions of positive and negative secondary ions with lanthanum, with nickel, and oxygen-containing lanthanum-nickel cluster secondary ions in the mass spectra. The resulting oxide compounds have a bulk structure and occupy dozens of monolayers. In such a bulk oxide structure, the outer monolayers are characterized by the highest ratio of the oxygen atoms number to the matrix atoms number. This ratio decreases along with the transition from the superficial to the underlying monolayers of the alloy. The quantitative and qualitative ratio of elements in the formed oxide structure depends mainly on the oxygen partial pressure and to a much lesser extent on the sputtering action of the primary beam.

The observed secondary ions are not a product of association between sputtered surface fragments and oxygen in the gas phase at the fly-off stage after sputter-ejection, but they are products of the oxide compounds being sputtered, hence they characterize the composition of surface and near-surface region.

ORCID IDs

✉ Viktor O. Litvinov, <https://orcid.org/0000-0003-2311-2817>; ✉ Ivan I. Okseniuk, <https://orcid.org/0000-0002-8139-961X>;
✉ Dmytro I. Shevchenko, <https://orcid.org/0000-0002-4556-039X>; ✉ Valentyn V. Bobkov, <https://orcid.org/0000-0002-6772-624X>

REFERENCES

- [1] J.H.N. van Vucht, F.A. Kuijpers, and H.C.A.M. Bruning, Philips Research Report, **25**(2), 133 (1970). OSTI Identifier: 4129528.
- [2] P. Dantzer, Materials Science and Engineering, **A329–331**, 313 (2002). [https://doi.org/10.1016/S0921-5093\(01\)01590-8](https://doi.org/10.1016/S0921-5093(01)01590-8)
- [3] B.P. Tarasov, M.V. Lototsky, and V.A. Yartys, Russian Chem. J. **L**(6), 34 (2006). <http://www.chem.msu.ru/rus/jvho/2006-6/34.pdf> (In Russian)
- [4] S Luo, J.D Clewley, Ted B Flanagan, R.C Bowman Jr., and L.A Wade, J. Alloys Comp. **267**(1-2), 171 (1998), [https://doi.org/10.1016/S0925-8388\(97\)00536-7](https://doi.org/10.1016/S0925-8388(97)00536-7)
- [5] L. Schlapbach, A. Seiler, F. Stucki, and H.C Siegmann, J. Less Common Metals, **73**, 145 (1980). [https://doi.org/10.1016/0022-5088\(80\)90354-9](https://doi.org/10.1016/0022-5088(80)90354-9)
- [6] F. Schweppe, M. Martin, and E. Fromm, Journal of Alloys and Compounds, **253-254**, 511 (1997). [https://doi.org/10.1016/S0925-8388\(96\)03002-2](https://doi.org/10.1016/S0925-8388(96)03002-2)
- [7] G.D. Sandroek, and P.D. Goodell, J. Less Common Metals, **73**(1), 161 (1980). [https://doi.org/10.1016/0022-5088\(80\)90355-0](https://doi.org/10.1016/0022-5088(80)90355-0)
- [8] P.D. Goodell, and P.S. Rudman, J. Less Common Metals, **89**(1), 117-125 (1983). [https://doi.org/10.1016/0022-5088\(83\)90255-2](https://doi.org/10.1016/0022-5088(83)90255-2)
- [9] P.D. Goodell, J. Less Common Metals, **89**(1), 45 (1983). [https://doi.org/10.1016/0022-5088\(83\)90247-3](https://doi.org/10.1016/0022-5088(83)90247-3)
- [10] H.C. Siegmann, L. Schlapbach, and C.R. Brundle, Phys. Rev. Lett. **40**(14), 972 (1978). <https://doi.org/10.1103/PhysRevLett.40.972>
- [11] W.E. Wallace, R.F. Karlicek, and H. Imamura, J. Phys. Chem. **83**(13), 1708 (1979). <https://doi.org/10.1021/j100476a006>
- [12] J.J. Burton, and E.S. Machlin, Phys. Rev. Lett. **37**(21), 1433-1436 (1976). <https://doi.org/10.1103/PhysRevLett.37.1433>
- [13] S.H. Overbury, P.A. Bertrand, and Q.A. Somorjai, Chemical Reviews, **75**(5), 547-560 (1975). <https://doi.org/10.1021/cr60297a001>
- [14] P. Selvam, B. Viswanathan, C.S. Swamy, and V. Srinivasan, J. Less Common Metals, **163**, 89 (1990), [https://doi.org/10.1016/0022-5088\(90\)90088-2](https://doi.org/10.1016/0022-5088(90)90088-2)
- [15] P. Selvam, B. Viswanathan, and V. Srinivasan, Jnt. J. Hydrogen Energy, **14**(9), 687 (1989). [https://doi.org/10.1016/0360-3199\(89\)90048-7](https://doi.org/10.1016/0360-3199(89)90048-7)
- [16] P. Selvam, B. Viswanathan, C.S. Swamy, and V. Srinivasan, Int. J. Hydrogen Energy, **16**(1), 23 (1991). [https://doi.org/10.1016/0360-3199\(91\)90057-P](https://doi.org/10.1016/0360-3199(91)90057-P)
- [17] J.H. Weaver, A. Franciosi, W.E. Wallace, and H. Kevin Smith, J. App. Phys. **51**, 5847-5851 (1980). <https://doi.org/10.1063/1.327544>
- [18] J.H. Weaver, A. Franciosi, D.J. Peterman, T. Takeshita, and K.A. Gschneidner Jr. J. Less Common Metals, **86**, 195 (1982). [https://doi.org/10.1016/0022-5088\(82\)90205-3](https://doi.org/10.1016/0022-5088(82)90205-3)

- [19] L. Schlapbach, Solid State Communications, **38**(2), 117 (1981), [https://doi.org/10.1016/0038-1098\(81\)90802-4](https://doi.org/10.1016/0038-1098(81)90802-4)
- [20] H. Züchner, R. Dobrleit, and T. Rauf, Fresenius J. Anal. Chem. **341**, 219 (1991). <https://doi.org/10.1007/BF00321552>
- [21] H. Züchner, P. Kock, T. Bruning, and T. Rauf, J. Less Common Metals, **172-174**(Part A), 95 (1991). [https://doi.org/10.1016/0022-5088\(91\)90437-9](https://doi.org/10.1016/0022-5088(91)90437-9)
- [22] V.A. Litvinov, I.I. Okseniuk, D.I. Shevchenko, and V.V. Bobkov, J. Surf. Invest. X-ray, Synchrotron and Neutron Techniques, **12**(3), 576 (2018). <https://doi.org/10.1134/S1027451018030321>
- [23] *Sputtering by Particle Bombardment I: Physical Sputtering of Single-Element Solids* edited by R. Behrisch (Springer-Verlag, Berlin-Heidelberg, 1981), pp. 284. <https://doi.org/10.1007/3-540-10521-2>

РОЗПИЛЕННЯ ОКСИДІВ З ПОВЕРХНІ LaNi₅

В.О. Літвінов, І.І. Оксенюк, Д.І. Шевченко, В.В. Бобков

Харківський національний університет ім. В.Н. Каразіна

61022, Україна, м. Харків, пл. Свободи, 4

Методом вторинної іонної мас-спектрометрії (ВІМС) проведено дослідження змін хімічного складу поверхневих моношарів інтерметалевого сплаву LaNi₅ в процесі взаємодії з киснем. Досліджувані зразки представляли собою таблетки, спресовані з дрібнозернистого сплаву LaNi₅. В якості первинних іонів використовувалися іони Ar⁺ з енергією 10 – 18 кеВ. Щільність струму первинного пучка становила 9-17 мкА·см⁻², що відповідає динамічному режиму ВІМС. Інтенсивності емісій вторинних іонів вимірювалися у динамічному діапазоні не менше 6 порядків. Перед вимірами зразки відпалювали у залишковому вакуумі при температурі ~ 1000 К. Після відпалу проводилась очистка поверхні пучком первинних іонів до повної стабілізації складу мас-спектра та інтенсивності емісій вторинних іонів. Склад газової фази контролювався за допомогою газового мас-спектрометра. Проведені дослідження показали, що в результаті впливу кисню, на поверхні і в приповерхневої області LaNi₅ утворюється комплексна хімічна структура, що включає кисень, лантан і нікель. Кисень, в такій структурі утворює міцні хімічні зв'язки з обома компонентами сплаву. Про це свідчить наявність в мас-спектрах великого набору кисневмісних емісій позитивних і негативних вторинних іонів з лантаном, з нікелем, а також кисневмісних кластерних лантан-нікелевих вторинних іонів. Оксидні сполуки, що утворюються, мають об'ємну структуру і займають десятки моношарів. У такої об'ємної оксидної структурі зовнішні моношари характеризуються найбільшим відношенням кількості атомів кисню до кількості атомів матриці. При переході до нижчого моношару це відношення зменшується. Цей процес відбувається рівномірно, без будь-яких фазових трансформацій. Спостережувані вторинні іони є продуктами розпилення оксидних сполук і не є продуктом асоціації розпилених фрагментів поверхні з киснем газової фази на етапі відльоту. Вони характеризують хімічний склад поверхневої і приповерхневої області сплаву при його взаємодії з киснем.

Ключові слова: ВІМС, інтерметалевий сплав LaNi₅, кисень, поверхня, оксиди

TENSOELECTRICAL PROPERTIES OF ELECTRON-IRRADIATED n-Si SINGLE CRYSTALS[†]

 **Sergiy Luniov^{a,*}, Petro Nazarchuk^a,  Volodymyr Maslyuk^b**

^a*Lutsk National Technical University*

Str. Lvivska, 75, Lutsk, 43018, Ukraine

^b*Institute of electron physics NAS of Ukraine*

Str. Universitetska, 21, Uzhgorod, 88017, Ukraine

*Corresponding Author: luniovs@ukr.net

Received May 18, 2021; revised June 1, 2021; accepted July 28, 2021

Tensoresistance at uniaxial pressure for electron-irradiated n-Si single crystals at room temperature has been studied. Silicon single crystals for research were doped with phosphorus, concentration $N_d=2.2 \cdot 10^{16} \text{ cm}^{-3}$, and irradiated by the electron flows of $5 \cdot 10^{16} \text{ el./cm}^2$, $1 \cdot 10^{17} \text{ el./cm}^2$ and $2 \cdot 10^{17} \text{ el./cm}^2$ with the energy of 12 MeV. Measurements of tensorresistance and Hall constant were performed for the uniaxially deformed n-Si single crystals along the crystallographic directions [100] and [111]. Mechanisms of tensorresistance for the investigated n-Si single crystals were established based on the measurements of the tenso-Hall effect and infrared Fourier spectroscopy. It is shown that the tensorresistance of such single crystals is determined only by changes in the electron mobility under the deformation. In this case, the electron concentration will not change under the action of uniaxial pressure, because the deep levels of radiation defects belonging to the VO_i VO_iP complexes will be completely ionized. Ionization of the deep level of $E_v+0.35 \text{ eV}$, which belongs to the defect of C_iO_i , under the deformation will not be manifested and will not be affect on the tensorresistance of n-Si. It is established that the anisotropy of electron scattering on the created radiation defects, which occurs at the uniaxial pressure along the crystallographic direction [100], is the cause of different values of the magnitude of tensorresistance of n-Si single crystals, irradiated by different electron flows. For the case of tensorresistance of the uniaxially deformed n-Si single crystals along the crystallographic direction [111], the dependence of its magnitude on the electron irradiation flow is associated with changes in the screening radius due to an increase in the effective electron mass. For the first time obtained at room temperature the increase of the magnitude of tensorresistance for the n-Si single crystals due to their irradiation by the electron flows of $\Omega \geq 1 \cdot 10^{17} \text{ el./cm}^2$ can be used in designing high uniaxial pressure sensors based on such n-Si single crystals with the higher value of tensorsensitivity coefficient regarding available analogues. Such sensors will have increased radiation resistance and a wide scope of operation.

Keywords: n-Si single crystals, radiation defects, tensorresistance, electron irradiation, tenso-Hall effect, infrared Fourier spectroscopy, scattering anisotropy.

PACS: 72.20.My, 72.20.Fr, 72.10.-d

Monocrystalline silicon is one of the promising materials for the manufacture of pressure sensors, which are used in many areas of science and technology, such as aerospace, cryo energy, nuclear and atomic power, instrument engineering and others [1-6]. The use of such sensors in these industries at the presence of radiation fields makes demands on the accuracy and stability of their parameters. The solution of these problems is possible due to the optimization of the performance of pressure sensors and the development of technologies for their production. Among the known methods of obtaining silicon and other semiconductor materials is metallurgical doping by the isovalent and rare earth impurities, impurity complexes and impurities with the deep levels [7-10]. However, these technologies have several disadvantages, such as limited solubility of doping impurities, which significantly narrows the range of possible concentrations of charge carriers, increasing the concentration of structural defects and reducing the degree of homogeneity of the material with increasing doping concentration. Another method of obtaining semiconductor materials with the necessary properties is the modification of these properties by radiation defects that are created in semiconductors under the irradiated with high-energy quanta or particles [8, 11]. In [12-14], the effect of gamma irradiation and annealing on the tensorresistive effect in n-Si single crystals was studied. It was established that the tensoelectrical properties of the investigated silicon single crystals are determined by the radiation defects belonging to A-centers [12, 13], or both A-centers and thermodonors [14]. However, the effect of these defects on the n-Si tensorresistance will be manifested only at temperatures slightly higher than the temperature of liquid nitrogen, and the energy levels of A-centers and thermodonors will be ionized at room temperature. This significantly narrows the scope of operation of pressure sensors that are manufactured based on such gamma-irradiated n-Si single crystals, as the use of gamma irradiation and thermal annealing technologies for this case does not allow to control the n-Si tensorsensitivity at room temperature. Therefore, this work aimed to study the mechanisms of tensorresistance of electron-irradiated n-Si single crystals at the uniaxial pressure and establishing optimal electron irradiation conditions to increase the tensorsensitivity of these single crystals at room temperature.

EXPERIMENTAL RESULTS AND DISCUSSION

Measurements of tensorresistance and Hall constant were performed for the uniaxially deformed n-Si single crystals along the crystallographic directions [100] and [111]. The investigated silicon single crystals were doped by the

[†] *Cite as:* S. Luniov, P. Nazarchuk, and V. Maslyuk, East. Eur. J. Phys. 3, 37 (2021), <https://doi.org/10.26565/2312-4334-2021-3-05>

phosphorus impurity, concentration $N_d=2.2 \cdot 10^{16} \text{ cm}^{-3}$, and irradiated by the electron flows of $5 \cdot 10^{16} \text{ el./cm}^2$, $1 \cdot 10^{17} \text{ el./cm}^2$ and $2 \cdot 10^{17} \text{ el./cm}^2$ with the energy of 12 MeV at room temperature. The method of preparation of silicon samples and experimental measurements of tensorial properties is described in detail in [15]. In [16], measurements of infrared Fourier spectroscopy have been conducted for these n-Si single crystals, irradiated by the electron flow of $1 \cdot 10^{17} \text{ el./cm}^2$. It was found that the absorption lines with frequencies of 836 and 885 cm^{-1} correspond to the A-center (VO_i complex), and the absorption line with the frequency of 865 cm^{-1} - the C_iO_i complex. These defects are the main ones and determine the electrical properties of these single crystals. The activation energy of radiation defects for irradiated silicon by the electron flow of $\Omega=1 \cdot 10^{17} \text{ el./cm}^2$, which is determined in this work based on Hall effect measurements turned out to be equal to $E_A = E_c - (0,107 \pm 0,005) \text{ eV}$, which corresponds to the A-center, additionally modified with impurity of phosphorus (VO_iP complex). This allowed us to establish that VO_iP complexes will be created under the irradiation of silicon in addition to VO_i complexes. The analysis of temperature dependences of electron concentration for irradiated silicon single crystals by the electron flows of $5 \cdot 10^{16} \text{ el./cm}^2$, $1 \cdot 10^{17} \text{ el./cm}^2$ and $2 \cdot 10^{17} \text{ el./cm}^2$ showed that at room temperature the radiation defects belonging to A-centers, will be ionized, and the deep levels $E_v+0,35 \text{ eV}$ belonging to the C_iO_i defects will be filled with electrons. Also, these conclusions are in good agreement with our measurements of the IR absorption spectra for irradiated n-Si single crystals by the electron flows of $5 \cdot 10^{16} \text{ el./cm}^2$ and $2 \cdot 10^{17} \text{ el./cm}^2$ at room temperature (Fig. 1).

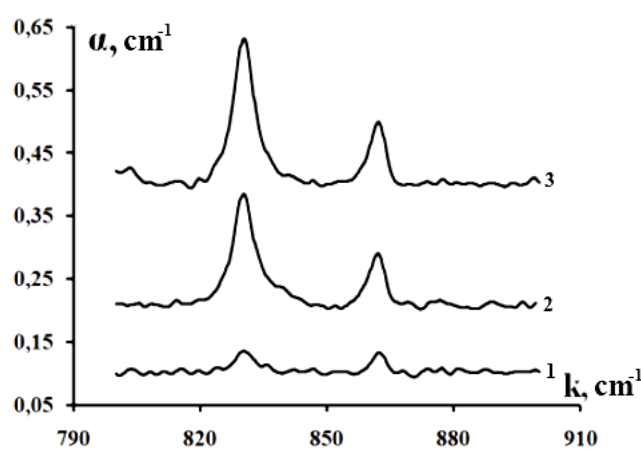


Figure 1. Absorption spectra at room temperature for irradiated n-Si single crystals by the different electron flows Ω , el./cm^2 :
1 – $5 \cdot 10^{16}$; 2 – $1 \cdot 10^{17}$ [16]; 3 – $2 \cdot 10^{17}$.

As follows from Fig. 1, in the absorption spectrum of irradiated silicon there is no line 885 cm^{-1} , which corresponds to the negatively charged state of the A-center, and there are absorption lines 836 cm^{-1} (corresponds to the neutral state of the A-center) and 865 cm^{-1} . Therefore, only radiation defects belonging to the C_iO_i complex will be electrically active at room temperature. The increase in the area under the curves that correspond to these absorption lines indicates that the concentration of the considered defects increases with the increasing electron irradiation flow. This statement is also confirmed by the quantitative calculations conducted in [16].

Dependences of the tensorial resistance for unirradiated and irradiated n-Si single crystals by the electron flows of $5 \cdot 10^{16} \text{ el./cm}^2$, $1 \cdot 10^{17} \text{ el./cm}^2$ and $2 \cdot 10^{17} \text{ el./cm}^2$ at the uniaxial pressure along the crystallographic directions [100] and [111] at room temperature show in Fig. 2 and Fig. 3.

The change in resistivity during deformation can occur both due to changes in mobility and electron concentration. As is known [12], the decrease in electron mobility of the unirradiated silicon single crystals at the uniaxial pressure along the crystallographic direction [100] occurs due to the redistribution of electrons between two minima of the conduction band with lower mobility, which descend down, and four minima with higher mobility, which ascend up on the energy scale under the action of deformation. That is, mobility in this case becomes anisotropic. The decrease in electron mobility of n-Si at the uniaxial pressure along the crystallographic direction [111] is associated with the increase in the effective mass of electrons during the transformation of a two-axis isoenergetic ellipsoid of rotation in the three-axis and the emergence of non-parabolicity of the silicon conduction band under the deformation [15].

In [15], it was established that changes in the electron mobility under the uniaxial pressure for the same n-Si single crystals with radiation defects are also associated with the additional mechanisms of electron scattering, which are not manifested for unirradiated n-Si single crystals. In so doing, the electron concentration during deformation increases due to the reduction of the ionization energy of the VO_i and VO_iP complexes. These two reasons will determine the tensorial resistance of irradiated n-Si single crystals at an uniaxial pressure. It should be noted that in [15] studies of the tensorial properties of electron-irradiated n-Si single crystals were performed for the temperature range 130-300 K. According to the temperature dependences of the electron concentration and infrared Fourier spectroscopy measurements [16], the energy levels of VO_i and VO_iP complexes will not be ionized at the temperatures $T < 250 \text{ K}$ and will contribute to the changes in the electron concentration under the deformation and, accordingly, to the

tensoresistance of the irradiated Si. In our case, these defects will be ionized and will not affect the tensoresistance n-Si at room temperature. The change in the electron concentration under the action of deformation is possible only due to the ionization of the C_iO_i complex, which will not be ionized at room temperature. Therefore, to interpret the obtained results of tensoresistance, presented in Fig. 2 and Fig. 3, the measurements of tenso-Hall effect have been conducted. In Fig. 4 shows the dependences of the Hall constant for unirradiated and irradiated n-Si single crystals by the electron flows of $5 \cdot 10^{16}$ el./cm², $1 \cdot 10^{17}$ el./cm² and $2 \cdot 10^{17}$ el./cm² on the uniaxial pressure along the crystallographic directions [100] and [111] at room temperature.

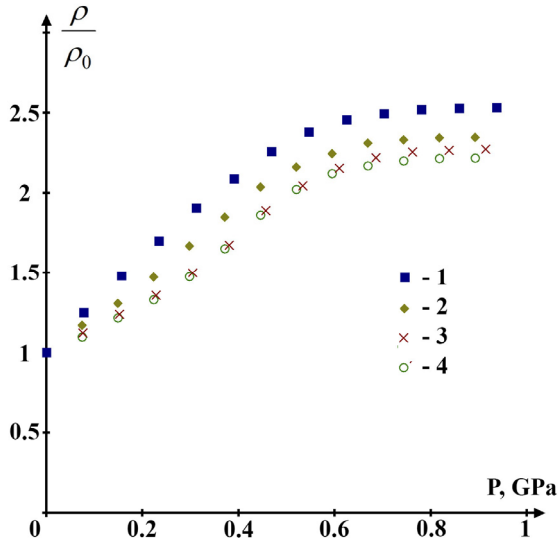


Figure 2. Dependences of tensoresistance at the uniaxial pressure along the crystallographic direction [100] for irradiated n-Si single crystals by the different electron flows Ω , el./cm²: 1 – $2 \cdot 10^{17}$, 2 – $1 \cdot 10^{17}$ el./cm², 3 – 0, 4 – $5 \cdot 10^{16}$.

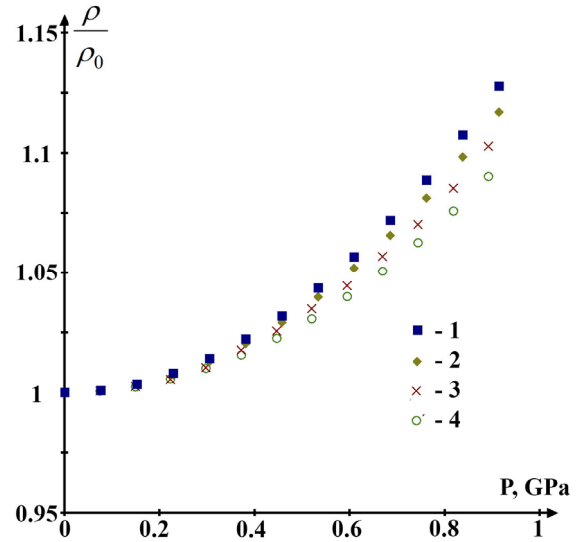


Figure 3. Dependences of tensoresistance at the uniaxial pressure along the crystallographic direction [111] for irradiated n-Si single crystals by the different electron flows Ω , el./cm²: 1 – $2 \cdot 10^{17}$, 2 – $1 \cdot 10^{17}$ el./cm², 3 – 0, 4 – $5 \cdot 10^{16}$.

The value of the Hall constant does not depend on the orientation of the uniaxial pressure, so curves 1 and 2, 3 and 4, 5 and 6, 7 and 8 in Fig. 4 coincide at the deformation along the crystallographic directions [100] and [111] for the same electron irradiation flows.

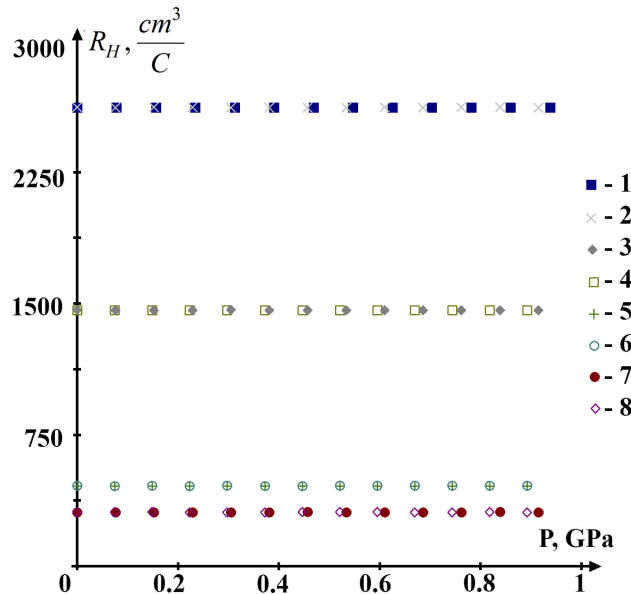


Figure 4. Dependences of the Hall constant on the uniaxial pressure along the crystallographic directions [100] and [111] at room temperature for irradiated n-Si single crystals by the different electron flows Ω , el./cm²: 1, 2 – $2 \cdot 10^{17}$; 3, 4 – $1 \cdot 10^{17}$; 5, 6 – $5 \cdot 10^{16}$; 7, 8 – 0.

As follows from Fig. 4, the Hall constant does not depend on the uniaxial pressure for both unirradiated and irradiated silicon samples. This is explained by the fact that at room temperature ionization of the deep level of $E_v+0,35$

eV belonging to the C_iO_i defect will not be manifested under the action of deformation. In this case, the radiation defects corresponding to the VO_i and VO_iP complexes will be ionized and will not in any way affect the changes in the electron concentration during deformation, in accordance with the Fig. 1 and obtained in [16] of the temperature dependences of electron concentration. Therefore, the presence of tensorresistance for irradiated n-Si single crystals, as well as for unirradiated ones, will be determined only by changes in the electron mobility at uniaxial pressure. Also, a characteristic feature of the dependences of the tensorresistance (Fig. 2 and Fig. 3) is the increase in the magnitude of the tensorresistance for the flows of $\Omega \geq 1 \cdot 10^{17}$ el./cm². To quantitatively explain this feature, the relative decrease of Hall mobility for undeformed and uniaxially deformed n-Si single crystals was estimated. The relative decrease in Hall mobility with the increasing magnitude of the electron flow can be represented as follows:

$$\alpha = \frac{\mu_h(0) - \mu_h(\Phi)}{\mu_h(0)} \cdot 100\%, \quad (1)$$

where $\mu_h(0)$ is the Hall mobility for unirradiated silicon single crystals; $\mu_h(\Omega)$ is the Hall mobility for irradiated silicon single crystals by the flow Ω .

Table presents the calculated values of the relative decrease of Hall mobility for undeformed and uniaxially deformed n-Si single crystals with increasing electron irradiation flow (values of uniaxial pressures for elastically deformed n-Si single crystals, for which assessments were conducted, are presented in parentheses).

Since the tensorresistance for unirradiated and irradiated n-Si single crystals, as established above based on the analysis of the Hall constant dependences (Fig. 4), will be determined by changes in the electron mobility, then

$$\frac{\rho(P)}{\rho(0)} = \frac{\mu(0)}{\mu(P)}. \quad (2)$$

As follows from the Table, the relative decrease in electron mobility for undeformed n-Si single crystals irradiated by the electron flow of $5 \cdot 10^{16}$ el./cm² is greater than for uniaxially deformed. This explains, according to (2), the decrease of the value of the tensorresistance $\frac{\rho(P)}{\rho(0)}$ under irradiation for these single crystals relative to the unirradiated silicon single crystals.

Table. Relative decrease of the Hall mobility of undeformed and uniaxially deformed n-Si single crystals.

Electron irradiation flow of Ω , el./cm ²	Relative decrease of Hall mobility α , %		
	Undeformed silicon single crystals	Uniaxially deformed silicon single crystals along the crystallographic direction [100]	Uniaxially deformed silicon single crystals along the crystallographic direction [111]
$5 \cdot 10^{16}$	2.7	0.5 (0.89 GPa)	1.3 (0.89 GPa)
$1 \cdot 10^{17}$	5.4	8 (0.82 GPa)	6 (0.84 GPa)
$2 \cdot 10^{17}$	7	16.6 (0.86 GPa)	8.4 (0.84 GPa)

For irradiated n-Si single crystals by the electron flows of $1 \cdot 10^{17}$ el./cm² and $2 \cdot 10^{17}$ el./cm² the situation, according to Table, changes to the opposite. In this case, the relative decrease in the electron mobility and, accordingly, the value of a tensorresistance for the uniaxially deformed n-Si single crystals increases with increasing electron irradiation flow. Such features of the dependences of electron mobility on the irradiation flow for undeformed and uniaxially deformed n-Si single crystals along the crystallographic direction [100] can be explained by the influence of the mobility anisotropy factor that arises in silicon for this deformation orientation. As is known [12], for undeformed silicon single crystals the electron mobility

$$\mu = \frac{1}{3} \mu_{\parallel} + \frac{2}{3} \mu_{\perp}, \quad (3)$$

where μ_{\perp} and μ_{\parallel} is the electron mobility across and along the axis of the ellipsoid.

Electrons will be in two minima of the conduction band with less mobility μ_{\parallel} at the strong uniaxial pressures along the crystallographic direction [100]. In doing so, the sensitivity of the mobility μ and μ_{\parallel} to the influence of electron irradiation will be different, which explains the data in Table 1 and the dependence of tensorresistance for the uniaxially deformed n-Si single crystals along the crystallographic direction [100]. Mobility anisotropy will not be arise at the uniaxial pressure along the crystallographic direction [111]. But in this case the effective mass of electrons increases. The increase in the effective mass leads to changes in the screening radius, which, in turn, impact on the potential energy of the electron's interaction with the scattering centre and, accordingly, the electrons mobility. Such scattering centres for electrons in irradiated silicon single crystals are impurity phosphorus ions and created radiation

defects. The change in the electron scattering conditions during deformation, in this case, is the cause of different dependences of the Hall mobility on the electron irradiation flow for undeformed and uniaxially deformed n-Si single crystals. These dependencies will determine the features of the tensorresistance of uniaxially deformed n-Si single crystals along the crystallographic direction [111] for different electron irradiation flows (Fig. 3).

CONCLUSIONS

Studies of the tenso-Hall effect and infrared Fourier spectroscopy have made it possible to establish the mechanisms of tensorresistive effect at the uniaxial pressures along the crystallographic directions [100] and [111] for electron-irradiated n-Si single crystals at room temperature. Dependences of the resistivity of the investigated n-Si single crystals on the uniaxial pressure are determined only by the change in the electron mobility. The electron concentration does not depend on the uniaxial pressure, because the deep levels of radiation defects belonging to the VO_i and VO_iP complexes will be completely ionized. Ionization of the deep $E_v+0.35$ eV level belonging to the C_iO_i defect will not occur under the action uniaxial pressure at room temperature. Dependence of the tensorresistance on the electron irradiation flow at uniaxial pressure along the crystallographic direction [100] is explained by the deformation-induced anisotropy of electron scattering on the created radiation defects. This leads to an increase of the scattering efficiency of electrons on radiation defects and, accordingly, to a greater relative decrease of electron mobility for the uniaxially deformed n-Si single crystals relative to undeformed n-Si single crystals. The increase in the value of the tensorresistance of uniaxially deformed n-Si single crystals along the crystallographic direction [111] at the flows of $\Omega \geq 1 \cdot 10^{17}$ el./cm² is associated with changes in the screening radius due to the increase in the effective electron mass and, according, of the conditions of their scattering on radiation defects during deformation. In [17], it was found that the magnitude of the tensorresistance of silicon, uniaxially deformed along the crystallographic direction [100], can vary depending on the relative contribution of f- and g-transitions to intervalley scattering. In this case, the increase in the tensorresistance and, accordingly, the tensorsensitivity of n-Si single crystals is achieved by reducing the temperature. Need for an additional cooling system with the aim of increasing tensorsensitivity and the temperature calibration of pressure sensors, manufactured on the basis of such silicon single crystals, significantly complicates their structure, increases cost and reduces the scope of operation. Also, the use of doping technologies by the donor or acceptor impurities does not increase the tensorsensitivity of silicon at room temperature [18]. In our case, such an increase in the tensorsensitivity of n-Si can be achieved only by increasing the flow of electron irradiation, which is an advantage. Therefore, the obtained results can be used in the design of high uniaxial pressure sensors based on irradiated n-Si single crystals with the predetermined coefficient of tensorsensitivity.

FUNDING

The presented work was financed under the project of the State Budget of Ukraine "Development of a complex of managed properties of many-valley semiconductors and polymer composite materials for operation in extreme conditions of operation", registration number 0117U000630.

ORCID IDs

 **Sergiy Luniov**, <https://orcid.org/0000-0003-0737-8703>;  **Volodymyr Maslyuk**, <https://orcid.org/0000-0002-5933-8394>

REFERENCES

- [1] I. Maryamova, A. Druzhinin, E. Lavitska, I. Gortynska, and Y. Yatzuk, *Sensors and Actuators A: Physical*, **85**, 153 (2000), [https://doi.org/10.1016/S0924-4247\(00\)00376-9](https://doi.org/10.1016/S0924-4247(00)00376-9)
- [2] A. Druzhinin, I. Ostrovskii, Y. Khoverko, and R. Koretskii, *Materials Science in Semiconductor Processing*, **40**, 766-771 (2015), <https://doi.org/10.1016/j.mssp.2015.07.015>
- [3] T. Toriyama, Y. Tanimoto, and S. Sugiyama, *Journal of microelectromechanical systems*, **11**, 605 (2002), <https://doi.org/10.1109/JMEMS.2002.802905>
- [4] A. Vlasov, S. Milesin, T. Tsivinskaya, and V. Shakhnov, *Problems of Perspective Micro- and Nanoelectronic Systems Development*, **4**, 190-196 (2018), <http://www.mes-conference.ru/data/year2018/pdf/D007.pdf>
- [5] P.I. Baranskii, and G.P. Gaidar, *Semiconductor Physics Quantum Electronics & Optoelectronics*, **19**(1), 39 (2016), <https://doi.org/10.15407/spqeo.19.01.039>, (in Ukrainian)
- [6] G.P. Gaidar, *Physics and Chemistry of Solid State*, **18**(1), 34 (2017), <https://doi.org/10.15330/pcss.18.1.34-40> (in Ukrainian).
- [7] Ya. Kost, I. Bolshakova, I. Duran, A. Vasyliiev, L. Viererb, R. Konopleva, M. Radishevskiy, V. Chekanov, and F. Shurygin, in: *12th International Conference "Interaction of Radiation with Solids"* (Belarusian state univ., Minsk, 2017), pp. 154-155.
- [8] I. Bolshakova, Ya. Kost, O. Makido, A. Shtabalyuk, and F. Shurygin, *Visnyk of Lviv Polytechnic National University, Electronics*, **734**, 28 (2012), <http://ena.lp.edu.ua:8080/handle/ntb/16051>. (in Ukrainian)
- [9] N. Kolin, *Russian physics journal*, **46**(6), 543 (2003), <https://doi.org/10.1023/B:RUPJ.0000008179.43324.96>
- [10] F. Shimura, in: *Semiconductor Silicon Crystal Technology*, edited by F. Shimura (Academic Press, London, 2012).
- [11] Y. Sun, and A. Chmielewski, in: *Applications of ionizing radiation in materials processing*, edited by Y. Sun, and A. Chmielewski (Institute of Nuclear Chemistry and Technology, Warszawa, 2017).
- [12] A.V. Fedosov, S.V. Luniov, and S.A. Fedosov, *Ukr. J. Phys.* **56**(1), 69 (2011), <http://archive.ujp.bitp.kiev.ua/files/journals/56/1/560108p.pdf>. (in Ukrainian)
- [13] G.P. Gaidar, and P.I. Baranskii, *Physica B: Condensed Matter*, **512**, 6 (2017), <https://doi.org/10.1016/j.physb.2017.02.015>
- [14] L.I. Panasyuk, V.V. Kolomoets, B.B. Sus, V.N. Ermakov, S.A. Fedosov, and P.P. Trokhimchuk, in: *10th International Conference "Interaction of Radiation with Solids"*, (Belarusian state univ., Minsk, 2013), pp. 137-139.

- [15] S.V. Luniov, V.V. Lyshuk, V.T. Maslyuk, and O.V. Burban, *Latvian Journal of Physics and Technical Sciences*, **56**(5), 45 (2019), <https://doi.org/10.2478/lpts-2019-0030>
- [16] S. Luniov, A. Zimych, M. Khvyshchun, M. Yevsiuk, and V. Maslyuk, *Eastern-European Journal of Enterprise Technologies*, **6**(12), 35 (2018), <https://doi.org/10.15587/1729-4061.2018.150959>. (in Ukrainian)
- [17] A.V. Fedosov, S.V. Luniov, and S.A. Fedosov, *Semiconductors*, **44**(10), 1263, <https://doi.org/10.1134/S1063782610100039>
- [18] P.I. Baranskii, A.E. Belyaev, and G.P. Gaidar, in: *Кінетичні ефекти в багатодолінних напівпровідниках [Kinetic Effects in Multi-Valley Semiconductors]*, (Naukova Dumka, Kyiv, 2019), pp. 448. (in Ukrainian)

ТЕНЗОЕЛЕКТРИЧНІ ВЛАСТИВОСТІ ОПРОМІНЕНИХ ЕЛЕКТРОНАМИ МОНОКРИСТАЛІВ n-Si

Сергій Лушов^a, Петро Назарчук^a, Володимир Маслюк^b

^aЛуцький національний технічний університет

вул. Львівська, 75, м. Луцьк, 43018, Україна

^bІнститут електронної фізики НАН України

вул. Університетська, 21, м. Ужгород, 88017, Україна

Досліджено тензоопір при одноосному тискові для опроміненних електронами монокристалів n-Si при кімнатній температурі. Досліджувані монокристали кремнію були леговані домішкою фосфору, концентрацією $N_d=2,2 \cdot 10^{16} \text{ см}^{-3}$, та опромінювались потоками електронів $5 \cdot 10^{16} \text{ ел./см}^2$, $1 \cdot 10^{17} \text{ ел./см}^2$ та $2 \cdot 10^{17} \text{ ел./см}^2$ з енергією 12 МеВ. Вимірювання питомого опору та сталої Холла проводились для одноосно деформованих вздовж кристалографічних напрямків [100] та [111] монокристалів n-Si. На основі вимірювань тензо-холл-ефекту та інфрачервоної Фур'є-спектроскопії були встановлені механізми виникнення тензорезистивного ефекту для досліджуваних монокристалів n-Si. Показано, що тензоопір для даних монокристалів визначається лише змінами рухливості електронів при деформації. При цьому концентрація електронів не залежить від одноосного тиску, оскільки глибокі рівні радіаційних дефектів, що належать комплексам VO_i VO_iP , будуть повністю іонізованими. Іонізація глибокого рівня $E_V + 0,35 \text{ eV}$, що належить дефекту SiO_i , за рахунок деформації не буде проявлятися та впливати на тензоопір n-Si. Встановлено, що анізотропією розсіяння електронів на утворених радіаційних дефектах, яка виникає при одноосному тискові вздовж кристалографічного напрямку [100], є причиною різної величини тензоопору опроміненних різними потоками електронів монокристалів n-Si. Залежність величини тензоопору одноосно деформованих вздовж кристалографічного напрямку [111] монокристалів n-Si від потоку електронного опромінення пов'язана зі змінами радіуса екранування за рахунок зростання ефективної маси електронів. Вперше одержане при кімнатній температурі зростання величини тензоопору монокристалів n-Si за рахунок опромінення потоками електронів $\Phi \geq 1 \cdot 10^{17} \text{ ел./см}^2$ може бути використане для конструювання сенсорів високого одноосного тиску на основі таких монокристалів n-Si з більшим значенням коефіцієнта тензочутливості відносно наявних аналогів. Такі сенсори матимуть підвищену радіаційну стійкість та широку сферу експлуатації.

Ключові слова: монокристали n-Si, радіаційні дефекти, тензоопір, електронне опромінення, тензо-холл-ефект, інфрачервона Фур'є-спектроскопія, анізотропія розсіяння.

STRUCTURE AND PHYSICAL PROPERTIES OF CAST AND SPLAT-QUENCHED CoCr_{0.8}Cu_{0.64}FeNi HIGH ENTROPY ALLOY[†]

 Oleksandr I. Kushnerov^{a,*},  Valerii F. Bashev^{b,‡}

*Department of Experimental Physics, Oles Honchar Dnipro National University
72 Gagarin ave., Dnipro, 49010 Ukraine*

**Corresponding Author: kushnrv@gmail.com, ‡E-mail: bashev_vf@ukr.net*

Received June 30, 2021; revised July 7, 2021; accepted July 27, 2021

The article investigates the structure and physical properties of the multicomponent high-entropy alloy CoCr_{0.8}Cu_{0.64}FeNi in the cast and quenched state. The composition of the alloy under study is analyzed using the criteria available in the literature for predicting the phase composition of high-entropy alloys. These parameters are based on calculations of the entropy and enthalpy of mixing and also include the concentration of valence electrons, the thermodynamic parameter Ω , which takes into account the melting point, entropy of mixing, and enthalpy of mixing. Another important parameter is the difference in atomic radii between the alloy components δ . Cast samples of the CoCr_{0.8}Cu_{0.64}FeNi alloy of nominal composition were prepared on a Tamman high-temperature electric furnace in an argon flow using a copper mold. The weight loss during the manufacture of ingots did not exceed 1%, and the average cooling rate was $\sim 10^2$ K/s. Thereafter, the cast ingot was remelted, and films were obtained from the melt. The splat quenching technique used in this work consisted of the rapid cooling of melt droplets when they collide with the inner surface of a rapidly rotating (~ 8000 rpm) hollow copper cylinder. The cooling rate, estimated from the film thickness, was $\sim 10^6$ K / s. X-ray structural analysis was performed on a DRON-2.0 diffractometer with monochromatic Cu K α radiation. Diffraction patterns were processed using the QualX2 program. The magnetic properties of the samples were measured using a vibrating sample magnetometer at room temperature. The microhardness was measured on a PMT-3 device at a load of 50 g. In accordance with theoretical predictions confirmed by the results of X-ray diffraction studies, the structure of the alloy, both in the cast and in the quenched state, is a simple solid solution of the FCC type. The lattice parameters in the cast and liquid-quenched states are 0.3593 nm and 0.3589 nm, respectively. Measurements of the magnetic properties showed that the CoCr_{0.8}Cu_{0.64}FeNi alloy can be classified as soft magnetic materials. In this case, quenching from a liquid state increases the coercivity. On quenched samples, increased microhardness values were also obtained. This can be explained by internal stresses arising during hardening.

Keywords: high entropy alloy, structure, phase composition, splat-quenching, microhardness, magnetic properties.

PACS: 81.05.Bx, 81.07.Bc, 81.40.Ef, 75.20.En, 75.50.Tt

The development of theories and technologies in the field of creating new materials has led to an increase in the number of elements in the composition of multicomponent alloys. In recent decades, a new class of metal compounds has been developed - the so-called multicomponent high-entropy alloys (HEAs) [1–3]. Such alloys contain at least five elements in equiatomic or close enough to equiatomic concentrations (usually from 5 to 35 at.%). The main feature of HEAs is the formation of single-phase, thermodynamically stable substitutional solid solutions with a cubic body-centered (BCC) or face-centered (FCC) lattice. Stabilization of the solid solution during crystallization is provided by the high entropy of mixing the components in the melt. The maximum value of the entropy of mixing, obviously, is achieved at equimolar ratios of elements.

Studies of HEAs have shown that they can form nanoscale structures and even amorphous phases [1-7]. This is due to significant distortions of the lattice, which are due to the difference in the atomic radii of the substitution elements. This also reduces the rate of diffusion processes, which decreases the growth rate of crystallites, which in turn leads to a fine crystalline structure.

Recently, it has been proposed in the literature to consider as HEAs only equimolar alloys in the structure of which there are exclusively simple solid solutions with crystal lattices of BCC and FCC. For other alloys with high entropy but with non-equimolar component content or more complex phase composition, in which there are also ordered solid solutions and intermetallic compounds, it was proposed to introduce new terms, namely: multi-principal element alloys (MPEA), or complex concentrated alloys (CCA) [3]. However, at present, these terms are not yet common.

Casting methods are usually used as methods for producing high-entropy alloys. However, it should be noted that the formation of the structure of the solid solution, doped with many elements, should complicate the casting process, in particular, we can assume a heterogeneous distribution of elements, as well as the presence of significant internal stresses in the ingot. There is an obvious need to increase the number of melts to increase the homogeneity of the chemical composition and control the cooling rate during crystallization.

One of the widespread methods of improving the physical, chemical, mechanical and other properties of metals and alloys is quenching from a liquid state [8]. The development of quenching methods has led to a growing interest in materials with thermodynamically nonequilibrium structures worldwide. In these methods, the cooling rate of the melt reaches values above 10^4 K/s, due to which a wide range of metastable structural states is formed in the alloys, including

[†] *Cite as:* O.I. Kushnerov, V.F. Bashev, East. Eur. J. Phys. 3, 43 (2021), <https://doi.org/10.26565/2312-4334-2021-3-06>

nanocrystalline and amorphous, with unique sets of properties [9]. Due to this, quenching from the liquid state is a promising method for obtaining high-entropy alloys with improved characteristics.

The properties of HEAs are determined by their elemental composition and structure. Due to the resistance to ionizing radiation, wear resistance, high hardness, and, at the same time, sufficient ductility, they can be promising materials for many fields of technology [10-17].

One of the possible applications of HEAs as not only structural but also functional materials is their use as magnetic materials. In work [18], using the density-functional theory (DFT) and a magnetic mean-field model, the possible ferromagnetic properties for a set of four- and five-component high entropy alloys were predicted. Some of these alloys look promising in terms of combining high mechanical and magnetic properties. Substances that combine the properties of several different types of materials have always been of considerable scientific interest [19,20]. This work aims to obtain a multicomponent high-entropy alloy $\text{CoCr}_{0.8}\text{Cu}_{0.64}\text{FeNi}$ and to study the effect of rapid quenching from the melt on its phase composition, microhardness, and ferromagnetic properties.

EXPERIMENTAL DETAILS

The as-cast samples of $\text{CoCr}_{0.8}\text{Cu}_{0.64}\text{FeNi}$ alloy with nominal composition presented in Table 1. were prepared by means of a Tamman high-temperature electric furnace in the argon gas flow using a copper mold.

Table 1. Nominal chemical composition of $\text{CoCr}_{0.8}\text{Cu}_{0.64}\text{FeNi}$ alloy

	Co	Cr	Cu	Fe	Ni
Composition of $\text{CoCr}_{0.8}\text{Cu}_{0.64}\text{FeNi}$, at. %	22.52	18.02	14.42	22.52	22.52

The mass losses during ingot preparation did not exceed 1% and the average rate of cooling was $\sim 10^2$ K/s. The as-cast ingot was thereafter remelted and the films were obtained from the melt by splat quenching (SQ) technique. A technique for splat quenching used in the present work consisted of rapid cooling of melt drops upon their collision with the internal surface of a rapidly rotating (~ 8000 RPM) hollow cylinder of copper. The cooling rate was estimated using the expression [8,21]

$$V = \frac{\alpha \vartheta}{c\rho\delta}, \quad (1)$$

where c is the heat capacity of film, ρ is the film density, α is the coefficient of heat transfer, ϑ is the excess temperature of the film and δ is the thickness of the film.

Taking into consideration the thickness of fabricated splat quenched films, i.e., ~ 40 μm , the estimated rate of cooling was $\sim 10^6$ K/s. The X-ray diffraction analysis (XRD) was carried out using a DRON-2.0 diffractometer with monochromatized Cu $K\alpha$ radiation. The diffraction patterns were processed using QualX2 software [22]. The magnetic properties of the samples were measured by a vibrating sample magnetometer (VSM) at room temperature. The microhardness was examined using a tester PMT-3 at a load of 50 g.

RESULTS AND DISCUSSION

Electronic, thermodynamic and atomic-size criteria of phase formation in high-entropy alloys

There are two main criteria by which the high-entropy alloys are usually characterized. This is the entropy of mixing ΔS_{mix} and the enthalpy of mixing ΔH_{mix} . However, to predict the phase composition of HEAs, some additional parameters were proposed [1-3]. These parameters include in particular the valence electron concentration (VEC), the thermodynamic parameter Ω , which takes into account the melting temperature, mixing entropy and the mixing enthalpy. The important parameter is an atomic-size difference between alloy components which is denoted as δ . Let's take a closer look at the above parameters

The basic principle of HEAs is the solid solution phase stabilization by the significantly higher configurational entropy of mixing ΔS_{mix} compared to conventional alloys. The configurational entropy of mixing during the formation of regular solution alloy can be determined as

$$\Delta S_{mix} = -R \sum_{i=1}^n c_i \ln c_i, \quad (2)$$

c_i - atomic fraction of the i -th component, R - universal gas constant. Increasing of mixing entropy reduces the Gibbs free energy of the alloy and improves the stability of the solid solution. For the alloy where n is the number of components maximum mixing entropy is when they are mixed in equal atomic fractions.

Usually in HEAs ΔS_{mix} value is in the range of 12-19 J/(mol·K). Due to the high mixing entropy HEAs are solid solutions typically having simple crystal structures (FCC or BCC), but to avoid the appearance of brittle intermetallic

compounds, complex microstructures and amorphous phases in the structure of alloys, some phase formation criteria are required to be completed. According to [1, 2], the Ω parameter can be used to estimate the phase composition of HEA.

$$\Omega = \frac{T_m \Delta S_{mix}}{|\Delta H_{mix}|}, \quad (3)$$

where T_m is the average melting temperature of alloy and ΔH_{mix} - mixing enthalpy

$$T_m = \sum_{i=1}^n c_i (T_m)_i, \quad (4)$$

$$\Delta H_{mix} = \sum_{i=1, i \neq j}^n \Omega_{ij} c_i c_j, \quad (5)$$

where the regular melt-interaction parameter between i -th and j -th elements $\Omega_{ij} = 4\Delta H_{mix}^{AB}$, and ΔH_{mix}^{AB} - mixing enthalpy of binary liquid AB alloy. Alloy components should not have a large atomic-size difference, which is described by the parameter

$$\delta = 100 \sqrt{\sum_{i=1}^n c_i \left(1 - \frac{r_i}{\bar{r}}\right)^2}, \quad (6)$$

where $\bar{r} = \sum_{i=1}^n c_i r_i$; r_i - the atomic radius of the i -th element.

According to [1,2] the HEA alloys for which $\Omega \geq 1.1$ and $\delta \leq 6.6\%$ can form the solid solutions without intermetallic compounds and amorphous phases. However, simple (not ordered) solid solutions form if $-15 \text{ kJ/mol} < \Delta H_{mix} < 5 \text{ kJ/mol}$ and $\delta \leq 4.6\%$.

The other useful parameter is the valence electron concentration, VEC , which has been proven useful in determining the phase stability of high entropy alloys [1,2]. VEC is defined by:

$$VEC = \sum_{i=1}^n c_i (VEC)_i, \quad (7)$$

where $(VEC)_i$ - valence electron concentration (including the d -electrons) of the i -th element. As pointed in [1,2] at $VEC \geq 8.0$, the sole FCC phase exists in the alloy; at $6.87 \leq VEC < 8.0$, mixed FCC and BCC phases will co-exist and the sole BCC phase exists at $VEC < 6.87$. It should be noted, however, that the exact boundaries of the valence electron concentration range, in which one should expect the formation of solid solutions based on BCC and FCC lattices are rather individual for each specific alloy. For example, the VEC criteria work on the assumption that solid solutions are the only constituents of the alloy, that is, no intermetallics or amorphous phases are formed [1,2]. In addition, the VEC criteria are most effective for HEAs containing mainly 3d or 4d transition metal elements [1,2]. Despite the above limitations, the empirical rules for predicting the phase composition of alloys are widely used in the literature and have recently been confirmed by the computational thermodynamic approach [23]. Using the data from [24], we calculated ΔS_{mix} , ΔH_{mix} , δ , VEC , and Ω of the CoCr_{0.8}Cu_{0.64}FeNi HEA (Table 2).

Table 2. Electronic, thermodynamic and atomic-size parameters of the CoCr_{0.8}Cu_{0.64}FeNi high-entropy alloy

Alloy	ΔS_{mix} , J/(mol·K)	ΔH_{mix} , kJ/mol	Ω	VEC	δ , %
CoCr _{0.8} Cu _{0.64} FeNi	13.26	1.68	14.05	8.75	1.26

The analysis of these parameters shows that in CoCr_{0.8}Cu_{0.64}FeNi alloy the formation of a single-phase solid solution of the FCC type without intermetallic compounds should take place.

Structure and properties of CoCr_{0.8}Cu_{0.64}FeNi high-entropy alloy

The phase composition of the studied alloy and the crystal lattice parameters (Table 3) were determined from the XRD patterns (Fig. 1).

An analysis of the X-ray diffraction patterns made it possible to establish the following: a single-phase FCC structure is formed in both cast and SQ samples. Thus, for this alloy, the consistency of the previously considered theoretical criteria for predicting the phase composition has been confirmed. We can also see that quenching from the liquid state does not change the phase composition of the CoCr_{0.8}Cu_{0.64}FeNi alloy.

Fig. 2 shows the magnetic hysteresis loops of the as-casted and splat quenched high-entropy $\text{CoCr}_{0.8}\text{Cu}_{0.64}\text{FeNi}$ samples measured at room temperature. Both are characterized by typical ferromagnetic behavior. According to the values of coercivity H_c of the samples (Table 4), they can be classified as soft magnetic materials. As can be seen from Fig. 2 and Table 4, the value of the specific saturation magnetization M_S practically does not change with an increase in the cooling rate. This is because the magnetization M of the alloy mainly depends on the composition and crystal structure, which are unchanged for both samples. At the same time, the coercivity value has doubled. Obviously, this is due to internal stresses arising in the material during quenching from the liquid state, as well as to the formation of a microcrystalline structure containing many defects and nanoprecipitates, which complicates the displacement of domain walls during magnetization reversal [25].

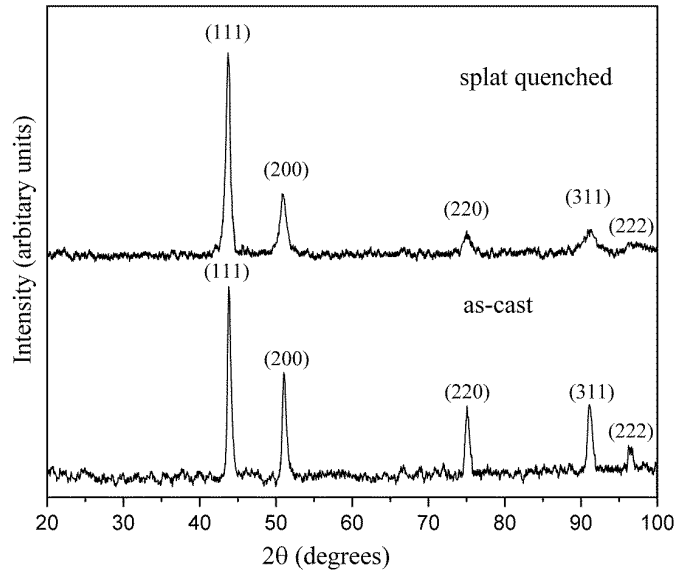


Figure 1. XRD patterns of $\text{CoCr}_{0.8}\text{Cu}_{0.64}\text{FeNi}$ high_entropy alloy

Table 3. The phase composition of $\text{CoCr}_{0.8}\text{Cu}_{0.64}\text{FeNi}$ high_entropy alloy

Alloy	Phase composition
As-cast $\text{CoCr}_{0.8}\text{Cu}_{0.64}\text{FeNi}$	FCC ($a=0.3593$ nm)
SQ film $\text{CoCr}_{0.8}\text{Cu}_{0.64}\text{FeNi}$	FCC ($a=0.3589$ nm)

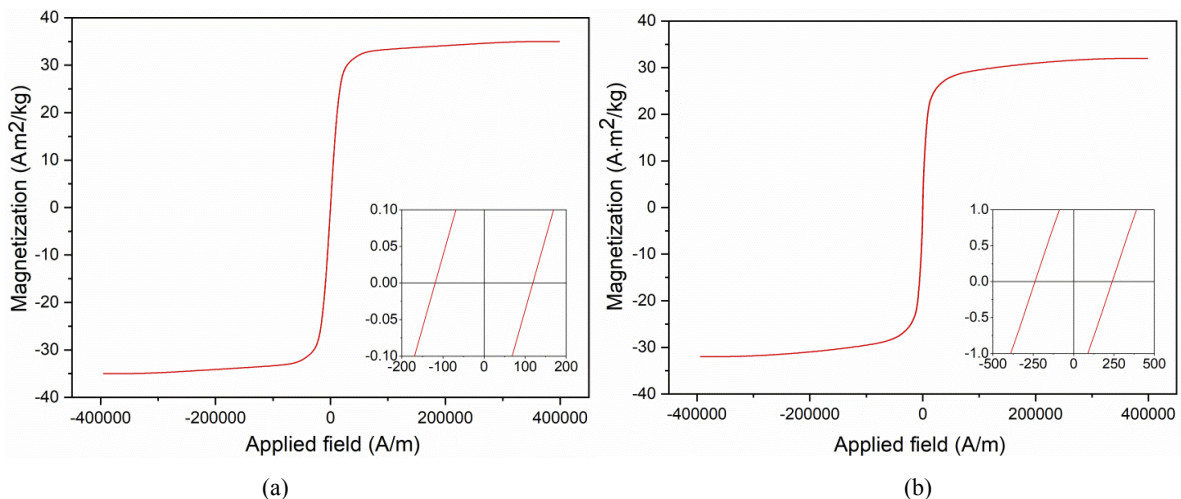


Figure 2. Hysteresis loops of as-cast (a) and splat-quenched (b) samples of $\text{CoCr}_{0.8}\text{Cu}_{0.64}\text{FeNi}$ HEA

Table 4. Magnetic characteristics of $\text{CoCr}_{0.8}\text{Cu}_{0.64}\text{FeNi}$ high_entropy alloy

Alloy	Specific saturation magnetization M_S , $\text{A}\cdot\text{m}^2/\text{kg}$	Coercivity H_c , A/m
As-cast $\text{CoCr}_{0.8}\text{Cu}_{0.64}\text{FeNi}$	35 ± 3	120 ± 10
SQ film $\text{CoCr}_{0.8}\text{Cu}_{0.64}\text{FeNi}$	32 ± 3	240 ± 20

Measurement of the microhardness of the SQ CoCr_{0.8}Cu_{0.64}FeNi alloy showed that the value of H_{μ} is higher than for the alloy in the as-cast state. (Table 5).

Table 5. Microhardness of CoCr_{0.8}Cu_{0.64}FeNi high-entropy alloy

Alloy	H_{μ} , MPa
As-cast CoCr _{0.8} Cu _{0.64} FeNi	2200±100
SQ film CoCr _{0.8} Cu _{0.64} FeNi	2600±100



This result is not unexpected, since, taking into account the results of [21], it can be concluded that in the cast alloy in the process of segregation, a microstructure with typical morphology of dendrites and interdendritic joints is formed. In the structure of the SQ alloy, the structure of a thin conglomerate of phases is observed. Thus, the microstructure and mechanical properties of the as-cast alloy significantly differ in its more equilibrium multiphase state, while the splat quenched alloy provides higher values of hardness and strength due to internal elastic stresses.

It should be noted that the relatively low value of microhardness is specific for HEAs with an FCC lattice, which is characterized by plasticity and not very high values of hardness. At the same time, alloys with a BCC lattice have a much higher microhardness but are brittle.

CONCLUSIONS

In this work, a CoCr_{0.8}Cu_{0.64}FeNi high entropy alloy was obtained for the first time in the as-cast and splat quenched state. The studies carried out made it possible to establish that the alloy has an FCC structure, which is not affected by the cooling rate. The CoCr_{0.8}Cu_{0.64}FeNi HEA shows ferromagnetic properties, and quenching from a liquid state increases the coercivity practically without changing the magnetization value. An increase in the cooling rate also increases the value of the microhardness of the alloy. Thus, the splat quenched CoCr_{0.8}Cu_{0.64}FeNi alloy can be recommended for applications where the ductility characteristics of the FCC alloy together with increased microhardness values are important.

ORCID IDs

 Oleksandr I. Kushnerov, <https://orcid.org/0000-0002-9683-2041>;  Valerij F. Bashev, <https://orcid.org/0000-0002-3177-0935>

REFERENCES

- [1] B.S. Murty, J.W. Yeh, S. Ranganathan, and P.P. Bhattacharjee, *High-Entropy Alloys 2nd Edition* (Elsevier, 2019).
- [2] T.S. Srivatsan and M. Gupta, editors, *High Entropy Alloys. Innovations, Advances, and Applications* (CRC Press, Boca Raton, 2020).
- [3] D.B. Miracle and O.N. Senkov, *Acta Mater.* **122**, 448 (2017). <https://doi.org/10.1016/j.actamat.2016.08.081>.
- [4] Y. Dong, Z. Yao, X. Huang, F. Du, C. Li, A. Chen, F. Wu, Y. Cheng, and Z. Zhang, *J. Alloys Compd.* **823**, 153886 (2020). <https://doi.org/10.1016/j.jallcom.2020.153886>.
- [5] Y.K. Kim, S. Yang, and K.A. Lee, *Sci. Rep.* **10**, 1 (2020). <https://doi.org/10.1038/s41598-020-65073-2>.
- [6] C. Gadelmeier, S. Haas, T. Lienig, A. Manzoni, M. Feuerbacher, and U. Glatzel, *Metals (Basel)*. **10**, 1412 (2020). <https://doi.org/10.3390/met10111412>.
- [7] L. Sang and Y. Xu, *J. Non. Cryst. Solids* **530**, 119854 (2020). <https://doi.org/10.1016/j.jnoncrysol.2019.119854>.
- [8] I.S. Miroshnichenko, *Закалка из жидкого состояния [Quenching From The Liquid State]*, (Metallurgy, Moscow, 1982). (in Russian).
- [9] V.F. Bashev, S.I. Ryabtsev, O.I. Kushnerov, N.A. Kutseva, and S.N. Antropov, *East Eur. J. Phys.* (3), 81 (2020). <https://doi.org/10.26565/2312-4334-2020-3-10>.
- [10] E. Zhou, D. Qiao, Y. Yang, D. Xu, Y. Lu, J. Wang, J.A. Smith, H. Li, H. Zhao, P.K. Liaw, and F. Wang, *J. Mater. Sci. Technol.* **46**, 201 (2020). <https://doi.org/10.1016/j.jmst.2020.01.039>.
- [11] C. Xiang, E.-H. Han, Z.M. Zhang, H.M. Fu, J.Q. Wang, H.F. Zhang, and G.D. Hu, *Intermetallics* **104**, 143 (2019). <https://doi.org/10.1016/j.intermet.2018.11.001>.
- [12] D. Patel, M.D. Richardson, B. Jim, S. Akhmaliev, R. Goodall, and A.S. Gandy, *J. Nucl. Mater.* **531**, 152005 (2020). <https://doi.org/10.1016/j.jnucmat.2020.152005>.
- [13] Y.H. Chen, W.S. Chuang, J.C. Huang, X. Wang, H.S. Chou, Y.J. Lai, and P.H. Lin, *Appl. Surf. Sci.* **508**, 145307 (2020). <https://doi.org/10.1016/j.apsusc.2020.145307>.
- [14] G. Perumal, H.S. Grewal, M. Pole, L.V.K. Reddy, S. Mukherjee, H. Singh, G. Manivasagam, and H.S. Arora, *ACS Appl. Bio Mater.* **3**, 1233 (2020). <https://doi.org/10.1021/acsabm.9b01127>.
- [15] G.S. Firstov, T.A. Kosorukova, Y.N. Koval, and V.V. Odnosum, *Mater. Today Proc.* **2**, S499 (2015). <https://doi.org/10.1016/j.matpr.2015.07.335>.
- [16] Y. Li, S. Wang, X. Wang, M. Yin, and W. Zhang, *J. Mater. Sci. Technol.* **43**, 32 (2020). <https://doi.org/10.1016/j.jmst.2020.01.020>.
- [17] J. Lu, Y. Chen, H. Zhang, N. Ni, L. Li, L. He, R. Mu, X. Zhao, and F. Guo, *Corros. Sci.* **166**, 108426 (2020). <https://doi.org/10.1016/j.corsci.2019.108426>.
- [18] F. Körmann, D. Ma, D.D. Belyea, M.S. Lucas, C.W. Miller, B. Grabowski, and M.H.F. Sluiter, *Appl. Phys. Lett.* **107**, 142404 (2015). <https://doi.org/10.1063/1.4932571>.
- [19] S. V. Akimov, V.M. Duda, E.F. Dudnik, A.I. Kushnerev, and A.N. Tomchakov, *Phys. Solid State* **48**, 1073 (2006). <https://doi.org/10.1134/S1063783406060175>.
- [20] E.F. Dudnik, V.M. Duda, and A.I. Kushnerov, *Phys. Solid State* **43**, 2280 (2001). <https://doi.org/10.1134/1.1427957>.

- [21] V.F. Bashev, and O.I. Kushnerov, Phys. Met. Metallogr. **118**, 39 (2017). <https://doi.org/10.1134/S0031918X16100033>.
- [22] A. Altomare, N. Corriero, C. Cuocci, A. Falcicchio, A. Moliterni, and R. Rizzi, Powder Diffr. **32**, S129 (2017). <https://doi.org/10.1017/S0885715617000240>.
- [23] S. Yang, J. Lu, F. Xing, L. Zhang, and Y. Zhong, Acta Mater. **192**, 11 (2020). <https://doi.org/10.1016/j.actamat.2020.03.039>.
- [24] A. Takeuchi and A. Inoue, Mater. Trans. **46**, 2817 (2005). <https://doi.org/10.2320/matertrans.46.2817>.
- [25] A.N. Gulivets, V.A. Zabudovsky, E.P. Shtapenko, A.I. Kushnerev, M.P. Dergachov, and A.S. Baskevich, Trans. IMF **80**, 154 (2002). <https://doi.org/10.1080/00202967.2002.11871457>.

СТРУКТУРА ТА ФІЗИЧНІ ВЛАСТИВОСТІ ВИСОКОЕНТРОПІЙНОГО СПЛАВУ $\text{CoCr}_{0.8}\text{Cu}_{0.64}\text{FeNi}$ У ЛИТОМУ ТА ЗАГАРТОВАНОМУ З РІДИНИ СТАНАХ

О. І. Кушнеров, В. Ф. Башев

*Кафедра експериментальної фізики, Дніпровський національний університет імені Олеся Гончара
72 пр. Гагаріна, Дніпро, 49010 Україна*

У статті досліджено структуру та фізичні властивості багатокомпонентного високоентропійного сплаву $\text{CoCr}_{0.8}\text{Cu}_{0.64}\text{FeNi}$ у литому та загартованому стані. Склад досліджуваного сплаву проаналізований з використанням наявних у літературі критеріїв для прогнозування фазового складу високоентропійних сплавів. Ці параметри базуються на розрахунках ентропії та ентальпії змішування, а також включають концентрацію валентних електронів, термодинамічний параметр Ω , який враховує температуру плавлення, ентропію змішування та ентальпію змішування. Ще одним важливим параметром є різниця в атомних радіусах між компонентами сплаву δ . Литі зразки сплаву $\text{CoCr}_{0.8}\text{Cu}_{0.64}\text{FeNi}$ номінального складу отримані за допомогою високотемпературної електричної печі Таммана в потоці аргону за допомогою мідної форми. Втрати ваги під час виготовлення злитків не перевищувала 1%, а середня швидкість охолодження становила $\sim 10^2$ К/с. Потім литий зразок переплавляли, а з розплаву отримували плівки. Техніка гартування з рідкого стану, використана в даній роботі, полягала в швидкому охолодженні крапель розплаву при зіткненні їх із внутрішньою поверхнею порожнього мідного циліндра, що обертався із великою швидкістю (~ 8000 об / хв). Швидкість охолодження, оцінена за товщиною плівки, становила $\sim 10^6$ К / с. Рентгеноструктурний аналіз проводили на дифрактометрі DRON-2.0 у монохроматичному випромінюванні $\text{Cu K}\alpha$. Дифрактограми оброблялися за допомогою програми QualX2. Магнітні властивості зразків вимірювалися за допомогою вібраційного магнітометра при кімнатній температурі. Мікротвердість вимірювали на приладі ПМТ-3 при навантаженні 50 г. Відповідно до теоретичних прогнозів, підтверджених результатами рентгенівських досліджень, структура сплаву як у литому, так і в загартованому стані є простим твердим розчином типу ГЦК. Параметри решітки в литому та швидкозагартованому станах становлять відповідно 0.3593 нм та 0.3589 нм. Вимірювання магнітних властивостей показало, що сплав $\text{CoCr}_{0.8}\text{Cu}_{0.64}\text{FeNi}$ можна класифікувати як магнітом'який матеріал. При цьому гартування з рідкого стану збільшує коерцитивну силу зразків. На загартованих зразках також були отримані підвищені значення мікротвердості. Це можна пояснити внутрішніми напруженнями, що виникають під час гартування.

Ключові слова: високоентропійний сплав, структура, фазовий склад, гартування з рідкого стану, мікротвердість, магнітні властивості.

PECULIARITIES IN THE STRUCTURE FORMATION AND CORROSION OF QUASICRYSTALLINE $\text{Al}_{65}\text{Co}_{20}\text{Cu}_{15}$ ALLOY IN NEUTRAL AND ACIDIC MEDIA[†]

 Olena V. Sukhova*,  Volodymyr A. Polonskyy

*Oles Honchar Dnipro National University,
72, Haharin Ave., Dnipro, 49010, Ukraine*

**Corresponding Author: sukhovaya@ukr.net*

Received June 23, 2021; revised August 16, 2021; accepted August 28, 2021

In the present study, the structure and corrosion properties of quasicrystalline conventionally solidified $\text{Al}_{65}\text{Co}_{20}\text{Cu}_{15}$ alloy cooled at 5 K/s were investigated. Structure was characterized by metallography, X-Ray diffraction, scanning electron microscopy, and energy dispersive spectroscopy. Corrosion properties were determined by gravimetric and potentiodynamic methods at room temperature. The investigations performed confirm the peritectic formation of stable quasicrystalline decagonal D-phase that coexists with crystalline $\text{Al}_4(\text{Co,Cu})_3$ and $\text{Al}_3(\text{Cu,Co})_2$ phases in the structure of $\text{Al}_{65}\text{Co}_{20}\text{Cu}_{15}$ alloy. According to energy dispersive spectroscopy, the stoichiometric composition of D-phase is $\text{Al}_{63}\text{Co}_{24}\text{Cu}_{13}$. The susceptibility of the $\text{Al}_{65}\text{Co}_{20}\text{Cu}_{15}$ alloy to corrosion significantly decreases with increasing pH from 1.0 (acidic media) to 7.0 (neutral medium). A corrosion rate of the $\text{Al}_{65}\text{Co}_{20}\text{Cu}_{15}$ alloy in the aqueous acidic solutions (pH=1.0) increases in the order $\text{HNO}_3 \rightarrow \text{HCl} \rightarrow \text{H}_2\text{SO}_4 \rightarrow \text{H}_3\text{PO}_4$. The mass of the specimens decreases in the solutions of H_2SO_4 or H_3PO_4 and increases in the solutions of HNO_3 or HCl which relates to different rate ratios of accumulation and dissolution of corrosion products. The $\text{Al}_{65}\text{Co}_{20}\text{Cu}_{15}$ alloy exhibits the highest corrosion resistance in the NaCl solution (pH=7.0) in which it corrodes under electrochemical mechanism with oxygen depolarization. The better corrosion resistance in sodium chloride solution is achieved due to the formation of passive chemical compounds blocking the surface. Free corrosion potential of the $\text{Al}_{65}\text{Co}_{20}\text{Cu}_{15}$ alloy has value -0.43 V, the electrochemical passivity region extends from -1.0 V to -0.4 V, and a corrosion current density amounts to 0.18 mA/cm². Depending on media, two typical surface morphologies are revealed after corrosion of quasicrystalline specimens of the $\text{Al}_{65}\text{Co}_{20}\text{Cu}_{15}$ alloy. In the H_2SO_4 and H_3PO_4 acidic solutions, clean specimens' surface due to its homogeneous dissolution is observed except for the more defective areas, such as boundaries of crystalline $\text{Al}_3(\text{Cu,Co})_2$ phase containing less Co, which dissolve at a higher rate. In the HNO_3 , HCl or NaCl solutions, a porous layer on the surface is formed which is visually revealed as surface darkening. After staying in the NaCl solution, on the surface of the $\text{Al}_{65}\text{Co}_{20}\text{Cu}_{15}$ alloy, the pits are also found due to preferential dissolution of components where the boundaries of $\text{Al}_3(\text{Cu,Co})_2$ phase and flaws are located.

Keywords: quasicrystalline $\text{Al}_{65}\text{Co}_{20}\text{Cu}_{15}$ alloy, decagonal quasicrystals, structure, neutral and acidic aqueous solutions, corrosion resistance.

PACS: 61.50.Lt, 61.72.Ff, 62.23.Pq, 68.35.Fx, 68.35.Np, 81.05.Je, 81.40.Cd

The quasicrystalline alloys are considered to be particularly interesting metallic materials because of exceptional properties, or combinations of physical and chemical properties, that distinguish these alloys from conventional crystalline materials [1-5]. The quasicrystalline alloys are useful for industrial applications as engineering, structural and surface coating materials [6-17] due to their outstanding properties, including high strength and hardness, a low friction coefficient and excellent wear resistance, together with other remarkable engineering properties such as good oxidation resistance, high toughness etc. [18-26].

After the discovery of a metastable icosahedral quasicrystal in the Al-Mn system, many alloy systems have been identified in which icosahedral or decagonal quasicrystalline phases are stable up to melting temperature. Among them, the Al-Cu-Co system in which a stable decagonal phase (D-phase) has been found in a slowly solidified $\text{Al}_{65}\text{Co}_{20}\text{Cu}_{15}$ alloy [27-31]. D-phase is quasiperiodic in a plane and periodic in the ten-fold direction perpendicular to this plane [32-35]. From such crystal structure arises an attractive combination of certain properties that are not achievable with conventional crystalline alloys [36-39].

The presence of elements such as cobalt in the alloy composition may inhibit corrosion [40,41] and lead to greater corrosion resistance of quasicrystalline Al-Cu-Co alloys as compared with that of Al-Cu-Fe alloys that form icosahedral quasicrystalline phase [42-44]. But only limited information has been found in the literature concerning the susceptibility of the Al-Cu-Co alloys to corrosion. Therefore, in this study we explored the behaviour of the $\text{Al}_{65}\text{Co}_{20}\text{Cu}_{15}$ alloy in neutral and acidic media, which allows us to evaluate its corrosion resistance under conditions comparable to application of aviation and rocket-and-space equipment.

MATERIALS AND METHODS

The $\text{Al}_{65}\text{Co}_{20}\text{Cu}_{15}$ alloy was produced of high purity (99.99 %) components melted using Tamman furnace in a graphite crucible. The cooling rate of the alloy was 5 K/s. The alloy composition was verified by atomic absorption spectroscopy with Sprut CEΦ-01-M device. The relative precision of the measurements was better than ± 1 at. %.

Microstructural characterization of the investigated alloy was done using Neophot and GX-51 optical microscopes, Epique quantitative analyzer, JVC scanning electron microscope (SEM) equipped with energy-dispersive

[†] Cite as: O. V. Sukhova, and V. A. Polonskyy. East. Eur. J. Phys. 3, 49 (2021), <https://doi.org/10.26565/2312-4334-2021-3-07>

spectrometer (EDS). The phase and structural compositions were also studied by powder X-ray diffraction (XRD) on ДРОН-УМ-1 diffractometer with Cu-K α radiation.

The corrosion properties were investigated by the gravimetric method after holding the Al₆₅Co₂₀Cu₁₅ alloy for 1-4 h in the HCl, H₂SO₄, HNO₃, and H₃PO₄ aqueous acidic solutions (pH=1.0) and for 1-8 days in the NaCl aqueous neutral solution (pH=7.0). The pH value of the media was measured with an EB-74 ionometer. After immersion in solutions, the specimens were weighed in a BA-21 analytical balance with error smaller than 0.1 mg. A corrosion rate was determined using the equation given in [45].

Electrochemical experiments were conducted in the NaCl solution (pH=7.0) by means of III-50-1 potentiostat and ПП-8 programmer using three-electrode electrolytic system consisted of the sample as working electrode, a platinum as counter electrode, and silver chloride as reference electrode. For each specimen, voltammograms were measured 2-3 times. A value of corrosion current density was determined by extrapolating the linear portion of the anodic and cathodic branches of the polarization curves to free corrosion potential. Model corrosion tests for 1-8 days in the NaCl solution were performed with specimens fully immersed in the medium. The surface morphology was examined using POMA 102-02 scanning electron microscope. Corrosion tests were carried out at the temperature of 293±2 K.

RESULTS AND DISCUSSION

Examination by optical and scanning electron microscopy reveals that Al₆₅Co₂₀Cu₁₅ alloy exhibits three-phase structure consisting of quasicrystalline decagonal D-phase and crystalline phases of Al₄(Co,Cu)₃ and Al₃(Cu,Co)₂ (Fig. 1a) [46]. The D-phase solidifies via a peritectic reaction, in which the primary Al₄(Co,Cu)₃ crystals are surrounded by the quasicrystalline phase. Later, liquid between D-quasicrystals solidifies to Al₃(Cu,Co)₂ phase. The identified phases are confirmed by X-ray investigation (Fig. 1b). EDS measurements show that D-phase has stoichiometric composition Al₆₃Co₂₄Cu₁₃ (Table 1). This phase takes about 65 % of a total alloy volume. The size of quasicrystals varies from 40 to 60 μ m due to differing local growth conditions.

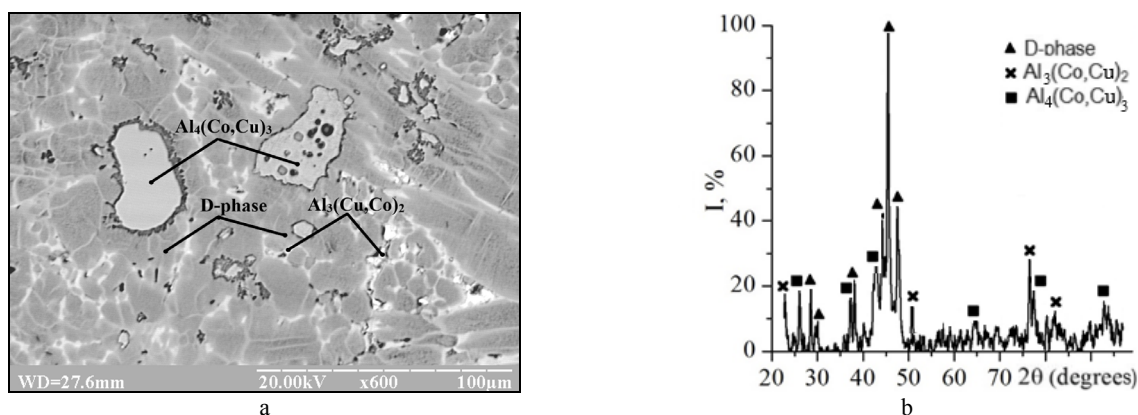


Figure 1. The Al₆₅Co₂₀Cu₁₅ alloy: a – SEM image; b – XRD pattern

Table 1. Elemental analysis (in at. %) of the Al₆₅Co₂₀Cu₁₅ alloy

Phase	Al	Co	Cu
D-phase	62.99	24.02	12.99
Al ₄ (Co,Cu) ₃	56.39	33.86	9.75
Al ₃ (Cu,Co) ₂	59.48	9.71	30.81

Corrosion tests of the Al₆₅Co₂₀Cu₁₅ alloy in the acidic media show that after the first hour of treatment a mass of the specimens gradually increases in the nitric and chloric acids. The mass gain in the chloric acid significantly exceeds that in the nitric acid reaching 4.58 g/m² against 0.98 g/m² after 4 holding hours. At that, the biggest relative change in the mass is observed after 2 holding hours in the chloric acid and after 3 holding hours in the nitric acid (Table 2).

Table 2. Relative changes in the mass (in %) of specimens of the Al₆₅Co₂₀Cu₁₅ alloy after corrosion tests

Solution	Holding time, hours				
	1	2	3	4	
HCl	0.02	0.04	0.12	0.14	
HNO ₃	0.00	0.00	0.01	0.03	
H ₂ SO ₄	-0.01	-0.09	-0.15	-0.18	
H ₃ PO ₄	-0.02	-0.09	-0.23	-0.25	
NaCl	Holding time, days				
	1	2	3	4	8
	0.04	0.15	0.20	0.22	0.24

After staying in the H_2SO_4 and H_3PO_4 acidic solutions, the mass of the specimens, on the contrary, decreases, and after 4 holding hours specific changes of the mass equal to -5.89 g/m^2 and -8.18 g/m^2 correspondingly. The $\text{Al}_{65}\text{Co}_{20}\text{Cu}_{15}$ alloy turns out to be the most corrosion-sensitive in the H_3PO_4 acid. The samples mainly lose their mass in the sulphuric acidic solution after 1 holding hour and in the orthophosphate acidic solution after 2 holding hours (Table 2). This conclusion is confirmed by scanning electron microscopy of the surface of the $\text{Al}_{65}\text{Co}_{20}\text{Cu}_{15}$ alloy affected by the sulphuric acidic solution (Fig. 2). The surface of the specimens quite homogeneously dissolves where Co-rich quasicrystalline D-phase and crystalline $\text{Al}_4(\text{Co,Cu})_3$ phase are located (Fig. 2b). Whereas, crystalline $\text{Al}_3(\text{Cu,Cu})_2$ phase, containing less Co, dissolves at a higher rate which may relate also to the fact that this phase crystallizes last and, therefore, may have more defective structure (Fig. 2a).

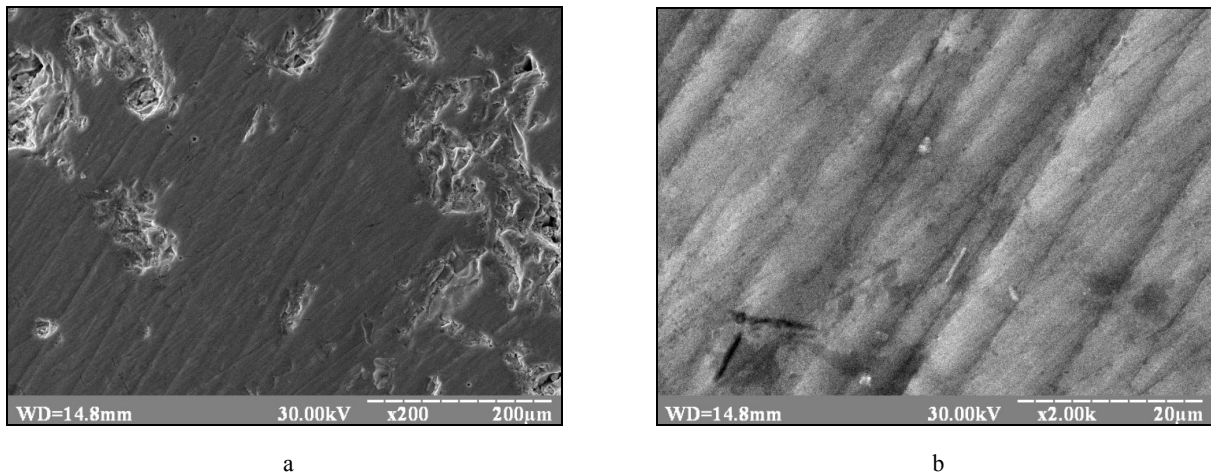


Figure 2. SEM-images of surface of the $\text{Al}_{65}\text{Co}_{20}\text{Cu}_{15}$ alloy after 4 holding hours in sulphuric acidic solution (pH=1.0)

The revealed differences in the mass changes of the corroded $\text{Al}_{65}\text{Co}_{20}\text{Cu}_{15}$ alloy affected by the acids may be explained by different rate ratios of selective dissolution of the alloy components and accumulation of corrosion products on the specimens' surface. Comparison of corrosion rates of the alloy for the investigated acidic solutions exhibits the following sequence $\text{HNO}_3 \rightarrow \text{HCl} \rightarrow \text{H}_2\text{SO}_4 \rightarrow \text{H}_3\text{PO}_4$ (in ascending order) (Fig. 3).

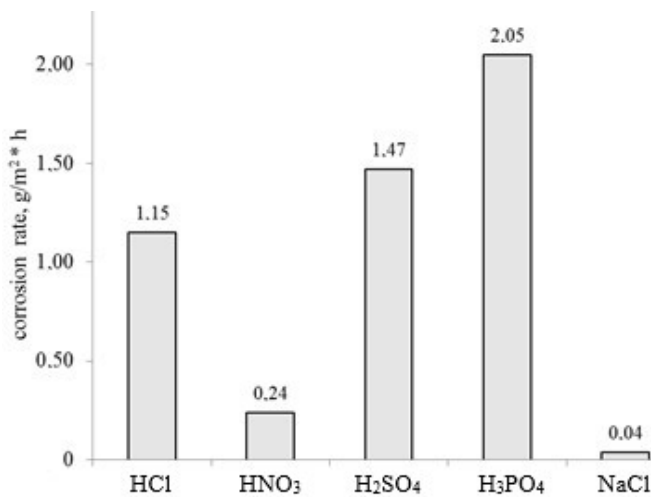


Figure 3. Corrosion rates of the $\text{Al}_{65}\text{Co}_{20}\text{Cu}_{15}$ alloy in the investigated corrosion media

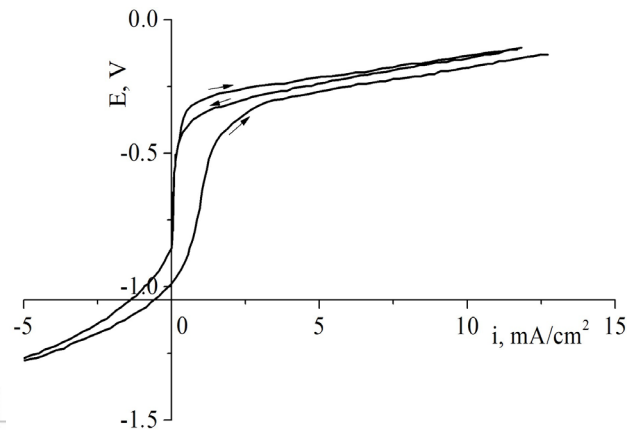


Figure 4. Potential versus current curves of the corrosion in NaCl solution (pH=7) of the $\text{Al}_{65}\text{Co}_{20}\text{Cu}_{15}$ alloy

When subjected to corrosion in the investigated media, the analyzed $\text{Al}_{65}\text{Co}_{20}\text{Cu}_{15}$ alloy is found to corrode much weaker in the NaCl solution (pH=7.0) than in the acidic solutions of HNO_3 , H_2SO_4 , HCl, and H_3PO_4 (pH=1.0). After 8 days of the tests in the aqueous sodium chloride solution, the specific mass change of the $\text{Al}_{65}\text{Co}_{20}\text{Cu}_{15}$ alloy equals to 8.0 g/m^2 . On the surface of the samples, a passivating oxide film is formed during the tests, which is revealed visually as surface darkening. That is why, the results on changes in the mass of specimens relative to the initial value indicate that the mass of specimens gradually increases, especially after 1 day of treatment (Table 2). Then, after 3 days of staying in the NaCl solution, the mass of specimens increases to a much lesser extent.

Chronopotentiometry measurements of free corrosion potential of the $\text{Al}_{65}\text{Co}_{20}\text{Cu}_{15}$ alloy show that potential stabilizes at a value of -0.43 V after ~ 17 minutes of measurements. A steady potential testifies that the passivation film build-up in the NaCl solution remains protective. Polarization measurements also evidence that corrosion of the $\text{Al}_{65}\text{Co}_{20}\text{Cu}_{15}$ alloy in the sodium chloride solution is typical to processes with oxygen depolarization (Fig. 4). Voltammograms recorded in semi-logarithmic coordinates indicate that anodic current gradually increases as potential changes towards more positive values. A sharp increase of an anodic current is observed at potential of ~ -0.3 V due to beginning of active dissolution of the alloy components. The appearance of a hysteresis loop in the anodic regime may be attributed to the surface passivation. After changing the direction of a potential sweep, in the cathodic area of a plot, a current limit in the mA range is observed. The zero value of a current density is reached at potential of -0.87 V. At potentials more negative than -1.0 V, cathodic current increases which relates to active hydrogen evolution. The value of corrosion current density for the alloy is 0.18 mA/cm². The electrochemical passivity region extends from -1.0 V to -0.4 V which indicates that the $\text{Al}_{65}\text{Co}_{20}\text{Cu}_{15}$ alloy is not susceptible to corrosion in the NaCl solution due to inhibition of anodic processes. That is why, the $\text{Al}_{65}\text{Co}_{20}\text{Cu}_{15}$ alloy exhibits the lowest corrosion rate at higher pH (Fig. 3).

Scanning electron microscopic investigations evidence that on the corroded surface of the $\text{Al}_{65}\text{Co}_{20}\text{Cu}_{15}$ alloy after staying in the NaCl solution for 8 days, pits about 10 μm in size are observed located mainly in the vicinity of defects (Fig. 5a). Corrosion is mainly concentrated in crystalline $\text{Al}_3(\text{Cu},\text{Co})_2$ phase containing less Co. The dissolution of this phase is most intense near the phase boundaries (Fig. 5b). Meanwhile, Co-rich quasicrystalline D-phase and crystalline $\text{Al}_4(\text{Co},\text{Cu})_3$ phase are less susceptible to corrosion.

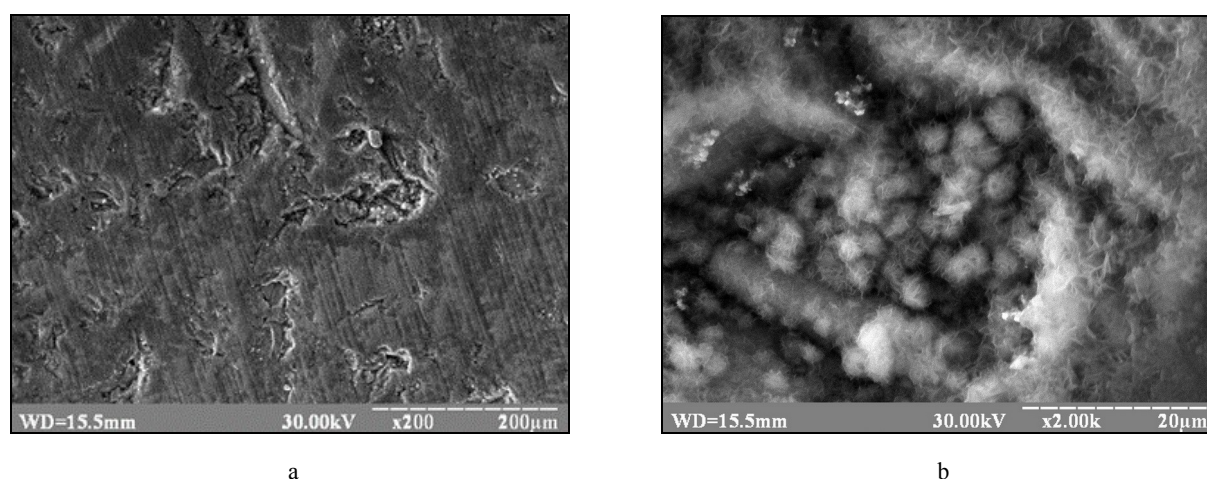


Figure 5. SEM-images of surface of the $\text{Al}_{65}\text{Co}_{20}\text{Cu}_{15}$ alloy after holding for 8 days in the NaCl solution (pH=7.0)

CONCLUSIONS

The investigations made on conventionally solidified $\text{Al}_{65}\text{Co}_{20}\text{Cu}_{15}$ alloy confirm that alloy system cooled at 5 K/s forms stable quasicrystalline decagonal D-phase by peritectic reaction. Its stoichiometric composition corresponds to $\text{Al}_{65}\text{Co}_{24}\text{Cu}_{13}$.

Corrosion of the $\text{Al}_{65}\text{Co}_{20}\text{Cu}_{15}$ alloy in the acidic solutions (pH=1.0) of HNO_3 , HCl , H_2SO_4 , H_3PO_4 (in ascending order) is much stronger than in the NaCl neutral solution (pH=7.0), intensifying with pH decreasing. The corrosion rate is lower by a factor between 6.0 and 51.25 as pH value is raised from 1.0 to 7.0. In the aqueous solutions of HNO_3 , HCl , and NaCl, a rate of accumulation of corrosion products on the specimens' surface exceeds a rate of dissolution of alloy components, but in the solutions of H_2SO_4 and H_3PO_4 – vice versa. The surface of the specimens is dissolved almost homogeneously except for the boundaries of crystalline $\text{Al}_3(\text{Cu},\text{Co})_2$ phase containing less Co which dissolve at a higher rate.

The corrosion of the $\text{Al}_{65}\text{Co}_{20}\text{Cu}_{15}$ alloy in the NaCl aqueous solution (pH=7.0) proceeds by the electrochemical mechanism with oxygen depolarization. The highest corrosion resistance of the $\text{Al}_{65}\text{Co}_{20}\text{Cu}_{15}$ alloy is observed in neutral media where a protective oxide film is developed. This alloy has free corrosion potential -0.43 V, electrochemical passivity region extending from -1.0 V to -0.4 V, and the value of corrosion current density – 0.18 mA/cm². On the surface affected by saline solution, the pits are revealed preferentially where the phase boundaries and flaws are located.

The work was performed within the framework of research project No. 0119U100977 “Electrode reactions of 3d-metal π -complexes” (2019-2021).

ORCID IDs

Olena V. Sukhova, <https://orcid.org/0000-0001-8002-0906>; Volodymyr A. Polonskyi, <https://orcid.org/0000-0002-4810-2626>

REFERENCES

- [1] C. Janot, *Quasicrystals*, (Springer, Berlin, Heidelberg, 1994), https://doi.org/10.1007/978-3-662-22223-2_9.
- [2] Z.M. Stadnik, *Physical Properties of Quasicrystals*, (Springer-Verlag, Berlin Heidelberg, 1999), <https://doi.org/10.1007/978-3-642-58434-3>.
- [3] H.R. Trebin, *Quasicrystals: Structure and Physical Properties*, (Wiley-VCH Verlag GmbH & Co., Weinheim, 2003), <https://doi.org/10.1002/3527606572>.
- [4] J.-M. Dubois, Chem. Soc. Rev. **41**, 4760-4777 (2012), <https://doi.org/10.1039/C2CS35110B>.
- [5] E. Huttunen-Saarivirta, J. Alloys Compd. **363**(1-2), 150-174 (2004), [https://doi.org/10.1016/S0925-8388\(0\)00445-6](https://doi.org/10.1016/S0925-8388(0)00445-6).
- [6] I.M. Spirydonova, O.V. Sukhova, and G.V. Zinkovskij, Metall. Min. Ind. **4**(4), 2-5 (2012). (in Russian)
- [7] W. Wolf, C. Bolfarini, C.S. Kiminami, and W.J. Botta, J. Mater. Res. **36**, 281-297 (2021), <https://doi.org/10.1557/s43578-020-00083-4>.
- [8] K. Jithesh, T.R. Prabhu, R.V. Anant, M. Arivarasu, A. Srinivasan, R.K. Mishra, and N. Arivazhagan, Mater. Sci. Forum. **969**, 218-224 (2019), <https://doi.org/10.4028/www.scientific.net/MSF.969.218>.
- [9] I.M. Spiridonova, E.V. Sukhovaya, S.B. Pilyaeva, and O.G. Bezrukavaya, Metall. Min. Ind. **3**, 58-61 (2002). (in Russian)
- [10] M. Kamalnath, B. Mohan, A. Singh, and K. Thirumavalavan, Mater. Res. Express. **7**(2), 1-11 (2020), <https://doi.org/10.1088/2053-1591/ab71c5>.
- [11] O.V. Sukhova, Phys. Chem. Solid St. **21**(2), 355-360 (2020), <https://doi.org/10.15330/pcss.21.2.355-360>.
- [12] M. Zhu, G. Yang, L. Yao, S. Cheng, and Y. Zhou, J. Mater. Sci. **45**(14), 3727-3734 (2010), <https://doi.org/10.1007/s10853-010-4421-8>.
- [13] O.V. Sukhova and Yu.V. Syrovatko, Metallofiz. Noveishie Technol. **33**(Special Issue), 371-378 (2011). (in Russian)
- [14] V.V. Cherdyn'tsev, S.D. Kaloshkin, I.A. Tomilin, E.V. Shelekhov, A.I. Laptev, A.A. Stepashkin, and V.D. Danilov, Phys. Met. Metallogr. **104**(5), 497-504 (2007), <https://doi.org/10.1134/S0031918X0711009>.
- [15] T.P. Yadav, D. Singh, R.S. Tiwari, and O.N. Srivastava, J. Mater. Lett. **80**, 5-8 (2012), <https://doi.org/10.1016/J.MATLET.2012.04.034>.
- [16] S.I. Ryabtsev, V.A. Polonsky, and O.V. Sukhova, Powder Metall. Met. Ceram. **58**(9-10), 567-575 (2020), <https://doi.org/10.1007/s11106-020-00111-2>.
- [17] J. Krawczyk, W. Gurdziel, W. Bogdanowicz, and K. Flisinski, Solid State Phenom. **163**, 282-285 (2010), <https://doi.org/10.4028/www.scientific.net/SSP.163.282>.
- [18] O.V. Sukhova and K.V. Ustinova, Funct. Mater. **26**(3), 495-506 (2019), <https://doi.org/10.15407/fm26.03.495>.
- [19] S.S. Kang and J.-M. Dubois, Phil. Mag. A. **66**(1), 151-163 (1992), <https://doi.org/10.1080/01418619208201520>.
- [20] U. Koster, W. Liu, H. Liebertz, and M. Michel, J. Non-Cryst. Solids. **153-154**, 446-452 (1993), [https://doi.org/10.1016/0022-3093\(93\)90393-C](https://doi.org/10.1016/0022-3093(93)90393-C).
- [21] X. Zhou, P. Li, J. Luo, S. Qian, and J. Tong, J. Mater. Sci. Technol. **20**(6), 709-713 (2009), <https://jmmst.org/CN/Y2004/V20/106/709>.
- [22] B.I. Wehner, J. Meinhardt, U. Koster, H. Alves, N. Eliaz, and D. Eliezer, Mater. Sci. Eng. A. **226-228**, 1008-1011 (1997), [https://doi.org/10.1016/S0921-5093\(96\)10848-0](https://doi.org/10.1016/S0921-5093(96)10848-0).
- [23] L.C. Jamshidi and R.J. Bodbari, J. Chilean Chem. Soc. **63**(2), 3928-3933 (2018), <https://doi.org/10.4067/s0717-97072018000203928>.
- [24] L.C. Jamshidi, R.J. Rodbari, L. Nascimento, E.P. Hernandez, and C.M. Barbosa, J. Met. Mater. Miner. **26**(1), 9-16 (2016), <https://doi.org/10.14456/jmmm.2016.2>.
- [25] K. Yubuta, K. Yamamoto, A. Yasuhara, and K. Hiraga, Mater. Trans. **55**(6), 866-870 (2014), <https://doi.org/10.2320/matertrans.M2014008>.
- [26] R.A. Varin, L. Zbroniec, T. Czujko, and Y.-K. Song, Mater. Sci. Eng. A. **300**(1-2), 1-11 (2001), [https://doi.org/10.1016/S0921-5093\(00\)01809-8](https://doi.org/10.1016/S0921-5093(00)01809-8).
- [27] A.-P. Tsai, A. Inoue, and T. Masumoto, Mater. Trans. JIM. **30**(4), 300-304 (1989), <https://doi.org/10.2320/matertrans1989.30.300>.
- [28] I.M. Zhang and P. Gille, J. Alloys Compd. **370**(1-2), 198-205 (2004), <https://doi.org/10.1016/j.jallcom.2003.09.033>.
- [29] D. Holland-Moritz, D.M. Herlach, B. Grushko, and K. Urban, Mater. Sci. Eng. A. **181-182**, 766-770 (1994), [https://doi.org/10.1016/0921-5093\(94\)90735-8](https://doi.org/10.1016/0921-5093(94)90735-8).
- [30] W. Bogdanowicz and J. Krawczyk, Cryst. Res. Technol. **45**(12), 1321-1325 (2010), <https://doi.org/10.1002/crat.201000313>.
- [31] D. Holland-Moritz, G. Jacobs, and I. Egry, Mater. Sci. Eng. **294-296**, 369-372 (2000), [https://doi.org/10.1016/S0921-5093\(00\)01126-6](https://doi.org/10.1016/S0921-5093(00)01126-6).
- [32] Y. Zou, P. Kuczera, J. Wolny, Acta Phys. Pol. A. **130**(4), 845-847 (2016), <https://doi.org/10.12693/aphyspola.130.845>.
- [33] B. Luca, J. Pham, and P.J. Steinhardt, Sci. Rep. **8**, 1-8 (2018), <https://doi.org/10.1038/s41598-018-34375-x>.
- [34] M. Widom, I. Al-Lehyani, W. Wang, and E. Cockayne, Mater. Sci. Eng. **294-296**, 295-298 (2000), [https://doi.org/10.1016/S0921-5093\(00\)01215-6](https://doi.org/10.1016/S0921-5093(00)01215-6).
- [35] E. Cockayne and M. Widom, Phys. Rev. Lett. **81**(3), 598-601 (1998), <https://doi.org/10.1103/PhysRevLett.81.598>.
- [36] A.R. Kortan, F.A. Thiel, H.S. Chen, A.P. Tsai, A. Inoue, and T. Masumoto, Phys. Rev. B. **40**(13), 9397-9399 (1989), <https://doi.org/10.1103/PhysRevB.40.9397>.
- [37] D. Holland-Moritz, J. Schroers, D.M. Herlach, B. Grushko, and K. Urban, Acta Mater. **46**(5), 1601-1615 (1998), [https://doi.org/10.1016/S1359-6454\(97\)00341-8](https://doi.org/10.1016/S1359-6454(97)00341-8).
- [38] X.Z. Liao, X.L. Ma, J.Z. Jin, and K.H. Kuo, J. Mater. Sci. Lett. **11**, 909-912 (1992), <https://doi.org/10.1007/BF00729091>.
- [39] L. Bindi, N. Yao, C. Lin, L.S. Hollister, C.L. Andronicos, V.V. Distler, M.P. Eddy, A. Kostin, V. Kryachko, G.J. MacPherson, W.M. Steinhard, M.P. Yudovskaya, and L. Steinhard, Sci. Rep. **5**, 1-5 (2015), <https://doi.org/10.1038/srep09111>.
- [40] K. Cooke, *Aluminum Alloys and Composites*, (Intechopen, London, 2020), <https://doi.org/10.5772/intechopen.81519>.
- [41] I.M. Spiridonova, E.V. Sukhovaya, V.F. Butenko, A.P. Zhudra, A.I. Litvinenko, and A.I. Belyi, Powder Metall. Met. Ceram. **32**(2), 139-141 (1993), <https://doi.org/10.1007/BF00560039>.
- [42] O.V. Sukhova, V.A. Polonsky, and K.V. Ustinova, Metallofiz. Noveishie Technol. **40**(11), 1475-1487 (2018), <https://doi.org/10.15407/mfint.40.11.1475>. (in Ukrainian)
- [43] O.V. Sukhova, V.A. Polonsky, and K.V. Ustinova, Voprosy Khimii i Khimicheskoi Technologii. **6**(121), 77-83 (2018), <https://doi.org/10.32434/0321-4095-2018-121-6-77-83>. (in Ukrainian)

- [44] O.V. Sukhova, V.A. Polonskyi, and K.V. Ustinova, *Phys. Chem. Solid St.* **18**(2), 222-227 (2017), <https://doi.org/10.15330/pcss.18.2.222-227>.
- [45] I.M. Zharskyi, N.P. Ivanova, D.V. Kuis, and N.A. Svidunovich, *Коррозия и защита металлических конструкций и оборудования [Corrosion and Protection of Metal Constructions and Equipment]*, (Vysh. shk., Minsk, 2012). (in Russian)
- [46] O.V. Sukhova and Yu.V. Syrovatko, *Metallofiz. Noveishie Technol.* **41**(9), 1171-1185 (2019), <https://doi.org/10.15407/mfint.41.09.1171>. (in Russian)

ОСОБЛИВОСТІ СТРУКТУРОУТВОРЕННЯ ТА КОРОЗІЇ КВАЗИКРИСТАЛІЧНОГО СПЛАВУ $Al_{65}Co_{20}Cu_{15}$ В НЕЙТРАЛЬНОМУ ТА КИСЛИХ СЕРЕДОВИЩАХ

Олена В. Сухова, Володимир А. Полонський

Дніпровський національний університет імені Олеся Гончара
49010, Україна, м. Дніпро, просп. Гагаріна, 72

В роботі досліджували структуру та корозійні властивості квазікристалічного сплаву $Al_{65}Co_{20}Cu_{15}$, закристалізованого зі швидкістю 5 К/с за звичайних умов. Структуру вивчали методами металографії, рентгеноструктурного аналізу, сканувальної електронної мікроскопії та рентгеноспектрального мікроаналізу. Корозійні властивості визначали гравіметричним та потенціодинамічним методами за кімнатної температури. Проведені дослідження підтвердили перитектичне утворення стабільної квазікристалічної декагональної D-фази, яка в структурі сплаву $Al_{65}Co_{20}Cu_{15}$ співіснує з кристалічними фазами $Al_4(Co,Cu)_3$ та $Al_3(Cu,Co)_2$. Згідно з результатами рентгеноспектрального мікроаналізу, стехіометричний склад D-фази відповідає $Al_{63}Co_{24}Cu_{13}$. Опір корозії сплаву $Al_{65}Co_{20}Cu_{15}$ суттєво збільшується з підвищенням рН розчинів з 1,0 (кислі середовища) до 7,0 (нейтральне середовище). Швидкість корозії сплаву $Al_{65}Co_{20}Cu_{15}$ у водних розчинах кислот (рН=1,0) збільшується в такому порядку: $HNO_3 \rightarrow HCl \rightarrow H_2SO_4 \rightarrow H_3PO_4$. Маса зразків зменшується в розчинах кислот H_2SO_4 та H_3PO_4 і збільшується в розчинах HNO_3 та HCl , що пов'язане з різним співвідношенням швидкостей накопичення та розчинення продуктів корозії. Найбільшу корозійну тривкість сплав $Al_{65}Co_{20}Cu_{15}$ має в розчині $NaCl$ (рН=7,0), в якому корозія сплаву проходить за електрохімічним механізмом з кисневою деполяризацією. Найкращий опір корозії в розчині натрій хлориду досягається за рахунок утворення пасивних хімічних сполук на поверхні сплаву, які блокують корозію. Вільний потенціал корозії сплаву $Al_{65}Co_{20}Cu_{15}$ становить $-0,43$ В, зона електрохімічної пасивності простягається від $-1,0$ В до $-0,4$ В, а густина струму корозії дорівнює $0,18$ мА/см². Залежно від корозійного середовища, спостерігаються два типи поверхні зразків квазікристалічного сплаву $Al_{65}Co_{20}Cu_{15}$, які зазнали корозійного руйнування. Після перебування в розчинах кислот H_2SO_4 та H_3PO_4 спостерігається чиста поверхня зразків внаслідок її відносно рівномірного розчинення за виключенням більш дефектних ділянок, таких як границі кристалічної фази $Al_3(Cu,Co)_2$, що містить менше Со, які розчиняються дещо швидше. В розчинах HNO_3 , HCl та $NaCl$ на поверхні утворюється пористий шар, який візуально спостерігається як потемніння поверхні. Після перебування в розчині $NaCl$ на поверхні сплаву $Al_{65}Co_{20}Cu_{15}$ також утворюються ділянки пітінгів внаслідок переважного розчинення компонентів в місцях розташування границь фази $Al_3(Cu,Co)_2$ та дефектів поверхні.

Ключові слова: квазікристалічний сплав $Al_{65}Co_{20}Cu_{15}$, декагональні квазікристали, структура, нейтральний та кислі водні розчини, корозійна тривкість.

DETERMINATION OF CALIBRATION X-RAY BEAM QUALITIES AND ESTABLISH A SET OF CONVERSION COEFFICIENTS FOR CALIBRATION OF RADIATION PROTECTION DEVICES USED IN DIAGNOSTIC RADIOLOGY[†]

 **Tanjim Siddiqua**^a,  **Md. Shakilur Rahman**^{a,*},  **Md. Sanaullah**^b,  **Zohora Akter Mitu**^c,
 **Imran Hossain**^d,  **Sadeka Sultana Rubai**^c

^aSecondary Standard Dosimetry Laboratory (SSDL), Bangladesh Atomic Energy Commission, Savar, Dhaka-1349, Bangladesh

^bDepartment of Nuclear Engineering, University of Dhaka, Dhaka-1000, Bangladesh

^cDepartment of Physics, University of Chittagong, Chittagong-4331, Bangladesh

^dDepartment of Physics, University of Barisal, Barisal-8200, Bangladesh

*Corresponding Author: shakilurssdl@baec.gov.bd

Received April 16, 2021; accepted August 27, 2021

The use of X-ray facilities in calibrating radiation measuring equipment in diagnostic radiology requires an exact knowledge of the radiation field. X-ray spectrums are made narrow beam by proper filtration recommended by several international organizations. In the present study, the experimental determination of X-ray calibration qualities and analysis of conversion coefficients from air Kerma to ambient and personal dose equivalent is carried for X-ray beam irradiator X80-225kV as per ISO narrow spectrum series at Secondary Standard Dosimetry Laboratory (SSDL) in Bangladesh. The X-ray beam involved in half value layer, effective energy, beam homogeneity coefficient and consistency of X-ray production from the generator (kV and mA) is conducted. A discrepancy of half value layer has been observed for N200 beam code by -8.5% which leads to the deviation of effective energy by -7.7% with a standard deviation of 1.3%. The conversion coefficients from the air kerma to dose equivalent that satisfying the condition of ICRU sphere is established to obtain radiation qualities and compared with values referred by other standard laboratories. A deviation of 0.87% has been observed for $H^*(10)$ and $H'(0.07)$ in between ISO and BCRU empirical relation which is insignificant. A set of conversion coefficients for $Hp(10)$ and $Hp(0.07)$ has also been calculated for ICRU four element tissue.

Keywords: X-ray qualities, radiation protection, ISO narrow beam, ambient dose equivalent, personal dose equivalent

PACS: 06.20.Fb; 28.41.Te; 52.38.Ph

Radiation protection is based on the principle of monitoring with the aim of verifying how requirements of the system of limits in deriving dose equivalent. X-rays are highly penetrating radiation and are widely used as a calibration source at standard laboratories for the calibration of dosimeters used at diagnostic radiology for the convenient use of their expected energies and qualities. Kerma in air is the most common and widely used reference quantity for X-ray photon fields specified by different calibration laboratories. Most of the national recommendations for the calibration of dosimeters are derived from the recommendations of ISO-4037 [1], which specifies characteristics of calibration beams. To reproduce these beams strictly according to the International Organization for Standardization (ISO) recommendation is difficult and has to look a close compromise. For achievement of required air kerma rates and Half Value Layers (HVL) adjusting the filtration is necessary. Some of the laboratories also extended the number of calibration beams, i.e. the energy range beyond ISO-4037. All these lead differences in the specification of standard beams between different laboratories. This leads the characterization of X-ray beam used for the protection of radiation as a whole [2].

As early as in 1985, the International Commission on Radiation Units and Measurements (ICRU) presented a concept of radiation protection quantities for measurement in area and individual monitoring of external radiation. The concept of operational quantities is to provide a reasonable and conservative approximation to the effective dose for most photon energies. Effective dose is the radiation protection quantity assessed control purpose in respect of stochastic effects of ionizing radiation. In 1985, the concept of operational quantities was introduced in ICRU Report-39 [3] which was further elaborated in ICRU Report 43 and 47 [4, 5]. The quantities applied during the calibration of dosimeter for area monitoring in units of dose equivalents are ambient dose equivalent $H^*(10)$ & directional dose equivalent $H'(0.07)$ and for individual monitoring it is represented by $Hp(10)$ and $Hp(0.07)$ [6, 7]. ISO-4037 also describes procedures for calibrating and determining the response of dosimeters and dose rate meters in terms of the ICRU operational quantities $Hp(10)$, $Hp(0.07)$, $H^*(10)$ and $H'(0.07)$ for radiation protection.

Air Kerma is widely used as reference quantities specified by different calibration laboratories and calibration of dosimeter used for individual and environmental monitoring requires the knowledge of conversion coefficients between the air Kerma and an appropriate protection quantity. The conversion coefficients (Sv/Gy) that relates ambient and personal dose equivalent to exposure and air kerma in free air is established by ISO for narrow spectrum in its publication 4037 [1, 8] as well as IAEA safety series-16 [9]. Conversion coefficients are the function of effective energy of the photon. The Conversion coefficients between the air kerma and these quantities have been calculated by different authors [10, 11]. The National

[†] **Cite as:** T. Siddiqua, Md.S. Rahman, Md. Sanaullah, Z.A. Mitu, I. Hossain, and S.S. Rubai, East. Eur. J. Phys. 3, 55 (2021), <https://doi.org/10.26565/2312-4334-2021-3-08>

© T. Siddiqua, Md.S. Rahman, Md. Sanaullah, Z.A. Mitu, I. Hossain, S.S. Rubai, 2021

Measurement Accreditation Service (NAMAS) [12] recommended for the calibration of radiological instruments using ISO recommended conversion coefficients (Sv/Gy) in its publication. The radiation fields from these reference radiations are normally standardized by the measurement of the air kerma rates. Such conversion coefficients (Sv/Gy) for monoenergetic photon have been recommended by various authors and organizations such as British Committee on Radiation Units and Measurements [BCRU] [13], International Commission on Radiological Protection (ICRP) [14], National Radiological Protection Board (NRPB) [15], Physikalisch-Technische Bundesanstalt (PTB) [16] etc. The calculations of conversion coefficients are usually performed by Monte Carlo simulations in standard condition of exposure of a simplified phantom.

On the other hand, operational dosimetric quantity recommended for individual monitoring is the personal dose equivalent $H_p(10)$ and $H_p(0.07)$, which would exist on a phantom approximately similar to a human body. The concept from which, calibration of personal dosimeter should be carried out on a suitable phantom surface as recommended by different international organizations related to the radiation protection standard. The calibration phantom should provide a backscatter contribution similar to that of the part of the body where the dosimeter is worn. In several times, different phantoms recommended for and later were rejected due to raised difficulties. In 1992, the ICRU-47 [5] gave a list of five different phantoms that were being used by several laboratories, which is considered to be enough within the accepted overall uncertainty in most radiation protection measurement of 30%. In this recommendation, calibration of personal dosimeter should be carried out on a PMMA slab phantom of size 30 cm × 30 cm × 15 cm. Recently, a recommended phantom is proposed by the ISO in its report ISO-4037-3 [1] is named as ISO water phantom of same dimension, which is represented as the human torso with regard to backscattering of the incident radiation. For calibration, this definition is extended to include a phantom having the composition of ICRU tissue and the same size and shape as the calibration phantom (30 cm × 30 cm × 15 cm, ICRU four element tissue phantom) [17]. However, since ICRU tissue is not readily available, a phantom of alternative composition must be specified. Calculated and measured photon backscatter results for the ICRU tissue phantom and calibration phantoms have been reported [18-19]. Kramar, H.M. *et al.* studies of the PMMA rectangular phantom indicated that photon energies in the range from about 10-500 keV, the backscatter factor could be 8% high relative to ICRU tissue [20]. Nelson and Chilton [21], for instance, have calculated dose equivalents in plastic and ICRU tissue equivalent semi-infinite slab phantoms for photon energies range 10-150 keV. Backscatter factor and tissue kerma at the phantom surface have been published by Bartlett *et al.* [22] for photon energies 15-662 keV for an ICRU tissue equivalent cube phantom and PMMA slab. R. J. Traub *et al.* [19] calculated MCNP generated backscattering correction factor for PMMA and ISO water phantom for narrow beam spectrum for the photon energy from 10 keV-2 MeV.

The aim of this work is to establish the calibration X-ray beam with a set of conversion factor for operational quantities for newly installed X-ray beam irradiator X80-225KV at Secondary Standard Dosimetry Laboratory (SSDL), Bangladesh Atomic Energy Commission.

MATERIALS AND METHODS

I. Calibration of X-ray Machine: The X-ray beam irradiator X80-225KV has been used to generate X-ray that permits its variable tube potentials 15-225 kV in 0.2 kV increments with accuracy ± 1% kV drift as a function of temperature is <100 ppm/°C and current selectable from 0-50 mA in 0.05 mA increments with a current accuracy ± 0.2% of set value for standard focal spot ± 0.2% for fine focuses. The quality of the X-ray production is checked in order to get of the desired uniformity of narrow beam. The linearity of tube voltage and tube current is tested for stability of the X-ray generator. The measurement is performed using secondary standard ionization chamber NE2575 coupled with an electrometer TW10002. Dose measurements were performed for each recommended beam quality of ISO narrow spectrum series at constant tube voltage varying tube current from 0-15 mA with an increment of 0.1 mA and vice versa. The stability of the X-ray generator was found to be good in agreement with SD variation of less than 1%. Output linearity is checked and found to be linearly increased with mAs and exposure time, beam output per unit time was also constant with exposure time which is shown in Figure 1.

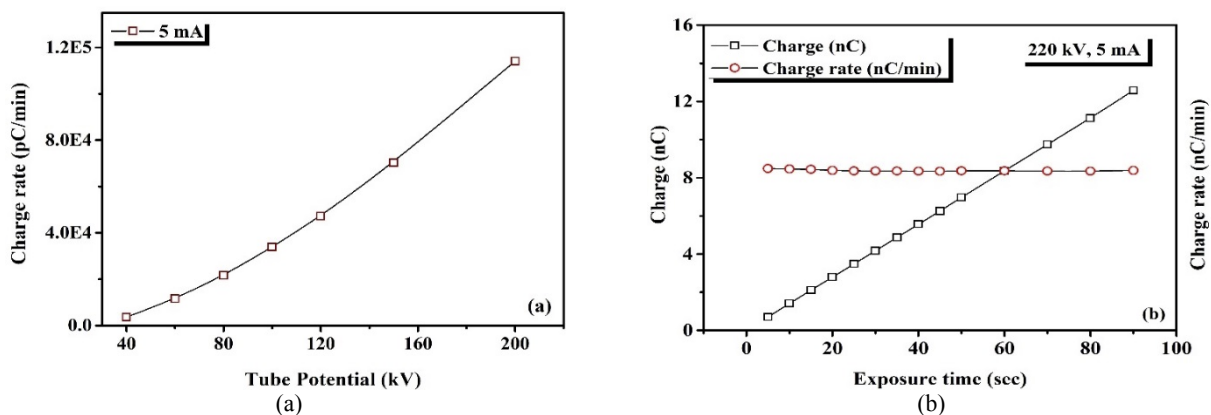


Figure 1. Variation of beam output with (a) Tube potential kVs and (b) Exposure time.

II. Half Value Layer (HVL) and Beam Homogeneity Coefficient: Attenuation measurements of a monoenergetic (monochromatic) beam of X- or gamma ray depends on the number of photons incident on an absorber, the number of photons transmitted through the absorber, and the absorber thickness. The expression; $\mu = \Delta N / \Delta x$. If ΔN and Δx are very small, they are known as differentials and the differential equation is solved by using calculus giving the following equations;

$$I = I_0 e^{-\mu x} \text{ and } N = N_0 e^{-\mu x} \quad (1)$$

where I_0 is beam intensity at an absorber thickness of zero, x absorber thickness, I is the beam intensity transmitted through an absorbent of thickness of x , e is base of the natural logarithm system, μ is attenuation coefficient, N = number of transmitted photons, and N_0 = number of incident photons.

The penetrating ability or quality of an X-ray beam is described explicitly by its spectral distribution, which indicates the energy present in each energy interval. However, the HVL or half-value thickness is the concept used most often to describe the penetrating ability of X-ray beams of different energy levels and the penetration through specific materials.

The HVL of an X-ray beam is obtained by measuring the exposure rate from the X-ray generator for a series of attenuating materials or attenuators placed in the beam. The HVL can be easily calculated from the linear attenuation coefficient for a monoenergetic photon beam and vice versa. The measurement of HVL is related to the Hubble's mass attenuation coefficient by relation; $HVL = \ln 2 / \mu$, where μ is linear attenuation coefficient of the material.

Hence beam homogeneity coefficient (h) has been obtained by using the relation stated below ;

$$h = \frac{1^{st} \text{ HVL}}{2^{nd} \text{ HVL}} \quad (2)$$

Effective energy, E_{eff} of narrow beam X-rays are calculated by the empirical relation obtained from the interpolation value from Hubble mass attenuation coefficients [23];

$$E_{eff} = 76.48 \cdot t^{0.356} + 2.543 \cdot t^{2.00}, \quad (3)$$

where t is the filter thickness in mm of Cu.

III. Measurement of Air Kerma Rate: The term dosimetry is used to describe the method by which the value of physical quantity characterizing the interaction of the radiation field with matter, which is measured in a given point by the use of a calibrated standard instrument. Dosimetry is the basis for calibration of radiation protection instruments and the determination of their response as a function of energy of interest. The output of calibration X-ray beam is measured by using a secondary standard ionization chamber NE2575 coupled with an electrometer TW10002. The chamber was previously calibrated at the National Physical Laboratory as well as from IAEA laboratory in terms of air kerma.

The air kerma rate at the reference point in air is given by simple relationship;

$$K'_a = M_u \cdot N_K, \quad (4)$$

where, M_u is the reading of the electrometer per unit time corrected for the influence quantities and N_K is the calibration factor in terms of air kerma. The corrected electrometer reading M_u , which is derived from the uncorrected instrument reading, M , by applying a number of measurement corrections;

$$M_u = M \cdot K_{tp} \cdot P_s \cdot P_{pol} \cdot C_k, \quad (5)$$

where, K_{tp} is the temperature and pressure correction factor, P_s is the recombination correction factor, P_{pol} is the correction factor for polarity effects in the user's beam and C_k is the correction factor for any difference in relative humidity between the reference conditions and conditions during measurement.

RESULTS

I. X-ray Beam Qualities: The experimentally measured and ISO reference values of HVL with tube potential (KV) for the ISO recommended filter combination for narrow beam spectrum is shown in Figure 2. The variation of HVL of measured value lies within 2 to -8.5% to ISO values with a standard deviation of 1.3%. The Beam homogeneity coefficients lie within 0.84 to 1.04 that meets well in agreement with ISO values (0.75 to 1.00). The experimental values of second HVL varies by -10.9% and -12.9% with ISO values for the beam code N150 and N200. It can be mentioned here that the deviation between the experimental and reference values of second HVL lies within 2% for five other beam codes. The effective energy (keV) is then calculated by established empirical relation which is obtained by the interpolation value from Hubble mass attenuation coefficients (Eqn. 3). It is shown that the -8.5% discrepancy of HVL for the beam code N200 leads to an effective energy deviation of -7.7%. The experimental measured 1st and 2nd HVL for ISO recommended filter combination with the reference values are summarized in Table 1.

II. Conversion Coefficients (Sv/Gy) for Reference Photon Radiation: The conversion coefficient enables calibration in terms of operational quantities to be derived from those the quantity currently determined by primary standardization laboratories. A set of conversion coefficients (Sv/Gy) for ambient dose equivalent $H^*(10)$ and $H'(0.07)$ and personal dose equivalent $H_p(10)$ and $H_p(0.07)$ has been calculated for ISO narrow beam spectrum series.

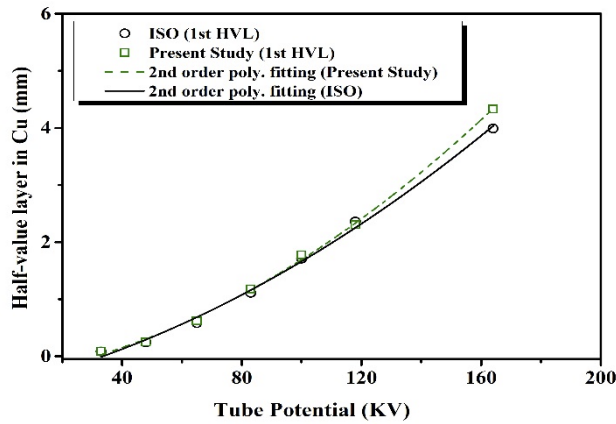


Figure 2. Experimental value of HVL in mm of Cu with ISO reference values

Table 1. Established radiation qualities and air kerma rate of X-ray beam irradiator X80-225KV

Beam code	Tube voltage in kV	Additional Filtration thickness in mm			1 st HVL in mm of Cu		HC	Effective photon energy in keV	Air kerma rate in mGy/h
		Pb	Sn	Cu	ISO reference	Experimental Value			
N40	40			0.21	0.084	0.088	0.957	32.21	37.12
N60	60			0.60	0.24	0.25	0.961	46.85	79.94
N80	80			2.00	0.58	0.62	1.016	65.49	14.28
N100	100			5.00	1.11	1.18	1.044	84.66	7.08
N120	120		1.00	5.00	1.71	1.775	0.947	102.00	10.45
N150	150		2.50	--	2.36	2.31	0.843	116.61	58.14
N200	200	1.00	3.00	2.00	3.99	4.33	0.947	176.544	22.20

II (a). Ambient Dose Equivalent $H^*(10)$ and $H'(0.07)$: The conversion coefficient for ambient dose equivalent is calculated from the fitted value of photon energy vs Conversion coefficient recommended by ISO and is given in Table 2 (SSDL, Bangladesh). The empirical mathematical functions for photon energy have been fitted from the data recommended by the British Committee on Radiation Units and Measurements (BCRU) for narrow spectrum series which is adopted under the condition of ICRU-39. These functions are convenient for user as their derivation is discussed elsewhere [23].

Table 2. Calculated values of Conversion Coefficients for ambient dose equivalent $H^*(10)$

Beam Quality	Effective Energy in keV	HVL in mm	Conversion Coefficients $H^*(10)$ (Sv/Gy)						
			Cu	ISO	BCRU	NPL	PTB	NRPB	AERE
N40	32.21	0.088	1.192	1.194	1.134	1.180	1.164	1.145	1.148
N60	46.85	0.250	1.615	1.618	1.547	1.579	1.579	1.528	1.558
N80	65.49	0.620	1.741	1.748	1.733	1.743	1.742	1.743	1.732
N100	84.66	1.180	1.713	1.704	1.706	1.706	1.705	1.706	1.706
N120	102.00	1.775	1.647	1.637	1.635	1.646	1.645	1.647	1.635
N150	116.61	2.305	1.599	1.585	1.587	1.597	1.697	1.598	1.588
N200	176.544	4.330	1.449	1.437	1.431	1.442	1.442	1.420	1.423

For monoenergetic photons with energies between 10 keV and 10 MeV, the relationship [24] between ambient dose equivalent $H^*(10)$ at 10 mm depth in ICRU tissue and air kerma free in air, K_a is given by;

$$\frac{H^*(10)}{K_a} = \frac{x}{ax^2+bx+c} + d \cdot \arctan(gx), \tag{6}$$

where $a = 1.465$, $b = -4.414$, $c = 4.789$, $d = 0.7006$, $g = 0.06519$, \arctan in radians and $x = \ln(E/E_0)$ where E is the photon energy in keV and $E_0 = 9.85\text{keV}$.

From this relationship (Eqn. 6) the $H^*(10)$ is calculated for the radiation quality obtained by the experiment is summarized in Table 2. For unidirectional monoenergetic photons with energies between 10 keV and 250 keV, the relationship [24] between directional dose equivalent at 0.07 mm depth in the ICRU sphere on the radius opposing the direction of the incident radiation, $H'(0.07)$, and air kerma free in air, K_a , is given by;

$$\frac{H'(0.07)}{K_a} = a + bx + cx^d \cdot \exp(gx^2) \text{ Sv/Gy} \quad (7)$$

Where, $a = 0.9505$, $b = 0.09432$, $c = 0.2302$, $d = 5.082$, $g = -0.6997$ and $x = \ln (E/E_0)$, where $E =$ photon energy (keV), and $E_0 = 9.85$ keV.

From this relationship (Eqn. 7) the $H'(0.07)$ is calculated for the radiation qualities obtained by the experiment which is shown in Table 3. A comparison of $H^*(10)$ and $H'(0.07)$ for the obtained photon energies measured by SSDL, Bangladesh and other standard laboratories are also presented.

Table 3. Calculated Conversion Coefficients for directional dose equivalent $H'(0.07)$

Beam Quality	Effective Energy in keV	HVL in mm	Conversion Coefficients $H'(0.07)$ (Sv/Gy)					
			Cu	ISO	BCRU	NPL	PTB	AERE
N40	32.21	0.088	1.263	1.266	1.238	1.258	1.220	1.243
N60	46.85	0.250	1.497	1.499	1.465	1.478	1.456	1.470
N80	65.49	0.620	1.600	1.609	1.602	1.592	1.582	1.602
N100	84.66	1.180	1.603	1.596	1.597	1.588	1.578	1.598
N120	102.00	1.775	1.546	1.547	1.546	1.547	1.536	1.545
N150	116.61	2.305	1.507	1.502	1.506	1.506	1.495	1.496
N200	176.544	4.330	1.369	1.371	1.369	1.377	1.366	1.369

The conversion coefficient for ambient dose equivalent $H^*(10)$ is calculated for monoenergetic photon by the mathematical equation stated above lies within -0.16% and 0.87% with ISO reference values shows a very good in agreement. It is made clear that $H^*(10)$ calculated by mathematical equation provides a conservative approximation of effective dose equivalent at lower energies up to 65.49 keV than ISO but above this energy ISO showed the similar. However, the deviation between the calculated values for ISO and BCRU are insignificant. Compared to the values by other laboratories, ISO and BCRU values provide us more conservative estimation which is an important concept in radiation protection.

For directional dose equivalent, $H'(0.07)$ the calculated values by mathematical equation lies within -0.13% to 0.43% showed a very good in agreement. In comparison with the measured values by other laboratories i.e. NPL, PTB, AERE, NAMAS, it can be stated that ISO values are more conservative estimation for the measurement of dose equivalent.

II (b). Personal Dose Equivalent $Hp(10)$ and $Hp(0.07)$: A set of conversion coefficients of $Hp(10)$ and $Hp(0.07)$ for ISO narrow beam series is presented in Table 4. As personal dosimeter has more or less significant sensitivity to backscattering component of radiation; therefore the suitability of the calibration phantom as compared with theoretical MCNP generated backscatter factor [25] for PMMA and ISO water phantom was used in this study is shown in Figure 3.

Table 4. Calculated conversion coefficient for personal dose equivalent $Hp(10)$ and $Hp(0.07)$

Beam Quality	Effective Energy in keV	HVL in mm Cu	Conversion Coefficients $Hp(10)$ (Sv/Gy)			Conversion Coefficients $Hp(0.07)$ (Sv/Gy)		
			ICRU Tissue Slab	PMMA Slab	ISO water slab phantom	ICRU Tissue Slab	PMMA Slab	ISO water
N40	32.21	0.088	1.139	1.0551	1.1388	1.253	1.1607	1.2528
N60	46.85	0.250	1.623	1.5131	1.6511	1.531	1.4273	1.5575
N80	65.49	0.620	1.885	1.7925	1.9315	1.723	1.6384	1.7655
N100	84.66	1.180	1.877	1.8239	1.9217	1.718	1.6694	1.7589
N120	102.00	1.775	1.805	1.7651	1.8473	1.665	1.6282	1.7040
N150	116.61	2.305	1.740	1.7085	1.7820	1.617	1.5877	1.6560
N200	176.544	4.330	1.542	1.5323	1.5739	1.469	1.4598	1.4994

DISCUSSION

The fundamental requirements for an adequate characterization of reference radiations for ISO narrow beam spectrum is established based on experimental condition. All radiation qualities should be chosen in accordance with the relevant standard which generally is useful to select an appropriate radiation quality taking into account the specified energy range and range of dose equivalent or dose equivalent rate of the device to be calibrated. To reproduce calibration X-ray beams in experimental condition differs, which is difficult to maintain strictly the ISO recommendation which leads to make in radiation protection optimization. Half value layer, air Kerma, photon energy could vary in experimental condition at different laboratory which leads the differences in producing standard beams. The process analyzed obtained by this experiment could give the message in minimizing the difficulties to standardize the calibration X-ray beam at

different laboratories. The discrepancies of experimental value of HVL lies within -8.5% which leads the variation of effective energy -7.64% to ISO values.

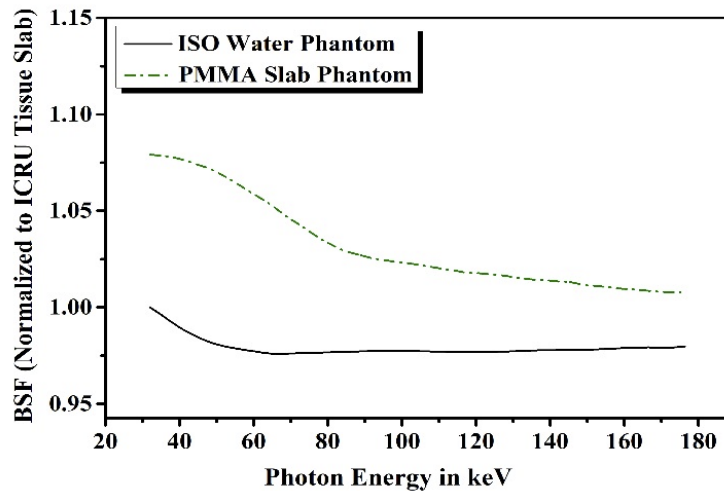


Figure 3. MCNP generated Backscattering Factor (BSF) for PMMA and ISO water phantom [25] that normalized with ICRU tissue slab

The conversion coefficients $H^*(10)/K_a$ and $H'(0.07)/K_a$ for ISO narrow beam series have been calculated from ISO data and compared with the value recommended by different laboratories. Empirical mathematical functions have been fitted from the data recommended by the BCRU for narrow spectrum series which is adopted under the condition ICRU-39. It is seen that ISO values meets very good in agreement with calculated value by empirical mathematical equation. This leads the use of these functions convenient for users as their derivation of ambient and directional dose equivalents. It is also observed that ISO value provides us more conservative approximation for the dose equivalent compared to other laboratories.

MCNP generated backscattering correction factor for PMMA and ISO water phantom for narrow beam spectrum is also used to derive conversion coefficients for individual monitoring $Hp(10)$ and $Hp(0.07)$.

CONCLUSION

In this work calibration X-ray beam was characterized by determining half value layer, effective energy, beam homogeneity coefficient and consistency of X-ray production from the generator (kV and mA) and also a set of conversion factor for operational quantities was established for newly installed X-ray beam irradiator X80-225KV at Secondary Standard Dosimetry Laboratory (SSDL), Bangladesh Atomic Energy Commission following recommendations from ISO-4037. In this study, the variation of HVL of measured value lies within 2 to -8.5% to ISO values with a standard deviation of 1.3%. The effective energy (keV) is then calculated by established empirical relation which is obtained by the interpolation value from Hubble mass attenuation coefficients. A set of conversion coefficients (Sv/Gy) for ambient dose equivalent $H^*(10)$ and $H'(0.07)$ and personal dose equivalent $Hp(10)$ and $Hp(0.07)$ has been calculated for ISO narrow beam spectrum series. The conversion coefficient for ambient dose equivalent $H^*(10)$ is calculated for monoenergetic photon lies within -0.16% and 0.87% with ISO reference values which shows a very good in agreement. It is made clear that $H^*(10)$ calculated by mathematical equation provides a conservative approximation of effective dose equivalent at lower energies up to 65.49 keV than ISO but above this energy ISO showed the similar. For directional dose equivalent, $H'(0.07)$ the calculated values by mathematical equation lies within -0.13% to 0.43% showed a very good in agreement. A set of conversion coefficients for individual monitoring $Hp(10)$ and $Hp(0.07)$ has also been established using the MCNP generated backscattering factor for PMMA and new ISO water slab phantom. The result obtained from this work could be used in characterizing radiation beams at different laboratories.

ORCID IDs

- Tanjim Siddiqua**, <https://orcid.org/0000-0001-8920-340X>;
 Md. Shakilur Rahman, <https://orcid.org/0000-0002-7873-7999>;
Md. Sanaullah, <https://orcid.org/0000-0001-8930-485X>;
 Zohora Akter Mitu, <https://orcid.org/0000-0002-0476-1523>;
Imran Hossain, <https://orcid.org/0000-0003-2898-1405>;
 Sadaka Sultana Rubai, <https://orcid.org/0000-0002-3977-8229>

REFERENCES

- [1] *X-ray and Gamma Reference Radiations for Calibrating Dosimeters & Dose rate meters and for determining their response as a Function of Photon Energy, Part-3: Calibration of Area and Personal Dosimeters and the Determination of Their Response as a Function and Angle of Incidence, ISO 4037-3* (International Organization for Standardization, Geneva, 1999).
- [2] R.D. Evans, *X-Ray and Gamma-Ray Interactions*; in: *Radiation Dosimetry I*, edited by Attix and Roesch, 2nd Ed. (Academic Press, New York and London, 1968).
- [3] *Determination of Dose Equivalents Resulting from External Radiation Sources, ICRU Report 39*, (International Commission on Radiation Units and Measurements, Bethesda, MD, 1985).

- [4] *Determination of Dose Equivalents from External Radiation Sources, ICRU Report 43*, (International Commission on Radiation Units and Measurements, Bethesda, MD, 1988).
- [5] *Measurement of Dose Equivalents from External Photon and Electron Radiation, ICRU Report 47*, (International Commission on Radiation Units and Measurements, Bethesda, MD, 1992).
- [6] *Quantities and Units in Radiation Protection, ICRU Report 51*, (International Commission on Radiation Units and Measurements, Bethesda, MD, 1993).
- [7] *Conversion Coefficients for Use in Radiological Protection against External Radiation, ICRP Publication 74*, Annals of the ICRP **26** (3-4), (International Commission on Radiological Protection, Oxford, Pergamon Press, 1996).
- [8] *X-ray and Gamma Reference Radiations for Calibrating Dosimeters & Dose Rate Meters and for Determining their Response as a Function of Photon Energy, Part-2: Dosimetry for Radiation Protection Over the Energy Range 8keV to 1.3MeV and 4MeV to 9MeV, ISO 4037-2*, (International Organization for Standardization, Geneva, 1997).
- [9] *Calibration of Radiation Protection Monitoring Instruments, Safety Report Series-16*, (International Atomic Energy Agency, Vienna, 1999).
- [10] *Data for Use in Radiation Protection against External Radiation Report*, (International Commission on Radiological Protection, Oxford, Pergamon Press, 1987).
- [11] S.R. Wagner, B. Grosswendt, J.R. Harvey, A.J. Mill, H.J. Selbach, and B.R. Siebert, Radiation Protection Dosimetry, **12**, 231 (1985), https://inis.iaea.org/search/search.aspx?orig_q=RN:17027979.
- [12] I.M.G. Thompson, Journal of Radiation Protection, **9**(3), 203 (1989), <https://doi.org/10.1088/0952-4746/9/3/007>.
- [13] Anon – BCRU, Radiation Protection Dosimetry, **14**, 337 (1986), <https://doi.org/10.1093/oxfordjournals.rpd.a079667>.
- [14] *Data for Use in Protection against External Radiation, ICRP Publication 51*, (International Commission on Radiological Protection, Oxford: Pergamon, 1987).
- [15] W.J. Iles, Conversion Coefficients from Air-kerma to Ambient Dose Equivalent for the International Standards Organizations Wide, Narrow and Low series of Reference Filtered X-Radiation, NRPB-R206 (1987).
- [16] W.W. Seelentag, W. Panzer, G. Drexler, L. Plantz and F. Santer, A Catalogue of Spectra for the Calibration of Dosimeters, GSF Report 560 (1979).
- [17] National Voluntary Laboratory Accreditation Program bulletin. Dosimetry, II:1, NVLAP (1995).
- [18] *Personnel Dosimetry Performance – Criteria for Testing, McLean, ANSI/HPS N13 11*, (Health Physics Society, Virginia, 1993).
- [19] R.J. Traub, J.C. McDonald, and M.K. Murphy, Radiation Protection Dosimetry, **74**, 13 (1997), <https://doi.org/10.1093/oxfordjournals.rpd.a032176>.
- [20] H.M. Kramer, J. Böhm, W.J. Iles, and I.M.G. Thompson, Radiation Protection Dosimetry, **54**, 267 (1994), <https://doi.org/10.1093/oxfordjournals.rpd.a082348>.
- [21] R.F. Nelson, and A.B. Chilton, *Low-energy Photon Dose Deposition in Tissue Slab and Spherical Phantoms, Report NUREG/CR-3425*, (Washington, DC; US Nuclear Regulatory Commission, 1983).
- [22] D.T. Bartlett, P.J. Dimbylow, and T.M. Francis, Radiation Protection Dosimetry, **32**, 123 (1990), <https://doi.org/10.1093/oxfordjournals.rpd.a080727>.
- [23] M.S. Rahman, *Report of MEXT Fellowship Program. Calibration and Standardization of Radiation Measuring devices*, (JAEA, 2003), pp. 23.
- [24] Anon – BCRU, Radiation Protection Dosimetry, **14**(4), 337 (1986), <https://doi.org/10.1093/oxfordjournals.rpd.a079667>.
- [25] M. Ginjaume, X. Ortega, and A. Barbosa, in: *IRPA-10: 10 International Congress of the International Radiation Protection Association*, (Japan Health Physics Society, Japan, 2000), pp. 1-7.

ВИЗНАЧЕННЯ ЯКОСТІ КАЛІБРУВАННЯ РЕНТГЕНІВСЬКОГО ВИПРОМІНЮВАННЯ ТА ВСТАНОВЛЕННЯ НАБОРУ КОЕФІЦІЄНТІВ ПЕРЕТВОРЕННЯ ДЛЯ КАЛІБРУВАННЯ ПРИСТРОЇВ РАДІАЦІЙНОГО ЗАХИСТУ, ЩО ВИКОРИСТОВУЮТЬСЯ В ДІАГНОСТИЧНІЙ РАДІОЛОГІЇ

Танджим Сіддіку^a, Мд. Шаکیلур Рахман^a, Мд. Санаулах^b, Зохора Актер Міту^c,
Імран Хусейн^d, Садека Султана Рубаї^c

^aЛабораторія вторинної стандартної дозиметрії (SSDL), Комісія з атомної енергії Бангладеш, Савар, Дакка, Бангладеш

^bФакультет ядерної інженерії, Університет Дакки, Дакка, Бангладеш

^cФізичний факультет, Університет Читтагонг, Читтагонг, Бангладеш

^dФізичний факультет Барішальського університету, Барішал, Бангладеш

Використання рентгенівських апаратів для калібрування радіаційно-вимірювального обладнання в діагностичній радіології вимагає точного знання радіаційного поля. Спектри рентгенівського випромінювання робляться вузько-променевими шляхом належної фільтрації, рекомендованої кількома міжнародними організаціями. У цьому дослідженні було проведено експериментальне визначення якостей рентгенівського калібрування та аналіз коефіцієнтів перетворення з повітряної керми в еквівалент дози для навколишнього середовища та персональної дози при використанні рентгенівського опромінювача X80-225 кВ відповідно до стандарту ISO для серії вузьких спектрів у Лабораторії Вторинної Стандартної Дозиметрії (SSDL) у Бангладеш. Були проведені дослідження рентгенівського пучка промінів, що задіяні у шарі половинного значення, ефективної енергії, коефіцієнту однорідності пучка та послідовності рентгенівського випромінювання від генератора (кВ та мА). Для коду пучка N200 спостерігалася розбіжність шару половинного значення на 8,5%, що призводить до відхилення ефективної енергії на 7,7% зі стандартним відхиленням 1,3%. Коефіцієнти перетворення з повітряної керми в еквівалент дози, що задовольняє умовам сфери ICRU встановлюються для отримання радіаційних якостей та порівнюються із значеннями, зазначеними іншими стандартними лабораторіями. Для $H^*(10)$ та $H_{\square}(0.07)$ спостерігалася відхилення 0,87% між емпіричним співвідношенням ISO та BCRU, яке є незначним. Набір коефіцієнтів перетворення для $H_p(10)$ та $H_p(0,07)$ також був розрахований для чотирьохелементної тканини ICRU.

Ключові слова: якості рентгенівського випромінювання, радіаційний захист, вузький пучок промінів згідно з ISO, еквівалент дози для навколишнього середовища та еквівалент персональної дози

FUNDAMENTAL PHYSICAL PROPERTIES OF LiInS_2 AND LiInSe_2 CHALCOPYRITE STRUCTURED SOLIDS[†]

 Jyoti Kumari^a,  Shalini Tomar^a,  Sukhendra^b,  Banwari Lal Choudhary^a,
 Upasana Rani^a,  Ajay Singh Verma^{c,*}

^aDepartment of Physics, Banasthali Vidyapith, Rajasthan, (India) 304022

^bDepartment of Physics, GDC Memorial College, Bahal, Bhiwani, (India) 127028

^cDepartment of Natural and Applied Sciences, Glocal University, Saharanpur (India) 247232

*Corresponding Author: ajay_phy@rediffmail.com

Received April 6, 2021; accepted June 6, 2021

For the couple of chalcopyrite compounds, we have theoretically studied the various properties for example structural, electronic optical and mechanical properties. The band structure curve, the density of states as well as the total energy have been investigated with the help of ATK-DFT by using the pseudo-potential plane wave method. For the LiInS_2 and LiInSe_2 chalcopyrites, we have found that these compounds possess direct band gap; which is 3.85 eV and 2.61 eV for LiInS_2 and LiInSe_2 respectively. It shows that the band gap is decreasing from 'S' to 'Se' as well as the B/G ratio called Pugh's ratio is 2.10 for LiInS_2 and 2.61 for LiInSe_2 so these compounds are ductile in nature also these compounds are found to be mechanically stable. The study of this work display that the couple of these chalcopyrite compounds can be the promising candidate for the substitution of absorbing layer in the photovoltaic devices.

Keywords: Ab-initio calculations; electronic properties; optical properties; elastic constants

PACS: 31.15.A-; 46.70.-P; 62.20.D-; 62.20.de; 65.40.De; 65.40.-b; 65.60.+a; 71.20.-b

The demand of energy is increasing day by day but the generation of energy without polluting environment is a great challenge now days. The main abundant origin of renewable energy is solar energy and the investigators are concentrated on finding a substitute material which can be used to operate the solar energy as electric power. The photoelectric effect is discovered very firstly by Becquerel [1] and Einstein [2] has given detailed explanation about it. After that the first transistor is made by Shockley et al [3] and gave description about the p-n junction then the work is started on semiconductor devices. Practically the first silicon p-n junction solar cells with the efficiency of 4.5% have been invented by Chapin et al [4]. After that the efficiency of the photovoltaic device approached 6% and then reached 10% [5]. The generation of electricity from the rays of sun is safe, it is reliable, eco-friendly and very rich in resources. Generally, in the manufacturing of a solar cell consists many layers likewise layer of antireflection, layer of window, front electrode, layer of buffer, back electrode, absorbing layer, substrate etc. but the most important layer is absorbing layer in the solar cells and all researchers are concentrated to finding the substitute material for the absorbing layer of the solar cell which should be lower in cost, non-toxic, pollution free and having better efficiency [6]. For the purpose of conversion of energy, the perovskites and the chalcogenides are considered as potential materials but the chalcopyrite display some extent of distinctive performance [5]. The silicon based solar cells are very expensive and for the global application of solar cells needs a huge reduction in the cost of photovoltaic cells. In photovoltaic technology, renewable energy resource is the main source having the biggest possibility in the reduction of cost and efficiency gains. If we are comparing the perovskite and the chalcogenides; then we will get that the chalcogenides having the good potential for the photovoltaic applications in some aspects. In the recent scenario [7-9], the ternary chalcopyrite compounds attract the interest of researchers towards themselves. The chalcopyrite based photovoltaic devices have the very excessive tolerance to every radiation also their life time was found 50 times longer than a silicon-based device [10]. The variation in the band gaps of these chalcopyrite compounds from IR region to UV region matches with the solar spectrum and these compounds can be grown up in the form of thin films by which these compounds are potential candidate for the employment in the solar cells [11]. The chalcopyrite compounds have the general composition $\text{A}^{\text{I}}\text{B}^{\text{III}}\text{X}_2^{\text{VI}}$ and these compounds having many applications likewise light emitting diodes [12], optical devices, non-linear optical devices [13], tunable laser system [14]. The chalcopyrite structured solids having tetragonal symmetry space group I42d (N^o 122) [15]. LiInSe_2 chalcopyrite compound is the most promising candidate for the applications in photovoltaic devices [16]. The properties like thermodynamic, mechanical properties, lattice dynamics are investigated theoretically of the chalcopyrite compounds LiInS_2 , LiInSe_2 and LiInTe_2 [17-20] also the piezoelectric and mechanical properties of LiMX_2 compound, (where M = Ga, In and X = S, Se) have reported [21]. Also, by using the CASTEP code the optical, structural and electronic properties of LiInSe_2 and LiInTe_2 chalcopyrite material have reported [17]. Now days the efficiency of lithium-based chalcopyrite materials have crossed from 22.8% [22,23].

Here, we have investigated the lattice dynamics, elastic properties, total energy, optical spectrum, electronic properties of the LiInS_2 and LiInSe_2 chalcopyrite compounds. There is lack of information is provided about the optical properties of these compounds so we are working on these crystal compounds to fill this lack of information.

[†] Cite as: J. Kumari, S. Tomar, Sukhendra, B.L. Choudhary, U. Rani, A.S. Verma, East. Eur. J. Phys. 3, 62 (2021), <https://doi.org/10.26565/2312-4334-2021-3-09>

COMPUTATIONAL METHOD

For the group of chalcopyrite compounds, we have theoretically investigated the structural properties, optical properties, mechanical properties, electronic properties, total energy by using the ATK-VNL (Atomistic Tool Kit-Virtual Nano Lab) simulation package [24]. It is a pseudo-potential plane wave method within the framework of (DFT) density functional theory [25-26]. ATK-VNL is a commercially licensed simulation package. For the investigation of above-mentioned properties, we have used the double zeta polarized basis sets for the electron wave function expanding and for the exchange correlation function we have used the GGA-PBE. The structures are permitted to optimize until each atom achieve force convergence criteria 0.05 eV/Å and the maximum stress is 0.05 eV/Å³. Maximum numbers of steps performed are 200 for the process of optimization and during this process maximum step size 0.2 Å which is also fixed. The convergence is achieved by deciding mesh cut-off energy on the ground of convergence principle and for this calculation 75 Hartree has been projected all over calculation as the most favourable after several convergence tests. For the spin polarization, no spin initial state has been selected for the atoms. We used the 24 x 24 x 24 Monk Horst-Pack k-mesh for the brillouin zone sampling to maintain balance between the calculation time and the results accuracy [27]. Further, all the constrain cell in x, y and z directions are removed for the optimization of crystal structure.

RESULTS AND DISCUSSION

Structural properties

The ternary chalcopyrite compounds LiInS₂ and LiInSe₂ are crystallize in the symmetry of body centred tetragonal and the space group is I42d and the space group number is 122. The configuration of atoms in the crystal structure after optimization of LiInS₂ and LiInSe₂ compounds have been illustrated in the Fig. 1 and the optimized lattice constants (a and c in Å) for these configurations in comparison with the experimental data are described in Table 1 and have been concluded that the calculated lattice constants are closer to the experimental values of the lattice constants. Also, the calculated total energy of LiInS₂ compound is -2617.97794 eV and for LiInSe₂ compound is -2756.35359 eV at which these compounds are optimized.

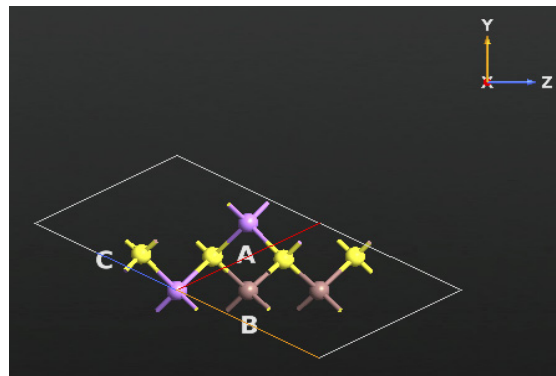


Figure 1. Atomic arrangement in chalcopyrite compounds LiInX₂ (X=S, Se) configurations. Purple color represents A-atom (Li), Brown color represents B-atom (In) and Yellow color represents C-atom (S and Se).

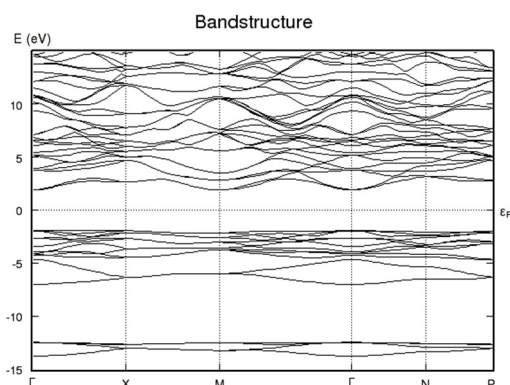
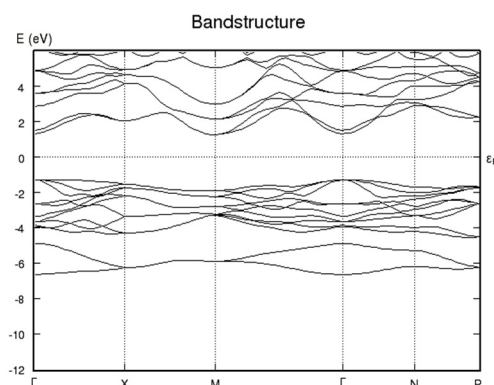
Table 1. Structural Parameters of LiInX₂ (X=S, Se) chalcopyrite compounds.

Compounds	Lattice Constants			
	Calculated		Experimental	
	a (Å)	c (Å)	a (Å)	c (Å)
LiInS ₂	5.523	11.120	5.996 ^{Ref [38],*}	11.078 ^{Ref [38],*}
LiInSe ₂	5.618	11.303	5.807 ^{Ref [38]}	11.810 ^{Ref [38]}

* experimental data.

Electronic properties

The optical properties of a compound are basically depending on the results of the electronic properties of that compound it means if we are getting more accurate band structure then we will be get more accurate optical properties. We have described the band structure of LiInS₂ and LiInSe₂, in this investigation of band structure the GGA-PBE exchange correlation potential have been used to execute the scf calculations using optimized lattice dynamics. The band structure curves between the wave vector 'k' and the energy functional of these compounds, plotted in the first brillouin zone are shown in the Figure 2 (a) and (b). This investigation of electronic band structure reveals that these couple of compounds are direct band gap semiconductors and the directivity of these compounds lies on $\Gamma - \Gamma$, for these compounds the computed energy band gap of LiInS₂ is 3.85 eV and for LiInSe₂ is 2.61 eV respectively.

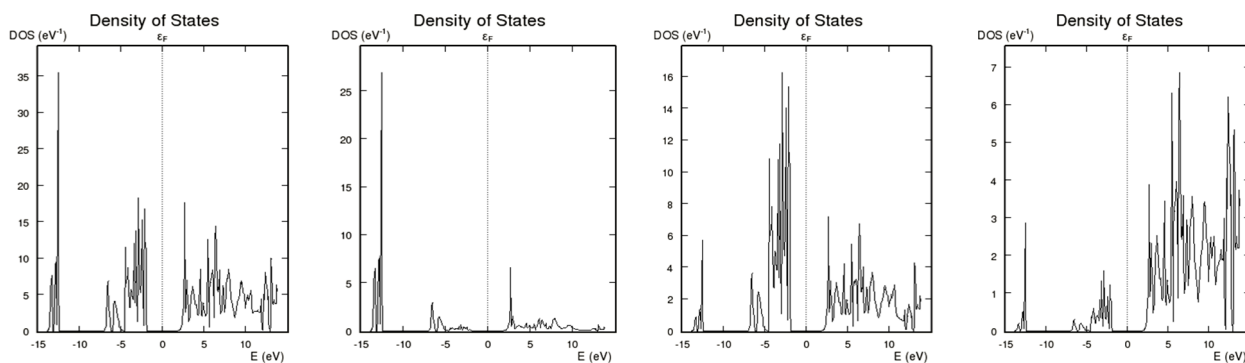
Figure 2 (a): Band structure plots of LiInS₂Figure 2 (b): Band structure plots of LiInSe₂

The reduction in the energy band gaps from the replacement of sulphur atom to the selenium atom in LiInX₂ chalcopyrite compound can be accredited to the modification of the conduction bands near the Fermi level, which reflects the important role of S in the band gap opening if the valence band is remains unaffected [28]. The calculated values of band gap are closer to the experimentally extracted energy band gap 3.57 eV for LiInS₂ and 2.83 eV for LiInSe₂ [29]. By doing the study of band structure of a compound, we have find out the band-gap of a compound; which is helpful to deciding the nature of the material likewise it is semiconductor, metallic or non-metallic in nature. We find out these couple of compounds LiInX₂ (X = S and Se) are the direct band-gap semiconductors and values are presented in Table 2.

Table 2. Electronic and Optical Parameters of LiInX₂ (X=S, Se) Chalcopyrite compounds.

Compounds	Band Gap (eV)		Dielectric Constant
	Calculated	Experimental	
LiInS ₂	3.85	3.57 ^{Ref [29]}	2.085
LiInSe ₂	2.61	2.83 ^{Ref [29]}	2.884

For the further understanding of electronic properties, we have been investigated the DoS (Density of States) of these compounds. The computed electronic band have been allocated with the help of the graphs of density of state and shown in the Figure 3 (i) DoS of LiInS₂ and (ii) DoS of LiInSe₂ by using the GGA-PBE exchange correlation potential.

Figure 3 (i). (a) Total DOS of LiInS₂ compound.Figure 3 (i). (b) Contribution of s-state in LiInS₂ compound.Figure 3 (i). (c) Contribution of p-state in LiInS₂ compound.Figure 3 (i). (d) Contribution of d-state in LiInS₂ compound.

We have plotted the total density of state graphs for the analysis of the influence of the different states of atoms for the valence and the conduction band. In the Figure 3 (i) (a) we have plotted the graph of total density of states of LiInS₂ chalcopyrite compound, in which the combined contribution of s, p and d states in the valence and conduction band region. In the Figure 3 (i) (b) we have plotted the density of state graph of the contribution of s-state, we got the major peak of s-state separated by small energy intervals so in this region the contribution of s-state is very high on the other hand, the contribution of s-state in the conduction band is very less as compare it's contribution in valence band. In Figure 3 (i) (c) shows the graph of density of state of the contribution of p-state, we got the major peaks of p-states at a particular energy intervals so the contribution of p-state in the valence band region is more than it's contribution in the conduction

band region, Figure 3 (i). (d). shows the graph of density of state of contribution of d-state, we got the major peaks of d-state at the particular energy intervals so the contribution of d-state is more in the conduction band region as compare it's contribution in the valence band region. Similarly, we have presented for LiInSe₂ in Figure 3 (ii) (a-d).

From the analysis of these graphs of density of states of LiInS₂ chalcopyrite compounds we observed that in the region of valence band there is s-p hybridization is formed and the contribution of d-state is very less as compare to the contribution of s and p states on the other hand in the conduction band there is p-d hybridization is formed and the contribution of s state is less as compare to the contribution of p and d states. We have observed that the calculated band structure and the density of states exhibit identical behaviour.

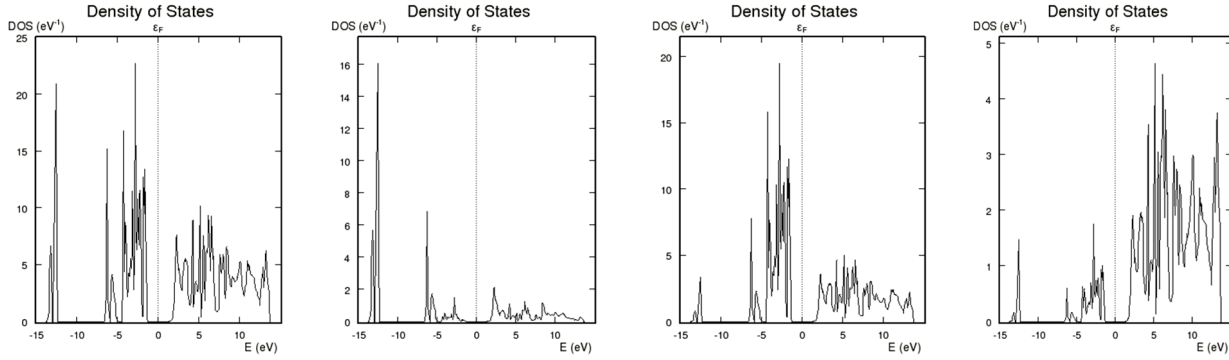


Figure 3 (ii). (a) Total DOS of LiInSe₂ compound.

Figure 3 (ii). (b) Contribution of s-state in LiInSe₂ compound.

Figure 3 (ii). (c) Contribution of p-state in LiInSe₂ compound.

Figure 3 (ii). (d) Contribution of d-state in LiInSe₂ compound.

Elastic Properties

The most fundamental properties of a semiconducting material are the elastic properties. As we all know very well the elastic properties gives the valued data regarding the binding characteristics between the adjacent planes. Usually, the anisotropic coefficients of binding and the stability of structure are described by the elastic constants C_{ij} . These elastic constants provide us the very significant data likewise stability of the crystal structure, mechanical properties, bond indexes and the anisotropy of material. These elastic moduli need the good information regarding the derivative of the energy as a function of the lattice strain [30]. From the elastic constants we can derive the mechanical properties likewise the bulk modulus, shear modulus, young's modulus, and poisson's ratio etc. and these moduli are playing most important role in finding the strength of the materials also these elastic properties defines that how a material undergoes stress deforms and then recovers and returns to its original shape after stress ceases. Moreover, the elastic constants of crystal structure of solids give the relation in between the mechanical and dynamical behaviours of solids also provide the essential data about the nature of the forces applying in the solids.

For a stable tetragonal crystal structure of a solid, mainly there are six independent elastic constants C_{ij} (C_{11} , C_{12} , C_{13} , C_{33} , C_{44} and C_{66}) must fulfil the well-known Born–Huang conditions for the stability of the solid crystals [31]. These elastic constants are related to the bulk modulus B_0 and the five shear constants ($C_{11} + C_{12}$, $C_{11} + C_{12} + 2C_{33} - 4C_{13}$, $1/2C_{33}$, $C_{11} - C_{12}$ and $1/2C_{66}$). Hereafter, a set of five equations required to determine all constants, the first equation contains the bulk modulus B_0 , which is related to the elastic constant by

$$B_0 = \frac{(C_{11} + C_{12})C_{33} - 2C_{13}^2}{C_{11} + C_{12} + 2C_{33} + 4C_{13}^2} \quad (1)$$

In the body centred tetragonal crystal structure of a solid the necessities of the mechanical stability having limitations on the elastic constants which are as follows;

- $C_{11} > 0$, $C_{33} > 0$, $C_{44} > 0$, $C_{66} > 0$,
- $(C_{11} - C_{12}) > 0$, $(C_{11} + C_{33} - 2C_{13}) > 0$,
- $\{2(C_{11} + C_{12}) + C_{33} + 4C_{13}\} > 0$.

The most important elastic properties are Zener anisotropy factor generally we denoted by 'A', Young's modulus denoted by 'E', Poisson's ratio denoted by 'σ' for the applications are computed with help of following relations [32];

$$A = \frac{C_{44}}{C_{11} - C_{12}} \quad (2)$$

The stability of the crystal structure is obtained by the anisotropic factor 'A', the material is isotropic if the value of 'A' is equal to one and the material is anisotropic if the value of 'A' deviate from one. The isotropic materials are those materials whose properties does not depends on the direction called isotropic materials.

$$\sigma = \frac{1}{2} \left[\frac{B-2/3 G}{B+1/3 G} \right] \quad (3)$$

The [3] is the value of Poisson's ratio in the terms of b and G and for most of the materials the value of σ lies in between 0 to 0.5.

$$E = \frac{9GB}{G+3B} \quad (4)$$

The 'E' [4] is young's modulus in the terms of B and G and it is used to determine the stiffness of the materials.

$$G = \frac{G_V + G_R}{2} \quad (5)$$

Here, G is the anisotropic shear modulus,

G_V is the Voigt's shear modulus corresponding to the upper bound values of G,

and G_R is the Reuss's shear modulus corresponding to the lower bound values of G.

- $G_V = 1/30 (4C_{11} + 2C_{33} - 4C_{13} - 2C_{12} + 12C_{44} + 6C_{66})$
- $G_R = 15 [(18B_V / C^2) + [6/ (C_{11} - C_{12})] + (6/C_{44}) + (3/C_{66})]^{-1}$
- $B_V = (1/9) [2(C_{11} + C_{12}) + C_{33} + 4C_{13}]$
- $C^2 = (C_{11} + C_{12}) C_{33} - 2(C_{13})^2$

In the above stated formulas, the subscript refers V to Voigt bound, R refers to Reuss bound [33]. The material is soft or hard it can be decided by the value of bond index if the value of bond index is less than 12 then the material is soft if the value of bond index is more than 12 then the material is hard [34]. The material is brittle or ductile it can be decided by the Pugh's ratio B/G if this ratio is less than 1.75 then the material is brittle and if this ratio is more than 1.75 then the material is ductile. The ratio B/G is a simple relationship related to the brittle or ductile nature of the material [35]. We can determine the mechanical properties of the material by the young's modulus 'E', Bulk modulus 'B', shear modulus 'G', Poisson's ratio ' σ ' by the Voigt-Reuss-Hill averaging method [36]. All the calculated elastic constants are presented in table 3, 4 and 5.

Table. 3. The calculated elastic constants of LiInX₂ (X=S, Se) chalcopyrite compounds.

Compounds	Elastic constants (GPa)					
	C ₁₁	C ₁₂	C ₁₃	C ₃₃	C ₄₄	C ₆₆
LiInS ₂	55.34	55.77	71.75	30.58	29.39	27.26
LiInSe ₂	72.13	72.11	81.82	27.53	27.43	26.81

From the table 3, we conclude that the mechanical stability limitations for the tetragonal crystal structure $C_{11} > 0$, $C_{33} > 0$, $C_{44} > 0$, $C_{66} > 0$, $(C_{11} - C_{12}) > 0$, $(C_{11} + C_{33} - 2C_{13}) > 0$ and $2((C_{11} + C_{12}) + C_{33} + 4C_{13}) > 0$ are satisfied by all these three chalcopyrite compounds LiInX₂ where (X=S, Se). So, by this calculation of elastic constants, we can say that these compounds possess the tetragonal symmetry.

From the Table 4 (a) and 4 (b) we observed that the value of Poisson's ratio lies in between 0 to 0.5 for these chalcopyrite compounds so we can say that the interatomic forces in these compounds are central forces because the one and only Poisson's ratio gives the more information regarding the characteristics of the bonding forces than any other of the elastic constants. For the central forces in the solid crystals the lower and the upper limits of this ratio are given 0.25 to 0.5 respectively. It shows that, the interatomic forces in these compounds are central forces. From Table 5, we have concluded that the anisotropy factor 'A' deviated from one for these chalcopyrite compounds so these compounds are anisotropic in nature also, the value of B/G is more than 1.75 for all compounds so it confirms that these compounds are ductile in nature.

Table 4. (a) and (b) Elastic Parameters of LiInX₂ (X=S, Se) Chalcopyrite compounds

(a) For LiInS₂		Reuss	Voigt	Hill
Bulk modulus:		42.9693	44.1156	43.5425
Shear modulus:		18.8437	22.4971	20.6704
Young's modulus:	X		Y	Z
		31.0883	31.3485	40.589
Poisson's ratio:	XY		XZ	YZ
		0.3772	0.4212	0.4184
	YX		ZX	ZY
		0.3740	0.3226	0.3231
(b) For LiInSe₂		Reuss	Voigt	Hill
Bulk modulus:		55.4550	55.7677	55.6114
Shear modulus:		20.2216	22.2306	21.2261
Young's modulus:	X		Y	Z
		38.2671	38.3226	44.6953
Poisson's ratio:	XY		XZ	YZ
		0.4005	0.3998	0.3972
	YX		ZX	ZY
		0.4000	0.3423	0.3406

Table 5. Calculated anisotropy factor (A) and Pugh's ratio (B/G) of the LiInX₂ (X=S, Se) compounds.

Compounds	A	B / G
LiInS ₂	-68.3488	2.1055
LiInSe ₂	1371.5	2.6199

From all the above calculations of elastic properties we concluded that these LiInX₂ (X=S, Se) chalcopyrite compounds are mechanically stable compounds.

Optical Properties

Whenever a material is used in optoelectronic device then for knowing the behaviour of that material the optical properties play an important role. The interaction of a material with electromagnetic radiation can be described by the optical properties and this interaction defines its optoelectronic applications [37-39]. We have been studied the optical properties of the couple of chalcopyrite compounds LiInX₂ (X = S and Se). In the present work, we have calculated the optical parameters, likewise the dielectric function, absorption coefficient and electron energy loss as a function of photon energy. The optical parameters of the interested materials have been computed for the rising energy of the incident electromagnetic radiation ranging from 0 to 5 eV, which is shown in Figure 4. From the computation of these parameters, we can say that these compounds are homogeneous as well as isotropic compounds it means for these compounds the values of different optical parameters are constant with changing the direction of incident electromagnetic radiation's electric field vector, but they are variable with its frequency.

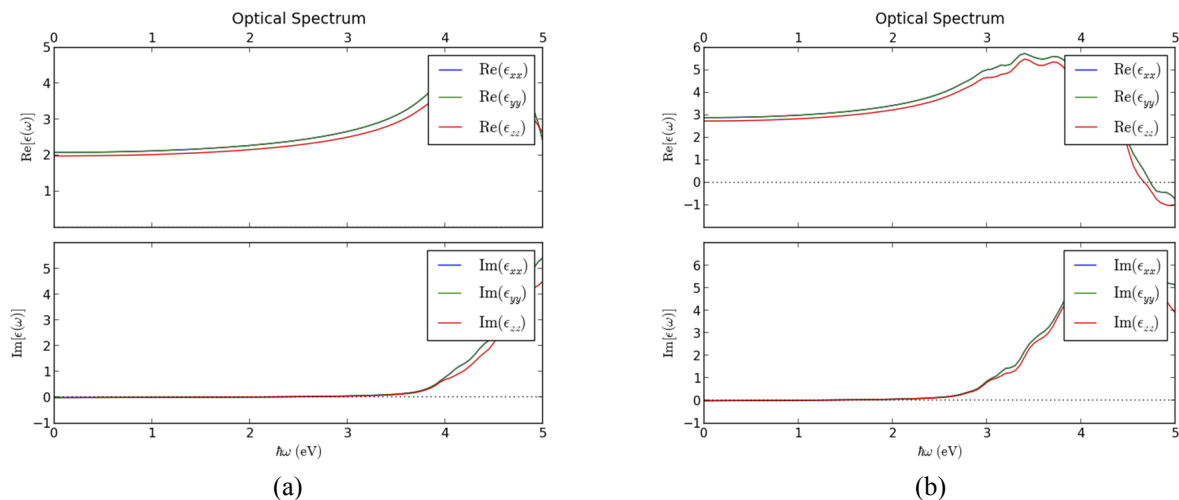
**Figure 4.** Dielectric tensor spectra (a) LiInS₂ and (b) LiInSe₂ compounds for its real part and imaginary part.

Figure 4 shows the real and the imaginary elements of the dielectric tensor spectra $\epsilon(\omega)$ for the energy of incident radiation. The dielectric constant of the compound expresses by the stationary value of its real component also can be defined via a trivial perimeter of the energy. It has been noted that the value of real component of LiInS₂ compound is

2.085 and 2.884 for LiInSe₂ compound. The higher value of real component is responsible for a compound's better response to the incident electromagnetic radiations. Figure 4 displays the variation in real component of the chalcopyrite compounds with the energy of incident radiation. We are clear from the figures of the considered compounds that the value of real component at the particular range of energy (0 eV to 2.98 eV for LiInS₂ and 0 eV to 2.69 eV for LiInSe₂) as the value of energy increases then the value of real component starts raising at a particular range of energy (3.90 eV to 4.78 eV for LiInS₂ and 2.96 eV to 3.97 eV for LiInSe₂) then decreases rapidly and becomes negative (negative is only for the LiInSe₂ compound), later a slightly rising towards zero is observed (only in LiInSe₂ compound). For these two chalcopyrite compounds, the highest value of real component has been observed in UV region i.e., in the UV region of EM spectrum these chalcopyrite compounds give the extreme response. Also, we have observed that the threshold energy of imaginary component varies from 3.92 eV to 4.16 eV for LiInS₂ compound and 2.97 eV to 4.15 eV for LiInSe₂ compound. The value of threshold energy displays the optical band gap of a material and in this study, it is found to be identical to the measured electronic energy band-gap which confirms the good accuracy of proposed results. Moreover, it has been noticed that these compounds, displays a sharp peak of imaginary component. The main peak of imaginary component can be given to the transition of electrons among the valence band maxima and conduction band minima. In this study the optical band gap is found close to the electronic energy band gap so these materials can be the promising material for the photovoltaic applications.

SUMMARY AND CONCLUSIONS

In this research paper, we inspected several physical properties such as structural, electronic, optical and the mechanical properties of LiInX₂ (X = S and Se) chalcopyrite compounds by using ATK-VNL simulation package. These compounds crystallize in tetrahedral symmetry with the space group I42d. They exhibit the direct electronic energy band gap (Γ - Γ) 3.85 eV for LiInS₂ and 2.61 eV for LiInSe₂, which are having the good agreement with the experimental results. Also, satisfied the optical band gap these materials are good photovoltaic in the UV region of the EM spectrum so these materials act as robust shields for the high energy UV radiations also these can be better photovoltaics in the IR region and the visible region of the EM spectrum. The computed dielectric constant for LiInS₂ is 2.085 and 2.884 is for LiInSe₂ compounds, which is responsible for a compound's better response to the incident electromagnetic radiations. These compounds are mechanically stable compounds and these are ductile in nature because the Pugh's ratio is greater than 1.75 for both of these compounds. Moreover, Poisson's ratio lies in between 0 to 0.5 for these chalcopyrite compounds so we can say that the interatomic forces in these compounds are the central forces. Also, in this computation these compounds are found to be anisotropic because the value of A is < 1 for LiInS₂ and A is > 1 for LiInSe₂. From the study of this work, we conclude that these materials can be the potential candidate for the photovoltaic applications. The majorities of the parameters explored are reported for the first time to the best of our knowledge and will further stimulate research in the related field.

ORCID IDs

● Jyoti Kumari, <https://orcid.org/0000-0002-1895-158X>; ● Shalini Tomar, <https://orcid.org/0000-0001-7385-3061>;
● Sukhendra, <https://orcid.org/0000-0002-2149-5669>; ● Banwari Lal Choudhary, <https://orcid.org/0000-0002-0446-8984>;
● Upasana Rani, <https://orcid.org/0000-0003-2550-0442>; ● Ajay Singh Verma, <https://orcid.org/0000-0001-8223-7658>

REFERENCES

- [1] E. Becquerel, *Compt. Rend.* **9**, 561 (1839).
- [2] P.C. Deshmukh, and S. Venkataraman, *100 years of Einstein's photoelectric effect*, Bulletin of Indian Physics Teachers Association. (2006).
- [3] S.M. Sze, *Semiconductor devices: physics and technology*, (Wiley John & Sons, 2008).
- [4] D.M. Chapin, C.S. Fuller, and G.L. Pearson, *J. Applied Physics*, **25**, 676-677 (1954), <https://doi.org/10.1063/1.1721711>.
- [5] M. Jing, J. Li, and K. Liu, *IOP Conference Series: Earth and Environmental Science IOP Publication*, **128**, 012087 (2018), <https://doi.org/10.1088/1755-1315/128/1/012087>.
- [6] Q. Lei, Z. Chunmei, and C. Qiang, *Sci. Technol.* **16**, 45 (2014), <https://doi.org/10.1088/1009-0630/16/1/10>
- [7] A.H. Reshak, M.G. Brik, and S. Auluck, *J. Applied Physics*, **116**, 103501 (2014), <https://doi.org/10.1063/1.4894829>.
- [8] J.E. Jaffe, and A. Zunger, *Physical Review B*, **28**, 5822 (1983), <https://doi.org/10.1103/PhysRevB.28.5822>.
- [9] C. Rincon, and C. Bellabarba, *Physical Review B*, **33**, 7160 (1986), <https://doi.org/10.1103/PhysRevB.33.7160>.
- [10] S. Sharma, A.S. Verma, R. Bhandari, and V.K. Jindal, *Computational materials science*, **86**, 108-117 (2014), <https://doi.org/10.1016/j.commatsci.2014.01.021>.
- [11] A.H. Reshak, and M.G. Brik, *J. Alloys and Compounds*, **675**, 355-363 (2016), <https://doi.org/10.1016/j.jallcom.2016.03.104>.
- [12] J.L. Shay, L.M. Schiavone, E. Buehler, and J.H. Wernick, *J. Applied Physics*, **43**, 2805-2810 (1972), <https://doi.org/10.1063/1.1661599>.
- [13] B.F. Levine, *Physical Review B*, **7**, 2600 (1973), <https://doi.org/10.1103/PhysRevB.7.2600>.
- [14] A. Sajid, S. Sajid, G. Murtaza, R. Khenata, A. Manzar, and S.B. Omran, *J. Optoelectronics and Advanced Materials*, **16**, 76-81 (2014), <https://joam.inoe.ro/articles/electronic-structure-and-optical-properties-of-chalcopyrite-cuyz2-yal-ga-in-zs-se-an-ab-initio-study/fulltext>.
- [15] A. Rockett, and R.W. Birkmire, *J. Applied Physics*, **70**, 81-97 (1991), <https://doi.org/10.1063/1.349175>.
- [16] M. Magesh, A. Arunkumar, P. Vijayakumar, G.A. Babu, and P. Ramasamy, *Optics and Laser Technology*, **56**, 177-181 (2014), <https://doi.org/10.1016/j.optlastec.2013.08.003>.

- [17] C.G. Ma, and M.G. Brik, Solid State Communications, **203**, 69-74 (2015), <https://doi.org/10.1016/j.ssc.2014.11.021>.
- [18] A.V. Kosobutsky, and Y.M. Basalae, Solid State Communications, **199**, 17-21 (2014), <https://doi.org/10.1016/j.ssc.2014.08.015>.
- [19] A.V. Kosobutsky, and Y.M. Basalae, J. Physics and Chemistry of Solids, **71**, 854-861 (2010), <https://doi.org/10.1016/j.jpcs.2010.03.033>.
- [20] A.V. Kosobutsky, Y.M. Basalae, and A.S. Poplavnoi, Physica Status Solidi (b), **246**, 364-371 (2009), <https://doi.org/10.1002/pssb.200844283>.
- [21] B. Lagoun, T. Bentria, and B. Bentria, Computational materials science, **68**, 379-383 (2013), <https://doi.org/10.1016/j.commatsci.2012.11.010>.
- [22] L. Isaenko, P. Krinitsin, V. Vedenyapin, A. Yelisseyev, A. Merkulov, J.J. Zondy, and V. Petrov, Crystal Growth and Design, **5**, 1325-1329 (2005), <https://doi.org/10.1021/cg050076c>.
- [23] M.S. Yaseen, G. Murtaza, and R.M.A. Khalil, Current Applied Physics, **18**, 1113-1121 (2018), <https://doi.org/10.1016/j.cap.2018.06.008>.
- [24] Atomistic Toolkit-Virtual Nano lab (ATK-VNL) Quantum wise Simulator, Version. 2014.3, <http://quantumwise.com/>.
- [25] Y.J. Lee, M. Brandbyge, M.J. Puska, J. Taylor, K. Stokbro, and R.M. Nieminen, Physical Review B, **69**, 125409 (2004), <https://doi.org/10.1103/PhysRevB.69.125409>.
- [26] K. Schwarz, J. Solid-State Chemistry, **176**, 319-328 (2003), [https://doi.org/10.1016/S0022-4596\(03\)00213-5](https://doi.org/10.1016/S0022-4596(03)00213-5).
- [27] H.J. Monkhorst, and J.D. Pack, Physical Review B, **13**, 5188 (1976), <https://doi.org/10.1103/PhysRevB.13.5188>.
- [28] A. Khan, M. Sajjad, G. Murtaza, and A. Laref, Zeitschrift für Naturforschung A, **73**, 645-655 (2018), <https://doi.org/10.1515/zna-2018-0070>.
- [29] L. Isaenko, A. Yelisseyev, S. Lobanov, P. Krinitsin, V. Petrov, and J.J. Zondy, J. Non-Crystalline Solids, **352**, 2439-2443 (2006), <https://doi.org/10.1016/j.jnoncrysol.2006.03.045>.
- [30] R. Khenata, A. Bouhemadou, M. Sahnoun, A.H. Reshak, H. Baltache, and M. Rabah, Computational Materials Science, **38**, 29-38 (2006), <https://doi.org/10.1016/j.commatsci.2006.01.013>.
- [31] J. Sun, H.T. Wang, N.B. Ming, Applied Physics Letters, **84**, 4544-4546 (2004), <https://doi.org/10.1063/1.1758781>.
- [32] B. Mayer, H. Anton, E. Bott, M. Methfessel, J. Sticht, J. Harris, and P. C. Schmidt, Intermetallics, **11**, 23-32 (2003), [https://doi.org/10.1016/S0966-9795\(02\)00127-9](https://doi.org/10.1016/S0966-9795(02)00127-9).
- [33] H. Fu, D. Li, F. Peng, T. Gao, and X. Cheng, Computational Materials Science, **44**, 774-778 (2008), <https://doi.org/10.1016/j.commatsci.2008.05.026>.
- [34] D.G. Pettifor, Materials Science and Technology, **8**, 345-349 (1992), <https://doi.org/10.1179/mst.1992.8.4.345>.
- [35] S.F. Pugh, Philosophical Magazine and J. Science, **45**, 823-843 (1954), <https://doi.org/10.1080/14786440808520496>.
- [36] R. Hill, Proceedings of the Physical Society. Section A, **65**, 349 (1952), <https://doi.org/10.1088/0370-1298/65/5/307>.
- [37] T. Lantri, S. Bentata, B. Bouadjemi, W. Benstaali, B. Bouhafs, A. Abbad, and A. Zitouni, J. Magnetism and Magnetic Materials **419**, 74-83 (2016), <https://doi.org/10.1016/j.jmmm.2016.06.012>.
- [38] S. Sharma, A.S. Verma, and V.K. Jindal, Materials Research Bulletin, **53**, 218-233 (2014), <https://doi.org/10.1016/j.materresbull.2014.02.021>.
- [39] C.M.I. Okoye, J. Physics: Condensed Matter, **15**, 5945-5958 (2003), <https://doi.org/10.1088/0953-8984/15/35/304>.

ОСНОВНІ ФІЗИЧНІ ВЛАСТИВОСТІ СТРУКТУРОВАНИХ СПОЛУК ХАЛЬКОПІРИТУ LiInS_2 та LiInSe_2

Джуоті Кумар^a, Шаліні Томар^a, Сухендра^b, Банварі Лал Чоудхарі^a, Упасана Рані^a, Аджай Сінх Верма^c

^aФізичний факультет, Банастанлі Від'яніт, Раджастан, (Індія) 304022

^bФізичний факультет, Меморіальний коледж GDC, Бахал, Бхівані, (Індія) 127028

^cФакультет природничих та прикладних наук, Університет Глокал, Сахаранпур (Індія) 247232

Для деяких сполук халькопіриту ми теоретично вивчили їхні різні властивості, наприклад структурні, електронні, оптичні та механічні. Криву зонної структури, щільність станів, а також загальну енергію досліджували за допомогою ATK-DFT методом псевдопотенціальної плоскої хвилі. Для халькопіритів LiInS_2 та LiInSe_2 ми виявили, що ці сполуки мають пряму енергетичну щільну, яка становить 3,85 eV та 2,61 eV для LiInS_2 та LiInSe_2 , відповідно. Це показує, що ширина енергетичної щільності зменшується від «S» до «Se», а також відношення V/G , яке називається коефіцієнтом П'ю, становить 2,10 для LiInS_2 та 2,61 для LiInSe_2 , таким чином ці сполуки є пластичними за своєю природою, також ці сполуки виявляються механічно стабільними. Дослідження цієї роботи показує, що пара цих сполук халькопіриту може бути перспективним кандидатом для заміни поглинаючого шару у фотоелектричних пристроях.

Ключові слова: неемперічні (Ab-initio) розрахунки; електронні властивості; оптичні властивості; пружні константи

SYNTHESIS AND CHARACTERIZATION OF METHYLAMMONIUM LEAD BROMIDE PEROVSKITE BASED PHOTOVOLTAIC DEVICE[†]

 Shaily Choudhary^a,  Shalini Tomar^a,  Depak Kumar^b,
 Sudesh Kumar^c,  Ajay Singh Verma^{d,*}

^aDepartment of Physics, Banasthali Vidyapith, Banasthali, Rajasthan 304022, India

^bDepartment of Chemical Engineering, Banasthali Vidyapith, Banasthali 304022, India

^cDepartment of Physics, Banasthali Vidyapith, Banasthali, Rajasthan 304022, India

^dDepartment of Natural and Applied Sciences, Glocal University, Saharanpur 247232, India

*Corresponding author: ajay_phy@rediffmail.com

Received April 17, 2021; accepted August 5, 2021

Hybrid electronic devices give a reasonable path for feasible power sources and other further applications due to its easy arrangement, preparation, producing, ease of materials, and less environmental impact. In this paper, we have discussed electrical properties of hybrid bromide perovskite nanoparticles and current progressions in perovskite photovoltaic devices have also been discussed. In order to fabricate, low-temperature solution-processed devices using one-step spin coating methods play a key role in producing uniform thin films. The spin coating technique has been used for the deposition of the precursor solution including methylammonium bromide (MABr) and lead bromide (PbBr₂) with molar ratio (3:1) to prepare the thin films onto FTO-substrate. One-step solution processes has been used for deposition of the CH₃NH₃PbBr₃ absorber layers and have explained an overview of material composition, deposition technique and the architecture of the device, the selection of charge transport layer and electrode.

Keywords: metal halide perovskites; charge carrier mobility; resistance; capacitance; electrochemical impedance spectroscopy

PACS: 61.30.Hn; 61.41.+e; 61.46.Df; 61.82.Fk; 68.37.Hk; 73.21.-b; 73.30.+y; 73.40.Lq; 73.50.Gr

The speed up world population expansion and post industrialized period bring to consideration a unexpected requirement of energy, answerable for environment dilemma, sustainable growth concerns with financial challenges [1-3]. Presently, finite sources of energy like fossil fuels are the resource for greater than 85% of the world main power and accountable in support of most of the green house gas emission. Wind, sun, hydraulic, biomass and geothermal have been studied for the technologies that take benefit of renewable energy sources. Sunbeams has an huge potential as energy resource among an irradiance 1.8×10^{14} kW at earth's outside, which can be convert in electrical energy as well as heat with negligible natural impact. Photovoltaic devices are one of the great hopeful mechanization for producing electricity from sunlight [4-6].

Kojima et al. [7] have demonstrated that organometal halide perovskites as light absorber with 3.8% power conversion efficiency. The organometallic hybrid halide perovskite material used, with the nonspecific structure of CH₃NH₃PbX₃, quickly proved to have an amazing high efficiency as light absorber displaying also very strong hole and electron conductivity. This disrupting result led to the appearance of a new thin film photovoltaic family— in today's world one of the most investigated families of photovoltaic devices are Perovskite photovoltaic devices [8]. The rapid attention on the perovskite photovoltaic devices has correlated to the great enhance on energy conversion efficiency, this technology experienced in the last 7 years, from 3.8% in 2009 to 22.1% in 2017 [9]. The essential property of Hybrid organic-inorganic Perovskites is their phase complexity from cubic, tetragonal, orthorhombic and monoclinic polymorphs (orthorhombic (space group -Pna21) to tetragonal (space group- P4/mmm) transition at 161.4 K and tetragonal to cubic (space group- Pm₃m) at 340.4 K). The main reason for phase transitions is a change in temperature, pressure, and applied field [10]. Theoretically number of first principles calculations for CH₃NH₃PbI₃ has been reported in recent years, for instance, Li Lang et. al and Yuan Ye et. al. reported that band gap and lattice constant depends upon A, B and X in ABX₃ they reported that as A increases from Cs to CH₃NH₃⁺ or NH₃CHNH₃⁺ and X changes from Cl to Br to I lattice constant increase and B varies from Sn to Pb band gap increase [11-12]

The promising organic-inorganic hybrid halide perovskite photovoltaic device (PPVs) represent one of the life-changing technology, just like organic photovoltaic devices (OPVs), and DSSCs, Perovskite also potentially can be converted into light-weight, adjustable and low in cost power sources throughout the high-throughput solution fabrication [13-15]. Perovskite photovoltaic devices have therefore acquired the exhaustive efforts in research from both academic world and industry. It fundamentally benefits from the outstanding electrical properties of semi-conducting organic-inorganic hybrid perovskite, such as the strong optical absorption coefficient, a long carrier life time, diffusion length, direct band gap, and high electron/hole mobility in crystalline state [16-17]. Most prominently, organic-inorganic lead halide perovskite produces loosely bonded exciton with truly little bonding energy, which facilitates the manufacture of free charge carriers within the Perovskite by the cost of negligible dynamic force [18].

[†] Cite as: S. Choudhary, S. Tomar, D. Kumar, S. Kumar, A.S. Verma, East. Eur. J. Phys. 3, 70 (2021), <https://doi.org/10.26565/2312-4334-2021-3-10>

© S. Choudhary, S. Tomar, D. Kumar, S. Kumar, A.S. Verma, 2021

EXPERIMENTAL METHODS

The heterojunction device has been fabricated onto coated glass-substrate. The zinc powder and hydrochloric acid (HCl) (2.0 M) have been used to etch the fluorine-doped tin oxide (FTO) substrate to acquire the required electrode pattern. After that the substrate was cleaned. The cleaning process of FTO substrate has been displays in Fig. 1.

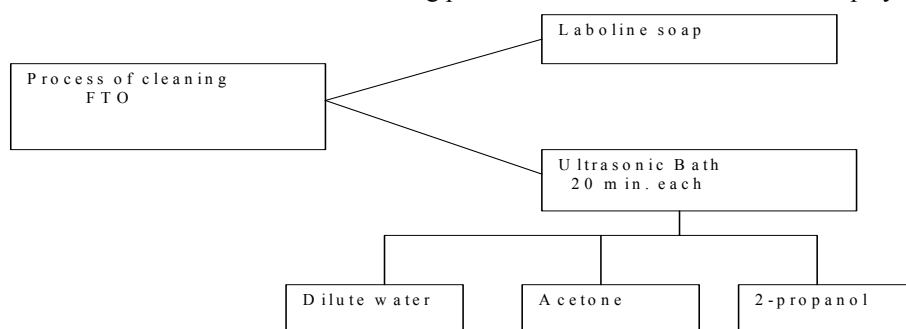


Figure 1. Illustration of method to clean FTO coated glass-substrate before fabrication of device.

Synthesis of $\text{CH}_3\text{NH}_3\text{PbBr}_3$ precursor solution. $\text{CH}_3\text{NH}_3\text{Br}$ has been synthesized at 0°C by reacting aqueous hydrobromic acid (HBr) under continuous stirring of 2 hr. After that to remove the solvent the solution has evaporated for 45 min at 60°C . Through this process the solution transforms into white powder crystals that have washed three times by diethyl ether attend by overnight drying at 60°C in vacuum oven. The field emission scanning electron microscopy (FESEM) image of methylammonium lead bromide ($\text{CH}_3\text{NH}_3\text{PbBr}_3$) perovskite precursor solution onto glass-substrate has been prepared by the deposition of one-step spin coating technique and displays in Fig 2. This image exhibits large domain size of perovskite material with uniform grains distribution and complete surface coverage.

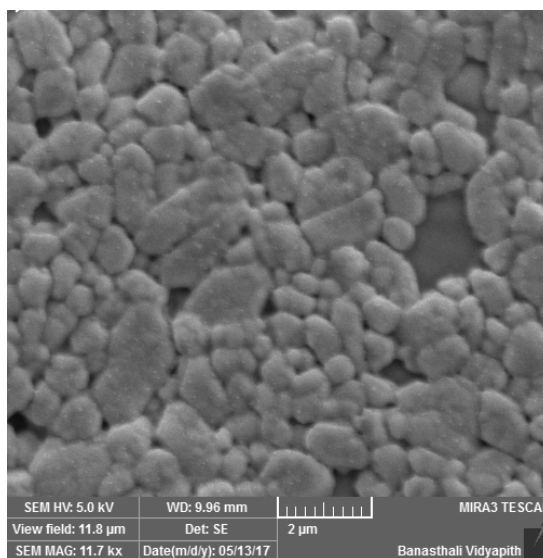


Figure 2. FESEM image shows the surface morphology of perovskite precursor solution.

Photovoltaic device fabrication. The fabrication procedure is following as,

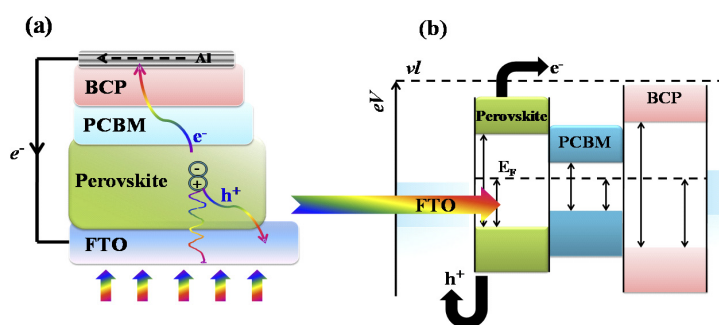


Figure 3. (a) Layout of fabricated device heterostructure, (b) Energy diagram of corresponding device with charge carrier transportation from perovskite to respective electrodes in illumination.

Firstly, the FTO coated glass-substrate has been cleaned as shown in Fig. 1 and then giving it an ozone treatment for 15 minutes for the better deposition. After that, the $\text{CH}_3\text{NH}_3\text{PbBr}_3$ Perovskite layer (photoactive layer) has been directly coated onto FTO substrate by 2500 rpm for 40 sec and then heated up-to 110°C for 5 minutes. A layer of Phenyl-

C₆₁-butyric acid methyl ester (PC₆₁BM) has been deposited onto perovskite layer by 3000 rpm for 40 sec and then heated for 2 min. Now, the Bathocuprione (BCP) buffer layer has coated onto PC₆₁BM layer by 4500 rpm for 40 second and annealed the device for 5 min. All the layers have been deposited by spin-coating technique inside the glove box under nitrogen gas. Finally, the device has been completed by thermal evaporation of Al to make the top electrode (cathode). The fabrication steps and architecture of the planer perovskite photovoltaic device has displayed in Fig. 3(a). The resultant device is composed of Al/BCP/PCBM/Perovskite/FTO and the energy level diagram of the device has shown in Fig. 3(b) with transportation of the charge carriers excited from Perovskite layer in illumination and then transport to their respective electrodes.

RESULT AND DISCUSSIONS

The surface morphology of perovskite precursor solution characterized by field emission scanning electron microscopy (FESEM) which grown on glass-substrate has displayed in Fig 2. The top view of FESEM image exhibits large grain size of perovskite material with uniform grain distribution and complete surface coverage without agglomeration. We have used band gap value is 2.3 eV, which is investigated in our previous paper [19]. I-V characteristics of the fabricated perovskite (photoactive layer) based device in dark and illumination condition have shown in Fig. 4 (-10V to +10V). We have seen from the figure that in forward biasing current increases exponentially, on the other hand the current vary slowly in dark with the applied voltage. By interpretation of current-voltage curve, applying Shockley model we have acquired the main diode characteristics. The photocurrent is calculated by using following formula:

$$I = I_0 [exp(qV/nkT) - 1]$$

Where, e is electron charge; K is Boltzmann constant; V is ideality voltage; T is absolute temperature; I₀ is reverse saturation current. The value saturation current can be described from the intercept at V = 0 can be obtained from the slope of the linear portion of forward bias region of the semi-logarithmic J-V characteristic shown in Fig. 4(a) as shown in Fig. 4(b), the saturation current (I_s) has been calculated in the value of 1.02×10⁻⁴mA by intercept at V=0 using semi-logarithmic scale of I-V curve.

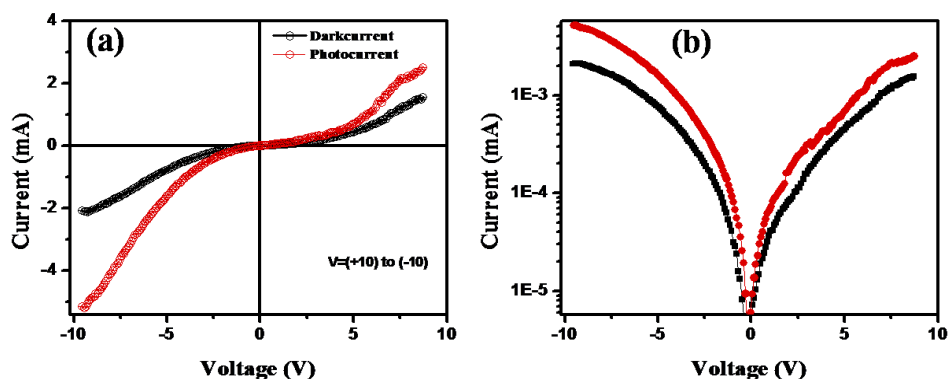


Figure 4. (a) Current-voltage curve of heterojunction devices under the dark and illumination, (b) I-V curve repotting in semilogarithmic scale of corresponding device.

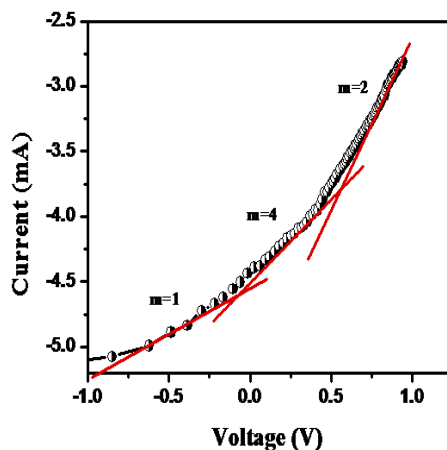


Figure 5. Log-Log scale of I-V curve; m represents the slope of the curve






By analyzing the double logarithmic I-V plots as shown in Fig. 5 the charge transport properties of the device were studied.

General power law dependence of J-V^m exhibit from the curve, where m represents the slope of the curve, a important quantity to define voltage dependent charge transport regions. Number of charge carriers at low applied voltage is miner. The injected charge carriers relatively high as applied voltage is increased beyond the ohmic region. Therefore, the density of injected carriers inside the organic layer reaches to the maximum value. Here the current is limited by the space charge and increased quadratically with the voltage as shown in region m = 2 in the curve. This characteristic represent the trap free space charge limited conduction phenomenon. Therefore, within the band gap presence of traps influence the conduction mechanism, distribution and location of the trap centers governs the current conduction.

SUMMARY AND CONCLUSIONS:

In this paper, we have synthesized and characterized of methylammonium lead bromide perovskite and prepared a thin film. This film has strong surface coverage and negligible pin holes represented by FESEM image. In I-V characteristics, we have shown that the perovskite thin film exhibit rectification behavior. The calculated saturation current is 1.02×10^{-4} mA. We believe that this study will be beneficial in the developments of $\text{CH}_3\text{NH}_3\text{PbBr}_3$ based devices, mainly for photodetectors and solar cells.

ORCID IDs

-  Shaily Choudhary, <https://orcid.org/0000-0003-4211-0921>;  Shalini Tomar, <https://orcid.org/0000-0001-7385-3061>
 Depak Kumar, <https://orcid.org/0000-0002-2958-8309>;  Sudesh Kumar, <https://orcid.org/0000-0002-7507-4712>
 Ajay Singh Verma, <https://orcid.org/0000-0001-8223-7658>

REFERENCES

- [1] I. Mesquita, L. Andrade, and A. Mendes, *Renewable and Sustainable Energy Reviews*, **82**, 2471 (2018), <https://doi.org/10.1016/j.rser.2017.09.011>
- [2] Y. Dkhissi, F. Huang, S. Rubanov, M. Xiao, U. Bach, L. Spiccia, and Y. B. Cheng, *J. Power Sources*, **278**, 325 (2015), <https://doi.org/10.1016/j.jpowsour.2014.12.104>
- [3] N. Adhikari, D. Khatiwada, A. Dubey, and Q. Qiao, *J. Photonics for Energy*, **5**, 057207 (2015), <https://doi.org/10.1117/1.JPE.5.057207>
- [4] H. Tang, S. He, and C. Peng, *Nanoscale research letters*, **12**, 410 (2017), <https://doi.org/10.1186/s11671-017-2187-5>
- [5] P. Docampo, J.M. Ball, M. Darwich, G.E. Eperon, and H.J. Snaith, *Nature communications*, **4**, 2761 (2013), <https://doi.org/10.1038/ncomms3761>
- [6] S. Masi, S. Colella, A. Listorti, V. Roiati, A. Liscio, V. Palermo, and G. Gigli, *Scientific reports*, **5**, 7725 (2015), <https://doi.org/10.1038/srep07725>
- [7] A. Kojima, K. Teshima, Y. Shirai, and T. Miyasaka, *J. American Chemical Society*, **131**, 6050 (2009), <https://doi.org/10.1021/ja809598r>
- [8] M.M. Lee, J. Teuscher, T. Miyasaka, T.N. Murakami, and H.J. Snaith, *Science*, **338**, 643 (2012), <https://doi.org/10.1126/science.1228604>
- [9] C. Liu, M. Hu, X. Zhou, J. Wu, L. Zhang, W. Kong, and C. Cheng, *NPG Asia Materials*, **10**, 552 (2018), <https://doi.org/10.1038/s41427-018-0055-0>
- [10] P. Nandi, C. Giri, B. Joseph, S. Rath, U. Manju, and D. Topwal, *J. Phys. Chem. A*, **120**, 9732 (2016), <https://doi.org/10.1021/acs.jpca.6b09718>
- [11] L. Lang, J.H. Yang, H.R. Liu, H.J. Xiang, and X.G. Gong, *Physics Letters A*, **378**, 290 (2014), <https://doi.org/10.1016/j.physleta.2013.11.018>
- [12] Y. Ye, X. Run, X. H. Tao, H. Feng, X. Fei, and W. L. Jun, *Chin. Phys. B*, **24**, 116302 (2015), <https://doi.org/10.1088/1674-1056/24/11/116302>
- [13] T. Qiu, Y. Hu, F. Bai, X. Miao, and S. Zhang, *J. Materials Chemistry A*, **6**, 12370 (2018), <https://doi.org/10.1039/C8TA00948A>
- [14] J. You, Z. Hong, Y. Yang, Q. Chen, M. Cai, T. B. Song, and Y. Yang, *ACS nano*, **8**, 1674 (2014), <https://doi.org/10.1021/nm406020d>
- [15] C. Manspeaker, S. Venkatesan, A. Zakhidov, and K. S. Martirosyan, *Current opinion in chemical engineering*, **15**, 1 (2017), <http://dx.doi.org/10.1016%2Fj.coche.2016.08.013>
- [16] Y. Ling, Y. Tian, X. Wang, J. C. Wang, J. M. Knox, F. Perez-Orive, and H. Gao, *Advanced Materials*, **28**, 8983 (2016), <https://doi.org/10.1002/adma.201602513>
- [17] M. Zhang, M. Lyu, H. Yu, J. H. Yun, Q. Wang, and L. Wang, *Chemistry—A European Journal*, **21**, 434 (2015), <https://doi.org/10.1002/chem.201404427>
- [18] S. Yang, W. Fu, Z. Zhang, H. Chen, and C.Z. Li, *J. Materials Chemistry A*, **5**, 11462 (2017), <https://doi.org/10.1039/C7TA00366H>
- [19] J. Chaudhary, S. Choudhary, C.M.S. Negi, S.K. Gupta, and A.S. Verma, *Physica Scripta*, **94**, 105821 (2019), <https://orcid.org/0000-0001-8223-7658>

СИНТЕЗ І ХАРАКТЕРИСТИКА ФОТОЕЛЕКТРИЧНОГО ПРИСТРОЮ НА ОСНОВІ ПЕРОВСКІТНОГО
 МЕТИЛАММОНІЙНОГО БРОМІДУ СВИНЦЮ

Шайлі Чоудхарі^a, Шаліні Томар^a, Дepak Кумар^a, Судеш Кумар^c, Аджай Сінгх Верма^d

^aФізичний факультет, Банастхалі Відьяпітх, Банастхалі, Раджастан, 304022, Індія

^bDepartment of Chemical Engineering, Банастхалі Відьяпітх, Банастхалі 304022, Індія

^cФізичний факультет, Банастхалі Відьяпітх, Банастхалі, Раджастан, 304022, Індія

^dФакультет природничих та прикладних наук, університет Глокал, Сахаранпур, 247232, Індія

Гібридні електронні пристрої дають прийнятний підхід до можливих джерел живлення та інших подальших застосувань завдяки простоті розташування, підготовки, виробництва, легкості використання матеріалів та меншому впливу на навколишнє середовище. У цій роботі було розглянуто електричні властивості гібридних бромідних наночастинок перовскіта, а також обговорювався шлях розвитку перовскітних фотоелектричних пристроїв. Для виготовлення пристроїв, що обробляються низькотемпературним розчином, ключову роль у виробництві однорідних тонких плівок відіграє використання одноетапних методів спінового покриття. Технологія спінового покриття була використана для нанесення розчину попередника, включаючи бромід метиламмонію (MABr) та бромід свинцю (PbBr₂) з молярним співвідношенням (3:1) для нанесення тонких плівок на FTO-підложку. Одноетапний процес розчину був використаний для нанесення шарів поглинача $\text{CH}_3\text{NH}_3\text{PbBr}_3$ та відобразив загальне уявлення щодо складу матеріалу, техніки нанесення та архітектури пристрою, вибір шару транспортування заряду та електрода.

Ключові слова: перовскітні металогалогеніди; мобільність носія заряду; опір; ємність; спектроскопія електрохімічного імпедансу

INVESTIGATIONS OF LEAD FREE HALIDES IN SODIUM BASED DOUBLE PEROVSKITES $\text{Cs}_2\text{NaBiX}_6$ (X=Cl, Br, I): AN AB INITIO STUDY[†]

 Shaily Choudhary^a,  Shalini Tomar^a,  Depak Kumar^b,
 Sudesh Kumar^c,  Ajay Singh Verma^{d,*}

^aDepartment of Physics, Banasthali Vidyapith, Banasthali, Rajasthan 304022, India

^bDepartment of Chemical Engineering, Banasthali Vidyapith, Banasthali 304022, India

^cDepartment of Physics, Banasthali Vidyapith, Banasthali, Rajasthan 304022, India

^dDepartment of Natural and Applied Sciences, Glocal University, Saharanpur 247232, India

*Corresponding author: ajay_phy@rediffmail.com

Received April 19, 2021; accepted July 14, 2021

Despite the excellent merits of lead based perovskite optoelectronic devices; their unstable nature and toxicity still present a bottleneck for practical applications. Double perovskite has emerged as a candidate for optoelectronics and photovoltaic application because of its nontoxic behaviour and stability in air. We have presented ab-initio study of $\text{Cs}_2\text{NaBiX}_6$ (X=Cl, Br, I) lead free halide double perovskites. The calculation is carried out using the FP-LAPW method in the DFT framework within PBE potential using the WIEN2k code. The structural, electronic and optical properties of $\text{Cs}_2\text{NaBiI}_6$, $\text{Cs}_2\text{NaBiBr}_6$ and $\text{Cs}_2\text{NaBiCl}_6$ have been analysed. We have obtained the band gap of 2.0, 2.6 and 3.7 for $\text{Cs}_2\text{NaBiI}_6$, $\text{Cs}_2\text{NaBiBr}_6$ and $\text{Cs}_2\text{NaBiCl}_6$ respectively. Throughout the study, we have shown that the variation in the structure of double perovskite within $\text{Cs}_2\text{NaBiX}_6$ (X=Cl, Br, I) that leads to the variation in band gap, density of states and in optical properties such as extinction coefficient, absorption spectra, optical reflectivity, dielectric coefficient, refractive index that shows the variety of this material for optoelectronic devices and other purposes.

Keywords: double perovskites; band gap, dielectric constant, optical conductivity

PACS: 73.21.-b; 73.30.+y; 73.40.Lq; 73.50.Gr

Nearly 85% of world's population are depending for energy on exhaustible fossil fuels that have deleterious out-turn on human health & environmental consequences. Furthermore, this demand of energy will be double by 2050. The evolution of sustainable energy, like as hydrolic energy, wind energy and solar energy becomes an impending prerequisite [1]. Therefore, research to achieve high-efficient solar cells is currently very active. Perovskite becomes the most quickly developing solar cell because of their high power conversion efficiency and low cost. We all know that halide perovskite based solar cells are currently the fastest growing photovoltaic technology in terms of research and development. Firstly, reported hybrid organic inorganic halide perovskite $\text{CH}_3\text{NH}_3\text{PbI}_3$ as a light sensitizer in a dye-sensitize solar cell and demonstrated a power conversion efficiency of 3.8% [2].

Hybrid perovskites, such as $\text{NH}(\text{CH}_3)_3\text{SnX}_3$ (X = Cl, Br), [1] ABi_3 (A = CH_3NH_3 , NH_2CHNH_2 ; B = Sn, Pb) [3] and $\text{CH}_3\text{NH}_3\text{PbI}_3$ [4] have been identified as potential candidates for fabricating high performance photovoltaic cells. Indeed, hybrid perovskites have considerable solar energy-conversion efficiency (greater than 19% [5]); however, they have some disadvantages, such as instability, a low resistance to moisture and heat when they are exposed for a long time to light and toxicity, which is caused by the presence of lead (Pb) [6,7]. Because of the mentioned diverse disadvantages of the hybrid perovskites, numerous researchers are working to identify an alternative to lead-halide perovskite semiconductors. Researchers have implemented a partial or full substitution of lead metal with tin or germanium in the perovskite structure. These modified materials, however, have resulted in inferior device performance due to the unstable +2 oxidation state of tin and germanium. Earlier predictions of new perovskite materials were based on the simple Goldschmidt tolerance factor to determine the stability of the structure. Recently, Travis et al. showed that the Goldschmidt tolerance factor fails to predict the stability of 32 known inorganic iodide perovskites. Researchers have been performed high throughput ab initio calculations on hypothetical three dimensional halide perovskites (ABX_3) obtained by substitution of lead with other divalent cations from the periodic table. The authors considered hundreds of material combinations and concluded that only Pb, Sn and Ge based perovskite show promising properties for optoelectronic devices. Attempts have also been made to find perovskite like structures via double perovskites, wherein two neighbouring divalent lead cations are replaced by monovalent and trivalent ones [8]. Double perovskites, a broad class of condensed materials has been started to investigated since 1960 [9, 10]. It was perhaps the most studied family of compound due to the flexibility of their structure, which permits novel device application originating from their low reactivity, magnetic and optical properties [11]. Double perovskites oxides, $\text{AA}'\text{BB}'\text{O}_6$, where A is alkaline-earth or rare-earth metal and B and B' are transition metals, which are derived from simple ABO_3 perovskite, A-site atoms are alkaline earth metals such as Ba, Sr or a lanthanide and the B atoms are the transition metals. They constitute an important class of materials, characterized by structural distortion from the cubic, space group $\text{Fm}\bar{3}\text{m}$ (No. 225), structure. In this work, we contribute to the study of double perovskite $\text{Cs}_2\text{NaBiX}_6$ (X=Cl, Br, I) by performing a first principles study of their

[†] Cite as: S. Choudhary, S. Tomar, D. Kumar, S. Kumar, A.S. Verma, East. Eur. J. Phys. 3, 74 (2021), <https://doi.org/10.26565/2312-4334-2021-3-11>

© S. Choudhary, S. Tomar, D. Kumar, S. Kumar, A.S. Verma, 2021

electronic and optical properties using the FPLAPW method in the DFT framework with PBE using the WIEN2k code [12]. We have performed the first principles calculations using the WIEN2k code based upon the framework of density functional theory (DFT) [13].

COMPUTATIONAL DETAILS

In this work, first principles calculations were executed within the framework of Kohn-Sham DFT to study the structural, electronic and optical properties of lead free halide double perovskite $\text{Cs}_2\text{NaBiX}_6$ ($X = \text{I}, \text{Br}, \text{Cl}$) by using Wien2k code [14, 15]. To optimize the lattice constant and ground state energy of lead free halide double perovskite the structural calculation was performed to properly relax the system in cubic phase using Wu-Cohen generalized gradient approximation (WC-GGA) giving optimized lattice constants. We employ a Perdew- Burke- Ernzerhof (PBE) generalized gradient approximation (GGA) exchange correlation functional [16]. For a well converged SCF calculation, we used cut off energy -6.0 Ry, $R_{\text{MT}} \times K_{\text{max}} = 7$ and 125 k-points to create $5 \times 5 \times 5$ k-mesh in the first Brillouin zone [17]. All present calculations were conducted using the full potential linearized augmented plane wave (FP-LAPW) method within the framework of density functional theory (DFT), as embodied in the WIEN2k code. The optical properties were determined for dense unit cell with 10000 k-mesh points. All the predictions are made using 0 K DFT relaxed structures and do not account for lattice expansion and temperature induced phase changes.

RESULTS AND DISCUSSIONS

Structural properties

The structural optimization based on Murnaghan's equation of state was performed to obtain the relax structure with minimum energy. $\text{Cs}_2\text{NaBiX}_6$ ($X = \text{Cl}, \text{Br}, \text{I}$) crystallizes in cubic phase ($\alpha = \beta = \gamma = 90^\circ$) with space group. The exchange correlation effect is treated using Perdew-Burke Ernzerhof-Generalized-Gradient Approximation (PBE-GGA). By fitting the total energy versus the reduced and extended volume of the unit cell into third order Birch-Murnaghan's equation of states (EOS), the ground state structural properties such as equilibrium volume (V), Bulk modulus (B), pressure derivative of Bulk modulus (B') and ground state energy (E_o) are determined [18,19].

$$E(V) = E_o + \frac{9VB}{16} \left\{ \left[\left(\frac{V_o}{V} \right)^{2/3} - 1 \right]^3 B' + \left[\left(\frac{V_o}{V} \right)^{2/3} - 1 \right]^2 \times \left[6 - 4 \left(\frac{V_o}{V} \right)^{2/3} \right] \right\} \quad (1)$$

The energy vs. volume curve for $\text{Cs}_2\text{NaBiX}_6$ ($X = \text{Cl}, \text{Br}, \text{I}$) (obtained by geometry optimization) has been shown in figure (1) with displaying lattice parameters (a), equilibrium volume (V), bulk modulus (B), pressure derivative of bulk modulus (B') for GGA-PBE potentials respectively. The value of internal parameter is decided by the convergence of total energy. The values of structural parameters are presented in table 1.

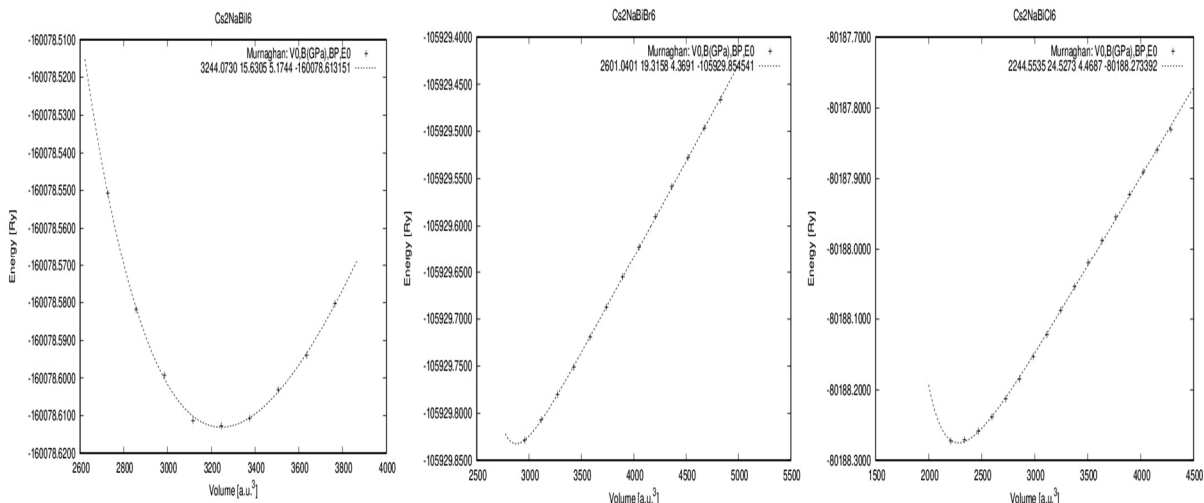


Figure 1. Volume optimization of $\text{Cs}_2\text{NaBiI}_6$, $\text{Cs}_2\text{NaBiBr}_6$ and $\text{Cs}_2\text{NaBiCl}_6$.

Table 1. Structural parameters of $\text{Cs}_2\text{NaBiX}_6$ ($X = \text{Cl}, \text{Br}, \text{I}$) perovskites.

Compounds	$a_0(\text{\AA})$	$V(\text{\AA}^3)$	B (GPa)	B'
$\text{Cs}_2\text{NaBiI}_6$	21.75	3244.073	15.63	5.174
$\text{Cs}_2\text{NaBiBr}_6$	21.75	2601.040	19.31	4.369
$\text{Cs}_2\text{NaBiCl}_6$	21.72	2244.553	24.52	4.468

Electronic properties

The band structures of these compounds are presented in figure 2. From the band structure diagrams of $\text{Cs}_2\text{NaBiX}_6$ ($X = \text{Cl}, \text{Br}, \text{I}$) it is clear that there is a difference in band gap of three compounds and belongs to indirect band gap material,

because the maxima of valance band and minima of conduction band does not coincide at Γ -point. In this Ab- initio study, we have focused on lead free halide double perovskite $\text{Cs}_2\text{NaBiX}_6$ ($X = \text{Cl, Br, I}$). The most prominent difference among the studied compounds $\text{Cs}_2\text{NaBiI}_6$, $\text{Cs}_2\text{NaBiBr}_6$, and $\text{Cs}_2\text{NaBiCl}_6$ is their anions, which is responsible for the variation in the calculated band gap. From the graphs it has been observed the value of band gap is decreases rapidly from Cl to Br to I. It is due to the effect of anions. Anions play an important role and through the valence electron contribution they decrease the band gap. It's clear that the basic study of anions are plays an important role for the electronic and optical characteristic of photovoltaic devices. The calculated band gap for $\text{Cs}_2\text{NaBiX}_6$ ($X = \text{Cl, Br, I}$) along the high symmetric point of Brillion zone is 3.7, 2.6 and 2.0 eV respectively with the GGA–PBE exchange-correlation potential.

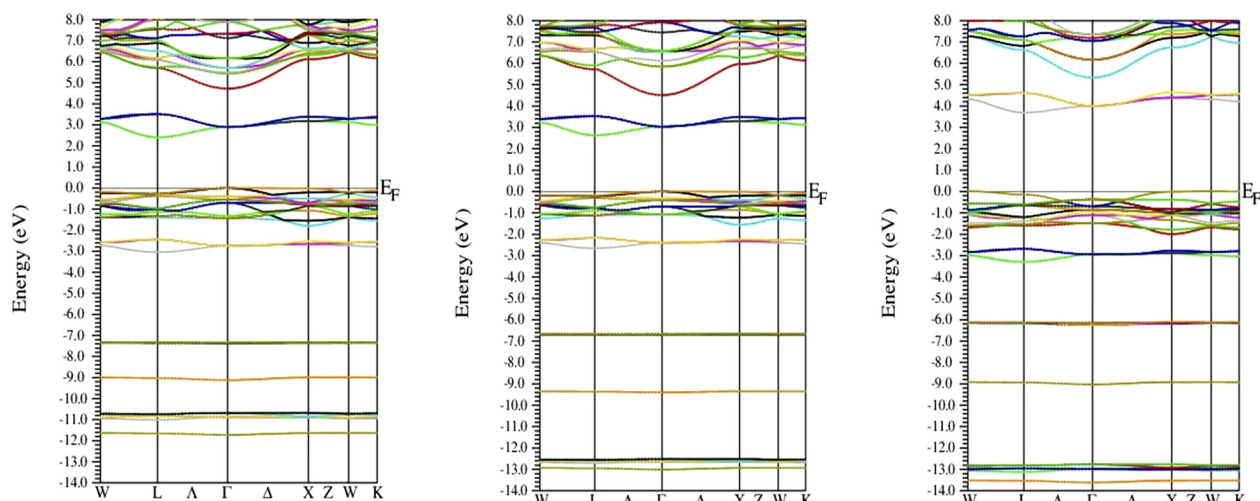


Figure 2. Band structure diagrams of $\text{Cs}_2\text{NaBiI}_6$, $\text{Cs}_2\text{NaBiBr}_6$ and $\text{Cs}_2\text{NaBiCl}_6$.

In diagram 3 the PDOS and TDOS of states of $\text{Cs}_2\text{NaBiX}_6$ ($X = \text{Cl, Br, I}$) has been presented. As we have seen in the plotted digram of PDOS for $\text{Cs}_2\text{NaBiCl}_6$ s and p orbital in upper valance band overlapped within the s and p of Na and Bi while s orbital of Cs and Na overlapped with s and p orbital of Cl. The lower valance band formed due to the overlapping of p orbital of Cs, Na, Bi and Cl. Similarly, in the case of $\text{Cs}_2\text{NaBiBr}_6$ and $\text{Cs}_2\text{NaBiI}_6$ the upper valance band mainly formed due to contribution of s orbital of Cs, Na, Bi and ($X = \text{Cl, Br, I}$) and lower valance band formed due to the p orbital overlapping in above compounds. From the above discussion, it can be said that the s orbital contribute more in all the case for formation of upper valance bands. Mutual hybridization of p orbital does not contribute that much to form upper valance band as compare to s orbital. We know that the position of the electron can be determined in all the compounds $\text{Cs}_2\text{NaBiCl}_6$, $\text{Cs}_2\text{NaBiBr}_6$ and $\text{Cs}_2\text{NaBiI}_6$ within upper valance band, lower valance band and conduction band. The total density of states (TDOS) for the lead free halide double perovskite $\text{Cs}_2\text{NaBiCl}_6$, $\text{Cs}_2\text{NaBiBr}_6$ and $\text{Cs}_2\text{NaBiI}_6$ represent the distribution of electrons in the energy spectrum. These figures describe the TDOS of $\text{Cs}_2\text{NaBiX}_6$ ($X = \text{Cl, Br, I}$) as well as for Na, Bi and ($X = \text{Cl, Br, I}$).

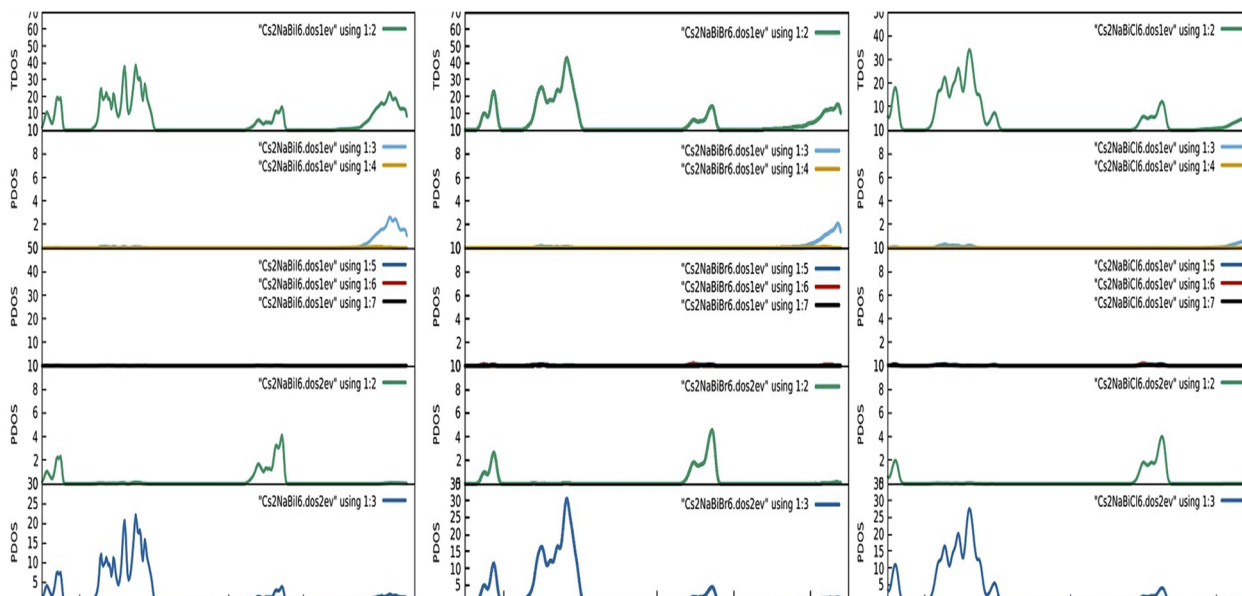


Figure 3. PDOS and TDOS diagrams of $\text{Cs}_2\text{NaBiI}_6$, $\text{Cs}_2\text{NaBiBr}_6$ and $\text{Cs}_2\text{NaBiCl}_6$

Optical properties

The dielectric properties are of great importance in giving insight into the fundamental physical properties and potential applications. The macroscopic optical response function of a compound is expressed by the dielectric function in the range of linear response. It is known that the dielectric function is mainly connected with the electronic response [20].

Basically, dielectric behavior of any compound is a quantity measuring the ability of a substance to store electrical energy in an electric field. The dielectric function known for describes the optical response of the medium at all photon energies [21] and gives a better understanding of electronic structure [22, 23]. The optical properties of $\text{Cs}_2\text{NaBiX}_6$ ($X = \text{Cl, Br, I}$) have been calculated from the complex dielectric function,

$$\varepsilon(\omega) = \varepsilon_1(\omega) + \varepsilon_2(\omega)$$

The imaginary part $\varepsilon_2(\omega)$ was calculated from momentum matrix elements between the occupied and unoccupied wave functions within the selection rules. The imaginary part $\varepsilon_2(\omega)$ of dielectric function can be express energy loss or describe the density of Plasmon excitation in a system. The variation of real part $\varepsilon_1(\omega)$ and imaginary part $\varepsilon_2(\omega)$ of dielectric function with respect to photon energy are shown in figure 4. This can be observed from the results that from IR to visible to UV region (0 – 4.31 eV), $\text{Cs}_2\text{NaBiX}_6$ (Cl, Br, I) shown higher dielectric constant ranges. In case of $\text{Cs}_2\text{NaBiCl}_6$ it reaches its first maximum value 5.29 at 4.38 eV. Similarly in $\text{Cs}_2\text{NaBiBr}_6$ and $\text{Cs}_2\text{NaBiI}_6$ shown higher peaks 6.47 at 2.9eV and 7.28 at 2.8 eV respectively corresponding to first and second inter band transition at R and M symmetry points of Brillouin zone for $\text{Cs}_2\text{NaBiX}_6$ (Cl, Br, I) along with $\varepsilon_1(\omega)$. Figure 4 shows the frequency dependent absorptive part $\varepsilon_2(\omega)$ of dielectric function $\varepsilon(\omega)$, the maximum absorption behaviour of these materials represented by the value of real part of dielectric constant as well as the value of $\varepsilon_2(\omega)$ start increasing sharply with the incident electromagnetic radiation. The threshold energy points occur for $\text{Cs}_2\text{NaBiX}_6$ (Cl, Br, I) at 2.8 eV, 2.24 eV and 2.18 eV respectively. After these threshold energy points many peaks can be seen that corresponds to the inter band transition for valence band to transition band. We can directly calculate the optical quantities like optical conductivity, absorption coefficient, refractive index, reflectivity etc. by using the real and imaginary part of dielectric function by the relation described in the reference [24].

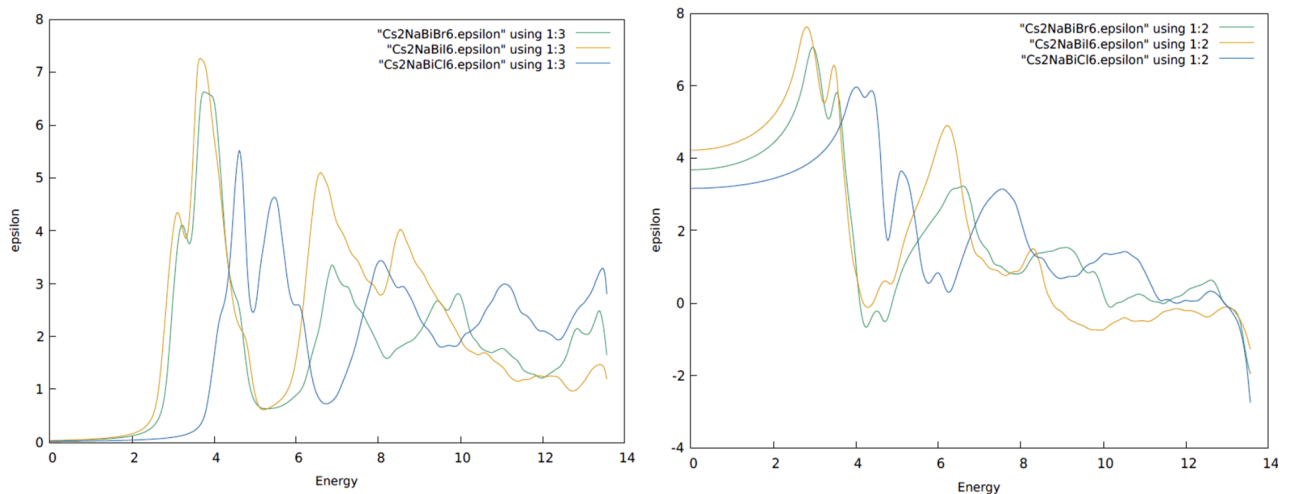


Figure 4. The plotted curve between photon energy and dielectric parameters imaginary epsilon ($\varepsilon_2(\omega)$) and real epsilon ($\varepsilon_1(\omega)$)

The absorption coefficient determines how far into a material light of a particular wavelength can penetrate before it get absorbed; it depends on the material and also on the wavelength of light which is being absorbed. Figure 5 gives a wide interpretation of absorption spectra $\text{Cs}_2\text{NaBiX}_6$ ($X = \text{Cl, Br, I}$) and its clear from the graph that the stronger absorption is seen from visible region to the commence of UV region i.e., in case of $\text{Cs}_2\text{NaBiCl}_6$ it ranges from 2.8-4.9eV, for $\text{Cs}_2\text{NaBiBr}_6$ it ranges from 2.2- 4.1eV and for $\text{Cs}_2\text{NaBiI}_6$ it ranges from 2.1- 4.2eV respectively. Instead of photon absorption there are several numbers of ways of exciting electrons in a compound. First is subjected to optical spectra is the excitation of electrons by other electrons that is done by shining a beam of mono-energetic electrons at a sample and analyzing the energy of the transmitted or reflected beam. It is found that the incident electrons loss energy in discrete amounts. The loss spectrum arises both from the excitation of single electrons in solid, just as in the case of photon absorption and also from the excitation of collective oscillations called Plasmon's. In case of inter-band transitions, which consist most of the Plasmon excitations, the scattering probability of volume losses is directly related to the energy loss function $L(\omega)$ [19]. The energy loss function $L(\omega)$ is also displayed in figure 5. This function plays an important role describing the energy loss of a fast electron traversing in a material. The peaks in $L(\omega)$ spectra represent the characteristic associated with the plasma resonance. The resonant energy loss from the help of the graph can be seen at 6.24eV, 4.52eV and 4.4eV in $\text{Cs}_2\text{NaBiCl}_6$, $\text{Cs}_2\text{NaBiBr}_6$ and $\text{Cs}_2\text{NaBiI}_6$ respectively.

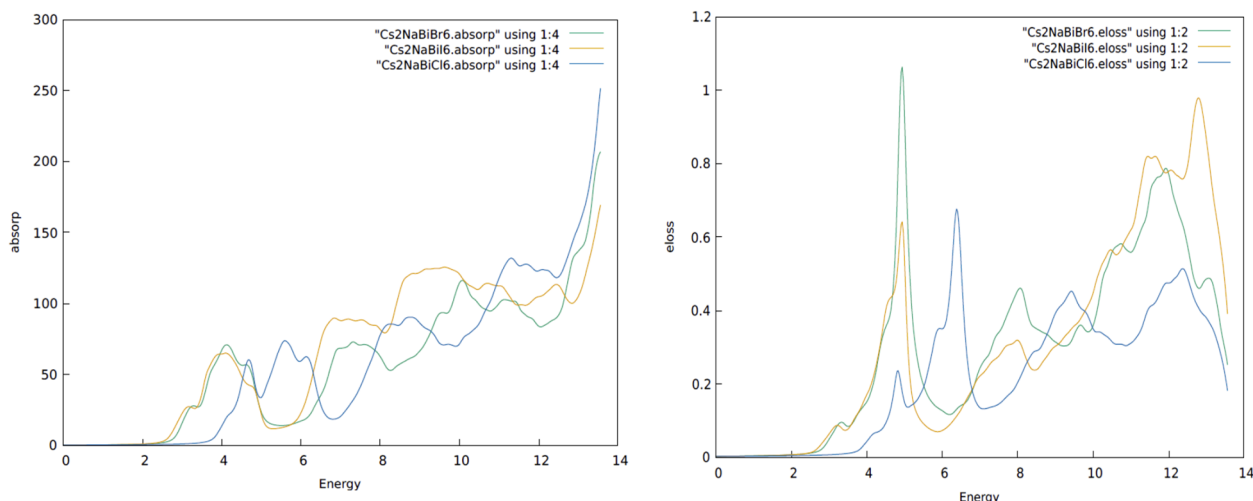


Figure 5. Absorption spectra and Energy loss function $L(\omega)$ of $\text{Cs}_2\text{NaBiX}_6$ ($X = \text{Cl, Br, I}$).

Refractive index of any material is a dimensionless number that describes how fast light travels through the materials. The refractive index and extinction coefficient are displayed in figure 6. We have observed the optically isotropic nature of this compound in the lower energy range. For lower energies the refractive index value is almost constant and as the energy increases it attains a maximum value and exhibits decreasing tendency for higher energy values. The static refractive index $n(0)$ is found to have the value 1.78, 1.90, and 2.1 in cases of $\text{Cs}_2\text{NaBiCl}_6$, $\text{Cs}_2\text{NaBiBr}_6$ and $\text{Cs}_2\text{NaBiI}_6$ respectively. It increases with energy in the transparent region reaching a peak in the ultraviolet range at 4.6 eV for $\text{Cs}_2\text{NaBiCl}_6$, and in visible region at 3.0 eV and 2.8 eV for $\text{Cs}_2\text{NaBiBr}_6$ and $\text{Cs}_2\text{NaBiI}_6$ respectively. The refractive index is greater than one because as photons enter a material they are slowed down by the interaction with electrons [20]. The more photons are slowed down while travelling through a material, the greater the material's refractive index. Generally, any mechanism that increases electron density in a material also increases refractive index. However, refractive index is also closely related to bonding. In general, ionic compounds are having lower values of refractive index than covalent ones. In covalent bonding more electrons are being shared by the ions than in ionic bonding and hence more electrons are distributed through the structure and interact with the incident photons to slow down.

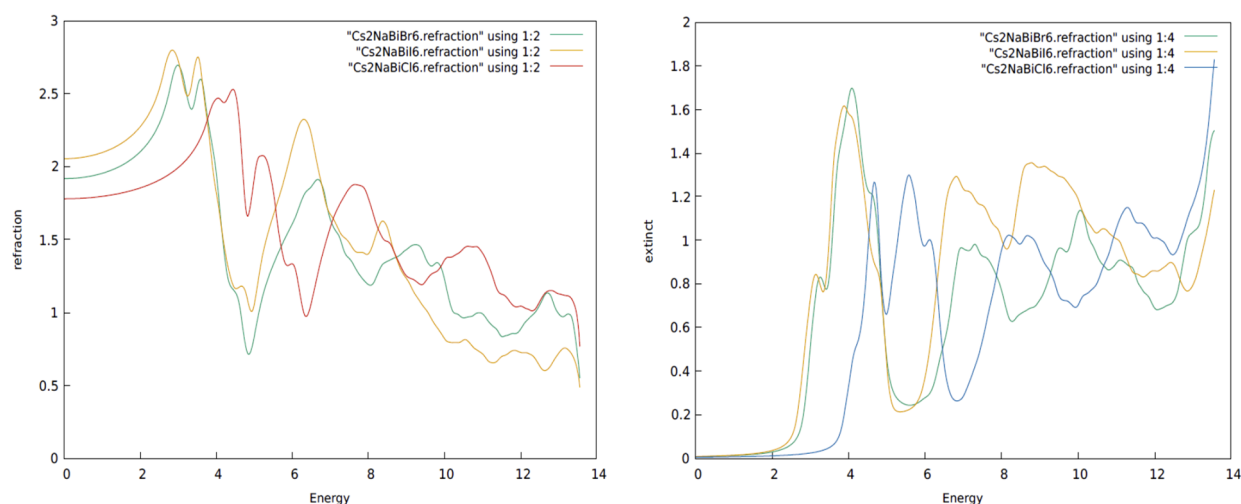


Figure 6. Refraction coefficient $n(\omega)$ and Extinction coefficient $K(\omega)$ of $\text{Cs}_2\text{NaBiX}_6$ ($M = \text{Cl, Br, I}$).

As extinction coefficient (K) is a measure of light lost due to scattering and absorption per unit volume, hence, high values of K in lower wavelength range show that these films are opaque in this range. Extinction coefficient reached its highest peaks at 4.8 eV, 4.0 eV and 3.8 eV for $\text{Cs}_2\text{NaBiCl}_6$, $\text{Cs}_2\text{NaBiBr}_6$ and $\text{Cs}_2\text{NaBiI}_6$ respectively. As we have observed the extinction coefficient and imaginary part of dielectric parameters they show a similar trend. $\text{Cs}_2\text{NaBiCl}_6$ and $\text{Cs}_2\text{NaBiBr}_6$ shows highest peaks in UV region and $\text{Cs}_2\text{NaBiI}_6$ shows a highest peak in UV region and a small peak in visible region as we have seen from the plotted figure 7. Reflectivity is an optical property of material, which describes how much light is reflected from the material in relation to an amount of light incident on the material. The reflectance occurs always on the surface of the material, for the light diffusing materials also in the volume of the materials. As shown in figure 7 the reflective coefficient as a function of photon energy. Reflective spectra of $\text{Cs}_2\text{NaBiCl}_6$ shows promise in UV region ranges between 4.0eV to 6.0eV. From these figures of $\text{Cs}_2\text{NaBiCl}_6$, it is clear that these materials show good reflectivity in UV region so that it can be a promising material to use as a UV detector.

As in the case of $\text{Cs}_2\text{NaBiCl}_6$, the reflective spectra of $\text{Cs}_2\text{NaBiBr}_6$ show a good agreement in between visible to UV range in the spectra. The reflectivity of this material ranges from 3.0eV to 4.8eV. This material will be useful as an optoelectronic device as well as in UV generators. $\text{Cs}_2\text{NaBiI}_6$ shows good spectra in visible to UV range. It ranges from 2.8 eV to 4.1 eV. The optical conductivity is shown in figure 7. In case of $\text{Cs}_2\text{NaBiCl}_6$ it ranges from 3.9 eV to 13.5 eV, similarly in $\text{Cs}_2\text{NaBiBr}_6$ it ranges from 2.8 eV to 13.3 eV and in case of $\text{Cs}_2\text{NaBiI}_6$ it ranges in between 2.3 to 8.3 eV.

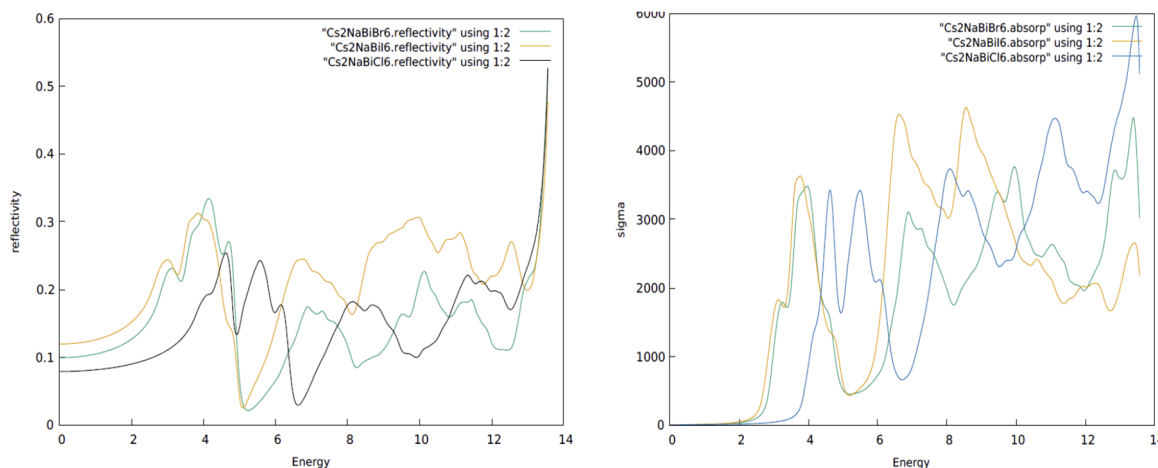


Figure 7. Optical Reflectivity $R(\omega)$ and (I) Optical conductivity $\sigma(\omega)$ of $\text{Cs}_2\text{NaBiX}_6$ ($X = \text{Cl}, \text{Br}, \text{I}$).

SUMMARY AND CONCLUSIONS:

In this work, we have studied the structural, electronic, and optical properties of the lead free halide double perovskite $\text{Cs}_2\text{NaBiCl}_6$, $\text{Cs}_2\text{NaBiBr}_6$ and $\text{Cs}_2\text{NaBiI}_6$ using the FP-LAPW method within the local density approximation (LDA), generalized gradient approximation (GGA) in the framework of density functional theory. The optical properties such as dielectric function, reflectivity, absorption coefficient, optical conductivity, refractive index, and extinction coefficient and energy loss are studied. These calculations reveals that $\text{Cs}_2\text{NaBiCl}_6$ and $\text{Cs}_2\text{NaBiBr}_6$ shows better behavior in UV range and can be used as UV generators while $\text{Cs}_2\text{NaBiBr}_6$ and $\text{Cs}_2\text{NaBiI}_6$ shows a good band gaps in visible region and can be used in lead free, non-toxic optoelectronic devices. However, we expect that this present study will motivate to experimental investigation on electronic and optical properties of lead free halide double perovskite.

ORCID IDs

- Shaily Choudhary**, <https://orcid.org/0000-0003-4211-0921>; **Shalini Tomar**, <https://orcid.org/0000-0001-7385-3061>
Depak Kumar, <https://orcid.org/0000-0002-2958-8309>; **Sudesh Kumar**, <https://orcid.org/0000-0002-7507-4712>
Ajay Singh Verma, <https://orcid.org/0000-0001-8223-7658>

REFERENCES

- [1] H. Tang, S. He, and C. Peng, *Nanoscale Research Letters*, **12**, 410 (2017), <https://doi.org/10.1186/s11671-017-2187-5>
- [2] F. Giustino, and H.J. Snaith, *ACS Energy Letters*, **1**, 1233 (2016), <https://doi.org/10.1021/acsenerylett.6b00499>
- [3] Y. Dang, C. Zhong, G. Zhang, D. Ju, L. Wang, S. Xia, H. Xia, and X. Tao, *Chem. Mater.* **28**, 6968 (2016), <https://doi.org/10.1021/acs.chemmater.6b02653>
- [4] C. Lee, J. Hong, A. Stroppa, M.H. Whangbo, and J.H. Shim, *RSC Adv.* **5**, 78701 (2015), <https://doi.org/10.1039/C5RA12536G>
- [5] T. Zhao, W. Shi, J. Xi, D. Wang, and Z. Shuai, *Sci. Rep.* **7**, 19968 (2016), <https://doi.org/10.1038/srep19968>
- [6] H.S. Jung, and N.G. Park, *Small*, **11**, 10 (2015), <https://doi.org/10.1002/sml.201402767>
- [7] A.H. Slavney, R.W. Smaha, I.C. Smith, A. Jaffe, D. Umeyama, and H.I. Karunadasa, *Inorg. Chem.* **56**, 46 (2017), <https://doi.org/10.1021/acs.inorgchem.6b01336>
- [8] F. Giustino, and H.J. Snaith, *ACS Energy Lett.* **1**, 1233 (2016), <https://doi.org/10.1021/acsenerylett.6b00499>
- [9] J. Cheng, and Z.Q. Yang, *Physica Status Solidi B*, **243**, 1151 (2006), <https://doi.org/10.1002/pssb.200541381>
- [10] H. Wu, *Phys. Rev. B*, **64**, 125126 (2001), <https://doi.org/10.1103/PhysRevB.64.125126>
- [11] Y. Shimakawa, M. Azuma, and N. Ichikawa, *Materials*, **4**, 153 (2011), <https://doi.org/10.3390/ma4010153>
- [12] P. Blaha, G.K.H. Madsen, D. Kvasnicka, and J. Luitz, *WIEN2K, an augmented plane wave plus local orbitals program for calculating crystal properties* (Vienna, Austria) 2008.
- [13] P. Hohenberg, and W. Kohn, *Phys. Rev.* **136**, B864 (1964), <https://doi.org/10.1103/PhysRev.136.B864>
- [14] W. Kohn, and L.J. Sham, *Phys. Rev.* **140**, A1133 (1965), <https://doi.org/10.1103/PhysRev.140.A1133>
- [15] J.P. Perdew, A. Ruzsinszky, G.I. Csonka, O.A. Vydrov, G.E. Scuseria, L.A. Constantin, X. Zhou, and K. Burke, *Phys. Rev. Lett.* **100**, 136406 (2008), <https://doi.org/10.1103/PhysRevLett.100.136406>
- [16] J.P. Perdew, K. Burke, and M. Ernzerhof, *Phys. Rev. Lett.* **77**, 3865 (1996), <https://doi.org/10.1103/PhysRevLett.77.3865>
- [17] H.J. Monkhorst, and J.D. Pack, *Phys. Rev. B*, **13**, 5188 (1976), <https://doi.org/10.1103/PhysRevB.13.5188>
- [18] F. Birch, *Physical Review*, **71**, 809 (1947), <https://doi.org/10.1103/PhysRev.71.809>
- [19] F.D. Murnaghan, *Proc. Natl. Acad. Sci. USA*, **30**, 244 (1994), <https://dx.doi.org/10.1073%2Fpnas.30.9.244>

- [20] E.E. Eyi, and S. Cabuk, Philosophical Magazine, **90**, 2965 (2010), <https://doi.org/10.1080/14786431003752159>
- [21] K.E. Babu, N. Murali, K.V. Babu, P.T. Shibeshi, and V. Veeraiah, Acta Physica Polonica A, **125**, 1179 (2014), <http://dx.doi.org/10.12693/APhysPolA.125.1179>
- [22] M.L. Ali, and M.Z. Rahaman, Int. J. Mater. Sci. Appl. **5**, (2016) 202-206, <https://doi.org/10.11648/j.ijmsa.20160505.14>
- [23] S. Choudhary, A. Shukla J. Chaudhary, and A.S. Verma, Int. J. Energy Res. **44**, 11614 (2020), <https://doi.org/10.1002/er.5786>
- [24] R. Gautam, P. Singh, S. Sharma, S. Kumari, and A.S. Verma, Superlattice Microst. **85**, 859 (2015), <https://doi.org/10.1016/j.spmi.2015.07.014>

ДОСЛІДЖЕННЯ БЕЗСВИНЦЕВИХ ГАЛІДІВ У ПОДВІЙНИХ ПЕРОВСКІТАХ НА ОСНОВІ НАТРІЮ Cs₂NaBiX₆ (X = Cl, Br, I): НЕЕМПЕРІЧНЕ (AB INITIO) ДОСЛІДЖЕННЯ

Шайлі Чоудхарі^a, Шаліні Томар^a, Дєпак Кумар^a, Судеш Кумар^c, Аджай Сінгх Верма^d

^aФізичний факультет, Банастхалі Відьяпітх, Банастхалі, Раджастан, 304022, Індія

^bDepartment of Chemical Engineering, Банастхалі Відьяпітх, Банастхалі 304022, Індія

^cФізичний факультет, Банастхалі Відьяпітх, Банастхалі, Раджастан, 304022, Індія

^dФакультет природничих та прикладних наук, університет Глокал, Сахаранпур, 247232, Індія

Незважаючи на значні переваги перовскітних оптоелектронних пристроїв на основі свинцю, їх нестабільний характер та токсичність все ще є перешкодою для практичного застосування. Подвійний перовскіт став кандидатом для застосування в оптоелектроніці та фотоелектричній техніці через його нетоксичний характер та стабільність у повітрі. Ми представили неемперічне (ab-initio) дослідження безсвинцевих галогенідних подвійних перовскітів Cs₂NaBiX₆ (X=Cl, Br, I). Розрахунок проводиться за допомогою методу FP-LAPW в рамках DFT в межах потенціалу PBE з використанням коду WIEN2k. Були проаналізовані структурні, електронні та оптичні властивості Cs₂NaBiI₆, Cs₂NaBiBr₆ та Cs₂NaBiCl₆. Ми отримали ширину енергетичної щілини 2,0, 2,6 та 3,7 для Cs₂NaBiI₆, Cs₂NaBiBr₆ та Cs₂NaBiCl₆ відповідно. Протягом усього дослідження ми показали, що зміна структури подвійного перовскіту в межах Cs₂NaBiX₆ (X = Cl, Br, I), що призводить до зміни ширини енергетичної щілини, щільності станів та оптичних властивостей, таких як коефіцієнт згасання, спектри поглинання, оптична відбивна здатність, діелектричний коефіцієнт, показник заломлення свідчить про різноманітність цього матеріалу для оптоелектронних пристроїв та інших цілей.

Ключові слова: подвійні перовскіти, ширина енергетичної щілини, діелектрична проникність, оптична провідність

THE PLASMA PARAMETERS OF PENNING DISCHARGE WITH NEGATIVELY BIASED METAL HYDRIDE CATHODE AT LONGITUDINAL EMISSION OF H⁻ IONS[†]

 Ihor Sereda*,  Yaroslav Hrechko,  Ievgeniia Babenko

*V.N. Karazin Kharkiv National University
31, Kurchatov av., 61108, Kharkiv, Ukraine*

**Corresponding author: igorsereda@karazin.ua*

Received June 30, 2021; revised July 27, 2021; accepted August 8, 2021

The enhancement of negative ion production in a volume Penning based source could be performed by the application of metal hydride cathode. Hydrogen isotopes are stored there in a chemically bound atomic state and desorbed from the metal hydride under the discharge current impact. Highly vibrationally / rotationally excited molecules H₂^{*} are formed by recombination of H-atoms at the metallic surface, which then can be easily converted to H⁻ by dissociative electron attachment without the pre-excitation of a H₂ molecule in plasma. Changing the discharge properties opens the way of source design simplification by negative ions extraction along the external magnetic field in comparison with traditional volume sources, where the extraction is performed perpendicular to magnetic field. The separation of negative ions from the extracted in longitudinal direction flux of charged particles was performed by an electromagnetic filter basing on numerical calculations of particles trajectories. The dependence of electron temperature and plasma density on the bias potential is carried out by Langmuir probe method. The measurement of electron energy was performed by an electrostatic energy analyzer. It was shown that the yield of H⁻ ions depends on the electrical bias on the metal hydride cathode with strong dependences on the plasma electrons temperature. The estimation of the bias potential versus T_e was performed under the assumption of electron Boltzmann distribution near the cathode. The presence of additional groups of electrons with higher energies distorts the behavior of H⁻ current, but generally the experimental results are in good agreement with estimation based on the physics behind the Boltzmann distribution. The optimum for the effective extraction of H⁻ ions was revealed, when the metal hydride cathode had been electrically biased at -20V and higher, and plasma density reaches the maximum value to 2×10^9 cm⁻³.

Keywords: negative ions, hydrogen, Penning type ion source, metal hydride

PACS: 52.80.Sm

In 1963 Ehlers et al. [1] extracted a beam of negative deuterium ions through the apertures in the anode with a current of 0.5 mA from a Penning discharge with cold cathodes at a discharge voltage of 3 kV. Further, sources of this type were developed and studied in many laboratories [2]. It can easily be built into the center of cyclotrons and was used in many cyclotrons for accelerating negative ions. It had been used until 1987 in the TRIUMF cyclotron, but the source was installed outside [3]. The Ehlers type source was also used in a Van de Graaf accelerator which accelerated H⁻ ions up to 1.5 MeV with the current of 1 mA and the pulse duration of 1.5 ms [4]. Then some basic understanding of the operation of the Penning type H⁻ ion source was presented.

Today there are two known methods for increasing the current of negative ions from a volume source without cesium using. This is an increase in pressure and plasma density, but this way is limited by destruction of H⁻ ions in plasma [5]. The second method is the choice of the electrode's material [6], which indicates the decisive role of processes on the surface facing hydrogen plasma.

Hydride-forming getter materials based on Zr-V alloys are a promising base for the manufacture of such electrodes [7]. They are characterized by high hydrogen storage capacity and low activation temperatures. They easily uptake hydrogen when heated to moderately elevated temperatures. This circumstance determines the high efficiency of hydrogen pressure adjusting according to the scheme of "adjustable parameter – thermal effect." Hydrogen uptake is accompanied by its excitation with following reduction of ionization potential by 0.3 - 0.5 eV and an increase in cross section for the dissociative attachment of slow electrons to neutral hydrogen molecules [8].

So, the application of metal hydrides as the electrodes of plasma devices opens the possibility of increase the efficiency of negative ion formation in plasma devices and provides an internal local hydrogen supply directly into a gas-discharge cell. The features of metal hydride application in hydrogen plasma of Penning discharge were carefully described in [9].

Highly rotationally/vibrationally excited molecules H₂^{*} are formed by recombination of H-atoms at the metallic surface, which then can be easily converted to H⁻ ions by dissociative electron attachment. The efficiency of H⁻ ion production sufficiently increases, because one does not need any more wasting energy on the pre-excitation of a H₂ molecule [10].

Activated hydrogen desorbed from a metal hydride cathode impacts on the Penning discharge properties [11]. It was cleared that at high discharge voltages negative ions along with electrons and positive ions starts outgoing along the external magnetic field through an aperture in the cathode. So, the simple replacement of a cathode by a metal hydride one and the reverse of polarity on pulling electrodes could make a negative ion source from traditional positive one.

[†] Cite as: I. Sereda, Y. Hrechko, Ie. Babenko, East. Eur. J. Phys. 3, 81 (2021), <https://doi.org/10.26565/2312-4334-2021-3-12>

In [13] the H^- ion current of $10 \mu A$ at an input power of 6W from Penning type ion source with metal-hydride cathode has been obtained. Maximum extracted current of H^- ions was observed at negative electrical bias of metal hydride cathode to 50 V. The purpose of the paper is to investigate the discharge properties in order to explain carried out results and to give advices on increasing the extracted current.

EXPERIMENTAL SETUP

Experimental investigations were performed on a device shown in Figure 1. This is a H^- ion source based on Penning discharge with metal hydride cathode equipped with an electromagnetic filter for H^- ions separation from extracted charged particle flux. Between a metal hydride cathode 1 and a copper cathode-reflector 3 a tubular anode 2 made from stainless steel was set. The positive potential U_a was supplied to the anode. On the metal hydride cathode there was a possibility of supplying a negative electric bias. An electromagnetic filter for negative ions separation was set behind the central aperture in the cathode-reflector. It includes of a grid 7 for positive ions reflection, a magnetic coil 9 for electrons diversion, a collector of diverted electrons 8 and a collector of extracted axial beam of H^- ions 10.

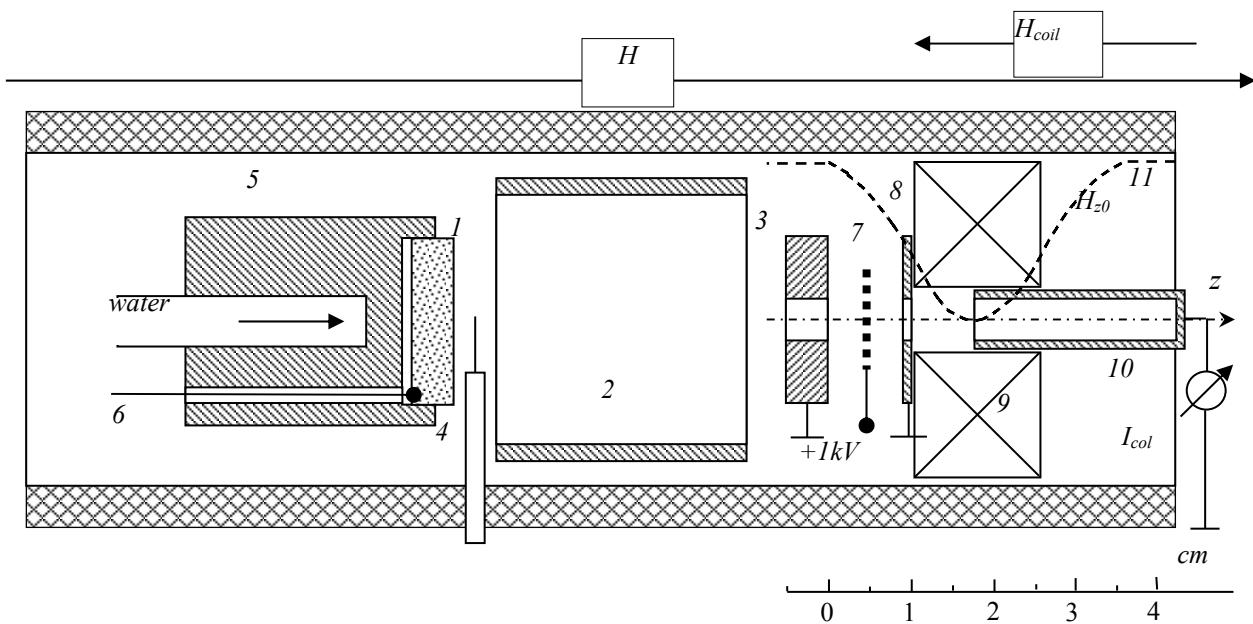


Figure 1. The scheme of discharge cell

1 – metal hydride cathode, 2 – anode, 3 – copper cathode with an aperture, 4 – Langmuir probe, 5 – cathode-holder, 6 - thermocouple, 7 – retarding grid, 8 – electrons collector, 9 – coil of magnetic field H_{coil} , 10 – H^- ion collector, 11 – distribution of the magnetic field H_{z0} in the filter

The metal hydride cathode 1 was pressed from a powder of hydride-forming alloy $Zr_{50}V_{50}$ with a copper binder by a method including melting of the alloy, its activation and filling with hydrogen. The quantity of hydrogen stored in the cathode was $\sim 870 \text{ cm}^3$ under normal atmospheric pressure and room temperature. The metal hydride cathode had a water-cool and its temperature ($\sim 20 \text{ }^\circ\text{C}$) was much lower than the minimal temperature of thermal desorption of hydrogen ($\sim 80 \text{ }^\circ\text{C}$). So, H_2^* uptake was determined only by a discharge current and is provided mainly by ion-stimulated processes from the surface of metal hydride [12]. Langmuir probe 4 made from tungsten wire and embedded in ceramic insulator was set perpendicular to discharge axis on the half distance between anode and metal hydride cathode. The working area of the probe was a cylinder 0.35 mm in diameter with the length of 4 mm faced the center of the cathode. The discharge worked only in desorbed from metal hydride hydrogen at initial residual pressure of 1.5×10^{-6} Torr without any external gas injection.

RESULTS AND DISCUSSION

Previously we reported about the possibility of enhancement of H^- ions yield by the application of a negative electric bias on metal hydride cathode [13]. Following decreasing in inter electrode distance induced significant modification in the negative ions current behavior under the negative electrical bias on metal hydride cathode [14]. More detailed results carried out within the frame work of the paper is shown in Figure 2. One can see, the inflection of H^- current is observed only at low magnetic fields (to 0.06 T) and is already not so pronounced. And when the electric bias $-U_{MH}$ and magnetic fields take higher values the H^- current does not decrease, as it was in [13], but on the contrary it grows.

In [13] a decrease in the H^- current was explained by electrons depletion by the metal hydride cathode owing to their reflection by $-U_{MH}$ potential which is reduced the rate of the dissociative electron attachment. The neglect of

secondary ion-electron emission from the surface of the cathode, which was slowed down the electrons depletion, caused a moderate discrepancy between experiment and calculation.

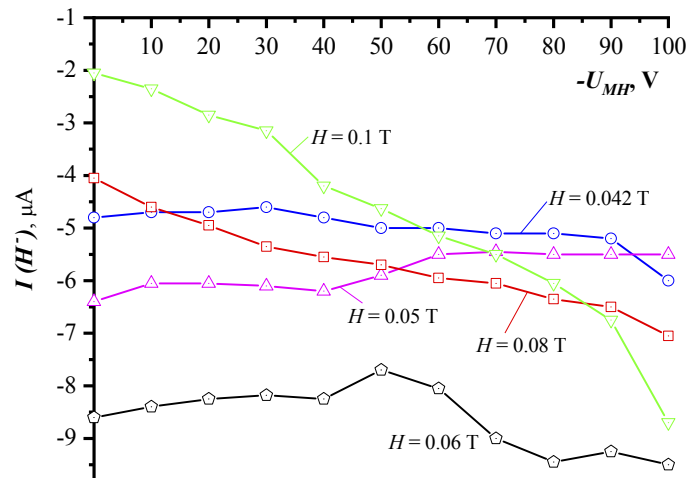


Figure 2. H^- ion current versus negative electric bias on metal hydride cathode at $U_a = 5$ kV, $P = 5 \times 10^{-6}$ Torr

The typical volt-ampere characteristics measured by cylindrical Langmuir probe is shown in Figure 3. The calculation of plasma density n was performed from Bohm current. The electron temperature T_e was calculated from transition section of volt-ampere characteristic near the point of floating potential using standard methodic. The applicability of this technique for determining the electron temperature for moderate magnetic fields has been confirmed in [15], mainly because of large (~ 1 cm) Larmor radius of H_2^+ ion compared with probe dimension.

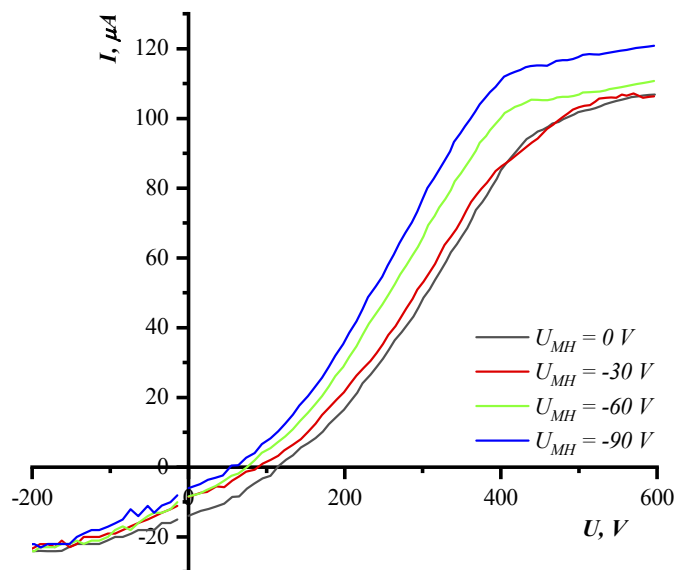


Figure 3. The typical volt-ampere characteristics measured by cylindrical Langmuir probe at $U_a = 5$ kV, $I_d = 0.8$ mA, $H = 0.1$ T, $P = 5 \times 10^{-6}$ Torr

The plasma parameters measured on the axis of discharge cell close to metal hydride cathode is shown in Figure 4. Negative electrical potential on metal hydride cathode $-U_{MH}$ impacts the density and plasma electron temperature. It is seen they behave in the same way at low electric bias. The density surely grows since the bias potential increase to -20 V. T_e drops wherein and takes the value of approximately from 14 eV to 28 eV depending on the magnetic field.

In [13] it was suggested that the inflection point of $I(H^-)$ in the Figure 2 corresponds to plasma electron temperature T_e . And the more T_e , the closer electron reflects from the metal hydride cathode which is under negative bias potential. Figure 4 has primarily proved this statement. At low magnetic field, when the inflection of H^- current is observed under the bias potential of -40 V, the electron temperature takes smaller value, and electrons could be easily reflected reducing the value of H^- current. If T_e takes larger values, there is no H^- current inflection, or it is not so pronounced.

Plasma density and electron temperature T_e takes on increased values when the pressure raises. But it depends in the same way as for those shown in Figure 4 and does not specially represented in the paper.

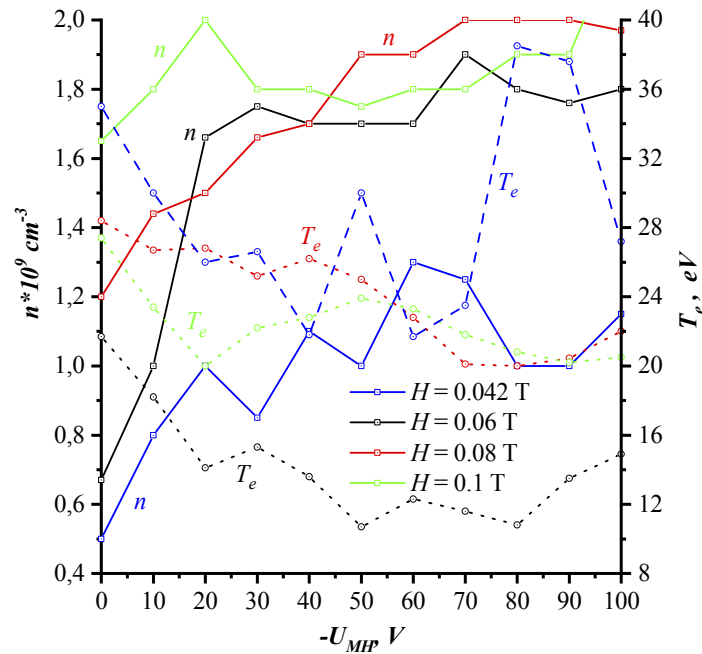


Figure 4. Plasma density and electron temperature on the axis of discharge cell by metal hydride cathode at $U_a = 5$ kV, $I_d = 0.8$ mA, $P = 5 \times 10^{-6}$ Torr

Another explanation of H^- current behavior could be the existence of electrons groups with different higher energy. To test this assumption, the electromagnetic filter was replaced with an electrostatic energy analyzer, which was used to measure the electron energy that outgoes in longitudinal direction (Figure 5).

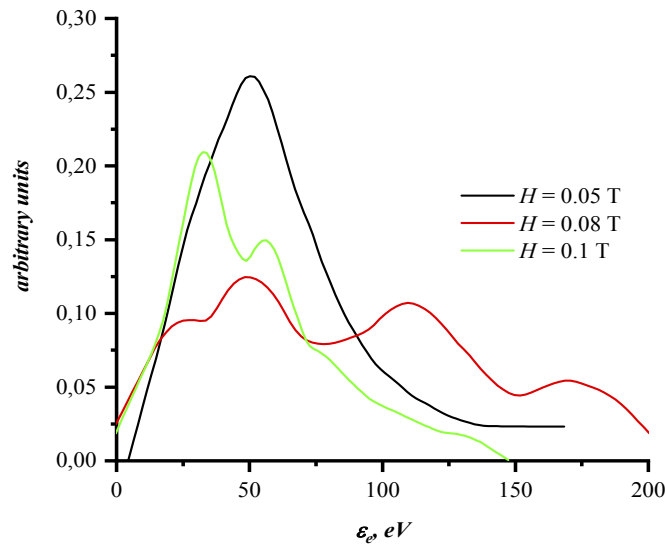


Figure 5. Electron energy at $U_a = 5$ kV, $I_d = 0.8$ mA, $U_{MH} = -20$ V, $P = 5 \times 10^{-6}$ Torr

As seen from Figure 5 the groups of high-energy particles appear in the spectrum of registered electron current at high magnetic field and distribution function strongly distorted by the “non-Maxwellian” tail of high-energy electrons with energies more than 100 eV. But the studies carried out in [16] pointed out, that in the central region of the discharge it close to the Maxwellian one, what determines the applicability of Langmuir probe set on the axis of the cell.

The highest value of electron energy there is much bigger, than the electric bias of metal hydride cathode, which could explain the increase of H^- current at high bias potential (Figure 2).

If we assume that decline in the H^- current is explained by electrons depletion by the metal hydride cathode because of the physics behind the Boltzmann distribution, then the factor e/T_e will be responsible for the inflection point of the H^- current. The higher values of T_e , the closer the inflection point to the cathode surface and higher values of $|U_{MH}|$ needed. This dependence was calculated in [14] and presented in Figure 6 (solid line).

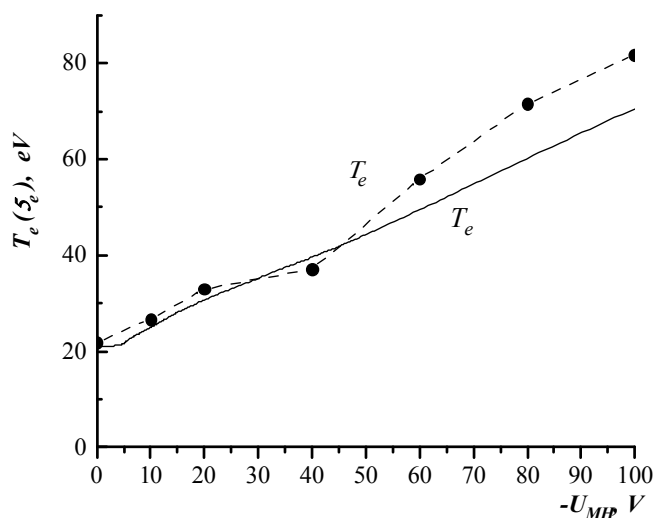


Figure 6. The dependence of needed metal-hydride electric bias on plasma electrons temperature (calculated) and electron energy (measured) at $U_a = 5$ kV, $I_d = 0.8$ mA, $H = 0.1$ T, $P = 5 \times 10^{-6}$ Torr

The electron energy ϵ_e is measured by energy analyzer. The presented data (dash line) correspond to the dynamic of the first maximum in distribution function, which is agreed with previously calculated values for T_e . It is, obviously, the group of electrons which are oscillated along the axis of Penning cell. The groups of electrons with higher energies appear due to heating on the instability of the anode layer. The characteristic dependence of the oscillation frequency on the magnetic field indicates on a diocotron type instability (Figure 7).

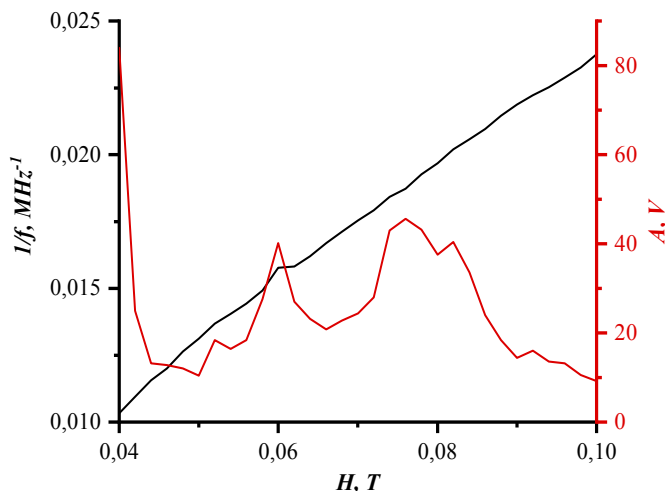


Figure 7. The dependence of frequency and arbitrary amplitude of oscillation in anode layer on magnetic field at $U_a = 5$ kV, $I_d = 0.8$ mA, $P = 5 \times 10^{-6}$ Torr

So, the presence of additional groups of electrons with energies significantly exceeding T_e distorts the behavior of H^- current in Figure 2 in comparison with the results obtained in [13]. Considering that the arbitrary amplitude of oscillation in anode layer is irregular, the behavior of H^- ion current in Figure 2 is irregular as well. The only clear fact here is that at low magnetic field the distortion of distribution function takes minimal value and weekly impact on H^- ion current behavior at negative electric bias of metal hydride cathode.

CONCLUSION

Thus, the application of metal hydride cathode in the Penning type ion source allows for producing axial H^- ion flow along the external magnetic field. The production of negative ions takes place in the near-cathode region caused by the dissociative attachment of thermal electrons to vibrationally / rotationally excited hydrogen, desorbed from metal hydride. The large mean free path of the H^- ions ensures their unimpeded yield together with an axial flow of charged particles. The configuration of the discharge electrodes, electromagnetic filter and electrical field of the discharge ensures the registration of only the paraxial group of particles. For increasing the H^- current a negative potential on metal hydride cathode should be supplied. The plasma density by metal hydride cathode surely grows since the bias

potential increase and T_e drops. The smaller T_e , the far electron reflects from the metal hydride cathode which is under negative bias potential. At low magnetic field, when the inflection of H^- current is observed under the bias potential of -40 V, the electron temperature takes smaller value (~ 15 eV), and electrons could be easily reflected reducing the value of H^- current. If T_e takes larger values, there is no H^- current inflection, or it is not so pronounced. The existence of electron groups with higher energies heated on anode layer instability sufficiently impacts the H^- current behavior and explains discrepancy between experiments and calculation results. The optimum bias potential for the effective extraction of H^- ions is -20V and higher, when plasma density reaches the maximum value to $2 \times 10^9 \text{ cm}^{-3}$.

ACKNOWLEDGMENTS

This research was partially supported by the National Research Foundation of Ukraine (Grant No. 2020.02/0234).

ORCID ODs

 Ihor Sereda, <https://orcid.org/0000-0002-9111-9853>;  Yaroslav Hrechko, <https://orcid.org/0000-0001-9198-3660>
 Ievgeniia Babenko, <https://orcid.org/0000-0001-9339-3365>

REFERENCES

- [1] K.W. Ehlers, B.F. Gavin, and E.L. Hubbard, Nucl. Instrum. Methods, **22**, 87 (1963). [https://doi.org/10.1016/0029-554X\(63\)90232-5](https://doi.org/10.1016/0029-554X(63)90232-5)
- [2] K. Jimbo, K. Ehlers, K. Leung, and R. Pyle, Nucl. Inst. Methods, **248**(2-3), 282 (1986). [https://doi.org/10.1016/0168-9002\(86\)91009-0](https://doi.org/10.1016/0168-9002(86)91009-0)
- [3] G.I. Dimov, Review of Scientific Instruments, **67**, 3393 (1996). <https://doi.org/10.1063/1.1147513>
- [4] G.I. Dimov, G.V. Roslyakov, Pribory i Tekhnika Eksperimenta, **1**, 29 (1967), <https://inis.iaea.org/search/searchsinglelrecord.aspx?recordsFor=SingleRecord&RN=5144624> (in Russian)
- [5] M. Bacal, R. McAdams, and B. Lepetit, in: *Second International Symposium on Negative Ions, Beams and Sources, AIP Conf. Proc.*, (vol. 1390, 2011), pp.13.
- [6] T. Inoue, Y. Matsuda, Y. Ohara, Y. Okumura, M. Bacal, and P. Berlemont, Plasma Sources Sci. Technol. **1**, 75 (1992). <https://doi.org/10.1088/0963-0252/1/2/001>
- [7] M.V. Lototsky, V.A. Yartys, Ye.V. Klochko, V.N. Borisko, R.I. Starovoitov, V.M. Azhazha, P.N. V'yugov, J. Alloys Compounds, **404-406**, 724 (2005). <https://doi.org/10.1016/j.jallcom.2005.02.086>
- [8] Yu.F. Shmal'ko, Ye.V. Klochko, and N.V. Lototsky, Int. J. Hydrogen energy, **21**(11-12), 1057 (1996), [https://doi.org/10.1016/S0360-3199\(96\)00040-7](https://doi.org/10.1016/S0360-3199(96)00040-7)
- [9] I. Sereda, A. Tseluyko, and N. Azarenkov, in: *Hydrides: Types, Bonds and Applications*, edited by Patrick C. Dam. (New York: Nova Science Publishers Inc, 2018), pp. 149-192.
- [10] M. Bacal, and M. Wada, Applied Physics Reviews, **2**, 021305 (2015). <https://doi.org/10.1063/1.4921298>
- [11] Ie.V. Borgun, D.L. Ryabchikov, I.N. Sereda, and A.F. Tseluyko, J. Phys. Conf. Ser. **514**, 012051 (2014), <https://doi.org/10.1088/1742-6596/514/1/012051>
- [12] I. Sereda, A. Tseluyko, N. Azarenkov, D. Ryabchikov, and Ya. Hrechko, International Journal of Hydrogen Energy, **42**(34), 21866-21870 (2017). <https://doi.org/10.1016/j.ijhydene.2017.07.129>
- [13] I. Sereda, A. Tseluyko, D. Ryabchikov, Ya. Hrechko, and N. Azarenkov, Vacuum. **162**, 163 (2019), <https://doi.org/10.1016/j.vacuum.2019.01.046>
- [14] I. Sereda, D. Ryabchikov, Ya. Hrechko, Ie. Babenko, Problems of atomic science and technology. Series: Plasma Physics, **6**(26), 107 (2020), https://vant.kipt.kharkov.ua/ARTICLE/VANT_2020_6/article_2020_6_107.pdf
- [15] J.R. Sanmartin, Phys. Fluids, **13**(1), 103 (1970), <https://doi.org/10.1063/1.1692776>
- [16] A.A. Petrushenya, Ph.D. dissertation, V.N. Karazin Kharkiv National University, 2005.

ПАРАМЕТРИ ПЛАЗМИ РОЗРЯДУ ПЕННІНГА З НЕГАТИВНО-ЗМІЩЕННИМ МЕТАЛОГІДРИДНИМ КАТОДОМ ПРИ ПОЗДОВЖНІЙ ЕМІСІЇ ІОНІВ H^-

I. Середя, Я. Гречко, Є. Бабенко

Харківський національний університет імені В.Н. Каразіна, Харків, Україна

Підвищення ефективності формування негативних іонів в об'ємному джерелі іонів на основі Пеннінговського джерела може бути здійснено за допомогою застосування металогідридного катода. Ізотопи водню зберігаються там у хімічно зв'язаному атомарному стані та десорбуються з металогідриду під впливом струму розряду. Коливально / оберально збуджені молекули H_2^* утворюються шляхом рекомбінації H -атомів на металевій поверхні, які потім можуть бути легко перетворені в іони H^- шляхом дисоціативного прилипання електронів без попереднього збудження молекули H_2 у плазмі. Зміна властивостей розряду відкриває шлях для спрощення конструкції джерела шляхом екстракції негативних іонів вздовж зовнішнього магнітного поля в порівнянні з традиційними об'ємними джерелами, де екстракція здійснюється перпендикулярно магнітному полю. Відокремлення негативних іонів від витягнутого в поздовжньому напрямку потоку заряджених частинок здійснювалося електромагнітним фільтром базуючись на чисельних розрахунках траєкторій заряджених частинок. Залежність температури електронів та щільності плазми від потенціалу зміщення проводилося методом зонда Ленгмюра. Вимірювання енергії електронів проводилося електростатичним аналізатором енергії. Було показано, що вихід іонів H^- залежить від потенціалу зміщення на металогідридному катоді і визначається температурою електронів плазми. Оцінка потенціалу зміщення від T_e проводилася за припущення розподілу електронів по Больцману поблизу катода. Наявність додаткових груп електронів з вищими енергіями спотворює поведінку струму H^- , але загалом результати експерименту добре узгоджуються з оцінкою, заснованою на фізиці, що лежить в основі розподілу Больцмана. Було виявлено оптимальне значення потенціалу зміщення металогідридного катода для ефективного вилучення іонів H^- на рівні -20 В та вище, коли щільність плазми досягає максимального значення до $2 \times 10^9 \text{ cm}^{-3}$.

Ключові слова: негативні іони, водень, джерело іонів типу Пеннінга, металогідрид

RESEARCH OF THE MECHANICAL PROPERTIES OF FUEL ELEMENT SHELLS MADE OF Zr1% Nb ALLOYS AT RADIAL STRESSES SIMILAR TO REACTOR CONDITIONS[†]

V.I. Savchenko^a, N.N. Belash^a, Y.A. Krainyuk^{a,*}, V.N. Voyevodin^{a,b}

^aNational Science Center Kharkov Institute of Physics and Technology (NSC KIPT), Kharkov, Ukraine

^bV.N.Karazin Kharkov National University, Kharkov, Ukraine

*Corresponding Author: krainyuk@kipt.kharkov.ua

Received June 16, 2021; revised June 30, 2021; accepted August 26, 2021

When determining the mechanical properties of ring specimens, a feature of a uniaxial (standard) loading scheme is that the method of applying a load to a specimen is somewhat remote from that to which the pipe walls can be subject in real operating conditions, in particular, these are tubes of fuel element shells. As an alternative loading method, the method of strain of a ring specimen on a cylindrical rod was considered and tested. By compressing the cylindrical rod from the ends, which in this case expanded and exerted pressure on the inner walls of the ring specimen in the radial direction, the specimen was deformed. The plasticity of fuel element shells made of Zr-1%Nb alloy on ring specimens under different loading methods is evaluated: uniaxial tension on half-disk supports, on a cylindrical rod, and on a tapered rod. Uniaxial tensile strain was determined in accordance with the normative documentation for the test method. When testing on a tapered rod, a specimen with a thinned working part was used. For the proposed loading method, the radial strain was measured by the change in the sample diameter. The results of testing the samples on a cylindrical rod were compared with the previously obtained results on half-disk supports and a tapered rod. The method of deformation of a ring specimen on a cylindrical rod makes it possible to obtain higher values of plasticity in comparison with uniaxial tension. In addition, the proposed method of deformation of a sample on a cylindrical rod, in contrast to uniaxial tension, in terms of the nature of the stress state, approaches to the operating reactor conditions.

Keywords: mechanical properties, ring sample, fuel element shell (TVEL), radial stress.

PACS: 62.20.-x

Investigations of the mechanical properties of pipes of small diameters, in particular, fuel element shells, both with and without coating, have been devoted to a lot of works [1-7]. Until now, there is extensive information on the mechanical properties of fuel element shells in the longitudinal and transverse directions at 20 °C and at elevated temperatures of ~700 °C. However, most of the works relate to tests in the uniaxial direction of tension, like on the fragments of tubes from the fuel element shells, and on ring samples in accordance with the normative documentation [8-10]. This method of tensile strain does not fully reflect the loading conditions of the walls of the fuel element shells during the operation of reactor facilities and does not give a complete picture of the properties of the material.

At NSC KIPT, steps were also taken [4] to assess the plastic characteristics of the material by a method different from the standard uniaxial testing of ring specimens on half-disk supports, in which the tensile strain of the ring to the yield strength point is often not taken into account, which is not unimportant for comparison with reactor conditions. Since when the ring is stretched in the deformation area to the yield strength point, conditions are created for the development of microdefects, which can contribute to a decrease in plasticity. This is manifested, for example, when testing ring samples with a nanostructured chrome coating with a thickness of 5-8 microns. In this case, if the coating was applied before deformation by ring tension, this leads to a noticeable decrease in the relative elongation $\delta\%$ [2, 3]. In [4], tests were carried out by distributing ring specimens on a tapered rod [11]. During these tests, significant differences in mechanical properties were noted, especially in the increase in ductility at elevated temperatures up to 350 °C. However, this method also has some nuances associated with the conditions of loading and deformation of the sample.

Taking into account the applied test methods of branch pipes and ring specimens made of fuel element shells, and noting the shortcomings of the methods about non-compliance with reactor conditions. In this work, a method of deformation of ring specimens in the radial direction is proposed. This method consists in expanding the annular specimen by compression of a metal cylindrical core, which brings this method of deformation and stress state closer to real conditions in which fuel element shells is operating.

SAMPLES AND TEST PROCEDURE

The circumference of the ring specimen $C = \pi D$, where D is the outer diameter of the ring. For the fuel tube in the initial state, $D_0 = 9.15$ mm, $C_0 = 28.73$ mm. At the yield strength point of the fuel element shell (a ring made of Zr1%Nb alloy)

$$\delta\% = ((C_1 - C_0)/C_0) \times 100 = 0,2\%$$

[†] Cite as: V.I. Savchenko, N.N. Belash, Y.A. Krainyuk, V.N. Voyevodin, East. Eur. J. Phys. 3, 87 (2021), <https://doi.org/10.26565/2312-4334-2021-3-13>

© V.I. Savchenko, N.N. Belash, Y.A. Krainyuk, V.N. Voyevodin, 2021

where C_1 is the circumference at the yield strength point.

From here it is possible to calculate the increment in the value of the absolute deformation at the yield strength point on the surface of the annular specimen during radial expansion, which is equal to $\Delta C_1 \approx 0.04$ mm. The amount of deformation is recording using a contact extensometer (Fig. 1).

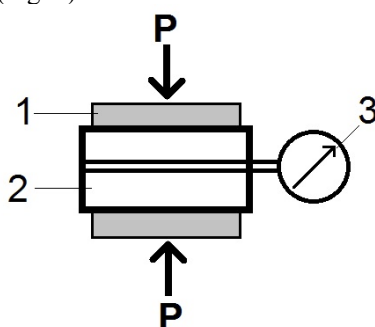


Figure 1. Test scheme

P - load (in compression), 1 - a rod made of ductile metal (alloy), 2-ring specimen of fuel element shell, 3-pin extensometer

It should be note that research of the mechanical characteristics of ring specimens made from fuel element shells can be performe on any mechanical testing facility, and testing on an Instron-5581 facility makes it possible to expand and simplify research.

One should take into account the limited possibility of deformation of a ring specimen on a compressive cylindrical rod (made of copper), which may not achieve destruction due to the significant plasticity of the Zr1%Nb alloy. Therefore, to compare the ductility of ring specimens made of Zr1%Nb alloy during standard uniaxial tests on half-disk supports and in deformation of rings on a compressing cylindrical rod (rod cooper), the achieved ductility of the specimen at the maximum level of core compression can be used. If the destruction of the ring specimen is not achieved, the obtained value of $\delta\%$ will be conditional.

The proposed deformation method makes it possible to test ring specimens of fuel element shells in the radial direction, which brings the stress state of the specimen walls closer to the conditions that arise during the operation of fuel element shells.

EXPERIMENTAL PART

When studying the strength and plastic characteristics of ring specimens from various materials using the device in Fig. 1 for loading, it is necessary to take into account some of the features that exist for brittle and ductile materials. The main difference is that brittle materials reach destruction and the characteristics of strength and ductility have finite values, for example, samples from chromium alloys. For plastic materials, which include the Zr1% Nb alloy and its δ (%) uniaxial tensile strain at normal temperature is $\delta \approx 27\%$, the samples may not reach destruction (when loaded according to the scheme in Fig. 1), therefore, determine the final values of δ (%) does not seem possible.

In this case, it is advisable to consider the values of δ (%) in stages, for example: at the first stage - deformation to the conditional yield strength $\sigma_{0.2}$ (the most significant in the deformation of the fuel element shell under reactor conditions), and then at the second stage - above the value of the conditional yield strength $\sigma_{0.2}$. In this case, the values $\sigma_{0.2}$ and δ (%), with uniform deformation, and other values obtained on this alloy under uniaxial tensile strain of ring specimens (on 2 half-disk supports) can be used. In such comparisons, some "conventional" values of δ (%) can be obtained at various points on the stress-strain diagram.

As an example, we can consider the tests carried out on an ring specimen made of Zr1%Nb alloy with a diameter of $D = 7.70$ mm and a height of $h = 4.0$ mm, into which a cylindrical rod (made of copper) with parameters $D = 7.65$ mm and $h = 12.37$ mm. Compressive strain of the rod was carried out on an Instron-5581 setup at normal temperature at a rate of 0.1 mm / min.

At the first stage, with a load $P_1 = 1335$ kg, the outer diameter of the ring specimen was $D_1 = 9.16$ mm and $\Delta D_1 = 0.06$ mm. At the second stage of deformation with a load $P_2 = 2100$ kg $D_2 = 9.77$ mm, and $\Delta D_2 = 0.62$ mm, which corresponds to $\delta_2 = 24.2\%$.

When comparing $\delta_2 = 24.2\%$ of the deformation δ obtained at the 2nd stage with the value of δ_{\max} (%) for ring specimens tested according to the standard method uniaxial tensile strain, which reached $\delta_{\max} \approx 24\%$ at destruction, it can be seen that with radial deformation using the loading scheme in Fig. 1, the plasticity is much higher, since the value $\delta_2 = 24.2\%$ already exceeds $\delta_{\max} \approx 24\%$ for uniaxial tension. With further deformation of the ring on the rod, δ_2 (%) will increase significantly. It should be note that under the applied loads, the specimen was not brought to destruction.

Figure 2 shows the dependence of the plasticity δ_2 (%) of the Zr1%Nb alloy on the loading method. With uniaxial tensile strain of the ring specimen on half-disk supports until destruction - item No.1 in Figure. 2.

Under radial tension of specimens on a cylindrical rod (made of copper) during its compression, the load P reached 1335 ... 2100 kg (without destruction of the specimen, since with this method of loading the plastic alloy cannot reach

destruction, and in this case δ_2 (%) is a conventional value - item No.2 in Figure 2). Ring specimens (item No.3 in Figure 2) refer to the method of expansion in the radial direction on a tamper rod [4] until destruction, while $\delta_2 = 40\%$.

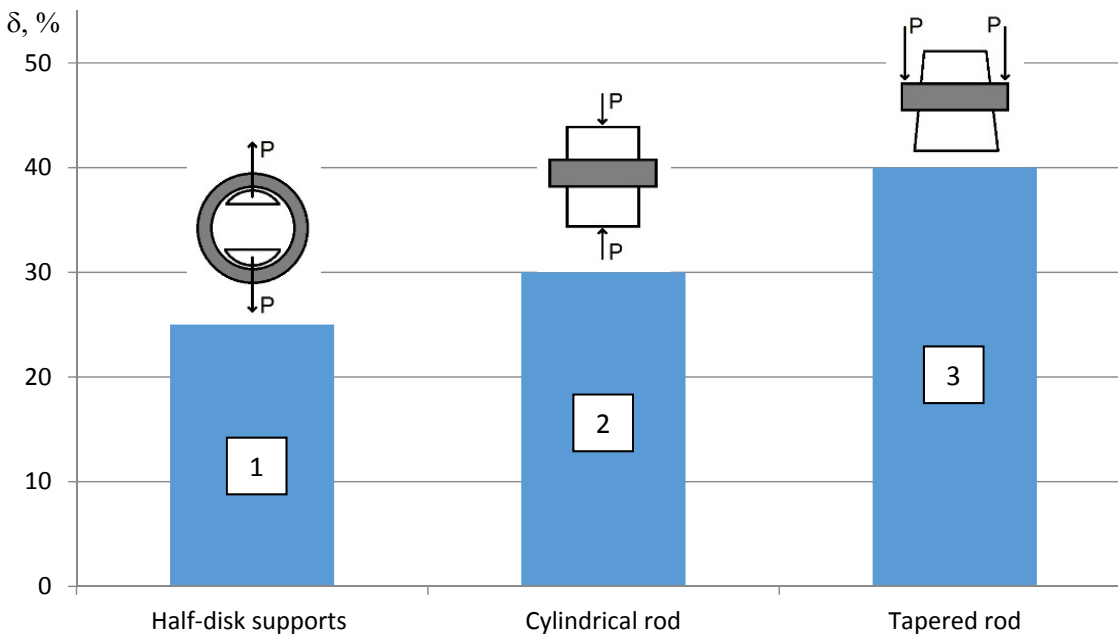


Figure 2. The dependence of plasticity δ_2 (%) of the Zr1%Nb alloy on the loading method.

From the presented results, it can be seen that under uniaxial tensile strain of ring specimens on half-disk supports, the maximum plasticity is the lowest in destruction (item No.1 in Figure 2). In the second case (item No.2 in Figure 2), the plasticity increases and even in the stress range $\approx \sigma_{0.2}$ it already exceeds δ_2 (%) in comparison with uniaxial tension. With the loading method (item No.3 in Figure 2) on a tamper rod, δ_2 (%) of the ring specimen at destruction is maximum in comparison with the plasticity for the first two cases (item No.1, No.2 in Figure 2). The stress in the ring specimen in the radial direction is determined by the formula

$$\sigma = \frac{E_t}{1-\nu^2} \left(\frac{1}{a_0} - \frac{1}{a_1} \right),$$

where σ is tensile stress, E_t is Young's modulus, ν is Poisson's ratio, d_0 , d_1 are the initial and final diameters of the specimen [4].

In the study of radial deformation in the range below the yield strength point, it is possible to compare δ (%), $\sigma_{0.2}$ and σ_B when removing a ring specimen from a cylindrical rod (copper), and performing a test. This makes it possible to compare the effect of uniaxial and radial loading on the strength uniaxial tensile strain and plastic properties of ring specimens. Thus, when using and comparing stress-strain diagrams by new and other methods, the plastic and strength characteristics that are closest to the reactor conditions can be obtained.

DISCUSSION

It is necessary to note the influence of the stress state scheme on the results of mechanical tests, which is especially significant in the region of elastic and uniform deformations occurring under reactor conditions in the fuel element shells made of Zr1% Nb alloy.

To assess the "softness" of the stress state circuit, the "softness" coefficient is used - (coefficient according to Ya. B. Fridman): $\alpha = t_{\max} / S_{\max}^n$, where t_{\max} is the maximum shear stress, S_{\max}^n is the maximum reduced principal normal stress. Hence it follows that the more t_{\max} and less S_{\max}^n (i.e., more α), the better the conditions for the development of plastic deformation. In practice, for example, in experiments with taper loading [4] or when loading in the radial direction in the fuel element shell, a noticeable increase in plasticity occurs in comparison with uniaxial loading, when the coefficient = 0.5, which is a significantly low indicator.

Thus, when using and comparing stress-strain diagrams during deformation of a ring on a rod with other methods, plastic and strength characteristics can be obtained that are closest to reactor conditions.

CONCLUSIONS

In order to assess the plasticity of the metal of thin-walled pipes of small diameters, in particular, of the fuel element shells, an alternative to the standard method of deformation of the ring specimen was used. By compressing the cylindrical



rod from the ends, which expanded and exerted pressure on the inner walls of the ring specimen in the radial direction, the specimen was deformed.

The results of the plasticity characteristics of ring specimens of fuel element shells under different methods of deformation are compared.

It is shown that under deformation of a ring specimen on a cylindrical rod, the value of plasticity is characterized by a large value, in contrast to the standard, uniaxial test method.

In the process of deformation of ring specimen on a cylindrical rod, the nature of the stress state of the specimen walls is close to the state that arises during operation of a fuel element shells under reactor conditions.

ORCID IDs

 Yevgeniy A. Krainyuk, <https://orcid.org/0000-0002-2185-1838>;  Viktor N. Vovodin, <https://orcid.org/0000-0003-2290-5313>

REFERENCES

- [1] A. Yarlick, Journal Nuclear Materials, **49**, 209 (1974). [https://doi.org/10.1016/0022-3115\(73\)90009-3](https://doi.org/10.1016/0022-3115(73)90009-3)
- [2] P.I. Stoev, V.A. Belous, V.N. Vovodin, A.S. Kuprin, S.A. Leonov, V.D. Ovcharenko, M.A. Tikhonovsky, and V.M. Horoshih, PAST, **5(99)** 87 (2015). https://vant.kipt.kharkov.ua/ARTICLE/VANT_2015_5/article_2015_5_87.pdf
- [3] V.A. Belous, V.N. Vovodin, S.V. Gozhenko, Y.A. Krainyuk, A.S. Kuprin, V.D. Ovcharenko, V.I. Savchenko, and S.V. Shramchenko, PAST, **5(123)**, 142 (2019). https://vant.kipt.kharkov.ua/ARTICLE/VANT_2019_5/article_2019_5_142.pdf
- [4] L.S. Ozhigov, A.S. Mitrofanov, V.I. Savchenko, Y.A. Krainyuk and ect. Industrial laboratory. Diagnostics of materials, **80(3)**, 60 (2014).
- [5] A.K. Andreyev, O.Y. Grydin, D.V. Shyshatskiy, M.Y. Panyushkin, M. Shaper, and Ya.V. Frolov, Materials working by pressure, Collection of science papers, **2(43)**, 77 (2016), [http://www.dgma.donetsk.ua/science_public/omd/omd_2\(43\)_2016/article/15.pdf](http://www.dgma.donetsk.ua/science_public/omd/omd_2(43)_2016/article/15.pdf)
- [6] S.V. Barsanova, A.V. Kozlov, M.V. Yevseyev, and V.I. Pastukhov, Сб. тезисов докладов научно-технической конференции «Институту реакторных материалов 50 лет» [Collection of abstracts of the scientific and technical conference "Institute of Reactor Materials 50 years"], 2016, pp. 84. (in Russia), <http://www.benran.ru/exh/ris1.aspx?par=216360&par1=600&par2=5&par3=6>
- [7] S.V. Barsanova, O.B. Shylo, M.V. Yevseyev, and A.V. Kozlov, PAST «Materials technology and new materials» series, **5(96)**, 88 (2018). http://bochvar.ru/download_files/Рефераты5-96.pdf
- [8] Метод испытання растяжением кольцевых образцов в условиях нагрева. ДСТУ 2528-94 [Tensile test method of annular specimens under heating conditions. DSTU 2528-94] (Kyiv, State Standard of Ukraine, 1995), pp. 10.
- [9] ОИ 001.325-2006. Методика выполнения испытаний для определения механических свойств при растяжении образцов труб в поперечном направлении из сплавов циркония [OI 001.325-2006. Test procedure for determining the characteristics of the mechanical properties under tension of pipe specimens in the transverse direction from zirconium alloys], (АО «ВНИИМ», Moscow, 2006), pp. 30.
- [10] Національний стандарт України. Металеві матеріали. Труби. ДСТУ ISO 8496-2002 (ISO 8496:1998, IDT), [National standard of Ukraine. Metal materials. Pipes. DSTU ISO 8496-2002 (ISO 8496:1998, IDT)], (State Standard of Ukraine, Kyiv, 2003), pp. 7, http://online.budstandart.com/ua/catalog/doc-page?id_doc=67275. (in Ukrainian)
- [11] Металеві матеріали. Труби. Випробування на роздання кільця. ДСТУ ISO 8495:2004 (ISO 8495:1998, IDT), [Державний стандарт України [Metallic materials. Pipes. Ring distribution test. DSTU ISO 8495: 2004 (ISO 8495: 1998, IDT), State Standard of Ukraine], (State Standard of Ukraine, Kyiv, 2003), http://online.budstandart.com/ua/catalog/doc-page.html?id_doc=67596. (in Ukrainian)

ДОСЛІДЖЕННЯ МЕХАНІЧНИХ ВЛАСТИВОСТЕЙ ОБОЛОНОК ТВЕЛ З Zr1%Nb СПЛАВІВ ПРИ РАДІАЛЬНИХ НАПРУЖЕННЯХ, АНАЛОГІЧНИХ РЕАКТОРНИМ УМОВАМ

Савченко В.І.^а, Белаш М.М.^а, Крайнюк Є.О.^а, Воводін В.М.^{а,б}

^аНаціональний науковий центр «Харківський фізико-технічний інститут» (ННЦ ХФТІ), Харків, Україна

^бХарківський національний університет ім. В.Н. Каразіна, Харків, Україна

При визначенні механічних властивостей кільцевих зразків особливість одноосної (стандартної) схеми навантаження полягає в тому, що спосіб прикладання навантаження до зразком кілька віддалений від того, яким можуть піддаватися стінки труб в реальних умовах експлуатації, зокрема це трубки ТВЕЛ. В якості альтернативного способу навантаження було розглянуто і випробувано спосіб деформації кільцевого зразка на циліндричній стрижні. Шляхом стиснення циліндричного стержня з торців, який при цьому розширювався і тиснув на внутрішні стінки кільцевого зразка в радіальному напрямку, відбувалася деформація зразка. Проведено оцінку пластичності оболонок ТВЕЛ зі сплаву Zr-1%Nb на кільцевих зразках при різних способах навантаження: одноосне розтягнення на напівдисківих опорах, на циліндричній стрижні і на конусній оправі. Деформація при одноосному розтягуванні визначалася відповідно до нормативної документації на метод випробування. При випробуванні на конусі застосовувався зразок з стоншеною робочою частиною. Для запропонованого способу навантаження радіальна деформація вимірювалася зі зміни діаметра зразка. Результати випробувань зразків на циліндричному стрижні були зіставлені з раніше отриманими результатами на напівдисківих опорах і конусній оправі. Спосіб деформації кільцевого зразка на циліндричному стрижні дозволяє отримати великі значення пластичності в порівнянні з одноосовим розтягуванням. Крім того, запропонований спосіб деформації зразка на циліндричній стрижні на відміну від одноосного розтягу за характером напруженого стану наближається до експлуатаційних реакторних умов.

Ключові слова: механічні властивості, кільцевий зразок, оболонка ТВЕЛ, радіальні напруження.

BREMSSTRAHLUNG GENERATION BY 7.5 MEV ELECTRONS IN CONVERTERS MADE OF DIFFERENT MATERIALS[†]

 Vladimir G. Rudychev^{a,*},  Nikolay A. Azarenkov^a,  Igor A. Girka^a,
 Yegor V. Rudychev^{a,b}

^aV.N. Karazin Kharkiv National University, 61022 Kharkov, Ukraine

^bNSC "Kharkov Institute of Physics and Technology"

Akademicheskaya, 1, 61108 Kharkov, Ukraine

*Corresponding Author: vrudychev@karazin.ua

Received July 2, 2021; accepted August 31, 2021

The present paper shows that, besides the technologically complex water-cooled converters made of Ta or W, a simple and efficient converter in the form of air-cooled Mo and Al plates can be fabricated for a number of tasks. The generation of bremsstrahlung by electrons with the energy of 7.5 MeV in the converter plates made of Ta, W, Cu or Mo and in the Al filter was studied by the Monte Carlo method in the PENELOPE software package. The thicknesses range of the plates made of Ta, W, Cu or Mo was chosen on condition that the total mass thickness of the converter and filter made of Al (in g/mm²) provided complete absorption of the primary electrons. It is shown that the photon yields from Mo at mass thicknesses above 25 g/mm² are higher than those from Ta and W, but the energy transferred from electrons to BS is lower. With the same mass thicknesses of Ta and W converters, practically all characteristics of bremsstrahlung and the absorbed energy in the target are the same. The conditions for cooling the converter elements with water and air are determined for the level of heat release in the converter up to 10 kW. The minimum dimensions of the electron-irradiated region of Ta and Mo converters, cooled by water, are determined. It is shown that with the really existing air compressors taken into account, the permissible heat release of air-cooled Mo converters should not exceed 4 kW.

Keywords: radiation technologies, converter, bremsstrahlung, electron beams.

PACS: 29.25.Bx; 61.82.Bg; 41.75.Fr; 47.85.Dh; 47.80.jk

At present, the radiation technologies, intended mainly for sterilization by electron beams, use accelerators with energies $E_e \leq 10$ MeV and power from several kilowatts to tens of kilowatts. The same accelerators can serve as sources of bremsstrahlung (BS), with energy not exceeding $E_e = 7.5$ MeV, i.e. the maximum bremsstrahlung energy allowed for food processing. Generally, refractory materials with a large atomic number, such as Ta and W, are used for the converters [1-3]. For the manufacture of such converters, complex technologies are used: tungsten carbide (WC) is spattered on the aluminum plate, and the tantalum plate is welded to aluminum by explosion welding [2]. In this paper simple design options for bremsstrahlung converters with air and water cooling are considered. The air-cooled converter model comprises a plate, made of Ta, W, Cu or Mo, and an air-spaced aluminum filter. The water-cooled converter is a rectangular tube made of aluminum or steel filled with water, whose front wall is made of Ta, W, Cu or Mo. In addition to the commonly used Ta and W the generation of bremsstrahlung by electrons with the energy of 7.5 MeV in targets made of Cu or Mo was investigated with these designs of the converters taken into account. The calculations of the spectral-angular characteristics of the bremsstrahlung and the energy release of electrons with energy $E_e=7.5$ MeV in the designs of the converters, subject to the target thickness, were performed by the Monte-Carlo method. The conjugate problem of thermodynamics and hydrodynamics (gas dynamics), when the converter elements were cooled with water and air, was solved with the heat release in the converter taken into account.

CALCULATIONS OF THE BREMSSTRAHLUNG BEAM CHARACTERISTICS

In [1-3] the characteristics of bremsstrahlung radiation generated by converters were investigated subject to the thickness of Ta or W. As the characteristics of bremsstrahlung, the yield (number) of photons into the front hemisphere, or the fraction of energy transferred from electrons to bremsstrahlung photons, was used. Virtually, there are no data on the fraction of the absorbed energy of electrons in the material of the converter, as well as on the fraction of the energy carried away by the electrons reflected from the surface of the converter. Note, that at the Ta or W optimal thickness, which provides the maximum bremsstrahlung yield, some of the primary electrons pass through the converter material [2]. These electrons, falling on the surface of the irradiated object, can increase the near-surface dose in addition to the bremsstrahlung photons. The applied designs of converters for cooling, as a rule, use water flowing through pipes made of steel or aluminum, which serve as absorbers (filters) for the electrons that passed through the Ta or W plates.

It was assumed that the electron beam with the energy of 7.5 MeV fell perpendicular to the converter surface, while the transverse dimensions of the converter were larger than the electron beam diameter. To calculate the bremsstrahlung characteristics we used the PENELOPE software package [4,5], which made it possible to calculate the

[†] Cite as: V.G. Rudychev, N.A. Azarenkov, I.A. Girka, Y.V. Rudychev, East. Eur. J. Phys. 3, 91 (2021), <https://doi.org/10.26565/2312-4334-2021-3-14>

© V.G. Rudychev, N.A. Azarenkov, I.A. Girka, Y.V. Rudychev, 2021

transport of electrons, positrons, and photons through layered structures made of different materials. For Ta layers of different thicknesses, the characteristics both of bremsstrahlung and the number of primary transmitted and reflected electrons were calculated. Figure 1 shows the bremsstrahlung yields ($N_{\gamma}^{\text{tot}}/N_e$) both into the front hemisphere and in the range of angles 0-48° (N_{γ}^{48}/N_e), which is actually used, when objects are irradiated. The bremsstrahlung yields and the number of primary transmitted (N_e^{tr}/N_e) and reflected (N_e^{back}/N_e) electrons are normalized to 1 initial electron.

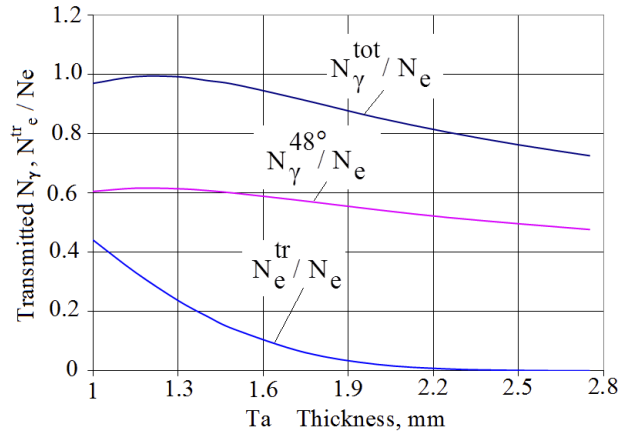


Figure 1. Yields of bremsstrahlung and primary transmitted and reflected electrons.

From the data given in Fig. 1, it follows that at the maximum bremsstrahlung yield with the layer thickness of ~ 1.2 mm, the number of primary electrons, transmitted through Ta, is ~ 30%. To reduce the amount of transmitted primary electrons to ~ 2%, a Ta layer of ~ 2 mm is required. The number of reflected primary electrons does not change in dependence of the thickness of the Ta layer and makes ~ 15%.

In [6] it was shown, that at $E_e = 10$ MeV, starting with a certain thickness of the converters, the bremsstrahlung forward yield is greater for converters with a lower atomic number (Mo or Cu). In this work, the characteristics of bremsstrahlung, produced by converters of Ta, W, Cu or Mo with different thicknesses upon absorption of the electrons transmitted through the material of the converter by Al filters, are studied.

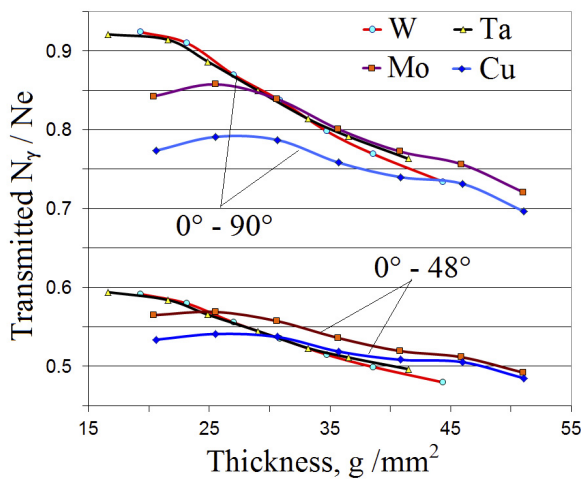


Figure 2. Bremsstrahlung yields versus mass thickness Ta, W, Cu, Mo.

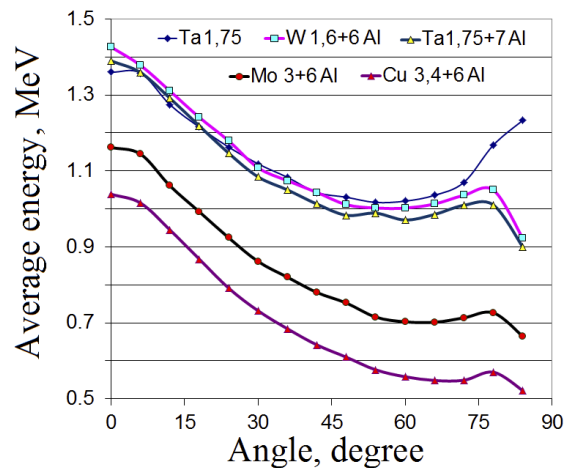


Figure 3. Dependences of the average photon energies on the emission angle for the Ta target and Ta, W, Cu, Mo with the Al filter

The characteristics of bremsstrahlung for the converters made of different materials and thickness of the converters will be compared with the same mass thickness, expressed in g/mm^2 . The thickness of the Al filter is determined on condition that the number of transmitted primary electrons is less than 0.2-0.3%. The optimization of bremsstrahlung calculations showed, that this condition was fulfilled for the total mass thickness of the converter materials (Ta, W) and Al filter of 45-49 g/mm^2 , and for (Cu, Mo) of 46-51 g/mm^2 . Figure 2 shows the bremsstrahlung yields subject to the thickness of the converter made of different materials at the optimal thickness of Al filters. The bremsstrahlung yields for Ta, W are practically the same (atomic numbers 73 and 74, respectively), and a decrease in atomic numbers 42 for Mo and 29 for Cu at small converter thicknesses leads to a decrease in the bremsstrahlung yield for these materials. Note, that the bremsstrahlung yields for Mo in the range of 0-48° at thicknesses > 25 g/mm^2 are greater than those for Ta, W. The PENELOPE package allows calculating the spectral - angular characteristics of bremsstrahlung. One of the

main characteristics of bremsstrahlung is the average photon energy. Figure 3 shows the dependences of the average photon energies on the emission angle for the Ta target and converters made of Ta, W, Cu, Mo with the Al filter. The average photon energies for the converters made of elements with a large atomic number such as Ta, W are significantly higher than those for Cu and Mo. Figure 4 shows fractions of the energy from the initial $E_e = 7.5$ MeV, converted into bremsstrahlung energy (E_γ), and that of the energy, carried away by reflected electrons (E_e^{back}), subject to the thickness of the converter made of different materials.

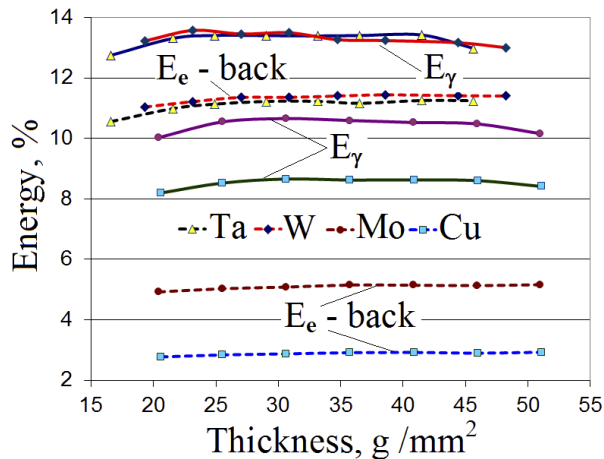


Figure 4. Fractions of bremsstrahlung energy (E_γ) and of the energy, carried bremsstrahlung away by reflected electrons (E_e^{back}), subject to the converter thickness.

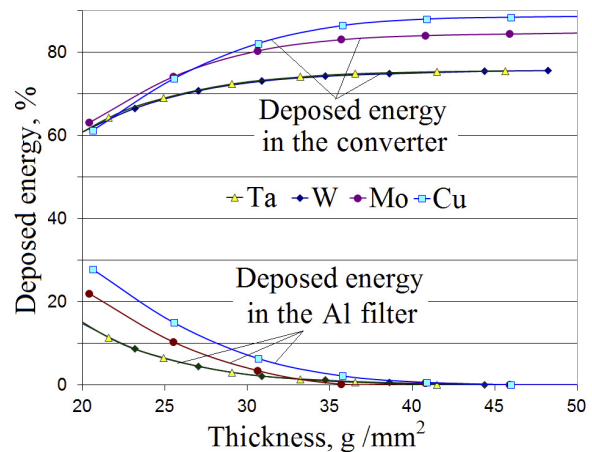


Figure 5. Fractions of the absorbed energy in the converter made of different materials, subject to its thickness, and in the Al filter.

The fractions of bremsstrahlung energy for Ta, W are practically the same, and the energies of the reflected electrons are also the same. Despite the fact that the bremsstrahlung yields (N_γ/N_e) for Mo (see Fig. 2) are the same or even higher than those for Ta and W, the fraction of the initial electrons energy, converted to bremsstrahlung, is lower. This is due to the fact that the average energies of the bremsstrahlung formed on Cu, Mo materials are lower than those on Ta, W, (Fig. 3). Figure 5 shows the fraction of the absorbed energy in the converter, made of different materials, subject to its thickness and in the Al filter. The total mass thickness of the converter materials (Ta, W) and of the Al filter is 45-49 g/mm^2 , and for the converter made of Cu or Mo it is 46-51 g/mm^2 . The absorbed energies determine the thermal loads on the converter material and on the converter design that ensures its cooling.

CALCULATION OF THERMAL MODES OF THE CONVERTERS WITH WATER AND AIR COOLING

In this section, simple designs of bremsstrahlung converters with different types of cooling are investigated, and the main parameters such as dimensions of the converter target and the material, as well as permissible thermal loads (electron beam power) are determined.

The calculation of thermohydraulic parameters and cooling conditions for the converters is carried out by solving the conjugate problem of thermodynamics and hydrodynamics. In 3D geometry, the most precise solution can be obtained by using Computational fluid dynamics (CFD) and finite volume technique. Simulation was carried out using the SolidWorks Flow Simulation software package [7, 8]. SolidWorks is a versatile tool for analyzing fluid dynamics and heat transfer processes. We use volumetric anisotropic heat sources. In the SolidWorks Flow Simulation software package, the heat transfer is simulated using the Navier-Stokes equations, which describe the laws of conservation of mass, momentum and energy in a non-stationary setting. In addition, the equation of state of the flowing medium components, as well as the empirical dependences of the viscosity and thermal conductivity of these components of the medium on the temperature, are used. The transition between laminar and turbulent flows is determined by the critical value of the Reynolds number. Since the used differential and integral equations do not have an analytical solution, they are reduced to a discrete form and solved on a certain computational grid (discretization in space or in time is possible). After generating the computational domain and grids, volumetric heat sources are determined for computation. To take into account the anisotropy of heat distribution in the converter, its area was uniformly divided into cells. For each of these cells, the corresponding heat source was determined [9], which was averaged over the cell volume, taking into account the results of the energy release calculation by the Monte Carlo method.

To determine the acceptable operating characteristics of the converters, we carried out studies of both standard water cooling and air cooling. In the case of water cooling, a three-dimensional solid model of the converter structure was built in the SolidWorks system. The model consists of a rectangular aluminum tube, inside of which water flows and a target, made of tantalum or other metal, is built into one of its walls. Within the framework of the model, we can vary the length and width of the converter, the volumetric flow rate of water, as well as the material of the converter and

the volumetric heat release in it. For this model, thermohydraulic calculations of the tantalum converter cooling were carried out in the SolidWorks Flow Simulation package.

Fig. 1A shows an option of the water cooled converter design with the flow rate of 0.5 liters per second, the dimensions of the irradiated volume of tantalum ($L = 500$) \times 20 \times 1.6 mm, and the power released in this volume is 10 kW. The figure also presents the temperature distribution both in tantalum and in the outflowing water. It is shown, that at the water flow rate of 0.5 l/s the maximum temperature on the tantalum outer surface does not exceed 123°C. The water temperature in the cooling channel does not exceed 35°C. The possibility of reducing the length of the converter L, while maintaining the power allocated in this volume of 10 kW, was investigated. Fig. 6B and Fig. 6C present the results of heat release calculations for converters made of Ta ($L=200$) \times 20 \times 1.6 mm, and ($L=50$) \times 20 \times 1.6 mm, respectively. From Fig. 6C it follows, that with the converter length of 5 cm, the maximum temperature of the converter outer surface is about 857°C.

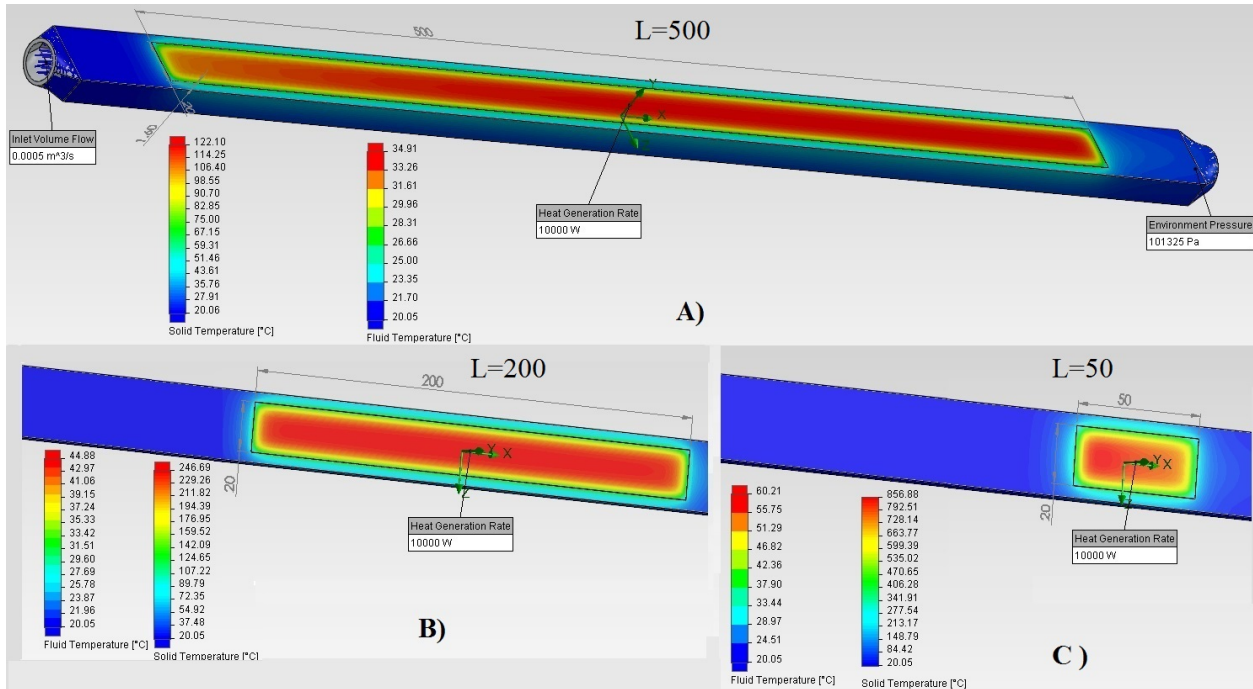


Figure 6. Options of the water cooled converter design with the flow rate of 0.5 l/s with the dimensions of the irradiated tantalum ($L=500, 200, 50$) \times 20 \times 1.6 mm

And although the maximum water temperature in the cooling channel is slightly lower than 60°C, a further reduction in the converter size in this case is not advisable, since the surface temperature at the interface between the converter and the aluminum system is about 500°C, and further decrease in the converter length can lead to the pipe melting (melting point of Al is \sim 660°C). However, this problem can be easily solved by changing the material of the cooling pipe, for example by steel. The calculations have shown, that in this case the temperature at the converter-cooling pipe interface is also about 500°C, what will not cause melting (steel melting temperature is \sim 1400°C). Structurally, it is possible to reduce the length of the converter to $L = 30$, then the temperature at the interface will be \sim 650°C.

We carried out similar calculations for the converters made of molybdenum and copper. As long as the densities of molybdenum and copper are lower than those of tantalum, the effective thicknesses for these materials will be greater. For the molybdenum converter dimensions ($L=500$) \times 20 \times 3.0 mm the results of simulation, carried out under the same conditions of cooling and heat load, showed that the maximum temperature of molybdenum does not exceed \sim 740°C, and at the boundary with the aluminum (steel) pipe it is \sim 500°C. Note, that the water flow in the channel is laminar, what provides good conditions for cooling the converter. Since the thermal conductivity of air within the temperature range of hundreds of degrees C° is an order of magnitude less than that of water, it is obvious that the air cooling is much less effective. We have chosen the most simplified model of the air cooling system, which is a box in the form of a parallelepiped with an air cooling channel inside which there is a converter ($L=500$) \times 100 \times 3.0 mm. For a heterogeneous distribution of the absorbed energy caused by irradiation, this converter is divided along its length into 50 zones, in each of which it is possible to vary the heat source. To determine the efficiency of the air channel at small thicknesses, the converter is displaced by 10 mm from the center of the box, thus the distance from one wall to the converter is 10 mm and from the other wall it is 17 mm. The general view of the converter model and the directions of air and electron flows are shown in Fig. 7.

For the molybdenum converter, the boundary conditions are determined for the air flow at the power yield of 10 kW. It is shown that for stable cooling of this converter design, it is necessary to provide a volumetric air flow rate of at least 9 m³/min. Figure 8 shows the temperature distribution in molybdenum and in cooling air. Similar results were

obtained for the targets of the converters made of tantalum and tungsten. Note, that the air flow rate of 9 m³/min is provided using industrial compressors with the power of about 50 kW. The calculations have shown that a decrease in heat release in the converter to 4 kW will reduce the volumetric air flow rate to ~ 300 l/min, while keeping to the permissible temperature regime. For example, the 2.2 kW Dnipro-M AC-50 VG air compressor provides the air flow of 290 l/min. The analysis of the obtained data allowed to conclude, that at the air cooling of the molybdenum converter the maximum power in the converter should not exceed 4 kW, and a further increase in the power could lead to melting of the molybdenum converter (2623°C). Thus, for heat-resistant materials such as tantalum, tungsten, or molybdenum at air cooling, based on conventional compressors for converters with plates 500×100×(t=1.6, 1.7, 3.0) mm in size, the allocated power should not exceed 4 kW.

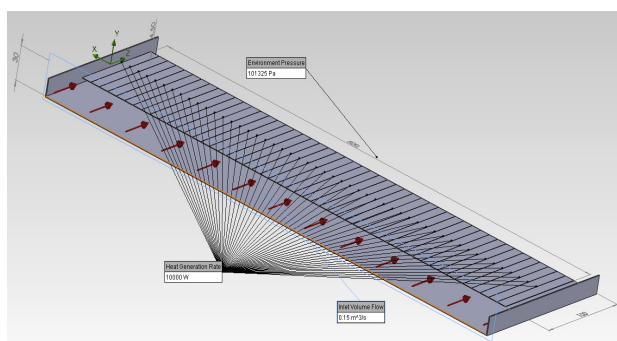


Figure 7. General view of the converter model and the directions of air and electron flows

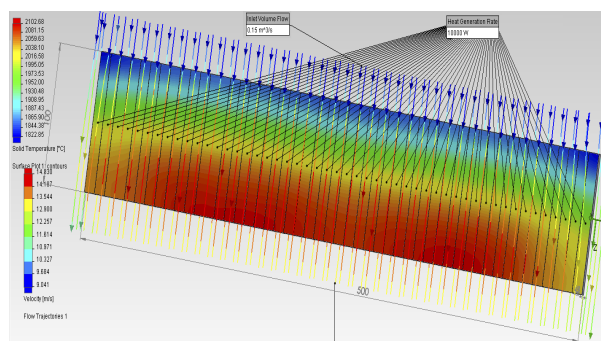


Figure 8. Temperature distribution in molybdenum and in the cooling air.

CONCLUSIONS

The generation of bremsstrahlung by electrons with the energy of 7.5 MeV for the converters, made of Ta, W, Cu or Mo with different thicknesses, was investigated. The thicknesses range of the converter plates made of Ta, W, Cu or Mo is chosen on condition that the total mass thickness of the converter and the Al filter (in g/mm²) provides complete absorption of the primary electrons. It is shown that for the same mass thicknesses of the converters made of Ta and W, practically all characteristics of BS: photon yields, average energies in the angular intervals, the energy transferred from electrons to BS, as well as the absorbed energies in the converter and the number of reflected electrons are the same. It is shown that the photon yields from Mo at mass thicknesses above 25 g/mm² are greater than those for Ta and W, but the energy, transferred from electrons to BS, is lower due to the lower average photon energy. The absorbed energies in the Mo and Cu converter are slightly higher than those of Ta and W due to the smaller number of reflected electrons.

The conjugate problem of thermodynamics and hydrodynamics (gas dynamics) was solved for the level of heat release in the converter up to 10 kW, when the converter elements were cooled with water and air. The minimum dimensions of the electron-irradiated region of a Ta or Mo converter, cooled by water, at which water efficiently removes heat, have been determined. For the option with air cooling of a Mo converter with the heat release of 10 kW, boundary conditions for the air flow are determined. It is shown that with the really existing air compressors taken into account, the permissible heat release of air-cooled Mo converters should not exceed 4 kW.

The present paper shows that, besides the technologically complex water-cooled Ta or W converters a simple and efficient converter in the form of air-cooled Mo and Al plates can be fabricated for a number of tasks.

ORCID IDs

Vladimir G. Rudychev, <https://orcid.org/0000-0002-7749-7858>; Nikolay A. Azarenkov, <https://orcid.org/0000-0002-4019-4933>
 Igor A. Girka, <https://orcid.org/0000-0001-6662-8683>; Yegor V. Rudychev, <https://orcid.org/0000-0002-1453-2062>

REFERENCES

- [1] M. Meissner, M.R. Abs at all. *Rad. Phys. Chem.* **57**, 647 (2000), [https://doi.org/10.1016/S0969-806X\(99\)00431-4](https://doi.org/10.1016/S0969-806X(99)00431-4)
- [2] V.L. Auslender, A.D. Bukin at all. *Rad. Phys. Chem.* **71**, 297 (2004), <https://doi.org/10.1016/j.radphyschem.2004.04.007>
- [3] F. Stichelbaut, J.-L. Bol at all. *Phys. Chem.* **71**, 297 (2004), <https://doi.org/10.1016/j.radphyschem.2004.03.062>
- [4] Salvat, F., Fernández-Varea, J.M., Sempau, J., PENLOPE 2011: A Code System for Monte Carlo Simulation of Electron and Photon Transport. (2012) Nuclear Energy Agency, <https://doi.org/10.1787/ef77b746-en>
- [5] V.T. Lazurik, S.A. Pismenesky, G.F. Popov, D.V. Rudychev, V.G. Rudychev, *Radiat. Phys. Chem.* **76**, 1787 (2007), <https://doi.org/10.1016/j.radphyschem.2007.03.019>.
- [6] V.T. Lazurik, S.A. Pismenesky, V.G. Rudychev, and D.V. Rudychev. *The Journal of Kharkiv National University, physical series: "Nuclei, Particles, Fields"*, **946**(1), 14 (2011) (in Russian).
- [7] John Matsson. *An Introduction to SolidWorks Flow Simulation*. (SDC Publications, 2010).
- [8] <http://www.solidworks.com/sw/products/simulation/flow-simulation.htm>.
- [9] A. Lukhanin, A. Belyaev, Y. Rudychev et al. *ASME 2012 Summer Heat Transfer Conf.* (Puerto Rico, 2012), No: HT2012-58173, pp. 129-133; <https://doi.org/10.1115/ht2012-58173>

**ГЕНЕРАЦІЯ ГАЛЬМІВНОГО ВИПРОМІНЮВАННЯ ЕЛЕКТРОНАМИ З ЕНЕРГІЄЮ 7.5 МЕВ
В КОНВЕРТЕРАХ З РІЗНИХ МАТЕРІАЛІВ**

Володимир Г. Рудичев^а, Микола О. Азаренков^а, Ігор О. Гірка^а, Єгор В. Рудичев^{а,б}

^а*Харківський національний університет імені В.Н. Каразіна
61022, Україна, м. Харків, пл. Свободи, 4*

^б*Національний науковий центр «Харківський фізико-технічний інститут»
61108 Україна, м. Харків, вул. Академічна, 1*

У даній роботі показано, що крім технологічно складних конвертерів з Та, W з водяним охолодженням, можна для ряду завдань виготовити простий і ефективний конвертер у вигляді пластин з Мо і Al з повітряним охолодженням. Досліджено генерація гальмівного випромінювання електронами з енергією 7.5 MeV в Та, W, Cu, Мо і фільтри з Al методом Монте-Карло в пакеті PENELOPE. Діапазон товщини з Та, W, Cu, Мо вибраний з умови, що сумарна масова товщина конвертера і фільтра з Al (в одиницях g / mm²) забезпечує повне поглинання первинних електронів. Показано, що виходи фотонів з Мо більше ніж для Та і W при масовій товщині вище 25 g / mm², але передана енергія від електронів в гальмівне випромінювання менше. При однакової масової товщини конвертерів з Та і W практично всі характеристики гальмівного випромінювання і поглиненої енергії в мішені однакові. Для рівня тепловиділення в конвертері до 10 кВт визначені умови охолодженні водою і повітрям елементів конвертера. Визначено мінімальні розміри області конвертера з Та і Мо що опромінюється електронами при водяному охолодженні. Показано, що з урахуванням реально існуючих повітряних компресорів допустиме тепловиділення конвертерів з Мо з повітряним охолодженням не повинно перевищувати 4 кВт.

Ключові слова: радіаційні технології, конвертер, гальмівне випромінювання, електронні пучки.

FORMATION OF OPTICAL IMAGES WITH SYNCHROTRON RADIATION FLUX OF RELATIVISTIC ELECTRONS IN THE X-RAY GENERATOR "NESTOR"[†]

 Aleksandr Mazmanishvili*,  Nataliya Moskalets

National Science Center "Kharkiv Institute of Physics and Technology"
1 Akademichna str., 61108, Kharkiv, Ukraine

*Corresponding Author: mazmanishvili@gmail.com

Received June 10, 2021; revised June 29, 2021; accepted August 28, 2021

When setting up physical experiments involving the use of the polarization properties of synchrotron radiation (SR) or a monoenergetic photon beam, detailed calculation of the spectral angular distribution of SR and its polarization components is of interest. Consideration of the electron beam size shows that in real conditions the radiation propagating in the plane of the equilibrium orbit will not be completely polarized, and the shape and dimensions of the angular distribution of radiation will be distorted. The motion of electrons in the uniform magnetic field and SR of the beam of relativistic particles in the storage ring of "NESTOR" are considered. The effect of the size of the electron beam with the energy of $E=225$ MeV in the 6-dimensional space on the formation of images of the flux of quanta of SR is analyzed. It is shown that the main contribution to the formation of images is made by the two-dimensional distribution of particles along the vertical direction axis and vertical oscillations. A software simulation code has been developed, the use of which made it possible to simulate the process of optical image formations by the flux of SR quanta (Этого предложения нет в русской аннотации). The formation of images of the radiation of electrons with an energy of $E=225$ MeV with change in the longitudinal distance L to the registration plane is considered. It is determined that at small longitudinal distances the main contribution to the image is made by the vertical distribution of particles in the beam. With an increase in the basic distance L , the contribution of the distribution of particles over vertical oscillations increases, which becomes decisive for large L value. Numerical simulation of image formation has been carried out. For the base distance of 300 cm and beam parameters with the vertical root mean square size σ_y of 0.2 mm and a vertical root mean square size $\sigma_{y'}$ of 0.15 mrad, the family of angular distributions is presented in the form of two-dimensional histograms for wavelengths $\lambda = 0.5 \lambda_c$, $\lambda = \lambda_c$, $\lambda = 2 \lambda_c$, where λ_c is the critical wavelength of SR. The dimensions of the optical window are obtained, the size of which makes it possible to reliably register the entire flux of SR quanta for the indicated registration characteristics.

Keywords: electron storage ring, electron beam, synchrotron radiation, angular distribution, polarization, σ component, π component, formation of optical image.

PACS: 29.20.-c, 41.60.Ap, 29.27.Fh

The movement of relativistic electrons in a magnetic field is accompanied by the emission of synchrotron radiation (SR) quanta. This radiation has many remarkable properties. These include, first of all, its unconditional reproducibility and metrological calculability [1, 2]. The problem of analytically describing the properties of SR in the ideal case has received a complete solution [3]. Practical application of SR implies the possibility of calculating the parameters of the flux of SR quanta in real conditions.

MAIN RESEARCH SUBJECT

Ideally, the emitting particle moves in a magnetic field along circular reference orbit. In practice, an intense flux of SR quanta is emitted by a distributed electron beam, conducted through an extraction channel, and recorded at a selected base distance in the image plane.

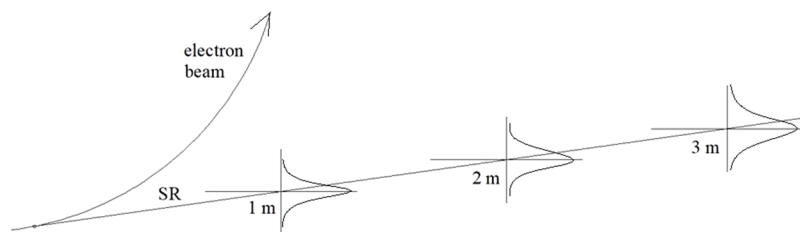


Figure 1. Scheme of registration of the flux of SR quanta

MATHEMATICAL MODEL

SR of a relativistic electron is characterized by a high degree of polarization [2]. In particular, in the ideal case, at zero angle ($\psi = 0$) to the orbital plane, it is linearly polarized. The spectral-angular dependences of the flux of SR quanta of one electron in this case are calculated in accordance with the expressions that describe the flux density

[†] Cite as: A. Mazmanishvili, N. Moskalets, East. Eur. J. Phys. 3, 97 (2021), <https://doi.org/10.26565/2312-4334-2021-3-15>

$w_\sigma(\psi)$ for the σ -component of polarization (in the plane of the orbit) and π -component $w_\pi(\psi)$ (perpendicular to the plane orbits)

$$w_\sigma(\psi) = \frac{8\pi e_0^2 R^2 f}{3c\hbar\lambda^3 \gamma^4} (1 + \gamma^2 \psi^2)^2 K_{2/3}^2 \left(\frac{\lambda_c}{2\lambda} (1 + \gamma^2 \psi^2)^{3/2} \right),$$

$$w_\pi(\psi) = \frac{8\pi e_0^2 R^2 f}{3c\hbar\lambda^3 \gamma^4} \gamma^2 \psi^2 (1 + \gamma^2 \psi^2) K_{1/3}^2 \left(\frac{\lambda_c}{2\lambda} (1 + \gamma^2 \psi^2)^{3/2} \right),$$
(1)

where $\gamma = E/E_0$ is the relativistic factor, E_0 is the electron rest energy, R is the orbital radius, f is the orbital frequency, $\lambda_c = 4\pi e_0^2 R f / \sqrt{3} c \hbar \gamma^3$ is the critical radiation wavelength. The total angular density is: $w(\psi) = w_\sigma(\psi) + w_\pi(\psi)$.

The photon flux of each electron is characterized by the angular distribution, the axis of which coincides with the direction of motion of the particle, and the top of the distribution coincides with the place of emission. The electrons in the storage ring oscillate around the reference orbit. These oscillations are due to recoil during emission of SR quanta, as well as intrabeam scattering and scattering by residual gas particles. As a result, the beam particles are distributed around the reference orbit with the normal Gaussian law in the 6-dimensional space.

Let us consider the effect of the particle distribution on the properties of the flux of SR quanta. The distribution in the longitudinal direction does not affect the spectral-angular characteristics of the flux of SR quanta due to azimuthal symmetry. For the same reason, the radial distribution of particles also does not affect the characteristics of the SR flux. For the vertical distribution of particles, we use the formula:

$$\rho(y, y') = \frac{1}{2\pi\sigma_y\sigma_{y'}} \exp\left(-\frac{y^2}{2\sigma_y^2} - \frac{y'^2}{2\sigma_{y'}^2}\right),$$
(2)

where σ_y and $\sigma_{y'}$ are, respectively, the root-mean-square dimensions of the beam in y and y' . Bearing in mind (2), we consider the receiving plane at the base distance L that is perpendicular to the tangent of a circular orbit at the radiation emission point. The angle of emission of the quantum ψ , as well as the coordinates of emission (y, y') and reception h in the vertical direction, are related by the relation $h - \psi L = y + Ly'$. Therefore, for the angular distributions of the flux of SR quanta averaged over the beam, we obtain:

$$N_\sigma(\beta) = \int_{-\pi/2}^{\pi/2} d\psi \int_{-\infty}^{\infty} dy \int_{-\infty}^{\infty} dy' \rho(y, y') \delta(h - y - y'L - \psi L) w_\sigma(\psi),$$
(3)

$$N_\pi(\beta) = \int_{-\pi/2}^{\pi/2} d\psi \int_{-\infty}^{\infty} dy \int_{-\infty}^{\infty} dy' \rho(y, y') \delta(h - y - y'L - \psi L) w_\pi(\psi),$$

where $\beta = h/L$ and $\delta(\cdot)$ is the Dirac delta function. Due to the Gaussian normal distribution of y and y' the random variable h is also Gaussian normal with the mathematical expectation ψL and the variance:

$$\sigma_L^2 = \sigma_y^2 + \sigma_{y'}^2 L^2.$$
(4)

Therefore, for the average angular distributions of the flux of SR quanta, we obtain:

$$N_\sigma(\beta) = L \int_{-\pi/2}^{\pi/2} \frac{d\psi}{\sqrt{2\pi}\sigma_L} \exp\left[-\frac{(\beta-\psi)^2 L^2}{2\sigma_L^2}\right] w_\sigma(\psi),$$

$$N_\pi(\beta) = L \int_{-\pi/2}^{\pi/2} \frac{d\psi}{\sqrt{2\pi}\sigma_L} \exp\left[-\frac{(\beta-\psi)^2 L^2}{2\sigma_L^2}\right] w_\pi(\psi).$$
(5)

It follows from (5) that the forming optical image is the convolution of the normal density of particles in the beam with the angular distribution that describes the emission of SR quanta. The dispersion of the resulting angular distribution $\langle(\beta-\psi)^2\rangle$ will decrease with increasing base L by $\sigma_L^2 = \sigma_y^2 + \sigma_{y'}^2/L^2$. For sufficiently large L , it will be determined only by the distribution of particles along the directions of vertical oscillations. The distribution for the σ -component of polarization, due to its unimodality, is more resistant to this influence. The angular spectrum of the π -component of polarization has two symmetric maxima; therefore, its deformation and broadening by virtue of (5) turn out to be more noticeable. In this case, with an increase in the base distance L , the spatial picture along the vertical axis will also expand. The gradual distribution normalization for π -component of polarization will take place at $\sigma_y^2 \gg \langle\psi_\pi^2(\lambda)\rangle$, where $\langle\psi_\pi^2(\lambda)\rangle$ is the angular dispersion of π -component at the wavelength λ . Otherwise, when $\langle\psi_\pi^2(\lambda)\rangle \gg \sigma_y^2$, the angular distribution will be not normalized for any base L value.

NUMERICAL RESULTS

Based on expressions (4), the software was developed that makes it possible to calculate the necessary characteristics of the fluxes of SR quanta of both polarizations that have passed the selected base distance and to analyze the optical images formed in the given geometry of emission and observation. Let us present the results of calculations of the distribution of the optical image of the SR components in the "NESTOR" of electrons with an energy of $E = 225$ MeV [4-6]. Parameters for the "NESTOR" summarized in Table.

Table. The main parameters of the "NESTOR"

Parameter	Specification
Energy of electron beam E , MeV	40-225
Storage ring circumference, m	15.418
The maximum stored current I , mA	360
Number of electrons in orbit	1.1×10^{11}
Bending radius in magnets R , m	0.5
Magnetic field at maximum energy B , T	1.5
Electron beam size at radiation points σ_y , m (for the maximum energy of the electron beam)	2.08×10^{-4}
Electron beam divergence σ_y' at radiation point (for the maximum energy of the electron beam)	1.51×10^{-4}

In Fig. 2 the family of angular distributions of flux densities for σ - and π -components of polarization calculated for one of the SR output channels in the generator, with $\sigma_y = 0.2$ mm and $\sigma_y' = 0.15$ mrad are shown. The dependences are presented in the form of two-dimensional histograms for different wavelengths $\lambda = 0.5 \lambda_c$, $\lambda = \lambda_c$, $\lambda = 2 \lambda_c$, as well as for different base lengths L , with $L_{max}=300$ cm. For the chosen base and at $\lambda_c = 2.45 \times 10^{-6}$ cm, the range of polar angle values β was $|\beta| \leq 10$ mrad. It can be seen that with the base of $L_{max}=300$ cm and the vertical size of the receiving window of $H=6$ cm, almost complete registration of quanta of the σ - and π -components at the selected SR wavelengths is provided. For large wavelengths of SR quanta, capture with a constant size of the receiving window H will be less effective due to the corresponding increase in of the root-mean-square angle of the distributions $w_\sigma(\psi)$ and $w_\pi(\psi)$ while the presence of two maxima in the distribution of the π -component becomes more evident.

Dependencies in Fig. 2 and Fig. 3 are given for the case when one electron turn around in the orbit.

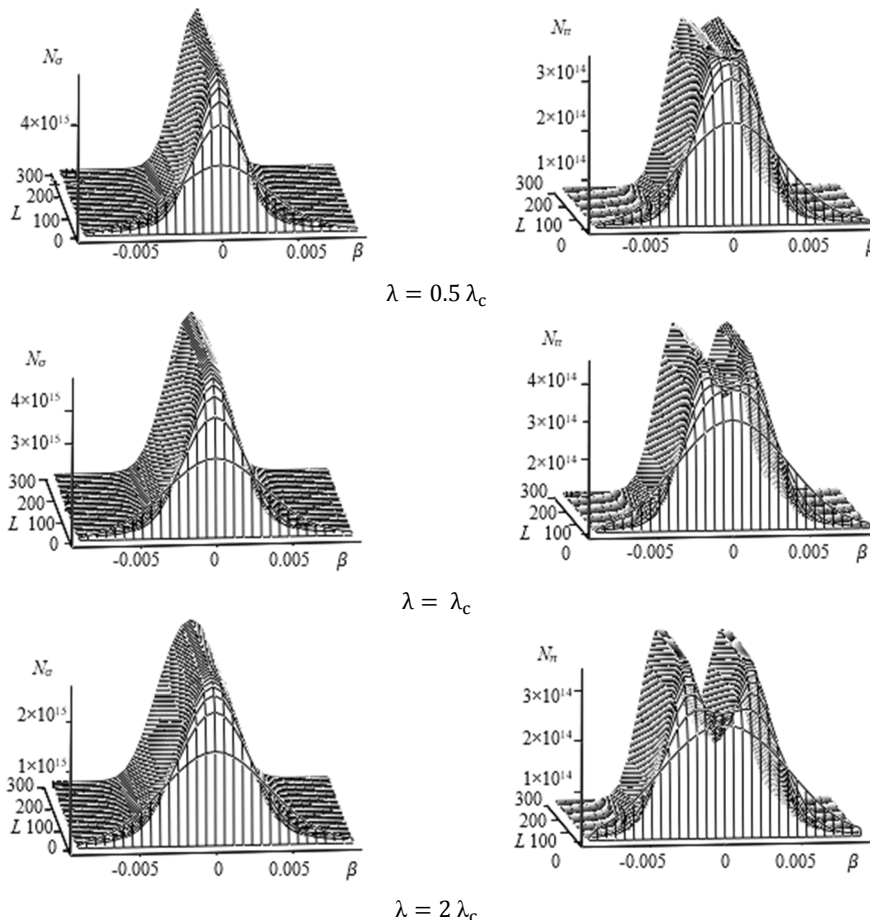


Figure 2. Family of angular distributions of the flux density of the σ -component (left) and the π -component (right) of the polarization of synchrotron radiation at an electron energy $E=225$ MeV and wavelengths, $\lambda = 0.5 \lambda_c$, $\lambda = \lambda_c$, $\lambda = 2 \lambda_c$, respectively

The rearrangement of optical images can be seen in Fig. 3. It shows the distributions that formed directly after the electron beam ($L=5$ cm) and distributions that formed on the basis of $L=300$ cm for different wavelengths of $\lambda = 0.5 \lambda_c$, $\lambda = \lambda_c$, $\lambda = 2 \lambda_c$ in addition to ideal angular distributions. From Fig. 3 one can see that at $L=5$ cm the angular distribution reflects the vertical imprint of the beam. At $L=300$ cm, the angular distribution is determined by the density of vertical oscillations of the electrons.

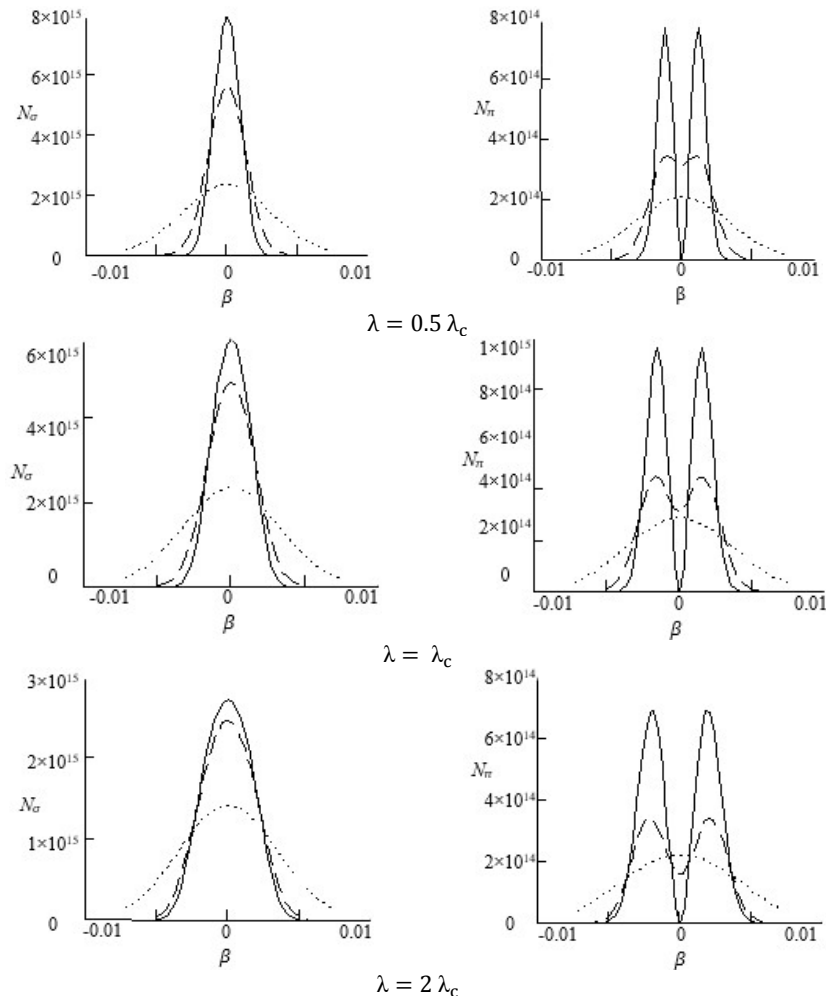


Figure 3. Family of angular distributions of flux density of the σ -component (left) and π -component (right) of the polarization of the SR at the electron energy $E=225$ MeV and wavelengths $\lambda = 0.5 \lambda_c$, $\lambda = \lambda_c$, $\lambda = 2 \lambda_c$, respectively. Line – ideal distribution; dotted line – distribution at $L=5$ cm, points – distribution at $L=300$ cm

CONCLUSION

The paper presents analytical expressions are obtained for the intensity of the flux of SR quanta of given wavelength for the selected registration geometry and algorithms for calculating the fluxes under consideration are proposed. It is shown that the forming optical image is the convolution of the normal density of particles in the beam with the angular distribution describing the emission of quanta. The dependences characterizing the intensity and spectral-angular properties of the SR photon flux are given. For the selected base distance and beam parameters with a vertical root-mean-square size σ_y and a root-mean-square size $\sigma_{y'}$ of vertical oscillations, the family of angular distributions is presented, which are presented in the form of two-dimensional histograms. The dimensions of the optical window are obtained, the value of which makes it possible to reliably register the flux of quanta of SR for the indicated registration characteristics. The paper presents the main characteristics of the angular distribution of the flux of SR quanta of relativistic electron beam in the storage ring of the "NESTOR" with a maximum electron energy of $E_{\max}=225$ MeV.

ORCID IDs

✉ Aleksandr Mazmanishvili, <https://orcid.org/0000-0003-0373-0626>; ✉ Nataliya Moskalets, <https://orcid.org/0000-0002-2163-9116>

REFERENCES

- [1] I. M. Ternov, V. V. Mikhailin, *Синхротронное излучение. Теория и эксперимент. [Synchrotron radiation. Theory and experiment]*, (Energoatomizdat, Moscow, 1986, pp. 219-250 (in Russian).

- [2] G. Bruk, *Циклические ускорители заряженных частиц [Cyclic charged particle accelerators]*, (Atomizdat, Moscow, 1970) (in Russian).
- [3] N. Kulipanov, A. N. Skrinskii, *Sov. Phys. Usp.* 20, 559 (1977) <http://dx.doi.org/10.1070/PU1977v020n07ABEH005444>
- [4] I.M. Karnaukhov et al., *Problems of Atomic Science and Technology*, series "Nuclear Physics Investigation", №5, (48), 156-159 (2007), <https://vant.kipt.kharkov.ua/TABFRAME.html>
- [5] A.A. Shcherbakov et al., in: *4th International Particle Accelerator Conference*, (IPAC, Shanghai, 2013), pp.2253-2255, <http://hal.in2p3.fr/in2p3-00823292>
- [6] V. Androsof et al., in: *9th International Particle Accelerator Conference*, (IPAC, Vancouver, 2018), pp. 4307-4309, <https://accelconf.web.cern.ch/ipac2018/papers/thpmk008.pdf>

**ФОРМУВАННЯ ОПТИЧНИХ ЗОБРАЖЕНЬ ПОТОКОМ КВАНТІВ
СИНХРОТРОННОГО ВИПРОМІНЮВАННЯ РЕЛЯТИВІСТСЬКИХ ЕЛЕКТРОНІВ
В РЕНТГЕНІВСЬКОМУ ГЕНЕРАТОРІ «НЕСТОР»**

О.С. Мазманішвілі, Н.В. Москалець

*Національний Науковий Центр Харківський фізико-технічний інститут
вул. Академічна, 1, 61108, Харків, Україна*

При постановці фізичних експериментів, пов'язаних з використанням поляризаційних властивостей синхротронного випромінювання (СВ) або моноенергетичного пучка фотонів, представляє інтерес детальний розрахунок спектрального кутового розподілу СВ і його поляризаційних компонент. Урахування розмірів пучка показує, що в реальних умовах випромінювання, що поширюється в площині рівноважної орбіти, не буде повністю поляризованим, а форма і розміри кутового розподілу випромінювання будуть спотворені. Розглянуто рух електронів в однорідному магнітному полі і СВ пучка релятивістських частинок в накопичувачі "НЕСТОР". Проаналізовано вплив на формування зображень потоку квантів СВ розмірів пучка електронів з енергією $E=225$ MeV в 6-вимірному просторі. Показано, що в формування зображень основний внесок вносить двовимірний розподіл часток по вертикалі і по вертикальним коливанням. Побудовано програмний засіб, використання якого дало можливість промоделювати процес формування оптичних зображень потоком квантів СВ. Розглянуто формування зображень випромінювання електронів з енергією $E=225$ MeV при зміні поздовжньої відстані L до площини реєстрації. Визначено, що на малих поздовжніх відстанях основний внесок в зображенні вносить вертикальний розподіл часток в пучку. Зі збільшенням базової відстані L зростає внесок розподілу часток по вертикальним коливанням, який для великих L стає визначальним. Проведено чисельне моделювання формування зображень. Для базової відстані в 300 см і параметрів пучка з вертикальним середньоквадратичним розміром σ_y , що становить 0.2 мм, і середньоквадратичним розміром σ_y вертикальним коливань, що становить 0.15 мрад, наведено сімейство кутових розподілів, які оформлені у вигляді двовимірних гістограм для довжин хвиль $\lambda = 0.5 \lambda_c$, $\lambda = \lambda_c$, $\lambda = 2 \lambda_c$, де λ_c – критична довжина хвилі СВ. Отримано розміри оптичного люка, величина яких дозволяє гарантовано реєструвати весь потік квантів СВ для зазначених характеристик реєстрації.

Ключові слова: накопичувач електронів, електронний пучок, синхротронне випромінювання, кутовий розподіл, поляризація, σ -компонента, π -компонента, формування оптичного зображення.

THE IMPACT OF PULSE PLASMA TREATMENT ON THE MICROHARDNESS OF STEEL 40X10C2M: EXPERIMENT AND NUMERICAL SIMULATIONS[†]

 **Nikolay A. Savinkov^{a,*}**,  **Oleh M. Bulanchuk^b**,  **Aleksander A. Bizyukov^c**

^a*Azovskiy Maritime Institute of NU «OMA», 19 Chornomors'ka str., Mariupol, 87517, Ukraine*

^b*Donetsk State University of Management, 58 Karpinskogo str., Mariupol, 87513, Ukraine*

^c*V.N.Karazin Kharkiv National University, 4 Svobody Sq., Kharkiv, 61022, Ukraine.*

*Corresponding Author: nik.sv2010@yandex.ua, phone: +380-98-376-03-75

Received June 6, 2021; revised July 29, 2021; accepted August 28, 2021

This paper presents a study of operating characteristics of steel 40X10C2M after treatment it of high-energy plasma pulses. The steel is used to manufacture the elements of ships' power plants. For pulsed plasma treatment of steel samples, we used an electrothermal plasma accelerator (ETPA). A high-current pulsed high-pressure arc discharge was initiated in a restricted dielectric chamber of ETPA. The discharge duration was 1.4 ms, the maximum current reached the value of 5 kA, the discharge voltage was up to 5 kV. We investigated the microhardness and microstructure of the processed (modified) layer and determined the optimal parameters of steel processing that provide the best characteristics of the modified layer when the microhardness increases by ≈ 5 times. Microhardness maxima were discovered in the depth of the modified layer. The paper studies the possibilities of controlling the maxima localization to form the desired performance characteristics of the treated layer. Mathematical modeling of rapid pulsed heating of the steel surface layer is performed within the framework of the two-phase "melt-solid" model, taking into account the dynamics of the thermodynamic characteristics of steel. For this purpose, we used the classical equation of thermal conductivity with varying steel parameters: density, heat capacity, and coefficient of thermal conductivity during the transition of a substance from the liquid to the solid phase. Within the chosen mathematical model, numerical calculations of the rapidly pulsed heating phenomenon of the steel surface were performed, taking into account melting and solidification in the Comsol Multiphysics package using the finite element method. The numerical simulation results are in good agreement with the experimental distribution of the microhardness of the treated steel layer deep into the sample.

Keywords: plasma treatment, modified layer, microhardness, microstructure, thermal conductivity equation, melting and solidification, melt cooling rate.

PACS: 07.90.+c; 52.90.+z; 44.05.+e; 02.60.-x; 68.35.Rh; 61.50.Ks

The surface treatment of metals and alloys using high-energy electron and ion beams, laser radiation, high-temperature thermal plasma stream was widely used to modify the properties of a thin surface layer of various materials [1-3]. In this case, the modification of the surface layer occurs due to a whole complex of processes: rapid heating and cooling (quenching), formation of defects and structural stresses, ion implantation, deposition, epitaxy of atoms and molecules, and radiation-stimulated diffusion. Such processing can result in the surface layer melting of the metal followed by ultrafast crystallization and the formation of a modified layer with a thickness of (10-200) microns [4-6]. As a consequence of various structural and phase transformations occurring in the modified layer, many operational characteristics of the product are improved, such as microhardness, durability, heat, corrosion, and erosion strength.

Here it is necessary to highlight the pulse-plasma technology (PPT) [2,7] for material processing, the advantages of which are high heating and cooling rates of the metal surface (106-108 K/s), the ability of varying the plasma stream parameters (number of pulses, specific power) and the ability of creating layered structures with various phase composition. Another advantage is the ability to impact the item locally by pulsed plasma.

In various works researchers observed an increase in the microhardness of the modified layer and an ambiguous change of the microhardness along the depth of the layer. For instance, in work [7] the microhardness maxima on the surface of the modified metal layer and a decrease of microhardness deep into this layer up to values typical for the base were obtained. The electro-explosive boron-copper plating of the steel-45 surface resulted in a threefold increase of the surface microhardness [8]. Microhardness of 17-4PH stainless steel behaves oppositely and increases linearly along with the layer depth (up to 600 microns) after steel treatment by pulsed energy streams [9]. In work [10], when processing steel with high-current electron beams, the microhardness values decreased exponentially along with the depth of the modified layer. Thus, using PPT the authors observed contractionary behavior of microhardness with the depth of the treated layer, so that aspect demands additional investigations.

The use of PPT can be associated with both "heating-cooling" processes and phase transformations of the first kind: melting and solidification. The size of the molten zone, the processes of transferring the heat stream into the interior, and the cooling rate depend on the modes of plasma exposure and the thermophysical properties of the processed material [11]. To determine the influence of each of these factors, it is necessary to simulate the space-time distributions of the temperature and the dynamics of phase transitions with the subsequent comparison with experimental data. For this purpose various mathematical models [12-15] are used. Some of the models can be solved analytically [14], but most of them are solved numerically [6,12,13]. In this case it is possible to consider the single-phase model of

[†] **Cite as:** N.A. Savinkov, O.M. Bulanchuk, A.A. Bizyukov, East. Eur. J. Phys. 3, 102 (2021), <https://doi.org/10.26565/2312-4334-2021-3-16>

transmission of heat to solid during the “fast heating – cooling” process (that is, without melting the surface [14.15]) or a two-phase model of “rapid heating and melting of the surface layer–hardening” [16.17])

Numerical calculations of heat transfer processes in two-phase systems during the solidification process of the molten surface layer obtained by many authors [12,13,16,17] assumed that the thermodynamic characteristics of the medium remain stationary. In fact, in two-phase models, it is necessary to take into account the dynamics of the main thermodynamic characteristics of a substance (density, heat capacity, coefficient of thermal conductivity). The simulation also did not determine the cooling rate $\Delta T / \Delta t$ of the melt and its distribution over the depth of the molten zone. The cooling rates determine the strength properties of the treated layer, and the cooling rate should correlate with the microhardness values.

The purpose of this work is, first, to study the microhardness and microstructure of the modified layer of 40X10C2M steel after the pulsed plasma treatment; second, to obtain the distribution of microhardness over the depth of the treated layer; third, to simulate numerically the rapid pulse heating process of the steel layer surface in the framework of the two-phase model “melt - solid” while taking into account the dynamics of thermodynamic characteristics of steel; forth, to compare the simulation results with experimental data.

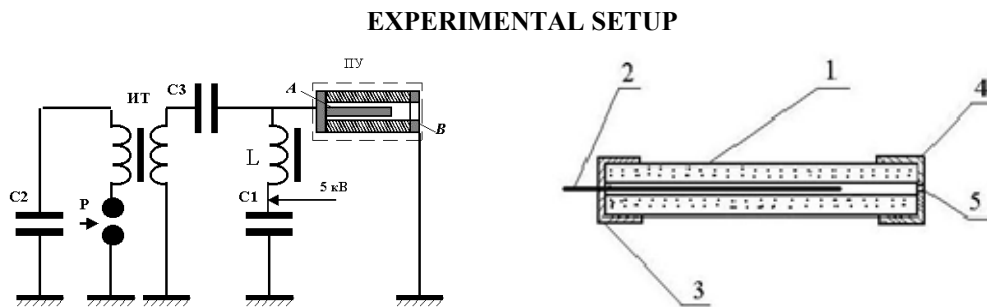


Figure 1. The electrothermal plasma accelerator (right)

and its electrical power supply circuit (left) For pulsed plasma treatment of steel samples, we used an electrothermal plasma accelerator (ETPA) – Fig. 1. A high-current pulsed high-pressure arc discharge was initiated in a restricted dielectric chamber (1) at atmospheric pressure between a consumable rod-shaped iron cathode (2) and an axially located ring-shaped anode (4) [18]. The edges of dielectical chamber is molded by metallic barrels 3 and 4. The anode was grounded, and we applied the voltage from the capacitive energy storage to the rod cathode. The discharge duration was 1.4 ms, the maximum current reached 5 kA, the discharge voltage was up to 5 kV, and the maximum stored energy in a pulse was (20-37) kJ. The working substance entered the discharge chamber due to the intense evaporation of the iron cathode. As a result, the chamber pressure rises for a short time up to (100-150) atm. The discharge led to the appearance of liquid metal in the form of vapor and plasma of the cathode medium. In this case, a pulsed injection of a dense gas-plasma beam occurred through the hole (5) in the ring-shaped anode in the direction of the sample under study. According to the obtained estimations, the plasma parameters: density and temperature approximately 10^{16}cm^{-3} and (1-2) eV, respectively.

EXPERIMENTAL RESULTS AND DISCUSSION

As specimens, we used plates with dimensions of (0.5x2x2) cm made of 40X10C2M steel. The samples were installed outside the discharge chamber near the anode and irradiated with one or more ETPA pulses. Before irradiation, the samples underwent standard thermal treatment: quenching and low tempering. We analyzed the modified layer microstructure of the processed specimens at a metallographic microscope “Neophot-21”. The Vickers microhardness of the samples was measured using a PMT-3 device.

The microstructure investigations, thickness, and microhardness of the modified layer of irradiated samples were carried out depending on the parameters of pulsed plasma treatment. The optimal distance from the plasma source to the specimen surface was determined experimentally on the level of 30 mm, at optimal discharge voltage of the ETPA of 4 kV. For these distance and voltage value, the power density on the sample surface was calculated as $q_0 = W / S \approx 10^9 \text{ W/m}^2$. Such a power density value provided the maximum rate of the “heating-ultrafast cooling” cycle of the near-surface layer. The quick cycle ensured a formation of dispersed alloyed crystal structure with a high dislocation density, and a hardened modified layer was formed. Fig. 2 shows the microstructure of the modified steel layer after pulsed plasma treatment. As we can see, the best structure is formed when the number of pulses is $N = 4$, the discharge voltage is $U = 4.0 \text{ kV}$ and the distance from the source to the sample is 30 mm (Fig. 2b).

As the distance from the ETPA to the sample surface decreases or as the discharge voltage increases to the maximum possible value of 5 kV, the power density increases, but the cathode starts ejecting metal droplets. Finally, the modified layer microstructure worsens and becomes loose and inhomogeneous (Fig. 2c). At a greater distance from the source to the sample, the thickness of the modified layer decreases (Table 1). At a distance of $l = 70 \text{ mm}$, the thickness drops to $\approx 53 \mu\text{m}$.

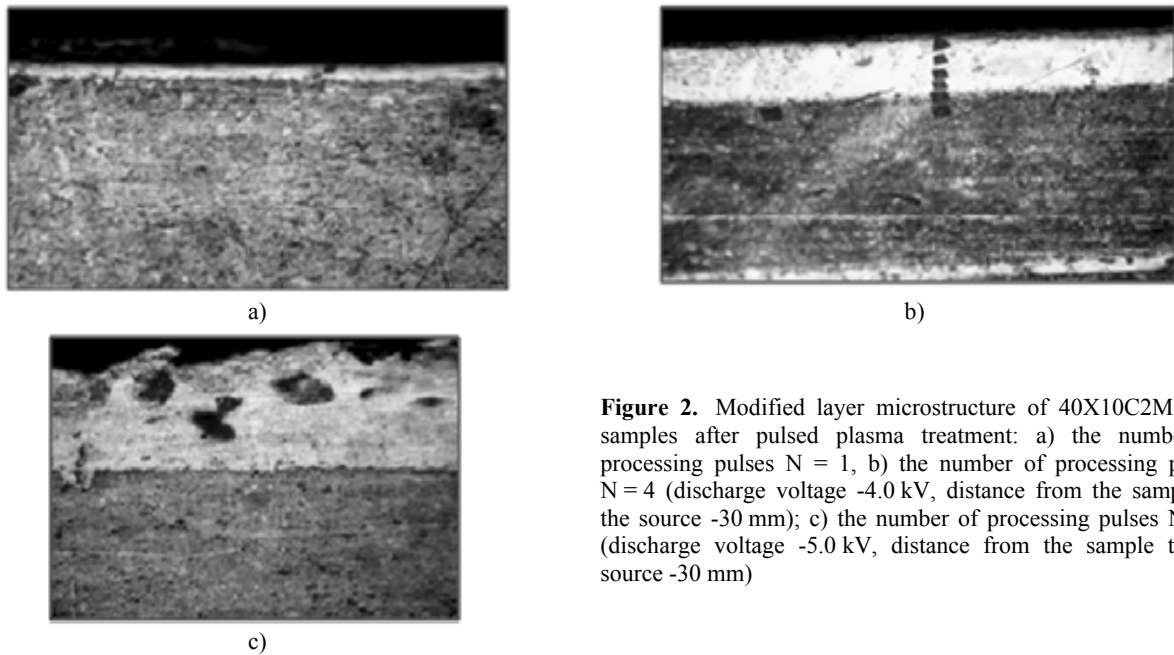


Figure 2. Modified layer microstructure of 40X10C2M steel samples after pulsed plasma treatment: a) the number of processing pulses $N = 1$, b) the number of processing pulses $N = 4$ (discharge voltage -4.0 kV, distance from the sample to the source -30 mm); c) the number of processing pulses $N = 6$ (discharge voltage -5.0 kV, distance from the sample to the source -30 mm)

Table 1. Values of the modified layer average thickness of steel samples at various modes of pulsed plasma treatment.

The discharge voltage of the ETPA, kV	The number of processing pulses	The distance from the plasma source to the sample, mm	The modified layer average thickness, μm
2.0	1	30	18.4
2.5	1	30	25.6
3.0	1	30	27.1
4.0	1	30	35.5
4.0	3	30	75.8
4.0	4	30	118.8
4.0	5	30	128.1
4.0	6	30	125.5
4.0	7	30	128
4.0	8	30	122.7
4.0	4	70	53

Table 1 shows the results of pulsed plasma treatment of 40X10C2M steel samples. The table shows the modified layer's average thickness at different power densities load of the plasma stream to the sample surface. Influence of the power density was determined by three factors: 1) the discharge voltage of the ETPA; 2) the number of processing pulses; 3) the distance from the plasma source to the sample.

From the analysis of the data in the table, it is advisable to increase the number of processing pulses to (4-5). A further increase in the number of pulses does not lead to a significant increase in the modified layer thickness. As we can see from the table, within the statistical error, the thickness does not change with an increase in the number of pulses $N > (4-5)$.

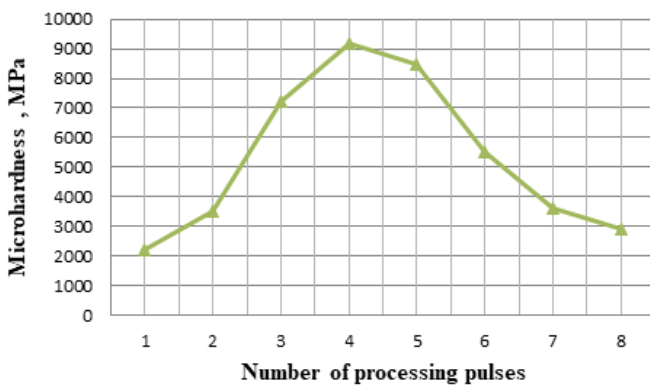


Figure 3. Dependence of the modified layer surface microhardness of 40X10C2M steel samples on the number of processing pulses

are shown in Fig. 4 depending on the different number of processing pulses.

The dependence of the microhardness on the number of processing pulses was plotted for the optimal distance values from the source to the sample – of 30 mm and the discharge voltage – $U = 4\text{kV}$ – Fig. 3.

The resulting curve correlates well with the data in the table: the thicker the homogeneous layer, the higher microhardness. The maximum microhardness value on the surface were also observed at 4 processing pulses.

For the processed samples, the microhardness values were determined at various points from the surface of the specimen cross-section into the depth of the modified layer. The microhardness curves

As we can see from Fig. 4, the position of the microhardness maximum depends on the plasma treatment modes. The microhardness maximum moves in depth when the number of processing pulses increases. For the number of pulses $N = 2$, the microhardness maximum (4700 MPa) is at a depth of 30 μm . With an increase in the number of pulses to $N = 3$, the microhardness maximum (7500 MPa) shifts to a depth of $\approx 40 \mu\text{m}$; at $N = 4$, a strongly marked maximum (12900 MPa) is observed at a depth of $\approx 60 \mu\text{m}$. With an increase in the number of pulses to $N = 5$, we observe a microhardness maximum (11200 MPa) at a distance from the surface of $\approx 80 \mu\text{m}$.

The presented curves also show that the microhardness values for all samples grow at power density rise on the sample surface load. The microhardness of the modified layer at its maximum rises by about five times compared to the untreated surface.

NUMERICAL SIMULATIONS AND DISCUSSION

To compose a mathematical model of heat transfer, while taking into account the melting-solidification process of the near-surface layer, we used the classical equation of thermal conductivity with a modified density, specific heat, and coefficient of thermal conductivity [19]:

$$\rho c_p \frac{\partial T}{\partial t} = \frac{\partial}{\partial x} \left(k \frac{\partial T}{\partial x} \right), \quad (1)$$

where T is the temperature, t and x are the time and coordinate, respectively, k is the coefficient of thermal conductivity of the substance, ρ is the density of the substance, c_p is the specific heat at constant pressure.

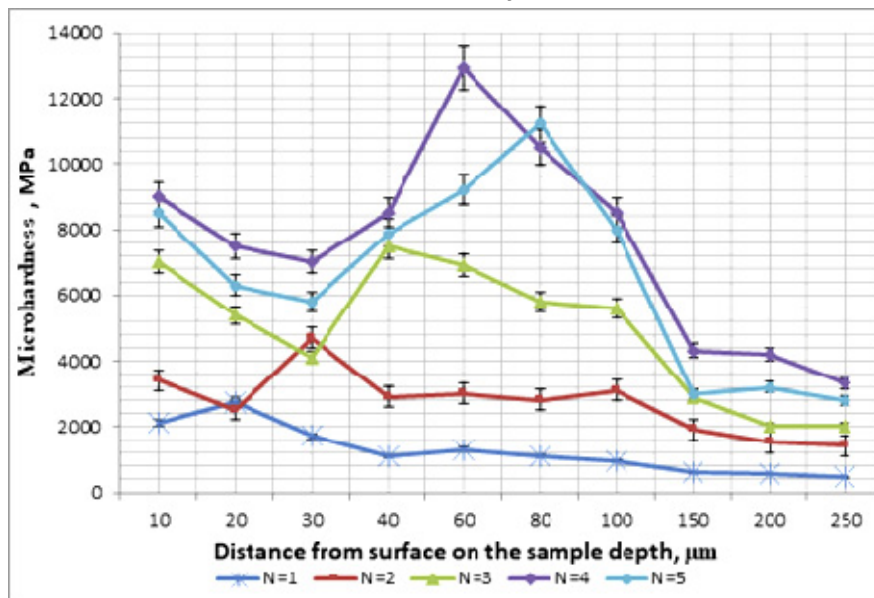


Figure 4. Microhardness dependence of the of 40X10C2M steel samples on the depth of the modified layer after a various number of processing pulses: curve 1 - the number of processing pulses $N = 1$; cr. 2 - $N = 2$; cr. 3 - $N = 3$; cr. 4 - $N = 4$; cr. 5 - $N = 5$. The discharge voltage is 4.0 kV, the distance from the sample to the plasma source is 30 mm.

The thermal conductivity coefficient was determined by the equation $k = (1 - \theta)k_1 + \theta k_2$, where k_1 and k_2 are the thermal conductivity coefficients of the solid and liquid phases, respectively; α - a smoothing function that depends on the temperature T and simulates the two-phase state of the surface layer substance. The type of $\theta(T)$ is set on the assumption that the phase transition occurs in the temperature range from $T_{pc} - \Delta T / 2$ to $T_{pc} + \Delta T / 2$, where T_{pc} is the temperature of the metal-melt phase transition (melting point), ΔT is the width of the temperature range where the substance is in a two-phase state.

We define $\theta(T)$ in such a way that it is equal to one when the substance is a liquid and zero when it is a solid:

$$\theta(T) = \begin{cases} 0, & T \leq T_p - \Delta T / 2 \\ 1, & T \geq T_{pc} + \Delta T / 2 \end{cases}.$$

In the case of an infinitely narrow interval ($\Delta T \rightarrow 0$), the function $\theta(T)$ is the Heaviside function equal to zero at $T < T_{pc}$ and is unity at $T > T_{pc}$.

For the specific heat at constant pressure, we applied the equation

$$c_p = \frac{(1-\theta(T))\rho_1 c_{p,1} + \theta(T)\rho_2 c_{p,2}}{(1-\theta(T))\rho_1 + \theta(T)\rho_2} + \lambda \frac{d\alpha(T)}{dT}$$

where λ is the specific heat of steel melting, $c_{p,1}$ and $c_{p,2}$ are the specific heat capacities of a solid and a melt, respectively; ρ_1, ρ_2 - are the density of the solid and liquid phases, respectively. Where $\alpha(T)$ - is the mass fraction

$$\alpha(T) = -\frac{1}{2} \frac{(1-\theta(T))\rho_1 - \theta(T)\rho_2}{(1-\theta(T))\rho_1 + \theta(T)\rho_2}$$

In this case, the condition $\int_{T_{pc}-\Delta T/2}^{T_{pc}+\Delta T/2} \frac{d\alpha(T)}{dT} dT = 1$ is met. In case of an infinitely narrow interval ($\Delta T \rightarrow 0$) $\frac{d\alpha}{dT}$ is -

the Dirac function.

The substance density in (1) was given by the expression

$$\rho = (1-\alpha(T))\rho_1 + \alpha(T)\rho_2$$

Thus, in the presented model, there is a jump of the thermal conductivity coefficient, heat capacity, and substance density during the transition from a liquid to a solid phase. Taking this phenomenon into account leads to the fact that the heat equation (1) has a quasilinear character.

Within the chosen framework of the mathematical model, we carried out the numerical simulation of steel surface heating by rapid pulses, taking into account the melting and solidification of the substance in the Comsol Multiphysics package using finite element method. The mesh settings were fitted empirically to have a sufficient number of mesh nodes in the range with very rapidly changing values (first of all, the rate of temperature change dT/dt). The space step was taken equal to $2.5 \cdot 10^{-7}$ m, the maximum time -step was $2.5 \cdot 10^{-6}$ s. Table 2 shows the parameters for numerical calculations [20].

On the left boundary of the sample, we selected the following boundary condition

$$q(0) = f(t) \cdot q_0 - \sigma(T^4 - T_0^4) \tag{2}$$

where $q_0 = 10^9$ W/m² is the power density load on the sample irradiated surface, $f(t)$ is a function in the form of a smoothed rectangular pulse with a duration of 1.4 ms, T_0 is the temperature of the cold surface (room temperature), T is the temperature of the substance, σ is the Stefan-Boltzmann constant.

Table 2. Parameters of steel and steel melt for numerical simulation in the Comsol Multiphysics package.

Value Description	Notation	Value
Solid phase temperature (steel)	T_0	293 K
Liquid phase temperature (melt)	T_1	1480 °C
Transition temperature interval	ΔT	49 K
Specific heat of melting	λ	84 kJ/kg
Steel density	ρ_1	7620 kg/m ³
Melt density	ρ_2	7250 kg/m ³
Steel specific heat	$c_{p,1}$	532 J/kg · K
Melt specific heat	$c_{p,2}$	825 J/kg · K
Steel thermal conductivity coefficient	k_1	52 W/m · K
Melt thermal conductivity coefficient	k_2	22 W/m · K
Thickness of metal layer (specimen)	l	2 mm
Power density on the sample surface	q_0	10^9 W/m ²

At the initial moment of time, the temperature was the same and equal to T_0 throughout the sample. In the expression (2), the second term takes into account the energy loss at the sample boundary due to thermal radiation. Boundary conditions on the right (back) side of the sample $q(l) = -\sigma(T^4 - T_0^4)$. We didn't consider the reflection and evaporation process from the boundary.

Figs. 5-7 show the results of numerical simulations. Fig. 5 shows a non-standard behavior of the melt cooling rate $-dT/dt$: the rate at certain times reaches its maximum not on the surface (as is usually in the case of solid heating), but in the depth of $\approx 20 \mu\text{m}$ of the sample.

As it is known, at the highest metal cooling rate, the regions of increased hardness are formed in the processes of quenching and hardening. The positions of the cooling rate maxima are somewhat different from the experimental values of the microhardness maxima (30-80) μm . However, the qualitative variation of the dependencies in Fig. 5 correlates well with the experimental results.

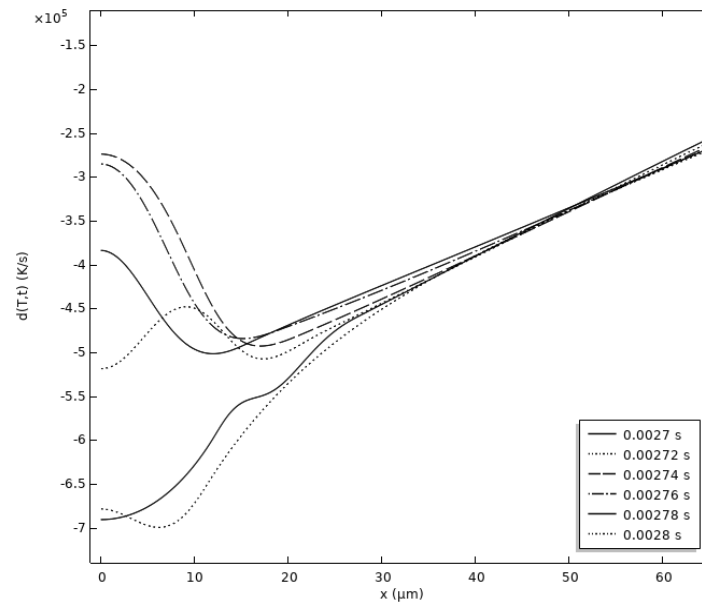


Figure 5. Dependencies of the temperature change rate (cooling rate) of the melt on the coordinate x deep into the sample for different points in time after the pulse power input: 0.00270 s, 0.00272 s, 0.00274 s, etc.

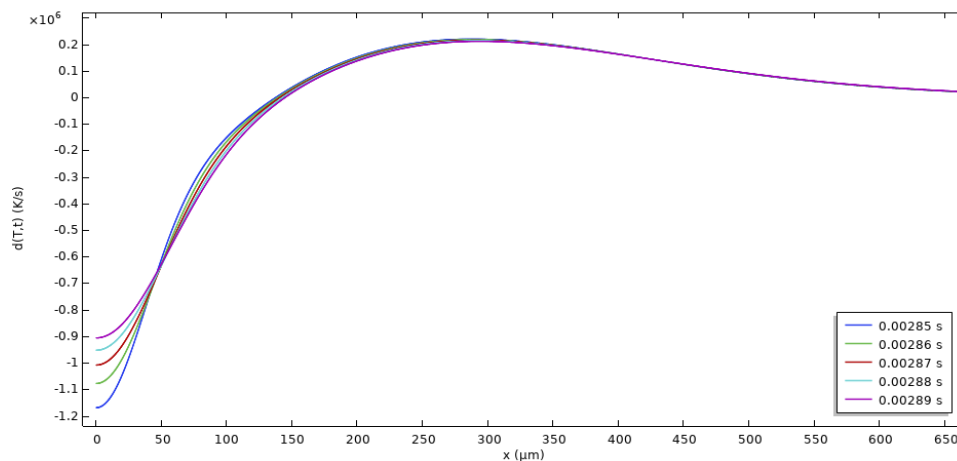


Figure 6. Dependencies of the temperature change rate (cooling rate) of the melt on the x coordinate into the depth of the sample for the moments of time 0.00285 s; 0.00286 s; 0.00287 s; 0.00288 s; 0.00289 s after impulse power input.

The regions of extreme cooling rates are preserved for the moment $t = 0.00285 \text{ s}$ when the complete solidification of the melt occurs. With the complete solidification of the sample, the zone of abnormally rapid cooling disappears, and the dependencies of the temperature change rate dT/dt become monotonous – (Fig. 6). One can see that the cooling rate monotonically decreases from the surface into the sample's interior.

Fig. 7 shows the cooling rate dependence of the melt on the cooling time on the surface and several points in the depth of the sample.

One can see that at distances (15, 20, 30) μm from the surface deep into the sample for a certain period, the cooling rate has maxima which is much higher than the cooling rate on the surface (curve 0 μm in the figure), which corresponds to the creation of a maximum microhardness in the modified layer depth.

The results of numerical simulations also show that the cooling rate is a nonlinear function of time, which corresponds to our mathematical model, in which the thermal conductivity coefficient k is a nonlinear function. The

nonmonotonic dependence of the cooling rate on time also indicates the correctness of the two-phase model “melt-solid” chosen for modeling.

As one can see from the presented results (Fig. 5-7), the dependences obtained during modeling correlate well with the experimentally observed distribution of the modified layer microhardness.

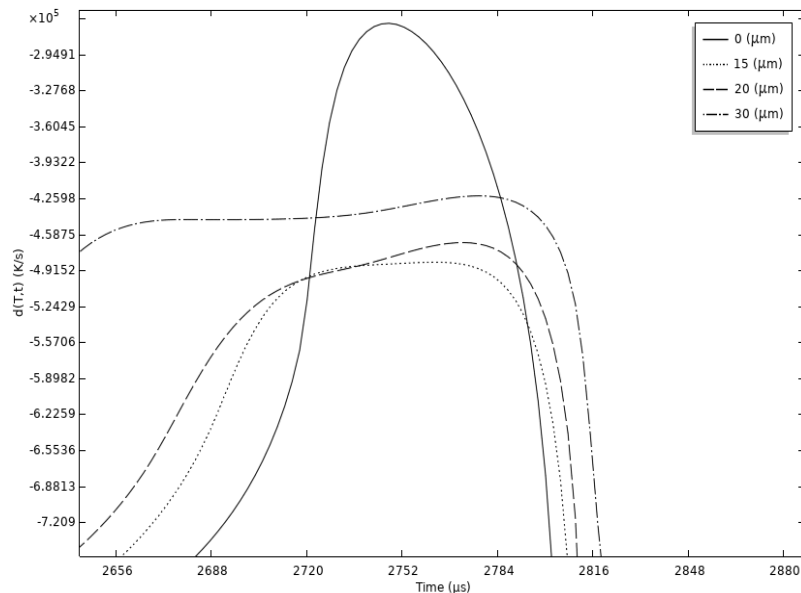


Figure 7. Dependencies of the temperature change rate (cooling rate) dT / dt of the melt on the cooling time on the sample surface ($0 \mu\text{m}$) and at various points deep into the sample ($15 \mu\text{m}$, $20 \mu\text{m}$, $30 \mu\text{m}$, etc).

The formation of microhardness maxima is in the depth of the modified layer and it shifts with increasing depth of the heat-affected zone “heating – cooling” can be explained as follows. It is known that the creation of a hardened layer on the surface occurs as a result of the ultrafast heating-cooling cycle due to two mechanisms: thermal radiation from the surface and the heat conduction mechanism deep into the sample. Due to the implementation of the first mechanism, a “traditional” microhardness maximum on the surface is formed. With a power density growth on the sample surface because of the formation of a molten zone, the second cooling mechanism is also activated - due to the release of heat during the transition of a material part from the liquid to the solid phase. Due to this mechanism, a second microhardness maximum is formed in the modified layer depth [21].

Microhardness growth is associated with structural changes during treatment process. The base of steel 40X10C2M in the initial hypoeutectoid state is ferrite with pearlite ($\alpha\text{-Fe}$) with a BCC lattice. At the “heating and melting” stage, the surface layer temperature rises to 1480°C . This results in the transformation of pearlite into austenite ($\gamma\text{-Fe}$) and forming a phase with an FCC lattice [22]. The transition from the ferrite BCC-structure to the austenite FCC-structure is also facilitated by alloying the molten region with atoms and ions of the consumable iron cathode, nitrogen, oxygen, and other ionized air particles. Thus, at the heating stage, a highly alloyed two-phase solution of α -iron and γ -iron is formed, and the crystallites size of the treated steel ferrite component decreases. At the cooling stage, this solution is partially converted into martensite. As a result, a fine-grained austenitic-martensitic structure occurs, that is, a strengthened alloyed layer. Structural changes lead to substantial growth of layer hardness, microhardness increases by ≈ 5 times.

CONCLUSIONS




1. As a result of pulsed plasma treatment of the surface layer of 40X10C2M steel, a modified layer with improved operational properties is formed: the structure of this layer is homogeneous, without pores and cracks; the microhardness of the layer increases by ≈ 5 times.

2. We discovered a maximum of microhardness in the depth of the modified layer; the localization of the maximum depends on the modes of pulsed plasma treatment. By changing these parameters, it is possible to get the desired profile of the microhardness distribution along with the depth of the modified layer, which makes it possible to form specific operational characteristics of the treated layer.

3. We performed numerical simulations of the rapid pulsed heating of the surface layer using the two-phase model “melt - solid”. We took into account the dynamics of the thermodynamic characteristics of steel. Within the chosen mathematical model framework, numerical simulation was carried out in the Comsol Multiphysics package by the finite element method.

4. We obtained a good agreement of simulation results with experimental data. The chosen computational model allowed us to obtain the character of the change in microhardness deep into the sample, which we observed experimentally.

ORCID IDs

-  Nikolay A. Savinkov, <https://orcid.org/0000-0003-0549-7127>;  Oleh M. Bulanchuk, <https://orcid.org/0000-0002-2801-2244>;
 Aleksander A. Bizyukov, <https://orcid.org/0000-0003-0192-5219>

REFERENCES

- [1] Y. Zhao, B. Gao, G.F. To, S.W. Li, S.Z. Zhao, and C. Dong, Applied Surface Science. **257**, 3913 (2011), <https://doi.org/10.1016/j.apsusc.2010.11.118>
- [2] A.D. Pogrebnjak, and Y.N. Tyurin, Physics-Uspekhi. **48**(5), 487 (2005), <http://dx.doi.org/10.1070/PU2005v048n05ABEH002055>
- [3] A.D. Korotaev, Surface and Coatings Technology. **185** (1), 38-49 (2004), <https://doi.org/10.1016/j.surfcoat.2003.11.021>
- [4] A.A. Skvortsov, S.G. Kalenkov, and M.V. Koryachko, Письма в ЖТФ [Letters in ZhTF], **40**(18), 24 (2014). (in Russian)
- [5] E.V. Haranzhevskiy, D.A. Danilov, M.D. Krivilyov, and P.K. Galenko, Mater. Sci. Eng. A. **375**, 502 (2004), <https://doi.org/10.1016/j.msea.2003.10.040>
- [6] A.G.M. Pukaszewicz, Jr.P.R. C. Alcover, A.R. Capra, and R.S.C. Paredes, Journal of Thermal Spray Technology, **23**(1-2), 51 (2014), <https://doi.org/10.1007/s11666-013-0001-1>
- [7] Y.D. Shitsyn, D.S. Belinin, S.D. Neulybin, and P.S. Kuchev, Modern Applied Science. **9**(6), 64-75 (2015), <https://doi.org/10.5539/mas.v9n6p64>.
- [8] E.S. Vaschuk, E.A. Budovsky, S.V. Raykov, and V.E. Gromov, Фундаментальные проблемы современного материаловедения [Fundamental problems of modern Materials Science]. **10**(1), 68-71 (2013). (in Russian)
- [9] D. Karthik, S. Kalainathan, and S. Swaroop, Surface and Coatings Technology, **278**, 138 (2015), DOI:10.1016/j.surfcoat.2015.08.012
- [10] E.A. Ochoa, D. Wisniveski, T. Minea, M. Ganciu, C. Tauziade, P. Chapon, and F. Alvarez, Surface and Coatings Technology, **203**(10-11), 1457 (2009), <https://doi.org/10.1016/j.surfcoat.2008.11.025>
- [11] V.D. Sarychev, S.V. Kononov and B.B. Haimzon, Известия вузов. Чёрная металлургия [News of universities. Ferrous metallurgy]. **8**, 52 (2011). (in Russian)
- [12] S. Alavi, M. Passandideh-Fard, and J. Mostaghimi. Journal of Thermal Spray Technology. **21**, 248 (2012), <https://doi.org/10.1007/s11666-012-9804-8>.
- [13] D.N. Trushnikov, D.S. Belinin, and Yu.D. Schitsyn, Современные проблемы науки и образования [Modern problems of science and education]. **2**, 95 (2014). (in Russian), <http://www.science-education.ru/ru/article/view?id=12706>
- [14] H. Qu, Ch. Wang, X. Guo, and A. Mandelis. Journal of Applied Physics. **104**(11), 113518 (2008), <https://doi.org/10.1063/1.3035831>.
- [15] V.S. Verkhoribov, Yu.S. Korobov, S.V. Nevezhin, Yu.D. Shitsyn, and I.A. Gilev, Master's Journal. **1**, 81 (2015). (in Russian)
- [16] W. Piekarska, and M. Kubiak. Applied Mathematical Modelling, **37**(4), 2051 (2013), <https://doi.org/10.1016/j.apm.2012.04.052>
- [17] F.Kh. Mirzade, V.G. Niziev, V.Ya. Panchenko, M.D.Khomenko, R.V.Grishaevm, S.Pityana, and Corney van Rooyen, Physica B: Condensed Matter, **423**, 69 (2013), <https://doi.org/10.1016/j.physb.2013.04.053>
- [18] Yu.E. Kolyada, A.A. Bizyukov, O.N. Bulanchuk, and V.I. Fedun, PAST, Series: Plasma Electronics and New Methods of Acceleration, **4**(98), 319 (2015), https://vant.kipt.kharkov.ua/ARTICLE/VANT_2015_4/article_2015_4_319.pdf
- [19] C. Bonacina, G. Comini, A. Fasano, and M. Primicerio, International Journal of Heat and Mass Transfer. **16**, 1825 (1973), [https://doi.org/10.1016/0017-9310\(73\)90202-0](https://doi.org/10.1016/0017-9310(73)90202-0)
- [20] A. I. Volkov, and I. M. Zharvsky, Большой химический справочник [Big chemical reference book], (Soviet School, Moscow, 2005), pp.608. (in Russian)
- [21] N.A. Savinkov, and Yu.E. Kolyada, Вісник Приазовського державного технічного університету: Збірник наукових праць [Bulletin of the Priazovsky State Technical University: Collection of scientific works], **29**, 70 (2014). (in Russian).
- [22] I.K. Razumov, Yu.N. Gornyostrev, and M.I. Katsnelson, Физика металлов и материаловедение [Metal physics and metal studies], **118**(4), 380 (2017). (in Russian)

ВПЛИВ ІМПУЛЬСНОЇ ПЛАЗМОВОЇ ОБРОБКИ НА МІКРОТВЕРДІСТЬ СТАЛІ 40X10C2M: ЕКСПЕРИМЕНТ І ЧИСЕЛЬНЕ МОДЕЛЮВАННЯ

М.О. Савінков^{a,*}, О.М. Буланчук^b, О.А. Бізюков^c

^aАзовський морський інститут НУ «ОМА», вул. Чорноморська 19., Маріуполь, 87517, Україна

^bДонецький державний університет управління, вул. Карпінського 58, Маріуполь, 87513, Україна

^cХарківський національний університет ім. В.Н. Каразіна, пл.Свободи 4, Харків, 61022, Україна

В роботі вивчаються експлуатаційні характеристики сталі 40X10C2M, що застосовується для виготовлення елементів силових установок судна, після високоенергетичної імпульсної плазмової обробки. Для цього використовувалася електротермічний плазмовий прискорювач, в камері якого ініціювався потужнострумний імпульсний дуговий розряд високого тиску з параметрами: тривалість розряду - 1,4 мс, максимальний струм - 5 кА, напруга розряду до 5кВ. Досліджується мікротвердість і мікроструктура обробленого (модифікованого) шару. Визначено оптимальні параметри обробки сталі, які забезпечують найкращі характеристики модифікованого шару: мікротвердість збільшується в ≈ 5 разів. Виявлено максимуми мікротвердості в глибині модифікованого шару. Вивчаються можливість управління локалізацією максимумів, як способу формування потрібних експлуатаційних характеристик обробленого шару. Виконано математичне моделювання швидкого імпульсного нагріву поверхневого шару сталі в рамках двофазної моделі "розплав - тверде тіло" з урахуванням динаміки термодинамічних характеристик сталі. Для цього використовувалося класичне рівняння теплопровідності зі змінними параметрами сталі: густиною, теплоємністю і коефіцієнтом теплопровідності при переході речовини з рідкої в тверду фазу. В рамках обраної математичної моделі були зроблені чисельні розрахунки явища швидкого імпульсного нагріву поверхні сталі з урахуванням плавлення і затвердіння в пакеті Comsol Multiphysics з використанням методу скінчених елементів. Отримано добре узгодження результатів чисельного моделювання з отриманим в експерименті розподілом мікротвердості обробленого шару сталі вглиб зразка.

Ключові слова: плазмова обробка, модифікований шар, мікротвердість, мікроструктура, рівняння теплопровідності, плавлення і затвердіння, швидкість охолодження розплаву.

RESEARCH AND DEVELOPMENT OF FUEL RODS METALLURGICALLY BONDED WITH FUEL CLADDING FOR NUCLEAR INSTALLATIONS[†]

Nikolay N. Belash^a, Anton V. Kushtym^{a*}, Vladimir V. Zigunov^a, Elena A. Slabospyska^a,
Gennadiy A. Holomeyev^b, Ruslan L. Vasilenko^b, Aleksandr I. Tymoshenko^c

^a«Nuclear Fuel Cycle» Science and Technology Establishment

^bInstitute of Solid-State Physics, Materials Science and Technologies

^cInstitute of Plasma Physics, National Science Center «Kharkiv Institute of Physics and Technology»

1, Akademichna St., Kharkiv, 61108, Ukraine

*Corresponding Author: kushtym@kipt.kharkov.ua

Received June 24, 2021; revised July 29, 2021; accepted August 27, 2021

The design and scheme for manufacturing fuel rods metallurgically bonded with ribbed aluminum claddings using hot isostatic pressing and contact-reactive brazing are presented. It is shown that the developed scheme can be used both for production of dispersive fuels and high-density fuels based on uranium alloys. The results of investigations of brazed joints of aluminum cladding with a matrix composition based on aluminum and with samples of E110 alloy through copper and silumin coatings are presented. The results of research of brazed joints of an aluminum cladding with an aluminum-based matrix composition and samples of zirconium alloy E110 made through copper and silumin coating are presented. The strength of brazed joints, composition of diffusion layers formed as a result of contact-reactive brazing in a high vacuum have been determined. The modes of hot isostatic pressing that provide crimping of the ribbed cladding of fuel pellets and rods and obtaining a metallurgical bonding between their surfaces have been defined. It is shown that satisfactory bond strength is provided starting from the temperature of 610 °C. The maximum strength values obtained on the compounds Al-(Al+12% Si)-Zr and Al-Cu-Zr are 57.0 MPa and 55.3 MPa respectively. The fracture of the of aluminum samples joints, obtained with the Cu layer at a temperature of 620 °C, occurs on threaded joints at the strength value of 82 MPa. The results of research of the composition of diffusion layers formed by brazing compounds Al-(Al + 12% Si)-Zr and Al-Cu-Zr are presented. It was established that hot pressing provides the best results for manufacturing of fuel rod dummies in the studied range of modes at a temperature of 630 °C, a pressure of 380 MPa and exposure of 20 minutes.

Keywords: fuel rod, aluminum alloys, dispersive fuel, alloys of uranium, hot isostatic pressing, contact-reactive brazing.

PACS: 28.41.Bm, 81.05.Ni, 81.15.Ef, 81.40.Vw, 81.70.Bt

In connection with the implementation of nuclear non-proliferation programs, the world's initiated work is aimed at the development and production of fuel for research nuclear installations (RNI), with an enrichment of ²³⁵U up to 20% [1-3]. Efforts to develop a promising fuel for most reactors are focused on solving two problems: improving existing fuel and developing new high-density fuel. In this regard, medium-alloyed uranium alloys are considered as promising fuels: U + 7% wt. Mo + 1% wt. Zr ($\rho_U = 16.0 \text{ g/cm}^3$), U + 6% wt. Zr + 4% wt. Nb ($\rho_U = 15.8 \text{ g/cm}^3$), U + 9% wt. Mo ($\rho_U = 15.5 \text{ g/cm}^3$) and uranium compounds: U₃Si ($\rho_U = 15.0 \text{ g/cm}^3$), U₃Si₂ ($\rho_U = 11.3 \text{ g/cm}^3$), UO₂ ($\rho_U = 9.2 \text{ g/cm}^3$) [4,5]. At the initial stage, compositions UAl_x-Al, UO₂-Al, U₃O₈-Al were used, which became widespread. Then much attention was paid to silicide fuel. The U₃Si₂-Al composition with a uranium content loading of 4.8 g/cm³, after successful tests in Oakridge in 1987 was approved by the US Nuclear Regulatory Commission (NRC), and is widely used around the world [5, 6]. This fuel has certain disadvantages. This is a relatively low uranium content and a problem of silicide fuel processing. At the same time, denser fuels based on uranium alloys were developed. Alloys U-(8...10)% Mo by weight are considered promising [7]. Despite the fact that the study of medium-alloyed uranium alloys has produced a significant number of results, it turned out that there are some obstacles to their qualification as fuel for research reactors. The main ones can be summarized as follows [8]: under irradiation, a fuel-aluminum matrix interaction zone consisting of uranium aluminides UAl₂, UAl₃ and UAl₄ is formed; starting from some burnup, gas bubbles begin to form at the aluminum matrix - interaction zone interface due to fission products, introduced into the matrix; with increasing burnup, in the cross sections of the fuel rods located in the zone of maximum energy release, along the line of contact of the zone of interaction with the matrix, gas cavities up to 1...2 mm are formed; further increase in burnup leads to formation of gaps in the fuel core and ballooning of the cladding. Specialists in the development of fuel for research reactors have identified ways to overcome the problem of uranium alloys interaction with aluminum matrix and cladding. These ways consist in alloying of aluminum alloys with 2-8% wt. of silicon, alloying of uranium alloy U+7% wt. Mo with 1% wt. of zirconium or titanium; application of protective coatings of Si, Nb, Zr, ZrN and other materials on fuel cores. The development of fuel rods is carried out using the technology of filling the niobium layer coated fuel composition U-9% wt. Mo with a melt of silumin (Al+12% wt. Si) [6,9]. A prominent place among various designs of fuel for RNI is occupied by fuel rods in aluminum and zirconium claddings. Fuel rods in claddings with spacer ribs are considered promising [3, 8, 10]. Hexagonal, square, circular and other shape fuel assemblies are produced with such fuel rods. Moreover, in most cases they provide metallurgical bonding between the cladding and the core. This allows to significantly reduce operating temperatures of fuel compositions, increase their service life and structural rigidity [4]. Various

[†] Cite as: [N.N. Belash], A.V. Kushtym, V.V. Zigunov, E.A. Slabospyska, G.A. Holomeyev, R.L. Vasilenko, A.I. Tymoshenko, East. Eur. J. Phys. 3, 110 (2021), <https://doi.org/10.26565/2312-4334-2021-3-17>

© N.N. Belash, A.V. Kushtym, V.V. Zigunov, E.A. Slabospyska, G.A. Holomeyev, R.L. Vasilenko, A.I. Tymoshenko, 2021

methods are used for the metallurgical bonding of the cladding and the fuel core, such as hot isostatic pressing, drawing, extrusion, filling with braze melt, for example, with silumin. It is of interest to use the method of hot isostatic pressing (HIP) for manufacturing of rod-type fuel elements [5, 6].

This method allows separate production of claddings with a preset configuration, fuel pellets (rods), to carry out their operative control, product assembly, following which to bring into contact the connected surfaces, and to carry out their metallurgical bonding. The purpose of this work is to develop metallurgically bonded fuel rods and to study the possibility of obtaining bonds of the ribbed cladding with fuel cores by means of HIP in combination with contact-reactive brazing.

SAMPLES, FUEL ROD DUMMIES, RESEARCH METHODS

Preparation procedure, materials, design of samples

The possibility of implementation of the technological scheme for the production of metallurgically bonded fuel rods was introduced in the research. It includes the following main operations:

- production of pellets or rods;
- production of a profiled cladding and plugs of aluminum alloy;
- production of fuel pellets or cores of uranium alloy;
- applying a coating of the materials that form a liquid phase in the temperature range of 550...620 °C on the surface of the pellets;
- attaching the plug to the cladding by argon-arc welding;
- filling the inner space of the cladding with fuel pellets (or a rod-type integral core);
- fuel rod sealing;
- processing of the fuel rod dummy by the HIP method;
- fuel rod leakage control and geometry control.

The following composition of aluminum alloy 6082 (AD35) was used in the research as the cladding material (in wt.%): Al + 0.8% Mg + 1.1% Si + 0.5% Mn + +0.27% Fe + 0.12% Cr + 0.09% Zn + +0.1% Cu. Its chemical composition and characteristics are close to the alloys SAV-1 and 6061, that are used for production of fuel claddings for research reactors [3,4]. UO₂-Al was used as the pellet composition, and HfO₂-Al was used as the simulating composition. Powders of planetary milled alloy 6082 swarf and the industrially produced aluminum powder of the PA-4 brand were chosen as the matrix materials. Pellets of HfO₂-Al composition were produced using the powder metallurgy methods described in detail in [12-14]. Characteristics of fuel pellets are given in Table 1. Uranium alloy core dummies were rods made of alloy E110 (Zr+1% wt. Nb). The choice was made due to the fact that in the future, uranium metal alloys with a protective zirconium coating on the surface can be used.

Two methods of coating formation have been developed: vacuum arc deposition and the method using centrifugal casting in thin-walled zirconium mould [15, 16].

The latter method provides not only strong adhesion of the core surface with the cladding, but also formation of a compensating central hole, moving to the central zone of impurities in the form of oxides, carbides and other compounds, additional doping with zirconium. It should be noted that the experimental metallurgically bonded fuel rods produced using centrifugal casting of uranium alloys in zirconium cladding have proved successful during the in-pile tests at the water coolant temperature of 282 °C, energy density of 21.6 kW/kg at thermal and fast neutron fluxes of 1.16×10^{17} n/m²·s and 0.9×10^{17} n/m²·s [16]. After a burnup of 22 MW day/kgU, they maintained integrity, metallurgical bonding of the fuel cores with the cladding and leak tightness. Testing of the technology and examination research of samples were carried out in two stages. The first stage included studying the characteristics of brazed joints of aluminum with aluminum and zirconium with aluminum made through layers of copper and silumin.

Table 1. Characteristics of dummy fuel pellets

Composition	Fuel dummies (fraction/volume ratio)	Matrix particle shape/fraction	Density of pellets (avg.)
UO ₂ -Al	-400 + 200 μm / 20%	Al-alloy / 112... 315 μm	0.96
Al-alloy	without dummies	grain / 112... 315 μm	0.98
ПА-4	without dummies	grain / 112... 200 μm	0.97
HfO ₂ -Al	-400 + 200 μm / 20%	Al-alloy / 112... 315 μm	0.96

These samples were two cylinders made of aluminum alloy 6082, with threaded ends for securing in the grips of the tensile testing machine. A recess of cylindrical shape with a diameter of 15 mm and a height of 5 mm was made in one of them to center the test samples. Some of the samples were produced of alloy 6082, and some – of alloy E110. Layers of copper or silumin with a thickness of 5...8 μm were applied on the surface of the samples by the vacuum arc deposition technique.



Figure 1. Sample for studying characteristics of brazed joints: Al-Cu-Zr, Al-(Al+12% Si)-Zr, Al-Cu-Al, Al-(Al+12% Si)-Al

Before coating, the surface of the samples was cleaned of oxide films by bombardment with ions of a vacuum arc at a bias voltage -800 V. The current of the vacuum arc was 120 A. The cleaning of samples was carried out in pulsed mode to avoid overheating. The temperature of the samples was monitored with a pyrometer, and it did not exceed 410 °C throughout the process. Coatings on aluminum cylindrical samples and pellets with dispersion compositions were also carried out in pulsed mode at a bias voltage -40 V. The rate of the deposition when using a silumin cathode was ~82 μm/h, and when using copper ~25 μm/h. Coating of E110 alloy products was performed in a continuous mode at a bias voltage -40 V. At the end of the process the samples temperature did not exceed 670 °C. The appearance of pellets with copper and silumin coatings is shown in Fig. 2 a, b.

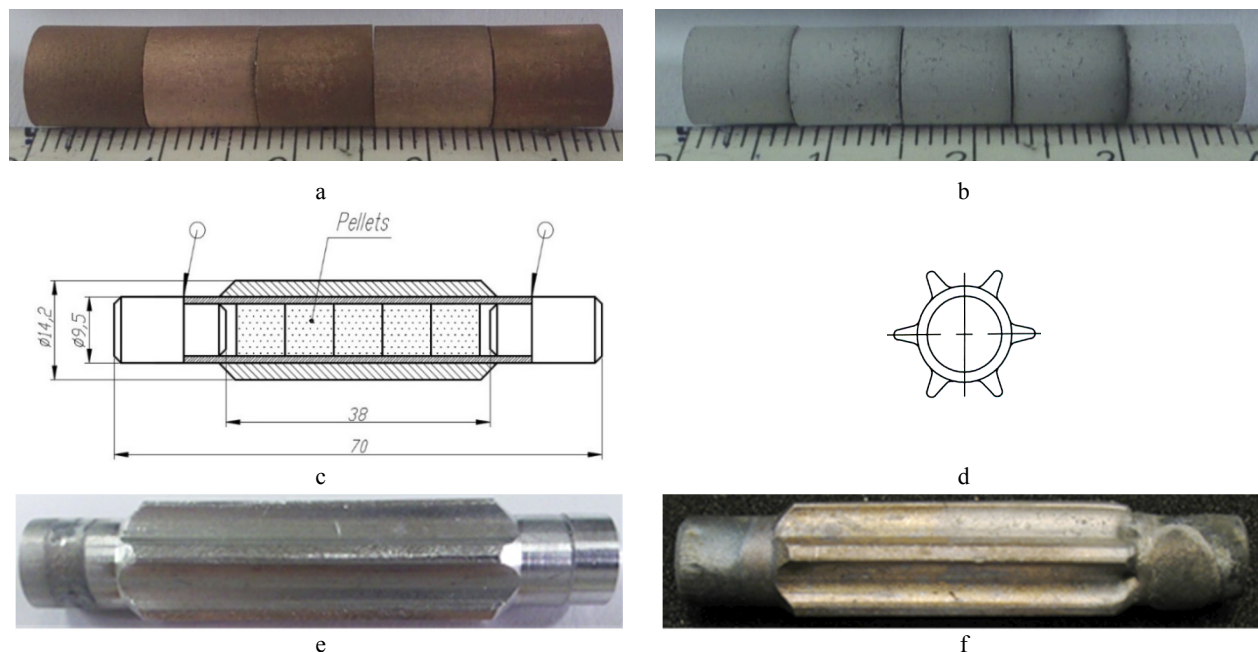


Figure 2. Fuel rod dummies before and after HIP treatment: a, b – pellets of dispersion composition $\text{HfO}_2\text{-Al}$ with copper and silumin coatings; c, d – design of fuel rod dummy; e, f – appearance of the dummy workpiece and fuel rod dummy before and after HIP treatment

Methods

Diffusion bonding of samples (Fig. 1) was performed in a vacuum of 10^{-3} Pa in the temperature range of 600...630 °C. Exposure time ranged from 5 to 30 minutes. The heating rate was 7 °C/min, and cooling rate was 5 °C/min. In the process of testing the modes, the strength of the connection was measured, the interface was studied using metallography, SEM and EDX microanalysis with a scanning electron microscope JSM 7001F at a voltage of 10 kV. EDX microanalysis was performed with an INCA PentaFET*3 detector. Research of influence of HIP modes on characteristics of fuel rod dummies were carried out in the temperature range of 580...630 °C and the pressure range of 340...380 MPa. Exposure time was 10, 15 and 20 minutes. The microstructure of pellets and claddings, as well as the interface between them, were studied on sections produced of molded fuel rod dummies. The degree of contact of the surface of pellets with the surface of cladding was determined by the formula:

$$\varphi = (L_k / L_{total}) \cdot 100\% \quad (1)$$

where φ is the contact factor, L_{total} is the circumference, $L_k = a \cdot R$ is the arc length of the segment (contact), R is the radius of the inner hole of the cladding; a is the angle of the segment.

EXPERIMENTAL RESULTS

Mechanical tests of brazed joints revealed that starting from a brazing temperature of 610 °C, a satisfactory bond strength is provided. The maximum strength values obtained on the bonds Al-(Al + 12% Si)-Zr and Al-Cu-Zr, respectively, were equal to 57.0 MPa and 55.3 MPa. A diffusion layer with a width of 1...6 μm of the following elemental composition (22...40)%wt. Al + (10... 18)% wt. Si + (38...64)% wt. Zr is formed at the interface of the samples with the silumin layer after brazing (Fig. 3a). When using a copper coating after the process that occurs as a result of formation of the liquid phase due to the eutectic interaction in the Al-Cu system, formation of two diffusion layers is observed (Fig. 3b). A layer 30...40 μm thick is formed on the aluminum side. Its composition is: The composition of this layer: (94... 95)% wt. Al + (3...4)% wt. Cu.

A layer 20...30 μm thick is formed on zirconium side. The concentration of elements in the layer varies in the range of (24...40)%wt. Al + (1...13)%wt. Cu + (44...65)% wt. Zr. On all tested samples, destruction occurred at the interface, i.e. along the diffusion layers. In the process of mechanical tests of aluminum samples bonded through a layer of Cu (Al-Cu-Al) at a brazing temperature of 620 °C, their destruction occurred along the thread (screw) joint (Fig. 5a).

Estimations revealed that the strength of the connection in this case exceeds 82 MPa. A thin diffusion layer 1...3 μm thick is formed at the interface of brazed samples (Fig. 5b). The results of research of the influence of HIP modes on the characteristics of joints in the fuel rod dummies are presented in Table 2 and in Fig. 6. The obtained results reveal that in mode 1 (Table 2), there is only 45...50% contact of the cladding and the core (Fig. 6a). Increasing the temperature up to 610 °C and the pressure up to 360 MPa leads to an increase in the contact surface to ~ 65...75% (Fig. 6b). The pellet-to-cladding gap varies from 18 μm to 211 μm. In mode 3 (T = 630 °C, P = 380 MPa, τ = 20 min), the coefficient of contact of the core with the cladding is ~ 90...95% (Fig. 6c).

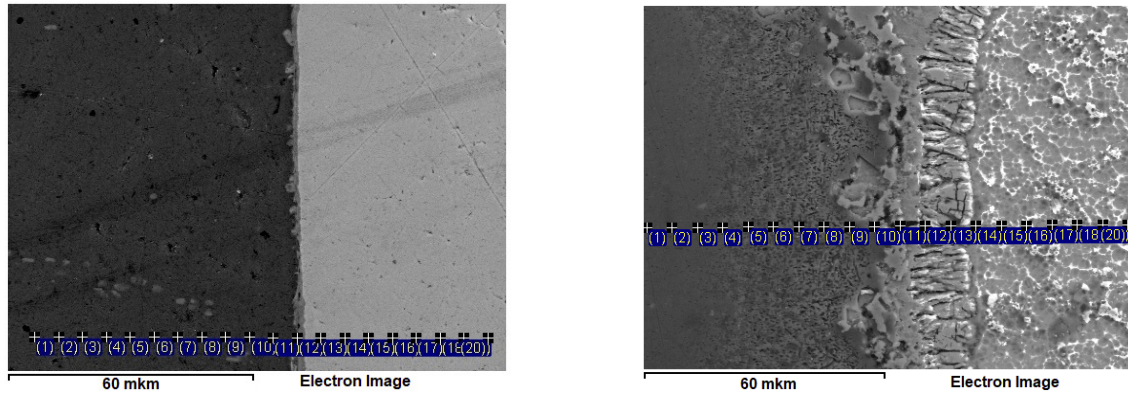


Figure 3. Brazed joint interface: a – Al-(Al+12% Si)-Zr; b – Al-Cu-Zr

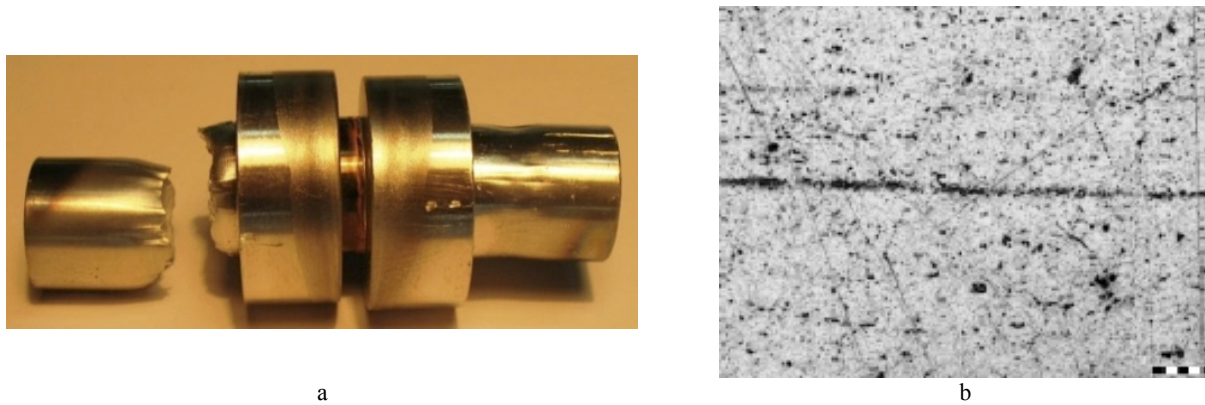


Figure 4. Results of mechanical tests and research of Al-Cu-Al connection: a – the destruction after mechanical tests; b – interface of the section

Table 2. Influence of HIP modes on the characteristics of fuel rod dummies

Test modes	Temperature, °C,	Pressure, MPa,	Exposure, min,	Contact factor (φ),%
#1	590	340	10	40...50
#2	610	360	15	65...75
#3	630	380	20	≥95

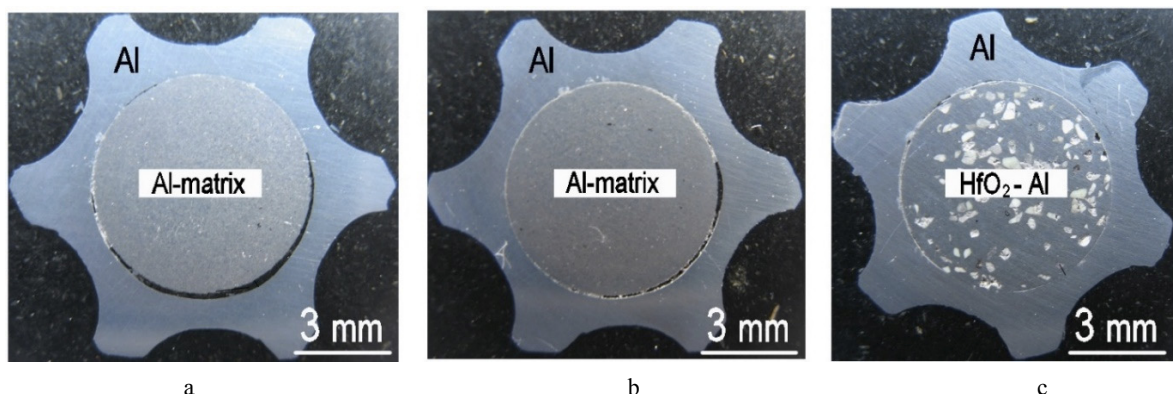


Figure 6. Appearance of cross sections of fuel rod dummies after HIP treatment in different modes: a – mode #1; b – mode #2; c – mode #3

These data indicate the presence of metallurgical bonding between the cladding and the surface of the pellet. The boundary of the connection of the cladding with the aluminum matrix and the core dummy with the matrix are shown in Fig. 7. Vickers microhardness values of the aluminum cladding, aluminum matrix and fuel dummies are: 500...560 MPa, 608...620 MPa and 686...735 MPa respectively.

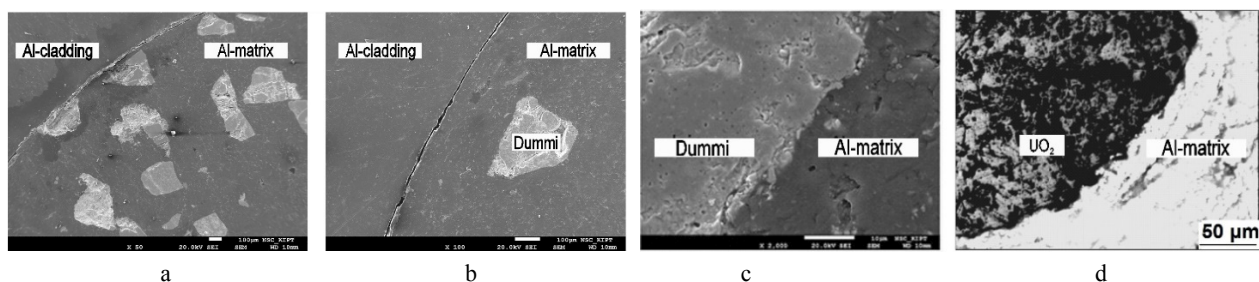


Figure 7. SEM microstructure cross-section of fuel rod dummy with dispersion composition pellets of UO_2 and dispersion composition $\text{UO}_2\text{-Al}$: a – $\times 50$; b – $\times 100$; c – $\times 2000$; d – dispersion composition $\text{UO}_2\text{-Al}$

CONCLUSIONS

The directions for the development of fuel compositions and designs of fuel rods for research nuclear installations have been determined. The possibility of implementation realization of the technological scheme for production of rod-type metallurgically bonded fuel elements with ribbed cladding by hot isostatic pressing in a combination with contact-reactive brazing is shown. The modes of applying copper and silumin coatings on aluminum and zirconium samples by vacuum arc deposition technique and obtaining joints by contact-reactive brazing and hot isostatic pressing have been worked out. It is shown that satisfactory bond strength is provided starting from the temperature of 610 °C. The maximum strength values obtained on the compounds Al-(Al+ 12% Si)-Zr and Al-Cu-Zr are 57.0 MPa and 55.3 MPa respectively. The fracture of the of aluminum samples joints, obtained with the Cu layer at a temperature of 620 °C, occurs on threaded joints at the strength value of 82 MPa. The results of research of the composition of diffusion layers formed by brazing compounds Al-(Al + 12% Si)-Zr and Al-Cu-Zr are presented. It was established that hot pressing provides the best results for manufacturing of fuel rod dummies in the studied range of modes at a temperature of 630 °C, a pressure of 380 MPa and exposure of 20 minutes.

ORCID IDs

- Anton V. Kushtym, <https://orcid.org/0000-0001-7058-373X>; Vladimir V. Zigunov, <https://orcid.org/0000-0002-2663-1033>;
 Elena A. Slabospyska, <https://orcid.org/0000-0002-0749-220X>; Gennadiy A. Holomeyev, <https://orcid.org/0000-0003-1779-9050>;
 Ruslan L. Vasilenko, <https://orcid.org/0000-0002-4029-9727>; Oleksandr I. Tymoshenko, <https://orcid.org/0000-0001-9163-1067>

REFERENCES

- [1] V.G. Aden, E.F. Kartashev, V.A. Lukichev, P.I. Lavrenyuk, V.M. Chernyshov, A.V. Vatulin, A.V. Morozov, V.B. Suprun, A.B. Alexandrov, and A.A. Enin. PAST, **5**, 3 (2005), https://vant.kipt.kharkov.ua/ARTICLE/VANT_2005_5/article_2005_5_3.pdf
- [2] R.G. Muranaka, IAEA Bulletin, **25**(1), 18 (1983), <https://www.iaea.org/sites/default/files/25105381821.pdf>
- [3] A.V. Vatulin, I.V. Dobrikova, V.B. Suprun, and G.V. Kulakov, Questions of atomic science and technology. Series: Materials Science and New Materials, **1**(74), 39 (2013), <https://elibrary.ru/item.asp?id=21397636>
- [4] A.G. Samoilov, A.I. Kashtanov, and V.S. Volkov, *Dispersion fuel elements of nuclear reactors*, (Atomizdat, Moskov, 1969), p. 584.
- [5] B.W. Pace, and E.A. Marinak, in: *International Meeting on Reduced Enrichment for Research and Test Reactors* (RERTR) (Budapest, 1999), <https://www.rertr.anl.gov/Web1999/Abstracts/14pace99.html>
- [6] Y.S. Kim, and G.L. Hofman, J. of Nucl. Mat. **410**, 1 (2011), <https://doi.org/10.1016/j.jnucmat.2010.12.031>
- [7] G.L. Hofman, M.K. Meyer, J.L. Snelgrove, M.L. Dietz, R.V. Strain, and K-H. Kim, in: *International Meeting on Reduced Enrichment for Research and Test Reactors* (RERTR). (Budapest, 1999), <https://www.rertr.anl.gov/Web1999/Abstracts/08hofman99.html>
- [8] G.A. Birzhevoy, R.Kh. Gibadullin, A.D. Karpin, V.V. Popov, V.N. Sugonyaev, and Yu.A. Fedorov, in: *IX Russian Conference on Reactor Materials Science*, (Dimitrovgrad, 2009), pp. 436-443.
- [9] H.J. Ryu, J.M. Park, K.H. Lee, B.O. Yoo, Y.H. Jeong, Y.J. Jeong, and Y.S. Lee, in: *European Research Reactor Conference*, (St. Petersburg, 2013), pp.115-123.
- [10] A.V. Vatulin, Yu. A. Stetsky, V.B. Suprun, I.V. Dobrikov, V.A. Mishunin, A.B. Alexandrov, and A.A. Enin, Patent RU No. 2267175 (14 october 2003) (in Russian).
- [11] S.Yu. Sayenko, Nuclear and radioactive safety, **1**(65), 41 (2015), <https://nuclear-journal.com/index.php/journal/article/view/355>
- [12] N.N. Belash, A.V. Kushtym, V.V. Zigunov, V.S. Krasnorutsky, Patent Ukraine No. 112268, (10 August 2016). (in Ukrainian).
- [13] N.N. Belash, A.V. Kushtym, V.V. Zigunov, V.A. Zuek, A.I. Bol'shak, and A.M. Stepanenko, in: *3 International conference "High-purity materials: obtaining, applications, properties"*, (NSC KIPT, Kharkov, 2015), pp. 94.
- [14] A.V. Kushtym, N.N. Belash, I.A. Chernov, V.M. Evseev, E.A. Slabospitskaya, E.B. Valezhny, V.A. Zuek, V.V. Zigunov, in: *International Conference "Improving the Safety and Efficiency of Nuclear Energy"*, (ONPU, Odessa, 2014), pp. 271-281.
- [15] Belash N.N., Tatarinov V.R., Ragulina N.I., Danilova O.V., and Semenov N.A. Problems of Atomic Science and Technology. Series: "Physics of radiation damage and radiation materials science". **3**(81), 88 (2002), <http://dspace.nbu.gov.ua/handle/123456789/80090>
- [16] V.S. Krasnorutsky, N.N. Belash, V.R. Tatarinov, Problems of Atomic Science and Technology. Series: "Physics of radiation damage and radiation materials science". **6**(82), 120 (2002), https://vant.kipt.kharkov.ua/ARTICLE/VANT_2002_6/article_2002_6_120.pdf

**РОЗРОБКА ТА ДОСЛІДЖЕННЯ ТВЕЛІВ З МЕТАЛУРГІЙНИМ З'ЄДНАННЯМ СЕРДЕЧНИКА
І ОБОЛОНКИ ДЛЯ ЯДЕРНИХ УСТАНОВОК****М.М. Бєлаш^а, А.В. Куштим^а, В.В. Зігунов^а, О.О. Слабоспицька^а****Г.О. Холомєєв^б, Р.Л. Василенко^б, О.І. Тимошенко^с**^а*Науково-технічний комплекс «Ядерний паливний цикл»*^б*Інститут фізики твердого тіла, матеріалознавства і технологій*^с*Інститут фізики плазми Національного наукового центру «Харківський фізико-технічний інститут»**вул. Академічна, 1, м. Харків, 61108, Україна*

Приведені конструкція та схема виготовлення стрижневих твелів з ребристою алюмінієвою оболонкою зчепленого варіанту з використанням методів гарячого ізостатичного пресування та контактної-реактивної пайки. Показано, що розроблена схема може бути використана як для виготовлення дисперсійного, так і високощільного палива на основі сплавів урану. Представлені результати досліджень паяних з'єднань алюмінієвої оболонки з матричною композицією на основі алюмінію та із зразками зі сплаву E110 через мідне та силумінове покриття. Визначені міцність паяних з'єднань, склад дифузійних шарів, що утворюються в результаті контактної-реактивної пайки у високому вакуумі. Визначені режими гарячого ізостатичного пресування, що забезпечують обжимання ребристою оболонкою паливних таблеток і стрижнів та одержання металургійного з'єднання між їхніми поверхнями. Показано, що починаючи з температури 610 °С забезпечується задовільна міцність зчеплення паяних з'єднань, а максимальні значення міцності, отримані на з'єднаннях Al-(Al+12%Si)-Zr і Al-Cu-Zr, відповідно, становлять 57,0 МПа і 55,3 МПа. Приведені результати досліджень складу дифузійних шарів, що утворюються в результаті пайки з'єднань: Al-(Al+12%Si)-Zr і Al-Cu-Zr. Встановлено, що при використанні гарячого пресування найкращі результати для виготовлення макетів твелів в досліджуваному діапазоні режимів забезпечуються за температури 630 °С, тиску 380 МПа і тривалості процесу 20 хвилин. Відпрацьовані режими нанесення мідного і силумінового покриттів на алюмінієві та цирконієві зразки вакуумно-дуговим методом (КІБ) та одержання з'єднань контактної-реактивною пайкою в комбінації з гарячим ізостатичним пресуванням.

Ключові слова: стрижневі твели, сплави алюмінію, дисперсійне паливо, сплави урану, гаряче ізостатичне пресування, контактної-реактивна пайка.

MECHANISMS OF DEGRADATION OF THE DETECTING PROPERTIES OF CdTe AND CdZnTe UNDER GAMMA RADIATION EXPOSURE[†]

 **Alexandr I. Kondrik**

National Science Center "Kharkiv Institute of Physics and Technology"

1, Academichna str., 61108 Kharkiv, Ukraine

E-mail: kondrik@kipt.kharkov.ua

Received June 9, 2021; revised July 27, 2021; accepted July 29, 2021

This work is devoted to the study of the mechanisms of the influence of radiation defects, arising under the influence of gamma irradiation, on the change in resistivity ρ , lifetime of nonequilibrium electrons τ_n and holes τ_p , in CdTe:Cl and Cd_{0.9}Zn_{0.1}Te as well as the collection efficiency η of uncooled radiation detectors based on these materials, by computer simulation method. Radiation defects, that are corresponded by deep energy levels in the band gap, act as trapping centers of nonequilibrium charge carriers, noticeably affect the degree of compensation by changing ρ of the detector material, the recombination processes by decreasing τ_n and τ_p , what ultimately can cause degradation of the charges collection efficiency η . The specific reasons for the deterioration of the detector properties of CdTe:Cl and Cd_{0.9}Zn_{0.1}Te under the influence of gamma irradiation were identified, and the main factors leading to complete degradation of the recording ability of detectors based on these semiconductors during their bombardment by ⁶⁰Co gamma quanta were determined. The gradual degradation of the spectroscopic performance of CdTe:Cl-based detectors during gamma irradiation occurs due to the continuous formation of cadmium vacancies V_{Cd} and acceptor complexes $V_{Cd} - Cl$, which continuously shift Fermi level towards valence band and decrease ρ . The complete performance degradation of CdTe detectors takes place mainly due to the capture of nonequilibrium electrons at energy level of interstitial tellurium Te(I). The invariable spectroscopic properties of CdZnTe-based sensors under gamma irradiation up to 25 kGy occur due to the mechanism of radiative self-compensation by formation of substitutional defect Te_{Zn}. At the final stage of irradiation, a sharp deterioration in the detector properties of CdZnTe occurs, mainly due to the capture and recombination of nonequilibrium charge carriers at the level of the Te(I) defect. The different radiation resistances of CdZnTe and CdTe:Cl can be explained by different behavior of Fermi level E_F in these semiconductors under gamma irradiation. E_F in CdZnTe under radiation exposure remains near the middle of band gap, and in CdTe it drifts to the valence band. The rate of capture and recombination through Te(I) donor level in CdTe:Cl is lower than in CdZnTe due to the larger difference between the Fermi level and the radiation defect Te(I) level in cadmium telluride. Thereby, the complete degradation of the CdTe:Cl detector occurs at a higher concentration of radiation defect Te(I), and hence after a higher irradiation dose of 50 kGy compared with a dose of 30 kGy required for degradation of CdZnTe detector properties.

Keywords: detector properties, simulation, CdTe, CdZnTe, gamma irradiation, radiation defects

PACS: 29.40.Wk; 61.72.Ji; 61.82.Fk

CdTe is considered as a promising material for semiconductor uncooled gamma-ray sensors used in radiation control and monitoring systems of radiation materials, in nuclear power, in imaging systems, as well as in nuclear medicine and solar power engineering [1-4]. A certain disadvantage of CdTe detectors is appeared in the polarization effect that appears in the matrix after long term operation. Currently, cadmium telluride is usually doped with zinc up to 10 – 15 wt% in order to increase the bandgap E_G and resistivity ρ , what allows increasing the bias voltage to prevent the polarization effects [5]. At present, Cd_{0.9}Zn_{0.1}Te (CZT), which has the band gap of about 1.57 eV at 300 K and the resistivity ρ higher by 1–2 orders of magnitude as compared to that of CdTe, is very common semiconductor material for γ -ray sensors operating at room temperature [6, 7]. The application of up-to-date CZT-based detectors, for example, with orthogonal coplanar strip electrodes, allows to achieve the photo-peak resolution in pulse amplitude spectra of about 1% at 662 keV [8, 9].

In the process of achieving the detecting quality in CdTe and CZT, some intrinsic defects appear in their matrix with the corresponded energy levels in the band gap, which change the degree of compensation, decreasing ρ , and act as traps of nonequilibrium charge carriers generated by the registered gamma radiation. To electrically compensate the charged states of the trap levels and increase the crystal resistivity, CdTe is often doped with chlorine, and CZT is doped with aluminum, indium, or yttrium. Al, In, Y act as substitutional impurities instead of cadmium, and Cl - instead of tellurium [10]. These compensating donor dopants are introduced to CdTe and CZT materials in the amount of 1-2 ppm or $\sim 10^{16}$ cm⁻³ [11, 12].

When CdTe and CZT detectors are used in an aggressive radiation environment, they are exposed to irradiation with gamma quanta, which can cause radiation damage in the crystal structure and, therefore, significantly affect their spectroscopic performance. Elucidation of the mechanisms of this effect is of great importance for detectors application in various fields, as well as for the improvement of radiation monitoring methods. Previous studies of ⁶⁰Co gamma irradiation [13–15] have shown that CdTe materials are insensitive to radiation damage up to an absorbed dose of several thousand gray. When the dose exceeds this value, the resistivity begins to decrease gradually. The spectroscopic performance continuously deteriorates, although the detectors can still operate in spectroscopic mode under irradiation of

[†] Cite as: A.I. Kondrik. East. Eur. J. Phys. 3, 116 (2021), <https://doi.org/10.26565/2312-4334-2021-3-18>

25 kGy. Irradiation doses over 30 kGy cause the actual degradation of the electrophysical and detector properties [14, 15]. Low-dose gamma-irradiation of CZT causes an increase in resistivity with its subsequent decrease at larger doses [16, 17]. High doses of gamma irradiation of CZT induce radiation defects that accumulate negative space charges, which significantly distorts the distribution of the electric field and reduces the mobility of electrons due to increase of the effect of scattering on clusters of ionized impurities [18]. This experimental fact is in agreement with the numerical simulations results obtained in [19], where it was shown that a decrease in the electron mobility μ_n in $\text{Cd}_{0.9}\text{Zn}_{0.1}\text{Te}$ by approximately two to three times could be caused by the scattering of conductivity electrons on clusters of charged point defects. Earlier experimental studies of radiation damage caused by gamma-quanta bombardment in CdTe and CZT detectors were mainly devoted to the effect of radiation dose on device performance [1, 3, 13–17]. Detector materials CdTe and CZT have a high resistivity of 10^9 – 10^{11} $\Omega\cdot\text{cm}$, what greatly complicates investigating at a microscopic scale the mechanisms of change and degradation of their electrophysical and detector properties under the influence of radiation defects, basing only on experimental techniques. In this regard, it is very important to use mathematical and computer simulation as an additional research tool based on known experimental results and proven physical models.

The object of the work was a model study of the effect of radiation defects arising under the influence of gamma irradiation on the degradation mechanisms of the electrophysical and detector properties of CdTe:Cl and $\text{Cd}_{0.9}\text{Zn}_{0.1}\text{Te}$. Calculations of the electron mobility μ_n , resistivity ρ , lifetime of nonequilibrium electrons τ_n and holes τ_p , and charge collection efficiency η , depending on the concentration of doping shallow donors for different impurity and defect compositions of the samples, before and after gamma irradiation, have been carried out.

MATERIALS AND MODELS

The main parameters of the i -th deep levels of defects that determine the detector properties of CdTe, CdZnTe are the concentration N_i , capture cross section σ_i , and position in the band gap (activation energy) E_i [17, 20, 21]. Measurements of N_i , σ_i , E_i are carried out using techniques based on the forced filling of energy levels with electrons and holes, followed by their emission into the corresponding bands. The measurements at certain instants of the currents of charge carriers emitted from the levels in a wide temperature range make it possible to obtain spectra with pronounced peaks at certain temperatures corresponding to the certain positions of the energy levels E_i . The height of the peaks and their width are determined, respectively, by the concentration of levels N_i and the capture cross section σ_i of nonequilibrium charge carriers. Overlapping these peaks can significantly distort the true values of N_i , E_i , and σ_i . In this regard, in published works, as a rule, there are disagreements in measuring the positions of energy levels in the band gap and even the lack of reproducibility of these values in different papers of the same authors. Nevertheless, in [14–16, 20], as well as in some other papers of these authors, there is an acceptable repeatability of E_i measurements, based on a well-developed technology of CdTe and CZT detectors production, what allows using the results, obtained by these authors, for correct identification of levels of radiation-induced and technological defects, as well as for studies of their evolution under radiation exposure. To get more accurate values of the capture cross sections σ_i , one can use the results of paper [22], where the contribution of all levels to the currents emitted into the corresponding bands was simultaneously taken into account.

The applied models and their testing are described in detail in [19], and the spectral characteristics of the initial and irradiated CdTe:Cl and $\text{Cd}_{0.9}\text{Zn}_{0.1}\text{Te}$ are taken from [14, 15]. First, an equation of electroneutrality was compiled with all impurities and defects, which were experimentally recorded in [14], taken into account. This equation was solved numerically with respect to the Fermi level E_F , then the concentrations of free electrons n and holes p were determined in the parabolic band approximation. The electron mobility μ_n was calculated in the momentum relaxation time approximation (tau-approximation) taking into account the mechanisms of scattering by ionized and neutral centers, acoustic and piezoelectric phonons, optical phonons, as well as scattering by clusters of point defects. The hole mobility μ_p was assumed to be invariable and equal to 70 $\text{cm}^2/(\text{V}\cdot\text{s})$. Specific conductivity was calculated using the formula: $e\cdot n\cdot\mu_n + e\cdot p\cdot\mu_p$. Resistivity was calculated as the reciprocal of conductivity. Basing on the experimentally measured band-to-band recombination coefficients [23], it was found that the rate of band-to-band recombination in the materials under study at room temperature was approximately ten orders of magnitude lower than the rate of recombination through deep levels of impurities and defects, described by the Shockley-Reed-Hall statistics which was therefore assumed to be the basis for calculating the lifetimes of nonequilibrium charge carriers τ_n , τ_p . The charge collection efficiency η of the detector was determined by the Hecht equation [24, p. 489]. As in [14, 15], the distance between the electrodes was assumed to be 1 mm, and the electric field strength was 500 V/cm for CdTe:Cl and 3000 V/cm for CZT.

The specific composition of the materials was taken from [14, 15], then the concentrations of background impurities and defects were determined, which ensured the coincidence of the calculated values $\rho = 2\cdot 10^9$ and $\rho = 1\cdot 10^{11}$ $\Omega\cdot\text{cm}$ respectively for CdTe and CZT with the values experimentally measured by the authors of paper [15] before irradiation. A typical initial composition of the CdTe detector material is presented in Table 1, and $\text{Cd}_{0.9}\text{Zn}_{0.1}\text{Te}$ -based material – in Table 2. In addition to [14, 15], a similar composition is described, for example, in [12, 17, 25, 26]. The table also lists the capture cross sections for the levels σ_i , whose order of magnitude was determined in [22]. The charge state of defects is indicated as plus (+) for the donors, whose energies are measured relative to the bottom of the conduction band E_C , and by minus (–) for the acceptor levels with energy relative to the top of the valence band E_V .

Indications and the probable nature of some levels are described in [12, 17, 25]. The alloying impurities of the shallow donor levels (Cl_{Te} , In_{Cd}) introduced into the matrix of the studied materials are designed to compensate for

acceptors (AX, A0, A, A1, K, X) and achieve a high-resistance state required for detectors operation. The defects AX, A0, A, A1, K, X, according to the authors [14, 15, 16, 20], as well as to the most of the researchers, are complexes of cadmium vacancies with various alloying and background impurities. Similarly, the vacancy of cadmium may correspond to D or J defect [17, 27]. Donor levels I⁺ and H1⁺ represent, respectively, a tellurium vacancy V_{Te} and substitutional defect Te_{Zn} or Te_{Cd} [28-30]. At the final stage of gamma irradiation, the donor defect Z appears in the PICTS spectra, which apparently corresponds to the interstitial tellurium Te(I). At the final stage of gamma irradiation, a donor level Z appears in the PICTS spectra, the nature of this defect is not unambiguous: it can be either interstitial cadmium Cd(I) or interstitial tellurium Te(I) [27, 28]. The author of this paper assume that the defect Z is interstitial tellurium.

Table 1. Composition of the initial CdTe with a resistivity of 2·10⁹ Ω·cm

Defect	Cl _{Te} ⁺	AX ⁻	A0 ⁻	A ⁻	A1 ⁻	X ⁻	D ²⁻	G ⁻	H ⁻	H1 ⁺	I ⁺
E _i , eV	0.014	0.11	0.12	0.14	0.16	0.28	0.35	0.64	0.77	0.82	1.01
σ _i , cm ²	1·10 ⁻²¹	3·10 ⁻²⁰	4·10 ⁻²⁰	10 ⁻¹⁹	2·10 ⁻¹⁹	4·10 ⁻¹⁹	7·10 ⁻¹⁷	3·10 ⁻¹⁷	1.3·10 ⁻¹⁷	4·10 ⁻¹⁷	10 ⁻¹⁸
N _i , cm ⁻³	1.7·10 ¹⁶	3.3·10 ¹⁴	7·10 ¹⁵	2·10 ¹⁵	2·10 ¹⁵	2·10 ¹⁵	2·10 ¹⁵	8·10 ¹⁵	9·10 ¹⁵	7·10 ¹⁵	8.5·10 ¹⁵

Table 2. Composition of the initial CdZnTe with a resistivity of 1·10¹¹ Ω·cm

Defect	In _{Cd} ⁺	A ⁻	A1 ⁻	K ⁻	X ⁻	D ²⁻	J ⁻	Y ⁻	W ⁻	H1 ⁺	I ⁺
E _i , eV	0.019	0.14	0.16	0.25	0.29	0.35	0.53	0.67	0.70	0.86	1.1
σ _i , cm ²	1·10 ²¹	2·10 ⁻¹⁹	2·10 ⁻¹⁹	6·10 ⁻¹⁹	4·10 ⁻¹⁹	7·10 ⁻¹⁷	5·10 ⁻¹⁷	10 ⁻¹⁷	10 ⁻¹⁷	10 ⁻¹⁸	10 ⁻¹⁸
N _i , cm ⁻³	1.9·10 ¹⁶	2·10 ¹⁵	2·10 ¹⁵	2.5·10 ¹⁵	2.5·10 ¹⁵	2·10 ¹⁵	5·10 ¹⁴	3·10 ¹⁵	3·10 ¹⁵	5·10 ¹⁵	4.5·10 ¹⁵

The calculated electrophysical properties of the unirradiated materials corresponded to known values: μ_n~1200 cm²/(V·sec), the lifetimes of electrons τ_n and the holes τ_p were about 10⁻⁶ seconds for both materials. The changes in ρ, μ_n, τ_n, τ_p, the positions of the Fermi level E_F in the band gap of CdTe:Cl and CZT, as well as the change in the charge collection efficiency η of the detector based on these materials were simulated depending on the content of radiation defects and the concentration of alloying donors N_D at T = 20°C – operating temperature of the detectors.

RESULTS AND DISCUSSION

The effect of radiation damage caused by the ⁶⁰Co gamma irradiation of two sets of detectors based on CdTe:Cl and Cd_{0.9}Zn_{0.1}Te, on the changes of their resistivity and spectroscopic properties, was experimentally investigated in [14, 15]. The initial dose of γ-irradiation of both sets of sensors in a ⁶⁰Co gamma cell was 10 kGy. The total doses up to 50 and 30 kGy were delivered in steps of 5 kGy each to CdTe:Cl and Cd_{0.9}Zn_{0.1}Te detectors, respectively. The resistivity and the energy resolution of the main photopeak of the ⁵⁷Co spectrum recorded using the detectors under study were determined before and after gamma irradiation. The energy levels in the band gap were determined by photoinduced current transient spectroscopy - PICTS. The measurement results obtained in [14, 15] served as the source data in present work to simulate the change and degradation of electrophysical and detector properties of CdTe:Cl and CZT under the influence of gamma irradiation.

CdTe:Cl-based detectors

CdTe:Cl-based detectors were exposed to 122 keV ⁶⁰Co gamma irradiation by the dose of 10 to 50 kGy. With an increase in the radiation dose, there was a gradual degradation of ⁵⁷Co and ¹²²Am spectra and a shift of the main photopeaks toward lower energies and their gradual broadening by 7-8%, what indicated a decrease in charge collection. In the process of exposure, a gradual decrease in the specific resistance of Δρ for CdTe:Cl was recorded, and Δρ reached 60% at the moment of complete degradation of detector properties after the radiation dose of 50 kGy. The PICTS technique, used to study the behavior of radiation defects, registered an increase in the concentrations of A-centers (AX, A0, A, A1 levels) and a decrease in the relative content of defects G, H, H1, I at an increase in the radiation dose. The peak of defect Z in PICTS spectra appears only in a completely degraded detector. The results obtained in [14, 15] were used in the present work to simulate changes in the electrophysical and detector properties of CdTe:Cl in the process of gamma irradiation.

Fig. 1 shows the changes in the specific resistance of CdTe:Cl subject to the concentration of alloying chlorine impurity after different doses of gamma irradiation. The concentrations of irradiation-induced A-centers are gradually increasing and after the dose of 50 kGy reach the following values, cm⁻³: N(AX)=2.5·10¹⁵, N(A0)=2,1·10¹⁶, N(A)= 2·10¹⁵; N(A1)=2.5·10¹⁵. The concentrations of deep levels are gradually decreasing and at the moment of complete degradation reach the following values, cm⁻³: N(G)=6·10¹⁵, N(H)=8·10¹⁵, N(H1)=6.5·10¹⁵, N(I)=7.5·10¹⁵. These concentrations are estimated values that gradually changed during irradiation. The variation range of N(Cl) in the figure is presented so that the curves of the specific resistance ρ would pass through the maxima. The vertical dashed line indicates the chlorine concentration at which the hole conductivity and the specific resistance ρ=2·10⁹ Ω·cm, measured in [15], is observed in the initial CdTe:Cl, therefore it can indicate the material under study. In Fig. 1 we see a confirmed experimentally gradual decrease in the resistivity with an increase in the radiation dose due to the shift of the curves ρ(N(Cl)) towards greater

chlorine concentrations. This shift is caused by a gradual increase in the content of electrically active acceptor A-centers (AX, A0, A, A1), whose compensation requires increased concentrations of the shallow chlorine donor. We see that after the dose of 50 kGy, the resistance decreases markedly, which leads to an increase in leakage currents and complete degradation of the detector properties. A significant decrease in ρ occurred due to the shift of the Fermi level towards the A centers levels and valence band.

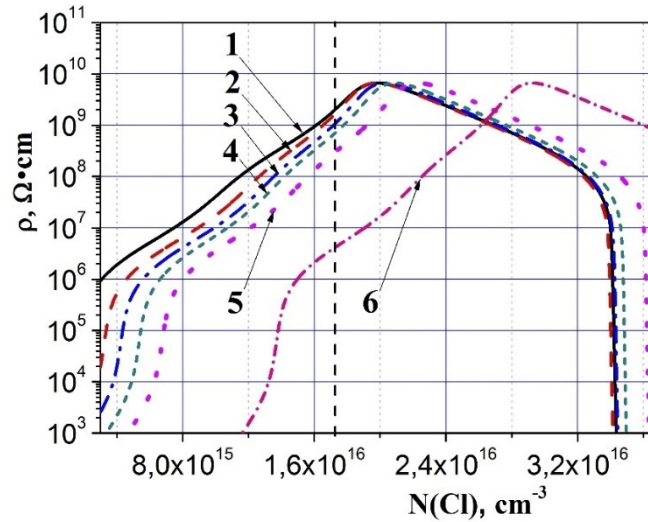


Figure 1. Dependences of the of CdTe:Cl resistivity on the Cl concentration after different doses of gamma irradiation, kGy: 1 – initial, whose composition is shown in Table 1; 2 - 10; 3 - 15; 4 - 20; 5 - 25; 6 - 50. The vertical dashed line indicates the concentration of doping chlorine ($1.7 \cdot 10^{16} \text{ cm}^{-3}$) for the test sample

Fig. 2 shows the dependences of the Fermi level on the concentration of the substitutional impurity Cl_{Te} after different doses of gamma irradiation. For the sample under study, a shift in the Fermi level, which is accompanied by an increase in the hole conductivity and a decrease in ρ , is clearly visible. With an increase in the concentration of shallow levels of A-centers, the content of deep levels G, H, H1 slightly decreases and, for this reason, the Fermi level does not stabilize in the vicinity of these deep levels and, correspondingly, the electrophysical properties vary, what leads to a gradual degradation of the recording ability of the CdTe:Cl-based detector. This agrees with the experiment, described in [14, 15], where it has been demonstrated by the example of a number of PICTS spectra (Fig. 2, [15]), from which it can be concluded that the detector spectroscopic performance gradually deteriorates with simultaneous increase in the radiation dose and the content of radiation A-centers. The decrease in resistivity is accompanied by an increase in leakage currents and noise in the pulse amplitude spectra. Degradation of spectroscopic performance and decrease in charge collection may also occur due to the capture of nonequilibrium electrons by the level of the defect Z, as well as by the partially ionized levels H, H1, and G, through which the Fermi level passes during irradiation.

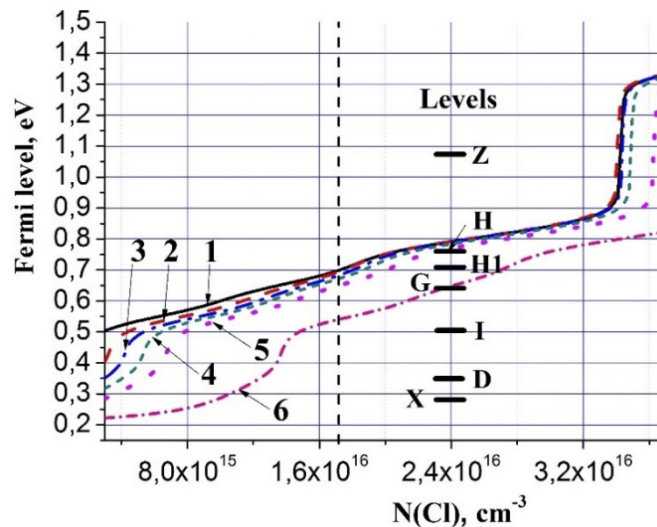


Figure 2. The Fermi level, measured from the valence band, subject to the concentration of the doping chlorine after different doses of gamma irradiation. The parameters of curves 1–6 correspond to the numbered curves in Fig. 1. The vertical dashed line indicates the test sample.

The change in the charge collection efficiency η was calculated subject to the content of radiation defects, which is shown in Fig. 3. It can be seen from the graphs that the radiation defect Z which presumably corresponds to the interstitial tellurium Te(I) exerts the decisive influence on the degradation of the detector spectroscopic properties. The authors of [14, 15] experimentally confirm that the peak of the Z defect in the PICTS spectrum appears only in a completely degraded detector. The simulation has also shown that the charge collection efficiency η of detector, whose initial composition is shown in Table 1, clearly correlates with the value of resistivity ρ : the higher is ρ , the higher is η , and, on the contrary, in the low-resistance state the collection of charges drops sharply. In this case, in order to realize the experimentally known fact of spectrometric performance degradation of CdTe due to the appearance of the defect Z, the capture cross section σ of nonequilibrium charge carriers for Z must be about 10^{-15} cm².

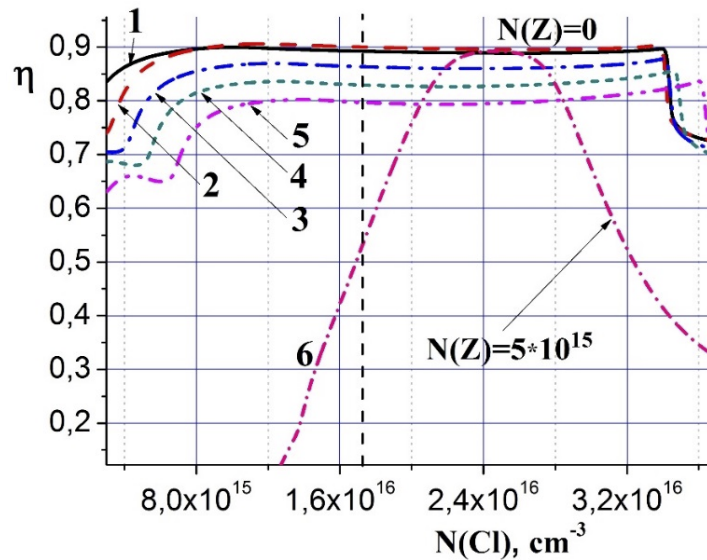


Figure 3. Dependences of the charge collection efficiency on the concentration of doping chlorine after different doses of gamma irradiation. The parameters of curves 1–6 correspond to the numbered curves in Fig. 1, and for 1–5 $N(Z) = 0$, for curve 6 – $N(Z) = 5 \cdot 10^{15}$ cm⁻³; The vertical dashed line indicates the test sample

An increase in the concentration of the radiation donor defect Z partly compensates the increase in the concentration of the acceptor A centers, and narrows the concentration range of the doping Cl_{Te}, in which high values of η take place (see Fig. 3, curve 6). The narrowing of the region of high η is caused by the capture of nonequilibrium electrons at the level of the defect Z. It should be noted that the necessary condition for the large capture cross section $\sigma \sim 10^{-15}$ cm² for complete degradation of the detector properties under the influence of the defect Z is explained by the large difference between level $E_Z = E_C - 0.47$ or $E_Z = E_V + 1.05$ eV and Fermi level E_F .

CdZnTe-based detectors

Let's consider the simulation results of changes in the electrophysical and detector properties of CZT under the influence of gamma irradiation, described in [14, 15], where a batch of Cd_{0.9}Zn_{0.1}Te detectors were irradiated with doses from 10 kGy to complete degradation of their detector properties after 30 kGy. The detectors did not change their performance during irradiation, and then, at the final stage, they suddenly lost their spectroscopic properties (see Fig. 8 [15]). It follows from the PICTS spectra shown in Fig. 5 in [14] and Fig. 11 of paper [15] that the content of radiation defects, presented by shallow levels A, K, X, D, slightly increases in the process of gamma quanta bombardment. However, the concentrations of defects corresponded to Y and W deep levels and, in particular, of the donor level H1 ($E_C - 0.82$ eV) located near the middle of the band gap, increase noticeably. Thus, the phenomenon of radiation self-compensation is realized by increasing the content of deep levels. A noticeable peak of the defect Z appears in the PICTS spectrum at the final stage of exposure after the dose of 30 kGy, when the spectroscopic properties are completely degraded. The calculations of the changes in ρ , η , and E_F in the process of gamma irradiation were performed with these features taken into account.

Fig. 4 shows the behavior of the Cd_{0.9}Zn_{0.1}Te resistivity after different irradiation doses; a) ρ as a function of the concentration of the doping shallow donor N_D , b) the dependence of ρ on the irradiation dose. The matrix composition of the initial, unirradiated detector is shown in Table 2. In the process of gamma irradiation, the concentration of radiation defects K, X, Y, W, H1 in the material gradually increases, and the relative content of the defect I decreases. After the irradiation dose of 25 kGy, these defects were assigned the following concentrations, cm⁻³: $N(K)=2,7 \cdot 10^{15}$, $N(X)=2,7 \cdot 10^{15}$, $N(Y)=3,2 \cdot 10^{15}$, $N(W)=3,2 \cdot 10^{15}$, $N(H1)=1 \cdot 10^{16}$, $N(I)=4 \cdot 10^{15}$.

The donor defect Z which appears in the spectrum at the final stage of gamma irradiation was assigned a concentration of $1 \cdot 10^{15}$ cm⁻³, and the defects, presented by deep levels, were assigned the following concentrations, cm⁻³: $N(Y)=4 \cdot 10^{15}$, $N(W)=4,2 \cdot 10^{15}$, $N(I)=2 \cdot 10^{15}$. Fig. 4b shows that at the initial stage of gamma irradiation the resistivity

increases and then decreases, that was confirmed experimentally in [14, 15, 17]. The simulation has shown that the effect of an increase in ρ is explained by an increase in the content of a deep donor H1 which can act as the Te_{Zn} antisite defect. An increase in the concentration of the radiation level H1 shifts the Fermi level E_F closer to the middle of the band gap, increasing ρ . In the course of further irradiation, the resistivity decreases, although it remains quite high even after a dose of 25 kGy $\rho = 1.1 \cdot 10^{11} \Omega \cdot \text{cm}$.

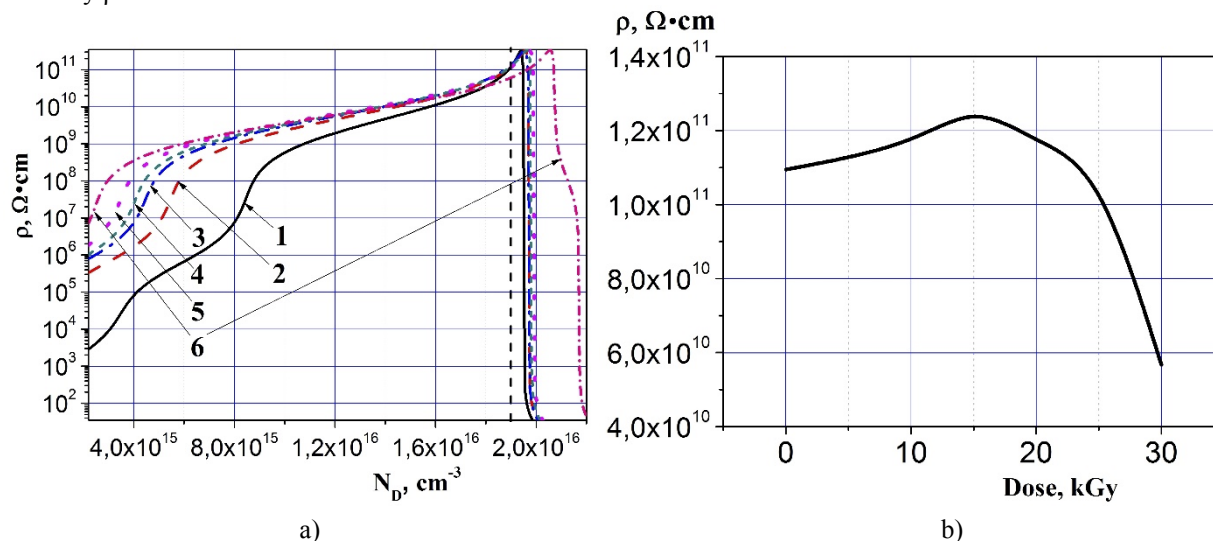


Figure 4. Dependences of the resistivity of $\text{Cd}_{0.9}\text{Zn}_{0.1}\text{Te}$ on the concentration of the dopant donor impurity after different irradiation doses. a) 1 – initial, unirradiated; 2 – 10 kGy; 3 – 15 kGy; 4 – 20 kGy; 5 – 25 kGy; 6 – 30 kGy. The vertical dashed line indicates the test sample. b) Dependence of ρ on the irradiation dose.

For this reason the spectroscopic properties of the detector remain at a high level, what is confirmed experimentally (see [15] Fig. 5). At the final stage after a dose of 30 kGy, when the spectroscopic properties are completely degraded, the resistivity decreases to a value of $\rho = 5.9 \cdot 10^{10} \Omega \cdot \text{cm}$. The simulation has shown that the main reason for the complete degradation of the detector is the capture of nonequilibrium electrons at the radiation defect Z, which can be represented by interstitial tellurium $\text{Te}(\text{I})$, that appears after the dose of 30 kGy with a noticeable decrease in the charge collection efficiency η to 0.3, as shown in Fig. 5. The charge collection is reduced due to the decrease in the lifetime of nonequilibrium electrons to the value of $9.3 \cdot 10^{-9}$ sec. The resistivity has little effect on the performance degradation, since it decreases slightly, remaining high in value $\sim 10^{10} \Omega \cdot \text{cm}$. Indeed, the simulation of the dependences $\rho(N_D)$ and $\eta(N_D)$ with the assumed concentrations of defects in the degraded detector shows that only introduction of the defect Z with a capture cross section of $7 \times 10^{-15} \text{ cm}^2$ and a concentration of $1 \times 10^{15} \text{ cm}^{-3}$ leads to obtaining a sharp decrease in the spectroscopic properties.

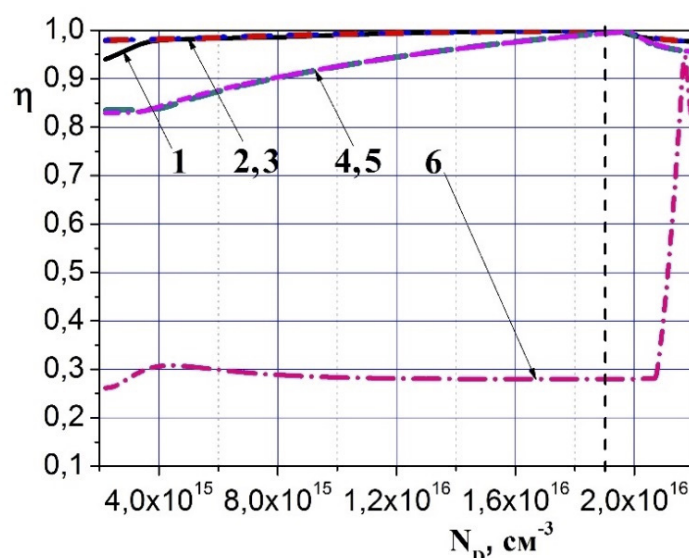


Figure 5. Dependences of the charge collection efficiency on the concentration of the dopant donor impurity after different gamma irradiation doses. Curves 1–6 correspond to the numbered curves in Fig. 4. The vertical dashed line indicates the test sample.

The simulation performed in this work is in qualitative agreement with the experimental results of [14, 15], according to which the resistivity in the degraded CZT-based detector remains higher than even in the initial CdTe:Cl , which

demonstrated an acceptable spectroscopic performance. Thus, a decrease in ρ of the CZT-based detector has less effect on the degradation of its recording properties compared to the effect of capture of nonequilibrium carriers at the level of the radiation donor defect Z (Te(I)).

CONCLUSIONS

Degradation of the spectroscopic performance of detectors based on high-purity CdTe:Cl occurs gradually during gamma irradiation due to the continuous formation of cadmium vacancies V_{Cd} and acceptor complexes $V_{Cd}-Cl$ when their concentration increase. As a result, the content of the donor impurity Cl and the compensation of acceptors somewhat decrease. The hole concentration and hole conductivity increase, and ρ decreases. Due to the relatively low initial resistivity of CdTe, its further decrease causes an increase in the leakage currents and increment of noise in amplitude spectrum. Along with the formation of V_{Cd} , tellurium atoms are knocked out into the interstice (defect Z), thereby increasing the content of donor defects - tellurium vacancies V_{Te} which, remaining neutral, do not affect the electrical compensation and capture processes due to the large difference between the V_{Te} level and the Fermi level. The continuously increasing concentration of the Te(I) at the final stage of gamma irradiation provides appearance of Z peak in the PICTS spectrum at the moment of complete degradation of the spectroscopic performance.

The spectroscopic properties of CZT during gamma irradiation remain unchanged up to 25 kGy due to the strong mechanism of radiative self-compensation in this semiconductor, and sharp degradation occurs only at the final stage of radiation exposure after a dose of 30 kGy with the appearance of a donor defect Z ($E_C - 0.52$ eV). The mechanism of radiative self-compensation is realized by increasing the relative content of the deep donor center H1 which is the Te_{Zn} antisite defect. In other words, tellurium in the irradiated CZT occupies mainly the sites of zinc vacancies V_{Zn} , and in a small amount – sites of V_{Cd} , since zinc atoms are almost two times lighter than those of cadmium, and a greater amount of Zn than that of Cd is knocked out from the lattice sites by gamma quanta. The deep donor Te_{Zn} fixes the position of the Fermi level near the middle of the band gap of CdZnTe, and at the same time stabilizes its electrophysical and detector properties. An increase in the content of the Te(I) (defect Z), at its certain concentration, leads to a complete degradation of the spectroscopic properties of a CZT-based detector due to the capture of nonequilibrium electrons at the Z level. This degradation occurs despite self-compensation by the H1 level and maintaining a fairly high resistivity of the detector material.

The noticeable difference in the radiation resistance of CdTe:Cl (50 kGy) and $Cd_{0.9}Zn_{0.1}Te$ (30 kGy) can be explained by different behavior of Fermi level E_F in these semiconductors during irradiation. In the case of CdTe:Cl, the Fermi level gradually shifts towards the valence band during irradiation and increase in Z concentration, and moves slightly away from the level Z ($E_C - 0.47$), thereby reducing the rate of capture of nonequilibrium charge carriers on it. However, at a certain Z concentration after the dose of 50 kGy, a complete degradation of properties occurs. For the case of CdZnTe, the Fermi level is approximately in the middle of the band gap due to self-compensation, and, therefore, it is closer to the donor level Z. For this reason, the rate of capture and recombination at this level in CdZnTe is higher than that in CdTe:Cl. Thus, the complete degradation of the CdZnTe-based detector properties occurs at a lower concentration of radiation defect Z or Te(I) and hence after the lower irradiation dose of 30 kGy.

ORCID ID

 Alexandr I. Kondrik, <https://orcid.org/0000-0001-9428-4830>

REFERENCES

- [1] Samira Abbaspour, Babak Mahmoudian, and Jalil Pirayesh Islamian, World Journal of Nuclear Medicine **16**(2), 101 (2017). <https://doi.org/10.4103/1450-1147.203079>
- [2] Hajir Al Hamrashdi, Stephen D. Monk, and David Cheneler, Sensors, **19**(11), 2638-1 (2019). <https://doi.org/10.3390/s19112638>
- [3] Tamotsu Okamoto, Tomoya Igari, Takahiro Fukui, Ryuto Tozawa, Yasuhito Gotoh, Nobuhiro Sato, Yasuki Okuno, Tomohiro Kobayashi, Mitsuru Imaizumi, and Masafumi Akiyoshi, Japanese Journal of Applied Physics, **60**, SBBF02-1 (2021). <https://doi.org/10.35848/1347-4065/abd6d8>
- [4] S. Dubos, H. Lemaire, S. Schanne, O. Limousin, F. Carrel, V. Schoepff, and C. Blondel, Nucl. Instrum. Meth. Phys. Res. Sec. A, **787**, 302 (2015). <https://doi.org/10.1016/j.nima.2014.12.111>
- [5] J. F. Butler, C. L. Lingren, and F. P. Doty, IEEE Trans. Nucl. Sci. (1992), **39**(4), 605. <https://doi.org/10.1109/23.159673>
- [6] Paul M. Johns, and Juan C. Nino, J. Appl. Phys., **126**, 040902-1 (2019). <https://doi.org/10.1063/1.5091805>
- [7] S. Del Sordo, L. Abbene, E. Caroli, A. Maria Mancini, A. Zappettini, and P. Ubertini, Sensors, **9**(5), 3491 (2009). <https://doi.org/10.3390/s90503491>
- [8] A.E. Bolotnikov, G.S. Camardaa, Y. Cuia, G. De Geronimo, J. Eger, A. Emerick, J. Fried, A. Hossain, U. Roy, C. Salwen, S. Soldner, E. Vernon, G. Yang, and R.B. James, Nuclear Inst. and Methods in Physics Research, A, **805**, 41 (2016). <https://doi.org/10.1016/j.nima.2015.08.051>
- [9] Qiushi Zhang, Congzhe Zhang, Yanye Lu, Kun Yang, and Qiushi, Sensors, **13**(2), 2447 (2013). <https://doi.org/10.3390/s130202447>
- [10] C. Szeles, Phys. Status Solidi B, **241**(3), 783 (2004). <https://doi.org/10.1002/pssb.200304296>
- [11] P.J. Sellin, A.W. Davies, A. Lohstroh, M.E. Ozsan, and J. Parkin, IEEE Trans. Nucl. Sci. **52**(6), 3074 (2005). <https://doi.org/10.1109/TNS.2005.855641>
- [12] Ruihua Nan, Tao Wang, Gang Xu, Man Zhu, and Wanqi Jie, Journal of Crystal Growth, **451**, 150 (2016). <https://doi.org/10.1016/j.jcrysgro.2016.07.032>
- [13] Santosh Kumar, M. Vinay Kumar, Manjunatha Pattabi, K. Asokan, Xavier Nini, Martin, B.N. Chandrashekar, Cheng Chune, and S. Krishnaveni, Materials Today: Proceedings, **5**(10), Part 3, 22570 (2018). <https://doi.org/10.1016/j.matpr.2018.06.630>

- [14] A. Cavallini, B. Fraboni, N. Auricchio, E. Caroli, W. Dusi, P. Chirco, M.P. Morigi, M. Zanarini, M. Hage-Ali, P. Siffert, and P. Fougeres, Nuclear Instrum. Meth. Phys. Res. A, **458**(1-2), 392 (2001). [https://doi.org/10.1016/S0168-9002\(00\)00931-1](https://doi.org/10.1016/S0168-9002(00)00931-1)
- [15] A. Cavallini, B. Fraboni, W. Dusi, N. Auricchio, P. Chirco, M. Zanarini, P. Siffert, and P. Fougeres, Nuclear Instruments and Methods in Physics Research A, **476**(3), 770 (2002). [https://doi.org/10.1016/S0168-9002\(01\)01674-6](https://doi.org/10.1016/S0168-9002(01)01674-6)
- [16] A. Cavallini, B. Fraboni, W. Dusi et al. Appl. Phys. Lett. **77**, 3212 (2000). <https://doi.org/10.1063/1.1324980>
- [17] Ruihua Nan, Wanqi Jie, Gangqiang Zha, Bei Wang, Yadong Xu, and Hui Yu Journal of Electronic Materials, **41**(11), 2044 (2012), <https://doi.org/10.1007/s11664-012-2204-5>
- [18] Rongrong Guo, Yadong Xu, Tao Wang, Gangqiang Zha, and Wanqi Jie, Journal of Applied Physics, **127**(2), 024501 (2020). <https://doi.org/10.1063/1.5126792>
- [19] A.I. Kondrik, and G.P. Kovtun, Tekhnologiya i Konstruirovaniye v Elektronnoi Apparature, **5-6**, 43 (2019), <https://dx.doi.org/10.15222/TKEA2019.5-6.43>. (in Russian)
- [20] B. Fraboni, L. Pasquini, A. Castaldini, A. Cavallini, and P. Siffert, Journal of Applied Physics, **106**(9), 093713-1 (2009), <https://doi.org/10.1063/1.3253748>
- [21] Lingyan Xu, Wanqi Jie, Gangqiang Zha, Yadong Xu, Xiaochuan Zhao, Tao Feng, Lin Luo, Wenlong Zhang, Ruihua Nana, and Tao Wang, CrystEngComm. **15**(47), 10304 (2013). <https://doi.org/10.1039/c3ce41734d>
- [22] Rui-hua Nan, Wan-qi Jie, Gang-qiang Zha, Xu-xu BAI, Bei Wang, and Hui Yu, Transactions of Nonferrous Metals Society of China, **22**, s148 (2012). [https://doi.org/10.1016/S1003-6326\(12\)61700-2](https://doi.org/10.1016/S1003-6326(12)61700-2)
- [23] G.F. Novikov, and N.A. Radychev, Russian Chemical Bulletin, **56**(5), 890 (2007). <https://doi.org/10.1007/s11172-007-0134-9>
- [24] G.F. Knoll, *Radiation detection and measurement*, 4th ed. (John Wiley & Sons, Inc., 2010), pp. 864.
- [25] A. Cavallini, and B. Fraboni, J. Appl. Phys. **94**(5), 3135 (2003). <https://dx.doi.org/10.1063/1.1600529>
- [26] B. Fraboni, L. Pasquini, A. Castaldini, A. Cavallini, and P. Siffert, Journal of Applied Physics, **106**, 093713 (2009). <https://dx.doi.org/10.1063/1.3253748>
- [27] M.A. Berding, Phys. Rev. B, **60**(12), 8943 (1999). <https://doi.org/10.1103/PhysRevB.60.8943>
- [28] R. Gul, A. Bolotnikov, H.K. Kim, R. Rodriguez, K. Keeter, Z. LI, G. GU, and R.B. James, Journal of Electronic Materials, **40**(3), 274 (2011). <https://doi.org/10.1007/s11664-010-1504-x>
- [29] M. Chu, S. Terterian, D. Ting, C.C. Wang, H.K. Gurgonian, and S. Mesropian, Appl. Phys. Lett. **79**(17), 2728 (2001). <https://doi.org/10.1063/1.1412588>
- [30] M. Fiederle, C. Eiche, M. Salk, R. Schwarz, K. Bens, W. Stadler, D.M. Hofmann, and J. Meyer, J. Appl. Phys. **84**(12), 6689 (1998). <https://doi.org/10.1063/1.368874>

МЕХАНІЗМИ ДЕГРАДАЦІЇ ДЕТЕКТОРНИХ ВЛАСТИВОСТЕЙ CdTe ТА CdZnTe ПІД ВПЛИВОМ ГАММА-ОПРОМІНЕННЯ









О.І. Кондрік

Національний науковий центр «Харківський фізико-технічний інститут» НАНУ
61108, вул. Академічна 1, Харків, Україна.

Представлена робота присвячена вивченню методом комп'ютерного моделювання механізмів впливу радіаційних дефектів, що виникають під дією гамма-випромінювання, на зміну питомого опору ρ , часу життя нерівноважних електронів τ_n і дірок τ_p в CdTe:Cl і Cd_{0.9}Zn_{0.1}Te, а також ефективності збору зарядів η неохолоджуваних детекторів випромінювання на основі цих матеріалів. Радіаційні дефекти, яким відповідають глибокі енергетичні рівні в забороненій зоні, діють як центри захоплення нерівноважних носіїв заряду, помітно впливають на ступінь компенсації, змінюючи ρ матеріалу детектора, процеси рекомбінації, зменшуючи τ_n і τ_p , що в кінцевому підсумку може викликати зниження ефективності збору зарядів η . Виявлені конкретні причини погіршення детекторних властивостей CdTe:Cl і Cd_{0.9}Zn_{0.1}Te під дією гамма-випромінювання від ⁶⁰Co, а також основні чинники, що призводять до повної деградації реєструвальної здатності детекторів на основі цих напівпровідників в процесі їх експлуатації. Поступове погіршення спектроскопічних характеристик детекторів на основі CdTe:Cl при гамма-опроміненні відбувається через безперервне утворення вакансій кадмію V_{Cd} і акцепторних комплексів V_{Cd}-Cl, які безперервно зміщують рівень Фермі в бік валентної зони і зменшують ρ . Повна деградація характеристик детекторів з CdTe відбувається в основному через захоплення нерівноважних електронів на рівні енергії міжвузельного телуру Te(I). Незмінні спектроскопічні властивості сенсорів на основі CdZnTe при гамма-опроміненні до 25 кГр обумовлені механізмом радіаційної самокомпенсації за рахунок утворення дефектів заміщення Te_{Zn}. На завершальній стадії опромінення відбувається різке погіршення детекторних властивостей CdZnTe через захоплення і рекомбінації нерівноважних носіїв заряду на енергетичному рівні дефекту Te(I). Різну радіаційну стійкість CdZnTe і CdTe:Cl можна пояснити різним поведінкою рівня Фермі E_F в цих напівпровідниках при гамма-опроміненні. E_F у CdZnTe при радіаційному впливі знаходиться поблизу середини забороненої зони, а в телуриді кадмію дрейфує в бік валентної зони. Швидкість захоплення і рекомбінації через донорний рівень Te(I) в CdTe:Cl менша, ніж в CdZnTe через більшу різницю між рівнем Фермі і рівнем радіаційного дефекту Te(I) в телуриді кадмію. Таким чином, повна деградація детектора CdTe:Cl відбувається при більш високій концентрації радіаційного дефекту Te(I) і, отже, після більш високої дози опромінення 50 кГр у порівнянні з дозою 30 кГр, необхідною для деградації детекторних властивостей CdZnTe.

Ключові слова: детекторні властивості, моделювання, CdTe, CdZnTe, гамма-опромінення, радіаційні дефекти

INFLUENCE OF FORMATION CONDITIONS, SUBSEQUENT ANNEALING AND ION IRRADIATION ON THE PROPERTIES OF NANOSTRUCTURED COATINGS BASED ON AMORPHOUS CARBON WITH GOLD, SILVER AND NITROGEN ADDITIVES[†]

 Aleksandr Kolpakov^a,  Aleksandr Poplavsky^{a,b},  Maksim Yapryntsev^a,
 Vseslav Novikov^a,  Sergey Manokhin^c,  Igor Goncharov^{a,b},
 Marina Galkina^{a,b},  Vyacheslav Beresnev^{d,*}

^aBelgorod National Research University, 308015 Belgorod, Russia

^bBelgorod State Technological University Named After V.G. Shoukhov, 308012, Belgorod, Russia

^cInstitute of Problems of Chemical Physics, Russian Academy of Sciences, 142432, Chernogolovka, Russia

^dV.N. Karazin Kharkiv National University Svobody Sq. 4, 61022, Kharkiv, Ukraine

*Corresponding Authors: v.beresnev@karazin.ua; novikov_v@bsu.edu.ru

Received June 14, 2021; revised July 27, 2021; accepted July 29, 2021

Nanostructured coatings based on amorphous carbon and carbon-doped with gold, silver, and nitrogen were obtained by the pulsed vacuum-arc method. Carbon coatings have been annealed in a vacuum as well as treated with argon ions. The alloying of carbon coatings with elements that do not form chemical bonds with the carbon matrix (Ag, Au) leads to the formation of gold or silver nanocrystallites with sizes of 2 - 20 nm in the matrix of amorphous carbon, whose density depends on the concentration of the doping element. Annealing of silver-doped carbon coatings leads to the formation of islands on the surface with the size of the order of micrometers. This is due to the silver diffusion and coalescence of small islands into larger ones. The HRTEM method discovered the effect of twinning in carbon nanocrystallites after vacuum annealing as well as silver and gold in the initial state (the formation of single-crystal regions with an altered orientation of the crystal structure) in the amorphous carbon matrix. Analysis of Raman spectra of pure carbon coating and silver-doped showed that the addition of silver leads to a decrease in sp³-phase in the carbon matrix. This effect is particularly evident in the nature of changes in the spectra after vacuum annealing at 600 °C. The addition of nitrogen in the carbon coating leads to an increase in the sp² - phase fraction, and additional annealing leads to a significant increase in the D - peak intensity and formation of clusters of the order of 5 - 15 nm, which are not localized but fill the entire space. Analysis of the coating a-C: Au irradiation with argon ions shows that the number of nanopitches decreased after ion irradiation, simultaneously decreased surface roughness degree, besides, decreased electrical conductivity of the coating as a result of decreased gold content. It was found that the conditions of nanostructured coatings and their subsequent processing allow controlling the properties of nanocoatings (structure, size of nanoparticles, surface topography, and electrical conductivity).

Keywords: Nanostructured coatings, Amorphous carbon, Alloying, Gold, Silver, Nitrogen, Annealing

PACS: 61.66.f, 61.46w

The peak of studies of coatings based on superhard carbon (mainly DLC) falls at the end of the twentieth and beginning of the twenty-first century. Several reviews are devoted to this object [1,2]. Despite the frustrations associated with the main drawbacks of DLC coatings (high internal stresses and defectiveness), their potential is far from being exhausted both in scientific terms [3] and in terms of purely applied research. According to Dr. Vetter [4], who has published the most objective and detailed review devoted to the history of these coatings and their many applications, this area of research should not be retired. One promising area of development of this research could be the creation of DLC-based nanostructures, which significantly expand the applications of these coatings.

According to the publications [5,6], solid DLC coatings obtained on a cold substrate by deposition of carbon particles with an energy of the order of 20-100 eV have a disordered quasiamorphous structure, and their properties approach the properties of the diamond as the content of the phase with sp³ hybridization of carbon atoms increases. Such coatings have come to be classified as ta-C. At present, attempts are being made to study more finely the structure of these coatings; in particular, nanoclusters with sizes on the order of 2.5 nm have been found in carbon coatings obtained by laser sputtering of a graphite target [7].

According to the data of [8] annealing in a vacuum at 600 °C allows initiating the formation of nanocrystallites with an ordered structure in the amorphous matrix of ta-C coatings. It was found that the size of nanocrystallites depends on the initial state of the carbon matrix and, first of all, on the content of the sp³ phase and the level of internal stresses in it, which is determined by the conditions of coating formation.

Another method of forming nanostructures based on the amorphous carbon matrix is the addition of elements that do not form stable chemical bonds with carbon atoms (Au, Ag, Pt, Cu) to the coating. Several studies have reported the detection of nanoclusters of these metals in the matrix of amorphous carbon [9,10]. In [11] using high-resolution HRTEM electron microscopy nanoclusters with an ordered structure (silver nanocrystallites with sizes of

[†] **Cite as:** A. Kolpakov, A. Poplavsky, M. Yapryntsev, V. Novikov, S. Manokhin, I. Goncharov, M. Galkina, and V. Beresnev. East. Eur. J. Phys. 3, 124 (2021), <https://doi.org/10.26565/2312-4334-2021-3-19>

the order of 10-50 nm) were found. It was found that the size of nanocrystallites depends on the conditions of coating formation.

Other method of nanostructured state formation is the creation of nanolayers based on DLC coatings with different densities by changing the energy of carbon ions arriving at the substrate [12]. In this case, layers with preferential growth in a certain direction are created.

The addition of nitrogen to the carbon coating formed by the pulsed vacuum-arc method and its subsequent annealing to increase the electrical conductivity leads to the formation of nanoclusters with sizes of the order of 3-10 nm [13]. At the same time, the structure of the coating is radically different from that obtained by annealing ta-C coatings [8], namely, the formation of local areas of nanocrystallites is not observed.

The state of the substrate, namely, the presence of defects in the initial state or created by directed actions, for example, ion bombardment or laser irradiation, allows changing the conditions of coating formation. In this regard, the peculiarities of nanostructured coating formation based on a matrix of amorphous carbon and silver nanoparticles on a substrate of NaCl single crystal can be noted. The effect of substrate defects in the form of steps and dislocation yield on the density and size of silver nanoparticles has been detected [11].

The subsequent processing of the coating is of particular interest. In [14] a nanocomposite thin coating containing gold nanoparticles in a carbon matrix (Au/a-C) was obtained on glass substrates by co-sputtering in a high-vacuum chamber. To increase the size of Au nanoparticles, thermal annealing of the deposited coatings was performed at temperatures ranging from 100 to 500 °C in an inert argon atmosphere. The growth of Au nanoparticles and the evolution of the carbon matrix during thermal treatment were investigated by PEM and Raman spectroscopy. PEM images of the deposited sample taken at different sections of the studied sample revealed spherical Au nanoparticles with an average diameter of 1.5 nm, whose size increases to 15.3 nm at a temperature of 500 °C.

A promising method of surface modification is irradiation with accelerated ions, which causes several physical processes (surface sputtering, ion implantation, formation of radiation defects) that can be used for etching, alloying with various elements, and accelerating diffusion processes [15,16].

Thus, the purpose of this work is to find common approaches to the formation of the nanostructured state of carbon-based coatings and to determine the possibility of comprehensive use of the above methods of subsequent processing to expand their areas of application.

EXPERIMENTAL PROCEDURE

Nanoscale carbon coatings 100-300 nm thick were deposited on an experimental setup equipped with a pulsed carbon plasma source of the original design (Fig. 1).

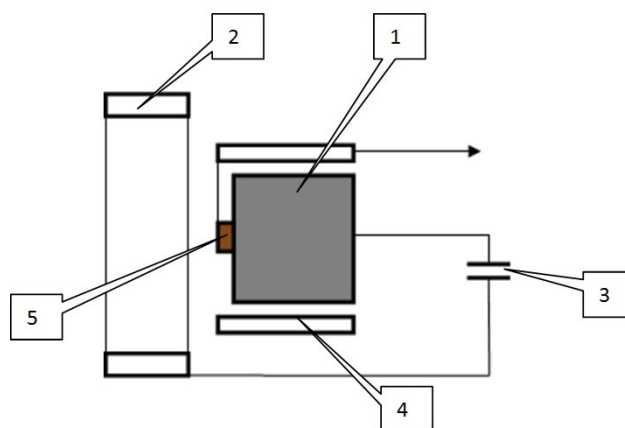


Figure 1. Pulsed carbon plasma source

1 - graphite cathode; 2 - anode; 3 - capacitive storage; 4 - ignition electrode; 5 - ignition assembly insulator

Carbon plasma source consists of graphite cathode 1 and ring anode 2, which are connected to the capacitive storage unit 3 with the capacitance of 2000 μF , charged from DC source to 300 V (not shown in Figure 1). The discharge is initiated between cathode 1 and anode 2 by applying a high-voltage pulse between the ignition electrode 4 and cathode 1, resulting in spark breakdown of the insulator surface 5 with excitation of cathode spots on cathode 1. Carbon coatings with silver and gold were applied using a similar pulsed plasma source equipped with a graphite cathode with silver and gold inserts. The firing pulse repetition rate was 1-5 Hz. Discharge pulse duration was set within the range of 0.8-1.0 ms. The productivity of this source was 0.6-0.7 nm/imp at 100 mm from the cathode.

For structural studies, coatings with a thickness of about 100 nm were deposited on polished plates of monocrystalline silicon and on a fresh chipped NaCl monocrystal. The coatings deposited on the NaCl monocrystal were separated from the substrate in distilled water according to the standard procedure.

The coatings were annealed in the Carbolite vacuum furnace GHA 10/600 at 600 °C for 10 minutes. At the same time, it took 40 minutes to reach the specified temperature mode. The samples were removed from the furnace the next

day after they had cooled completely. The subsequent irradiation was performed by argon ions with an energy of 1.0 keV. The internal stresses were determined before and after annealing by the laser-optical method based on the substrate deflection.

Carbon coatings with nitrogen addition were obtained in the modes indicated above, but with simultaneous irradiation with nitrogen ions at an energy of about 700 eV according to the procedure described in detail in [13]. The monocrystalline silicon substrate was previously degreased and placed in a vacuum chamber, which was evacuated to a pressure of $1 \cdot 10^{-3}$ Pa. Before coating, the substrate was treated with argon ions using an electron-ion source with a closed electron drift at a discharge voltage of 2.0 kV and a discharge current of 80 mA for 3 minutes. The coating thickness was set by the number of discharge pulses and determined preliminarily on crosssection chips using a QUANTA 600 FEG scanning electron microscope.

The surface morphology was studied using scanning electron microscopes QUANTA 600 and Nova NanoSEM 450 as well as a scanning probe microscope NTEGRA AURA. The elemental composition of the a-CN coatings was determined by X-ray microanalysis on a scanning electron microscope.

Structural studies were performed on a high-resolution Tecnai G2 F20 S-TWIN transmission electron microscope. To calculate the average particle size, histograms of horizontal and vertical secant size distributions were plotted for each of the samples. Then, the average histogram was plotted, from which the average particle size was determined. Raman spectra were obtained using a LabRAM HR Evolution spectroscopic (laser wavelength 532 nm, power 50 mW).

RESULTS

Carbon coating

Figure 2 shows a dark-field PEM image of the carbon coating in the initial state and after annealing in a vacuum at 600 °C. There is a significant difference between the structure of the coatings in the initial state and after annealing. The coating structure in the initial state is amorphous and close to homogeneous. The internal stresses in the initial state are 12 GPa.

After annealing, local bright areas appear on the PEM images, half of which have a size of 10 to 20 nm according to the histogram of their size distribution (Fig. 3). The value of internal stresses after annealing decreases to 2 GPa.

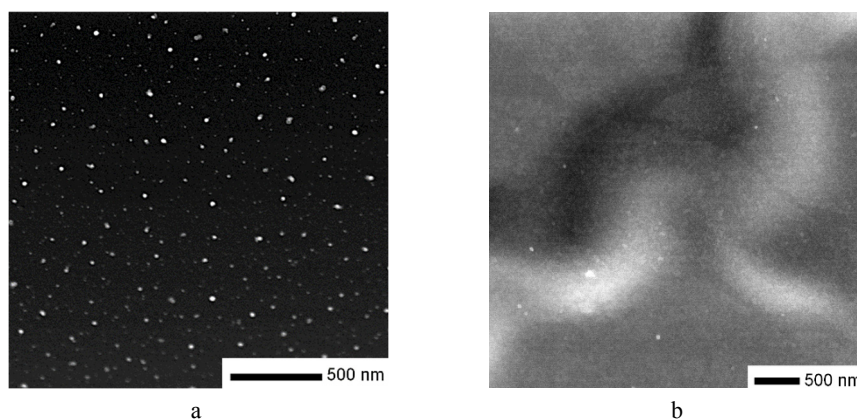


Figure 2. Dark-field PEM image of the carbon coating in the initial state (a) and after annealing in vacuum at 600 °C (b).

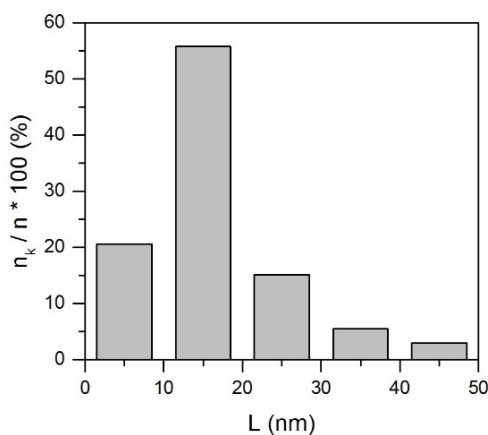


Figure 3. Histogram of the size distribution of local light regions for the carbon coating after annealing in vacuum at 600 °C.

Fig. 4 shows HRTEM images of light regions of different sizes in the amorphous matrix. The analysis of the light regions showed that they are nanosized crystallites with a HCC structure. The interplanar distances are 2.47 Å, 2.13 Å, and 1.51 Å. The calculated value of the lattice parameter was 4.27 ± 0.01 Å, and the unit cell volume was 0.78 Å^3 (note

that the unit cell volume of a diamond is 0.45 \AA^3). It can be seen that areas of larger size are an agglomeration of several crystallites, indicated by arrows in Fig. 4b.

The plasmon energies obtained from the electron energy loss spectra for the samples in the initial state and after annealing are 30 eV and 30.5 eV.

Figure 5 shows the Raman spectra of the coating in the initial state and after annealing in a vacuum at $600 \text{ }^\circ\text{C}$. It can be seen that the Raman spectra before and after annealing are almost identical, only the main G peak is observed. A more detailed analysis of these spectra by decomposition into the constituent D and G peaks showed the absence of structural changes in the sp^2 phase during annealing.

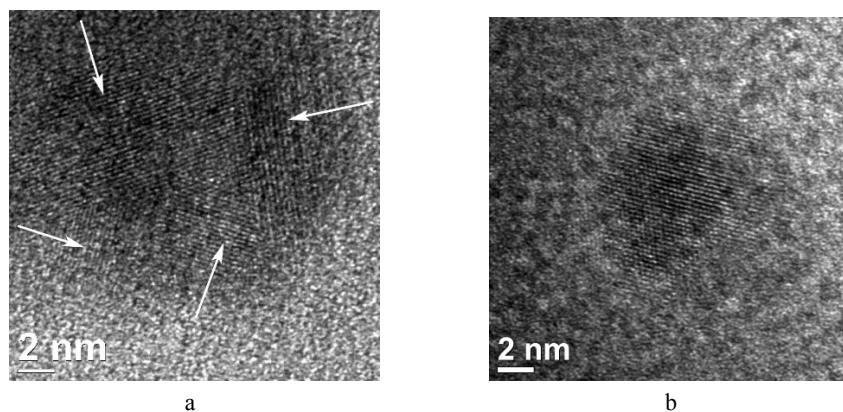


Figure 4. HRTEM-images of light regions in the carbon coating structure after annealing at $600 \text{ }^\circ\text{C}$ in a vacuum. Single nanocluster (a) and a cluster of nanocrystallites (b).

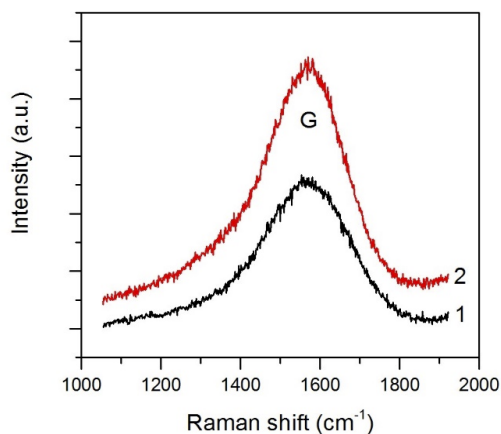


Figure 5. Raman spectra of the coating in the initial state (1) and after annealing in a vacuum at $600 \text{ }^\circ\text{C}$ (2).

Silver-doped carbon coating

Fig. 6a shows the picture of electron diffraction of carbon coating with silver additives (a-C:Ag), and in Fig. 6b its dark-field PEM image. The silver content in the coating is 10 at.%. Diffraction rings correspond to interplanar distances of crystalline silver (ring number - interplanar distance, \AA : 1 - 2.36, 2 - 2.04, 3 - 1.45, 4 - 1.24).

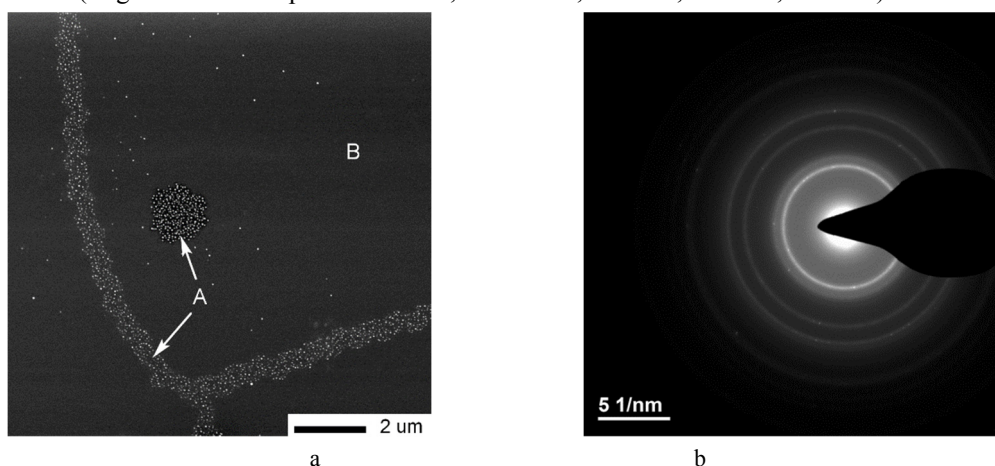


Figure 6. Coating a-C:Ag, electron diffraction (a), dark-field PEM image (b).

It was found that silver atoms are grouped into individual clusters, which are silver nanocrystallites. Their distribution density and size are determined by substrate defects and internal stresses occurring in the coating matrix. For example, silver nanocrystallites in the A region are much larger than those in the dark B region (Figure 6b). A single silver nanocrystallite is shown in Figure 7. It has face-centered cubic lattice (HCC), and the calculated interplanar distances and lattice parameters agree well with the tabulated data for silver.

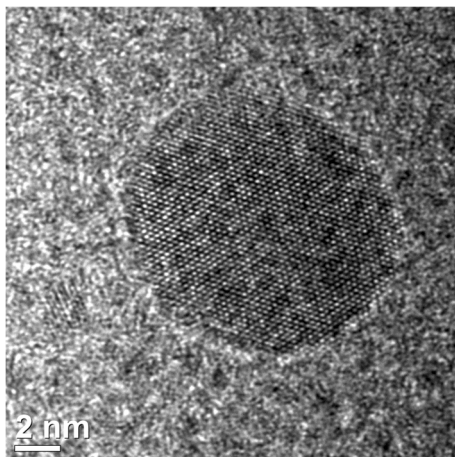


Figure 7. HRTEM images of silver nanocrystallite in the carbon matrix.

Figure 8a shows the appearance of the surface of a-C:Ag coating after annealing at 600 °C obtained by scanning electron microscopy. After annealing silver agglomeration from the coating volume into large objects with the size of 1 - 5 microns on the surface is observed.

Figure 8b shows the Raman spectra of silver-doped carbon coatings in the initial state and after annealing in vacuum at 600 °C. The intensity of the Raman spectrum of the coating after annealing increases significantly. This can be explained by the reduction of the surface reflection coefficient as a result of silver agglomeration from the coating volume into large objects. The development of the D - peak (about 1350 cm⁻¹) indicates the formation of sp² clusters in the carbon matrix.

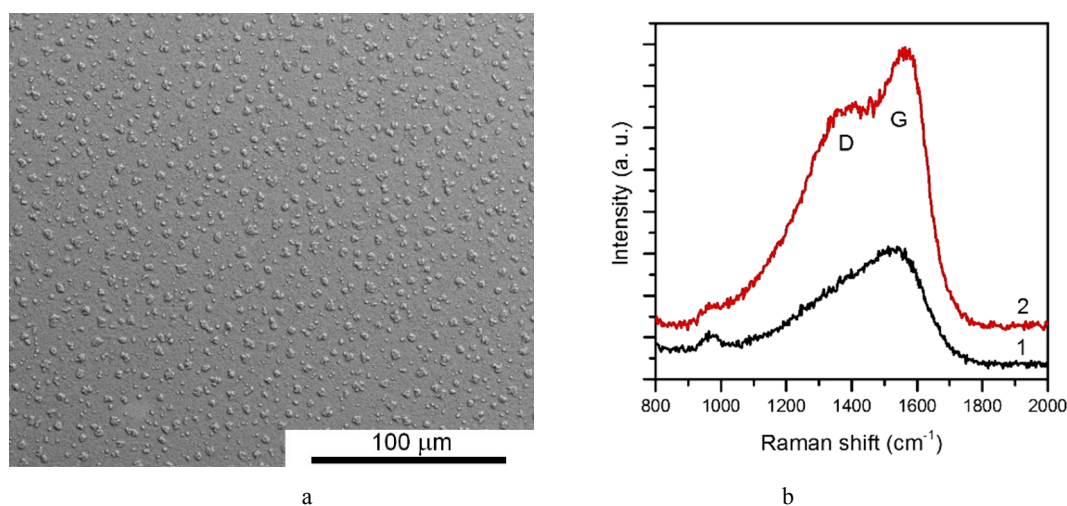


Figure 8. (a) - Surface appearance of a-C:Ag coating after annealing at 600 °C, (b) - Raman spectra of a-C:Ag coating in the initial state (1) and after annealing at 600 °C (2)

Nitrogen-doped carbon coating

Figure 9 shows a PEM image of a nitrogen-doped (a-C:N) carbon coating after annealing at 600 °C (a) and a histogram of the sp² cluster size distribution. In the dark-field image of the sample taken in the region of the 1st ring distribution of electron diffraction, the contrast characteristic of nanoscale phases is observed. No such bright features were observed prior to annealing. Analysis of the image, as well as the histogram, allows us to conclude that the structure of the a-C:N coating differs significantly from ta-C (see Figs. 2,3,4) after annealing.

The Raman spectra are shown in Figure 10 also differ dramatically, both in the initial state and after annealing. Annealing at 600 °C has no effect on the Raman spectrum intensity. The increase in the D peak intensity and the shift of the G peak position towards higher wavenumbers are related to the growth of sp² clusters in the carbon matrix. This indicates the evolution of the amorphous carbon matrix towards nanocrystalline graphite.

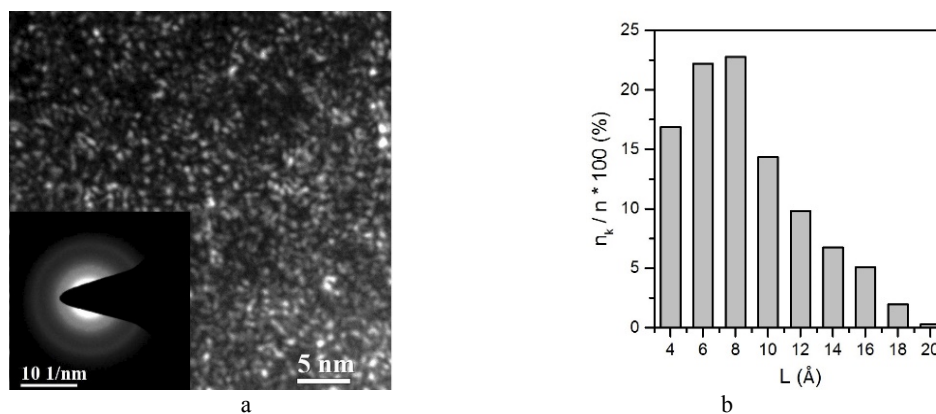


Figure 9. TEM image of a-C:N carbon coating after annealing at 600 °C (a) and histogram of the cluster size distribution (b)

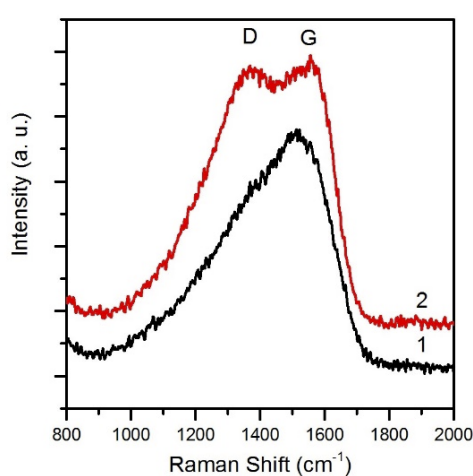


Figure 10. Raman spectra of a-C:N coating in the initial state (1) and after annealing (2)

Gold-doped carbon coating

Samples of carbon coatings with different concentrations of gold (a-C:Au) from 1 to 26 at.% were obtained, and everywhere the grouping of gold atoms into nanosized particles of globular morphology is observed. Figure 11 shows an electron microscopic image of a carbon coating with 18 at.% gold content and an electron diffraction pattern. The diffraction rings correspond to the gold structure (ring number - interplanar distance, Å: 1 - 2.30, 2 - 2.07, 3 - 1.41, 4 - 1.20). HRTEM study of individual particles also showed that their lattice parameters correspond to the known from literature values of gold (cubic face-centered lattice, spatial group Fm-3m, lattice parameters $a = b = c = 4.08$ Å). When fusing of two or more crystal individuals observed twinning effect (Fig. 12a). The histogram of gold particle size distribution is shown in Fig. 12b. The density of gold nanocrystallites increases with increasing of gold content.

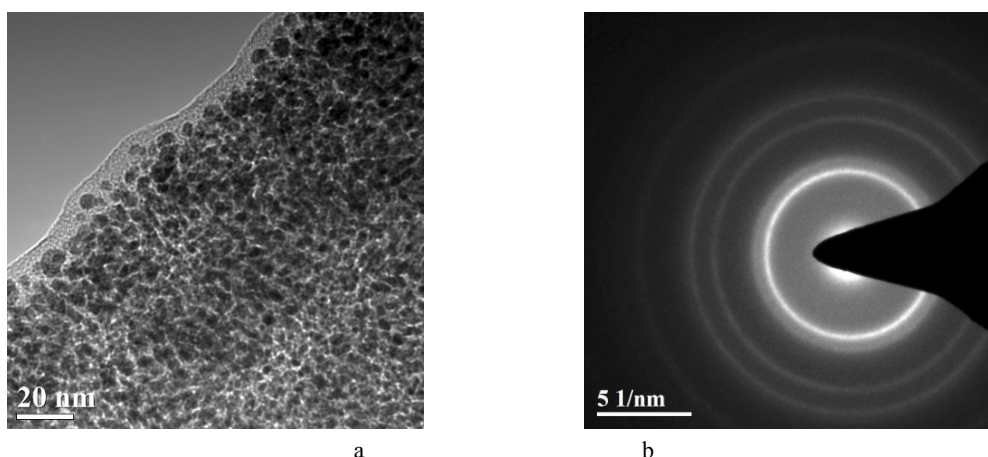


Figure 11. Electron microscopic image of carbon coating with 18 at.% gold (a) and its electron diffraction pattern (b)

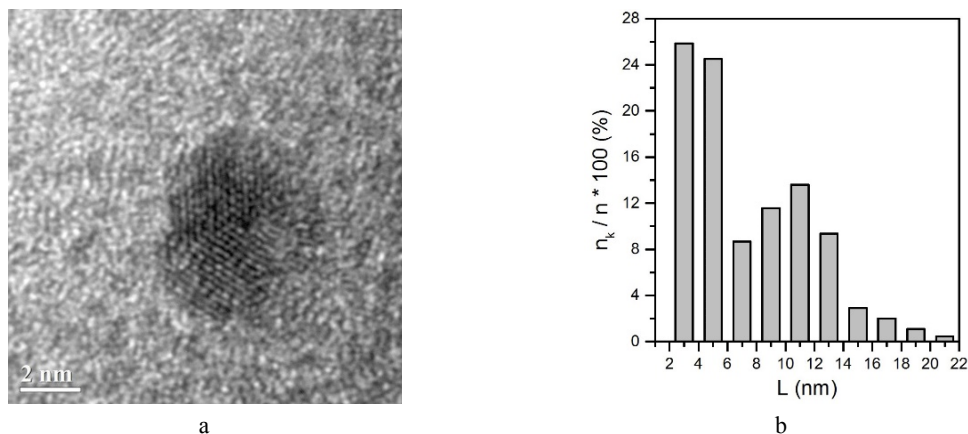


Figure 12. HRTEM image of gold nanocrystallite with the twinning effect (a) and histogram of the gold particle size distribution (b)

Figure 13 shows scans of the a-C:Au coating surface obtained by AFM in the initial state (a) and after irradiation with argon ions (b) at an energy of 1 keV for 10 min. After ion irradiation, the average surface roughness decreased from 21 nm to 10 nm.

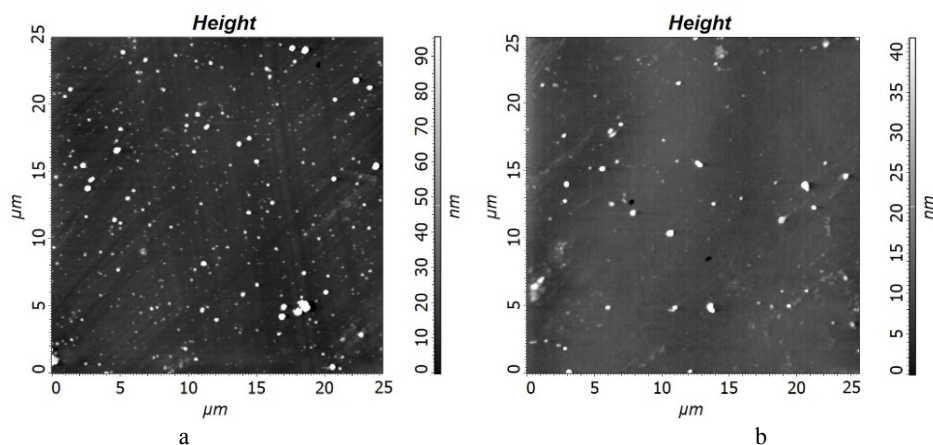


Figure 13. AFM scans of the a-C:Au coating surface in the initial state (a) and after irradiation with argon ions (b) at an energy of 1 keV for 10 min

To assess the electrical conductivity of the a-C:Au coating surface before and after the ion irradiation, we used the technique of determining the resistance of the flow-through, for which a potential of 1 V was applied to the probe. The results of scanning in this mode are shown in Fig. 14.

Analyzing the results of these scans, we can note that the number of nano increases decreased after ion irradiation, while the degree of surface roughness decreased. In addition, the electrical conductivity of the a-C:Au coating (see Fig. 14) decreased as a result of the reduction of the gold content from 26% to 10%.

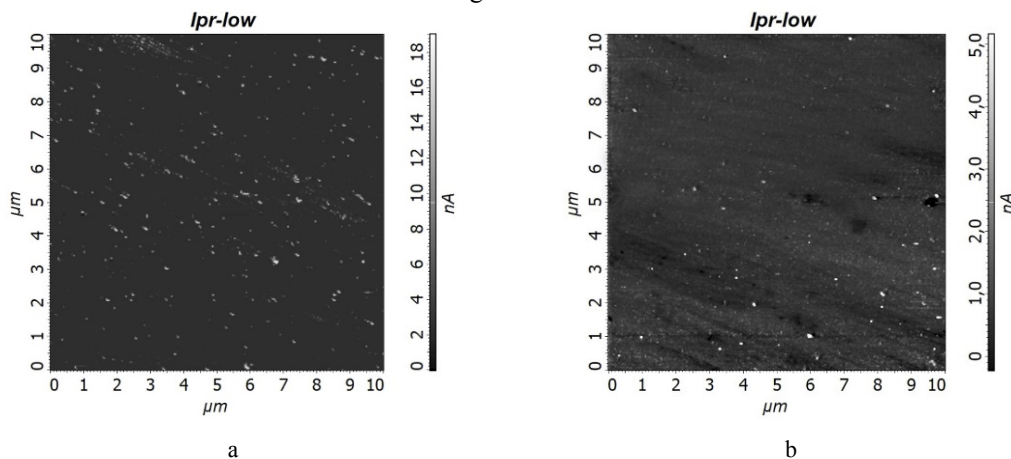


Figure 14. Scans of a-C:Au coating surface in the mode of determination of the flow resistance in the initial state (a) and after irradiation with argon ions with the energy of 1 keV for 10 min (b)

Figure 15 shows an electron microscopic image of the a-C:Au coating surface after etching with argon ions at 1 keV energy for 20 minutes. The initial gold content in the coating is 10%, and after ion etching, it approaches zero. The dark areas on the surface are most likely craters left by the etching of the gold particles.

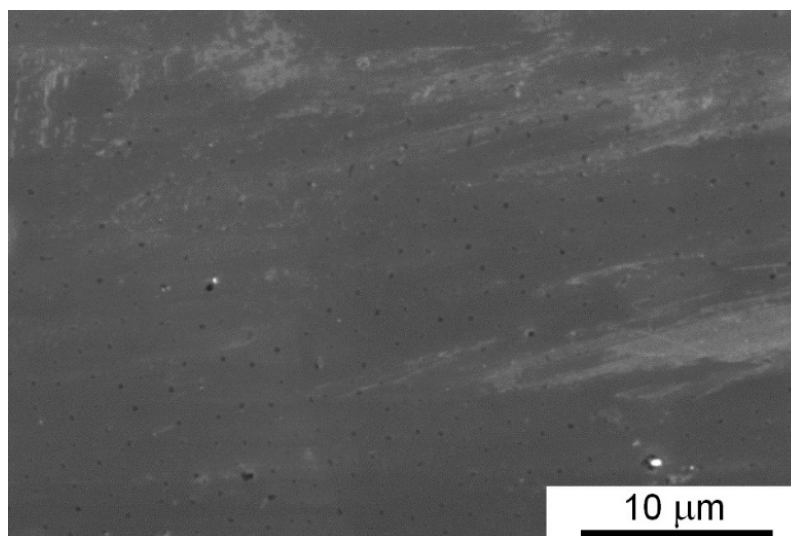


Figure 15. Electron microscopic image of a-C:Au coating surface after etching with argon ions at an energy of 1 keV for 20 minutes

ANALYSIS OF THE RESULTS

Analyzing the HRTEM images shown in Figure 4, it should be noted that a feature of the ordered regions formed during annealing is that they consist of several nanocrystallites (shown by arrows in Figure 4b). In addition, the crystallites are formed in the [011] direction of the GCC lattice, perpendicular to the coating surface. The size of the nanocrystallites after annealing depends on the initial value of internal stresses and increases as the value of internal stresses increases, which in turn is determined by the number of radiation defects.

It is known that the study by EELS (electron energy-loss spectroscopy) method allows determining the ratio of phases with different hybridization of valence electrons (sp^3 , sp^2) [17]. Plasmon energy value determined by this technique is related to the local density of valence electrons and correlates with the density of carbon coating. The plasmon energy values for diamond, DLC-coating, and graphite are 34 eV, 30 eV, and 27 eV, respectively [18]. Annealing of the coating leads to a slight increase in the plasmon energy. Consequently, we can conclude that annealing of DLC coatings deposited by the pulsed vacuum-arc method leads not to graphitization of the coating structure, but to partial ordering in the coating structure. This conclusion is confirmed by the identity of the Raman spectra of the coating in the initial state and after annealing in a vacuum at a temperature of 600 °C, shown in Fig. 5. It is especially necessary to note the increase of the plasmon energy to the value of 30.5 eV, which may indicate an increase in the coating density after annealing, which may be one of the reasons for the decrease in the value of internal stresses.

It was found that large silver nanoclusters are formed predominantly in the dislocation exit sites and steps on the NaCl monocrystal surface. The nucleation energy of nanoclusters is lower in these defective sites and favorable conditions for coalescence of smaller clusters into larger ones. Thus, the state of the substrate surface significantly affects the size and density of silver nanoclusters.

The analysis of the Raman spectra of the pure carbon coating and silver-doped one showed that the addition of silver leads to a decrease in the sp^3 -phase content in the carbon matrix, which coincides with the results of other publications. This effect is particularly evident in the nature of changes in the spectra after vacuum annealing at a temperature of 600 °C.

The addition of nitrogen to the carbon coating leads to an increase in the sp^2 -phase, and additional annealing to a significant increase in the intensity of the D - peak and the formation of clusters with sizes of about 5 - 15 nm, which are not localized but fill the entire space in contrast to ta-C - coating after the same annealing [8]. At the same time, the clusters in a-C:N -coating do not have an ordered structure. The element composition of the a-C:N coating is preserved after annealing, which indicates the absence of significant diffusion of elements to the natural sinks (surface and transition zone) [13].

The analysis of the results of the irradiation of the a-C:Au coating with argon ions allows us to conclude that the number of nanosteaks decreased after ion irradiation, the degree of surface roughness simultaneously decreased, and, in addition, the electrical conductivity of the coating decreased as a result of the decrease in the gold content. To explain this result, we used the simulation of the interaction of argon ions with gold and amorphous carbon targets in the SRIM program environment [19]. It was found that the sputtering coefficient of the gold target significantly exceeds the corresponding value for amorphous carbon (3.726 atom/ion and 0.218, respectively). Thus, the preferential etching of gold nanoparticles occurs.

CONCLUSIONS

Annealing of amorphous carbon coatings ta-C with a high level of internal stresses leads to the formation of nanocrystallites with preferential sizes of 10 - 20 nm, which is associated with a high concentration of radiation defects and their migration in the fields of internal stresses.

The alloying of carbon coatings with elements that do not form chemical bonds with the carbon matrix (Ag, Au) leads to the formation of gold or silver nanocrystallites with sizes of 2 - 20 nm in the matrix of amorphous carbon, whose density depends on the concentration of the alloying element.

The state of the substrate surface (surface energy) significantly affects the size of silver nanocrystallites and their density, which can be used to visualize surface defects.

The effect of twinning in carbon nanocrystallites after vacuum annealing as well as silver and gold in the initial state (formation of areas with the changed orientation of the crystal structure in the monocrystal) in the matrix of amorphous carbon was detected by the HRTEM method.

Annealing of silver-doped carbon coatings leads to the formation of islands on the surface with the size of the order of micrometers. This is due to the diffusion of silver and coalescence of small islands into larger ones.

The addition of nitrogen to the carbon coating leads to an increase in the proportion of sp² - phase, and additional annealing to the formation of clusters with sizes of the order of 5 - 15 nm, which are not localized but fill the entire space in contrast to the ta-C coating after the same annealing. The clusters in the a-C:N coating do not have an ordered structure.

The irradiation of the surface of the carbon coating with gold addition by argon ions leads to a decrease in its roughness and electrical conductivity, which is associated with the preferential etching of gold nanoparticles. Increasing the dose of ion irradiation leads to the complete etching of gold nanoparticles, which can be used in the future for the formation of nanomembranes based on amorphous carbon.

ACKNOWLEDGEMENTS

This work was supported by the Russian Foundation for Basic Research and the Belgorod Region Government in the framework of project No.18-42-310001.

ORCID ID

 Aleksandr Kolpakov, <https://orcid.org/0000-0003-4836-5677>;  Aleksandr Poplavsky, <https://orcid.org/0000-0001-6127-5874>;
 Maksim Yapyrintsev, <https://orcid.org/0000-0001-8791-8102>;  Vseslav Novikov, <https://orcid.org/0000-0002-3602-0746>;
 Sergey Manokhin, <https://orcid.org/0000-0002-1683-5614>;  Igor Goncharov, <https://orcid.org/0000-0002-7734-0535>;
 Marina Galkina, <https://orcid.org/0000-0003-0819-3153>;  Vyacheslav Beresnev, <https://orcid.org/0000-0002-4623-3243>

REFERENCES

- [1] Alfred Grill, *Diam. Relat. Mater.* **8**, 428 (1999). [https://doi.org/10.1016/S0925-9635\(98\)00262-3](https://doi.org/10.1016/S0925-9635(98)00262-3)
- [2] J. Robertson, *Mater. Sci. Eng. R.* **37**, 129 (2002). [https://doi.org/10.1016/S0927-796X\(02\)00005-0](https://doi.org/10.1016/S0927-796X(02)00005-0)
- [3] A.C. Ferrari, S.E. Rodil, J. Robertson, and W.I. Milne, *Diam. Relat. Mater.* **11**, 994, (2002). [https://doi.org/10.1016/S0925-9635\(01\)00705-1](https://doi.org/10.1016/S0925-9635(01)00705-1)
- [4] J. Vetter, *Surf. Coat. Technol.* **257**, 213 (2014). <https://doi.org/10.1016/j.surfcoat.2014.08.017>
- [5] S. Xu, B.K. Tay, H.S. Tan, L. Zhong, Y.Q. Tu, S.R.P. Silva, and W.I. Milne, *J. Appl. Phys.* **79**, 7234 (1996). <https://doi.org/10.1063/1.361440>
- [6] D.R. McKenzie, D. Muller, B.A. Pailthorpe, Z.H. Wang, E. Kravtchinskaja, D. Segal, P.B. Lukins, P.D. Swift, P.J. Martin, G. Amaratunga, P.H. Gaskell, and A. Saeed, *Diam. Relat. Mater.* **1**, 51, (1991). [https://doi.org/10.1016/0925-9635\(91\)90011-X](https://doi.org/10.1016/0925-9635(91)90011-X)
- [7] V.A. Plotnikov, B.F. Dem'yanov, A.P. Yeliseyev, S.V. Makarov, and A.I. Zyryanova, *Diam. Relat. Mater.* **91**, 225 (2019). <https://doi.org/10.1016/j.diamond.2018.11.022>
- [8] A.Ya. Kolpakov, A.I. Poplavsky, M.E. Galkina, S.S. Manokhin, and J.V. Gerus, *Appl. Phys. Lett.* **105**, 233110 (2014). <https://doi.org/10.1063/1.4903803>
- [9] R.J. Narayan, H. Abernathy, L. Riester, C.J. Berry, R. Brignon, *J. of Materi Eng and Perform.* **14**, 435 (2005). <https://doi.org/10.1361/105994905X56197>
- [10] A.S. Chaus, T.N. Fedosenko, A.V. Rogachev, L. Čaplovič, *Diam. Relat. Mater.* **42**, 64 (2014). <https://doi.org/10.1016/j.diamond.2014.01.001>
- [11] A.Ya. Kolpakov, A.I. Poplavsky, S.S. Manokhin, M.E. Galkina, I.Yu. Goncharov, R.A. Liubushkin, J.V. Gerus, P.V. Turbin, and L.V. Malikov, *J. Nano- Electron. Phys.* **8**(4), 04019 (2016). [https://doi.org/10.21272/jnep.8\(4\(1\)\).04019](https://doi.org/10.21272/jnep.8(4(1)).04019)
- [12] M.B. Taylor, D.W.M. Lau, J.G. Partridge, D.G. McCulloch, N.A. Marks, E.H.T. Teo, and D.R. McKenzie, *J. Phys.: Condens. Matter.* **21**, 225003 (2009). <https://doi.org/10.1088/0953-8984/21/22/225003>
- [13] A. Poplavsky, Yu. Kudriavtsev, A. Kolpakov, E. Pilyuk, S. Manokhin, and I. Goncharov, *Vacuum*, **184**, 109919 (2021). <https://doi.org/10.1016/j.vacuum.2020.109919>
- [14] Ritu Vishnoi, Kshipra Sharma, Ganesh D. Sharma, and Rahul Singhal, *Vacuum*, **167**, 40 (2019). <https://doi.org/10.1016/j.vacuum.2019.05.031>
- [15] *Ion Beam Modification of Solids: Ion-Solid Interaction and Radiation Damage*, (Switzerland: Springer International Publishing: 2016). <https://doi.org/10.1007/978-3-319-33561-2>
- [16] Carsten Bundesmann, and Horst Neumann, *J. Appl. Phys.* **124**, 231102 (2018). <https://doi.org/10.1063/1.5054046>
- [17] R.F. Egerton, *Rep. Prog. Phys.* **72**, 016502 (2008). <https://doi.org/10.1088/0034-4885/72/1/016502>
- [18] J. Kulik, Y. Lifshitz, G.D. Lempert, E. Grossman, J.W. Rabalais, D. Marton, *J. Appl. Phys.* **76**, 5063 (1994). <https://doi.org/10.1063/1.357218>
- [19] J.F. Ziegler, M.D. Ziegler, J.P. Biersack, *Nuclear Instruments and Methods in Physics Research B*, **268**, 1818 (2010). <https://doi.org/10.1016/j.nimb.2010.02.091>

**ВПЛИВ УМОВ ФОРМУВАННЯ, ВІДПАЛУ ТА ІОННОГО ОПРОМІНЕННЯ НА ВЛАСТИВОСТІ
НАНОСТРУКТУРНИХ ПОКРИТТІВ НА ОСНОВІ АМОРФНОГО ВУГЛЕЦЮ
З ДОБАВКАМИ ЗОЛОТА, СРІБЛА ТА АЗОТУ****Олександр Колпаков^a, Олександр Поплавський^{a,b}, Максим Япрінцев^a, Всеслав Новіков^a, Сергій Манохин^a,
Ігор Гончаров^{a,b}, Марина Галкіна^{a,b}, Вячеслав Береснев^g**^aБелгородський національний дослідницький університет, 308015, Белгород, Росія^bБелгородський державний технологічний університет імені В.Г. Шухова, 308012, Белгород, Росія^cІнститут проблем хімічної фізики Російської академії наук, 142432, Черноголовка, Росія^dХарківський національний університет імені В.Н. Каразіна, 61022, Харків, Україна

Імпульсним вакуумно-дуговим методом сформовані наноструктурні покриття на основі аморфного вуглецю та вуглецю, легованого золотом, сріблом і азотом. Проведено відпал покриттів у вакуумі, а також обробка іонами аргону. Легування вуглецевих покриттів елементами, що не утворюють хімічних зв'язків з вуглецевою матрицею (Ag, Au) призводить до виділення нанокристалітів золота або срібла з розмірами 2 - 20 нм в матриці аморфного вуглецю, густина цих виділень залежить від концентрації легуючого елемента. Відпал вуглецевих покриттів, легованих сріблом, призводить до утворення на поверхні острівців металу з розмірами порядку мікрометру. Це пов'язано з дифузією срібла і коалесценцією малих острівців до утворення більших за розмірами. Методом HRTEM виявлений ефект двійникування в нанокристалітах вуглецю після відпалу в вакуумі, а також срібла та золота у вихідному стані (утворення в монокристалі областей зі зміненою орієнтацією кристалічних ґратів) в матриці аморфного вуглецю. Аналіз спектрів Рамана чистого вуглецевого покриття і легованого сріблом показав, що добавка срібла призводить до зменшення вмісту sp^3 -фази в вуглецевій матриці. Найбільше цей ефект проявляється в характері зміни спектрів після вакуумного відпалу при температурі 600 °С. Додавання азоту до вуглецевого покриття призводить до збільшення частки sp^2 -фази, а додатковий відпал – до значного збільшення інтенсивності D-піку і формування кластерів з розмірами близько 5 - 15 нм, що не є локалізованими, а заповнюють весь об'єкт. Аналіз опромінення покриття а-С:Аu іонами аргону свідчить про зменшення кількості нановиступів після іонного опромінення, одночасно зменшується ступінь шорсткості поверхні, а також електропровідність покриття (це є наслідком зменшення вмісту золота). Технологічні чинники формування наноструктурних покриттів і їхньої подальшої обробки дають можливість керувати властивостями нанопокриттів (структурою, розміром наночастинок, рельєфом поверхні і електропровідністю).

Ключові слова: наноструктурні покриття, аморфний вуглець, легування, золото, срібло, азот, відпал.

BEAM SCANNING CONTROL SYSTEM FOR PROTON BEAM WRITING[†]

 **Sergey V. Kolinko^a**,  **Ivan S. Kolinko^b**,  **Hlib E. Polozhii^{a,*}**,
 **Aleksandr G. Ponomarev^a**

^a*Institute of Applied Physics National Academy of Sciences of Ukraine, Sumy, Ukraine*

^b*Sumy State University, Sumy, Ukraine*

*Corresponding Author: polojty_ge@ipflab.sumy.ua

Received June 14, 2021; revised July 6, 2021; accepted August 31, 2021

A scanning control system of the ion beam of MeV energies has been developed for the nuclear scanning microprobe and proton-beam writing channel as a part of accelerator-analytical complex based on the Sokol electrostatic accelerator of the Institute of Applied Physics of the National Academy of Sciences of Ukraine. The system was put into operation to replace the obsolete one based on microcontrollers. The scanning control system is based on a National Instruments reconfigurable module with a Field Programmable Gate Array. The module operates in real time and is connected to a personal computer by a high-speed PCI-Express interface with data buffering. The system provides two main modes of operation: exposure of sample areas with a given profile and raster secondary electrons imaging of the sample or a calibration grid. Profile exposure is possible both in raster and functional scanning modes. Automatic calibration of the profile scale and scan raster is also implemented. Using of reconfigurable logic makes it possible to quickly adjust the system to the conditions of a particular experiment and the available equipment. The hardware capabilities of the scanning control system allows in the future to connect up to 4 spectrometric ADC for mapping the elemental composition of samples using Proton Induced X-ray Emission and Proton Backscattering. The first experiments on the irradiation of polymethylmethacrylate have been carried out; images of the obtained microstructures taken with a scanning electron microscope are shown. The aim of this work is to develop a control system for scanning a high-energy focused beam in proton beam writing technique to create small-sized structures for special purposes, as well as to demonstrate the efficiency of the developed system.

Keywords: lithography, proton beam writing, scanning control, nuclear microprobe

PACS: 07.05.Dz; 85.40.Hp; 81.16.Nd

Scanning control systems (SCS) are an important part of the systems for collecting and processing data from the channels of a nuclear scanning microprobe and proton-beam writing, therefore, in the leading laboratories of the world, much attention is paid to their development and improvement. [1-5]. These systems, in addition to basic functions, are currently required versatility, modularity of design, interchangeability of modules, flexibility of the operation algorithm. Therefore, systems with a rigid logic of functioning gave way to reconfigurable systems based on a Field Programmable Gate Array (FPGA). The current level of development of FPGA technology allows the necessary functions in a single module to be implemented, and wide range of such modules is available for purchase. In particular, National Instruments company produces specialized reconfigurable data acquisition modules based on FPGAs manufactured by Xilinx, the functionality of which makes it possible to create a SCS based on them. An additional advantage of this approach is the possibility of widespread use of experimental equipment already available in laboratories as part of the designed SCS. From an economic point of view, using of modules with FPGAs is currently preferred.

The system is designed to control scanning a beam of charged particles both in raster and functional scanning modes. The raster mode (progressive scanning of the beam) is used to determine the dimension of the focused beam on the target and the scanning step size using the secondary electron image of the copper calibration grid. The functional mode is designed to expose specified areas of the sample in accordance with the digital scan profile. The movement of the beam in this mode obeys the rule of transition between the nearest neighboring pixels that require exposure.

SCANNING CONTROL SYSTEM

The SCS was developed and implemented on the channel of the nuclear scanning microprobe [6] and on the new channel of proton beam writing of the electrostatic accelerator Sokol of the Institute of Applied Physics of the National Academy of Sciences of Ukraine [7]. The basic features of the system are shown in Table 1.

Table 1. Basic features supported by the SCS.

Maximum resolution, points	65536×65536
Scan step	User-defined
Initial raster offset	User-defined
Scan type	Progressive, functional
Scan polarity	Unipolar, bipolar
Pixel exposure mode	By time, by fluence

[†] **Cite as:** S.V. Kolinko, I.S. Kolinko, H.E. Polozhii, and A.G. Ponomarev, East. Eur. J. Phys. 3, 134 (2021), <https://doi.org/10.26565/2312-4334-2021-3-20>

© S.V. Kolinko, I.S. Kolinko, H.E. Polozhii, A.G. Ponomarev, 2021

The block diagram of the SCS is shown in Fig. 1. The system consists of a scanner (Scan), two current-frequency converters for measuring the beam current on the target (Cur/Fre) and the current of secondary electrons (SE/Fre) (counting information channels), a reconfigurable input-output module (NI FPGA card) with a connector (Connector NI) and a connecting cable (Cable), a personal computer (PC). NI FPGA card is installed in the PCI-Express slot of a PC and is connected to all SCS modules via the supplied connecting cable and connector.

NI 7852R multifunctional reconfigurable I/O module contains 8 independent 16-bit ADCs and DACs, 96 universal digital I/O lines, user-configurable FPGA, high-speed PC communication interface. The FPGA includes 3 FIFO registers, which makes it possible to buffer data exchange with a PC. Digital logic circuits runs signals up to 40 MHz, the maximum sampling rate of the ADC is 750 kHz, the DAC is 1 MHz. The use of FPGA allows the system to be quickly configured for the specific requirements of the experiment and the required operation algorithm without mechanical reconnecting of circuits. The incomplete functional load of the module makes it possible to expand the functionality of the SCS by connecting additional equipment.

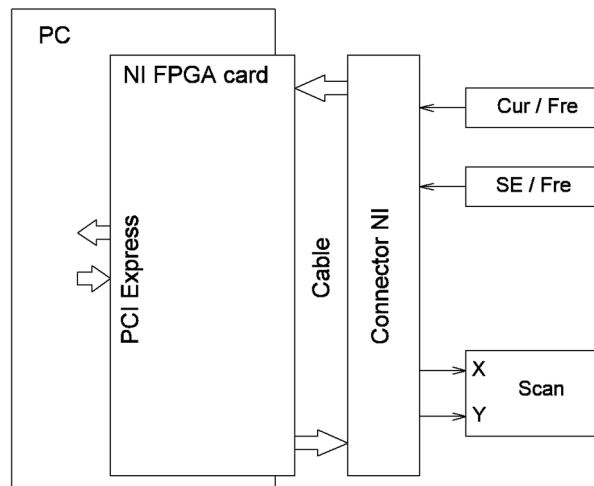


Figure 1. Block diagram of the SCS.

The functional diagram of the SCS is shown in Fig. 2. Sources of counting information are connected to the digital inputs-outputs of the NI FPGA card, which are configured by software during the system initialization. The analog outputs of the high-voltage amplifiers of the electrostatic scanner are connected to the outputs of two DACs X and Y of the NI FPGA card; the voltages across them determine the position of the focused beam (pixel) on the target. The NI FPGA card is connected to the system PCI slot of the computer, data exchange with the RAM is carried out by means of direct memory access. The configuration of the internal structure of the FPGA is carried out using specialized software with a convenient and intuitive graphical interface.

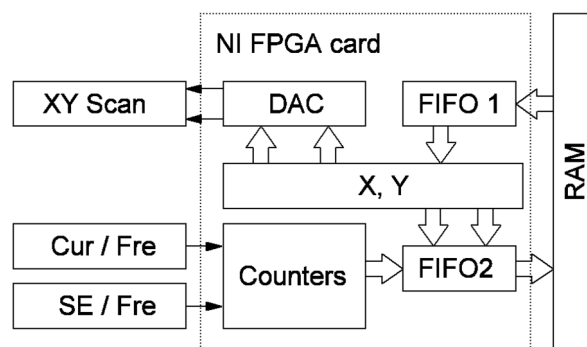


Figure 2. Functional diagram of the SCS.

When initializing the NI FPGA card in FPGA counters and timers are configured to collect counting information and control the scanning system, as well as logical circuits that set the algorithm for the entire system. After initialization, the system works in real time using an internal timer, communication with the PC is carried out via direct memory access channels using FIFO registers ("first in - first out") to buffering the data exchange.

The FIFOs are assigned to the functional load as follows. In FIFO1, the input from the PC of the scanning profile (the sequence of positions of the focused beam on the target, specified by the coordinates X, Y) is buffered. By means of

FIFO2, the counting information from the current-frequency converters with reference to the pixel coordinates is displayed in the PC in the format {current (fluence or dwell time in a pixel)} {SE current} {pixel coordinates}. The FPGA core configuration diagram is shown in Fig. 3. The main processes are indicated by rounded rectangles and run in parallel.

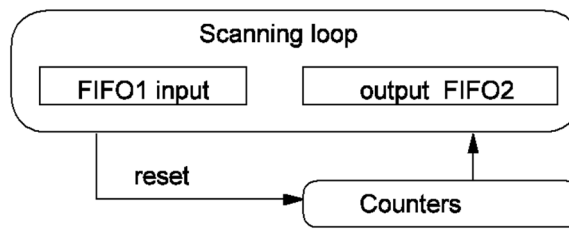


Figure 3. FPGA core configuration diagram.

The leader is the "Scanning loop", it is started by the operator with the "Start" command. At the beginning of the loop, the current coordinates of the scan profile are read from FIFO1 and fed to the DAC to control the scanner. At this time, a counter reset signal is generated, and after the time required to complete the transient process, a counting enable signal (Busy signal is passive) is generated. After the exposure time set in the internal timer has elapsed, counting is disabled (the Busy signal is active) and a word containing coordinates and counting information (fluence, SE current) is output to the FIFO2 register. Then the cycle repeats - the next pair of coordinates is read. The end of the cycle and the stop of data collection occurs on the signal of emptying FIFO1 or on the command of the operator "Stop".

When normalizing the accumulated dose in a pixel, the cycle duration is determined by counting pulses from a current-frequency converter or a scattered proton detector (SPD), and the fluence in the output data word is replaced by the pixel exposure time (if necessary).

The set of counters contains:

- fluence counter (signal from current-frequency converter or SPD),
- secondary electron current counter,
- pixel exposure time counter.

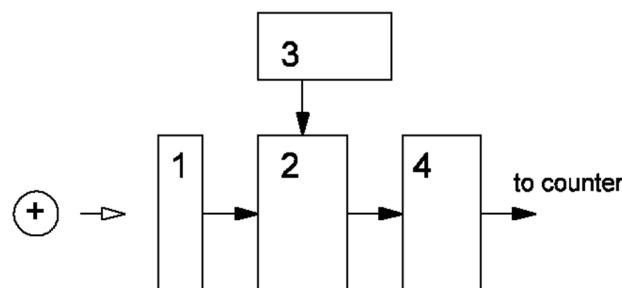


Figure 4. Block diagram of the SPD channel.

On the diagram, the numbers indicate:

- 1- surface-barrier charged particle detector,
- 2- preamplifier,
- 3- high voltage source for detector,
- 4- spectrometric amplifier-shaper.

Registration of secondary electrons is performed by a secondary electron multiplier (SEM). Secondary electrons are accelerated by a potential of 10 kV at the accelerating electrode and hit the scintillator SEM, at the output of which pulses are formed with a frequency proportional to the current of secondary electrons. The frequency signal is fed to the input of the counter in the NI FPGA card, the binary code at the output of which is proportional to the secondary electron current.

Normalization of the exposure time to fluence involves measuring the charge brought by the beam to the current pixel. For conducting samples, this problem is effectively solved using a charge-frequency converter. For non-conductive samples used in proton lithography, this method is unacceptable. Since the output of backscattered protons is proportional to the fluence, the signal from the counting output of the backscattered proton channel is used to control the radiation dose. The channel for detecting backscattered protons by the SPD is made according to the block diagram shown in Fig. 4.

The main program consists of two parts interacting with each other: a program in the NI FPGA card core (CORE) and a program in a PC with OS Windows (HOST). The CORE program is loaded into the NI FPGA card and initialized when

the HOST program is started on the PC. During initialization, data on the number of pixels (Pixels), the exposure time of the pixel (Dwell) and the time sufficient for the transition of the beam between pixels (Busy) are transmitted to the core. Also, a sequence of coordinates for scanning is loaded into the FIFO1 register.

After initialization, the core cyclically reads the next coordinate from FIFO1 using an internal timer and outputs the X, Y values to the corresponding DACs. Then, after the Busy time has elapsed, the counters of secondary electrons and pulses from the current integrator are enabled for the Dwell time. When the exposure time expires, a word is sent to FIFO2 containing coordinates and data from counters. The counters are reset during the Busy signal. The number of cycles corresponds to the number of exposed pixels.

The program monitors the FIFO1 register and loads the coordinates as it is emptied, and also reads information from FIFO2 and displays it in a graphical form, and at the end of the scan saves it to a file in a two-dimensional array format (when scanning an image in secondary electrons).

The external view of the HOST program control panel is shown in Fig. 5. Purpose of controls from top to bottom: FPI (SE) / LITOG – switches the operating mode of the SCS scanning in secondary electrons / lithography.

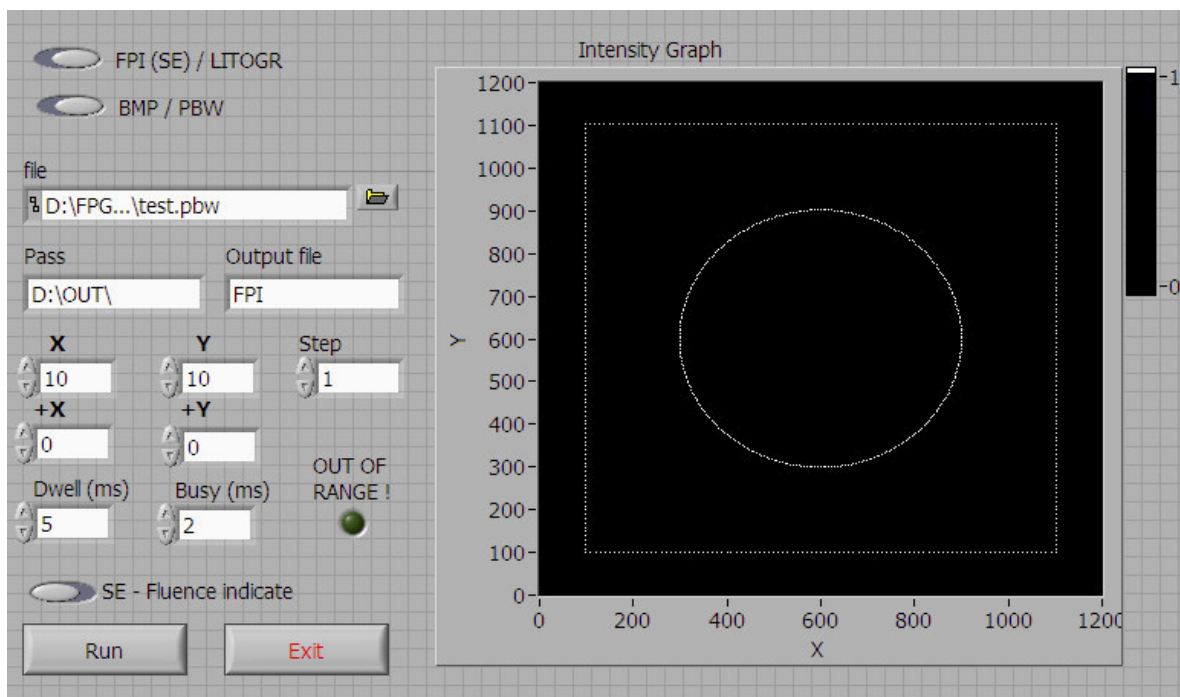


Figure 5. Appearance of the HOST program control panel.

BMP/PBW – allows with two formats of scanning profiles to be worked: directly graphic format *.BMP or functional sequence of coordinates *.PBW.

file – menu for selecting a scan profile file.

Pass, Output file – path and name for the output file of the SE scan.

X, Y, Step – raster sizes and scanning step value.

+X, +Y – scan raster offset.

Dwell, Busy – exposure and transient process time.

OUT_OF_RANGE! – out of coordinates range indicator.

SE-Fluence indicate – switch for displaying counting information sources on the chart.

In addition to the main program, a number of auxiliary programs have been developed to solve the following tasks:

- creating a scanning profile *.PBW from lines and parts of a circle.
- visualization of the scan profile file *.PBW.
- creation and conversion of raster *.BMP files into *.PBW scan profile format.
- converting a raster sequence of pixels into a functional one.

The algorithm for converting a raster sequence of pixels into a functional one is similar to that described in [8], but optimized for images with a high aspect ratio, which consist mainly of monospaced lines.

SCANNING CONTROL SYSTEM CALIBRATION

Functionally, the SCS provides control of the scanner's power supplies by setting the current in the coils or the voltage on the deflecting plates, depending on what type of scanner is used, ferromagnetic or electrostatic. To calibrate the scale of the scanning step and the size of the focused beam, a raster image in the secondary electrons of a calibration copper grid with a grid period of 400 mesh / inch is used (Fig. 6).

Initially, the size of the scanning step is determined based on the number of pixels in one period of the grid. Further, the size of the focused beam at half maximum of the distribution of the beam current density, which is proportional to the yield of secondary electrons, is determined from the size of the scanning step. In this case, the function of the exit of secondary electrons in the direction of X or Y coordinates in the form is used.

$$T_v(v_0, \lambda, \tau, \gamma, f_v, a_v) = \frac{\lambda}{2} \left[1 + \operatorname{Erf} \left(\frac{2\sqrt{\ln 2}}{f_v} (a_v - v_0) \right) \right] + \frac{\tau}{f_v} \sqrt{\frac{\ln 2}{\pi}} \exp \left[-\frac{\ln 16}{f_v^2} (a_v - v_0)^2 \right] + \gamma, \quad (1)$$

where λ – parameter describing the intensity of the output of secondary electrons from the grid surface perpendicular to the beam axis;

τ – parameter describing the intensity of the output of secondary electrons from the inner surface of the grid cells;

γ – the output of secondary electrons in the cavities of the grid, if the grid itself is located on the substrate;

$\operatorname{Erf}(z)$ – error function,

f_v - the size of the beam in the direction of the coordinate $v = (X, Y)$, which is determined by the full width at half maximum (FWHM) of the current density distribution of the focused beam,

a_v, v_0 – determine the position of the beam.

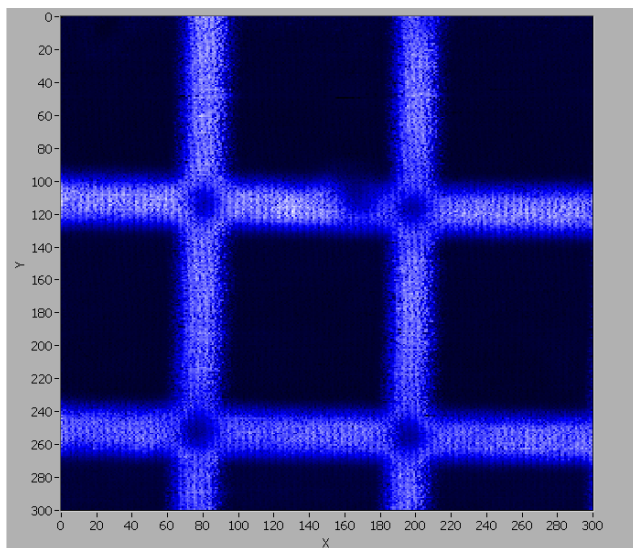


Figure 6. Secondary electron image of a copper calibration grid (scale in pixels).

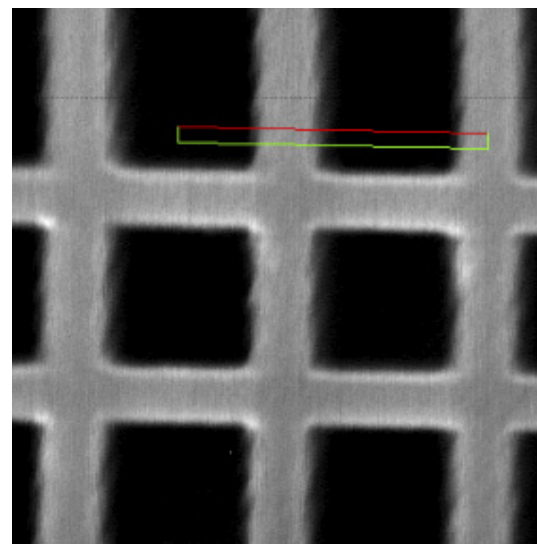


Figure 7. Selection of ten lines for processing experimental data for copper grid with 1000 mesh/inch period

Mathematical fitting of function (1) for the experimental data of the scanning line in the X, Y direction is carried out using the nonlinear Levenberg - Marquardt method. The initial data is taken on the grid image along the lines, the angle of inclination of which corresponds to the angle of inclination of the grid. Measurement along each axis uses ten parallel, side-by-side lines of equal length. The intensity values for each point are averaged (the arithmetic mean over the points of the same serial number in 10 lines). The line selection location is set manually in the graphical interface, as shown in Fig. 7.

Measurement results (shape and size of the beam) are displayed immediately after measurement. The division value (micron per pixel) is also calculated. This data is necessary to determine the geometry and dimensions of images obtained by lithography.

SCANNING CONTROL SYSTEM TESTING

The SCS testing was carried out in the proton-beam writing mode on samples where plates with a surface roughness of 50 nm and a layer of PMMA positive resist with a layer thickness of about 5 μm were used as a substrate. The samples were irradiated according to the specified templates. After processing the irradiated areas, images in secondary electrons were obtained using a scanning electron microscope, which are shown in Fig. 8. Bright artifacts visible in the images are due to poor-quality deposition of a metal coating, which is necessary for electron microscopy of non-conductive samples.

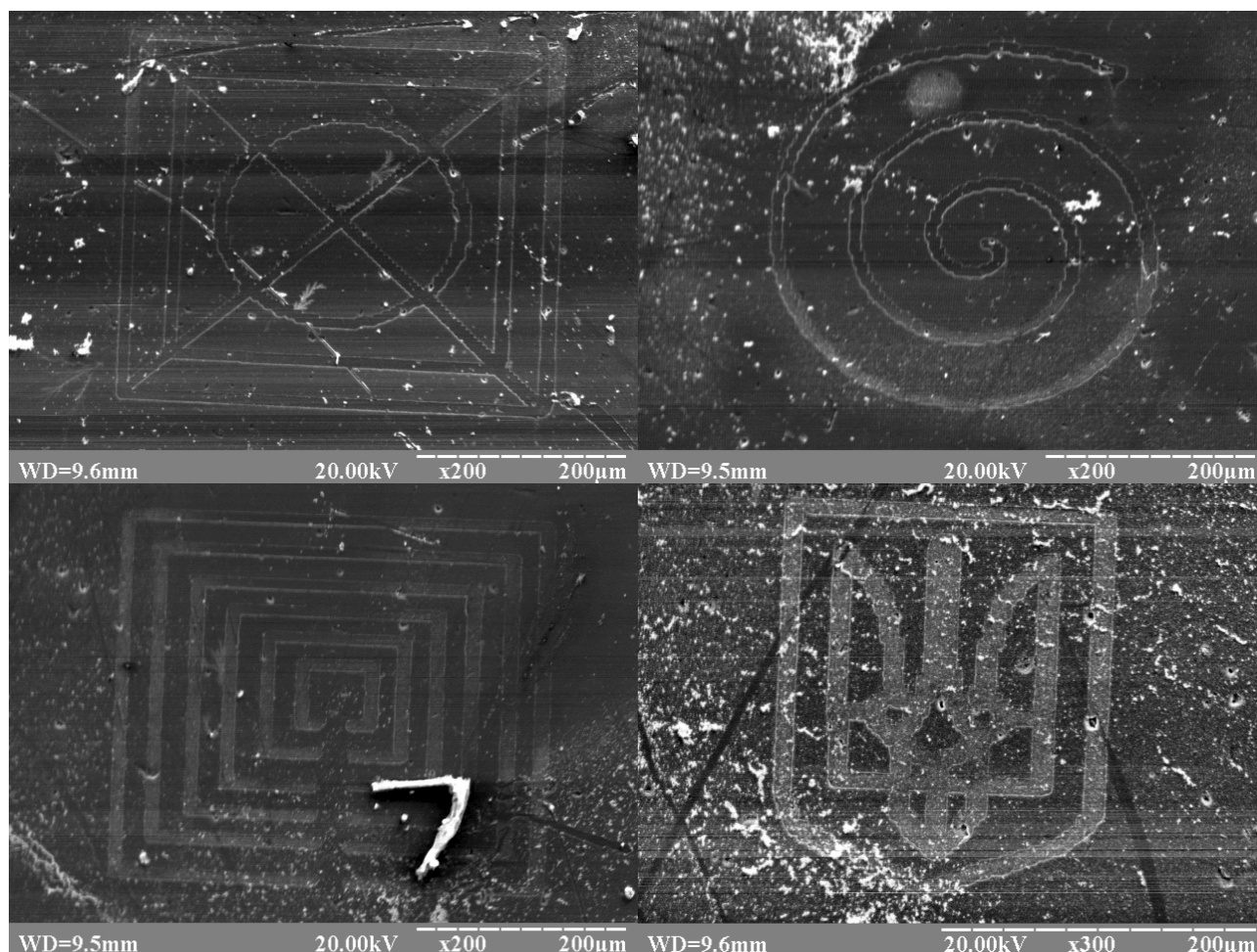


Figure 8. Scanning electron microscopy of test profiles on PMMA.

CONCLUSION

The new scanning control system for the channel of the nuclear scanning microprobe and the channel of proton-beam writing based on the Sokol electrostatic accelerator of the Institute of Applied Physics of the National Academy of Sciences of Ukraine is built on a modern platform and meets all the requirements for efficiently solving the problems of creating three-dimensional microstructures for various fields of engineering and technology, including number of X-ray optics [9, 10]. In the future, it is planned to expand this system with facility for collecting spectrometric information for use as a part of new microprobe [11]. It is also planned to improve the software with the addition of vector proton direct writing lithography.

ACKNOWLEDGMENT

The authors are grateful to the staff of the electrostatic accelerator at the Institute of Applied Physics of the National Academy of Sciences of Ukraine for their help in performing this work.

ORCID IDs

Sergey V. Kolinko, <https://orcid.org/0000-0003-0312-049X>; **Ivan S. Kolinko**, <https://orcid.org/0000-0001-8809-3915>

Hlib E. Polozhii, <https://orcid.org/0000-0002-5664-808X>; **Aleksandr G. Ponomarev**, <https://orcid.org/0000-0002-4517-5635>

REFERENCES

- [1] J. S. Laird, C. G. Ryan, R. Kirkhamc, T. Satoh, and A. Pages, Nucl. Instrum. Meth. Phys. Res. Sect. B **404**, 15 (2017), <https://doi.org/10.1016/j.nimb.2017.03.003>
- [2] L. Daudin, P. Barberet, L. Serani, and P. Moretto, Nucl. Instrum. Meth. Phys. Res. Sect. B **306**, 64 (2013), <https://doi.org/10.1016/j.nimb.2012.11.041>
- [3] J.S. Laird, R. Szymanski, C.G. Ryan, and I. Gonzalez-Alvarez, Nucl. Instrum. Meth. Phys. Res. Sect. B **306**, 71 (2013), <http://dx.doi.org/10.1016/j.nimb.2012.12.045>
- [4] C.G. Ryan et al., Nucl. Instrum. Meth. Phys. Res. Sect. B **268**(11–12), 1899 (2010), <https://doi.org/10.1016/j.nimb.2010.02.052>
- [5] A.A. Bettiol, C. Udalagama, and F. Watt, Nucl. Instrum. Meth. Phys. Res. Sect. B **267**(12–13), 2069 (2009), <https://doi.org/10.1016/j.nimb.2009.03.073>
- [6] D.V. Magilin, A.G. Ponomarev, V.A. Rebrov, N.A. Sayko, K.I. Melnik, V.I. Miroshnichenko, and V.Y. Storizhko, Nucl. Instrum. Meth. Phys. Res. Sect. B **267**, 2046 (2009), <https://doi.org/10.1016/j.nimb.2009.03.015>
- [7] A.G. Ponomarev, V.A. Rebrov, S.V. Kolinko, Nauka innov., **15**(4), 62 (2019), <https://doi.org/10.15407/scin15.04.062> (in Russian)

- [8] G. W. Grime, S. Al-Shehri, and V. Palitsin, Journal of Micromechanics and Microengineering, **29**, 035003 (2019), <https://doi.org/10.1088/1361-6439/aafa03>
- [9] V.N. Kolomiets, S.N. Kravchenko, I.M. Kononenko, A.G. Ponomarev, V.A. Rebrov, and S.V. Kolinko, Nanosystems, Nanomaterials, Nanotechnologies **16**(4), 645 (2018), file:///C:/Users/8523~1/AppData/Local/Temp/nano_vol16_iss4_p0645p0655_2018-1.pdf (in Ukrainian)
- [10] A.G. Ponomarev, S.V. Kolinko, V.A. Rebrov, V.N. Kolomiets, and S.N. Kravchenko, Questions of atomic sciences and technologies, **4**, 285 (2018), file:///C:/Users/8523~1/AppData/Local/Temp/article_2018_4_285.pdf
- [11] A.G. Ponomarev, V.A. Rebrov, S.V. Kolinko, A.S. Lapin, V.F. Salivon, and A.A. Ponomarov. Nucl. Instrum. Meth. Phys. Res. Sect. B, **456**, 21 (2019), <https://doi.org/10.1016/j.nimb.2019.06.048>

СИСТЕМА КЕРУВАННЯ СКАНУВАННЯМ ПУЧКА ДЛІЯ ПРОТОННОЇ ПРОМЕНЕВОЇ ЛИТОГРАФІЇ

Сергій В. Колінько^а, Іван С. Колінько^б, Гліб Є. Положій^а, Олександр Г. Пономарьов^а

^аІнститут прикладної фізики НАН України вул. Петропавлівська 58, 40000, Суми, Україна

^бСумський державний університет, Суми, Україна

Розроблено систему керування скануванням іонного пучку МеВ-них енергій для каналів ядерного скануючого мікрозонду та протонної літографії в складі прискорювально-аналітичного комплексу на базі електростатичного прискорювача “Сокіл” ІПФ НАН України. Систему введено в експлуатацію на заміну застарілій, яка працювала на мікроконтролерах. Систему побудовано на реконфігурованому модулі виробництва National Instruments з програмованою логічною інтегральною схемою (FPGA). Модуль працює в режимі реального часу та з’єднаний з комп’ютером швидодіючим інтерфейсом PCI-Express з буферизацією даних, що передаються. Система забезпечує два основних режими функціонування: експонування ділянок зразку за заданим профілем та отримання растрового зображення зразку або калібрувальної сітки у вторинних електронах. Експонування профілю можливе в режимах растрового та функціонального сканування. Також реалізовано автоматичне калібрування масштабу профілю та растру сканування. Застосування перепрограмованої логіки дає можливість оперативно налаштувати систему під умови конкретного експерименту та наявне обладнання. Апаратні можливості системи дозволяють в подальшому під’єднати до 4 спектрометричних перетворювачів для отримання картини елементного складу зразків методами характеристичного рентгенівського випромінювання та зворотного розсіювання протонів. Проведені перші експерименти з опромінення поліметилметакрилату, наведено зображення отриманих мікроструктур, зняті на растровому електронному мікроскопі. Метою цієї роботи є розробка системи управління скануванням високоенергетичного сфокусованого пучка в протонно променевої літографії для створення малорозмірних структур спеціального призначення, а також демонстрація ефективності розробленої системи.

Ключові слова: літографія, протонна літографія, система управління скануванням, ядерний мікрозонд

INFLUENCE OF THE ORDER OF ION IMPLANTATION ON LUMINESCENT SPECTRUM OF ZnSe NANOCRYSTALS[†]

 Anna Boichenko^a,  Sergiy Kononenko^a, Fadei Komarov^b,  Oganés Kalantaryan^a,
 Vitaliy Zhurenko^{a,*}, Stanislav Avotin^c, Nikolay Rokhmanov^c

^aV.N. Karazin Kharkiv National University

4 Svobody Sq., Kharkov, 61022, Ukraine

^bInstitute of Applied Physics Problems

7, Kurchatov Str., 220045 Minsk, Belarus

^cKharkiv National Agrarian University named after V. V. Dokuchaiev

«Dokuchaeske-2», Kharkiv region, Ukraine

*Corresponding Author: v.zhurenko@gmail.com

Received July 2, 2021; revised July 26, 2021, accepted July 22, 2021

The paper presents the results of mathematical treatment of the luminescent spectra of ZnSe nanocrystals. The samples were formed by the implantation of 150 keV Zn⁺ and 170 keV Se⁺ ions in silicon dioxide layer obtained by oxidation of a silicon substrate. We analyzed two sorts of the samples obtained with different implantation sequences: Zn⁺ were implanted first, and Se⁺ implanted next (sample A); reverse sequence with Se⁺ implanted at the beginning (sample B). The spectra obtained for different implantation sequences A and B differed from each other. It was found that besides the intensive evident bands with maxima at 2.3 eV (540 nm) and 2.85 eV (430 nm), which were associated with ZnSe intrinsic luminescent centers, there were two bands with maxima at 1.9 eV (650 nm) and 2.6 eV (480 nm), which were related to intrinsic SiO₂ defects. Hereby the effect of the medium (silicon dioxide matrix) on luminescent spectra of SiO₂ films with ZnSe nanocrystals formed by ion implantation was demonstrated. Mathematical treatment of the band shape with a maximum of 2.85 eV showed that the parameters such as full width at half maximum, skewness and kurtosis indicated the dependence of size distribution of ZnSe nanoparticles on the implantation sequence of ions. The results are in a good agreement with the data of Transmission Electron Microscopy.

Keywords: zinc selenide, ion implantation, luminescence spectrum, fitting by Gaussian functions.

PACS: 78.55.-m

Progress of science and technology requires the creation of new functional materials with special properties to solve various technical problems. In recent years, semiconductors and optical elements based on selenides have been widely studied and used [1–3]. Much attention is paid to the properties of nanosized crystals of zinc selenide (ZnSe) (see, for example, [1–2, 4]).

Zinc selenide has unique optical properties, due to which it is used in modern optical and electronic devices [5]. For example, an optical fiber with a ZnSe core has significantly improved signal transmission at infrared and visible range of the spectrum [6]. There are quite a few ways to get zinc selenide crystals production. The formation of the ZnSe agglomerate was carried out chemically by the deposition of the reaction products between dimethylzinc, dimethylselenide and hydrogen in the pores of the optical fibers under high pressure. It should be noted that zinc selenide crystals are usually grown in medium that are chemically neutral to them. For example, ZnSe was grown by organometallic chemical vapor deposition on a GaAs substrate at 280°C [4] or by precipitation on a neutral substrate (teflon) after a chemical reaction [7].

For some scientific and technical problems, zinc selenide crystals are grown in the form of certain geometric shapes, namely, nanowires and nanorods. The results of growing ZnSe in the form of a nanowire by the method of "vapor-liquid-crystal" are presented in [8]. There are also other methods of obtaining nanocrystals of zinc selenides. They can be formed from zinc and selenium atoms, which are injected into the surface layer of the sample or epitaxial film by bombarding the surface with a beam of high energy ions of these elements. In [2, 9], ZnSe nanocrystals were formed from implanted zinc and selenium atoms in the SiO₂ layer, which was created by oxidation on the surface of a silicon substrate.

Luminescent technique is widely used method of studying dielectrics and semiconductors [10]. Experimentally obtained spectra carry information about the energy structure of a sample being studied and the presence of different types of defects. In addition, the size of crystals also influences the parameters of these spectra [1]. It causes the appearance of characteristic bands in the structure of the spectrum. Some bands may overlap due to close arrangements of their maxima or certain correlation of intensities, which does not allow visualizing the shape of the bands in the experimental spectrum. In this case, a special mathematical processing of experimental data is used allowing identifying details and features of the spectrum structure. In this sense fitting of spectra by Gaussian functions is an effective method [11]. In general Gaussian approximation, namely single Gaussian and mixtures of Gaussians are most popular probability models, and they are used for many applications (see [12] and references herein). A progress of Gaussian representation was made by T. Kato and coauthors [12] by development a new probability model, 'asymmetric Gaussian', which is an extension of usual Gaussian

[†] **Cite as:** A. Boichenko, S. Kononenko, F. Komarov, O. Kalantaryan, V. Zhurenko, S. Avotin, and N. Rokhmanov, East. Eur. J. Phys. 3, 141 (2021), <https://doi.org/10.26565/2312-4334-2021-3-21>

© A. Boichenko, S. Kononenko, F. Komarov, O. Kalantaryan, V. Zhurenko, S. Avotin, N. Rokhmanov, 2021

and describes spatially asymmetric distributions. As applied to the processing of spectra, this method is often used for decomposing into different emission bands by fitting Gaussian functions. For example, recent study of silica glass luminescence during low energy H^+ , He^+ and O^+ irradiation performed at the 200 kV Ion Implanter was based on spectrum decomposition into four different emission bands by fitting Gaussian functions [13].

This paper presents the results of mathematical processing of photoluminescent spectra of ZnSe nanocrystals formed in an amorphous SiO_2 film by ion implantation [2].

MATHEMATICAL TREATMENT AND DISCUSSION

The nanocrystals of ZnSe was formed by sequential implantation of Zn^+ and Se^+ ions with energies of 150 and 170 keV, respectively, in the silicon dioxide matrix [2]. The energies of ions were chosen for reasons of maximum overlap of the concentration profiles of the implanted atoms. Both implantations of Zn^+ and Se^+ ions were done at the same fluence of 4×10^{16} ions/cm². The study was performed for two sets of samples with different implantation sequences: the first set (sample A) were implanted at first with Zn^+ ions and after that with Se^+ ions, the second set (sample B) was obtained by reverse order of implantation: at first with Se^+ ions and after that with Zn^+ ions.

For both samples, the photoluminescence spectra consisted of two broad bands with maxima of about 2.3 and 2.85 eV. The intensities of corresponding bands for the sample A were greater than for the sample B. To identify the structure of the spectra, we used the Gaussian fitting analysis of optical spectra (see, for example, [14]). Since luminescence is an equilibrium stochastic process, the probability of different electronic transitions is described by the Gaussian distribution function. Thus, it is important to perform the fitting of luminescent spectra represented in energy units. According to the chosen technique, the spectra were represented as the sum of several peaks, each of which is described by a Gaussian function.

The smallest error was achieved by the use of four Gaussians to fit the experimental spectra. The results of the processing for both samples are shown on Fig. 1. This procedure revealed, that in addition to ZnSe typical bands with maxima at 2.3 eV (540 nm) and 2.85 eV (430 nm), two more ones with maxima at 1.9 eV (650 nm) and 2.6 eV (480 nm) were found. The last two bands are associated with intrinsic silica defects [13]. Locations of the maxima of corresponding peaks are the same for both samples.

Bands with maximum at 1.9 eV corresponded to intrinsic silica defect such as non-bridging oxygen hole centers. One of the valence bonds of oxygen of such a defect has an unpaired electron: $\equiv Si-O\bullet$, where " \equiv " denotes three bonds, " \bullet " — an unpaired electron [15]. The band with a maximum at 2.6 eV was associated with another intrinsic silica defect — oxygen deficient centers: $\equiv Si-Si\equiv$ [15].

Thus, the analysis of the luminescent spectra of ZnSe nanocrystals allows obtaining information also about the medium in which they are formed — a layer of SiO_2 matrix on a silicon substrate. The luminescence was excited at room temperature by He-Cd laser at a wavelength of 325 nm. Such radiation effectively excites the luminescent centers of ZnSe nanocrystals [16]. It should be noted that although the SiO_2 layer is almost transparent to light with a wavelength of 325 nm, but the excitation of defects can take place on the "tails" of the absorption bands of silicon dioxide [17]. This explains relatively low intensity of the maxima.

Bands with maxima at 2.3 and 2.85 eV were associated with electronic transitions in ZnSe nanocrystals [2, 4, 8]. Their origin is connected with the presence of intrinsic crystallographic defects in the formed crystals, donors, acceptors and donor-acceptor pairs [2].

The luminescence intensity in the bands is proportional to the total number of ZnSe crystals that were created in the sample during implantation. The measured profiles of the distribution of elements by depth of penetration showed that there were areas where the concentration of one of the elements is greater than the other [2]. In these areas, a smaller number of ZnSe nanocrystals can be formed in comparison with the areas with the same concentration of both elements and, thus, the contribution to the total luminescence is also relatively smaller. The analysis of the measured profiles of element concentrations in both samples showed that in term of percentage ratio the area where the concentrations of elements coincide was larger for sample A than for sample B. Thus, the luminescence intensity of the first sample should be higher, which was confirmed by the spectra (see Fig. 1).

In addition to the factor of a medium, the shape of the luminescent spectra is also affected by the size of the nanocrystals, as suggested in [2]. As it was demonstrated earlier [1], the full width at half maximum (FWHM) of the band with a maximum at 2.85 eV is determined by the relationship between the size of ZnSe nanocrystals and the position of the maximum of the blue band luminescence. According to this work, the position of the maximum of the blue band depends on the size of the nanocrystals and shifts to the range of lower energies with increasing particle size (redshift). Thus, the shape of the blue band of the experimental spectrum is a superposition of the radiations from individual nanocrystals of different sizes. FWHM can allow finding qualitatively distribution of nanocrystals sizes.

In the case of sample A (Zn^+/Se^+ sequence of implantation), the blue band FWHM was 48 nm, for sample B (Se^+/Zn^+ sequence) — 51 nm. This indicates a larger variation in the size of the nanocrystals in the second sample. Such results are well confirmed by the data on the particle sizes obtained by electron microscopy [2]. In the case of initial implantation of Se ions, the layer of the formed clusters is thinner (150 nm compared to 200 nm for the case of initial implantation of Zn ions), and their size in the area of maximum concentration is larger (10–20 nm instead of 8–15 nm).

One of the methods of experimental luminescent spectrum analysis can be an analysis of curve shape deviation from Gaussian distribution function. Typically, such an analysis is performed by calculating such parameters of the

spectrum shape as skewness (A_s) and kurtosis (E_k) of the band [18]. Skewness and kurtosis as higher-order moments are widely used in modern data processing to analyze Gaussian distributions (see, for example [19]). Skewness characterizes the difference of the distribution shoulders (asymmetry) relative to its average value (Fig. 2). A positive skewness ($A_s > 0$) indicates a deviation of the distribution toward positive values (Fig. 2a). In our case, the positive skewness of the peak represented in energy units indicates a larger number of small particles. Negative skewness ($A_s < 0$) indicates a deviation of the distribution towards negative values (Fig. 2b), i.e. a larger number of nanocrystals of larger size compared to the average value for this distribution function [18].

Kurtosis characterizes the relative sharpness or planeness of the distribution peak (Fig. 2c). A sharp peak ($E_k > 3$) will indicate a strong nonuniform distribution of particle size relative to its average value; if maximum is flatter ($E_k < 3$), then size distribution is more uniform. Note that according to the definition, the Gaussian function has the following values of the parameters: $A_s = 0$, $E_k = 3$.

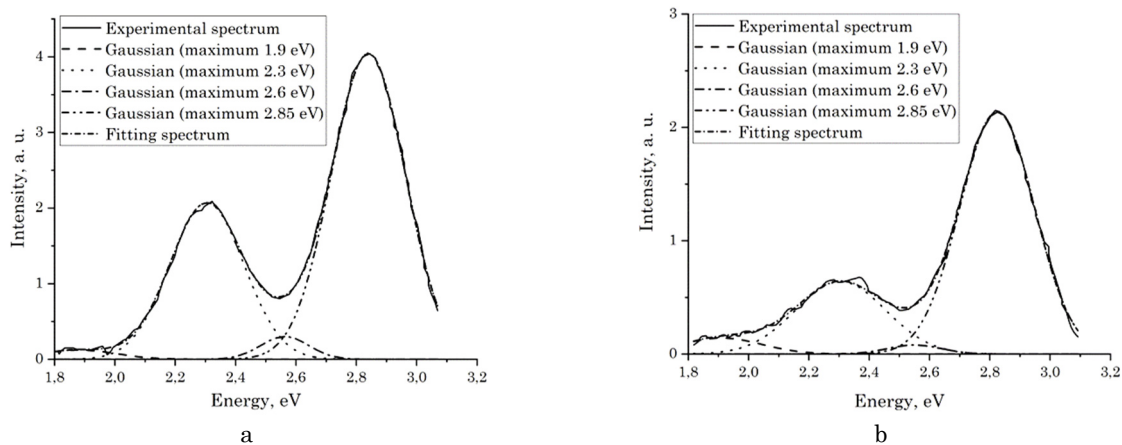


Figure 1. Luminescent spectra for samples A (a) and B (b): experimental data [2] and calculated curves obtained by fitting with four Gaussian functions.

For samples A and B, the values of skewness in energy units are -0.40 and -0.48 , respectively. The kurtosis is 2.33 for sample A and 1.84 for sample B. Fitting calculations were performed for the peak area where there was no effect of adjacent peaks.

Since the bands with a maximum at 2.85 eV were asymmetric and different in shape for samples A and B, the kurtosis and skewness being calculated allowed us to draw conclusions about the size distribution of nanocrystals.

For both spectra, the skewness was negative. Its larger modulo value in the case of sample B indicated the displacement of the spectrum wings toward red-wave direction (lower photon energies). It means a shift in the distribution of particles toward larger sizes. The flatter distribution, according to the calculated kurtosis, indicated that sample A had a narrower range of nanocrystal sizes than sample B. Such conclusions regarding the particle size distributions correlated well with the data obtained by electron microscopy, namely, $8\text{--}15$ nm for sample A and $10\text{--}20$ nm for sample B [2].

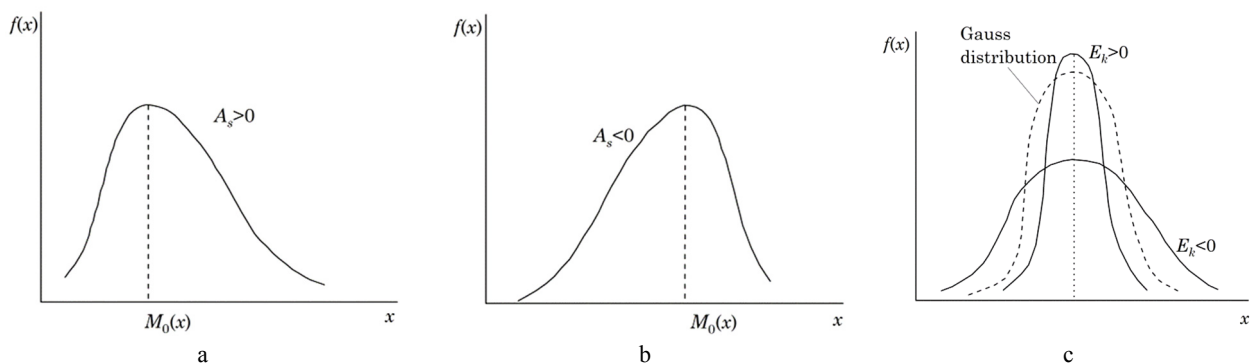


Figure 2. Illustration of definition of the terms that were calculated during the analysis of the deviation of the curve shape from the Gaussian distribution function: positive skewness (a), negative skewness (b), two different values of kurtosis (c).

CONCLUSION

The structure of the luminescent spectra of ZnSe nanocrystals in SiO_2 layer formed by oxidation on a silicon substrate was mathematically analyzed. Two cases of nanocrystal formation by sequential implantation of Zn and Se ions (two





different sequence of implantation: first Zn⁺, then Se⁺ and reverse one) were considered. Corresponding luminescent spectra, which differed slightly from each other, were treated by Gaussian fitting procedure. It was found that in addition to the intense bands with maxima at 2.3 eV (540 nm) and 2.85 eV (430 nm), associated with intrinsic ZnSe luminescent centers, there were two more bands with maxima of 1.9 eV (650 nm) and 2.6 eV (480 nm), corresponding to SiO₂ intrinsic defects, namely, non-bridging oxygen hole centre and oxygen deficiency center. Thus, an influence of the silicon dioxide matrix where zinc selenium nanocrystals were formed on luminescent spectra was shown.

The analysis of the measured profiles of element concentrations for both implantation sequences revealed that the luminescence intensity correlated with the number of ZnSe nanocrystals created in the samples.

Mathematical processing of the band with a maximum at 2.85 eV found that parameters such as full width at half maximum, skewness and kurtosis indicated narrower distribution in the size of ZnSe nanocrystals in the sample obtained by implanting first Zn⁺ and then Se⁺ ions, as compared with the case of the reverse order implantation. Such results are in a good agreement with the data from electron microscope.

Mathematical processing of the luminescent spectra of ZnSe nanocrystals allows one to obtain data on the size distribution of nanocrystals. It may also allow answering a question about a substance (matrix), in which the nanocrystals structures are formed. The results obtained can become the basis for an additional channel of information on nanocrystals for verifying finding measured by other methods.

ORCID IDs

 Anna Boichenko, <https://orcid.org/0000-0002-2444-2052>;  Sergiy Kononenko, <https://orcid.org/0000-0001-6060-2589>;
 Vitaliy Zhurenko, <https://orcid.org/0000-0002-4738-094X>;  Oganeg Kalantaryan, <https://orcid.org/0000-0002-5625-6908>

REFERENCES

- [1] P. Reiss et al., *Materials Chemistry and Physics*, **84**, 1 (2004), <https://doi.org/10.1016/j.matchemphys.2003.11.002>
- [2] M. Makhavikou et al., *Surface and Coatings Technology*, **344**, 25 (2018), <https://doi.org/10.1016/j.surfcoat.2018.03.017>
- [3] B. Dong et al., *Chem. Commun.* **46**, 39 (2010), <https://doi.org/10.1039/C0CC02042G>
- [4] J.Z. Zheng et al., *Appl. Phys. Lett.* **62**, 63 (1993), <https://doi.org/10.1063/1.108820>
- [5] H. Qi et al., *Optik*, **127**, 14 (2016), <https://doi.org/10.1016/j.ijleo.2016.03.079>
- [6] J.R. Sparks et al., *Adv. Mater.* **23**, 14 (2011), <https://doi.org/10.1002/adma.201003214>
- [7] B. Feng et al., *J. Mater Sci: Mater Electron*, **26**, 5 (2015), <https://doi.org/10.1007/s10854-015-2818-5>
- [8] U. Philipose et al., *J. Appl. Phys.* **100**, 084316 (2006), <https://doi.org/10.1063/1.2362930>
- [9] J.D. Budai et al., *Mat. Res. Soc. Symp. Proc.* **452** (1996), <https://doi.org/10.2172/425296>
- [10] P.D. Townsend et al., *J. Appl. Phys.* **121**, 145101 (2017), <https://doi.org/10.1063/1.4979725>
- [11] M.D. Mason et al., *Phys. Rev. Lett.* **80**, 24 (1998), <https://doi.org/10.1103/PhysRevLett.80.5405>
- [12] T. Kato, S. Omachi, H. Aso, *SSPR&SPR* (Windsor, Ontario, Canada: 2002), (Eds.) T. Caelli et al., LNCS 2396, 405 (2002), <https://doi.org/10.1007/3-540-70659-3>
- [13] Y. Chu et al., *Surface & Coatings Technology*, **348**, 91 (2018), <https://doi.org/10.1016/j.surfcoat.2018.05.008>
- [14] Y.B. Soskovets, A.Y. Khairullina, V.A. Babenko, *Journal of Applied Spectroscopy*, **73**, 4 (2006), <https://doi.org/10.1007/s10812-006-0121-1>
- [15] R. Salh, H.-J. Fitting, *Phys. Status Solidi (c)*, **4**, (3) (2007), <https://doi.org/10.1002/pssc.200673717>
- [16] P.J. Dean, A.D. Pitt, M.S. Skolnick, P.J. Wright, B. Cockayne, *Journal of Crystal Growth*, **59**, 1–2 (1982), [https://doi.org/10.1016/0022-0248\(82\)90341-4](https://doi.org/10.1016/0022-0248(82)90341-4)
- [17] M. Wakaki, K. Kudo, T. Shibuya, *Physical Properties and Data of Optical Materials* (New York: CRC Press LLC: 2007).
- [18] NIST/SEMATECH e-Handbook of Statistical Methods (NIST/SEMATECH: 2012), <https://doi.org/10.18434/M32189>
- [19] A.H. Ramezani, S. Hoseinzadeh, Zh. Ebrahimnejad, *Appl. Phys. A*, **126**, 481 (2020), <https://doi.org/10.1007/s00339-020-03671-7>

ВПЛИВ ПОРЯДКУ ЙОННОЇ ШІМПЛАНТАЦІЇ НА ЛЮМІНЕСЦЕНТНИЙ СПЕКТР НАНОКРИСТАЛІВ ZnSe

Г. Бойченко, С. Кононенко, Ф. Комаров, О. Калантар'ян, В. Журенко, С. Авотін, М. Рохманов

Харківський Національний університет ім. В.Н. Каразіна

61022, Україна, м. Харків, пл. Свободи, 4

Інститут проблем прикладної фізики

220045, Білорусь, м.Мінськ, вул. Курчатова, 7

Харківський Національний аграрний університет імені В.В. Докучаєва

62483, Харківська область, Харківський район, п/в "Докучаєвське - 2"

У статті представлені результати математичної обробки люмінесцентних спектрів нанокристалів ZnSe. Зразки були підготовлені шляхом імплантації йонів Zn⁺ з енергією 150 кеВ та йонів Se⁺ з енергією 170 кеВ в шарі діоксиду кремнію, отриманого окисненням кремнієвої підкладки. Ми проаналізували два типи зразків, отриманих за різною послідовністю імплантації: спочатку імплантували Zn⁺, а потім Se⁺ (зразок А); зворотна послідовність — з імплантованими на початку йонами Se⁺ (зразок В). Спектри, отримані для різних послідовностей імплантації А і В, відрізнялися один від одного. Було встановлено, що крім інтенсивних смуг з максимумами 2,3 еВ (540 нм) і 2,85 еВ (430 нм), які були пов'язані з власними люмінесцентними центрами ZnSe, існували дві смуги з максимумами 1,9 еВ (650 нм) і 2,6 еВ (480 нм), які були пов'язані із власними дефектами SiO₂. Цим було продемонстровано вплив середовища (матриці діоксиду кремнію), де утворювались нанокристали ZnSe, на його люмінесцентні спектри. Математична обробка форми смуги з максимумом 2,85 еВ показала, що такі параметри, як повна ширина при половині висоти максимуму, асиметрія та ексцес вказують на залежність розкиду розмірів нанокристалів ZnSe від порядку імплантації йонів. Результати добре узгоджуються з даними трансмісійної електронної мікроскопії.

Ключові слова: селенід цинку, йонна імплантація, люмінесцентний спектр, фітування функціями Гауса.

FAST ELECTROMAGNETIC WAVES ON METAMATERIAL'S BOUNDARY: MODELING OF GAIN[†]

 Viktor K. Galaydych*,  Alexandr E. Sporov,  Volodymyr P. Olefir,
 Mykola O. Azarenkov

V.N. Karazin Kharkiv National University, 4 Svobody Sq., Kharkov, 61022, Ukraine

*Corresponding Author: galaydych@karazin.ua

Received July 7, 2021; accepted September 27, 2021

The paper presents the results of the study of properties of fast surface electromagnetic waves that propagate along the flat interface between the active metamaterial and air (or vacuum). The case of homogeneous and isotropic metamaterial is considered. The dispersion properties, the wave spatial attenuation, the phase and group velocities, as well as the spatial distribution of the electromagnetic field of the eigen TE and TM modes of such a waveguide structure are studied in the frequency range where the metamaterial has a simultaneously negative permittivity and permeability. It is shown that fast surface electromagnetic waves can exist in this waveguide structure and their properties are studied. It is shown that the phase speed of TM mode is several times higher than the speed of light in vacuum, while the phase speed of TE mode is slightly higher than the speed of light in vacuum. The TM mode is a direct wave in which the phase and group velocities have the same direction. It is obtained that the group velocity of the TM mode varies from zero to the about half of speed of light in vacuum, and reaches a minimum at a certain value of wave frequency, which depends on the characteristics of the metamaterial. It is shown that the penetration depth of the TM mode into the metamaterial is much smaller than into the vacuum. The TE mode is a backward wave with opposite directed phase and group velocities. The absolute value of the group velocity of the TE mode is about six times less than the speed of light in vacuum. In contrast to the TM mode the penetration depth of the TE mode into the metamaterial is much greater than in vacuum. The obtained properties of the fast surface electromagnetic waves can be used for modeling and design of modern generation and amplification devices containing metamaterials.

Keywords: metamaterial, fast surface electromagnetic wave, dispersion, attenuation, spatial wave structure

PACS: 52.35g, 52.50.Dg

The metamaterials are referred to the materials consisting of a small-size cells that play the role of atoms for electromagnetic waves. It's possible for such artificial materials to get various combinations of electromagnetic characteristics including simultaneously negative value of permittivity and permeability, so-called left-handed materials [1].

The generating and amplifying devices use the backward electromagnetic waves (phase and group velocities are opposite) and the fast electromagnetic waves (phase velocity exceeds the speed of light in a vacuum) [2-4].

In our previous papers [5,6] we have studied the properties of slow surface electromagnetic waves on the left-handed materials. In the presented work we will study the fast surface electromagnetic waves on the left-handed materials.

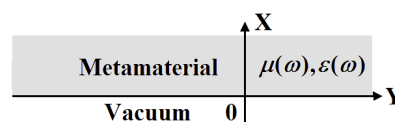


Figure 1. The geometry of problem

TASK SETTINGS

Let us investigate the electromagnetic waves of a surface type that propagate along a plane waveguide structure in the Z - axis direction (Fig. 1). The semi-infinite air (or vacuum) region with permittivity $\epsilon_v = 1$ and permeability $\mu_v = 1$ takes place at $x \leq 0$. The semi-infinite region $x \geq 0$ is filled by double negative metamaterial (DNM) that characterized by the commonly used the effective permittivity $\epsilon(\omega)$ and permeability $\mu(\omega)$ [5]:

$$\epsilon(\omega) = 1 - \frac{\omega_p^2}{\omega(\omega - i\nu_G)}, \quad (1)$$

$$\mu(\omega) = 1 - \frac{F\omega^2}{\omega(\omega - i\gamma_G) - \omega_0^2}, \quad (2)$$

where ω - is angular wave frequency, ν_G , γ_G - are effective electric and magnetic gain, respectively.

[†] Cite as: V.K. Galaydych, A.E. Sporov, V.P. Olefir, N.A. Azarenkov, East. Eur. J. Phys. 3, 145 (2021), <https://doi.org/10.26565/2312-4334-2021-3-22>

© V.K. Galaydych, A.E. Sporov, V.P. Olefir, M.O. Azarenkov, 2021

The modeling was carried out for the metamaterial with $\omega_p / 2\pi = 10$ GHz, $\omega_0 / 2\pi = 4$ GHz, and $F = 0.56$ [7]. Under these conditions it is possible to obtain $\varepsilon(\omega) < 0$ and $\mu(\omega) < 0$ simultaneously in the frequency range $1 < \Omega = \omega/\omega_0 < 1.5$.

Let us consider the fast electromagnetic waves that propagate along interface between the metamaterial and air (or vacuum) and possess the exponentially decreasing field far away from the interface. The spatial-temporal dependence of the wave components has such a form:

$$E, H \propto E(x), H(x) \exp[i(k_3 z - \omega t)], \tag{3}$$

where the amplitudes of the wave fields decrease exponentially from the boundary and k_3 is complex wavenumber. Real part of k_3 characterizes the wavelength and imagine part – the decrement in the propagation direction.

Under the considered assumptions the set of Maxwell equations split into two independent sub-systems. One of them describes the TE-waves that contain (H_x, E_y, H_z) -components and another – TM-waves that contain (E_x, H_y, E_z) -components.

The boundary conditions (the continuity of the tangential wave field components at metamaterial-vacuum interface $x = 0$) gives the dispersion equation as for the TM-mode:

$$\kappa_v \varepsilon(\omega) + \varepsilon_v \kappa_m = 0, \tag{4}$$

as for the TE-mode:

$$\kappa_v \mu(\omega) + \mu_v \kappa_m = 0, \tag{5}$$

where, $\kappa_v = \sqrt{k_3^2 - k^2}$, $\kappa_m = \sqrt{k_3^2 - \varepsilon(\omega)\mu(\omega)k^2}$ - are the transverse wave vectors in vacuum and metamaterial regions, respectively, $k = \omega/c$ and c is the light speed in vacuum.

The TM-wave possesses the components that have the following form in air (or vacuum) region $x < 0$:

$$\begin{aligned} H_y(x) &= e^{\kappa_v x} H_y(0) \\ E_x(x) &= \frac{e^{\kappa_v x} k_3 H_y(0)}{k}, \\ E_z(x) &= \frac{ie^{\kappa_v x} \kappa_v H_y(0)}{k}. \end{aligned} \tag{6}$$

In the metamaterial region $x > 0$ the components of TM-wave has such form:

$$\begin{aligned} H_y(x) &= e^{-\kappa_m x} H_y(0), \\ E_x(x) &= \frac{e^{-\kappa_m x} k_3 H_y(0)}{\varepsilon(\omega)k}, \\ E_z(x) &= \frac{-ie^{-\kappa_m x} \kappa_m H_y(0)}{\varepsilon(\omega)k}. \end{aligned} \tag{7}$$

The TE-wave components of the following form in vacuum region $x < 0$:

$$\begin{aligned} E_y(x) &= e^{\kappa_v x} E_y(0), \\ H_x(x) &= -\frac{e^{\kappa_v x} k_3 E_y(0)}{k}, \\ H_z(x) &= -\frac{ie^{\kappa_v x} \kappa_v E_y(0)}{k}. \end{aligned} \tag{8}$$

and in the metamaterial region $x > 0$:

$$\begin{aligned} E_y(x) &= e^{-\kappa_m x} E_y(0), \\ H_x(x) &= -\frac{e^{-\kappa_m x} k_3 E_y(0)}{\mu(\omega)k}, \\ H_z(x) &= \frac{ie^{-\kappa_m x} \kappa_m E_y(0)}{\mu(\omega)k}. \end{aligned} \tag{9}$$

MAIN RESULTS

To analyze obtained equations let’s introduce such dimensionless variables: the frequency $\Omega = \omega / \omega_0$, the wavenumber $\beta = \text{Re}(k_3)c / \omega_0$, the normalized decrement $\alpha = \text{Im}(k_3)c / \omega_0$, the normalized electric $\nu = \nu_G / \omega_0$ and magnetic $\gamma = \gamma_G / \omega_0$ gains, and distance $\zeta = x \omega_0 / c$.

At first, two obtained dispersion equations for TM- and TE-modes (4,5) were solved numerically for metamaterial with $\nu = 0, \gamma = 0$ (Fig. 2).

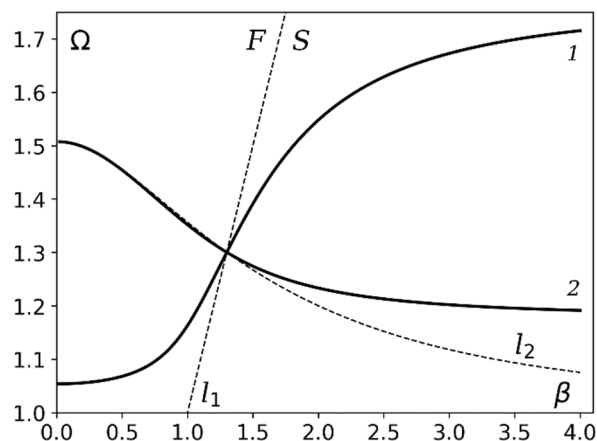


Figure 2. Normalized frequency as a function of the normalized wavenumber for TM and TE modes when $\nu = 0, \gamma = 0$ in equations (4,5).

The wave marked with number 1 corresponds to the wave of TM-polarizations, and by the number 2 – TE-wave. The dashed lines correspond to the conditions $\kappa_v = 0$ and $\kappa_m = 0$. These lines separate the regions where waves are fast or slow and bulk or surface.

It was previously shown [8] that the slow surface electromagnetic waves can exist in the right and upper region with respect to $\kappa_v = 0$ (line marked l_1 in Fig. 2) and $\kappa_m = 0$ (line marked l_2 in Fig. 2) lines. This region is marked by the letter S (see Fig. 2). The results obtained are in a good accordance with previously obtained results [8]. The fast electromagnetic waves can exist in the left region with respect to line l_1 that is marked by the letter F (Fig. 2). To study the properties of such fast waves it is necessary to take into account the non-zero values of ν and γ parameters in metamaterial permittivity $\epsilon(\omega)$ and permeability $\mu(\omega)$ expressions (1, 2), because in the case

of “ideal” metamaterial one obtain non-physical solutions of the dispersion equation. The results of the numerical solution of dispersion equations (4, 5) for this case for fast waves are presented in Figs. 3-6.

The numerical solutions of the dispersion equation (4) for fast TM-waves for the case when $\nu, \gamma \neq 0$ are presented in the Figs 3,4. These results have shown that the increase of the gain ν and γ leads to the strong decrease of wavelength under the fixed wave frequency value in the region of the rather low wave frequencies $\Omega < 1.15$ (see, Fig. 3). In the region when $1.15 < \Omega < 1.3$ the influence of ν and γ parameters variation is much smaller (see, Fig. 3). The dependence of the normalized decrement α versus ν and γ values are presented in the Fig. 4. This decrement has negative sign and the increase of gain ν and γ values leads to the α absolute value increase (see, Fig. 4).

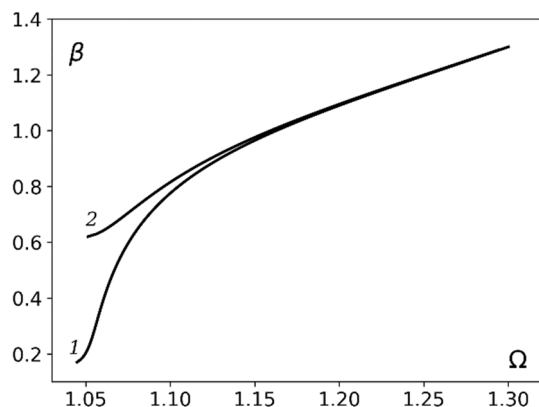


Figure 3. The normalized wavenumber β versus wave frequency Ω for the fast TM- wave. The line 1 corresponds to $\nu = 0.01, \gamma = 0.01$ and the line 2 corresponds to $\nu = 0.05, \gamma = 0.05$

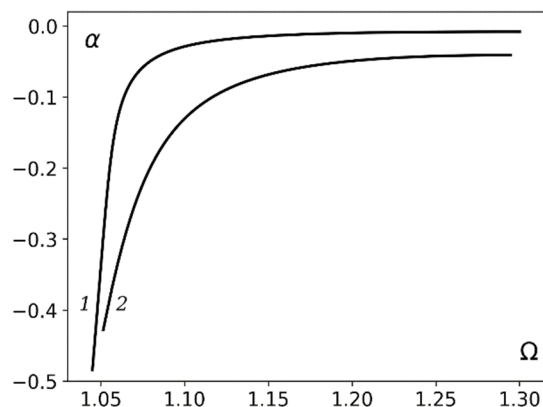


Figure 4. The normalized decrement α versus wave frequency Ω for the fast TM-waves. The parameters and curve numbering are the same as for the Fig. 3

The results of the numerical analysis of the dispersion equation (5) for fast TE-waves for the case $\nu, \gamma \neq 0$ are presented in the Figs 5,6. It is necessary to mention that simultaneously variation of ν, γ parameters make an extremely small influence on the TE-wave dispersion (see Fig. 5). But the influence of mentioned parameters of the TE-wave normalized decrement is much larger.

The increase of the parameters ν and γ values twice from 0.005 up to 0.01 leads to the increase on the normalized decrement α almost twice in the whole frequency range (see Fig. 6). It is also necessary to mention that for the fast TE-waves the normalized decrement $\alpha > 0$ and is much smaller by absolute value than α for the TM-wave.

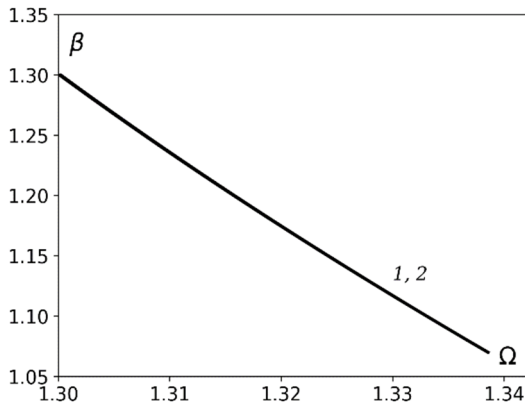


Figure 5. The normalized wavenumber β versus wave frequency Ω for the fast TE- wave. The coincident lines 1,2 corresponds to $\nu = 0.005, \gamma = 0.005$ and $\nu = 0.01, \gamma = 0.01$

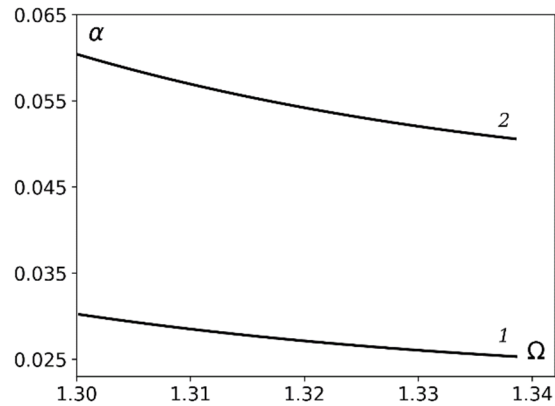


Figure 6. The normalized decrement α versus wave frequency Ω for the fast TE-modes. The parameters and curve numbering are the same as for the Fig. 5.

It was also studied the normalized phase ($V_{ph} = \Omega / \beta$) and group ($V_{gr} = d\Omega / d\beta$) velocities of the fast waves considered. The dependence of the V_{ph} for the fast TM-wave versus normalized frequency Ω for the same parameters as for the Fig. 3 are presented in the Fig. 7. It is shown that the wave is really fast wave ($V_{ph} > 1$) in appropriate frequency range. The simultaneously increase of the parameters ν and γ leads to the essentially TM-wave slowing in the region of rather low wave frequencies Ω ($\Omega < 1.1$ in Fig. 7).

The dependence of the V_{gr} for the fast TM-wave versus normalized frequency Ω for the same parameters as for the Fig. 3 are presented for the Fig. 8.

While the phase velocity is essentially greater than the speed of lighth (Fig. 7) the group velocity is much smaller than c (Fig. 8). TM-mode is forward, as can be seen from the figure above, i.e. the velocities V_{ph} and V_{gr} have the same sign. The normalized group velocity increases with the simultaneously increasing of the parameters ν and γ . It is necessary to mention that V_{gr} possesses the some minimum value in the region on rather small Ω values (see lines 1,2 in the Fig. 8 in the region $1.05 < \Omega < 1.1$). This minimum values shifts to the upper Ω values with the increase of the ν and γ .

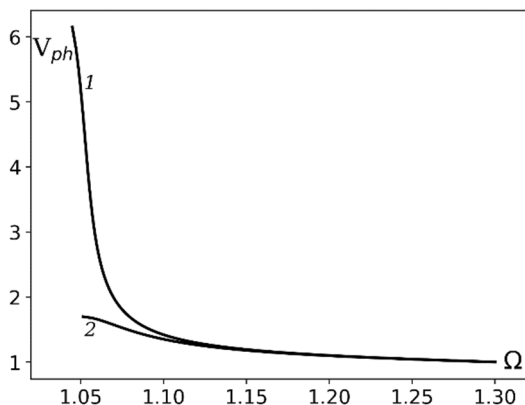


Figure 7. The normalized phase velocity of the fast TM- wave versus normalized frequency Ω . The parameters and curve numbering are the same as for the Fig. 3

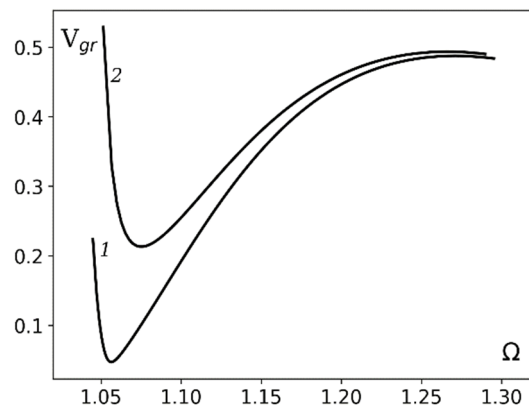


Figure 8. The normalized group velocity of the fast TM-wave versus normalized frequency Ω . The parameters and curve numbering are the same as for the Fig. 3

The dependence of the V_{ph} for the fast TE-wave versus normalized frequency Ω for the same parameters as for the Fig.5 are presented for the Fig. 9. It is shown that the wave is fast wave but more slowly than TM-wave. The characteristic

feature of the TE-wave is almost linearly dependence of the V_{ph} versus Ω (see Fig. 9) in the whole frequency range of fast wave existence. The phase velocity of the TE-wave is practically independent upon changing ν and γ .

The dependence of the V_{gr} for the fast TE-wave versus normalized frequency Ω for the same parameters as for the Fig. 5 are presented for the Fig. 10. The group velocity is negative, so the fast TE-wave is backward (V_{ph} and V_{gr} have the different signs). The absolute value of V_{gr} of TE-wave is much smaller than V_{gr} of TM-wave. This group velocity has weak dependence upon changing ν and γ and has almost linearly dependence versus Ω .

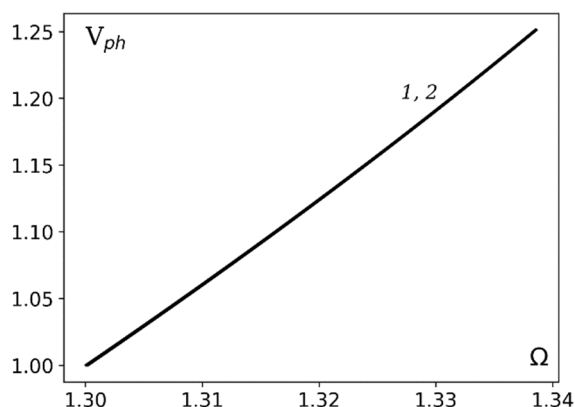


Figure 9. The normalized phase velocity of the fast TE-wave versus normalized frequency Ω . The parameters and curve numbering are the same as for the Fig. 5

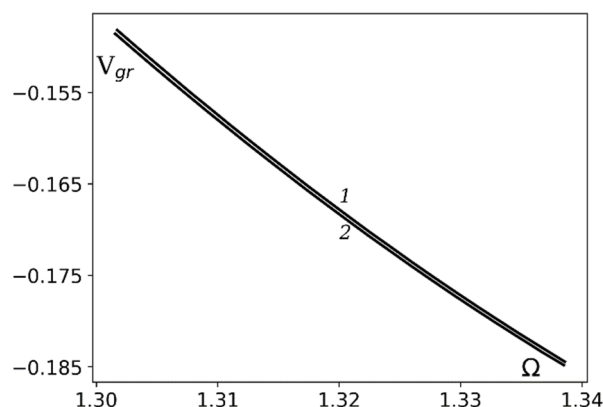


Figure 10. The normalized group velocity of the fast TE-wave versus normalized frequency Ω . The parameters and curve numbering are the same as for the Fig. 5

The absolute values of the normalized wave field components (upon the $H_y(0)$) for fast TM-wave for $\beta = 0.21$ (where wave phase velocity is much greater than c) are presented in the Fig. 11.

The absolute values of the normalized wave field components (upon the $E_y(0)$) for fast TE-wave for $\beta = 1.1$ (where wave phase velocity is much greater than c) are presented in the Fig. 12. It is necessary to mention that the normalized skin depth of the fast TM-wave in metamaterial region is much smaller that skin depth of the fast TE-wave. The obtained results can be important for modeling and designing of modern devices based on metamaterials.

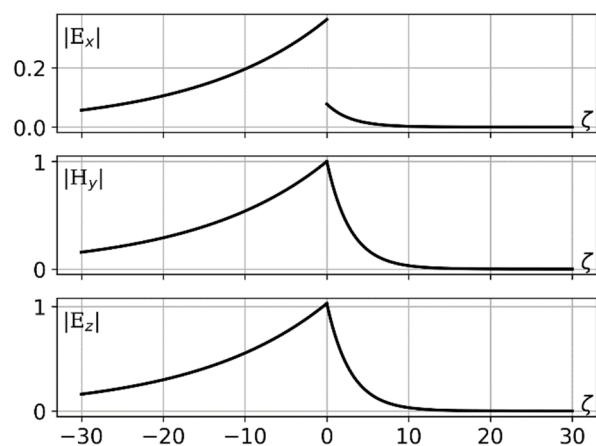


Figure 11. The absolute values of the normalized wave field components (upon the $H_y(0)$) for fast TM-wave for $\beta = 0.21$

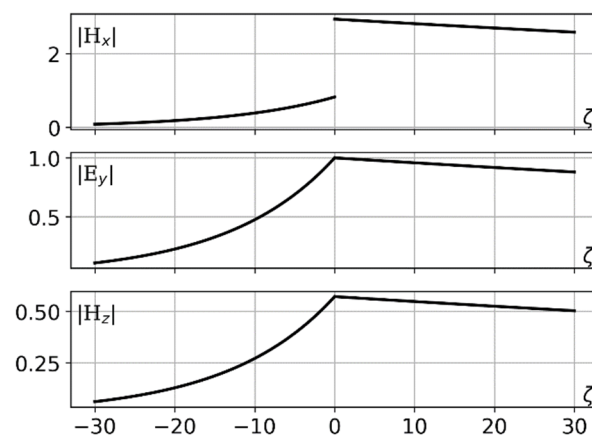


Figure 12. The absolute values of the normalized wave field components (upon the $E_y(0)$) for fast TE-wave for $\beta = 1.1$

CONCLUSIONS

It was shown that fast eigen TE- and TM-waves can exist in the considered waveguide structure. It was studied the dependence of the dispersion properties, wave attenuation, phase and group velocities, and spatial wave field structure of waves considered upon the metamaterial parameters. It is demonstrated that the eigen fast TM-wave is the direct wave and fast eigen TE-wave is backward wave.

The obtained results can be important for modeling and designing of modern generating and amplifying devices based on metamaterials.

ORCID IDs

 Viktor K. Galaydych, <https://orcid.org/0000-0002-2255-9716>;  Alexandr E. Sporov, <https://orcid.org/0000-0002-4610-9656>
 Volodymyr P. Olefir, <https://orcid.org/0000-0002-8022-2556>;  Mykola O. Azarenkov, <https://orcid.org/0000-0002-4019-4933>

REFERENCES

- [1] I.V. Shadrivov, M. Lapine, and Y.S. Kivshar, editors, *Nonlinear, tunable and active metamaterials*, (Springer, 2015), <https://doi.org/10.1007/978-3-319-08386-5>
- [2] S. Ramo, J.R. Whinnery, and T. Van Duzer. *Fields and Waves in Communication Electronics* (3rd ed.), (John Wiley & Sons, 1994), ISBN: 978-0-471-58551-0
- [3] R. Carter. *Fast-Wave Devices // Microwave and RF Vacuum Electronic Power Sources* (The Cambridge RF and Microwave Engineering Series), (Cambridge University Press, 2018), pp. 659-693, <https://doi.org/10.1017/9780511979231.018>
- [4] G.S. Nusinovich, M.K. Thumm, and M.I. Petelin, *Journal of Infrared, Millimeter, and Terahertz Waves*, **35**, 325 (2014), <https://doi.org/10.1007/s10762-014-0050-7>
- [5] V.K. Galaydych, N.A. Azarenkov, V.P. Olefir, and A.E. Sporov, *Problems of Atomic Science and Technology*, **4**, 306 (2015), https://vant.kipt.kharkov.ua/ARTICLE/VANT_2015_4/article_2015_4_306.pdf
- [6] V.K. Galaydych, N.A. Azarenkov, V.P. Olefir, and A.E. Sporov, *Problems of Atomic Science and Technology*, **1**, 96 (2017), https://vant.kipt.kharkov.ua/ARTICLE/VANT_2017_1/article_2017_1_96.pdf
- [7] D.R. Smith, W.J. Padilla, S.C. Vier, S.C. Nemat-Nasser, and S. Schultz, *Phys. Rev. Lett.* **84**, 4184, (2000), <https://doi.org/10.1103/PhysRevLett.84.4184>
- [8] R. Ruppin, *Phys. Lett. A*, **277**, 61 (2000), [https://doi.org/10.1016/S0375-9601\(00\)00694-0](https://doi.org/10.1016/S0375-9601(00)00694-0)

ШВИДКІ ЕЛЕКТРОМАГНІТНІ ХВИЛІ НА МЕЖІ МЕТАМАТЕРІАЛУ: МОДЕЛЮВАННЯ ПІДСИЛЕННЯ

В.К. Галайдич, О.Є. Споров, В.П. Олефір, М.О. Азаренков

*Харківський Національний університет ім. В.Н. Каразіна
61022, Україна, м. Харків, пл. Свободи, 4*

В статті представлено результати дослідження властивостей швидких поверхневих електромагнітних хвиль, що поширюються уздовж плоскої поверхні розділу між активним метаматеріалом та повітрям (або вакуумом). Розглянуто випадок однорідного та ізотропного метаматеріалу. Досліджено дисперсійні властивості, просторове загасання хвилі, фазову та групову швидкості, а також просторовий розподіл електромагнітного поля власних ТЕ та ТМ мод такої хвилеводної структури. Показано, що в цій хвилеводній структурі можуть існувати швидкі поверхневі електромагнітні хвилі та досліджено їх властивості. Показано, що фазова швидкість ТМ-моди у кілька разів перевищує швидкість світла у вакуумі, тоді як фазова швидкість ТЕ-моди незначно перевищує швидкість світла у вакуумі. ТМ-мода є прямою хвилею, в якій фазова та групові швидкості однаково спрямовані. Отримано, що групові швидкості ТМ-моди змінюються від нуля до половини швидкості світла у вакуумі, та досягає мінімуму за деякого значення частоти хвилі, що залежить від характеристик метаматеріалу. Показано, що глибина проникнення ТМ-моди в метаматеріал значно менша ніж у вакуум. ТЕ-мода є зворотною хвилею, в якій фазова та групові швидкості протилежно направлені. Абсолютне значення групової швидкості ТЕ-моди приблизно в шість разів менше за швидкість світла у вакуумі. На відміну від ТМ-моди, глибина проникнення ТЕ-моди в метаматеріал значно більша, ніж у вакуум. Визначені властивості швидких поверхневих електромагнітних хвиль можуть бути використані для моделювання та проектування сучасних приладів генерації та підсилення, що містять метаматеріали.

Ключові слова: метаматеріал, швидка поверхнева електромагнітна хвиля, дисперсія, загасання, просторова структура хвилі

DETERMINATION OF URANIUM ISOTOPIC RATIOS BY HRGS USING VARIOUS EFFICIENCY CALIBRATION APPROACHES[†]

 **Dmytro V. Kutnii**,  **Dmytro D. Burdeynyi**

National Science Center “Kharkiv Institute of Physics and Technology” of NAS of Ukraine

E-mail: d_kutniy@kipt.kharkov.ua

Received May 14, 2021; accepted September 27, 2021

The effect of various efficiency calibration approaches on the value and source of the HRGS measurement uncertainty of $^{234}\text{U} / ^{238}\text{U}$, $^{235}\text{U} / ^{238}\text{U}$, $^{234}\text{U} / ^{235}\text{U}$ isotopic ratios for the purposes of technological control, nuclear forensics, and environmental monitoring has been studied. The Canberra Broad Energy Germanium detector BEGe3830 and five samples of uranium certified reference materials CRM 969 and CRM 146 with a content of $^{235}\text{U} / \text{U}$ ranging from 0.7 to 20.0 wt. % have been used. To calculate the uranium isotope ratios, the acquired gamma spectra were processed using: commercial MGAU (LLNL), FRAM (LANL), ISOCS software (Canberra/Mirion Technologies), based on intrinsic and absolute efficiency calibration approaches. It has been found that maximum relative biases, for the $^{234}\text{U} / ^{238}\text{U}$ and $^{234}\text{U} / ^{235}\text{U}$ isotopic ratios determined using the MGAU \ FRAM \ ISOCS software, are $\sim 25\%$ \ $\sim 10\%$ \ $\sim 10\%$, and the random uncertainty is varied within $\pm [18-25\%$ \ $2-15\%$ \ $\leq 3\%]$, respectively. In the case of $^{235}\text{U} / ^{238}\text{U}$ isotopic ratio determination using the MGAU \ FRAM \ ISOCS software, maximum relative biases come to $\sim 3\%$ \ $\sim 4\%$ \ $\sim 1\%$, and the random uncertainty values decrease to $\pm [1\%$ \ 1% \ $1\%]$, respectively. In the present paper we propose a combined intrinsic efficiency calibration approach with the use of the polynomial functions for analytical description of the relation $\varepsilon_{rel,i}(E_i)$. In this approach a maximum relative biases, in the determination of the $^{234}\text{U} / ^{238}\text{U}$ and $^{234}\text{U} / ^{235}\text{U}$ isotopic ratios is 2.7% at a random uncertainty of $\leq 1\%$, and in the case of the $^{235}\text{U} / ^{238}\text{U}$ ratio a maximum relative deviation is 0.5% at a random uncertainty of $\leq 0.7\%$.

Keywords: high resolution gamma spectrometry, uranium isotope ratios, efficiency calibration, measurement uncertainty, uranium ore, MGAU, FRAM, ISOCS

PACS: 29.30. Kv

Natural uranium is a mixture of three isotopes: ^{238}U (isotopic abundance $^{238}\text{U} / \text{U} = 99.2745\%$, half-life $T_{1/2} = 4.468 \cdot 10^9$ years), ^{235}U ($^{235}\text{U} / \text{U} = 0.7200\%$, $T_{1/2} = 7.04 \cdot 10^8$ years) and ^{234}U ($^{234}\text{U} / \text{U} = 0.0055\%$, $T_{1/2} = 2.455 \cdot 10^5$ years) [1]. In some stages of the fuel nuclear cycle, and due to the radionuclide migration in the geosphere, the uranium isotopic composition can vary, therefore, there is a need to measure the uranium isotopic ratio in the view of economic and technologic strategy for the purposes of nuclear safety and environmental monitoring.

The values of the isotopic abundances ($^{234}\text{U} / \text{U}$, $^{235}\text{U} / \text{U}$, $^{238}\text{U} / \text{U}$) are a subject of technological control in the uranium material production. They are regulated by the international ASTM standards, e.g. C 787 and C 996. The standard test method for uranium isotopic abundance analysis using the inductively coupled plasma mass spectrometry (ICP-MS), described in the ASTM C 1477 standard, is applied in the destructive analysis (DA) of feed raw material in order to fabricate the nuclear fuel with a relative content of $^{235}\text{U} / \text{U} \leq 5.0\%$ for power reactors. Using this destructive method it is possible to reach the measurement uncertainty for $^{235}\text{U} / \text{U}$ at a level of $\leq 0.1\%$ and for $^{234}\text{U} / \text{U}$ at a level $\leq 1.0\%$, i.e. even minor variations in the isotopic composition can be quantified. A quantitative identification of uranium isotopes is also required in the complex of scientific methods known as nuclear forensics. As defined by the IAEA the nuclear forensics is a field of applied nuclear physics directed at the analysis of nuclear and radioactive materials, seized from the illicit trafficking, to obtain analytical data needed to reconstruct the history of the origin of these materials. In this field the uranium isotopic ratios ($^{234}\text{U} / ^{238}\text{U}$, $^{235}\text{U} / ^{238}\text{U}$, $^{234}\text{U} / ^{235}\text{U}$) are of particular interest compared to their isotopic abundances [2, 3].

The information on the geographic region of the material deposit plays a substantial role in tracking its deposit. The values of the uranium isotopic ratios in the complex may be used for establishing the origin of uranium ores (UO) and uranium ore concentrates (UOC).

Moreover, the $^{234}\text{U} / ^{238}\text{U}$ isotopic ratio is used in the hydroindication studies as a high-precision indicator of the source of groundwater flow formation. The values of the $^{234}\text{U} / ^{238}\text{U}$ ratios give important information for estimation of the groundwater recovery and flow separation, for determining mixing proportions of several sources and studying the dynamics of interaction in the water-ore system.

The $^{235}\text{U} / ^{238}\text{U}$ isotopic ratio in natural uranium has been widely accepted as 7.25×10^{-3} for many years and until recently has been invariant [4]. In 1972 the uranium ores from the Oklo deposit (Gabon, Western Africa) revealed a

[†] Cite as: D.V. Kutnii, D.D. Burdeynyi, East. Eur. J. Phys. 3, 151 (2021), <https://doi.org/10.26565/2312-4334-2021-3-23>

significant deviation in the $^{235}\text{U} / ^{238}\text{U}$ isotopic ratio [5]. It has been found that the $^{235}\text{U} / \text{U}$ isotopic abundance in the deposit ores is depleted nearly 2.5 times apparently due to the uranium “burn-up” as a result of a spontaneous chain nuclear reaction. Subsequent research has shown that variations of the $^{235}\text{U} / ^{238}\text{U}$ isotopic ratio in natural uranium usually do not exceed 1.3 % for different deposits and most often are caused by the physical-chemical factors [6].

The $^{234}\text{U} / ^{238}\text{U}$ ratio for natural uranium accepted as 5.5×10^{-5} , on the other hand, has been found to vary considerably due to the natural cause in many water, soil, sediments and uranium ores of different geographical origin [7]. The mechanism of such variation is a preferential leaching of ^{234}U compared with ^{238}U from the solid phase, caused by radiation damage of the crystal lattice upon the alpha decay of ^{238}U , oxidation of insoluble tetravalent ^{234}U to soluble hexavalent ^{234}U during decay, and alpha recoil of ^{234}Th (and its daughter ^{234}U) into solution phase [8]. The $^{234}\text{U} / ^{238}\text{U}$ ratio in water reportedly varies from 2.8×10^{-5} to 2.2×10^{-3} (variation quantified as a mean absolute deviation of about 100 %), that in soil typically ranges from 2.8×10^{-5} to 6.6×10^{-5} (variation of about 40 %), while that in uranium ores ranges from 5.2×10^{-5} to 8.4×10^{-5} (variation of about 20 %) [9].

The natural $^{234}\text{U} / ^{235}\text{U}$ isotopic ratio can also appreciably vary for different uranium deposits [10]. The $^{234}\text{U} / ^{235}\text{U}$ ratios of the high-temperature and non-redox deposits appear to lie close to the secular equilibrium value 7.6×10^{-3} , whereas the $^{234}\text{U} / ^{235}\text{U}$ ratios of the low-temperature deposits show a significant scatter. This difference is likely related to the nature of the deposits themselves as open or closed systems. Low-temperature deposits primarily consist of sandstone deposits that form below the water table. The relatively high porosity of the host sandstone allows for greater open system behavior than does the more compacted lithology of the host rocks of high-temperature and non-redox deposits. Whenever large amounts of groundwater interact with a deposit, the deposit is expected to contain either excesses of ^{234}U , if the deposition is still occurring or depletions in ^{234}U if the deposition has stopped. In the first case the $^{234}\text{U} / ^{235}\text{U}$ ratio can reach $\sim 1.3 \times 10^{-2}$, in the second case it is 6.3×10^{-3} , and the ratio variation is of about 30 %.

Furthermore, slight differences in the $^{234}\text{U} / ^{235}\text{U}$ ratio may point to the different enrichment processes at the enrichment stage of the nuclear fuel cycle [11]. Hence, when using the gas centrifugation process for uranium enrichment to the $^{235}\text{U} / \text{U}$ abundance ~ 93 %, a typical $^{234}\text{U} / \text{U}$ abundance increases to 0.89 %, the gaseous diffusion enrichment process under the same conditions increases the $^{234}\text{U} / \text{U}$ abundance to 0.93 % [12]. Thus, using different enrichment technologies the variations in the $^{234}\text{U} / ^{235}\text{U}$ isotopic ratio can be about 2 %.

A comparison of $^{235}\text{U} / \text{U}$ measurement uncertainty results obtained in [13] by destructive (ICP-MS) and non-destructive (high resolution gamma spectrometry – HRGS) methods show that in the range of $^{235}\text{U} / \text{U}$ abundance from 1.0 to 20.0% the international target values for measurement uncertainties of DA methods are 0.14 % and these of non-destructive (NDA) methods are 3.6 %.

In this paper we have studied the effect of various efficiency calibration approaches on the magnitude and sources of the HRGS measurements uncertainty of $^{234}\text{U} / ^{238}\text{U}$, $^{235}\text{U} / ^{238}\text{U}$, $^{234}\text{U} / ^{235}\text{U}$ isotopic ratios for the purposes of technological control, nuclear forensics, and environmental monitoring.

MATERIALS AND METHODS

The Canberra Broad Energy Germanium detector BEGe3830 with active area of 3800 mm² and thickness of 30 mm has been used for the spectra acquisition. The detector is equipped with a carbon composite input window of 0.6 mm thickness. The energy resolution (FWHM) of the detector is 720 eV at 122 keV.

Five samples of uranium certified reference materials CRM 969 and CRM 146 from the US National Bureau of Standards with $^{235}\text{U} / \text{U}$ abundance from 0.7 to 20.0 wt. % have been used in testing. The calculated reference uranium isotope ratios and their relative uncertainties are shown in Table 1. Reference samples were made of 200 or 230 g of U₃O₈ powder encased with a filling height of 20.8 or 15.8 mm in aluminum cans with bottom wall thickness of about 2 mm and side wall thickness of about 5 mm.

The sample cans were placed in front of the detector in the “bottom configuration” geometry keeping the symmetry of mutual position. The counting time for data acquisition was 2 h. The dead time varied typically from 0.62 to 2.65 %. The 185.7 keV peak of ^{235}U was checked to be at the channel 2476 corresponding to the required detector calibration gain of 0.075 keV per channel.

Table 1. Reference uranium isotopic ratios and relative uncertainties in the materials CRM 969 and CRM 146

Sample ID	$(^{235}\text{U} / \text{U})^{\text{Ref.}}$, wt. %	$(^{234}\text{U} / ^{238}\text{U})^{\text{Ref.}} \pm \text{Rel. Unc.}$	$(^{235}\text{U} / ^{238}\text{U})^{\text{Ref.}} \pm \text{Rel. Unc.}$	$(^{234}\text{U} / ^{235}\text{U})^{\text{Ref.}} \pm \text{Rel. Unc.}$
071	0.7119	$5.2376 \times 10^{-5} \pm 3.85$ %	0.00717 ± 0.07 %	$7.3044 \times 10^{-3} \pm 3.85$ %
194	1.9420	$1.7442 \times 10^{-4} \pm 1.17$ %	0.01981 ± 0.07 %	$8.8054 \times 10^{-3} \pm 1.17$ %
295	2.9492	$2.8757 \times 10^{-4} \pm 1.43$ %	0.03039 ± 0.07 %	$9.4602 \times 10^{-3} \pm 1.43$ %
446	4.4623	$3.7594 \times 10^{-4} \pm 0.84$ %	0.04673 ± 0.07 %	$8.0452 \times 10^{-3} \pm 0.84$ %
NBL0013	20.107	$1.8682 \times 10^{-3} \pm 0.25$ %	0.25277 ± 0.09 %	$7.3910 \times 10^{-3} \pm 0.25$ %

In order to calculate the uranium isotopic ratios, the gamma spectra were processed using:

- Commercial software MGAU (Ver. 3.2), developed at the Lawrence Livermore National Laboratory and FRAM (Ver. 5.0), developed at the Los Alamos National Laboratory;
- ISOCS efficiency calibration combined with Geometry Composer (Ver. 4.2.1) software, developed at the Canberra (Mirion Technologies);
- Intrinsic (relative) efficiency calibration approach [14-17].

The commercial software MGAU and FRAM use the «response function» approach for determination of the uranium isotopic composition [18, 19]. According to this approach, the response functions, describing the contribution of each isotope to the fitted energy range, are constructed or, in other words, the true intensities of uranium gamma lines are calculated. At constructing, the available prior information on the energies, peak shapes, energy resolution, branching ratios and relative intensities of gamma and x-rays is utilized.

To determine accurately the areas of the photoelectric absorption peaks, a relative efficiency curve is calculated using the intrinsic efficiency calibration. The efficiency calibration is intrinsic in the sense that it relates to a specific gamma spectrum, i.e. for each sample under study (a set of spectral data) it is necessary to perform its own intrinsic calibration based on the information coming directly from the measured spectrum. Mathematically, the intrinsic efficiency calibration is described in [20, 21]. The observed net count rate in the photopeak corresponding to the radioisotope of interest is expressed as:

$$n_i^R = \lambda^R \cdot N^R \cdot I_i^R \cdot \varepsilon_i, \quad (1)$$

where n_i^R is the net count rate in the peak at energy i of radioisotope R ; λ^R – the decay constant for radioisotope R ; N^R – the number of atoms for the radioisotope R ; I_i^R – the gamma-ray emission probability at energy i from radioisotope R ; ε_i – absolute detection efficiency at energy i .

To express equation given above in the relative terms, we need to introduce the ratio of the radioisotopes considered in the analysis by dividing their corresponding amounts N^T by an amount of a “reference” radioisotope. The reference radioisotope represents the radioisotope relatively to which the remaining radioisotopes considered in the analysis are normalized. In this case the counting efficiency becomes expressed in relative terms:

$$n_i^R = \lambda^R \cdot (N^T / N^R) \cdot I_i^R \cdot \varepsilon_{rel,i}. \quad (2)$$

If ^{238}U is used as the reference radioisotope, then the ratios $^{235}\text{U} / ^{238}\text{U}$ and $^{234}\text{U} / ^{238}\text{U}$ can be estimated. After the division by the primary radioisotope the counting efficiency is viewed in the relative term which is the detection efficiency for ^{234}U and ^{235}U gamma-ray peaks with respect to those of ^{238}U .

For a given pair of radioisotopes the atomic ratio is defined as division of the number of atoms N^T by the number of atoms corresponding to the reference radioisotope (in our case ^{238}U), thus for the gamma peaks corresponding to the reference radioisotope (^{238}U) the ratio N^T / N^R is equal to unity (since the atomic ratio $N^{238} / N^{238} = 1$), whereas for the gamma peaks of ^{234}U and ^{235}U radioisotopes their values are determined from the fitting routine.

If to analyze the isotope ratio, the $^{235}\text{U} / ^{238}\text{U}$ gamma-lines with energies of 258.3, 766.4, 1001.3 keV of ^{234m}Pa (daughter of ^{238}U) and 143.8, 163.3, 185.7 keV of ^{235}U are measured, then using the information from all the available gamma-ray signatures, corresponding to the radioisotopes considered in the analysis, a system of simultaneous equations is constructed, as given by the system of equations:

$$\begin{aligned} n_{258}^{238} &= \lambda^{238} \cdot 1 \cdot I_{258}^{238} \cdot \varepsilon_{rel,258}, \\ n_{766}^{238} &= \lambda^{238} \cdot 1 \cdot I_{766}^{238} \cdot \varepsilon_{rel,766}, \\ n_{1001}^{238} &= \lambda^{238} \cdot 1 \cdot I_{1001}^{238} \cdot \varepsilon_{rel,1001}, \\ n_{143}^{235} &= \lambda^{235} \cdot (N^{235} / N^{238}) \cdot I_{143}^{235} \cdot \varepsilon_{rel,143}, \\ n_{163}^{235} &= \lambda^{235} \cdot (N^{235} / N^{238}) \cdot I_{163}^{235} \cdot \varepsilon_{rel,163}, \\ n_{186}^{235} &= \lambda^{235} \cdot (N^{235} / N^{238}) \cdot I_{186}^{235} \cdot \varepsilon_{rel,186}. \end{aligned} \quad (3)$$

In such a way the system of n -equations is constructed for the available gamma-ray peaks. A minimum number of gamma peaks necessary for the fitting routine is determined as a total number of fitting parameters plus one, for at least one degree of freedom. In such a system of equations the atomic ratios are fitted altogether with the coefficients of the relative counting efficiency model applied to describe the shape of the counting efficiency curve using the data points from both radioisotopes.

If in the graphical representation Equation (1) is written as: $n_i^R / I_i^R = (\lambda^R \cdot N^R) \cdot \varepsilon_i$, then for different gamma-quantum energies i of a single radioisotope R we obtain $\varepsilon_i \sim n_i^R / I_i^R$. Plotting the n_i^R / I_i^R ratio as a function of gamma-quantum energy E_i and approximating its polynomial functions $f(E)$ we obtain a relative efficiency curve $\varepsilon_{rel,i}(E_i)$ for a radioisotope R . For single measurement geometry the curves $\varepsilon_{rel,i}(E_i)$ have the same shape for all the isotopes being analyzed and differ only by the coefficient $\lambda^R \cdot N^R$. The software FRAM uses for approximation the function such as: $\ln \varepsilon_{rel,i} = f(E_i) = c_1 + c_2/E_i^2 + c_3 \cdot \ln E_i + c_4 \cdot (\ln E_i)^2 + c_5 \cdot (\ln E_i)^3$ where $c_1 \dots c_5$ are the coefficients determined by fitting the reference isotope peaks. The type of approximating polynomial function, used in the MGAU software, is not given by the developers.

As a result, the software codes MGAU and FRAM fit normalized responses in the required energy range and then calculate relative abundances as follows, e.g. for $^{238}\text{U} / \text{U}$:

$$\frac{^{238}\text{U}}{\text{U}} = \frac{N^{238}}{N^{234} + N^{235} + N^{238}} = \frac{1}{N^{234}/N^{238} + N^{235}/N^{238} + 1} \quad (4)$$

The MGAU code performs an efficiency calibration in the 89-100 keV energy range, while FRAM code has a choice of the two alternative energy ranges: 60-210 keV and 120-1001 keV.

An ISOCS efficiency calibration software is a mathematical package built for the absolute detector efficiency ε_{abs} calculation using a MCNP Monte Carlo modeling code. For the efficiency calibration an accurate model of the sample geometry – position of the sample relative to the detector, distribution of the source in the sample, shape and thickness of the container, density of the original matrix, composition of the container and matrix – was created using a Geometry Composer software. After that, ISOCS effectively integrates the characterization function across the sample volume and, as a result, the absolute efficiency data points are generated which further are used for efficiency calibration of the measured gamma-spectrum. The activity A_i^R of the radioisotope R with gamma-line energies i is calculated as: $A_i^R = n_i^R / (I_i^R \cdot \varepsilon_{abs})$. Subsequently, using the specific activity values of the isotopes, their masses and isotope ratios can be calculated.

RESULTS AND DISCUSSIONS

To evaluate the results of uranium isotope ratios analysis by various software, statistical methods were used [22]. A comparison between the calculated values of isotope ratios with reference ones was based on a statistical quantity called the ζ -score, which is estimated as:

$$\zeta = \frac{(x - X)}{\sqrt{(u_x^2 + u_X^2)}}, \quad (5)$$

where x and u_x are the values of the calculated isotope ratio and its uncertainty; X and u_X are the values of the reference isotope ratio and its uncertainty. The results of the analysis are considered to be acceptable if $|\zeta| \leq 2$, i.e. the calculated and reference values are consistent. The value of $|\zeta|$ from 2 to 3 indicates that the results are of a questionable quality or inconsistent with a medium confidence. If $|\zeta| > 3$, the analysis was considered to be out of control, i.e. the results are inconsistent with a high confidence. The results of uranium isotope ratios evaluation using the statistical approach are shown in Fig. 1.

The values of $^{234}\text{U} / ^{238}\text{U}$ and $^{234}\text{U} / ^{235}\text{U}$ isotopic ratios, calculated using the MGAU and FRAM software and the relative efficiency calibration approach satisfy the statistical criterion $|\zeta| \leq 2$, i.e. they are in agreement with reference values. However, the value of ζ is negative and $|\zeta| \rightarrow 2$ for the results obtained by the MGAU software, i.e. probably, there occurs a systematic underestimation of the ^{234}U isotope abundance. The ISOCS results do not coincide with the reference values for samples 194, 295, 446. The biases have a diverse character and, probably, they are related with a ^{234}U isotope determination error. In the case of analysis of the $^{235}\text{U} / ^{238}\text{U}$ isotopic ratio there was observed a tendency to overestimate by the software MGAU and to underestimate by the software FRAM its value.

The written above is graphically shown in Fig. 2 where the results of $^{234}\text{U} / ^{238}\text{U}$, $^{235}\text{U} / ^{238}\text{U}$, $^{234}\text{U} / ^{235}\text{U}$ isotopic ratio measurement by different software are represented. In addition, there is a reference value of the isotopic ratio determined with measurement uncertainty limits, relative bias (systematic uncertainty) of the measured value from the reference and software measurement uncertainties (random uncertainties).

It is seen that the relative bias of $^{234}\text{U} / ^{238}\text{U}$ and $^{234}\text{U} / ^{235}\text{U}$ ratio values, measured by the MGAU software, is negative and its absolute value is $\sim 25\%$. So, really, the MGAU software significantly underestimates the ^{234}U isotope

abundance, and the agreement of $^{234}\text{U} / ^{238}\text{U}$ and $^{234}\text{U} / ^{235}\text{U}$ isotopic ratio values with the statistical criterion $|\zeta| \leq 2$ is explained only by a high value of the random uncertainty u_x ($\pm 18\text{-}25\%$), being in the denominator of Equation (5). The abundance of the ^{234}U isotope is determined by analysis of its single gamma-line with energy of 120.9 keV. As the software MGAU performs the efficiency calibration in the narrow energy range from 89 to 100 keV, the efficiency curve approximation up to 120.9 keV can introduce a significant error that, likely, is a cause of the ^{234}U isotope abundance underestimation.

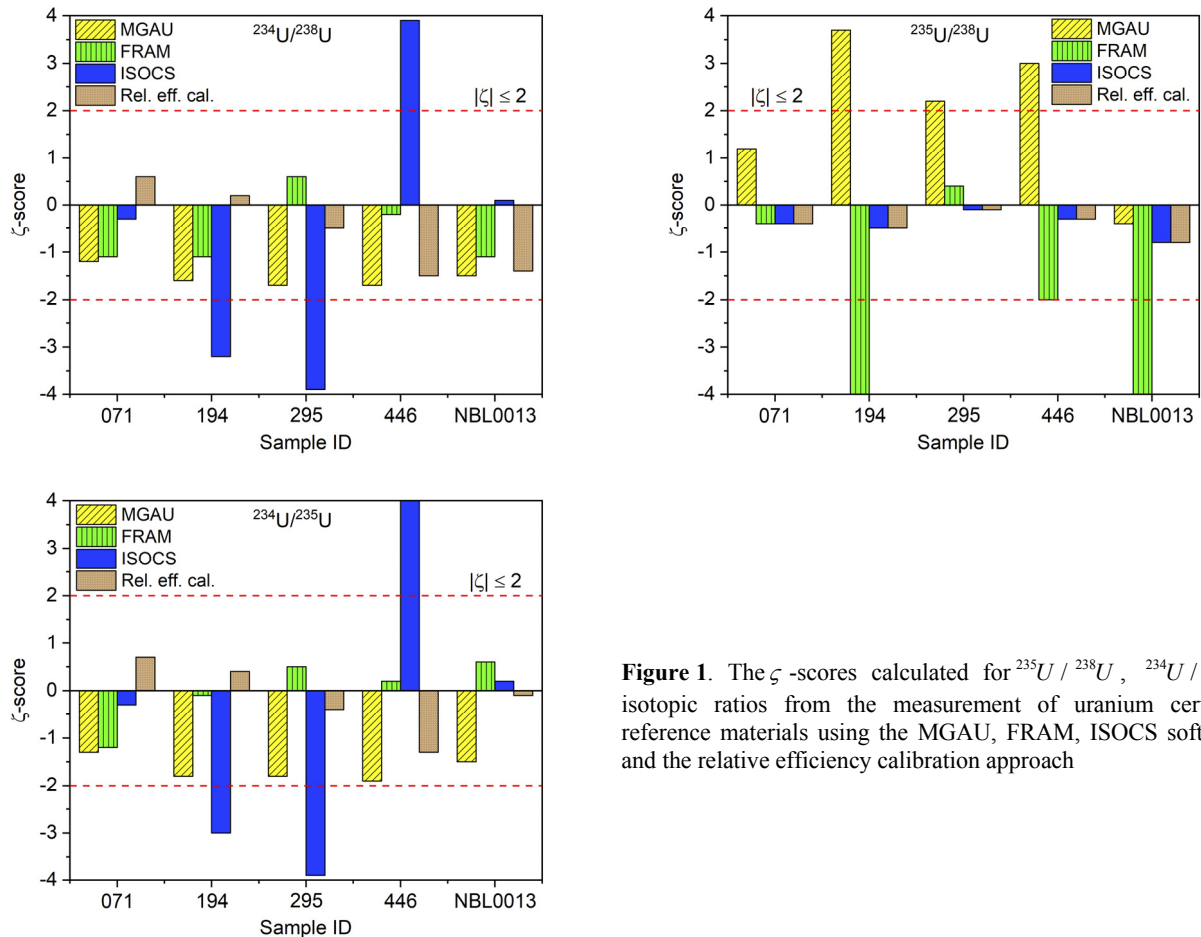


Figure 1. The ζ -scores calculated for $^{235}\text{U} / ^{238}\text{U}$, $^{234}\text{U} / ^{235}\text{U}$ isotopic ratios from the measurement of uranium certified reference materials using the MGAU, FRAM, ISOCs software and the relative efficiency calibration approach

In the case of $^{235}\text{U} / ^{238}\text{U}$ isotopic ratios the software MGAU gives, mainly a result overestimated by 1-3%, and the random uncertainty u_x does not exceed 1%. In Ref. [18] such a relative bias is explained by the ^{232}U , ^{233}U , ^{234}U , ^{236}U , ^{238}U contribution into the intensity of $\text{ThK}\alpha$ analytical lines (93.35 and 89.96 keV), emitted in the decay process $^{235}\text{U} \rightarrow ^{231}\text{Th}$, being the base lines for estimation of the ^{235}U isotopic abundance.

The FRAM software, compared to MGAU, determines the $^{234}\text{U} / ^{238}\text{U}$ and $^{234}\text{U} / ^{235}\text{U}$ isotopic ratios with a lesser systematic uncertainty. Thus, a maximum relative bias of $\sim 10\%$ was obtained for a sample of natural uranium (sample ID: 071). When the ^{235}U abundance and, consequently that of ^{234}U , increases (in the process of uranium enrichment with isotope ^{235}U the material is enriched with isotope ^{234}U more effectively) the systematic and random uncertainties decrease to 2-3%. This occurs due to the increase in the gamma-line 120.9 keV intensity of ^{234}U and, respectively, due to the decrease in the peak area determination error. Similarly to the case with the MGAU, the occurrence of a relative bias, when determining ^{234}U with the FRAM, can be explained by the shortcomings in the intrinsic efficiency calibration procedure. But FRAM, unlike MGAU, uses a larger energy range (from 143.8 keV to 1001.3 keV) directly for the relative efficiency curve calculating, therefore the curve approximation to 129.9 keV provides a lesser error. By determining the $^{235}\text{U} / ^{238}\text{U}$ isotopic ratio, FRAM, most often, underestimates the ratio by $< 5\%$ in the ^{235}U abundance range being studied, and the random uncertainty u_x does not exceed 1% that correlates with the data [23].

Despite the fact that the values of the $^{234}\text{U} / ^{238}\text{U}$ and $^{234}\text{U} / ^{235}\text{U}$ isotopic ratios, calculated with the ISOCs software, do not satisfy the statistical criterion $|\zeta| \leq 2$ for some samples, the values of the relative bias and random uncertainty obtained by such a method are lower than in MGAU and FRAM codes and do not exceed 10% and 3%

respectively. The $^{235}\text{U} / ^{238}\text{U}$ isotopic ratio can be calculated more accurately and in this instance the statistic parameters (relative bias and random uncertainty) do not exceed 1 %. A main disadvantage of the ISOCS efficiency calibration software is that the absolute efficiency can be calculated only from the exact measurement geometry data in order to take correctly into account the effects of absorption and scattering of gamma-quanta in the material under study, container material and other absorbers that is not always possible in the real conditions.

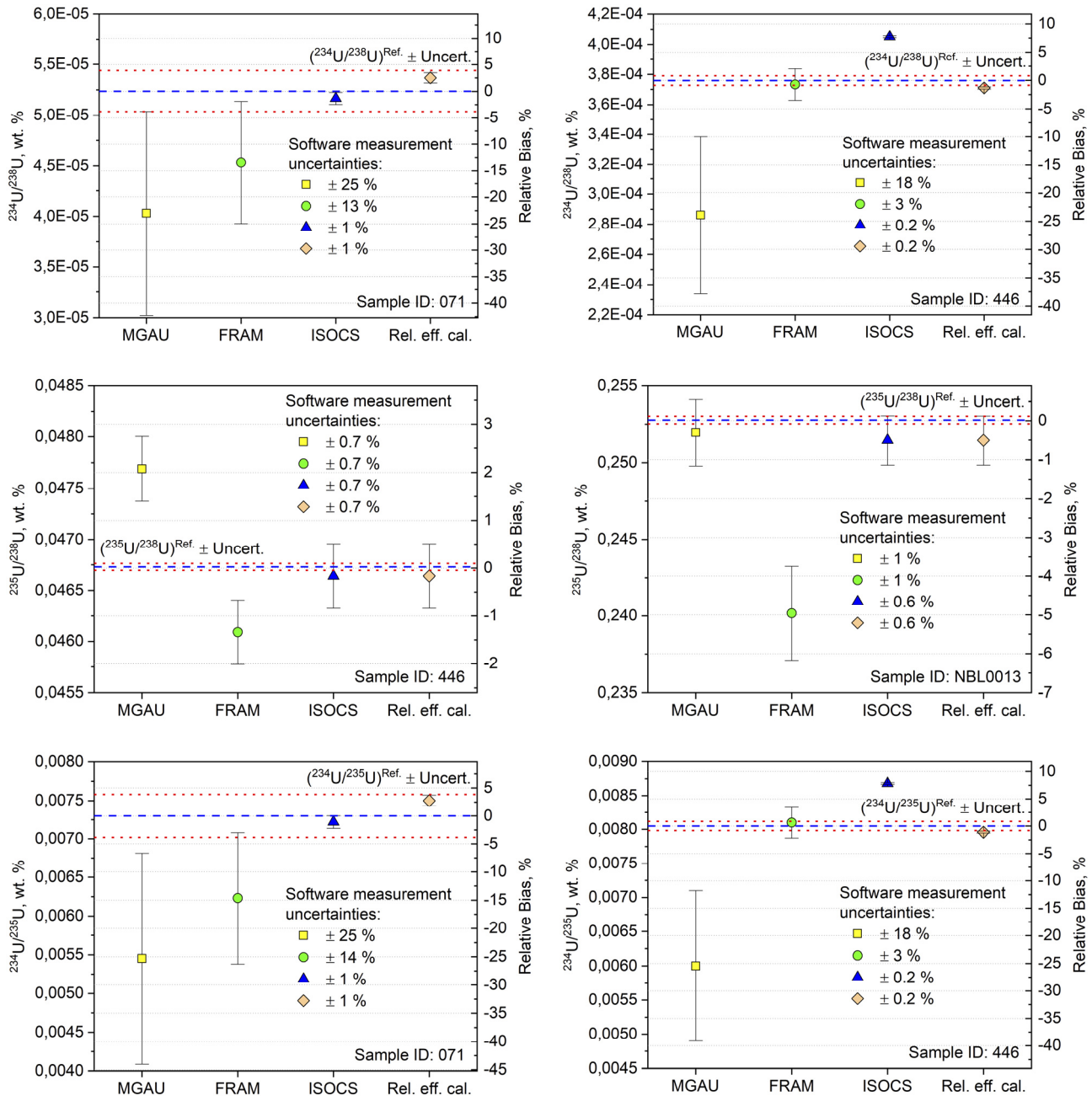


Figure 2. Calculated $^{234}\text{U} / ^{238}\text{U}$ (1st row), $^{235}\text{U} / ^{238}\text{U}$ (2nd row), $^{234}\text{U} / ^{235}\text{U}$ (3rd row) isotope ratios vs reference values, relative biases and measurement uncertainties in the uranium certified reference materials (samples ID: 071, 446 and NBL0013)

The uranium gamma-ray spectrum is essentially divided into two regions below 1 MeV. The low-energy region up to about 200 keV contains major gamma rays from ^{235}U at 143.8, 163.3, 185.7, 202.1, and 205.3 keV. The ^{238}U gamma rays in the high-energy region arise from its ^{234m}Pa daughter with energies of 742.8, 766.4, 786.3, and 1001.3 keV for the most intense lines [24]. This peak plays an important role in the routine intrinsic calibration approach for defining the relative efficiency curve. Data points from ^{235}U usually determines the low-energy portion of the relative efficiency curve. The high-energy portion of the curve is usually determined by a series of gamma rays from ^{234m}Pa with only a single point at 258.3 keV to make the normalization between the high- and low-energy portions of the curve.

We have proposed a combined intrinsic efficiency calibration approach consisting in the following. The $^{235}\text{U} / ^{238}\text{U}$ isotopic ratios can be rather correctly calculated using the MGAU, FRAM or ISOCS codes, then, taking into account the specific isotope activity, the relative efficiency curve can be obtained by fitting the data of a single polynomial functions $f(E)$ in the whole gamma-quantum energy range of ^{235}U and ^{234m}Pa , and thus the $^{234}\text{U} / ^{238}\text{U}$ and $^{234}\text{U} / ^{235}\text{U}$ isotopic ratios can be calculated.

In the present study for the $^{235}\text{U} / ^{238}\text{U}$ ratio estimations we have applied the results obtained with the ISOCS code, i.e. the absolute efficiency calibration approach. For experimental data fitting we have used three polynomial functions: $f_1(E_i) = c_1 \cdot E_i^{c_2} \cdot \exp(c_3 \cdot e^{c_4 \cdot E_i})$; $f_2(E_i) = c_1 + c_2 \cdot \ln(E_i) + c_3 \cdot \ln^2(E_i) + c_4 \cdot \ln^3(E_i) + c_5 \cdot \ln^4(E_i) + c_6 \cdot \ln^5(E_i)$; $f_3(E_i) = c_1 \cdot \ln(E_i) + c_2 \cdot \ln^2(E_i) + c_3 \cdot \ln^3(E_i) - c_4 \cdot E_i^{c_5}$ [25-27]. A gamma-quantum energy range was extended to 2 MeV including additional peaks of ^{234m}Pa : 1193.8, 1510.2, 1737.7 and 1831.3 keV. The extension of energy range and finding in it of an analytical function $\varepsilon_{rel,i}(E_i)$ can be fruitful for a tasks of uranium age-dating by means of a $^{214}\text{Bi} / ^{234}\text{U}$ chronometer in which the high-energy lines of ^{214}Bi : 609.3, 1120.3, 1764.5 keV are used.

Fig. 3 shows the results of fitting the relative efficiency vs. gamma-rays energy of ^{235}U and ^{234m}Pa by the $f_1(E)$, $f_2(E)$, $f_3(E)$ functions and residuals in the whole range of energies and in its low-energy portion. It can be seen that all the three proposed functions fit the experimental data in the range of gamma-ray energies up to 2 MeV with residuals of no more than ± 2 , and in the low-energy portion, no more than ± 1 . For purposes of determining $^{234}\text{U} / ^{238}\text{U}$ and $^{234}\text{U} / ^{235}\text{U}$ ratios, the accuracy of the low-energy fitting is critical, since this is where the relative efficiency for the 120.9 keV of ^{234}U line is calculated.

When the uranium isotope ratios was calculated by applying the combined intrinsic efficiency calibration approach, a minimum relative bias in most cases, has been obtained using a fitting function $f_3(E)$, for which the residuals in the low-energy region were minimum and did not exceed ± 0.5 . In some cases, the most reasonable results for uranium isotope ratios have been obtained using a fitting function $f_1(E)$.

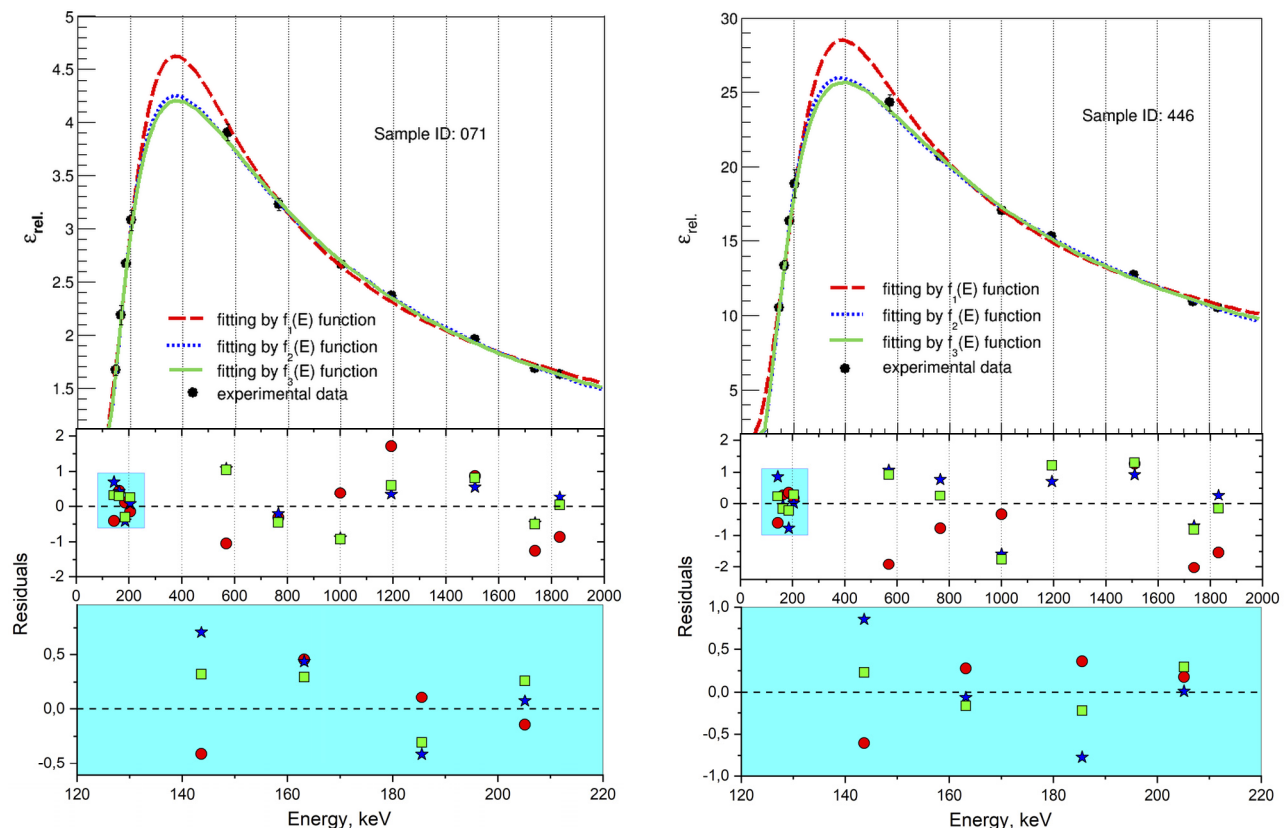


Figure 3. Fitting the relative efficiency vs. gamma-rays energy of ^{235}U and ^{234m}Pa using the $f_1(E)$, $f_2(E)$, $f_3(E)$ functions and residuals (● – residuals of $f_1(E)$ function; ★ – residuals of $f_2(E)$ function; ■ – residuals of $f_3(E)$ function)

A maximum relative bias in the $^{234}\text{U} / ^{238}\text{U}$, $^{235}\text{U} / ^{238}\text{U}$, $^{234}\text{U} / ^{235}\text{U}$ isotopic ratio calculation after the best fit was 2.7 % in the natural uranium (sample ID: 071), in the other samples the relative bias did not exceed 1 % at a random uncertainty of ≤ 1 %.

CONCLUSIONS

The effect of various efficiency calibration approaches on the value and sources of the HRGS measurement uncertainty of $^{234}\text{U}/^{238}\text{U}$, $^{235}\text{U}/^{238}\text{U}$, $^{234}\text{U}/^{235}\text{U}$ isotopic ratios for the purposes of technological control, nuclear forensics, and environmental monitoring was studied.

The calculations of uranium isotopic ratios were performed in the $^{235}\text{U}/\text{U}$ abundance range from 0.7 to 20.0 wt. % using commercial MGAU, FRAM and ISOCS software based on the intrinsic and absolute efficiency calibration approaches. It is shown that the values of maximum relative bias in the $^{234}\text{U}/^{238}\text{U}$ and $^{234}\text{U}/^{235}\text{U}$ ratio estimations using MGAU \ FRAM \ ISOCS software are $\sim 25\%$ \ $\sim 10\%$ \ $\sim 10\%$ and the random uncertainty is varied within the $\pm [18-25\% \ 2-15\% \ \leq 3\%]$, respectively. The estimation of the $^{235}\text{U}/^{238}\text{U}$ isotopic ratios using MGAU \ FRAM \ ISOCS software maximum relative bias are $\sim 3\%$ \ $\sim 4\%$ \ $\sim 1\%$ and the random uncertainty values decrease to $\pm [1\% \ 1\% \ 1\%]$, respectively.

For determining the $^{234}\text{U}/^{238}\text{U}$, $^{235}\text{U}/^{238}\text{U}$, $^{234}\text{U}/^{235}\text{U}$ isotopic ratios a combined intrinsic efficiency calibration approach has been proposed in which the range of measured gamma-quantum energies was extended up to 2 MeV by including the additional peaks of ^{234m}Pa : 1193.8, 1510.2, 1737.7 and 1831.3 keV, and for analytical description of the relation $\varepsilon_{rel,i}(E_i)$ there were used functions:

$$f_1(E_i) = c_1 \cdot E_i^{c_2} \cdot \exp(c_3 \cdot e^{-E_i}); \quad f_2(E_i) = c_1 + c_2 \cdot \ln(E_i) + c_3 \cdot \ln^2(E_i) + c_4 \cdot \ln^3(E_i) + c_5 \cdot \ln^4(E_i) + c_6 \cdot \ln^5(E_i);$$

$f_3(E_i) = c_1 \cdot \ln(E_i) + c_2 \cdot \ln^2(E_i) + c_3 \cdot \ln^3(E_i) - c_4 \cdot E_i^{c_5}$. In the present approach a maximum relative bias in the determination of $^{234}\text{U}/^{238}\text{U}$ and $^{234}\text{U}/^{235}\text{U}$ isotopic ratios is 2.7 % at a random uncertainty of $\leq 1\%$, and in the determination of $^{235}\text{U}/^{238}\text{U}$ ratio a maximum relative deviation is 0.5% at a random uncertainty of $\leq 0.7\%$.

It is clear that in the case of $^{235}\text{U}/^{238}\text{U}$ isotopic ratio measurement, in order to identify its natural variation as well as to control the uranium material fabrication process, the HRGS method cannot compete with a destructive method of mass-spectrometry. Nevertheless, the gamma-spectrometric measurement of ^{235}U isotope is widely applied in the problems of nuclear material safeguards and nuclear forensics for fast in-field categorization of radiological or nuclear material in order to identify the safety risk to first responders and to the public. Application of the absolute efficiency calibration approach makes it possible to decrease the measurement uncertainty to $\sim 1\%$ compared to the international target values of 3.6 % used for measurement uncertainties of NDA methods.

The commercial FRAM and ISOCS software can be used for environmental monitoring to determine the natural variations of the $^{234}\text{U}/^{238}\text{U}$ isotopic ratio in water, soil and sediments, while a proposed combined intrinsic efficiency calibration approach permits to expand the list of investigations with uranium ores for the purpose of determining their geographical origin. A similar situation takes place when determining the $^{234}\text{U}/^{235}\text{U}$ ratio variations in the different uranium deposits, limiting values of which can be $\sim 30\%$. Establishing uranium enrichment process characteristics using $^{234}\text{U}/^{235}\text{U}$ variation is probably not feasible for HRGS.

ORCID IDs

 Dmytro V. Kutnii, <https://orcid.org/0000-0001-9591-4013>;  Dmytro D. Burdeynyi, <https://orcid.org/0000-0003-4431-7264>

REFERENCES

- [1] G. Audi, O. Bersillon, J. Blachot, and A. Wapstra, Nuclear Physics A, **729**, 3 (2003), <https://doi.org/10.1016/j.nuclphysa.2003.11.001>
- [2] L. Meyer, Synopsis of Ph.D. dissertation, University of Cincinnati, 2013.
- [3] D. Reading, Synopsis of Ph.D. dissertation, University of Southampton, 2016.
- [4] R. Steiger, and E. Jaeger, Earth Planet Sci. Lett. **36**, 359 (1977), [https://doi.org/10.1016/0012-821X\(77\)90060-7](https://doi.org/10.1016/0012-821X(77)90060-7)
- [5] F. Gauthier-Lafaye, P. Holliger, and P. Blanc, Geochimica et Cosmochimica Acta. **60**, 4831 (1996), [https://doi.org/10.1016/S0016-7037\(96\)00245-1](https://doi.org/10.1016/S0016-7037(96)00245-1)
- [6] A. Baranova, (2011), <http://conf.nsc.ru/youngconf-2011/ru/reportview/48802>. (in Russian)
- [7] Y. Fujikawa, M. Fukui, M. Sugahara, E. Ikeda, and M. Shimada, in: *10th International Congress of the Radiation Protection Association Proceedings*, (JHPS, Hiroshima, 2000), pp. 1-6.
- [8] E. Yakovlev, G. Kiselev, S. Druzhinin, S. Zykov, Bulletin of the Northern (Arctic) Federal University. **3**, 15 (2016). (in Russian)
- [9] S. Richter, A. Alonso, W. De Bolle, R. Wellum, and P.D.P. Taylor, International Journal of Mass Spectrometry. **193**, 9 (1999), [https://doi.org/10.1016/S1387-3806\(99\)00102-5](https://doi.org/10.1016/S1387-3806(99)00102-5)
- [10] G. Brennecka, Synopsis of Ph.D. dissertation, Arizona State University, 2011.
- [11] Y. Hinrichsen, *Fingerprinting of nuclear material for nuclear forensics*. (Hausarbeit am ZNF, Hamburg, 2011), pp. 9-10.
- [12] H. Wood, A. Glaser, in: *INMM 49th Annual Meeting Proceedings*, (INMM, Nashville, 2008), pp. 921-928.
- [13] K. Zhao, M. Penkin, C. Norman, S. Balsley, K. Mayer, P. Peerani, C. Pietri, S. Tapodi, Y. Tsutaki, M. Boella, G. Renha, E. Kuhn, *International target values 2010 for measurement uncertainties in safeguarding nuclear materials*. (International Atomic Energy Agency, Vienna, 2010), pp. 29-30.
- [14] D. Reilly, N. Ensslin, H. Hastings, S. Kreiner, *Passive Nondestructive Assay of Nuclear Materials*. (LANL, Los Alamos, 1991), pp. 193-213.

- [15] R. Harry, J. Aaldijk, J. Braak, in: *IAEA Symposium on Safeguarding Nuclear Materials Proceedings*, (IAEA, Vienna, 1976), pp. 235.
- [16] T.C. Nguyen, and J. Zsigrai, *Nucl. Instr. and Meth.* **B243**, 187 (2006), <https://doi.org/10.1016/j.nimb.2006.01.011>
- [17] L. Lakosi, J. Zsigrai, T.C. Nguyen, in: *7th Conference on Nuclear and Particle Physics Proceedings*, (ENPA, Sharm El-Sheikh, 2009), pp. 413-424.
- [18] A. Berlizov, V. Tryshyn, *Study of the MGAU Applicability to Accurate Isotopic Characterization of Uranium Samples*. (Report # IAEA-SM-367/14/05/P, IAEA, Vienna, 2001), 13 p.
- [19] D.T. Vo, T.E. Sampson, *Uranium Isotopic Analysis, the FRAM Isotopic Analysis Code*, (Report # LA-13580, LANL, Los Alamos, 1999), 30 p.
- [20] I. Meleshkovskii, N. Pauly, and P. Labeau, *Eur. Phys. J. Plus.* **133**, 554 (2018), <https://doi.org/10.1140/epjp/i2018-12363-8>
- [21] A.V. Bushuev, *Методы измерений ядерных материалов [Methods of nuclear materials measurement]* (Moscow Engineering and Physics Institute, Moscow, Russia, 2007), pp. 65-103. (in Russian).
- [22] M. Thompson, S. Ellison, and R. Wood, *Pure Appl. Chem.* **78**, 145 (2006), <https://doi.org/10.1351/pac200678010145>
- [23] A.A. Solodov, S.E. Smith, J.S. Bogard, *Uranium Isotopic and Quantitative Analysis Using a Mechanically-Cooled HPGe Detector*, (Report # ORNL/TM-2006/150, ORNL, Oak Ridge, 2006), 67 p.
- [24] T.E. Sampson, T.A. Kelley, D.T. Vo, *Application Guide to Gamma-Ray Isotopic Analysis Using the FRAM Software*, (LANL, Los Alamos, 2003), pp. 21-32.
- [25] J. G. Williams, in: *ISR15 – International Symposium on Reactor Dosimetry Proceedings*, (Aix-en-Provence, France, 2015), 07004.
- [26] R.C. McFarland, Reprint of “From the Counting Room”, **2(4)**, 35-40 (1991), http://www.ezag.com/fileadmin/ezag/user-uploads/isotopes/pdf/Behavior_of_Several_Germanium_Detector_Full_Energy_Peak.pdf
- [27] A. Svec, *J. Appl. Radiat. Isot.* **66**, 786 (2008), <https://doi.org/10.1016/j.apradiso.2008.02.070>

ГАММА-СПЕКТРОМЕТРИЧНЕ (HRGS) ВИЗНАЧЕННЯ ІЗОТОПНИХ СПІВВІДНОШЕНЬ УРАНУ З ВИКОРИСТАННЯМ РІЗНИХ ПІДХОДІВ КАЛІБРУВАННЯ ПО ЕФЕКТИВНОСТІ

Д.В. Кутній, Д.Д. Бурдейний

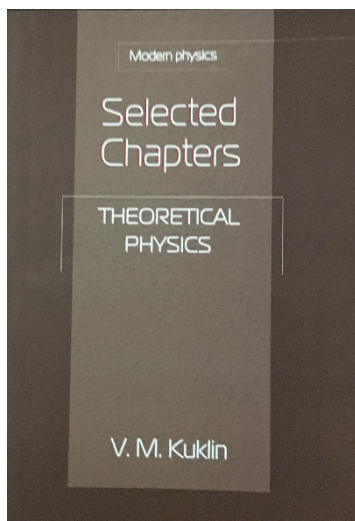
Національний науковий центр «Харківський фізико-технічний інститут» НАН України

Досліджувався вплив різних підходів калібрування по ефективності на величину і джерела невизначеності гамма-спектрометричних вимірювань ізотопних співвідношень урану $^{234}\text{U} / ^{238}\text{U}$, $^{235}\text{U} / ^{238}\text{U}$, $^{234}\text{U} / ^{235}\text{U}$ для цілей технологічного контролю, ядерної криміналістики і екологічного моніторингу. Напівпровідниковий детектор на основі HPGe (Canberra Broad Energy Germanium detector BEGe3830) і п'ять еталонних сертифікованих уранових зразків CRM 969 і CRM 146 із вмістом $^{235}\text{U} / \text{U}$ від 0.7 до 20.0 мас. % використовувалися при проведенні досліджень. Розрахунок ізотопних співвідношень урану виконували шляхом обробки експериментальних гамма-спектрів комерційними програмними продуктами: MGAU (LLNL), FRAM (LANL), ISOCS (Canberra/Mirion Technologies), які основані на підходах калібрування за абсолютною і відносною ефективністю. Показано, що величини максимальних відносних відхилень результатів при визначенні ізотопних співвідношень $^{234}\text{U} / ^{238}\text{U}$ і $^{234}\text{U} / ^{235}\text{U}$ програмним забезпеченням MGAU \ FRAM \ ISOCS складають $\sim 25\% \sim 10\% \sim 10\%$ при цьому випадкові невизначеності варіюються в інтервалі $\pm [18-25\% \sim 2-15\% \sim \leq 3\%]$, відповідно. При визначенні ізотопних співвідношень $^{235}\text{U} / ^{238}\text{U}$ програмним забезпеченням MGAU \ FRAM \ ISOCS, максимальні відносні відхилення складають $\sim 3\% \sim 4\% \sim 1\%$ при цьому випадкові невизначеності знижуються до $\pm [1\% \sim 1\% \sim 1\%]$, відповідно. Запропоновано комбінований підхід калібрування по відносній ефективності, в якому для аналітичного опису залежності $\varepsilon_{rel,i}(E_i)$ використані поліноміальні функції. В даному підході максимальне відносне відхилення при визначенні ізотопних співвідношень $^{234}\text{U} / ^{238}\text{U}$ і $^{234}\text{U} / ^{235}\text{U}$ складає 2.7 % при випадковій невизначеності $\leq 1\%$, а в разі визначення співвідношення $^{235}\text{U} / ^{238}\text{U}$ максимальне відносне відхилення дорівнює 0.5 % при випадковій невизначеності $\leq 0.7\%$.

Ключові слова: гамма-спектрометрія високої роздільної здатності, ізотопні співвідношення урану, калібрування по ефективності, невизначеність вимірювань, уранова руда, MGAU, FRAM, ISOCS

ANNOUNCEMENT

V.M. Kuklin, *Selected chapters (theoretical physics)*, (V.N. Karazin KhNU, Kharkiv, 2021), pp. 244.



The book considers spontaneous and induced emission of particles and waves. The formation of coherent pulses near a detected new threshold of induced radiation is discussed. It is shown how modulation instabilities generate self-similar structures and anomalous waves. A comparison is made of the dynamics of instability of Langmuir oscillations in plasma and heating of ions in Silin and Zakharov models. Turbulent-wave instability is discussed and a new approach to the description of the Mössbauer effect is presented. The similarity of processes of superradiation and dissipative instability is noted. Structural transitions in the convective layer and the appearance of large-scale vortices during modulation instability of developed convection and other relevant problems are discussed. It is of interest to specialists, graduate students and students of physics departments.

PACS: 52.35 Mw;41.60.-m; 05.45 Xt;03.65 Sq;47.55 pb.

In the monograph, the author presented the completed theories and developments, completed over four decades, together with colleagues and students. Simple relations are proposed that allow, knowing the contribution of the spontaneous emission of sources - particles and currents, to correctly determine the levels of their induced emission. On the basis of the new threshold of stimulated emission discovered by A.G. Zagorodny and the author, the conditions for the generation of sawtooth pulses, in particular those observed in space, were studied and a possible mechanism of periodic changes in the luminosity of stars – Cepheids – was considered. The mechanism of turbulence growth initiated by an external wave has been studied.

It is shown that at the same level of energy extraction from the system of moving radiators and resting oscillators, the processes of dissipative instability and superradiance regimes in the classical and quantum cases have comparable development times and values of the attainable amplitude, as well as a similar degree of radiation coherence.

The mechanism of formation of self-similar periodic structures near the threshold of modulation instability of a wave of finite amplitude is presented. A theory is presented of the formation of disturbances and waves of anomalous amplitude, in particular, on the ocean surface, due to the development of modulation instability of undamped waves. The mechanism of the formation of anomalous amplitude envelopes due to the disturbance-induced interference of developing disturbances is explained.

A completed one-dimensional theory of parametric instability of a Langmuir wave in a cold plasma (generalized model of V.P. Silin) is presented. It is compared with the V.E. Zakharov model of instability of such a wave for a non-isothermal plasma. The mechanism of thermalization of plasma ions is presented.

The process of a second-order phase transition in convective instability of a thin layer of liquid or gas is considered in detail. It is shown that the developing modulation instability of the field of convective cells is capable of generating large-scale vortices (the effect of a hydrodynamic dynamo).

The book contains almost three dozen appendices, which set forth, in particular, a new interpretation of the Mössbauer effect; the formation of self-similar structures in a solid; the nature of intense fluctuations in the reflection coefficient of an electromagnetic wave from the plasma surface; comparison of the spectral and visual characteristics of the defectiveness of structures, taking into account the effect of plasma on the operating mode of the gyrotron, attenuation of wave packets in plasma and in the active medium, lifetimes of waves of anomalous amplitude in the ocean, and a number of others.

У монографії автор представив виконані за чотири десятиліття разом з колегами і учнями завершені теорії і розробки. Запропоновано прості співвідношення, які дозволяють, знаючи внесок спонтанного випромінювання джерел - частинок і струмів, коректним чином визначити рівні їх індукованого випромінювання. На основі виявленого А. Г. Загороднім і автором книги, нового порога вимушеного випромінювання, вивчені умови генерації пілкоподібних імпульсів, зокрема спостережуваних в космосі і розглянуто можливий механізм періодичної зміни світності зірок-цефеїд. Вивчено механізм зростання турбулентності, ініційований зовнішньої хвилею.

Показано, що при одному рівні виведення енергії з системи рухомих випромінювачів і нерухомих осциляторів процеси дисипативної нестійкості і режими зверхвипромінювання (суперлюмінесценції) в класичному і квантовому випадках мають порівнянні часи розвитку і значення досяжної амплітуди, як, втім, і подібну ступінь когерентності випромінювання.

Представлений механізм формування самоподібних періодичних структур поблизу порога модуляційної нестійкості хвилі кінцевої амплітуди. Представлена теорія формування збурень і хвиль аномальної амплітуди, зокрема на поверхні океану, за рахунок розвитку модуляційної нестійкості невщухаючого хвилювання. Пояснений механізм формування огинаючої аномальної амплітуди за рахунок змущеної хвилюванням інтерференції збурень що розвиваються.

Представлена завершена одномірна теорія параметричної нестійкості ленгмюрівської хвилі в холодній плазмі (узагальнена модель В. П. Силіна). Проведено її порівняння з моделлю В. С. Захарова нестійкості подібної хвилі для неізотермічної плазми. Представлений механізм термалізації іонів плазми.

Детально розглянуто процес фазового переходу другого роду при конвективній нестійкості тонкого шару рідини або газу. Показано, модуляційна нестійкість поля конвективних осередків, що розвивається, здатна генерувати великомасштабні вихори (ефект гідродинамічного динамо). У книзі представлено майже три десятка додатків, де викладено зокрема нове трактування ефекту Месбауера; виникнення самоподібних структур в твердому тілі; природа інтенсивних коливань коефіцієнта відбиття електромагнітної хвилі від поверхні плазми; порівняння спектральних і візуальних характеристик дефектності структур, облік впливу плазми на режим роботи гіротрону, загасання хвильових пакетів в плазмі і в активному середовищі, час життя хвиль аномальної амплітуди в океані і ряд ін.

INSTRUCTIONS FOR PREPARING MANUSCRIPT IN THE EAST EUROPEAN JOURNAL OF PHYSICS

Nikita F. Author^{a,*}, Peter V. Co-Author(s)^{b,†}

^aAffiliation of first author

^bAffiliation of second author (if different from the first Author)

*Corresponding Author: corresponding_authors@mail.com, ^aORCID ID

[†]E-mail: co_authors@mail.com, ^bORCID ID

Received May 25, 2021; revised June 25, 2021 accepted July 5, 2021

Each paper must begin with an abstract. The abstract should be typed in the same manner as the body text (see below). Please note that these Instructions are typed just like the manuscripts should be. The abstract must have at least **1800 phonetic symbols**, supplying general information about the achievements, and objectives of the paper, experimental technique, methods applied, significant results and conclusions. Page layout: the text should be printed on the paper **A4** format, at least **5 pages**, with margins of: **Top - 3, Bottom, Left and Right - 2 cm**. The abstract, keywords should be presented in **English** (only for foreign authors), and **Ukrainian**.

Keywords: there, must, be, 5-10 keywords

PACS: specify PACS code(s) here

This is **Introduction** section. This paper contains instructions for preparing the manuscripts. The text should be prepared in “**doc**” or “**docx**” format.

INSTRUCTIONS

The text should be typed as follows:

- **title:** Times New Roman, 12 pt, ALL CAPS, bold, 1 spacing, centred;
- **authors:** name, initials and family names; Times New Roman, 12 pt, bold, 1 spacing, centred;
- **affiliation(s):** Times New Roman, 9 pt, italic, 1 spacing, centred;
- **abstract:** Times New Roman, 9 pt, 1 spacing, justified;
- **body text:** Times New Roman, 10 pt, 1 spacing, justified; paragraphs in sections should be indented right (tabulated) for 0.75 cm;
- **section titles:** Times New Roman, 10 pt, bold, 1 spacing, centred, without numbering, one line should be left, blank above section title;
- **subsection titles:** Times New Roman, 10 pt, bold, 1 spacing, centred, without numbering in accordance to the section (see below), one line should be left blank above subsection title;
- **figure captions:** width of the figure should be 85 or 170 mm, Figures should be numbered (**Figure 1.**) and titled below Figures using sentence format, Times New Roman, 9 pt, 1 spacing, centred (if one line) or justified (if more than one line); one line should be left blank below figure captions;
- **table captions:** width of the table should be 85 or 170 mm, tables should be numbered (**Table 1.**) and titled above tables using sentence format, Times New Roman, 10 pt, 1 spacing, justified, Tables should be formatted with a single-line box around the outside border and single ruling lines between rows and columns; one line should be left blank below tables;
- **equations:** place equations centred, numbered in Arabic: (1), flush right, equations should be specially prepared in **MathType** or “**Microsoft Equation**”, Times New Roman, 10 pt, one line should be left blank below and above equation.

Additional instructions

Numerated figures and tables should be embedded in your text and placed after they are cited. Only sharp photographs and drawings are acceptable. Letters in the figures should be 3 mm high. The figures should be presented in one of the following graphic formats: jpg, gif, pcx, bmp, tif.

REFERENCES

List of References must contain **at least 50% of articles published over the past 5 years and no more than 20% of links to their own work**. Cite References by number in AIP style (<https://aip.scitation.org/php/authors/manuscript>). Numbering in the order of referring in the text, e.g. [1], [2-5], etc. References should be listed in numerical order of citation in the text at the end of the paper (justified), Times New Roman, 9 pt, 1 spacing:

Journal Articles

- [1] T. Mikolajick, C. Dehm, W. Hartner, I. Kasko, M.J. Kastner, N. Nagel, M. Moert, and C. Mazure, *Microelectron. Reliab.* **41**, 947 (2001), [https://doi.org/10.1016/S0026-2714\(01\)00049-X](https://doi.org/10.1016/S0026-2714(01)00049-X).
- [2] S. Bushkova, B.K. Ostafyichuk, and O.V. Copenaiev, *Physics and Chemistry of Solid State.* **15**(1), 182 (2014), <http://page.if.ua/uploads/pcss/vol15/1501-27.pdf>. (in Ukrainian)
- [3] M. Yoshimura, E. Nakai, K. Tomioka, and T. Fukui, *Appl. Phys. Lett.* **103**, 243111 (2013), <http://dx.doi.org/10.7567/APEX.6.052301>.

E-print Resources with Collaboration Research or Preprint

- [4] M. Aaboud et al. (ATLAS Collaboration), *Eur. Phys. J. C*, **77**, 531 (2017), <http://dx.doi.org/10.1140/epjc/s10052-017-5061-9>
- [5] Sjöstrand et al., *Comput. Phys. Commun.* **191**, 159 (2015), <https://doi.org/10.1016/j.cpc.2015.01.024>.
- [6] Boudreau, C. Escobar, J. Mueller, K. Sapp, and J. Su, (2013), <http://arxiv.org/abs/1304.5639>.

Books

- [7] S. Inoue, and K.R. Spring, *Video Microscopy: The fundamentals*, 2nd ed. (Plenum, New York, 1997), pp. 19-24.
- [8] I. Gonsky, T.P. Maksymchuk, and M.I. Kalinsky, *Біохімія Людини [Biochemistry of Man]*, (Ukrmedknyga, Ternopil, 2002), pp. 16. (in Ukrainian)

Edited Books

- [9] Z.C. Feng, editor, *Handbook of Zinc Oxide and Related Materials: Devices and Nano Engineering, vol. 2*, (CRC Press/Taylor & Francis, Boca Raton, FL, 2012)

Book Chapters

- [10] P. Blaha, K. Schwarz, G.K.H. Madsen, D. Kvasnicka, and J. Luitz, in: *WIEN2K, An Augmented Plane Wave Plus Local Orbitals Program for Calculating Crystal Properties*, edited by K. Schwarz (Techn. Universität Wien, Austria, 2001).
- [11] M. Gonzalez-Leal, P. Krecmer, J. Prokop, and S.R. Elliot, in: *Photo-Induced Metastability in Amorphous Semiconductors*, edited by A.V. Kolobov (Wiley-VCH, Weinheim, 2003), pp. 338-340.
- [12] A. Kochelap, and S.I. Pekar, in: *Теорія Спонтанної і Стимульованої Хемілюмінесценції Газів [Theory of Spontaneous and Stimulated Gas Chemiluminescence]* (Naukova dumka, Kyiv, 1986), pp. 16-29. (in Russian)

Conference or Symposium Proceedings

- [13] C. Yaakov, and R. Huque, in: *Second International Telecommunications Energy Symposium Proceedings*, edited by E. Yow (IEEE, New York, 1996), pp. 17-27.
- [14] V. Nikolsky, A.K. Sandler, and M.S. Stetsenko, in: *Автоматика-2004: Матеріали 11 Міжнародної Конференції по Автоматичному Управлінню [Automation-2004: Materials of the 11th International Conference on Automated Management]* (NUHT, Kyiv, 2004), pp. 46-48. (in Ukrainian)

Patent

- [15] I.M. Vikulin, V.I. Irha, and M.I. Panfilov, Patent Ukraine No. 26020 (27 August 2007). (in Ukrainian)

Thesis / Dissertation

- [16] R.E. Teodorescu, Ph.D. dissertation, The George Washington University, 2009.

Special Notes

1. Use International System of Units (SI system). 2. It is undesirable to use acronyms in the titles. Please define the acronym on its first use in the paper. 3. Refer to isotopes as ¹⁴C, ³H, ⁶⁰Co, etc.

Наукове видання

СХІДНО-ЄВРОПЕЙСЬКИЙ ФІЗИЧНИЙ ЖУРНАЛ

Номер 3, 2021

EAST EUROPEAN JOURNAL OF PHYSICS

No 3, 2021

Збірник наукових праць
англійською та українською мовами

Коректор – Коваленко Т.О.
Технічний редактор – Гірник С.А.
Комп'ютерне верстання – Гірник С.А.

Підписано до друку 27.09.2021. Формат 60×84/8. Папір офсетний.

Друк цифровий.

Ум. друк. арк. 11,7. Обл.-вид. арк. 11,9
Тираж 50 пр. Зам. № . Ціна договірна

Видавець і виготовлювач
Харківський національний університет імені В.Н. Каразіна
61022, Харків, майдан Свободи, 4
Свідоцтво суб'єкта видавничої справи ДК № 3367 від 13.01.09

Видавництво Харківський національний університет імені В.Н. Каразіна
тел. +380-057-705-24-32